Fusheng Li
Yoshio Awaya
Koji Kageyama
Yongfen Wei *Editors*

River Basin Environment: Evaluation, Management and Conservation

Springer

River Basin Environment: Evaluation, Management and Conservation

Fusheng Li • Yoshio Awaya • Koji Kageyama • Yongfen Wei
Editors

River Basin Environment: Evaluation, Management and Conservation

Springer

Editors
Fusheng Li
River Basin Research Center
Gifu University
Gifu, Gifu, Japan

Yoshio Awaya
River Basin Research Center
Gifu University
Gifu, Gifu, Japan

Koji Kageyama
River Basin Research Center
Gifu University
Gifu, Gifu, Japan

Yongfen Wei
River Basin Research Center
Gifu University
Gifu, Gifu, Japan

ISBN 978-981-19-4069-9 ISBN 978-981-19-4070-5 (eBook)
https://doi.org/10.1007/978-981-19-4070-5

This Springer imprint is published by the registered company Springer Nature Singapore Pte Ltd.
The registered company address is: 152 Beach Road, #21-01/04 Gateway East, Singapore 189721, Singapore

Preface

River basin refers to a region drained by a main river and all its tributaries. It is shaped by terrain, ground, and rivers; and extends from mountains in upstream through middle plains to the downstream. As a social-ecological system, river basin provides crucial ecosystem functions and services that support plants and animals (including humans). River basin is also the basic hydrological unit for a country to plan and develop its resources for water, soil, and vegetation.

Long- and short-term environmental changes reflected and, in most cases, induced by global warming, urbanization, radioactive waste, heavy rain storms, earthquake, and intensifying human activities (including deforestation, resource excavation and utilization, and social, industrial, and agricultural development) have brought various changes to the river basin environment; and pollution, flood, biodiversity loss, ecosystem deterioration, and agricultural land degradation occurring in different basin scales are consistently and increasingly turning into issues of great concern. Moreover, many new challenges related, for example, to antibiotic-resistant genes, pathogenic microorganisms, and low carbon/decarbonization are emerging and require careful and urgent handling. To respond to the changes and needs, sustainable use and management of all resources in the river basin is necessary. Meanwhile, systematic evaluations of basin environment are also desired, along with studies that contribute to better understanding and sustainable utilization of the functions that each constituting ecosystem in the river basin may play.

This book provides updated and comprehensive information on evaluation, management, and conservation of river basin environment from the important aspects of vegetation, water, soil, hydrometeorological dynamics, and disaster mitigation. It is an entire work of the River Basin Research Center of Gifu University, based mainly on the recent research achievements of all its faculty members that link directly with the safety, security, and sustainability of river basin environment, the foundation for achieving the United Nations' Sustainable Development Goals (SDGs), particularly the goals for No Poverty (1), Zero Hunger (2), and Clean Water and Sanitation (6), as well as Affordable and Clean Energy (7), Sustainable Cities

and Communities (11), Climate Action (13), Life below Water (14), and Life on Land (15).

We hope this book will benefit the research community and environmental education and have reference value for students, water and forest resource managers, hydrologists, and all those who are engaging or interested in any aspect of evaluation, management, and conservation of river basin environment, contributing to sustainable development solutions through better management of water, soil, and vegetation resources.

We thank all referees who have generously contributed their time and talent to ensure the quality of this book. We also thank Springer Nature and its staff for their invaluable support and cooperation that helped in publishing this book.

Gifu, Japan

Fusheng Li
Yoshio Awaya
Koji Kageyama
Yongfen Wei

Contents

About the Editors

Fusheng Li is a professor at the River Basin Research Center, Gifu University, Japan. His teaching and research activities are in the fields from water quality to water and wastewater treatment, and recently also to resource and energy recovery from organic waste. The ongoing research projects in his lab include activated carbon adsorption, membrane filtration, biological water and wastewater treatment, vermicomposting treatment of vegetable waste and activated sludge, and physico-chemical and biological water quality evaluation. Dr. Li completed his PhD in March 1998 from Gifu University and has been a full professor at the research center since May 2008. He is also serving as the director of the research center now.

Yoshio Awaya has been a Professor at the River Basin Research Center, Gifu University, Japan, since 2009. His research interests are remote sensing of the land ecosystem, especially forest and forestry. His research covers leaf to global scale of changes in ecosystem structure or biomass using field data, airborne and satellite optical sensors, and airborne laser scanners. He received his PhD from Niigata University in 1995. He worked as a research scientist at the Forestry and Forest Products Research Institute of Forestry Agency of Japan from 1980 until 2009, prior to joining the River Basin Research Center, Gifu University. He was appointed as the president of the Remote Sensing Society of Japan between 2016 and 2018.

Koji Kageyama has been an Emeritus Professor at River Basin Research Center, Gifu University, Japan, since 2021. His research interests include plant pathology, mycology, and molecular ecology of soil fungi. He received his PhD from Hokkaido University in 1983. He worked as a researcher in Aichi Prefectural Agricultural Experiment Station, as an assistant and associate professor in the Department of Agriculture, Gifu University, and as a professor in the River Basin Research Center, Gifu University, until 2021.

Yongfen Wei is an associate professor at the River Basin Research Center, Gifu University, Japan. She is also a principal supervisor for master's course education in the Graduate School of Natural Science and Technology, and doctoral course education in the United Graduate School of Agricultural Science of this Japanese national university. She received her BS degree in environmental engineering from Lanzhou Jiaotong University of China in 1986, MS degree from Kitami Institute of Technology of Japan in 1995, and PhD degree from Gifu University in 2002. Her main research focus is environmental monitory and assessment, ranging from remote sensing application to mass dynamics analysis, and recently has also been working on topics relating to soil remediation. As a key member of the Gifu University Rearing Program for Basin Water Environmental Leaders (BWEL), she has been actively involving in all program teaching and managing activities with other faculty members together, leading to the achievement with 230 master's and doctoral graduates who learned under the program.

Part I
Vegetation Ecology and Functions

Chapter 1
Phenology of Photosynthesis in a Deciduous Broadleaf Forest: Implications for the Carbon Cycle in a Changing Environment

Hiroyuki Muraoka

Abstract Photosynthetic carbon assimilation in plant leaves supports biomass accumulation and developmental growth and contributes to the regulation of atmospheric CO_2 concentration via the carbon cycle. Photosynthesis and its environmental responses have been the central theme of plant physiological ecology and ecosystem ecology, as photosynthesis is involved in a broad range of natural systems from cells to the biosphere. In particular, the environmental responses of tree leaves and forest ecosystems and their seasonal and interannual changes under ongoing climate change are central research interests in ecology and Earth system science. This chapter reviews the studies of leaf and canopy photosynthesis conducted in a cool-temperate deciduous broadleaf forest site in Japan. Long-term observations and open-field warming experiments were conducted to assess leaf phenology in canopy trees, leaf photosynthesis, and the light environment of understory shrubs, and the application of optical remote sensing on forest canopy photosynthetic productivity helped to clarify single-leaf level ecophysiology and forest ecosystem function. The advancement of integrated ecosystem science coupled with climate monitoring should help us to respond to the urgent need for key data regarding biodiversity and ecosystem conservation and management across landscapes from local to regional scales.

Keywords Climate change · Deciduous broadleaf trees · Ecosystem master site · Phenology · Photosynthesis

H. Muraoka (✉)
River Basin Research Center, Gifu University, Gifu, Japan

Division of Biodiversity, National Institute for Environmental Studies, Tsukuba, Japan
e-mail: muraoka@green.gifu-u.ac.jp

F. Li et al. (eds.), *River Basin Environment: Evaluation, Management and Conservation*, https://doi.org/10.1007/978-981-19-4070-5_1

1.1 Introduction

The photosynthetic carbon assimilation that occurs in leaves supports plant developmental growth and biomass accumulation as well as the regulation of CO_2 concentration in the atmosphere via the carbon cycle (Chapin et al. 2012). Because photosynthesis affects natural systems from cells to the biosphere, photosynthesis and its environmental responses have been the central theme of plant physiological ecology and ecosystem ecology (Evans et al. 1988; Hikosaka et al. 2016). Photosynthesis is largely influenced by abiotic environmental conditions such as solar radiation, temperature, air humidity, soil water availability, and atmospheric CO_2 concentration, all of which vary spatially and temporally. In temperate regions where there are marked seasonal changes in meteorological conditions, the seasonal change of biological behavior in the natural environment, so-called phenology, has been studied with regard to leaf demography, photosynthesis, and shoot growth for various plants in grasslands (Monsi and Saeki 2005; Oikawa et al. 2006) and forests (Augspurger and Bartlett 2003; Kikuzawa and Lechowicz 2011; Wilson et al. 2000).

Recently, the phenology of vegetation has become a focus of Earth system science because its sensitivity to short- to long-term climate change in many organisms and its involvement in ecosystem functions through diverse biological and biogeochemical interactions have feedback effects on the climatic system (Piao et al. 2019; Richardson et al. 2013). Figure 1.1 illustrates the scheme of CO_2 exchange between the atmosphere and a forest ecosystem and the carbon cycle within an ecosystem. The CO_2 exchange can be roughly determined as the balance of photosynthetic absorption (gross primary production, GPP) and respiratory release of CO_2 by the ecosystem (ecosystem respiration, R_e). GPP is the total amount of carbon assimilated in single leaves across the entire forest canopy, and R_e is total amount of CO_2 respired from leaves, stem, root, and soil microorganisms. These CO_2 flux components change throughout the seasons in deciduous forests (e.g., Baldocchi et al. 2005; Richardson et al. 2007; Saigusa et al. 2005). Although numerous studies have investigated CO_2 exchange in response to environmental change across seasons and years, there are still knowledge gaps regarding the mechanistic and quantitative connections between single-leaf level ecophysiology, phenology, and the CO_2 flux of entire ecosystems in a changing environment across seasons and years (e.g., Piao et al. 2019; Rogers et al. 2017).

Long-term field studies have been conducted at various research sites around the world (cf. Mirtl et al. 2018). Such long-term research is needed to capture temporal changes and extreme events, thus improving our knowledge of ecosystem responses to environmental changes at decadal scales as well as the underlying mechanisms. These data also have been used to develop simulation models (e.g., Ichii et al. 2010; Ito et al. 2007) and to validate satellite remote sensing data (e.g., Turner et al. 2006; Xiao 2004), which allows findings to be scaled temporally from the past to the future and over spatially from local landscapes to regional to global for the evaluation of ecosystem function under climate change.

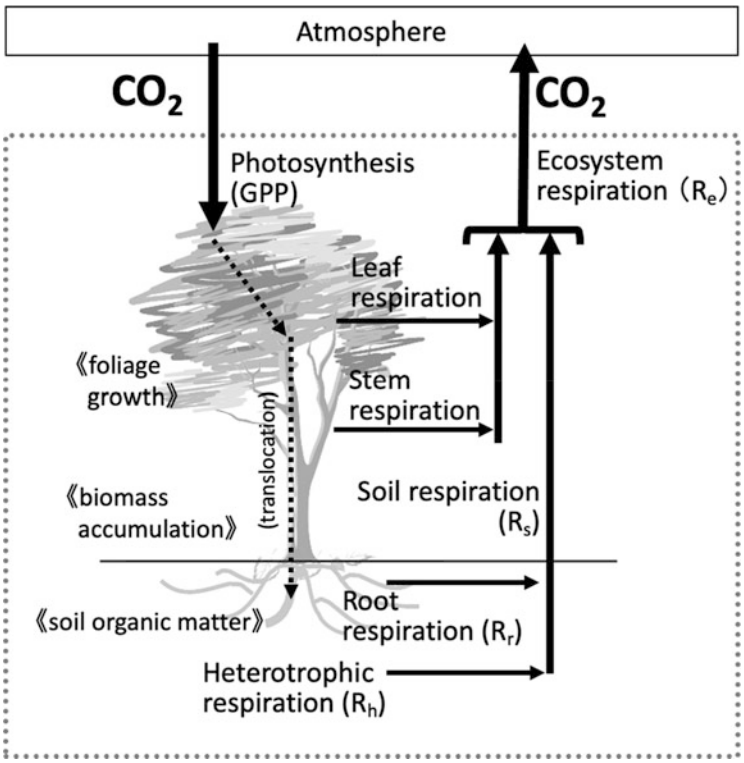

Fig. 1.1 Scheme of the carbon cycle in a forest ecosystem. CO_2 exchange between the atmosphere and the ecosystem is determined by photosynthesis (GPP) and respiration (R_e). The carbon fixed by photosynthesis is allocated for plant respiration (in leaves, stems, and roots) and growth, such as foliage growth and biomass accumulation. Plant litter (dead leaves, stems, and roots) is input to soil and consumed by heterotrophic organisms that release CO_2 by respiration (R_h)

A series of long-term studies on carbon dynamics was initiated in 1993 at a cool-temperate deciduous broadleaf forest in a mountainous region of central Japan by combining atmospheric science, ecology, soil biogeochemistry, simulation modeling, and remote sensing (Muraoka et al. 2015; Yamamoto and Koizumi 2005). The research site, called "Takayama site", has been a platform of these long-term ecosystem research and atmospheric observation contributing to ecosystem and Earth system sciences. In this chapter, I review the studies focused on the phenology of photosynthesis at the Takayama site and discuss the critical role of long-term and multidisciplinary studies conducted at an intensive research station, namely 'master site', for understanding and evaluating forest ecosystem function under climate change. Our research group initiated collaborative observation of phenology of the forest canopy in 2003 for a deeper understanding of the ecophysiological mechanisms of seasonal dynamics of CO_2 flux and short- to long-term changes in spectral signals obtained by satellite remote sensing (Fig. 1.2).

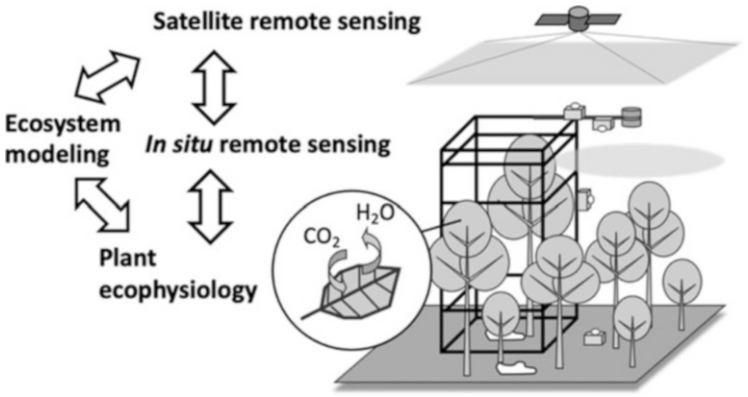

Fig. 1.2 Illustration of a long-term and multidisciplinary observation system for a forest ecosystem. Plant ecophysiological studies and in situ observations of tree and forest canopy enable a mechanistic understanding of the ecosystem function and scaling via model simulation. In addition, in situ optical remote sensing improves satellite remote sensing of ecosystem structure and function

1.2 Study Site and Plant Species

The Takayama site is located in a cool-temperate deciduous broadleaf forest (about 1420 m a.s.l.) at the Takayama Field Station (36°08.549′N, 137°25.340′E, 1342 m a.s.l.), River Basin Research Center, Gifu University, on complex terrain in a mountainous landscape in central Japan. Mean annual temperature and mean annual precipitation from 1996 to 2017 at the field station office (about 500 m south of the studied forest) was 7.2 °C and 2176.5 mm, respectively. The forest understory is covered with snow from December to April, and the maximum snow depth in the middle of winter reaches 1.5–1.8 m. The forest canopy of the study site has a height of approximately 18–20 m and is dominated by *Quercus crispula* Blume, *Betula ermanii* Cham., and *Betula platyphylla* Sukatchev var. *japonica* Hara. The subcanopy layer is represented by *Acer rufinerve* Sieb. et Zucc. and *Acer distylum* Sieb. et Zucc. and the understory layer by *Hydrangea paniculata* Sieb. and *Viburnum furcatum* Blume ex Maxim. The understory is dominated by the evergreen bamboo grass *Sasa senanensis* (Fr. et Sav.) Rehder and saplings of tree species.

At the Takayama site, the CO_2 flux between the atmosphere and forest ecosystem has been continuously observed since 1993 (Murayama et al. 2010; Saigusa et al. 2005; Yamamoto et al. 1999). Tree biomass and net primary production (Ohtsuka et al. 2009), soil respiration (R_s) and its components (root respiration, R_r; heterotrophic respiration, R_h; Mo et al. 2005), and leaf and canopy phenology (Muraoka and Koizumi 2005; Nasahara and Nagai 2015; Noda et al. 2015) have been measured, and in situ and satellite remote sensing (Muraoka et al. 2013; Nakashima et al. 2021; Noda et al. 2021; Shin et al. 2021) and modeling of the ecosystem carbon budget (e.g., Ito et al. 2007; Kuribayashi et al. 2017; Muraoka et al. 2010) have been intensively conducted. In addition, an open-field warming experiment on soil carbon

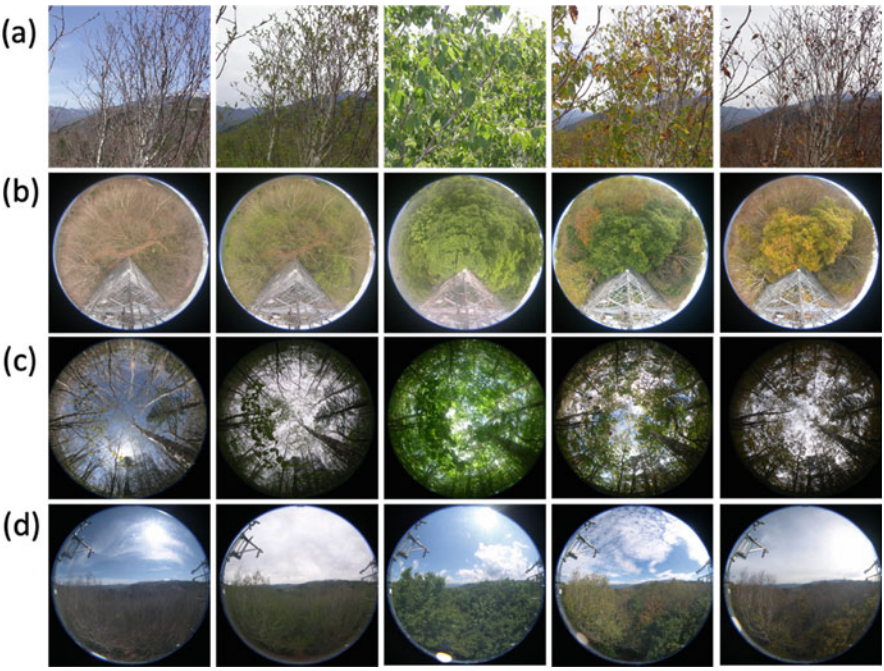

Fig. 1.3 Leaf phenology of (**a**) a branch of *Betula ermanii*, (**b**) forest canopy (view from above the forest), (**c**) forest canopy (view from understory), and (**d**) landscape, taken in 2021 on day of year 130, 140, 200, 289 and 300 (from left to right) at the Takayama site

dynamics was conducted (Chung et al. 2013; Noh et al. 2016, 2017). These long-term observations reveal remarkable seasonal changes in carbon flux and ecological processes at the site. These long-term and multidisciplinary studies in this research site are contributing to AsiaFlux (http://www.asiaflux.net/), Japan Long-Term Ecological Research Network (JaLTER, http://www.jalter.org/), International LTER Network (ILTER, https://www.ilter.network/), and Asia-Pacific Biodiversity Observation Network (APBON; Takeuchi et al. 2021, http://www.esabii.biodic.go.jp/apbon/index.html); for overviews of the multiple studies at this research site, see Muraoka (2015) and Muraoka et al. (2015).

In 2003, an automated system consisting of digital cameras and spectroradiometers was installed to observe individual tree branches and the forest canopy (Nasahara and Nagai 2015). Images from the digital cameras, taken hourly, provide visible and optical information about the forest canopy and tree crowns of respective species (Nagai et al. 2011). The spectroradiometers provide hyperspectral information of the incoming solar radiation and reflected radiation from the foliage, which can be used to calculate spectral vegetation indices (Motohka et al. 2010; Muraoka et al. 2013). These in situ remote sensing observations are conducted at several research sites in Japan and AsiaFlux sites, which together comprise the Phenological Eyes Network (PEN) (Nasahara and Nagai 2015). Figure 1.3 shows

representative images taken by the automated digital camera system installed at the Takayama site. The collection of visible images of tree foliage (branch), the canopy, and the landscape will help to improve the interpretation of satellite remote sensing signals at broad spatial scales from a local forest ecosystem to a mountainous landscape. By using the data collected in the deciduous broadleaf forest, for example, Inoue et al. (2014) clarified that the timing of leaf expansion is rather similar among the tree species and dependent on air temperature, whereas that of leaf fall is variable. The combined observations of tree foliage photographs and leaf traits will allow us to identify the relationships between color (i.e., spectral) information and the leaf ecophysiological characteristics (pigments, morphology, and photosynthetic capacity) of plants and improve optical remote sensing of forest canopies.

1.3 Phenology of Leaf and Canopy Photosynthesis

1.3.1 Seasonal Change of Leaf Ecophysiological Traits in a Deciduous Broadleaf Forest

The deciduous broadleaf forest at the Takayama site is characterized by multiple plant species including tall canopy trees, subcanopy trees, and understory trees and an evergreen bamboo grass in the understory. The forest floor is covered by snow from December through early April. The leaves of bamboo grass reappear after snowmelt in April, and then the leaves of understory trees emerge in early May. In mid- to late May the leaves of subcanopy and canopy trees emerge. In summer the entire forest canopy is filled by green leaves of various plant species, and in autumn the leaves change to yellow or red and then fall in October (Fig. 1.3). The various patterns of leaf emergence between the canopy layers or between species have been described in many deciduous broadleaf forests in many places in the world, and those differences are hypothesized to be related to successional status of species differing in leaf flushing types (Koike 1990), ontogenic differences within a species (Augspurger and Bartlett 2003; Seiwa 1999; Vitasse 2013), and as an adaptive response to the seasonality of light availability in the forest understory (Augspurger et al. 2005; Seiwa 1998).

The seasonal change of leaf traits of canopy trees (*Q. crispula* and *B. ermanii*), understory trees (*H. paniculata* and *V. furcatum*), and evergreen bamboo grass (*S. senanensis*) was assessed based on measurements of maximum photosynthetic rate (A_{max}, index of photosynthetic capacity in a single leaf), dark respiration rate (R), index of chlorophyll concentration (SPAD), and leaf mass per area (LMA) as the morphological characteristic. In 2005, A_{max} and R were measured in intact leaves on the trees and bamboo grass by using a portable photosynthesis measuring systems (LI-6400, Li-Cor, Inc., Lincoln, NE, USA), and SPAD was measured in the same leaves by using a SPAD meter (SPAD-502, Minolta, Tokyo, Japan). The LMA of the same leaves was calculated as the ratio of leaf dry weight (leaves were oven-dried

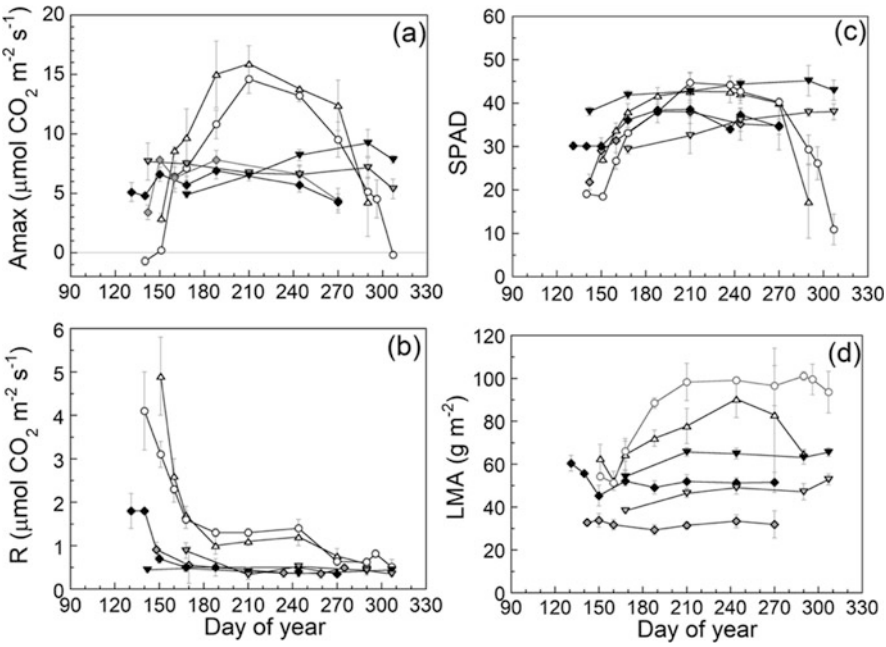

Fig. 1.4 Phenology of leaf ecophysiological characteristics in deciduous broadleaf trees at the Takayama site in 2005. (**a**) Leaf photosynthetic capacity (A_{max}), (**b**) dark respiration (R), (**c**) index of chlorophyll content (SPAD), and (**d**) leaf mass per area (LMA). Symbols and error bars indicate mean ± SD for three to five sample leaves. *Betula ermanii* (open triangle), *Quercus crispula* (open circle), *Hydrangea paniculata* (gray diamond), *Viburnum furcatum* (solid diamond), *Sasa senanensis* (overwintered leaf, solid reverse triangle; current-year leaf, gray reverse triangle). The current-year leaves of *S. senanensis* emerge in early summer and develop their photosynthetic capacity in summer and autumn. Data for *B. ermanii* and *Q. crispula* were included in Noda et al. (2015), and those for other plants are unpublished data by H. Muraoka

at 70 °C for 24 h) to leaf area in the laboratory. Canopy-top leaves were accessed via an 18-m-tall scaffold tower (for more details of measurement protocols, see Muraoka and Koizumi 2005; Noda et al. 2015).

The data show drastic changes in those leaf traits (Fig. 1.4). Leaves of understory trees and bamboo grass have relatively high A_{max} from the beginning of the snow-free season (i.e., growing season), corresponding with high SPAD and LMA. The leaf traits of these species were almost constant throughout the seasons until leaf fall in autumn. In contrast, A_{max} of canopy trees was remarkably low at the leaf emerging phase (~DOY 150) and increased rapidly until their maximum level in early summer (~DOY 200). In autumn, A_{max} and SPAD of canopy trees decreases and then leaf fall occurred. The seasonal development of A_{max} was associated with SPAD and LMA, whereas the decrease of A_{max} was associated only with SPAD. In this study we also found a drastic change of R, characterized by remarkably high values at the leaf emerging phase, a sharp decline along with physiological and morphological development, and stable values from early summer through the leaf senescence phase. The

high R value during the leaf emerging phase reflects high growth respiration due to the leaf construction cost, and the values in summer through autumn reflect mostly maintenance respiration.

The seasonal patterns of leaf development and fall are also reflected in the seasonal change of the leaf area index (LAI) in this forest, which was estimated by intensive measurement of leaf area and number, as well as a litter-trap survey (Nasahara et al. 2008). The data presented in Fig. 1.4 give us basic information about the ecological linkage between leaf characteristics and the contributions of photosynthesis from different species to that of the entire forest (GPP) and hence the CO_2 exchange with the atmosphere.

1.3.2 Interannual Changes in Canopy Leaf Photosynthesis and GPP

Multiple-year measurement of CO_2 flux in the deciduous broadleaf forest ecosystem at the Takayama site revealed remarkable seasonal change, characterized by negative net ecosystem production (NEP) in winter, a transition to positive NEP in spring after snowmelt, high values in summer, a decline in autumn, and then a transition to negative NEP in early winter (Saigusa et al. 2005). The seasonal change of NEP could occur via two major mechanisms: climatic control and ecological control. Because NEP is roughly the balance between GPP and R_e, climatic factors such as solar radiation, air temperature, air humidity, soil temperature, and soil water availability influence photosynthetic activity in leaves (i.e., the CO_2 absorption process) and respiratory activities of plants (leaf, stem, root) and soil microorganisms (the CO_2 release processes). Long-term CO_2 flux measurements at many terrestrial ecosystems demonstrate these temporal and interactive changes (e.g., Hirata et al. 2007; Owen et al. 2007; Saigusa et al. 2008). For a deeper understanding of the biological mechanisms underlying these ecosystem responses, we should consider the seasonal change of leaf photosynthetic capacity (e.g., A_{max}) as shown in Fig. 1.4.

To examine the extent to which the seasonal change of leaf-level photosynthetic capacity influences the GPP of the forest ecosystem, Ito et al. (2006) incorporated the leaf characteristics measured at the Takayama site into an ecosystem carbon cycle simulation model. Their simulations indicated that the leaf phenology is the main driver of the seasonal change and annual amount of GPP and hence NEP. If the leaf photosynthetic capacity were assumed to be constant throughout the season, then GPP would be overestimated by 8% and NEP by 38% (Ito et al. 2006). Likewise, Wilson et al. (2001) demonstrated that the phenology of leaf photosynthesis explained the seasonal change of CO_2 flux measured by the eddy covariance method in a North American deciduous broadleaf forest. A new finding by Ito et al. (2006) was that the phenology of dark respiration is also quantitatively responsible for the seasonal change of R_e in the deciduous forest. Thus, leaf photosynthetic capacity

varies throughout the seasons, especially for canopy trees, and is largely responsible for the seasonal change of GPP, since these species account for a major fraction of LAI of the entire forest canopy at the Takayama site.

Next, researchers aimed to identify the mechanism driving the interannual change of GPP in this forest, which was observed by the eddy covariance method. Saigusa et al. (2005) reported that the plant area index (similar to LAI) of the forest and the seasonal timing of development varied among years, indicating that phenological timing of the forest canopy leaves differ among years. In addition, Ohtsuka et al. (2009) investigated interannual changes in the annual NEP, net primary production (NPP) of woody biomass and tree foliage, R_s, and R_e at the Takayama site. They noted interannual variation in NPP of woody biomass, but NPP of foliage was rather stable. Thus, although the amount of foliage is relatively stable among years, the annual amount of photosynthetic carbon gain is variable. These findings led to important questions about the consequence of leaf photosynthetic activity, phenology, and ecosystem carbon sequestration in a changing environment over seasons and years.

To address these questions, we have been conducting periodic measurements of leaf photosynthetic capacity and corresponding traits in dominant canopy tree species at the Takayama site since 2003 (Muraoka and Koizumi 2005; Noda et al. 2015). Muraoka et al. (2010) estimated the impacts of phenology of leaf photosynthesis and canopy LAI as well as their interannual variation (i.e., early or late leaf growth in spring, early or late leaf senescence in autumn). They used 5 years of data on leaf photosynthetic characteristics, LAI, and micrometeorological factors in a process-based carbon cycle model and demonstrated drastic seasonality of GPP and its interannual changes (Fig. 1.5). These findings indicated that (1) spring temperature could affect GPP through leaf phenology, (2) incoming radiation determined GPP in summer in this forest located in the Asian monsoon region, and (3) annual GPP would be overestimated by 15% if leaf phenology were ignored. The results also suggested that interannual variation in the phenology of canopy LAI would influence photosynthetic productivity of evergreen bamboo grass through changes in the understory light environment. These findings provide important insights into the consequence of tree leaf ecophysiological response to a changing environment and photosynthetic activity at the forest canopy level, highlighting the need to consider the phenology of leaf-level photosynthesis in simulation models to better predict the ecosystem carbon cycle.

The seasonality of photosynthetic carbon fixation would affect not only CO_2 flux components but also biomass accumulation (i.e., plant growth) in the forest. In a recent study at the Takayama site, Shen et al. (2020) found that tree ring growth of *Fagus crenata* Blume, *Q. crispula*, and *B. ermanii* has a seasonal pattern, and it is correlated with the seasonality of meteorological conditions in the previous year and current year, particularly air temperature and water availability in summer and autumn. These environmental factors influence photosynthetic activity, consumption of photosynthetic products, and growth.

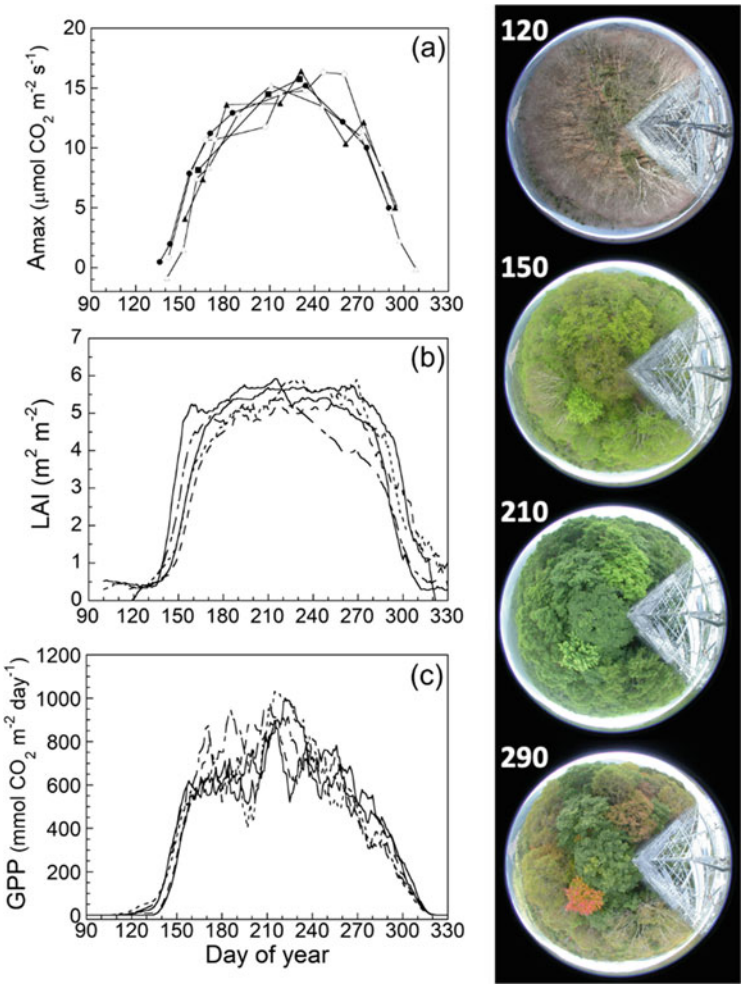

Fig. 1.5 Seasonal changes in (**a**) leaf photosynthetic capacity (A_{max}), (**b**) canopy leaf area index (LAI) and (**c**) estimated GPP of canopy at the Takayama site. A_{max} is the average of values for *Betula ermanii* and *Quercus crispula*. Different lines indicate different study years (2003–2007), and symbols indicate mean ± SD for three to five sample leaves. Canopy images in spring (DOY 120), early summer (DOY 150), late summer (DOY 210), and autumn (DOY 290) are also shown. Graphs (**b**) and (**c**) are redrawn from Muraoka et al. (2010)

1.3.3 Combining Long-Term Observations and an Open-Field Experiment on Leaf Phenology

Long-term ecological research (LTER) enables us to identify important aspects of ecosystems, such as the patterns of changes, their biotic and abiotic drivers, and the impacts of short-term and long-term climatic change on ecosystem structure and

function (e.g., Kim et al. 2018; Mirtl et al. 2018). Intensive data gathered from the single-leaf to forest ecosystem scale at the Takayama site can provide insights into the biological response of tree leaves to changing environments over seasons and years, as well as the consequence for single-leaf and ecosystem-scale CO_2 flux (Muraoka and Koizumi 2009; Tang et al. 2016).

Long-term monitoring of trees has revealed changes in the timing of leaf unfolding and flowering with changing temperatures in Japan (Doi and Katano 2008; Matsumoto et al. 2003), Europe (Menzel et al. 2006; Vitasse et al. 2009), and North America (Gunderson et al. 2012), and analyses suggest that these phenological changes are correlated with warming. The accumulated data on leaf phenology is useful for developing an empirical model to predict the timing of leaf emergence, leaf development and senescence, and leaf fall (Hänninen et al. 2019; Richardson et al. 2006). By integrating leaf data obtained from 2003 to 2010, Noda et al. (2015) investigated the relationships in *Q. crispula* and *B. ermanii* between an abiotic driver (temperature) and various leaf ecophysiological traits, including photosynthetic capacity (A_{max}), R, maximum velocity of carboxylation (V_{cmax}), chlorophyll and nitrogen content, and LMA. They demonstrated that the leaf phenological pattern could be consistently predicted by temperature. Seasonal growth—leaf physiological and morphological development—could be predicted by the cumulative temperature from early spring to early summer (growing degree days, GDD), and physiological senescence could be predicted by cumulative (decreasing) temperature from late summer to autumn (chilling degree days, CDD). The findings of this study are generally consistent with the outcomes from studying automated digital camera images of forest canopy, namely that GDD and CDD can be used as indicators of leaf onset and leaf fall timing (Inoue et al. 2014; Nagai et al. 2013). In addition to air temperature, leaf physiological and morphological development in deciduous broadleaf trees is dependent on environmental factors such as local light availability (Niinemets 2004).

This finding under interannual variation in meteorological conditions would further support us to apply empirical models to simulate the seasonal change of leaf photosynthetic capacity and foliage growth to predict forest canopy photosynthesis. By applying the leaf phenological patterns, Kuribayashi et al. (2017) investigated the impacts of increasing atmospheric CO_2 concentration and global warming (increase of 2.38–2.49 °C) on leaf phenology, GPP, R_e, and NEP of a cool-temperate deciduous broadleaf forest at the Takayama site. They demonstrated that GPP and NEP would be increased by 25.2% and 35.4%, respectively, due to rising temperature, which led to earlier leaf expansion and delayed leaf fall by about 10 days and higher photosynthetic activity in early summer and autumn, as well as to the CO_2 fertilization effect on photosynthesis in summer. Improving the leaf phenology model, however, will require integrated analysis that also considers physiological mechanisms, because leaf expansion is not only driven by temperature but also by photoperiod (Way and Montgomery 2015), and perhaps other environmental factors such as radiation and water availability (cf. Cleland et al. 2007; Polgar and Primack 2011; Tang et al. 2016).

The impacts of global warming on leaf phenology also have been investigated in open-field warming experiments (Chung et al. 2013; Richardson et al. 2018; Rustad et al. 2001). By installing an open-top chamber, heating cable, or heating lamp, the air temperature around a branch or the temperature of the branch itself can be raised to the desired experimental temperature conditions, while other environmental factors, particularly solar radiation, remain similar among the different temperature treatments (Nakamura et al. 2010, 2016; Yamaguchi et al. 2016). For example, open-field warming experiments on canopy-top leaves of adult *B. ermanii* trees in northern Japan showed that leaf flush advanced by 6.5 days under +1.18 to 1.35 °C conditions (Nakamura et al. 2016).

At the Takayama site, we conducted a warming experiment from 2011 to 2017 by installing open-top chambers on branches of *Q. crispula* and *B. ermanii* at the top of their crowns (ca. 14–16 m above ground). Each open-top chamber (1.15 m × 1.7 m × 1.75 m high) is made of transparent acrylic board and vinyl sheeting and surrounds the branch for about 1 m of its length. The daytime air temperature in the open-top chambers was higher than in the control treatment by 1.4–1.6 °C. On average, this warming treatment advanced leaf expansion by 1.6 days in *Q. crispula* and by 2.2 days in *B. ermanii*, while the leaf expansion in the ambient treatment changed by 14–16 days in response to a 5 °C temperature anomaly in spring (H. Muraoka et al., submitted). A rise in temperature not only influences leaf phenology but also photosynthetic capacity and its temperature-dependence (e.g., Yamaguchi et al. 2016). Figure 1.6 shows the relationship between A_{max} and leaf temperature in warmed and control leaves of *Q. crispula* (H. Muraoka, unpublished data). In early June, a few weeks after leaf emergence, A_{max} was higher in warmed leaves than in control leaves, reflecting the earlier leaf expansion in the former. A_{max} was also approximately 10% higher in warmed leaves in summer, which is consistent with the findings that warmed leaves had higher chlorophyll content (estimated by SPAD) and nitrogen concentration (H. Muraoka, unpublished data). The higher A_{max} in October indicates delayed senescence in warmed leaves. In a cool-temperate deciduous broadleaf forest, Hikosaka et al. (2007) and Yamaguchi et al. (2016) also showed that the temperature-dependence of photosynthesis changes in response to the temperature condition which changed across the growing season as well as being altered by open-top chambers.

To what extent do these changes in photosynthetic capacity and temperature-dependence influence photosynthetic productivity at the forest canopy level (i.e., GPP) in cool-temperate deciduous broadleaf forest? To answer this question, we must consider the impacts of current meteorological anomalies to explain the interannual changes of GPP over the past 30 years, as well as the impacts of future climate change. Although drought or extreme heat rarely impacts the forest at the Takayama site, as occurs in other terrestrial ecosystems in the world (e.g., Reichstein et al. 2013), we should consider how climate change stress affects photosynthesis through altered leaf phenology as extreme climate events are likely to occur under ongoing climate change.

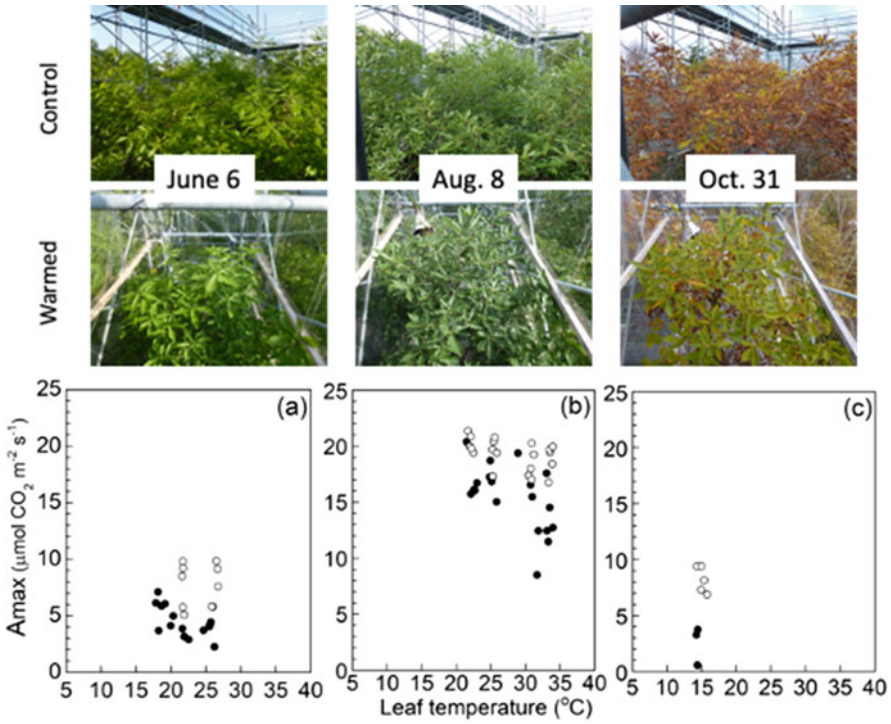

Fig. 1.6 Relationship between leaf temperature and leaf photosynthetic capacity (A_{max}) of *Quercus crispula* in control (solid circle) and warmed (open circle) treatments in the open-field warming experiment at the Takayama site. Photographs show branches of respective treatments on the measurement dates. On October 31, many leaves in the warmed treatment remain green, whereas those in the control treatment have already turned yellow

1.3.4 Leaf Photosynthesis and Phenology in Forest Understory Trees

The cool-temperate deciduous broadleaf forest at the study site has rich woody species diversity in the understory. *Hydrangea paniculata* and *V. furcatum* inhabit the understory and grow up to approximately 3 m. Forest understory plants generally experience limited light availability, which is the energy source for leaf photosynthesis (Montgomery and Chazdon 2001; Muraoka et al. 1997; Pearcy et al. 2005). In such a light-limited environment on the forest floor, Muraoka et al. (2003) reported that saplings of canopy and subcanopy trees and understory trees maximize their light interception by geometrical arrangement of leaf display in their given microhabitats. Mature *H. paniculata* and *V. furcatum* arrange their leaf display along the branches to minimize the overlap between the leaves and maximize the efficiency of light interception in the understory (Muraoka and Koizumi 2005). In a forest understory where leaf photosynthesis is generally limited by low light availability,

phenology and acclimation of leaf photosynthesis to light heterogeneity are also keys to understanding how the plants survive in such an environment (Augspurger et al. 2005; Montgomery and Chazdon 2001; Muraoka et al. 2002; Pearcy and Sims 1994). As shown in Fig. 1.4, A_{max} values of *H. paniculata* and *V. furcatum* are high even in the very early phase of their phenology, suggesting that these species are adapted to utilize the high light only available before leaf expansion of canopy trees.

To understand the relationships among canopy leaf phenology, light penetration to the forest understory, and leaf photosynthetic productivity of the understory trees, we conducted a 2-year study at the Takayama site. Figure 1.7 illustrates the light intensity (photosynthetically active photon flux density: PPFD) measured above the canopy-top and in forest understory, relative PPFD (ratio of understory to canopy-top PPFD), leaf photosynthetic capacity, and estimated daily photosynthesis of *H. paniculata* and *V. furcatum* (C. Ohashi and H. Muraoka, unpublished data). In this study, we selected two places in the forest understory, one where the canopy-top layer is dense and another where the canopy-top has a gap due to branch or tree fall. Light intensity is high throughout the seasons, but the daily integrated PPFD is influenced by solar angle and weather. With leaf expansion of the canopy trees, light penetration to the understory expressed as relative PPFD decreased from about 0.6 to 0.05 and remained low in the summer. In autumn, the relative PPFD increased with leaf fall of the canopy trees. Thus, understory plants are shaded for most of the growing season. A_{max} of understory leaves was high in the early growing season, and then decreased toward summer and autumn. Moreover, A_{max} was higher in leaves at the gap site than at the closed-canopy site in both species.

Based on measured PPFD and leaf photosynthetic characteristic, we then estimated daily photosynthesis (A_{day}), which reflects the seasonal change of A_{max}, penetration of light through the canopy-top layer, and the different light availability in the gap and closed-canopy sites (Fig. 1.7). The estimated A_{day} suggests that (1) photosynthetic productivity tends to be higher early in the growing season (which is obvious in the second year), (2) *H. paniculata* has higher A_{max} and hence higher A_{day} than *V. furcatum* throughout the seasons, and (3) higher A_{max} and light availability in the gap led to higher A_{day} in both species. We estimated that about 84% of photosynthetic production in *H. paniculata* is achieved after canopy closure, whereas in *V. furcatum* up to 39% of photosynthetic production is achieved before canopy closure. This study demonstrated the different strategy of the two shrub species to utilize the light resources in the understory. The high A_{max} of *H. paniculata* in the early and mid-growing season led to a high photosynthetic rate by utilizing sunflecks penetrating through gaps in the canopy. The higher A_{max} at the gap site, which can be considered as a light acclimation response to the heterogeneous light environment in the understory, also contributed to higher A_{day}. In *V. furcatum*, the relatively rapid leaf development early in the growing season enables the species to utilize the high light available before canopy closure, and this seems to be a strategy to avoid canopy shade (cf. Augspurger et al. 2005).

Our study of the light environment within a forest implies the possible influence of global warming on photosynthetic productivity in understory plants via the changes in leaf phenology of the canopy trees. Another question is how the timing

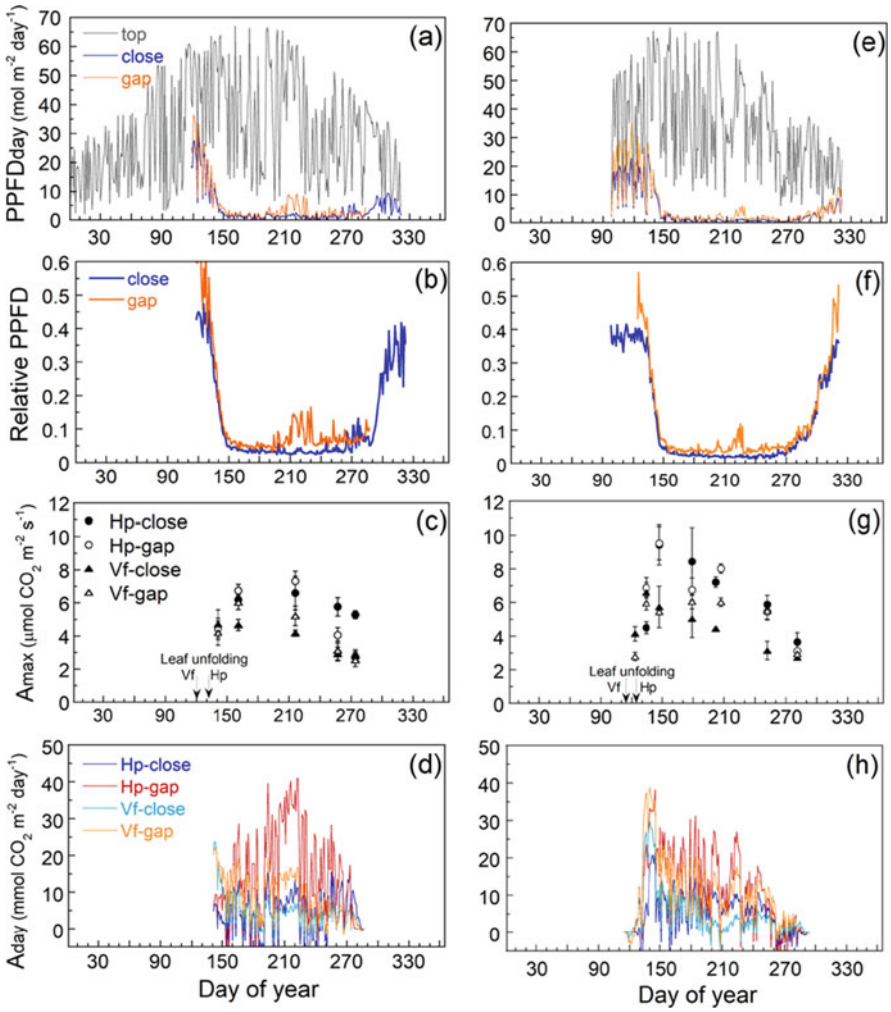

Fig. 1.7 Seasonal changes in (**a**, **e**) light intensity above the forest canopy and in the understory (PPFD), (**b**, **f**) relative PPFD in the understory, (**c**, **g**) leaf photosynthetic capacity (A_{max}), and (**d**, **h**) daily leaf photosynthesis (A_{day}) of *Hydrangea paniculata* and *Viburnum furcatum*, respectively. Measurements of PPFD and A_{max} were made in closed-canopy and gap sites in the forest understory. Symbols in (**c**) and (**g**) indicate mean ± SD for three sample leaves. (C. Ohashi and H. Muraoka, unpublished data)

of snowmelt on the forest floor interactively impacts leaf phenology and photosynthesis in the understory.

1.4 Combining In Situ Surveys and Satellite Remote Sensing for Phenology Observations

Satellite remote sensing of terrestrial ecosystems enables us to monitor the spatial and temporal dynamics in a changing environment (Running et al. 2004). With the advancement in spatial and temporal resolution as well as spectral characteristics, satellite remote sensing of the physiological characteristics of the vegetation canopy has provided invaluable information on biodiversity and ecosystem structure and function (e.g., Anderson 2018; Ustin et al. 2009; Vihervaara et al. 2017). The phenology of terrestrial vegetation serves as an indicator of the impacts of climate change on plant ecophysiological characteristics at the landscape, regional, and global scale (Piao et al. 2019; Richardson et al. 2013; Tang et al. 2016). To improve remote sensing observation techniques for its use in ecosystem studies, however, we must conduct intensive in situ studies to connect optical signals with the ecophysiological characteristics on the ground (Noda et al. 2021; Ustin et al. 2009). At the Takayama site, we have developed an observation system to link ecological and optical forest canopy information with the satellite remote sensing signals to advance the use of satellites in ecological research, known as the "Satellite Ecology" concept (Muraoka and Koizumi 2009). The importance of ground-truthing data in validating satellite observations is discussed by Nagai et al. (2020).

Satellite remote sensing of seasonal changes and the geographic distribution of canopy structure and photosynthetic productivity of terrestrial vegetation has been achieved through use of optical sensors onboard Earth observation satellites such as Landsat, Terra and Aqua with Moderate resolution Imaging Spectroradiometer (MODIS), Advanced Land Observing Satellite (ALOS), Global Change Observation Mission-Climate (GCOM-C), and Sentinel-2. The satellites' optical sensors measure the reflected spectrum for visible bands such as blue, green, and red, as well as an infrared band. Then these signals are used to calculate vegetation indices such as the Normalized Difference Vegetation Index (NDVI), Enhanced Vegetation Index (EVI), or Green-Red Vegetation Index (GRVI) which provide estimates of the greenness of the land surface as a proxy of canopy leaf area and photosynthetic productivity (Motohka et al. 2010; Muraoka et al. 2013; Nagai et al. 2010; Turner et al. 2006; Xiao 2004). While these vegetation indices have been used to estimate the canopy structure (e.g., LAI) or to detect the timing of leaf onset (greening) and offset (leaf fall) in the last 20–30 years (e.g., Piao et al. 2015; Running et al. 2004), detailed examination and verification of the optical information in relation to canopy structure and photosynthetic productivity (GPP) are essential for accurate estimation from space (Muraoka and Koizumi 2009; Noda et al. 2021).

To assess the applicability of vegetation indices for estimating photosynthetic productivity at spatial scales ranging from landscape to national in Japan, where forests are distributed mainly in mountainous areas, we investigated the relationship between vegetation indices and GPP estimated at the Takayama site (Muraoka et al. 2013). Vegetation indices were calculated from hyperspectral data obtained by a spectroradiometer mounted on the scaffold tower (Fig. 1.2); this spectroradiometer is

part of the PEN observation system. Measuring the spectral reflectance just above the canopy enables us to obtain data without any atmospheric noise, such as clouds and aerosols, which are problems with optical satellite remote sensing (Nagai et al. 2020). The vegetation indices were compared with GPP of the forest canopy predicted by an ecosystem model incorporating the observed leaf-level photosynthesis, canopy LAI, and micrometeorological conditions (for a discussion of the model, see Sect. 1.3.2). Among NDVI, EVI and GRVI, EVI showed the clearest relationship with GPP, for both its daily integrated value and maximum value within a day, throughout the seasons and years (Fig. 1.8). Here it should be noted that the relationship between EVI and GPP was not simply a linear function but showed hysteresis between the lines for spring—summer and summer—autumn, suggesting that optical properties of single leaves and hence canopies need to be considered carefully (see also Noda et al. 2021). Then the obtained relationship was used to convert the EVI value to daily maximum rate of GPP, an indicator of photosynthetic capacity of forest ecosystems, over the central region of the main island of Japan (Fig. 1.8).

The above study focused on the photosynthetic *capacity*, which is close to the potential (maximum) level of photosynthesis in an ecosystem. However, the Greenhouse gases Observing SATellite (GOSAT, launched in 2009) provides a signal of chlorophyll fluorescence emitted from the vegetation surface (e.g., Frankenberg et al. 2011), called sun-induced fluorescence (SIF). SIF has been assessed for its utility for estimating the photosynthetic *activity*, which should be close to the actual photosynthetic rate driven by physiological and meteorological factors (e.g., Yang et al. 2015). At the Takayama site, Nakashima et al. (2021) examined the accuracy and applicability of SIF to the estimation of GPP by combining in situ hyperspectral data of the canopy surface and CO_2 flux measurements. Because chlorophyll fluorescence indicates the physiological status of photosynthesis in leaves (Genty et al. 1989; Muraoka et al. 2000), SIF is expected to be an indicator of the environmental response as well as the impact of climate change stress on photosynthesis at the ecosystem scale. However, we still need to explore the ecophysiological mechanisms of SIF by considering underlying photosynthetic reactions at the single-leaf level as well as the canopy geometrical and optical structures to accurately utilize the SIF signals at broader scales ranging from canopy to landscape (cf. Hikosaka and Noda 2019). In addition, we need to develop a methodology to detect photosynthetic capacity or activity under cloudy conditions, which is crucial for observations in regions with a humid Asian monsoon climate.

1.5 Conclusion

In this chapter, I reviewed studies of leaf and canopy photosynthesis conducted in a cool-temperate deciduous broadleaf forest in Japan. The research findings from the Takayama site clearly describe the relationship between phenology and meteorological factors and phenologically influenced changes in carbon flux. Ecophysiological

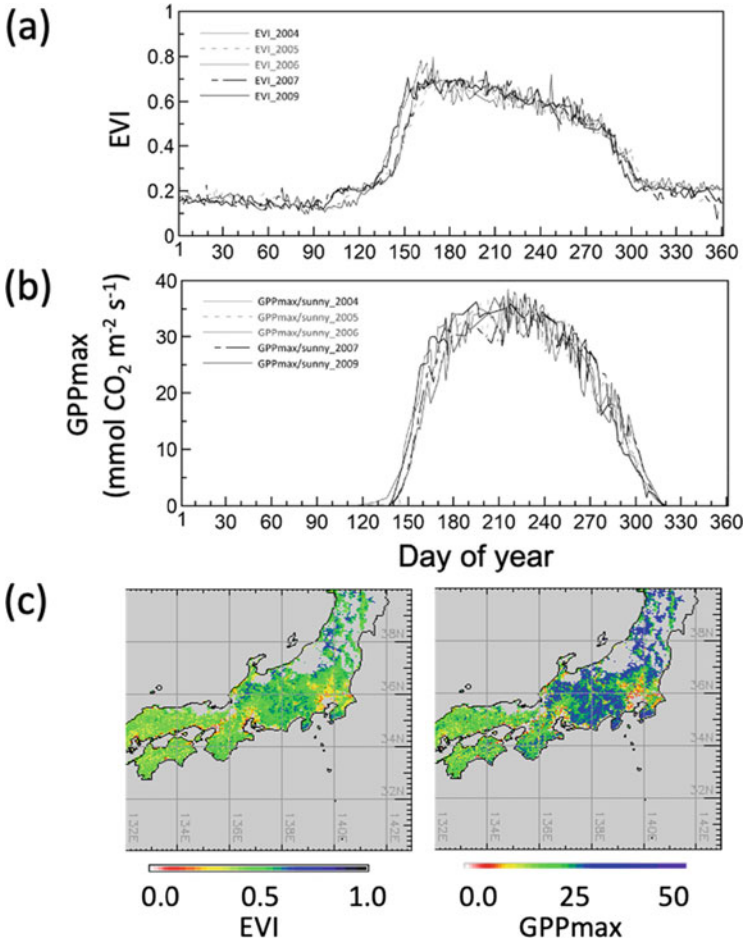

Fig. 1.8 Seasonal changes in the (**a**) Enhanced Vegetation Index (EVI) obtained by spectroradiometer and (**b**) daily maximum GPP under sunny conditions estimated by a model simulation at the Takayama site from 2004 to 2009. The relationship between daily maximum canopy photosynthetic rate, estimated by model simulation, and EVI obtained at the Takayama site was used to convert satellite-based EVI to GPP across central Japan (**c**). Graphs (**a**) and (**b**) were redrawn from the original data in the study by Muraoka et al. (2013)

studies focusing on photosynthesis and phenology highlight the temporal changes at daily, seasonal, and annual time scales, which deepens our understanding of the dynamic linkages of the processes to overall forest ecosystem function (Fig. 1.2). Long-term and multidisciplinary research reveals the time-dependent linkages among processes occurring in different ecosystem compartments; elaboration of these linkages is supported by advanced technology, such as measurement systems for physiology and biochemistry, sensors for in situ and satellite remote sensing, and CO_2 flux observation systems, as well as simulation models. These methodologies

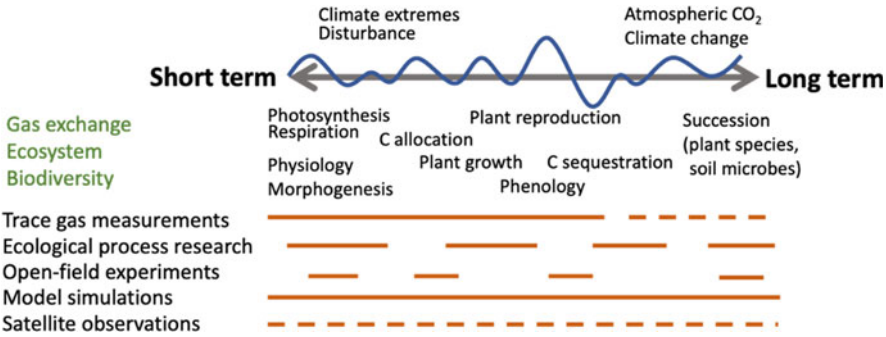

Fig. 1.9 Schematic of the relationships between research targets in gas exchange, ecosystem dynamics, and biodiversity as well as available technologies for in situ and satellite observations, experiments, and model simulations under environmental changes that occur over the short to long term. Research topics have unique temporal scales, resolution or continuity, and corresponding technologies, but combining the technologies (i.e., multidisciplinary studies) allows us to identify complicated mechanisms and consequences of ecosystem structure and functions over various spatial and temporal scales. The orange lines show image of temporal resolution or continuity of research: broken lines represent intermittent or periodical measurements, while a long line represents continuous measurements or estimation

have various spatial resolutions that can be applied to the scale of interest—from a single leaf to the landscape—and integration of the data obtained through these various methods provides an overall picture of ecosystems and their changes (Fig. 1.9; see also Muraoka and Koizumi 2009).

The challenges discussed in this chapter regarding a mechanistic understanding of the components involved in a given ecosystem can be overcome by conducting long-term observations and open-field experiments, coupled with observations of atmospheric dynamics at in situ research sites, that is, 'master sites' like the one at Takayama (Fig. 1.2). Developing an ecosystem research infrastructure—the integrated observation of ecosystem structure and function, followed by data analysis and sharing—is crucial for timely monitoring of the steady state and detecting the impacts of climate change (Chabbi and Loescher 2017). Networks of such research sites and scientists, such as JaLTER, JapanFlux, AsiaFlux, and APBON, will help us to integrate data and knowledge gathered from different scientific perspectives covering the broad geographic and climatic range found among various ecosystems. Comprehensive analysis of the system may allow us to identify key ecosystem variables, such as Essential Climate Variables (ECV; Global Climate Observing System 2016) and Essential Biodiversity Variables (EBV; Pereira et al. 2013), that are crucial to track and compare in future efforts to extend these principles to larger scales (cf. Haase et al. 2018). These essential variables should facilitate truly meaningful interpretation of satellite remote sensing data and the improvement of ecosystem models used to evaluate the potential consequences of climate change. The knowledge and observation designs generated from such comprehensive research are crucial for biodiversity and ecosystem conservation and management in landscapes from local to regional scales.

Acknowledgements The author thanks K. Kurumado, S. Yoshitake, K. Suzuki, and all technical staff of the Takayama Field Station, Gifu University, for logistical support. Studies introduced in this chapter were conducted with multiple collaborators, including H. Koizumi, S. Yamamoto, N. Saigusa, S. Murayama, A. Ito, T. Ohtsuka, K.N. Nasahara, S. Nagai, H.M. Noda, T. Akitsu, M. Kuribayashi, N. Noh, T. Nakaji, T. Hiura, T.M. Saitoh, Y. Son, Q. Wang, and J.D. Tenhunen. Open-field warming experiment was conducted as part of the bachelor's or master's thesis by C. Shoji and A. Nagao, and a study on forest understory trees was part of the master's thesis by C. Ohashi, who were in author's laboratory. Other lab members Y. Tamaki, A. Yamada, P. Liang, and I. Melnikova supported fieldwork. Concepts of the master site and networking have been discussed with A. Bombelli, H. Shibata, K. Ichii, O. Ochiai, and Y. Takeuchi. Our valued colleague, the late Dr. R. Suzuki provided foresighting insights in linking in situ and satellite research. The studies were supported in part by the Ministry of the Environment, Japan (S-1, D-0909), JSPS twenty-first Century COE Program, JSPS-KOSEF-NSFC A3 Foresight Program, a Global Change Observation Mission (PI#102) of the Japan Aerospace Exploration Agency, JSPS NEXT Program (GR048) and JSPS KAKENHI (18710006, 26241005, 19H03301).

References

Anderson CB (2018) Biodiversity monitoring, earth observations and the ecology of scale. Ecol Lett 21:1572–1585

Augspurger CK, Bartlett EA (2003) Differences in leaf phenology between juvenile and adult trees in a temperate deciduous forest. Tree Physiol 23:517–525

Augspurger CK, Cheeseman JM, Salk CF (2005) Light gains and physiological capacity of understorey woody plants during phenological avoidance of canopy shade. Funct Ecol 19: 537–546

Baldocchi DD, Black TA, Curtis PS, Falge E, Fuentes JD, Granier A, Gu L, Knohl A, Pilegaard K, Schmid HP, Valentini R, Wilson K, Wofsy S, Xu L, Yamamoto S (2005) Predicting the onset of net carbon uptake by deciduous forests with soil temperature and climate data: a synthesis of FLUXNET data. Int J Biometeorol 49:377–387

Chabbi A, Loescher HW (eds) (2017) Terrestrial ecosystem research infrastructure: challenges and opportunities. CRC Press, Boca Raton

Chapin FS III, Matson PA, Vitousek PM (eds) (2012) Principles of terrestrial ecology, 2nd edn. Springer, Berlin

Chung H, Muraoka H, Nakamura M, Han S, Muller O, Son Y (2013) Experimental warming studies on tree species and forest ecosystems: a literature review. J Plant Res 126:447–460

Cleland EE, Chuine I, Menzel A, Mooney HA, Schwartz MD (2007) Shifting plant phenology in response to global change. Trends Ecol Evol 22:357–365

Doi H, Katano I (2008) Phenological timings of leaf budburst with climate change in Japan. Agric For Meteorol 148:512–516

Evans JR, von Caemmerer S, Adams III WW (eds) (1988) Ecology of photosynthesis in sun and shade. CSIRO

Frankenberg C, Fisher JB, Worden J, Badgley G, Saatchi SS, Lee J-E, Toon GC, Butz A, Jung M, Kuze A, Yokota T (2011) New global observations of the terrestrial carbon cycle from GOSAT: patterns of plant fluorescence with gross primary productivity. Geophys Res Lett. https://doi.org/10.1029/2011GL048738

Genty B, Briantais JM, Baker NR (1989) The relationship between the quantum yield of photosynthetic electron transport and quenching of chlorophyll fluorescence. Biochim Biophys Acta 990:87–92

Global Climate Observing System (2016) The global observing system for climate: implementation needs. World Meteorological Organization. https://gcos.wmo.int/en/gcos-implementation-plan

Gunderson CA, Edwards NT, Walker AV, O'Hara KH, Campion CM, Hanson PJ (2012) Forest phenology and a warmer climate: growing season extension in relation to climatic provenance. Glob Chang Biol 18:2008–2025

Haase P, Tonkin JD, Stoll S, Burkhard B, Frenzel M, Geijzendorffer IR, Hauser C, Klotz S, Kuhn I, McDowell WH, Mirtl M, Muller F, Musche M, Penner J, Zacharias S, Schmeller DS (2018) The next generation of site-based long-term ecological monitoring: linking essential biodiversity variables and ecosystem integrity. Sci Total Environ 613-614:1376–1384

Hänninen H, Kramer K, Tanino K, Zhang R, Wu J, Fu YH (2019) Experiments are necessary in process-based tree phenology modelling. Trends Plant Sci 24:199–209

Hikosaka K, Noda HM (2019) Modeling leaf CO_2 assimilation and photosystem II photochemistry from chlorophyll fluorescence and the photochemical reflectance index. Plant Cell Environ 42: 730–739

Hikosaka K, Nabeshima E, Hiura T (2007) Seasonal changes in the temperature response of photosynthesis in canopy leaves of *Quercus crispula* in a cool-temperate forest. Tree Physiol 27:1035–1041

Hikosaka K, Niinemets Ü, Anten PR (eds) (2016) Canopy photosynthesis: from basics to applications. Springer, Berlin

Hirata R, Hirano T, Saigusa N, Fujinuma Y, Inukai K, Kitamori Y, Takahashi Y, Yamamoto S (2007) Seasonal and interannual variations in carbon dioxide exchange of a temperate larch forest. Agric For Meteorol 147:110–124

Ichii K, Suzuki T, Kato T, Ito A, Hajima T, Ueyama M, Sasai T, Hirata R, Saigusa N, Ohtani Y, Takagi K (2010) Multi-model analysis of terrestrial carbon cycles in Japan: limitations and implications of model calibration using eddy flux observations. Biogeosciences 7:2061–2080

Inoue T, Nagai S, Saitoh TM, Muraoka H, Nasahara KN, Koizumi H (2014) Detection of the different characteristics of year-to-year variation in foliage phenology among deciduous broad-leaved tree species by using daily continuous canopy surface images. Ecol Informatics 22:58–68

Ito A, Muraoka H, Koizumi H, Saigusa N, Murayama S, Yamamoto S (2006) Seasonal variation in leaf properties and ecosystem carbon budget in a cool-temperate deciduous broad-leaved forest: simulation analysis at Takayama site, Japan. Ecol Res 21:137–149

Ito A, Inatomi M, Mo W, Lee M, Koizumi H, Saigusa N, Murayama S, Yamamoto S (2007) Examination of model-estimated ecosystem respiration using flux measurements from a cool-temperate deciduous broad-leaved forest in Central Japan. Tellus B: Chem Phys Meteorol 59: 616–624

Kikuzawa K, Lechowicz MJ (2011) Ecology of leaf longevity. Springer, Berlin

Kim E-S, Trisurat Y, Muraoka H, Shibata H, Amoroso V, Boldgiv B, Hoshizaki K, Kassim AR, Kim Y-S, Nguyen HQ, Ohte N, Ong PS, Wang C-P (2018) The international long-term ecological research–East Asia–Pacific regional network (ILTER-EAP): history, development, and perspectives. Ecol Res 33:19–34

Koike T (1990) Autumn coloring, photosynthetic performance and leaf development of deciduous broad-leaved trees in relation to forest succession. Tree Physiol 7:21–32

Kuribayashi M, Noh NJ, Saitoh TM, Ito A, Wakazuki Y, Muraoka H (2017) Current and future carbon budget at Takayama site, Japan, evaluated by a regional climate model and a process-based terrestrial ecosystem model. Int J Biometeorol 61:989–1001

Matsumoto K, Ohta T, Irasawa M, Nakamura T (2003) Climate change and extension of the *Ginkgo biloba* L. growing season in Japan. Glob Chang Biol 9:1634–1642

Menzel A, Sparks TH, Estrella N, Koch E, Aasa A, Ahas R, Alm-Kubler K, Bissolli P, Braslavská OG, Briede A, Chmielewski FM, Crepinsek Z, Curnel Y, Dahl Å, Defila C, Donnelly A, Filella Y, Jatczak K, Mage F, Mestre A, Nordli Ø, Penuelas J, Pirinen P, Remisova V, Scheifinger H, Striz M, Susnik A, Van Vliet AJH, Wielgolaski F-E, Zach S, Zust ANA (2006) European phenological response to climate change matches the warming pattern. Glob Chang Biol 12:1969–1976

Mirtl M, Borer ET, Djukic I, Forsius M, Haubold H, Hugo W, Jourdan J, Lindenmayer D, McDowell WH, Muraoka H, Orenstein DE, Pauw JC, Peterseil J, Shibata H, Wohner C,

Yu X, Haase P (2018) Genesis, goals and achievements of long-term ecological research at the global scale: a critical review of ILTER and future directions. Sci Total Environ 626:1439–1462
Mo W, Lee MS, Uchida M, Inatomi M, Saigusa N, Mariko S, Koizumi H (2005) Seasonal and annual variation in soil respiration in a cool-temperate deciduous broad-leaved forest in Japan. Agric For Meteorol 134:81–94
Monsi M, Saeki T (2005) On the factor light in plant communities and its importance for matter production. Ann Bot 95:549–567
Montgomery RA, Chazdon RL (2001) Forest structure, canopy architecture, and light transmittance in tropical wet forests. Ecology 82:2707–2718
Motohka T, Nasahara KN, Oguma H, Tsuchida S (2010) Applicability of green-red vegetation index for remote sensing of vegetation phenology. Remote Sens 2:2369–2387
Muraoka H, Koizumi H (2005) Photosynthetic and structural characteristics of canopy and shrub trees in a cool-temperate deciduous broadleaved forest: implication to the ecosystem carbon gain. Agric For Meteorol 134:39–59
Muraoka H, Koizumi H (2009) Satellite ecology (SATECO)-linking ecology, remote sensing and micrometeorology, from plot to regional scale, for the study of ecosystem structure and function. J Plant Res 122:3–20
Muraoka H, Tang Y, Koizumi H, Washitani I (1997) combined effects of light and water availability on photosynthesis and growth of *Arisaema heterophyllum* in the forest understory and an open site. Oecologica 112:26–34
Muraoka H, Tang Y, Terashima I, Koizumi H, Washitani I (2000) Contributions of diffusional limitation, photoinhibition and photorespiration to midday depression of photosynthesis in *Arisaema heterophyllum* in natural high light. Plant Cell Environ 23:235–250
Muraoka H, Tang Y, Koizumi H, Washitani I (2002) Effects of light and soil water availability on leaf photosynthesis and growth of *Arisaema heterophyllum*, a riparian forest understorey plant. J Plant Res 115:419–427
Muraoka H, Koizumi H, Pearcy RW (2003) Leaf display and photosynthesis of tree seedlings in a cool-temperate deciduous broadleaf forest understory. Oecologia 135:500–509
Muraoka H, Saigusa N, Nasahara KN, Noda H, Yoshino J, Saitoh TM, Nagai S, Murayama S, Koizumi H (2010) Effects of seasonal and interannual variations in leaf photosynthesis and canopy leaf area index on gross primary production of a cool-temperate deciduous broadleaf forest in Takayama, Japan. J Plant Res 123:563–576
Muraoka H, Noda HM, Nagai S, Motohka T, Saitoh TM, Nasahara KN, Saigusa N (2013) Spectral vegetation indices as the indicator of canopy photosynthetic productivity in a deciduous broadleaf forest. J Plant Ecol 6:393–407
Muraoka H, Saitoh TM, Nagai S (2015) Long-term and interdisciplinary research on forest ecosystem functions: challenges at Takayama site since 1993. Ecol Res 30:197–200
Murayama S, Takamura C, Yamamoto S, Saigusa N, Morimoto S, Kondo H, Nakazawa T, Aoki S, Usami T, Kondo M (2010) Seasonal variations of atmospheric CO_2, $\delta^{13}C$, and $\delta^{18}O$ at a cool temperate deciduous forest in Japan: influence of Asian monsoon. J Geophys Res 115:D17304
Nagai S, Saigusa N, Muraoka H, Nasahara KN (2010) What makes the satellite-based EVI–GPP relationship unclear in a deciduous broad-leaved forest? Ecol Res 25:359–365
Nagai S, Maeda T, Gamo M, Muraoka H, Suzuki R, Nasahara KN (2011) Using digital camera images to detect canopy condition of deciduous broad-leaved trees. Plant Ecol Divers 4:79–89
Nagai S, Saitoh TM, Kurumado K, Tamagawa I, Kobayashi H, Inoue T, Suzuki R, Gamo M, Muraoka H, Nishida Nasahara K (2013) Detection of bio-meteorological year-to-year variation by using digital canopy surface images of a deciduous broad-leaved forest. SOLAIAT 9:106–110
Nagai S, Nasahara KN, Akitsu TK, Saitoh TM, Muraoka H (2020) Importance of the collection of abundant ground-truth data for accurate detection of spatial and temporal variability of vegetation by satellite remote sensing, in biogeochemical cycles: ecological drivers and environmental impact. Geophysical Monograph 251. Wiley, New York, pp 225–243

Nakamura M, Muller O, Tayanagi S, Nakaji T, Hiura T (2010) Experimental branch warming alters tall tree leaf phenology and acorn production. Agric For Meteorol 150:1026–1029

Nakamura M, Makoto K, Tanaka M, Inoue T, Son Y, Hiura T (2016) Leaf flushing and shedding, bud and flower production, and stem elongation in tall birch trees subjected to increases in aboveground temperature. Trees 30:1535–1541

Nakashima N, Kato T, Morozumi T, Tsujimoto K, Akitsu TK, Nasahara KN, Murayama S, Muraoka H, Noda HM (2021) Area-ratio Fraunhofer line depth (aFLD) method approach to estimate solar-induced chlorophyll fluorescence in low spectral resolution spectra in a cool-temperate deciduous broadleaf forest. J Plant Res 134:713–728

Nasahara KN, Nagai S (2015) Review: development of an *in situ* observation network for terrestrial ecological remote sensing: the phenological eyes network (PEN). Ecol Res 30:211–223

Nasahara KN, Muraoka H, Nagai S, Mikami H (2008) Vertical integration of leaf area index in a Japanese deciduous broad-leaved forest. Agric For Meterol 148:1136–1146

Niinemets Ü (2004) Within-canopy variation in the rate of development of photosynthetic capacity is proportional to integrated quantum flux density in temperate deciduous trees. Plant Cell Environ 27:293–313

Noda HM, Muraoka H, Nasahara KN, Saigusa N, Murayama S, Koizumi H (2015) Phenology of leaf morphological, photosynthetic, and nitrogen use characteristics of canopy trees in a cool-temperate deciduous broadleaf forest at Takayama, Central Japan. Ecol Res 30:247–266

Noda HM, Muraoka H, Nasahara KN (2021) Plant ecophysiological processes in spectral profiles: perspective from a deciduous broadleaf forest. J Plant Res 134:737–751

Noh NJ, Kuribayashi M, Saitoh TM, Nakaji T, Nakamura M, Hiura T, Muraoka H (2016) Responses of soil, heterotrophic, and autotrophic respiration to experimental open-field soil warming in a cool-temperate deciduous forest. Ecosystems 19:504–520

Noh NJ, Kuribayashi M, Saitoh TM, Muraoka H (2017) Different responses of soil, heterotrophic and autotrophic respirations to a 4-year soil warming experiment in a cool-temperate deciduous broadleaved forest in Central Japan. Agric For Meteorol 247:560–570

Ohtsuka T, Saigusa N, Koizumi H (2009) On linking multiyear biometric measurements of tree growth with eddy covariance-based net ecosystem production. Glob Chang Biol 15:1015–1024

Oikawa S, Hikosaka K, Hirose T (2006) Leaf lifespan and lifetime carbon balance of individual leaves in a stand of an annual herb, *Xanthium canadense*. New Phytol 172:104–116. https://doi.org/10.1111/j.1469-8137.2006.01813.x

Owen KE, Tenhunen J, Reichstein M, Wang Q, Falge EVA, Geyer R, Xiao X, Stoy P, Ammann C, Arain A, Aubinet M, Aurela M, Bernhofer C, Chojnicki BH, Granier A, Gruenwald T, Hadley J, Heinesch B, Hollinger D, Knohl A, Kutsch W, Lohila A, Meyers T, Moors E, Moureaux C, Pilegaard KIM, Saigusa N, Verma S, Vesala T, Vogel C (2007) Linking flux network measurements to continental scale simulations: ecosystem carbon dioxide exchange capacity under non-water-stressed conditions. Glob Chang Biol 13(4):734–760

Pearcy RW, Sims D (1994) Photosynthetic acclimation to changing light environments: scaling from the leaf to the whole plant. In: Caldwell MM, Pearcy RW (eds) Exploitation of environmental heterogeneity by plants. Academic, San Diego, pp 145–174

Pearcy RW, Muraoka H, Valladares F (2005) Crown architecture in sun and shade environments: assessing function and tradeoffs with a 3-D simulation model. New Phytol 166:791–800

Pereira HM, Ferrior S, Walters M, Geller GN, Jongman RHG, Scholes RJ, Bruford MW, Brummitt N, Butchart SHM, Cardoso AC, Coops NC, Dulloo E, Faith DP, Freyhof J, Gregory RD, Heip C, Hoft R, Hurtt G, Jetz W, Karp DS, McGeoch MA, Obura D, Onoda Y, Petteorelli N, Reyers B, Sayre R, Scharlemann JPW, Stuart SN, Turak E, Walpole M, Wegmann M (2013) Essential biodiversity variables. Science 339:277–278

Piao S, Tan J, Chen A, Fu YH, Ciais P, Liu Q, Janssens IA, Vicca S, Zeng Z, Jeong SJ, Li Y, Myneni RB, Peng S, Shen M, Penuelas J (2015) Leaf onset in the northern hemisphere triggered by daytime temperature. Nat Commun 6:6911

Piao S, Liu Q, Chen A, Janssens IA, Fu Y, Dai J, Liu L, Lian X, Shen M, Zhu X (2019) Plant phenology and global climate change: current progresses and challenges. Glob Chang Biol 25: 1922–1940

Polgar CA, Primack RB (2011) Leaf-out phenology of temperate woody plants: from trees to ecosystems. New Phytol 191:926–941

Reichstein M, Bahn M, Ciais P, Frank D, Mahecha MD, Seneviratne SI, Zscheischler J, Beer C, Buchmann N, Frank DC, Papale D, Rammig A, Smith P, Thonicke K, van der Velde M, Vicca S, Walz A, Wattenbach M (2013) Climate extremes and the carbon cycle. Nature 500: 287–295

Richardson AD, Bailey AS, Denny EG, Martin CW, O'Keefe J (2006) Phenology of a northern hardwood forest canopy. Glob Chang Biol 12:1174–1188

Richardson AD, Jenkins JP, Braswell BH, Hollinger DY, Ollinger SV, Simith ML (2007) Use of digital webcam images to track spring green-up in a deciduous broadleaf forest. Oecologia 152: 323–334

Richardson AD, Keenan TF, Migliavacca M, Ryu Y, Sonnentag O, Toomey M (2013) Climate change, phenology, and phenological control of vegetation feedbacks to the climate system. Agric For Meteorol 169:156–173

Richardson AD, Hufkens K, Milliman T, Aubrecht DM, Furze ME, Seyednasrollah B, Krassovski MB, Latimer JM, Nettles WR, Heiderman RR, Warren JM, Hanson PJ (2018) Ecosystem warming extends vegetation activity but heightens vulnerability to cold temperatures. Nature 560:368–371

Rogers A, Medlyn BE, Dukes JS, Bonan G, von Caemmerer S, Dietze MC, Kattge J, Leakey ADB, Mercado LM, Niinemets Ü, Prentice IC, Serbin SP, Sitch S, Way DA, Zaehle S (2017) A roadmap for improving the representation of photosynthesis in earth system models. New Phytol 213:22–42

Running SW, Nemani RR, Heinsch FA, Zhao M, Reeves M, Hashimoto H (2004) A continuous satellite-derived measure of global terrestrial primary production. Bioscience 54:547–560

Rustad L, Campbell J, Marion G, Norby R, Mitchell M, Hartley A, Cornelissen J, Gurevitch J, GCTE-News (2001) A meta-analysis of the response of soil respiration, net nitrogen mineralization, and aboveground plant growth to experimental ecosystem warming. Oecologia 126: 543–562

Saigusa N, Yamamoto S, Murayama S, Kondo H (2005) Inter-annual variability of carbon budget components in an AsiaFlux forest site estimated by long-term flux measurements. Agric For Meteorol 134:4–16

Saigusa N, Yamamoto S, Hirata R, Ohtani Y, Ide R, Asanuma J, Gamo M, Hirano T, Kondo H, Kosugi Y, Li S-G, Nakai Y, Takagi K, Tani M, Wang H (2008) Temporal and spatial variations in the seasonal patterns of CO_2 flux in boreal, temperate, and tropical forests in East Asia. Agric For Meteorol 148:700–713

Seiwa K (1998) Advantages of early germination for growth and survival of seedlings of *Acer mono* under different overstorey phenologies in deciduous broad-leaves forests. J Ecol 86:219–228

Seiwa K (1999) Changes in leaf phenology are dependent on tree height in *Acer mono*, a deciduous broad-leaved tree. Ann Bot 83:355–361

Shen Y, Fukatsu E, Muraoka H, Saitoh TM, Hirano Y, Yasue K (2020) Climate responses of ring widths and radial growth phenology of *Betula ermanii*, *Fagus crenata* and *Quercus crispula* in a cool temperate forest in Central Japan. Trees 34:679–692

Shin N, Saitoh TM, Nasahara KN (2021) How did the characteristics of the growing season change during the past 100 years at a steep river basin in Japan? PLoS ONE 16(7):e0255078. https://doi.org/10.1371/journal.pone.0255078

Takeuchi Y, Muraoka H, Yamakita T, Kano Y, Nagai S, Bunthang T, Costello MJ, Darnaedi D, Diway B, Ganyai T, Grudpan C, Hughes A, Ishii R, Lim PT, Ma K, Muslim AM, Si N, Nakaoka M, Nakashizuka T, Onuma M, Park CH, Pungga RS, Saito Y, Shakya MM, Sulaiman MK, Sumi M, Thach P, Trisurat Y, Xu X, Yamano H, Yao TL, Kim ES, Vergara S, Yahara T

(2021) The Asia-Pacific biodiversity observation network: 10-year achievements and new strategies to 2030. Ecol Res 36:232–257

Tang J, Körner C, Muraoka H, Piao S, Shen M, Thackeray S, Yang X (2016) Emerging opportunities and challenges in phenology: a review. Ecosphere 7:e01436. https://doi.org/10.1002/ecs2.1436

Turner DP, Ritts WD, Cohen WB, Gower ST, Running SW, Zhao M, Costa MH, Kirschbaum AA, Ham JM, Saleska SR, Ahl DE (2006) Evaluation of MODIS NPP and GPP products across multiple biomes. Remote Sens Environ 102:282–292

Ustin SL, Gitelson AA, Jacquemoud S, Schaepman M, Asner GP, Gamon JA, Zarco-Tejada P (2009) Retrieval of foliar information about plant pigment systems from high resolution spectroscopy. Remote Sens Environ 113:S67–S77

Vihervaara P, Auvinen A-P, Mononen L, Törmä M, Ahlroth P, Anttila S, Böttcher K, Forsius M, Heino J, Heliölä J, Koskelainen M, Kuussaari M, Meissner K, Ojala O, Tuominen S, Viitasalo M, Virkkala R (2017) How essential biodiversity variables and remote sensing can help national biodiversity monitoring. Global Ecol Conserv 10:43–59

Vitasse Y (2013) Ontogenic changes rather than difference in temperature cause understory trees to leaf out earlier. New Phytol 198:149–155

Vitasse Y, Delzon S, Dufrêne E, Pontailler J-Y, Louvet J-M, Kremer A, Michalet R (2009) Leaf phenology sensitivity to temperature in European trees: do within-species populations exhibit similar responses? Agric For Meteorol 149:735–744

Way DA, Montgomery RA (2015) Photoperiod constraints on tree phenology, performance and migration in a warming world. Plant Cell Environ 38:1725–1736

Wilson KB, Baldocchi DD, Hanson PJ (2000) Quantifying stomatal and non-stomatal limitations to carbon assimilation resulting from leaf aging and drought in mature deciduous tree species. Tree Physiol 20:787–797

Wilson KB, Baldocchi DD, Hanson PJ (2001) Leaf age affects the seasonal pattern of photosynthetic capacity and net ecosystem exchange of carbon in a deciduous forest. Plant Cell Environ 24:571–583

Xiao X (2004) Modeling gross primary production of temperate deciduous broadleaf forest using satellite images and climate data. Remote Sens Environ 91:256–270

Yamaguchi DP, Nakaji T, Hiura T, Hikosaka K (2016) Effects of seasonal change and experimental warming on the temperature dependence of photosynthesis in the canopy leaves of *Quercus serrata*. Tree Physiol 36:1283–1295

Yamamoto S, Koizumi H (2005) Long-term carbon exchange at Takayama site, a cool-temperature deciduous forest in Japan. Agric For Meteorol 134:1–3

Yamamoto S, Murayama S, Saigusa N, Kondo H (1999) Seasonal and inter-annual variation of CO_2 flux between a temperate forest and the atmosphere in Japan. Tellus 51B:402–413

Yang X, Tang J, Mustard JF, Lee J-E, Rossini M, Joiner J, Munger JW, Kornfeld A, Richardson AD (2015) Solar-induced chlorophyll fluorescence that correlates with canopy photosynthesis on diurnal and seasonal scales in a temperate deciduous forest. Geophys Res Lett 42:2977–2987

Chapter 2
Ecological Significance of Throughfall and Stemflow to the Carbon Cycle in Forest Ecosystems

Siyu Chen, Ruoming Cao, Shinpei Yoshitake, Yasuo Iimura, and Toshiyuki Ohtsuka

Abstract Rainfall enriches the dissolved organic carbon (DOC) after passing through the tree canopy. DOC is exported down stems as stemflow and through leaves, branches, and gaps as throughfall. In this paper, we synthesized the trends and factors that affect the DOC concentrations and fluxes of throughfall and stemflow in a cool-temperate deciduous broad-leaved forest (TDF) and a warm-temperate/subtropical evergreen broad-leaved forest (SEF), and reviewed the literature for various forests in different climatic zones around the world. The DOC concentrations were higher in stemflow (6–332 mg C L^{-1}) than in throughfall (5–29 mg C L^{-1}). The throughfall and stemflow DOC fluxes reported from natural forests in different climate zones range from 1.9 to 48 and 0.01 to 8 g C m^{-2} $year^{-1}$, respectively. The controls on throughfall and stemflow DOC concentrations are diverse, including rainfall characteristics, tree morphology, canopy phenology, and preceding atmospheric deposition. DOC fluxes in the forest carbon cycle act as a pathway, with water being essential to the carbon input of mineral soil. Studies of the fate of DOC in forest ecosystems may provide direct verification of soil C sequestration. Additional research is required to understand the significance of stemflow and throughfall DOC to forest C cycling.

S. Chen
School of Environmental and Life Science, Nanning Normal University, Nanning, China

R. Cao
River Basin Research Center, Gifu University, Gifu, Japan

School of Ecology and Environment, Northwestern Polytechnical University, Xi'an, China

S. Yoshitake
Faculty of Education and Integrated Arts and Sciences, Waseda University, Tokyo, Japan

Y. Iimura
School of Environmental Science, The University of Shiga Prefecture, Hikone, Japan

T. Ohtsuka (✉)
River Basin Research Center, Gifu University, Gifu, Japan
e-mail: ohtsuka@gifu-u.ac.jp

F. Li et al. (eds.), *River Basin Environment: Evaluation, Management and Conservation*, https://doi.org/10.1007/978-981-19-4070-5_2

Keywords Throughfall · Stemflow · Dissolved organic carbon · DOC concentration · DOC flux

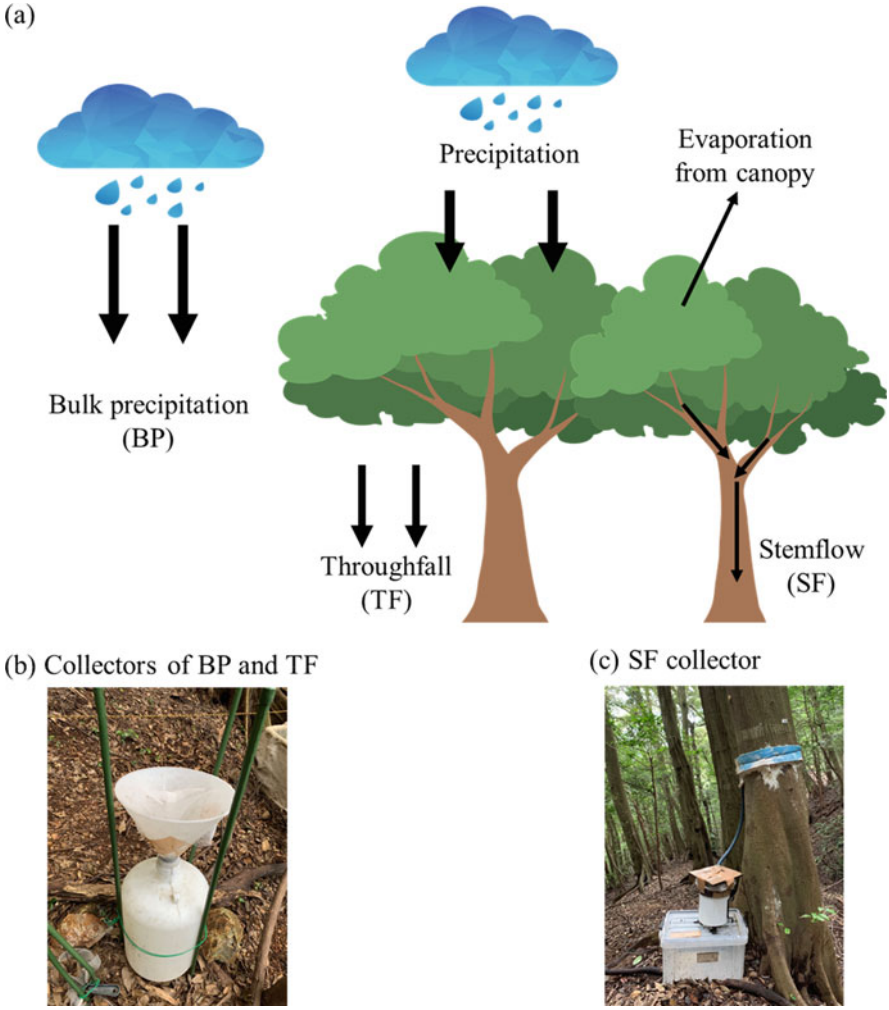

Fig. 2.1 Forest canopy redistributes rainfall into throughfall and stemflow (**a**). Funnel and a collection bottle for assessing bulk precipitation and throughfall (**b**); A stemflow collector attached to a rain gage to detect the volume of stemflow (**c**). Some of the water that passes through the rain gage is collected in a reservoir tank and sampled for analysis

2.1 Introduction

In forest ecosystems, precipitation that falls as rain, snow, or fog must first pass through the canopy before reaching the forest floor. This precipitation is partitioned into three fractions (Fig. 2.1a): (1) the interception that remains on the canopy and is evaporated after or during rainfall; (2) stemflow that flows to the ground via stems and boles; (3) throughfall that may or may not contact the canopy and that falls to the ground between the various components of the vegetation (Crockford and Richardson 2000). In other words, forest canopies redistribute rainfall into throughfall and stemflow, and these water fluxes wash various water-soluble materials out of the forest canopy, stems, and boles, and transfer them to the forest floor. Various nutrients (e.g., sulfur, nitrogen) are added when rain passes through the forest canopy, due to leaf leaching and/or anthropogenic deposition from the atmosphere onto the canopy (Bulter and Likens 1995). For example, dissolved inorganic nitrogen (e.g., NO_3^- and NH_4^+) and dissolved organic nitrogen are enriched by 8.8 and 1.5 kg N ha^{-1} $year^{-1}$, respectively, via throughfall in an urban evergreen broad-leaved forest in central Japan (Cao et al. 2020). The input of water to the forest floor is characterized by the forest composition, canopy structure, stand density, and basal area (Ford and Deans 1978; Crockford and Richardson 2000; Park and Hattori 2002); it is an important part of the material cycle in forest ecosystems.

Dissolved organic carbon (DOC) is operationally defined as organic molecules that pass through a filter, most often 0.45 μm in size. DOC can hydrologically transport carbon between different pools in the ecosystem. The DOC concentrations of rainfall are generally very low, but increase as rainwater passes through the canopy and the forest floor in the form of throughfall and stemflow (Kolka et al. 2008). Generally, the increase in the concentration of DOC due to precipitation is almost certainly a result of leaf and stem leaching, as well as microbial metabolites (biodegradable and hydrophilic neutral carbohydrates) that wash away from the canopy during this process (Guggenberger and Zech 1994; Michalzik et al. 2001; Levia et al. 2012). Thus, throughfall and stemflow are two flow paths by which DOC is removed from the canopy and transferred to the forest floor. Moreover, DOC is the major form of carbon that is transported from the soil solution to streams (Michalzik et al. 2001; Perakis and Hedin 2002).

We investigated the concentrations and fluxes of DOC in precipitation, throughfall, and stemflow in two contrasting forest ecosystems; a cool-temperate deciduous broad-leaved forest (TDF) and a warm-temperate/subtropical evergreen broad-leaved forest (SEF) (Chen 2019). These two types of secondary forests encompass the deciduous forest in a rural deep snow area and the evergreen forest in an urbanized area in the central region of the main island of Japan, where long-term forest monitoring have been intensively investigated. Annual measurements of the forest NPP began in 1998 using a permanent plot (Ohtsuka et al. 2009) beneath a flux tower (Yamamoto et al. 1999; Saigusa et al. 2002) on the site in the TDF, while the measurement of tree growth began in 1989 in the SEF (Chen et al. 2017a). The pattern and process of DOC fluxes in throughfall and stemflow should differ across

the contrasting two forests. Although some intensive research has already been conducted, few detailed annual studies have evaluated the contribution of throughfall and stemflow to the annual C budget using the permanent plots.

In this work, we summarized the DOC concentrations and fluxes within the throughfall and stemflow in the two contrasting forests, and reviewed studies of various forests in different climatic zones around the world. Moreover, we evaluated the contribution of DOC fluxes to the ecosystem carbon cycle. The two hydrologic pathways (stemflow and throughfall) in the forest canopy, particularly stemflow, have been rarely investigated within the context of the forest C cycle; this may be partly because DOC fluxes are generally not considered to be critical components of the carbon balance in an ecosystem, being extremely small relative to the carbon fluxes of primary productivity or heterotrophic respiration in terrestrial systems (Hope et al. 1994; Schimel 1995). The objectives of this article were: (1) to compare the dynamics of DOC concentrations and fluxes in throughfall and stemflow using current data, including that from our own studies; (2) to review current knowledge of the processes that influence the dynamics of throughfall and stemflow DOC concentrations and fluxes; and (3) to evaluate all current knowledge to identify major gaps.

2.2 Methodology

2.2.1 Site Description

The TDF used in this study is an experimental forest of the Takayama Field Station, belonging to the River Basin Research Center at Gifu University (36°08′N, 137°25′E, 1420 m a.s.l.). The dominant species are *Quercus crispula, Betula ermanii,* and *B. platyphylla* var. *japonica*, with a basal area of 32.3 m^2 ha^{-1} (Ohtsuka et al. 2005; Saitoh et al. 2012). A permanent plot of 1 ha (100 × 100 m) was set on a west-facing slope. The soil of the study site can be classified as andisol, as well as Japanese volcanic ash soil (Chen et al. 2017b). The annual mean air temperature of the site is 7.3 °C, the average annual precipitation is approximately 2400 mm (2014–2015) distributed throughout the year, and the snow depth is usually 1–2 m in the winter (December–April).

The SEF used in this study is located on Mt. Kinka, central Japan. The topography of the area is hilly with young soil. The bedrock is composed of sedimentary rock on a chert layer. In 1989, a 0.7-ha study plot (70 × 100 m) was established on the lower slopes of Mt. Kinka (ca. 60 m a.s.l., 35°26′ N, 136°47′ E), with a basal area of 46.1 m^2 ha^{-1}. The dominant tree species in this forest is *Castanopsis cuspidata,* which accounts for 87.9% of the basal area (Chen et al. 2017a). The annual mean temperature is 16.1 °C and the average annual precipitation is 1866 mm. It is slightly snowy in the winter.

2.2.2 Experimental Setup and Sample Collection

Nine throughfall collectors were set in each forest, with each throughfall collector consisting of a 21-cm diameter funnel and 12-L collection bottle; samples were collected monthly (Fig. 2.1b). Samples of bulk precipitation were collected using a 12-L bottle set up in a location without a canopy that was near the study area in both sites. Samples were collected from the TDF and SEF from May to November 2015, and from January to December 2017, respectively.

Stemflow collectors (Fig. 2.1c) consisted of a PE film surrounding a tree trunk like a collar, with a tube connecting the collar to a rain gage to measure water volume. Moreover, a reservoir tank (12 L) was set under the rain gage to collect monthly water samples. In the TDF, stemflow collectors were installed on three tree stems in each of the three main species (*Q. crispula, B. ermanii,* and *B. platyphylla* var. *japonica*). In the SEF, stemflow collectors were installed on 12 tree stems of various diameter at breast height classes (20–50 cm) of the dominant species, *C. cuspidata*. The sampled trees were evenly distributed across the both study plots.

During the snowy season in the TDF, snowpack samples were collected in January 2016 and January 2017, when the snowpack had accumulated to its thickest amount. Within the plot, three random locations were selected as sampling points. Snow samples were collected using a 100-mL soil corer from the snow surface to the soil surface (64.3 cm snow depth in January 2016, and 107 cm snow depth in January 2017). Because there was no tree canopy cover, and the understory was also overwhelmed by thick snowpack during the snow season, we assumed that throughfall was the same as bulk precipitation and that there was no stemflow.

2.2.3 Chemical Analysis and Calculation of Fluxes

All water samples were filtered through a 0.45-μm MF-Millipore nitrocellulose membrane. The concentrations of DOC in the solution were measured using a total organic carbon analyzer (TOC-V, Shimadzu, Japan). Additionally, DOC fluxes were calculated based on the average concentration (mg L^{-1}) and water depth (mm) during each sampling time. See Chen et al. (2017b) for further details.

We used the net throughfall (TF) and net stemflow (SF) to identify the DOC fluxes that were influenced by the canopy and trunk. Net TF and net SF were calculated using the following formulas:

$$\text{net TF} = (\text{DOC}_{\text{TF}} — \text{DOC}_{\text{BP}}) \times \text{V}_{\text{TF}};$$

$$\text{net SF} = (\text{DOC}_{\text{SF}} — \text{DOC}_{\text{BP}}) \times \text{V}_{\text{SF}};$$

where DOC_{TF} is the DOC concentration of collected samples of throughfall, DOC_{SF} is the DOC concentration of collected samples of stemflow, DOC_{BP} is the DOC

concentration of collected samples of bulk precipitation, V_{TF} is the volume of throughfall, and V_{SF} is the volume of stemflow.

2.3 Dynamics of DOC Concentrations in Forest Ecosystems

2.3.1 DOC Concentration in TDF and SEF

When bulk precipitation entered the forest, the DOC concentration increased in both the TDF and SEF (Table 2.1). During the growing season, in the TDF, the mean DOC concentration in stemflow (15.05 mg C L^{-1}) was much higher than that in throughfall (7.08 mg C L^{-1}) and was more than seven times higher than that in bulk

Table 2.1 Water budget of precipitation, and annual mean dissolved organic carbon (DOC) concentration and fluxes of different hydrological fluxes in a cool-temperate deciduous forest (TDF) and a warm-temperate/subtropical evergreen forest (SEF)

Forest type		Bulk precipitation	Throughfall	Stemflow
Water budget (mm period^{-1})				
	TDF (Growing season)	1592	1122	42.5
	TDF (Snow season)	864	≃864	≃0
	SEF	1864	1436	67.7
Proportion of bulk precipitation (%)				
	TDF (Growing season)	–	70.5	2.7
	TDF (Snow season)	–	≃100	≃0
	SEF	–	77.0	3.6
DOC concentration (mg C L^{-1})				
Mean	TDF (Growing season)	2.98 ± 0.45	7.08 ± 0.42	15.1 ± 0.98
	TDF (Snow season)	0.98 ± 0.10	–	–
	SEF	2.80 ± 0.37	6.62 ± 1.62	11.9 ± 0.96
Range	TDF (Growing season)	1.03 ~ 4.74	1.63 ~ 19.5	3.60 ~ 37.90
	TDF (Snow season)	0.33 ~ 2.20	–	–
	SEF	0.68 ~ 5.32	1.79 ~ 22.2	4.96 ~ 17.25
DOC flux (g C m^{-2} period^{-1})				
	TDF (Growing season)	4.55	7.94	0.62
	TDF (Snow season)	0.27	≃0.27	≃0
	TDF (Annual)	4.82	8.21	0.62
	SEF (Annual)	3.54	7.30	0.90
net DOC flux (g C m^{-2} period^{-1})				
	TDF (Growing season)	–	4.77	0.50
	TDF (Snow season)	–	≃0	≃0
	TDF (Annual)	–	4.77	0.50
	SEF (Annual)	–	4.82	0.62

We assumed no net flux of throughfall (throughfall ≃ bulk precipitation) and no stemflow in the snow season in the TDF. Data from Chen et al. (2017b) and Chen (2019)

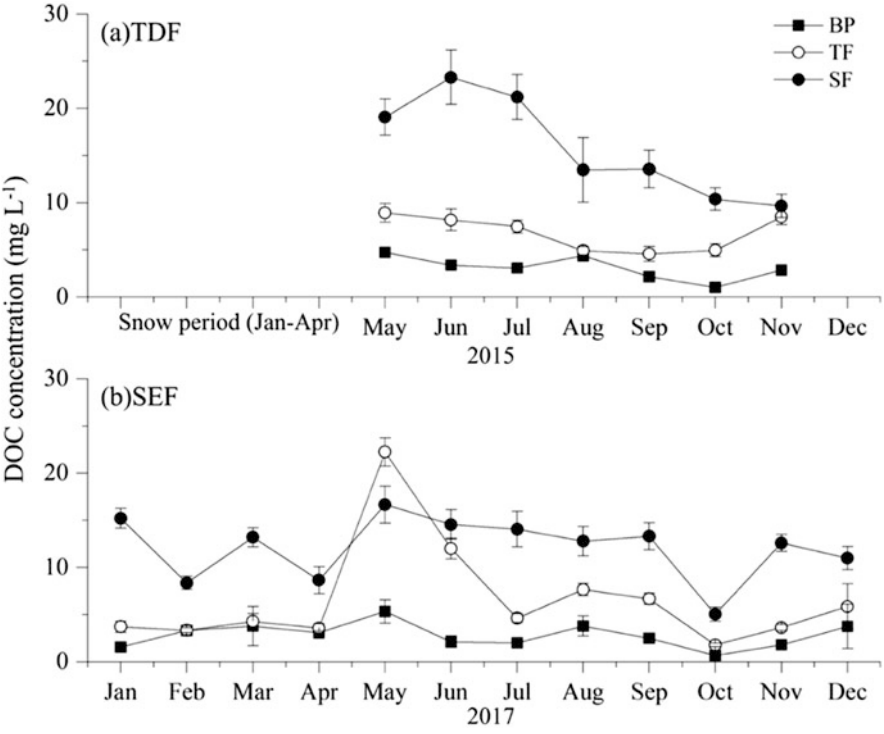

Fig. 2.2 Monthly average dissolved organic carbon (DOC) concentrations of bulk precipitation (BP), throughfall (TF), and stemflow (SF) in a cool-temperate deciduous forest (TDF) in 2015 (**a**), and a warm-temperate/subtropical evergreen forest (SEF) in 2017 (**b**). Data from Chen et al. (2017b) and Chen (2019)

precipitation (2.98 mg C L^{-1}; $p < 0.05$). In the SEF, the annual mean DOC concentrations in throughfall (6.62 mg C L^{-1}) and stemflow (11.87 mg C L^{-1}) were 2.4 and 4.2 times greater than that in precipitation (2.80 mg C L^{-1}), respectively (Table 2.1). The mean concentrations of DOC in bulk precipitation and throughfall were nearly the same in both forests.

There were seasonal changes in the stemflow DOC concentration in the TDF (Fig. 2.2a). The DOC concentration in stemflow was high during the early summer (June or July), then gradually decreased. Compared with stemflow, the DOC concentrations in throughfall and bulk precipitation did not show a distinct monthly variation in the TDF (Fig. 2.2a). Similarly, the DOC concentration in precipitation did not show a distinct monthly variation in the SEF; however, the DOC concentrations in throughfall and stemflow exhibited significant monthly variations (Fig. 2.2b). In May, the DOC concentrations in throughfall and stemflow were 22.24 and 17.24 mg C L^{-1}, respectively, which corresponded to the highest values of the year, before they gradually decreased (Fig. 2.2b).

2.3.2 *Factors Affecting DOC Concentration in Throughfall*

To date, throughfall has been sampled in most forest ecosystems, including various climatic zones, although research in boreal forests is sparse (Table 2.3). Previous studies have reported that the throughfall DOC concentration in subtropical and temperate forests ranges from 5 to 11 and 7.08 to 29 mg L^{-1}, respectively (Fig. 2.3a). Throughfall DOC concentration ranges are greatest in temperate forests, likely due to their pronounced differences in seasonal leaf states. Conversely, studies of evergreen forest types (subtropical and boreal forests) have noted the lowest variability in throughfall DOC concentrations. The lowest and second-lowest mean throughfall DOC concentrations have been noted in tropical and subtropical forests; this be attributed to their high rainfall conditions, with some studies reporting that large or intense storms are able to wash tree surfaces clean and dilute DOC concentrations (Goller et al. 2006; Levia et al. 2012). In this study, the DOC concentrations of stemflow and throughfall in the TDF and SEF (Table 2.1) were slightly lower than those in previous reports (9–29 mg C L^{-1}), while the DOC concentrations in the precipitation (2.98 and 2.80 mg C L^{-1}) was somewhat higher than those reported in other studies (1.8–2.7 mg C L^{-1}; Currie et al. 1996; Michalzik and Matzner, 1999; Moreno et al. 2001; Solinger et al. 2001).

In the SEF, there was a positive correlation between throughfall DOC concentration and the dry weight of litterfall (Table 2.2). Nitta and Ohsawa (1997) reported that the leaf phenology of *Castanopsis sieboldii* peaked in May, simultaneously with leaf emergence in central Japan. Altogether, we assumed that the amount of litter fall did not directly affect the DOC concentration, but the phenological phenomena on the canopy (e.g., new leaf emergence, florescence) had a great impact on the throughfall DOC concentration. The mean DOC concentration of snowpack (0.98 ± 0.10 mg C L^{-1}) in the TDF was much lower than that in throughfall (7.08 ± 0.42 mg C L^{-1}) during the growing season, due to the leafless conditions (Table 2.1). Comiskey (1978) reported that throughfall DOC concentrations beneath a summer, fully leafed canopy were more than 20 times greater than during the winter, under leafless conditions, in a temperate deciduous forest. Moreover, Solinger et al. (2001) observed obvious changes in throughfall DOC concentrations that significantly correlated with mean seasonal air temperature in a central European deciduous forest.

In both the SEF and TDF, there were no significant correlations between the DOC concentration in the different hydrological fluxes and the precipitation amount (Table 2.2). Rainfall amounts and intensity are uncertain factors with respect to their impact on DOC concentrations; some studies, including our study, have revealed that DOC concentrations are independent of rainfall amount (Solinger et al. 2001; Michalzik et al. 2001), whereas other studies have found that the DOC concentrations in throughfall and stemflow are inversely related to rainfall amount and intensity (Goller et al. 2006; Levia et al. 2012), indicating that large or intense storms may wash tree surfaces clean and dilute tree DOC. The rainfall dilution effect on DOC concentration may be offset by other covarying factors, such as biological

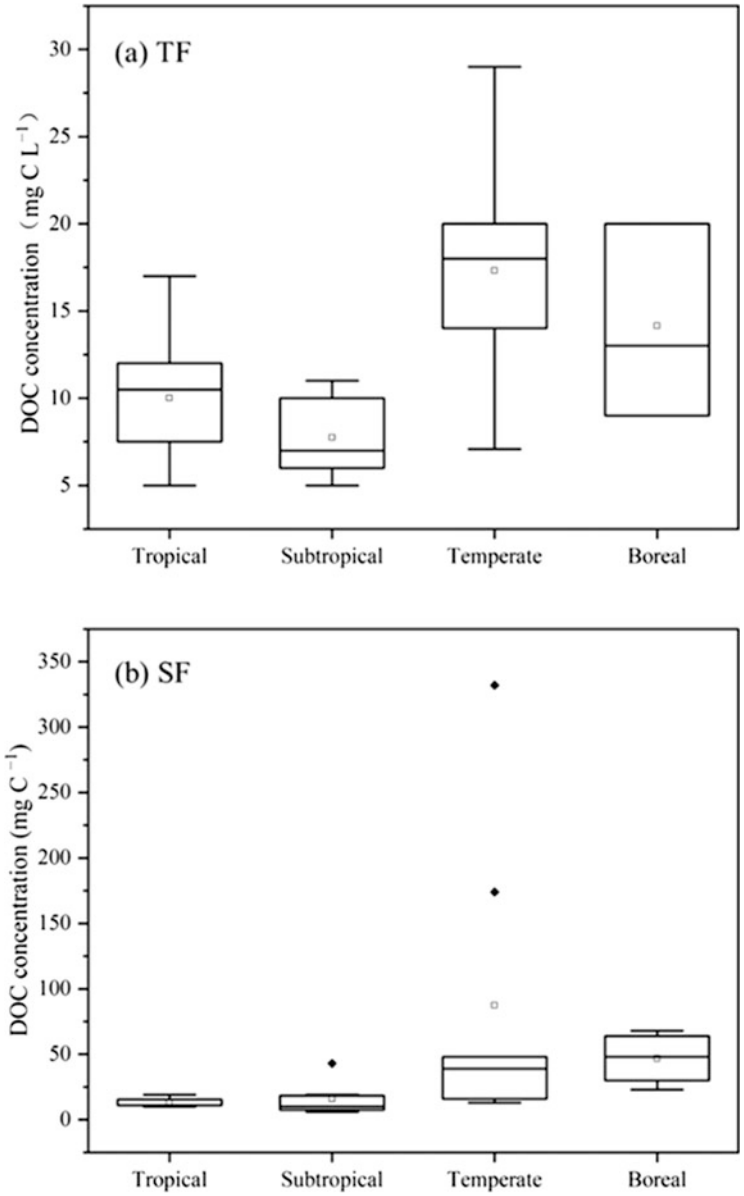

Fig. 2.3 Mean values and ranges of throughfall (**a**) and stemflow (**b**) dissolved organic carbon (DOC) concentrations in different forest types, across climate zones

Table 2.2 Correlation coefficients between the monthly mean DOC concentrations and the monthly DOC fluxes in throughfall and stemflow, with environmental factors such as monthly precipitation, monthly mean temperature, and litter fall in a cool-temperate deciduous forest (TDF, n = 7) and a warm-temperate/subtropical evergreen forest (SEF, n = 12)

	Monthly mean DOC concentrations		Monthly DOC fluxes				
	Throughfall	Stemflow	Throughfall	Stemflow	Monthly precipitation	Monthly mean temperature	Litter fall
	(mg C L^{-1})		(g C m^{-2} $month^{-1}$)		(mm)	(°C)	(g m^{-2} $month^{-1}$)
Temperate deciduous forest (TDF)							
DOC concentration							
Throughfall (TF)	–	0.842*	0.631	–	−0.109	0.072	−0.067
Stemflow (SF)	0.842*	–	–	0.399	−0.402	0.548	−0.289
DOC flux							
Throughfall (TF)	0.631	–	–	0.210	−0.226	0.211	−0.083
Stemflow (SF)	–	0.399	0.210	–	0.300	−0.077	−0.045
Warm-temperate/subtropical evergreen forest (SEF)							
DOC concentration (mg C L^{-1})							
Throughfall (TF)	–	0.708	0.726**	–	−0.210	0.364	0.716**
Stemflow (SF)	0.708**	–	–	−0.432	−0.475	0.318	0.414*
DOC flux (g C m^{-2} $month^{-1}$)							
Throughfall (TF)	0.726**	–	–	0.329	0.323	0.459	0.516
Stemflow (SF)	–	−0.432	0.329	–	0.917**	0.754*	0.071

Data from Chen et al. (2017a) and Chen (2019)
* indicates significant relationships at $p < 0.05$
** indicates significant relationships at $p < 0.01$

activities and changes in leaf leaching (Yan et al. 2015). Furthermore, variations in DOC concentration are profound between wet and dry seasons, with throughfall and stemflow DOC concentrations being ~10 times higher at the start of the rainy season due to the accumulation of materials during the dry season (Laclau et al. 2003; Ciglasch et al. 2004).

2.3.3 *Factors Affecting DOC Concentration in Stemflow*

Similarly to throughfall, stemflow DOC concentration ranges are large for most temperate forests and small for evergreen forests (Fig. 2.3b); the DOC concentration of stemflow in subtropical and temperate forests ranges from 6 to 43 and 13 to 332 mg L^{-1}, respectively (Fig. 2.3b). Stemflow DOC concentrations (volume-weighted means) show greater variabilities across forest types (6–332 mg C L^{-1}) than is noted with throughfall concentrations (5–29 mg C L^{-1}). From this study, the DOC concentrations of stemflow in the TDF and SEF were within the lower range of the previous reports, as was the case for throughfall (Table 2.1). The sources of stemflow DOC are dry deposition, canopy and trunk leaching, and incident precipitation. There were significant and positive relationships between the concentrations of DOC in stemflow and the DOC in throughfall in both the SEF and TDF (Table 2.2), with DOC concentration increasing in both forests in the sequence from precipitation to throughfall. Moreover, the stemflow was similar to those reported in other forests (Tesón et al. 2014). Levia et al. (2012) also reported that stemflow DOC concentrations diminished by 50–60% under leafless canopy conditions, compared to fully leafed conditions, likely due to dilution by the enhanced stemflow generation of leafless canopies, but possibly also due to the decrease in leaf surface area and biological activity associated with winter senescence. Phenological phenomena, such as leaf shed during the winter season in the TDF, and leaf and flowering flush in the spring in the SEF, also had indirect impacts on the DOC concentrations of stemflow.

For stemflow, the ability of tree species-specific canopy structures to funnel rainfall to their stem is a factor that affects DOC concentrations (Van Stan and Stubbins 2018). Although increasing rainfall amounts have been similarly shown to dilute throughfall DOC concentrations (Levia et al. 2012), no clear species-specific structural influences over throughfall DOC concentrations have been identified. In the TDF, the stemflow DOC concentration of *Quercus* species was significantly higher than that of either *Betula* species (Chen et al. 2017b); this is owed to the rough and multi-layered fibrous bark of *Quercus*, which retains precipitation longer than the single-layered bark of *Betula*, allowing more DOC to leach. These results match those observed in earlier studies (Inagaki et al. 1995; Levia and Herwitz 2002), in which the DOC concentrations in stemflow were regulated by the retention time of precipitation in the bark, implying that the DOC concentration in stemflow is affected by different bark morphologies.

2.4 Dynamics of DOC Fluxes in Forest Ecosystems

2.4.1 Water Partitioning

The partitioning of gross rainfall into throughfall, stemflow, and intercepted water is controlled by the forest composition, seasonality and canopy foliar status, rainfall characteristics, and meteorological conditions (Siegert and Levia 2014). During the growing season (May–November 2015), the bulk precipitation flux in the TDF was 1592.3 mm, which was partitioned into stemflow (42.5 mm, 2.7% of bulk precipitation) and throughfall (1122.3 mm, 70.5%; Table 2.1). The annual bulk precipitation flux in the SEF was 1864 mm, which was partitioned into stemflow (67.7 mm, 9.0% of bulk precipitation) and throughfall (1436 mm, 77.0%; Table 2.1). Throughfall inputs and canopy interception varied across the different kinds of forests; mean throughfall inputs are reported to range from 27 to 96%, whereas canopy interception loss is reported to range from 9.7 to 19.5% in deciduous forests (Price and Carlyle-Moses 2003). In Japan, the throughfall range has been reported to be from 64 to 97% (Ikawa 2007). In our study, the throughfall (70.5%) and canopy interception (11.6%) measured in the TDF were within the ranges reported from other forests. Conversely, although the proportion of canopy interception (19.4%) in the SEF is slightly lower than that (20.2–48.2%) for a warm-temperate evergreen broad-leaved forest in Kochi, Japan (Fujimoto 1997), it is within the widely reported range of 15–30% for many broad-leaved evergreen forests around the world (Crockford and Richardson 2000; Iroume and Huber 2002).

Stemflow is the smallest fraction of gross rainfall (Helvey and Patric 1965; Levia and Frost 2003). According to Levia and Frost (2003), the mean stemflow inputs range from 0.94 to 20% of the gross rainfall in temperate forests; the average stemflow input in temperate forests is 11.3%. In the TDF and SEF, the stemflow was 2.7 and 3.6% of the gross rainfall, respectively; these are both lower than the average for temperate forests, but are still within the range observed in other forests. Tree size and bark water storage capacity are among the key factors that control stemflow intrastorm generation from deciduous species in the eastern United States (Levia et al. 2010). The lower observed volume of stemflow in the TDF may be attributable to its higher bark water storage capacity. Moreover, González-Martínez et al. (2016) found that understory importantly contributes to stemflow, particularly if the density of the understory vegetation groups is high. Furthermore, this noted difference may be due to variation in the forest structures and rainfall characteristics, as well as the sampling designs (Lloyd 1988; Xu et al. 2005).

2.4.2 DOC Fluxes in Throughfall and Stemflow

Bulk precipitation in the TDF and SEF brought 4.82 and 3.54 g C m^{-2} $year^{-1}$ of DOC into the forest canopy, respectively (Table 2.1). In TDF and SEF, the DOC

fluxes in throughfall were 8.21 and 7.30 g C m^{-2} $year^{-1}$, respectively. Canopy and trunks leached 5.27 and 5.44 g C m^{-2} $year^{-1}$ of DOC as net throughfall + stemflow in TDF and SEF, respectively. The throughfall DOC fluxes reported from natural forests in different climate zones range from 1.9 to 48 g C m^{-2} $year^{-1}$ (Table 2.4). Subtropical forests produce the greatest mean and maximum throughfall DOC fluxes (Fig. 2.4a). Additionally, the range in reported throughfall DOC fluxes is greatest for subtropical forests and lowest for boreal forests (Fig. 2.4a). Stemflow DOC fluxes range from 0.01 to 8 g C m^{-2} $year^{-1}$ and vary in response to the species-specific canopy structure (Van Stan and Gordon 2018). The stemflow DOC flux ranges are greatest for tropical forests and lowest for boreal forests (Fig. 2.4b). Although stemflow DOC flux was overlooked in most studies of carbon budgets, Johnson and Lehmann (2006) reported that several large stemflow generating tree species throughout the primary forest ecological zones can generate substantial stemflow DOC to their near-stem soils. All the world's forest types are classified by their temperature and precipitation. DOC fluxes are related to the DOC concentration and water volume, and the drivers that modulate DOC concentration are diverse, including precipitation intensity and frequency, tree morphology, phenoseason, and preceding atmospheric deposition. Therefore, the variation in the DOC fluxes of throughfall and stemflow was attributable to storm duration, storm intensity, and the length of the antecedent dry period, in context with the DOC concentration in the different forest types.

Like the DOC concentrations, the throughfall and stemflow DOC fluxes also demonstrated marked seasonality in the TDF and SEF (Fig. 2.5). In the SEF, the DOC fluxes in throughfall were not significantly correlated with precipitation but were significantly related to its DOC concentration on a monthly scale ($R = 0.726$, $p < 0.01$, Table 2.2). Conversely, in the TDF, there was no significant positive correlation between the DOC fluxes and concentration in throughfall (Table 2.2). Winter is an important season in the TDF; it induces leafed and leafless seasons. As such, we assume that the throughfall DOC concentrations and fluxes were affected by the interaction between precipitation and distinct canopy changes in the TDF.

In the SEF, precipitation was the dominant driver of DOC fluxes in stemflow at a monthly scale ($r = 0.917$, $p < 0.01$, Table 2.2). This effect has also been found in previous studies (Michalzik et al. 2001; Fujii et al. 2009). In contrast, in the TDF, there was no significant correlation between monthly stemflow DOC fluxes and monthly precipitation. Within the leafed or leafless periods in the TDF, precipitation type can affect the stemflow amount. Levia and Underwood (2004) found that winter stemflow generation from leafless deciduous trees is affected by the precipitation event type (e.g., rain, rain-to-snow, and snow-to-rain); even with similar durations, magnitudes, and intensities, different types of precipitation events can produce drastically different stemflow amounts. Furthermore, the canopy state also has a great impact on stemflow amount. Staelens et al. (2007) found that, for various species, stemflow production is greater in a leafless state, which appears to contradict the results of Levia et al. (2012), who noted that stemflow DOC flux diminishes with leaf fall because there is less canopy area to receive dry deposited or organism-derived DOM.

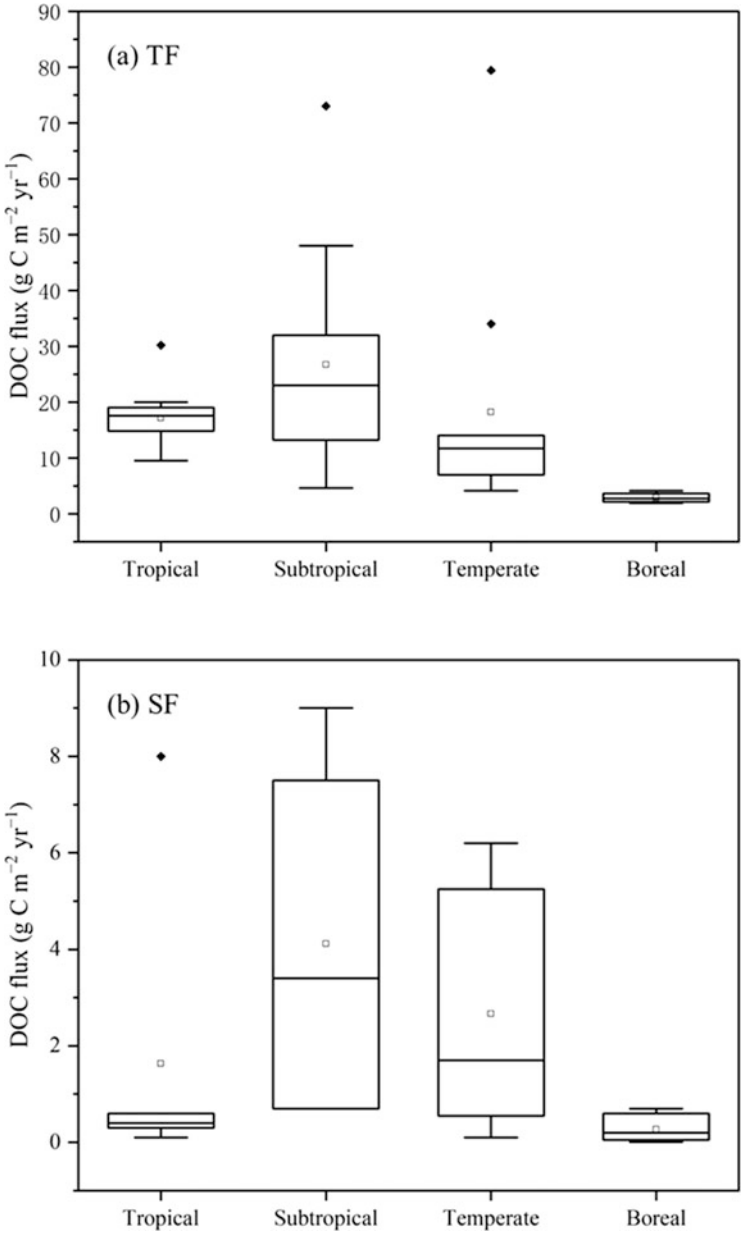

Fig. 2.4 The annual dissolved organic carbon (DOC) flux of throughfall (**a**) and stemflow (**b**) in different forest types, across climate zones

Chen et al. (2019) concluded that tree size is the main factor that controls the stemflow volume and percentage, but only when rainfall intensity is <15 mm h^{-1}.

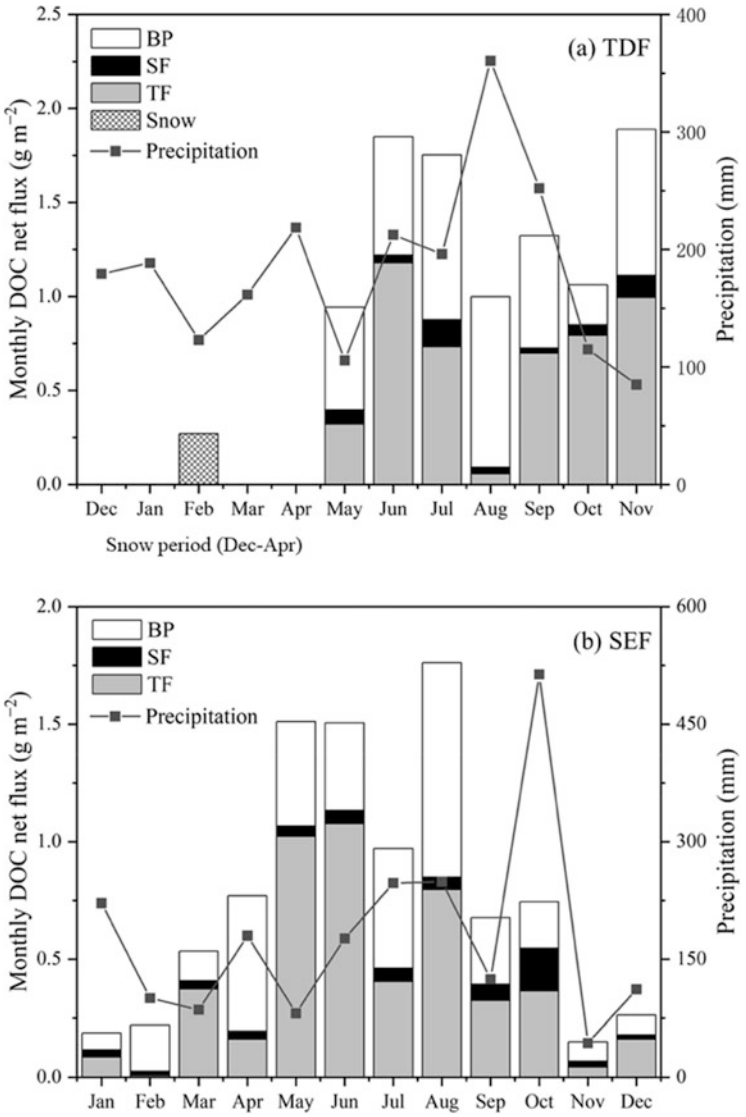

Fig. 2.5 Monthly net DOC flux (bar graph) of bulk precipitation (BP), stemflow (SF), and throughfall (TF), and monthly precipitation (line graph) in (**a**) a cool-temperate deciduous forest (TDF) and (**b**) a warm-temperate/subtropical evergreen forest (SEF). Data from Chen et al. (2017a) and Chen (2019)

The stemflow DOC fluxes were profoundly affected by tree size in the SEF. Furthermore, in the SEF, the monthly DOC fluxes in stemflow were statistically correlated with temperature ($r = 0.754$, $p < 0.05$, Table 2.2); this further supports the supposition that annual mean air temperature may be a main factor influencing

annual DOC fluxes, since many biological processes in the production and consumption of DOC depend on temperature (Michalzik and Matzner 1999; Watmough et al. 2004; Schaefer and Alber 2007). Altogether, the factors that drive both the throughfall and stemflow fluxes in the TDF were more complicated than those in the SEF; this is likely due to the profound seasonal canopy change and snow season in the TDF.

2.4.3 DOC Fluxes in the Context of the Carbon Cycle

Forest ecosystems play an important role in absorbing atmospheric CO_2 and temporarily accumulating it as organic matter. The process through which forest ecosystems accumulate organic matter, and their locations, is generally quantified by the biometric method (Ohtsuka et al. 2016). This method determines the balance between NPP, which is the amount of organic matter substantially produced by autotrophs through the absorption of CO_2, and the amount of CO_2 released by heterotrophs by decomposing organic matter, called the net ecosystem production (NEP). In forest ecosystems, the flux of water-mediated carbon (aquatic C), such as DOC, is far less than that of NPP and soil respiration, and has often been neglected in conventional biometric studies (e.g., Ohtsuka et al. 2010).

In recent years, DOC flux from soil has become a crucial component of the net ecosystem carbon budgets at the catchment scale (Webb et al. 2019). For example, in mangrove forests, part of the produced organic matter is released as DOC, but a large part of the decomposed CO_2 is released into the ocean with tidal changes as DIC (Ohtsuka et al. 2020) Furthermore, DOC leakage out of the system has been noted as the cause of differences in NEP estimates calculated using the biometric method, which quantifies organic matter accumulation in the ecosystem, and the eddy-covariance method, which quantifies the CO_2 balance in the forest canopy (Kindler et al. 2011).

In forest ecosystems, if the origin of DOC in throughfall and stemflow is plant leaching, these are part of the organic matter produced by plants. Thus, ignoring these sources is an underestimation of NPP in the biometric method. Ohtsuka (2012) reported 1.07 ± 0.26 ton C ha^{-1} $year^{-1}$ of woody production and 1.83 ± 0.12 ton C ha^{-1} $year^{-1}$ of foliage production in the TDF. In the SEF, woody production is 1.63 ± 0.08 ton C ha^{-1} $year^{-1}$ (Chen et al. 2017a), and the annual litter production of foliage and reproductive organs is 1.99 ± 0.04 and 1.35 ± 0.92 ton C ha^{-1} $year^{-1,}$ respectively (unpublished data, 2017–2019). DOC is also contained in rainfall, and the net DOC fluxes from throughfall and stemflow at the study sites were 52.7 and 54.4 kg C ha^{-1} $year^{-1}$ for the TDF and SEF, respectively (Table 2.1); these values are only 1 to 2% of the above-ground NPPs, thus the issue of underestimation is not very significant. Clark et al. (2001) stated that volatile emissions from plants, which are the source of leaching from the canopy, contribute to about 0–5% of the NPP.

Conversely, DOC flux is an important part of the process by which carbon is stored in the soil (Cotrufo et al. 2015). The DOC in the throughfall and stemflow in forest ecosystems eventually joins with the products of litter decomposition, which is supplied to the soil as litter leachate. For example, Chen (2019) studied the dynamics of litter leachate at these two sites and found that it was 311.5 kg C ha^{-1} within the growing season in the TDF and 309.5 kg C ha^{-1} per year in the SEF. The contribution of net throughfall and stemflow (Table 2.1) to litter leachate reached 16.9% in the TDF and 17.6% in the SEF. Thus, in forest ecosystems, the contribution of throughfall and stemflow to the DOC flux to the soil cannot be ignored. Moreover, the DOC flux of stemflow is often overlooked in water and carbon budgets due to the low contribution of litter leachate, compared to the throughfall; however, it can contribute substantial DOC fluxes to near-stem soils (Johnson and Lehmann 2006) and can be 10–100 times more chemically enriched than rainfall or throughfall (Van Stan and Gordon 2018).

Studies on the fate of supplied DOC to the mineral soil remain limited. Previous studies showed that nearly 50% of the DOC fluxes in throughfall consist of carbohydrates that are dominated by microbial metabolites washed from the canopy, and about 80% of these carbohydrates are easily decomposable. Thus, throughfall provides easily decomposable carbon compounds, which probably act as co-substrates or promoters for the decomposition and mineralization processes of organic carbon on the forest floor (Guggenberger and Zech 1994; Michalzik et al. 2001). Accordingly, although some DOCs are readily degradable, others are adsorbed stably by the soil and play a central role in soil carbon sequestration (Kawahigashi et al. 2006). Furthermore, some DOCs are discharged out of the system through groundwater at the watershed scale, but this does not occur to a large extent in forest ecosystems, except in mangrove forests (Webb et al. 2019). In general, the CO_2 absorbed in forest ecosystems accumulates either in the woody biomass pool of trees or in the soil carbon pool as NEP; however, biometric methods induce a great deal of uncertainty in estimates of the latter compared to the former, which can be directly quantified by allometry (Ohtsuka et al. 2013). Future studies of detailed dynamics, including input by DOC flux, as well as its short-term decomposition and DOC output at the watershed scale, may provide direct verification of soil carbon sequestration in forest ecosystems.

2.5 Conclusion

Although DOC fluxes in throughfall and stemflow are quantitatively significant fluxes of carbon, they remain poorly integrated into models, budgets, and conceptualizations of terrestrial and aquatic ecosystem biogeochemistry. Most studies have investigated the factors that control the amount and quality of throughfall and

stemflow. The factors that affect the throughfall and stemflow DOC concentrations are diverse, including rainfall chemistry, precipitation intensity and frequency, tree morphology, phenology, canopy change, and preceding atmospheric deposition.

Our results from two forest stands indicate that canopy phenological patterns (e.g., leafless snowy season, leaf and/or flowering flush) are the direct and indirect reasons for variability in throughfall and stemflow DOC concentrations. Moreover, the DOC concentrations in stemflow were regulated by species-specific retention time in the bark. The DOC flux is a result of DOC concentration and water budget. Current research suggests that rainfall frequency, rainfall amount, and rainfall partitioning all influence the throughfall and stemflow DOC fluxes. In addition to these hydrological drivers, biological drivers should also be assessed, such as tree morphology, canopy phenology, and the presence and type of epiflora and epifauna. In time, these assessments should improve our understanding and predictions of the quantity and quality of throughfall and stemflow DOC generation and export. Furthermore, stemflow brings abundant water and nutrients to the soils near stems, suggesting that stemflow may have an important influence on the ecological processes of near-stem soils, few rare studies have investigated this influence.

Acknowledgements We wish to thank the Gifu forest administration for giving us access to the Mt. Kinka site and Takayama Field Station for supporting the field surveys. We are grateful to the supports for field surveys from the members of Ohtsuka Lab. We thank Prof. Fusheng Li, River Basin Research Center, Gifu University, for providing TOC analyzer and suggestions of DOC method. We would like to thank Enago for the English language review.

Appendix Tables

Table 2.3 Annual volume-weighted mean concentrations of dissolved organic carbon (DOC) in throughfall (TF) and stemflow (SF) in various forest ecosystems across climate zones

Forest type	Mean TF (mg C L^{-1})	Mean SF (mg C L^{-1})	Study site description	References
Tropical	6 ± 3	–	Tabonuco (*Dacryodes excelsa*) forest type	McDowell (1998)
	9 ± 42	54 ± 270	Eucalypt	Laclau et al. (2003)
	10 ± 8	–	Savanna	
	12 ± 6	11 ± 12	Sedimentary plain (mature pristine rain forest)	Tobon et al. (2004)
	13 ± 12	11 ± 16	High Terrace (mature pristine rain forest)	
	11 ± 8	10 ± 14	Low Terrace (mature pristine rain forest)	
	8 ± 7	19 ±32	Floodplain (mature pristine rain forest)	
	5 ± 1	–	*Pinus kesiya*	Moller et al. (2005)
	12	15	Microcatchment 1 (evergreen montane forest)	Goller et al. (2006)
	11	14	Microcatchment 2.1 (evergreen montane forest)	
	12	–	Microcatchment 2.2 (evergreen montane forest)	
	15	–	Microcatchment 2.3 (evergreen montane forest)	
	17	19	Microcatchment 3 (evergreen montane forest)	
	9 ± 2	–	Mature forest	Schrumpf et al. (2006)
	12 ± 2	–	Secondary forest	
	7 ± 5	–	Tropical rainforest, Brazil	Germer et al. (2007)
	11 ± 4	16 ± 12	Fringe *Rhizophora mangle*	Wanek et al. (2007)
	6 ± 2	11 ± 11	Dwarf *R. mangle*	
	9 ± 0.7	–	*Shorea laevis* and *Dipterocarpus cornutus* (BS)	Fujii et al. (2009)
	5 ± 0.3	–	*Shorea laevis* and *Dipterocarpus cornutus* (BB)	
	–	40	Primary ridge forest	Hofhansl et al. (2012)
	–	16	Primary ravine forest	
	–	26	Secondary ravine forest	

(continued)

Table 2.3 (continued)

Forest type	Mean TF (mg C L^{-1})	Mean SF (mg C L^{-1})	Study site description	References
Subtropical				
	10 ± 4	10 ± 5	Secondary hardwood	Liu and Sheu (2003)
	8 ± 3	7 ± 4	Natural hardwood	
	5 ± 1	43 ± 28	*Cunninghamia lanceolate*	Wang et al. (2004)
	7 ± 3	8 ± 5	Secondary hardwood	
	6 ± 2	6 ± 2	Natural hardwood	
	11 ± 8	18 ± 14	*Schima superba*	Guo et al. (2005)
	10 ± 7	19 ± 17	*Cunninghamia lanceolata*	
	6 ± 24	–	Subtropical wet forest	Heartsill-Scalley et al. (2007)
	6.6 ± 1.3	12 ± 3.3		Present study
Temperate				
	17 ± 13	332 ± 820	Maimai (*Pinus radiata*)	Moore (1987)
	22 ± 13	43 ± 23	Larry river (*Leptospermum scoparium, P. radiata*)	
	9 ± 2	–	Deciduous forest	Qualls et al. (1991)
	25 ± 19	–	Pine forest	Currie et al. (1996)
	29 ± 44	–	Hardwood forest	
	20 ± 7	28 ± 17	*Populus tremuloides*	Kolka et al. (1999)
	20 ± 7	35 ± 32	*Betula papyrifera-Acer rubrum*	
	18 ± 4	39 ± 7	*Abies balsamea*	
	18 ± 4	174 ± 98	*Picea mariana*	
	16	16	Beech and oak	Chang and Matzner (2000)
	10	–	*Picea abies*	Frank et al. (2000)
	14	–	European deciduous forest	Solinger et al. (2001)
	–	13 ± 8	*Fagus grandifolia*	Levia et al. (2012)
	–	48 ± 35	*Liriodendron tulipifera*	
	7.08 ± 0.42	15.05 ± 0.98	Deciduous forest	Chen et al. (2017a)
Boreal				
	9	30	Broadleaved upland forest	Dalva (1991)
	13	23	Swamp forest	
	15	68	Needleleaved upland forest	
	20 ± 7	64 ± 26	*Pinus banksiana*	Moore (2003)
	20 ± 14	37 ± 19	*P. tremuloides*	
	13 ± 4	59 ± 25	*P. mariana*	
	9 ± 10	–	*Acer saccharum, Fagus grandifolia*	Turgeon and Courchesne (2008)

Table 2.4 Annual mean dissolved organic carbon (DOC) fluxes of throughfall (TF) and stemflow (SF) in various forest ecosystems across climate zones

Forest type	Mean TF ($g\ C\ m^{-2}\ year^{-1}$)	Mean SF ($g\ C\ m^{-2}\ year^{-1}$)	Study site description	References
Tropical		8	*Cyrilla racemiflora*	Frangi and Lugo (1985)
	15.1	–	Mature forest	Schrumpf et al. (2006)
	20	–	Secondary forest	
	14.8	0.3	Sedimentary plain	Tobon et al. (2004)
	19	0.3	High terrace	
	17.5	0.5	Low terrace	
	17.6	0.6	Floodplain	
	30.2	–	Tropical rainforest, Brazil	Germer et al. (2007)
	18.2		*Shorea laevis* and *Dipterocarpus cornutus* (BS)	Fujii et al. (2009)
	9.7		*Shorea laevis* and *Dipterocarpus cornutus* (BB)	
	9.5	0.1		Hofhansl et al. (2012)
Subtropical	4.6		Eucalypt	Laclau et al. (2003)
	4.8		Savanna	
	23.1	1.5	Secondary hardwood	Liu and Sheu (2003)
	18.9	0.7	Natural hardwood	
	13.2	–	Subtropical wet forest	Heartsill-Scalley et al. (2007)
	23	0.7	Oak with epiphytes	Van Stan and Stubbins (2018)
	48	5.3	Cedar with epiphytes	
	32	7.5	Bare cedar	
	73	9		Present study
Temperate	4.1	–	*Fagus grandifolia, Betula alleghaniensis, Acer saccharum*	McDowell and Likens (1988)
	34	5.6		Moore and Jackson (1989)
	13.1	–	Deciduous forest	Qualls et al. (1991)
	13.9	–	Pine forest	Currie et al. (1996)

(continued)

Table 2.4 (continued)

Forest type	Mean TF (g C m^{-2} $year^{-1}$)	Mean SF (g C m^{-2} $year^{-1}$)	Study site description	References
	11.7	–	Hardwood forest	
	6.8	0.8	*Populus tremuloides*	Kolka et al. (1999)
	14	0.5	*Betula papyrifera*	
	7.7	0.6	*Abies balsamea*	
	8.4	0.1	*Picea mariana*	
	7	–	European deciduous forest	Solinger et al. (2001)
	–	4.9	*Fagus grandifolia*	Levia et al. (2012)
	–	2.6	*Liriodendron tulipifera*	
	79.4	6.2	Deciduous forest	Chen et al. (2017a)
Boreal				
	1.9	0.1	Broadleaved upland forest	Dalva (1991)
	2.2	0.05	Swamp forest	
	2.1	0.2	Needleleaved upland forest	
	4.1	0.01	Woodland	Koprivnjak and Moore (1992)
	3.3	–	Forest	
	4	0.6	*Pinus banksiana*	Moore (2003)
	3.2	0.7	*P. tremuloides*	
	2.3	0.2	*P. mariana*	

References

Bulter TJ, Likens GE (1995) A direct comparison of throughfall plus stemflow to estimates of dry and total deposition for sulfur and nitrogen. Atmos Environ 29:1253–1265

Cao R, Chen S, Yoshitake S, Ohtsuka T (2020) Organic and inorganic nitrogen deposition in an urban evergreen broad-leaved forest in central Japan. Atmos Pollut Res 12:488–496

Chang SC, Matzner E (2000) The effect of beech stemflow on spatial patterns of soil solution chemistry and seepage fluxes in a mixed beech/oak stand. Hydrol Process 14:135–144

Chen S (2019) Controls on the dynamics of dissolved organic carbon in litter leachate in contrasting two forest ecosystems. Doctoral thesis, Gifu University

Chen S, Komiyama A, Kato S, Cao R, Yoshitake S, Ohtsuka T (2017a) Stand dynamics and biomass increment in a lucidophyllous forest over a 28-year period in central Japan. Forests 8(10):397

Chen S, Yoshitake S, Iimura Y, Asai C, Ohtsuka T (2017b) Dissolved organic carbon (DOC) input to the soil: DOC fluxes and their partitions during the growing season in a cool-temperate broad-leaved deciduous forest, central Japan. Ecol Res 32(5):713–724

Chen S, Cao R, Yoshitake S, Ohtsuka T (2019) Stemflow hydrology and DOM flux in relation to tree size and rainfall event characteristics. Agric For Meteorol 279:107753

Ciglasch H, Lilienfein J, Kaiser K, Wilcke W (2004) Dissolved organic matter under native Cerrado and *Pinus caribaea* plantations in the Brazilian savanna. Biogeochemistry 67:157–182

Clark DA, Brown S, Kicklighter W, Chambers JQ, Thomlinson JR, Ni J (2001) Measuring net primary production in forests: concepts and field methods. Ecol Appl 11:356–370

Comiskey CE (1978) Aspects of the organic carbon cycle on Walker branch watershed: a study in land/water interaction, p 509. Doctoral dissertation. University of Tennessee

Cotrufo MF, Soong JL, Horton AJ, Campbell EE, Haddix M, Wall DH, Parton J (2015) Formation of soil organic matter via biochemical and physical pathways of litter mass loss. Nat Geosci 8: 776–779

Crockford R, Richardson DJH (2000) Partitioning of rainfall into throughfall, stemflow and interception: effect of forest type, ground cover and climate. Hydrol Process 14(16–17): 2903–2920

Currie WS, Aber JD, McDowell WH, Boone RD, Magill AH (1996) Vertical transport of dissolved organic C and N under long-term N amendments in pine and hardwood forests. Biogeochemistry 35:471–505

Dalva T (1991) Sources and sinks of dissolved organic carbon in a forested swamp catchment. Biogeochemistry 15:1–19

Ford ED, Deans JD (1978) The effects of canopy structure on stemflow, throughfall and interception loss in a young Sitka spruce plantation. J Appl Ecol 15:905–917

Frangi JL, Lugo AE (1985) Ecosystem dynamics of a subtropical floodplain forest. Ecol Monogr 55:351–369

Frank H, Patrick S, Peter W, Hannes F (2000) Export of dissolved organic carbon and nitrogen from Gleysol dominated catchments – the significance of water flow paths[J]. Biogeochemistry 50 (2):137–161

Fujii K, Uemura M, Hayakawa C, Funakawa S, Sukartiningsih KT, Ohta S (2009) Fluxes of dissolved organic carbon in two tropical forest ecosystems of East Kalimantan, Indonesia. Geoderma 152:127–136

Fujimoto K (1997) Studies of elements originated from sea salt in stemflow and throughfall. Bull Kochi Univ Forest 24:147–185. (in Japanese with English abstract)

Germer S, Neill C, Krusche AV, Neto SCG, Elsenbeer H (2007) Seasonal and within-event dynamics of rainfall and throughfall chemistry in an open tropical rainforest in Rondonia, Brazil. Biogeochemistry 86:155–174

Goller R, Wilcke W, Fleischbein K, Valarezo C, Zech W (2006) Dissolved nitrogen, phosphorous, and sulfur forms in the ecosystem fluxes of a montane forest in Ecuador. Biogeochemistry 77: 57–89

González-Martínez TM, Williams-Linera G, Holwerda F (2016) Understory and small trees contribute importantly to stemflow of a lower montane cloud forest. Hydrol Process 31:1174–1183

Guggenberger G, Zech W (1994) Dissolved organic carbon in forest floor leachates: simple degradation products or humic substances. Sci Total Environ 152:37–47

Guo JF, Yang YS, Chen GS, Lin P (2005) Dissolved organic carbon and nitrogen in precipitation, throughfall and stemflow from *Schima superba* and Cunninghamia lanceolate plantations in subtropical China. J For Res 16:19–22

Heartsill-Scalley T, Scatena FN, Estrada C, McDowell WH, Lugo AE (2007) Disturbance and long-term patterns of rainfall and throughfall nutrient fluxes in a subtropical wet forest in Puerto Rico. J Hydrol 333:472–485

Helvey JD, Patric JH (1965) Canopy and litter interception of rainfall by hardwoods of the eastern United States. Water Resour Res 1:193–206

Hofhansl F, Wanek W, Drage S, Huber W, Weissenhofer A, Richter A (2012) Controls of hydrochemical fluxes via stemflow in tropical lowland rainforests: effects of meteorology and vegetation characteristics. J Hydrol 452-453:247–258

Hope D, Billett MF, Cresser MS (1994) A review of the export of carbon in river water: fluxes and processes. Environ Pollut 84:301–324

Ikawa R (2007) Literature review of stemflow generation and chemical characteristics in Japanese forests. J Jpn Assoc Hydrol Sci 37:187–200

Inagaki M, Saikai M, Ohnuki Y (1995) The effects of organic carbon on acid rain in a temperate forest in Japan. Water Air Soil Pollut 85:2345–2350

Iroume A, Huber A (2002) Comparison of interception losses in a broadleaved native forest and a *Pseudotsuga menziesii* (Douglas fir) plantation in the Andes Mountains of southern Chile. Hydrol Process 16:2347–2361

Johnson MS, Lehmann J (2006) Double-funneling of trees: stemflow and root-induced preferential flow. Ecoscience 13:324–333

Kawahigashi M, Kaiser K, Rodionov A, Guggenberger G (2006) Sorption of dissolved organic matter by mineral soils of the Siberian forest tundra. Glob Chang Biol 12:1868–1877

Kindler R, Siemens JAN, Kaiser K, Walmsley DC, Bernhofer C, Buchmann N, Cellier P, Eugster W, Gleixner G, GrÛNwald T, Heim A, Ibrom A, Jones SK, Jones M, Klumpp K, Kutsch W, Larsen KS, Lehuger S, Loubet B, McKenzie R, Moors E, Osborne B, Pilegaard KIM, Rebmann C, Saunders M, Schmidt MWI, Schrumpf M, Seyfferth J, Skiba UTE, Soussana JF, Sutton MA, Tefs C, Vowinckel B, Zeeman MJ, Kaupenjohann M (2011) Dissolved carbon leaching from soil is a crucial component of the net ecosystem carbon balance. Glob Chang Biol 17(2):1167–1185

Kolka RK, Nater E, Grigal DF, Verry ES (1999) Atmospheric inputs of mercury and organic carbon into a forested upland/bog watershed. Water Air Soil Pollut 113:273–294

Kolka R, Weishampel P, Fröberg M (2008) Measurement and importance of dissolved organic carbon. In: Hoover CM (ed) Field measurements for Forest carbon monitoring. Springer, Dordrecht

Koprivnjak JF, Moore TR (1992) Sources, sinks, and fluxes of dissolved organic carbon in subarctic fen catchments. Arct Alp Res 24:204–210

Laclau JP, Ranger J, Bouillet JP, de Dieu NJ, Deleporte P (2003) Nutrient cycling in a clonal stand of eucalyptus and an adjacent savanna ecosystem in Congo 1. Chemical composition of rainfall, throughfall and stemflow solutions. For Ecol Manag 176:105–119

Levia DF, Frost EE (2003) A review and evaluation of stemflow literature in the hydrologic and biogeochemical cycles of forested and agricultural ecosystems. J Hydrol 274(1):1–29

Levia DF, Herwitz SR (2002) Winter chemical leaching from deciduous tree branches as a function of branch inclination angle in central Massachusetts. Hydrol Process 16:2867–2879

Levia DF, Underwood SJ (2004) Snowmelt induced stemflow in northern hardwood forests: a theoretical explanation on the causation of a neglected hydrological process. Adv Water Resour 27(2):121–128

Levia DF, Van Stan JT, Mage SM, Kelley-Hauske PW (2010) Temporal variability of stemflow volume in a beech-yellow poplar forest in relation to tree species and size. J Hydrol 380(1–2, 112):–120

Levia DF, Van Stan JT, Inamdar SP, Jarvis MT, Mitchell MJ, Mage SM, Scheick CE, McHale PJ (2012) Stemflow and dissolved organic carbon cycling: temporal variability in concentration, flux, and UV-Vis spectral metrics in a temperate broadleaved deciduous forest in the eastern United States. Can J For Res 42:207–216

Liu CP, Sheu BH (2003) Dissolved organic carbon in precipitation, throughfall, stemflow, soil solution, and stream water at the Guandaushi subtropical forest in Taiwan. For Ecol Manag 172: 315–325

Lloyd CR (1988) Spatial variability of throughfall and stemflow measurements in Amazonian rainforest. Agric Forest Meterol 42:63–73

McDowell WH (1998) Internal nutrient fluxes in a Puerto Rican rain forest. J Trop Ecol 14:521–536

McDowell WH, Likens GE (1988) Origin, composition, and flux of dissolved organic carbon in the Hubbard Brook Valley. Ecol Monogr 58:177–195

Michalzik B, Matzner E (1999) Dynamics of dissolved organic nitrogen and carbon in a Central European Norway spruce ecosystem. Eur J Soil Sci 50(4):579–590

Michalzik B, Kalbitz K, Park JH, Solinger S, Matzner E (2001) Fluxes and concentrations of dissolved organic matter – a synthesis for temperate forests. Biogeochemistry 52:173–205

Moller A, Kaiser K, Guggenberger G (2005) Dissolved organic carbon and nitrogen in precipitation, throughfall, soil solution, and stream water of the tropical highlands in northern Thailand. J Plant Nutr Soil Sci 168:649–659

Moore TR (1987) An assessment of a simple spectrophotometric method for the determination of dissolved organic carbon in freshwaters. New Zealand J Mar Freshw Res 21:585–589

Moore TR (2003) Dissolved organic carbon in a northern boreal landscape. Global Biogeochem Cycles 17:1109

Moore TR, Jackson RJ (1989) Dynamics of dissolved organic carbon in forested and disturbed catchments, Westland, New Zealand 2. Larry River. Water Resour Res 25:1331–1339. https://doi.org/10.1029/WR025i006p01331

Moreno G, Gallardo JF, Bussotti F (2001) Canopy modification of atmospheric deposition in oligotrophic Quercus pyrenaica forests of an unpolluted region (central-western Spain). For Ecol Manag 149:47–60. https://doi.org/10.1016/S0378-1127(00)00544-2

Nitta I, Ohsawa M (1997) Leaf dynamics and shoot phenology of eleven warm-temperate evergreen broad-leaved trees near their northern limit in central Japan. Plant Ecol 130(1):71–88

Ohtsuka T (2012) Carbon cycling at Takayama Forest: results from intensive studies in the last decade, and further studies for a next decade. Jpn J Ecol 62:31–44. (in Japanese with English summary)

Ohtsuka T, Akiyama T, Hashimoto Y, Inatomi M, Sakai T, Jia S, Mo W, Tsuda S, Koizumi H (2005) Biometric-based estimates of net primary production (NPP) in a cool-temperate deciduous forest stand beneath a flux tower. Agric For Meteorol 134:27–38

Ohtsuka T, Saigusa N, Koizumi H (2009) On linking multiyear biometric measurements of tree growth with eddy covariance-based net ecosystem production. Glob Change Biol 15:1015–1024

Ohtsuka T, Shizu Y, Nishiwaki A, Yashiro Y, Koizumi H (2010) Carbon cycling and net ecosystem production at an early stage of secondary succession in an abandoned coppice forest. J Plant Res 123:393–401

Ohtsuka T, Negishi M, Sugita K, Iimura Y, Hirota M (2013) Carbon cycling and sequestration in a Japanese red pine *(Pinus densiflora)* forest on lava flow of Mt. Fuji. Ecol Res 28(5):855–867

Ohtsuka T, Saigusa N, Iimura Y, Muraoka H, Koizumi H (2016) Biometric-based estimations of net primary production (NPP) in forest ecosystems. In: Hikosaka K, Niinemets Ü, Anten N (eds) Canopy photosynthesis: from basics to applications volume 42 of the series advances in photosynthesis and respiration. Springer, Dordrecht, pp 333–351

Ohtsuka T, Onishi T, Yoshitake S, Tomotsune M, Kida M, Iimura Y, Kondo M, Suchewaboripont V, Cao R, Kinjo K, Fujitake N (2020) Lateral export of dissolved inorganic and organic carbon from a small mangrove estuary with tidal fluctuation. Forests 11:1041

Park HT, Hattori S (2002) Applicability of stand structural characteristics to stemflow modelling. J For Res 7:91–98

Perakis SS, Hedin LO (2002) Nitrogen loss from unpolluted south American forests mainly via dissolved organic compounds. Nature 415:416–419

Price AG, Carlyle-Moses DE (2003) Measurement and modelling of growing-season canopy water fluxes in a mature mixed deciduous forest stand, southern Ontario, Canada. Agric Forest Meteorol 119:69–85

Qualls RG, Haines BL, Swank WT (1991) Fluxes of dissolved organic nutrients and humic substances in a deciduous forest. Ecology 72:254–266

Saigusa N, Yamamoto S, Murayama S, Kondo H, Nishimura N (2002) Gross primary production and net ecosystem production of a cool-temperate deciduous forest estimated by the eddy covariance method. Agric For Meteorol 112:203–215

Saitoh TM, Nagai S, Noda HM, Muraoka H, Nasahara KN (2012) Examination of the extinction coefficient in the Beer-Lambert law for an accurate estimation of the forest canopy leaf area index. For Sci Technol 8:67–76

Schaefer SC, Alber M (2007) Temperature controls a latitudinal gradient in the proportion of watershed nitrogen exported to coastal ecosystems. Biogeochemistry 85:333–346

Schimel DS (1995) Terrestrial ecosystems and the carbon cycle. Glob Chang Biol 1:77–91
Schrumpf M, Zech W, Lehmann J, Lyaruu HVC (2006) TOC, TON, TOS and TOP in rainfall, throughfall, litter percolate and soil solution of a montane rainforest succession at Mt. Kilimanjaro, Tanzania. Biogeochemistry 78:361–387
Siegert CM, Levia DF (2014) Seasonal and meteorological effects on differential stemflow funneling ratios for two deciduous tree species. J Hydrol 519:446–454
Solinger S, Kalbitz K, Matzner E (2001) Controls on the dynamics of dissolved organic carbon and nitrogen in a Central European deciduous forest. Biogeochemistry 55:327–349
Staelens J, De Schrijver A, Verheyen K (2007) Seasonal variation in throughfall and stemflow chemistry beneath a European beech (*Fagus sylvatica*) tree in relation to canopy phenology. Can J For Res 37(8):1359–1372
Tesón N, Conzonno VH, Arturi M, Frangi JL (2014) Dissolved organic carbon in water fuxes of Eucalyptus grandis plantations in northeastern Entre Ríos Province, Argentina. Bosque 35:279–288
Tobon C, Sevink J, Verstraten JM (2004) Solute fluxes in throughfall and stemflow in four forest ecosystems in northwest Amazonia. Biogeochemistry 70:1–25
Turgeon JML, Courchesne F (2008) Hydrochemical behavior of dissolved nitrogen and carbon in a headwater stream of the Canadian shield: relevance of antecedent soil moisture conditions. Hydrol Process 22:327–339
Van Stan JT, Gordon DA (2018) Mini-review: stemflow as a resource limitation to near-stem soils. Front Plant Sci 9:248. https://doi.org/10.3389/fpls.2018.00248
Van Stan JT, Stubbins A (2018) Tree-DOM: dissolved organic matter in throughfall and stemflow. Limnol Oceanogr Lett 3(3):199–214
Wanek W, Hofmann J, Feller IC (2007) Canopy interactions of rainfall in an offshore mangrove ecosystem dominated by Rhizophora mangle (Belize). J Hydrol 345:70–79
Wang MC, Liu CP, Sheu BH (2004) Characterization of organic matter in rainfall, throughfall, stemflow and stream water from three subtropical forest ecosystems. J Hydrol 289:275–285
Watmough SA, Eimers MC, Aherne J, Dillon PJ (2004) Climate effects on stream nitrate concentrations at 16 forested catchments in south central Ontario. Environ Sci Technol 38:2383–2388
Webb JR, Santos IR, Maher DT, Kerri F (2019) The importance of aquatic carbon fluxes in net ecosystem carbon budgets: a catchment-scale review. Ecosystems 22:508–527
Xu X, Wang Q, Hirata E (2005) Precipitation partitioning and related nutrient fluxes in a subtropical forest in Okinawa, Japan. Ann For Sci 62:245–252
Yamamoto S, Murayama S, Saigusa N, Kondo H (1999) Seasonal and inter-annual variation of CO_2 flux between a temperate forest and the atmosphere in Japan. Tellus 51B:402–413
Yan J, Li K, Wang W, Zhang D, Zhou G (2015) Changes in dissolved organic carbon and total dissolved nitrogen fluxes across subtropical forest ecosystems at different successional stages. Water Resour Res 51:3681–3694

Chapter 3
Forest Carbon Sequestration in Mountainous Region in Japan Under Ongoing Climate Change: Implication for Future Research

Taku M. Saitoh, Nagai Shin, Jumpei Toriyama, Shohei Murayama, and Koh Yasue

Abstract Carbon sequestration is one of the most important ecological functions and services provided by forests in any catchment area. In addition, recent international framework requires detailed and accurate estimation of forest carbon stock, actual and potential forest carbon sequestration at national, regional, and administrative district scales under ongoing climate change. We, therefore, present an example of estimated change in potential carbon sequestration in a mountainous region of Japan under ongoing climate change at a spatial resolution of 1 km. In addition to (1) illustrating the importance of monitoring carbon processes in the field for simulating carbon fluxes at the regional scale and (2) characterizing changes in carbon sequestration in response to climate change in mountainous regions with large environmental gradients, we discuss (3) future directions of research on regional-scale carbon flux simulations from three distinct vantage points: ecological,

T. M. Saitoh (✉)
River Basin Research Center, Gifu University, Gifu, Japan
e-mail: taku@green.gifu-u.ac.jp

N. Shin
Research Institute for Global Change, Japan Agency for Marine-Earth Science and Technology (JAMSTEC), Yokohama, Japan
e-mail: nagais@jamstec.go.jp

J. Toriyama
Kyushu Research Center, Forestry and Forest Products Research Institute (FFPRI), Kumamoto, Japan
e-mail: jtori@affrc.go.jp

S. Murayama
Environmental Management Research Institute, National Institute of Advanced Industrial Science and Technology (AIST), Tsukuba, Japan
e-mail: s.murayama@aist.go.jp

K. Yasue
Mountain Research Institute, Shinshu University, Nagano, Japan
e-mail: yasue@shinshu-u.ac.jp

F. Li et al. (eds.), *River Basin Environment: Evaluation, Management and Conservation*, https://doi.org/10.1007/978-981-19-4070-5_3

forestry, and climatological/meteorological. Consequently, overcoming the challenges for three distinct vantage points will require not only further advances in individual disciplines but, also, interdisciplinary research by members of the ecology-atmospheric science community as well as transdisciplinary research linking ecology, forestry, and sociology.

Keywords Carbon sequestration · Forest · Global warming · Model simulation · Mountainous region

3.1 Introduction

Forest carbon sequestration plays a critical role in the global carbon cycle and is one of the main factors controlling the Earth's climate through biosphere–atmosphere interactions (Heimann and Reichstein 2008; Hui et al. 2015; Pugh et al. 2019). Accordingly, carbon sequestration is one of the most important ecological functions and services provided by forests in any catchment area (Chisholm 2010; Di Sacco et al. 2021). The Paris Agreement adopted at the 21st Conference of the Parties to the United Nations Framework Convention on Climate Change (COP21) held in 2015 committed signatory countries "to limit the global average temperature rise to well below 2 °C above preindustrial levels and to pursue efforts to limit the temperature increase to 1.5 °C" (IPCC 2018). A two-pronged approach for mitigating future global warming has thus been emphasized that includes the reduction of carbon emissions generated by human activity and the promotion of carbon sequestration by forests and other carbon sinks (Fawzy et al. 2020). This international framework requires detailed and accurate estimation of forest carbon stock, actual and potential forest carbon sequestration at national, regional, and administrative district scales under ongoing climate change (Lamb et al. 2021).

One of the main approaches to evaluating and forecasting future forest carbon sequestration for a given area involves the use of terrestrial ecosystem models (Cao and Woodward 1998a, b). Terrestrial ecosystem models typically consist of a physical module (water, heat, radiation balance, etc.) and a physiological module (photosynthesis, respiration, leaf phenology, carbon allocation, etc.) and enable estimation of carbon fluxes and carbon sequestration in terrestrial ecosystems (Bonan 2008). In terrestrial ecosystem models, forest carbon fluxes are expressed in terms of carbon absorption from the atmosphere via photosynthesis and carbon emissions to the atmosphere via respiration from different plant parts (leaves, branches, stems, roots) and respiration associated with microbial decomposition (Fig. 3.1). Changes in intensity and performance of various processes associated with photosynthesis and respiration in response to global warming are reflected in the carbon sequestration by forest ecosystems (Song et al. 2019). As such, in situ monitoring of fundamental carbon fluxes provides important basic information needed for forecasting future forest carbon sequestration (Ito et al. 2015). For example, among diagnostic research on the current state of forest carbon sequestration in Japan, ecological models validated by field data have been used to estimate

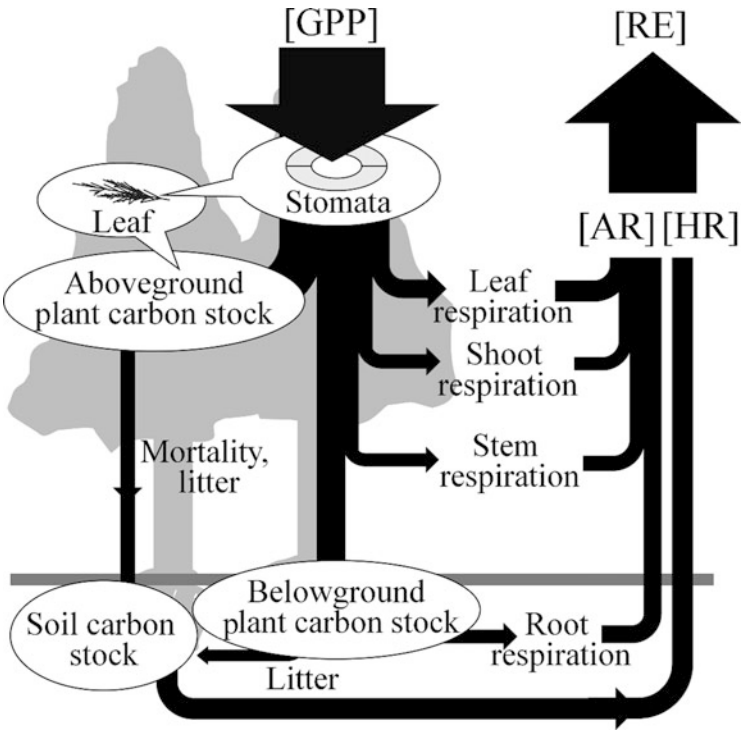

Fig. 3.1 Carbon allocation and partitioning in forest ecosystem. GPP is gross primary production, RE is ecosystem respiration, AR is autotrophic respiration, and HR is heterotrophic respiration

carbon sequestration at a spatial resolution of 1 km and to investigate environmental factors that govern this sequestration (Sasai et al. 2011; Setoyama and Sasai 2013). That said, although there are several studies that estimated future carbon sequestration in Japan at national and regional scales under ongoing climate change at a coarse spatial resolution (approx. over 10 km), much uncertainty remains (e.g., Sasai et al. 2016). One of the main reasons for this uncertainty has to do with the fact that 70% of Japan is mountainous, and there are vastly different climate zones ranging from 0 to 3000 m in elevation can be found within a horizontal distance of 100 km. The fact that forest mosaically cover 67% of the land area is likely another source of uncertainty. To be able to estimate future carbon sequestration in Japan at the administrative district (prefectural) scale, on the order of 10,000 km^2, it would be extremely useful to estimate carbon sequestration at a spatial resolution of 1 km or finer using ecological models that are validated and optimized using basic data obtained by monitoring forest carbon fluxes in the field.

In this chapter, we present an example of estimated change in potential carbon sequestration in a mountainous region of Japan under ongoing climate change at a spatial resolution of 1 km. In addition to (1) illustrating the importance of monitoring carbon processes in the field for simulating carbon fluxes at the regional scale and

(2) characterizing changes in carbon sequestration in response to climate change in mountainous regions with large environmental gradients, we discuss (3) future directions of research on regional-scale carbon flux simulations from three distinct vantage points: ecological, forestry, and climatological/meteorological.

3.2 Research Approach

3.2.1 Topography and Climate of the Target Site

We selected Gifu Prefecture, Japan, as the target site for simulations. Gifu Prefecture has a large elevation range (0 to greater than 3000 m above sea level) and experiences wide variability in annual mean temperatures and precipitation (approx. −3 to 16 °C; approx. 1800 to 3700 mm) (Fig. 3.2). Gifu Prefecture experiences distinct seasons: cold, dry winters; temperate springs and autumns; and humid and hot summers with a rainy season known as *tsuyu* in early summer under the East Asian monsoon zone. Higher elevation areas experience snow cover in winter.

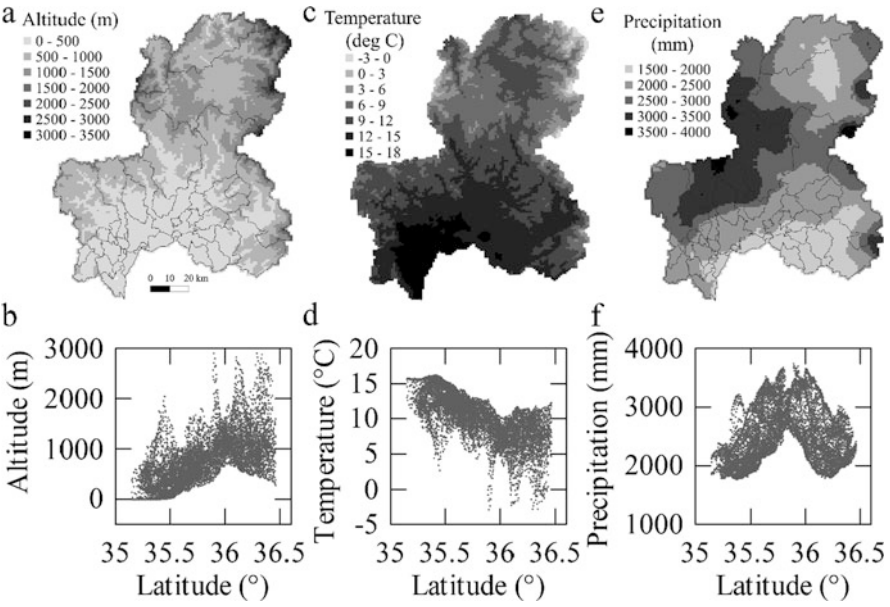

Fig. 3.2 Altitude, annual temperature, and annual precipitation under current climate condition

3.2.2 Model Validation Site

There are two flux tower sites in Gifu Prefecture: The Takayama evergreen coniferous forest site (TKC) (36°08′23′N, 137°22′15″E, 800 m a.s.l.) and the Takayama deciduous broad-leaf forest site (TKY) (36°08′46″N, 137°25′23″E, 1420 m a.s.l.). Descriptions of the vegetation and climate of both sites are provided in Table 3.1. The planted evergreen coniferous forest and natural or secondary broad-leaf forest are the two most common vegetation types in Gifu Prefecture and in Japan. In this study, we used forest carbon flux and stock data collected at these two sites to validate our ecological model.

3.2.3 Ecological Model

We used the Biome-BGC ecological model (version 4.2), which is capable of simulating carbon, water, and nitrogen fluxes in terrestrial ecosystems (Thornton 2010). The main components of ecosystem carbon flux in this model consist of a photosynthesis scheme, a carbon allocation scheme, an autotrophic respiration scheme, and a microbial decomposition scheme. Photosynthesis is primarily calculated using a photosynthesis model (Farquhar et al. 1980) and a stomatal

Table 3.1 Summary of vegetation and climate characteristics at Takayama evergreen coniferous forest (TKC) and Takayama deciduous broadleaf forest site (TKY)

	TKC	TKY
Vegetation type	Evergreen coniferous forest	Deciduous broadleaf forest
Dominant species	*Cryptomeria japonica* D. Don, *Chamaecyparis obtusa* Sieb. et Zucc.[a]	*Betula ermanii* Cham., *Quercus crispula* Blume[b]
Height of the tree canopy	20 to 25 m[c]	13–20 m[b]
Tree age	Approx. 40–50 years[a]	Approx. 60 years[b]
Understory vegetation	Sparse shrubs, herbs, and ferns[c]	Evergreen dwarf bamboo [(*Sasa senanensis* (Franch. Et Sav.) Rehder][b]
Annual mean air temperature	9.5 °C[d]	6.5 °C[e]
Annual mean rainfall	Approx. 1700 mm[d]	Approx.2100 mm[e]
Snow covered period	Late-December to late-March[f]	Early-December to mid-April[f]

[a] Saitoh et al. (2010)
[b] Ohtsuka et al. (2005)
[c] Lee et al. (2008)
[d] Average values from 2006 to 2010
[e] Saitoh et al. (2015)
[f] Visual inspection by using camera images (Nagai et al. 2018)

conductance model (Collatz et al. 1991). In the carbon allocation scheme, carbon fixed by photosynthesis is allocated to different plant parts (leaves, stems, coarse roots, fine roots, etc.) according to fixed ratios that are set in the plant physiology parameters. Autotrophic respiration is calculated as maintenance respiration expressed as a function based on temperature and plant nitrogen content plus growth respiration expressed as a proportion of productivity.

The ecological model is driven by daily maximum temperature, daily minimum temperature, daily average temperature, daily precipitation, daytime vapor pressure deficit, daytime solar radiation, and day length. In this study, we used the climate data set described in Sect. 3.2.4 as input data.

3.2.4 Climate Scenarios and Climatic Input Data

We used climate model output data (NAROv2.7r) obtained by statistical downscaling of five climate models (HadGEM2-ES, MRI-CGCM3, CSIRO-Mk3-6-0, MIROC5, and GFDL-CM3) (Nishimori et al. 2019). In this chapter, data from 1996 to 2000 were treated as current climate values and estimates from CMIP5 scenarios RCP2.6 and RCP8.5 as predicted future climate values for 2096 to 2100. For HadGEM2-ES, values for 2095 to 2099 were used as proxies for values for 2096 to 2100. We estimated daily average temperature, daytime vapor pressure deficit, daytime solar radiation, and day length using MT-CLIM module ver. 4.3 (Kimball et al. 1997; Thornton and Running 1999) based on output data from the five climate models (Toriyama et al. 2021). In this study, the atmospheric CO_2 concentration in 2000 is 369.4 ppm and it reaches 420.9 and 935.9 ppm in 2100 under RCP2.6 and RCP8.5 scenarios, respectively.

The climate models predicted that temperatures for Gifu Prefecture as a whole will increase compared to the current climate by 0.89 to 2.7 °C (mean = 1.9 °C) for scenario RCP2.6 and by 4.4 to 7.2 °C (mean = 5.3 °C) for scenario RCP8.5 (Fig. 3.3a). For both scenarios, most of the climate models predicted greater precipitation and lower solar radiation compared to current levels (Fig. 3.3b, c).

In this study, to reduce uncertainty in forest carbon sequestration estimates, we used mean values (e.g., daily maximum temperature, daily minimum temperature, precipitation, daytime solar radiation) obtained from the five climate models as input data for the ecological model. In Sect. 3.5.3, we report the results of using values from each of the five climate models separately as ecological model input values to illustrate the uncertainty of carbon sequestration estimates.

3.2.5 Model Simulations

First, to evaluate the accuracy of carbon flux simulations by the ecological model for evergreen coniferous forests and for deciduous broad-leaf forests, we ran model

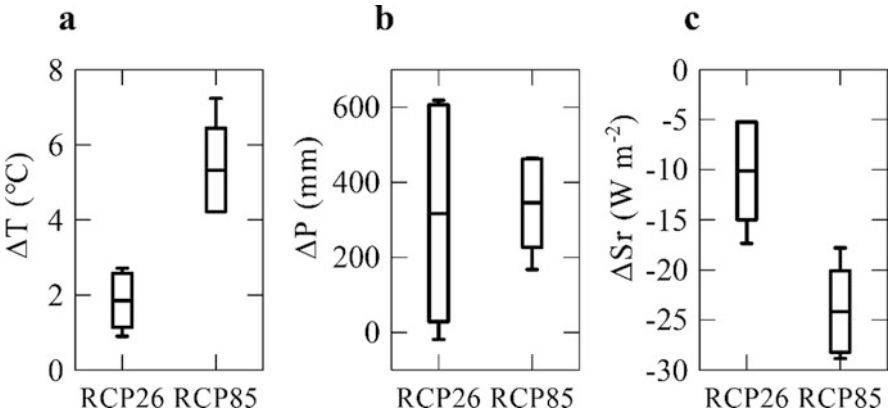

Fig. 3.3 The changes of annual temperature, annual precipitation, and annual solar radiation in the future projection relative to the current climate. Each box indicates average and standard deviation of five different climate model

simulations using meteorological data from the TKC and TKY sites (from 2006–2010 and 2002–2007, respectively) as input data. For the default simulation, we ran simulations using the default parameter settings for Biome-BGC v4.2. For modified simulations, we changed the parameters for evergreen coniferous forests and deciduous broad-leaf forests based on Toriyama et al. (2021) and Kondo et al. (2015), respectively, with some further modification and optimization.

For model simulations of Gifu Prefecture as a whole, we used the parameter sets from modified simulations. To eliminate the influence of stand age, in our analyses, we used five-year average carbon sequestration estimates for 46 to 50-year-old stands.

3.3 Importance of Field Research that Measures Actual Carbon Flux

The carbon flux of forests is expressed in terms of carbon absorption from the atmosphere through photosynthesis and carbon release to the atmosphere through respiration of various plant parts and microbial respiration associated with decomposition (Fig. 3.1). When major ecological disturbances such as fires, wind damage, snow damage, acid rain, or insect damage and non-CO_2 fluxes such as leaching, lateral transfers, harvesting, fire, herbivory, CH4, carbon monoxide, and emission of biogenic volatile organic compounds are not accounted for, net carbon sequestration can be expressed as net ecosystem production (NEP) using the following equation:

$$\mathrm{NEP} = \mathrm{GPP} - \mathrm{RE} \tag{3.1}$$

where GPP is gross primary production (carbon fixed by photosynthesis), RE is respiration of the entire ecosystem consisting of plant respiration (AR = autotrophic respiration) plus respiration associated with microbial decomposition (HR = heterotrophic respiration) (Bonan 2008; Keenan and Williams 2018). NEP can also be expressed as follows:

$$\mathrm{NEP} \cong \Delta\mathrm{B} + \mathrm{L} - \mathrm{HR} = \mathrm{NPP} - \mathrm{HR} \tag{3.2}$$

where ΔB is the change in biomass, L is litter, NPP is net primary production, and HR is microbial respiration associated with decomposition. In addition, AR can be expressed as:

$$\mathrm{AR} = \mathrm{GPP} - \mathrm{NPP} = \mathrm{RE} - \mathrm{HR} \tag{3.3}$$

Two methods can be used for monitoring each of these parameters: the eddy-covariance method and the biometric method (Chapin et al. 2006). The former method, calculate CO_2 exchange rate between ecosystem and atmosphere by measuring CO_2 concentration and 3-D wind speed at high frequencies (on the order of approximately 10 Hz) using observation towers, can be used to estimate all terms in Eq. (3.1) (Aubinet et al. 2012; Lee et al. 2004). The latter method estimates parameters via tree census or chamber method and can be used to estimate the terms in Eq. (3.2) (Ohtsuka et al. 2007). A certain level of uncertainty is associated with observations made using the eddy-covariance method and the biometric method. For example, measurements acquired at TKC and TKY using the two methods differ by approximately 40 g C m^{-2} $year^{-1}$ (Table 3.2). As such, whenever possible, it is best to use measurements obtained by both methods for model validation. Measurements for forest ecosystems in Global and East Asia obtained by both methods have been compiled and are available as Global dataset (Luyssaert et al. 2007) and, The Compilation Dataset of Ecosystem Functions in Asia (version 1.3) (Kondo et al. 2017; Chang et al. 2021), respectively.

Comparisons of default and modified simulation results (after parameter adjustment) and observed values from TKC and TKY sites are presented in Fig. 3.4 and Table 3.2. For both sites, modified simulations after parameter adjustment improved reproducibility of not only NEP but, also, other components of forest carbon flux and carbon stock (Fig. 3.4 and Table 3.2). As illustrated by this example, it is anticipated that the collection and publication of long-term continuous data using both methods over a wide range of ecosystems will facilitate improving the ability of ecosystem models to reproduce carbon fluxes.

Table 3.2 Performance of default and modified simulations of annual cumulative carbon fluxes and carbon stock in the evergreen coniferous forest at the TKC site and the deciduous broad-leaf forest at the TKY site

Site	Unit	Carbon flux and stocks	Default simulation	Modified simulation	Observation
TKC	g C m^{-2} $year^{-1}$	GPP	2330	2240	2220[a]
	g C m^{-2} $year^{-1}$	NPP	670	700	790[b]
	g C m^{-2} $year^{-1}$	NEP	90	390	390[a], 430[b]
	g C m^{-2} $year^{-1}$	RE	2240	1850	1830[a]
	g C m^{-2} $year^{-1}$	AR	1660	1540	1430[c], 1470[d]
	g C m^{-2} $year^{-1}$	HR	580	310	360[b]
	kg C m^{-2}	B	41.1	17.1	19.3[b]
TKY	g C m^{-2} $year^{-1}$	GPP	1260	1050	1000[e]
	g C m^{-2} $year^{-1}$	NPP	760	590	650[f]
	g C m^{-2} $year^{-1}$	NEP	30	170	250[e], 210[f]
	g C m^{-2} $year^{-1}$	RE	1200	880	750[e]
	g C m^{-2} $year^{-1}$	AR	500	470	350[c], 360[d]
	g C m^{-2} $year^{-1}$	HR	730	410	390[f]
	kg C m^{-2}	B	58.7	12.7	7.8[f]

GPP is gross primary production, NPP is net primary production, NEP is net ecosystem production, RE is ecosystem respiration, AR is autotrophic respiration, HR is heterotrophic respiration, and B is plant biomass

[a] Five years average (2006–2010) estimated using eddy-covariance method (Saitoh et al. 2010 and additional data)

[b] Four years average from May 2005 to March 2009 (Yashiro et al. 2010)

[c] The calculated value subtracted from GPP leaves NPP

[d] The calculated value subtracted from RE leaves HR

[e] Six years average (2002–2007) estimated using eddy-covariance method (Saigusa et al. 2005; AsiaFlux database)

[f] Five years average (1999–2003) estimated using biometric method (Ohtsuka et al. 2007)

3.4 Change in Carbon Sequestration Under Ongoing Climate Change

3.4.1 Elevation-Dependence of Cumulative Annual NEP Under the Current Climate and Contributing Factors

According to our simulations, under the current Gifu Prefecture climate with annual mean temperatures ranging from −2.9 to 16.3 °C, cumulative annual NEP was estimated to range from −32 to 515 g C m^{-2} $year^{-1}$ in evergreen coniferous forests and from −47 to 276 g C m^{-2} $year^{-1}$ in deciduous broad-leaf forests (Figs. 3.5 and 3.6). Furthermore, mean cumulative annual NEP for Gifu Prefecture (mean temperature for all grid squares: 10.5 °C) was estimated by simulations to be 436 g C m^{-2} $year^{-1}$ for evergreen coniferous forests and 229 g C m^{-2} $year^{-1}$ for deciduous broad-leaf forests. These simulated NEP values were similar to values

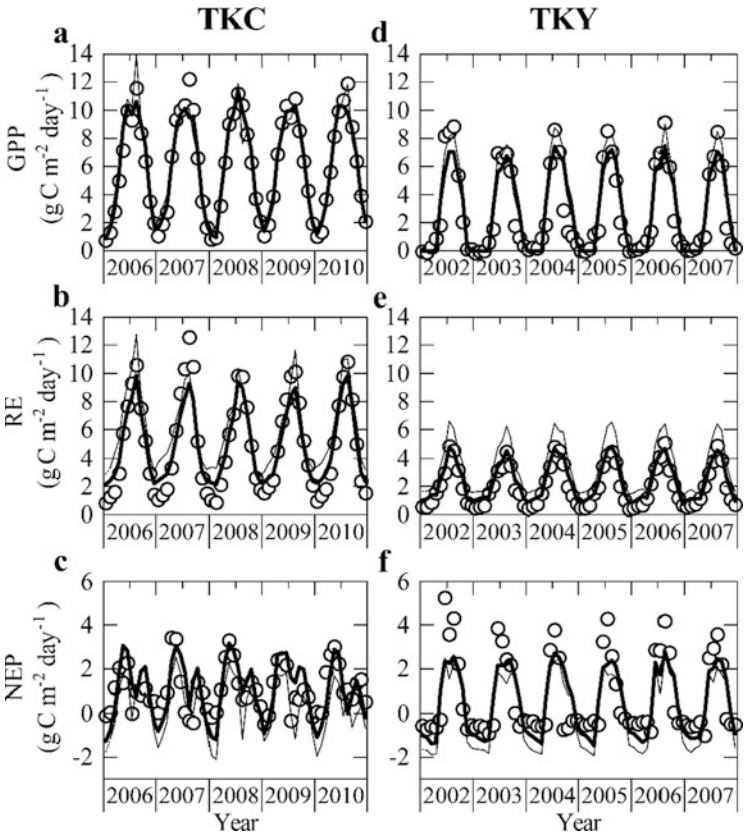

Fig. 3.4 Model performance of seasonal variation in gross primary production (GPP), ecosystem respiration (RE), and net ecosystem production (NEP) at Takayama evergreen coniferous forest (TKC) and Takayama deciduous broad-leaf forest (TKY) sites. Thin and solid lines indicate default and modified simulations, respectively. White circle indicates monthly values observed by eddy-covariance method at both forest sites

obtained previously in Japan using eddy-covariance and biometric methods: 290 to 479 g C m^{-2} $year^{-1}$ for evergreen coniferous forests (mean annual temperatures: 9.7 to 15.3 °C) and 258 to 357 g C m^{-2} $year^{-1}$ for deciduous broad-leaf forests (mean annual temperatures: 5.9 to 15.0 °C) (Table 3.3). Regarding the elevation-dependence of cumulative annual NEP, NEP tended to decrease with increasing elevation at elevations of 1000 m or higher in evergreen coniferous forests (typical mean annual temperatures of 10 °C or lower) and 500 m or higher in deciduous broad-leaf forests (typical mean annual temperatures of 13 °C or lower) but showed low sensitivity to elevation at lower elevations (Fig. 3.5c, f). These trends closely match the trends estimated for NPP with respect to elevation (Fig. 3.5b, f). In contrast, GPP tended to decrease with increasing elevation for all elevations (Fig. 3.5a, d). We attribute this result to the following three factors: (1) because

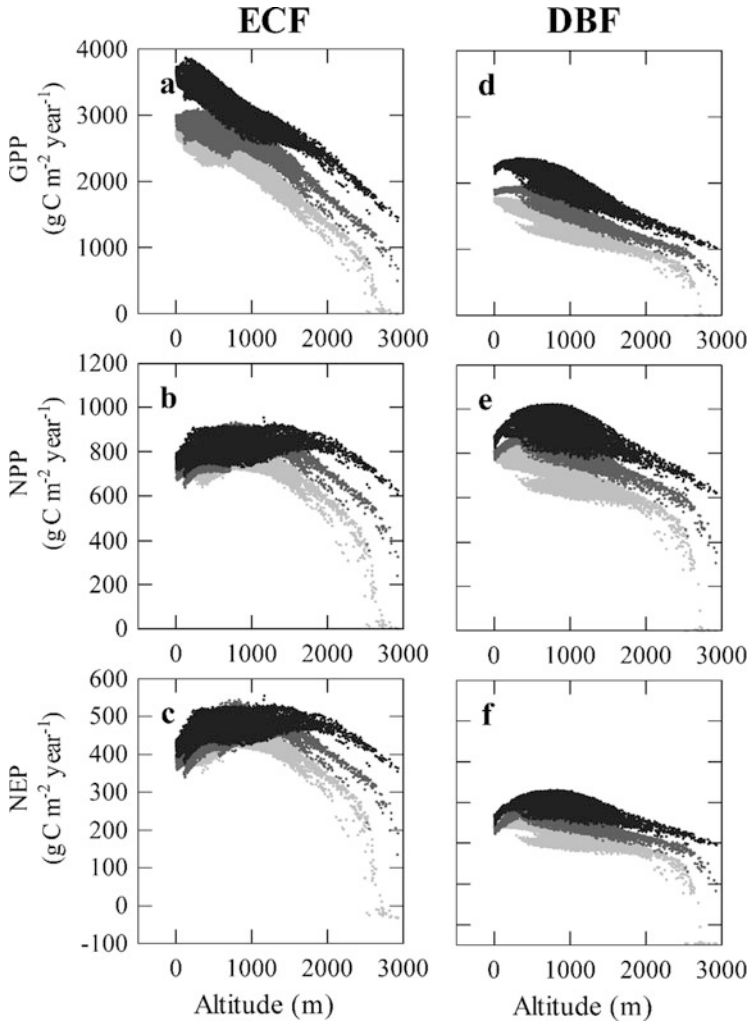

Fig. 3.5 Altitude dependency of (**a**, **d**) Annual GPP (g C m^{-2} $year^{-1}$), (**a**, **d**) Annual NPP (g C m^{-2} $year^{-1}$), and (**a**, **d**) Annual NEP (g C m^{-2} $year^{-1}$) under current (light grey), RCP26 future projection (dark grey) and RCP85 future projection (black) in evergreen coniferous forest (ECF) and deciduous broad-leaf forest (DBF)

mean annual temperature under the current climate is 20 °C or lower in this region, high temperature stress during summer is rare even in low-elevation areas and does not limit GPP; (2) because Gifu Prefecture is located in the East Asian monsoon zone, annual rainfall typically exceeds 1700 mm and summer rains known as *tsuyu* fall in June and July, summer drought stress has little impact on GPP; and (3) GPP and respiration exhibit different sensitivities to environmental factors.

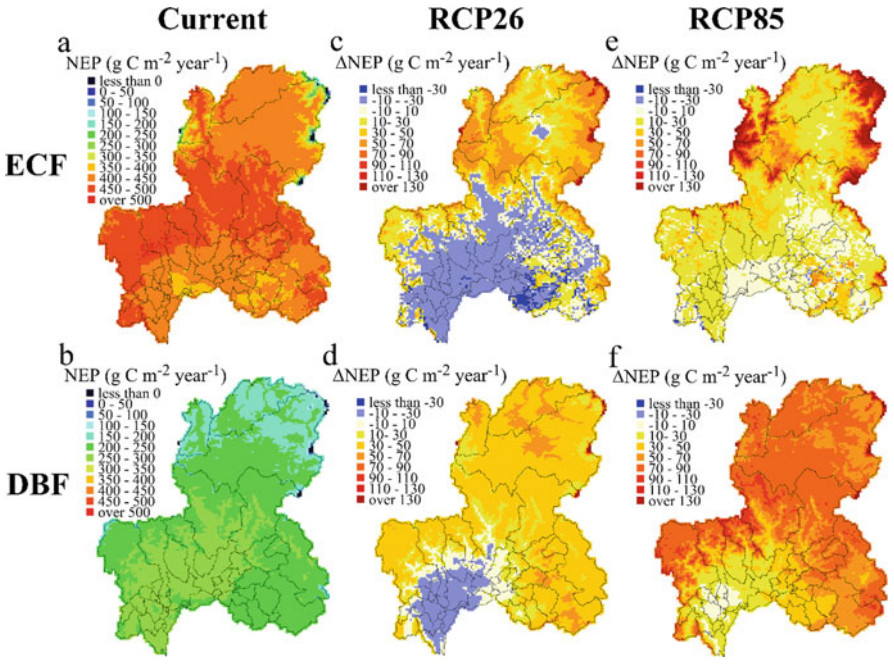

Fig. 3.6 (**a**, **b**) Annual NEP (g C m^{-2} $year^{-1}$) under current climate condition, (**c**, **d**, **e**, **f**) annual ΔNEP in the future projection relative to the current climate in evergreen coniferous forest (ECF) and deciduous broadleaf forest (DBF). Positive values in ΔNEP represent increased NEP in the future projection relative to the current climate

3.4.2 Spatial Distribution of Carbon Sequestration and its Control Factors

The spatial distributions of annual ΔNEP (predicted future NEP minus current NEP) are shown in Fig. 3.6. In both evergreen coniferous forest and deciduous broad-leaf forest simulations, whereas annual NEP in future climate projections tended to be higher than under the current climate in northern Gifu (i.e., low to moderate temperature zone), annual NEP tended to be slightly higher or lower in the south (i.e., high temperature zone) (Figs. 3.5 and 3.6). Meanwhile, annual ΔNEP showed low dependence on precipitation (Fig. 3.7). In the section below, we divide Gifu into high-, moderate-, and low-elevation zones and consider the factors contributing to ΔNEP in each of these zones.

In the high-elevation zone (generally with mean annual temperatures of 5 °C or lower), NEP was predicted to increase substantially under future climate in both evergreen coniferous forests and deciduous broad-leaf forests due to increases in summer productivity (Figs. 3.2 and 3.7). This effect was especially dramatic in the RCP8.5 scenario, which assumes the greatest temperature rise relative to present. Another contributing factor may be the lower magnitude of increase in respiration

Table 3.3 Annual cumulative net ecosystem production (NEP) in evergreen coniferous and deciduous broadleaf forests in Japan

Site Name	AsiaFlux site code	Forest type	Forest age (year)	Dominate species	Location	Annual temperature	Annual precipitation	NEP (g C m^{-2} $year^{-1}$)	References
Fujiyoshida	FJY	Temperate evergreen coniferous	90	*Pinus densiflora*	35° 27′ N, 138° 46′ E	9.7	2025	388[a], 290[b]	Mizoguchi et al. (2012), Ohtsuka et al. (2013)
Kiryu	KEW	Temperate evergreen coniferous	45	*Chamaecyparis obtuse*	34° 58′ N, 135° 59′ E	13.7–14.4	1179–1438	479[a]	Takanashi et al. (2005)
Kahoku	KHW	Temperate evergreen coniferous	32–55	*Cyptomeria japonica, Chamaecyparis obtuse*	33° 08′ N, 130° 42′ E	15.3	2130	427[a]	Ohtani et al. (2005)
Sapporo	SAP	Temperate deciduous broadleaf	90	*Betula platyphylla, Quercus crispula, Quercus mongolica*	42° 59′ N, 141° 23′ E	6.5	1100	261[a]	Nakai et al. (2003)
Tomakomai	TOE	Temperate deciduous broadleaf	45	*Quercus mongolica* var. *crispula, Acer mono*	42° 40′ N, 141° 36′ E	7.1	1200	258[a]	Shibata et al. (2005)
Appi	API	Temperate deciduous broadleaf	70	*Fagus crenata*	40° 00′ N, 140° 56′ E	5.9	2029	312[a]	Yasuda et al. (2012)

(continued)

Table 3.3 (continued)

Site Name	AsiaFlux site code	Forest type	Forest age (year)	Dominate species	Location	Annual temperature	Annual precipitation	NEP (g C m^{-2} $year^{-1}$)	References
Kawagoe	KWG	Temperate deciduous broadleaf	70	*Quercus serrata, Carpinus laxiflora, Purunus Jamasakura*	35° 52′ N, 139° 29′ E	15.0	1300	357[a]	Yasuda et al. (1998)

[a] Estimated value using eddy-covariance method
[b] Estimated value using biometric method

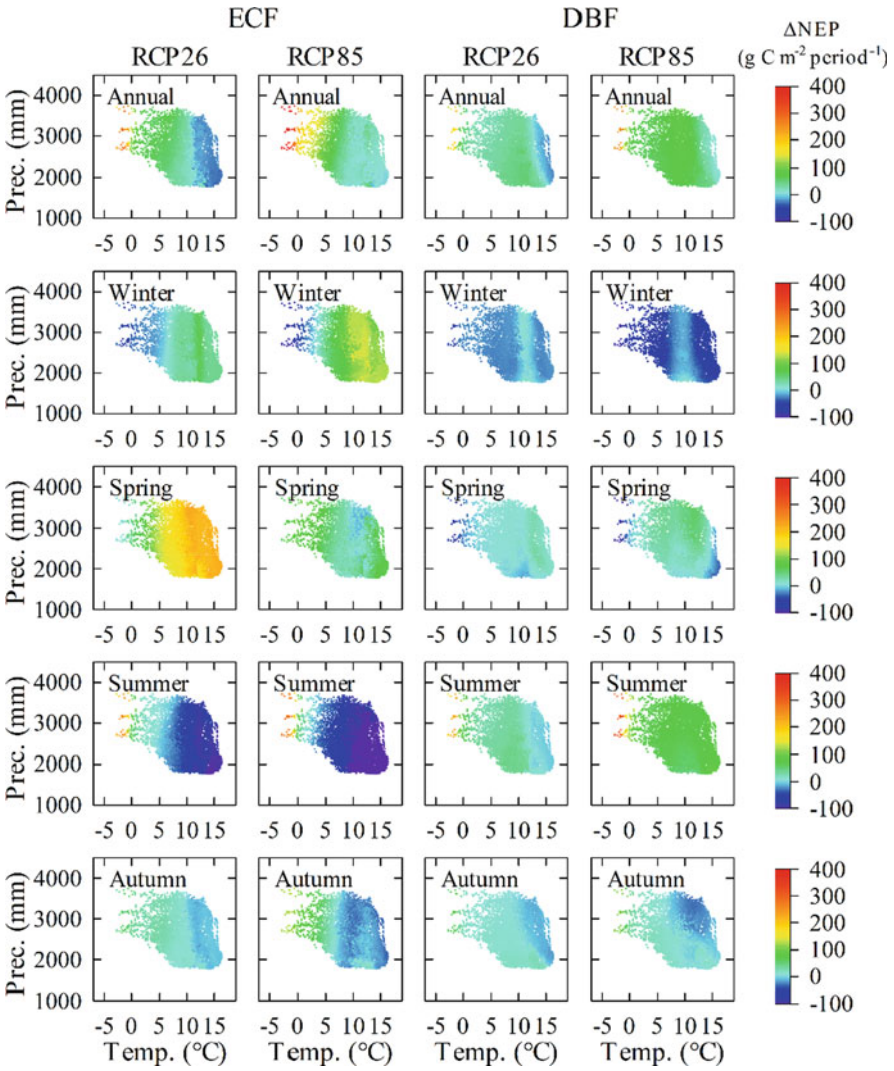

Fig. 3.7 Projected distribution of ΔNEP against annual temperature and precipitation under current climate in annual, winter (December–February), spring (March–May), summer (June–August), and autumn (September–November) periods in evergreen coniferous forest (ECF) and deciduous broadleaf forest (DBF). Positive values in ΔNEP represent increased NEP in the future projection relative to the current climate

due to soil organic matter decomposition compared to the moderate- and low-elevation zone. These trends are believed to reflect climate shift-driven conversion of high-elevation areas that are currently unsuitable for forest development into areas that are suitable for forest development.

In the moderate-elevation zone (typical mean annual temperatures between 5 and 10 °C), NEP was predicted to increase under future climate in both evergreen coniferous forests and deciduous broad-leaf forests. However, the mechanism is believed to differ between the two forest types. The increase in annual NEP of evergreen coniferous forests in future climate projections is thought to be the result of increased GPP due to warming-related improvement in photosynthetic function (Figs. 3.5 and 3.6). This effect appeared to be especially dramatic in winter and spring periods (Fig. 3.7). Investigations of cool-temperature evergreen coniferous forests in Japan based on camera monitoring and flux measurements suggest that, although the change in leaf area over an entire year is small (Nagai et al. 2012), high temperatures in early spring can increase photosynthetic potential and actual amount of photosynthesis by trees (Saitoh et al. 2010). In contrast, the increase in annual NEP of deciduous broad-leaf forests is thought to be due to an extension of the growth period due to warming. Regarding cool temperature deciduous broad-leaf forests in Japan, Saitoh et al. (2015) reported that acceleration of leafing in deciduous forests due to warming increases NEP, especially from spring to early summer. Meanwhile, NEP was found to increase only minimally or, in some scenarios, to decrease in the autumn—i.e., positive impacts of delayed leaffall were not observed. The main reason for this effect may be that cumulative light interception by the vegetation during the leaffall period, compared with leaf expansion period, was relatively low due to the different of solar elevation in both periods (Saitoh et al. 2015). Negative impacts of warming on NEP in the autumn have also been reported in North America and Europe (Piao et al. 2008). As can be seen from the above, although the mechanisms may differ between evergreen coniferous and deciduous broad-leaf forests, responses of leaf phenology to warming appears to be an important factor that should be accounted for when predicting NEP under warming conditions (Chung et al. 2013). Another possible contributing factor besides those discussed above is GPP increase due to CO_2 fertilization (e.g., Dusenge et al. 2019; Walker et al. 2021). The effect of CO_2 fertilization on GPP is current hot topics and future research is needed (e.g., Keenan et al. 2021; Wang et al. 2020).

In the low-elevation zone, whereas GPP was predicted to increase in both evergreen coniferous and deciduous broad-leaf forests (Fig. 3.5), increase in cumulative annual NEP due to warming tended to be inhibited, especially in evergreen coniferous forests. Like the moderate-elevation zone, the GPP increase in both forest types is thought to result from leaf phenology response to warming and CO_2 enrichment. The summer decrease in NEP in evergreen coniferous forests was especially dramatic compared to deciduous broad-leaf forests and kept cumulative annual NEP due to warming from increasing (Fig. 3.6). The substantial summer decrease in NEP in evergreen coniferous forests is believed to result from substantial warming-associated increase in plant respiration (particularly maintenance respiration), given that biomass in evergreen coniferous forests is higher than that in deciduous broad-leaf forests (Egusa et al. 2020).

The above results illustrate the possibility that, in mountainous regions with large environmental gradients, the impact of warming on forest sequestration differs substantially by climate zone and vegetation type even in an area as small as Gifu

Prefecture, which is on the order of 10,000 km^2. Furthermore, the results suggest that the changing carbon sequestration is determined by a variety of factors including the conversion of high-elevation areas unsuitable for forest development into areas that are suitable for forest development due to climate shift, leaf phenology response to warming, and warming-associated increase in respiration. In the next section, we will discuss the outlook for future research that emerges from the analysis above.

3.5 Outlook for Future Research

3.5.1 Ecological Perspective

3.5.1.1 Acclimation to Elevated Temperature and CO_2

Increases in temperature and atmospheric CO_2 concentration affect carbon sequestration through their influence on carbon metabolic pathways. One of the major challenges of ecosystem models is their treatment of changes in the temperature- and CO_2-sensitivities of carbon metabolic pathways (i.e., acclimation to elevated temperature and CO_2) (Dusenge et al. 2019). Previous simulated global warming experiments and free-air CO_2 enrichment (FACE) experiments have revealed that the acclimation of carbon metabolic processes to elevated temperature and CO_2 varies by tree and vegetation type (Ainsworth and Long 2005; Dusenge et al. 2020; Romero-Olivares et al. 2017). In response to this and other empirical evidence, many ecosystem models have been improved in recent years to account for acclimation to temperature and CO_2 (Smith and Dukes 2013). That said, regarding carbon estimation at the regional scale, the setting of parameter values related to temperature and CO_2 acclimation remains a challenge. For example, incorporating temperature and CO_2 acclimation into the model simulations discussed in this chapter would require the setting of parameter values that are appropriate for evergreen coniferous and deciduous broad-leaf forests in Gifu Prefecture. As a first step, this would require the compilation of data related to temperature and CO_2 acclimation for various vegetation types and tree species based on previously accumulated and new experimental results in a form that can be used to set parameter values in ecosystem models.

3.5.1.2 Change in Frequency of Extreme Weather Events and Forest Disturbances

It has recently been reported that climate change will very likely be accompanied by increased frequency of extreme weather events (IPCC 2018). Such extreme weather events are expected to impact terrestrial carbon sequestration through their disturbance of terrestrial ecosystems and mortality (Reichstein et al. 2013). For example, Allen et al. (2010) warn that climate change-related drought and heat stress will increase forest mortality across the globe, leading to a decline in carbon

sequestration. Certain areas of Japan are predicted to experience increased frequency of heavy snows and higher-intensity typhoons (Nishijima et al. 2012; Sasai et al. 2019) that will result in higher frequency of large-scale disturbances and a decline in forest carbon sequestration. Meanwhile, the main causes of natural disturbances that impact ecological services such as forest carbon sequestration are known to vary by region (Thom and Seidl 2016). For example, the main causes of forest disturbances in the Gifu region discussed in this chapter include wind and snow damage in cool temperate mountainous areas (Nagai et al. 2018; Morimoto et al. 2021), as opposed to fire damage, which is frequently observed in the European Mediterranean region and North America (Seidl et al. 2014; Amiro et al. 2006). That said, as is the case with the simulation results presented in this chapter, previous studies estimating future changes in carbon sequestration at national and regional scales have not sufficiently factored in the increased frequency of region-specific extreme weather events that are expected to accompany climate change or the increased frequency of disturbances and mortality associated with such events.

Accordingly, the following items should be incorporated into future ecosystem model simulations of carbon sequestration at the regional scale: (1) extreme weather events particular to each region that have a high probability of impacting forest carbon sequestration; (2) spatial distribution of changes in frequency of extreme weather events due to climate shift and changes in magnitude of accompanying forest disturbances; and (3) impacts of forest disturbances on forest carbon sequestration.

3.5.2 Forestry Perspective

3.5.2.1 Land Use Change

Historical land use (change over time in land cover) impacts the current soil composition, soil organic matter content, soil nitrogen content, and other soil characteristics and, consequently, current and future forest carbon sequestration (e.g., Compton et al. 1998; Goodale and Aber 2001). In Japan, fallow fields and land are often afforested with Japanese cedar and Japanese cypress. As such, currently forested areas have not always been continuously used as forest land. Furthermore, because warming can cause climate shift in mountainous areas, in the future, forests may spread to elevations that are currently above the tree line. Thus, it is necessary to account for historical land use and future land-use change when estimating future forest carbon sequestration (e.g., Erb et al. 2013).

The first method of accounting for historical land use in model simulations involves the use of current soil environment data. For example, in their estimates of future NPP of Japanese cedar forests, Toriyama et al. (2021) accounted indirectly for historical land use by entering current soil environment data in their model.

The second method involves the use of remote sensing data. If the period in question is from 1970 onwards, satellite data (e.g., Landsat, EROS, etc.) can be used

to reconstruct land use history and year-to-year land cover change. If the period in question is more recent than 1900, after the advent of airplane technology, aerial photographs taken by cameras installed on airplanes can be used. In Japan, for example, many aerial photographs taken by the US military after the end of the Second World War still exist. Although the information obtained is imprecise, it is also possible to estimate historical land use based on a survey of the literature. For example, in Japan, there are many works of literature from the Edo period from which the spatial distribution of historical land use from 1600 onward can be estimated. It is possible to reconstruct historical land use based on such data and to account for changes in soil composition, organic matter content, nitrogen content, and other soil parameters associated with land-use change by using this land-use history in the spin-up of model simulations.

Estimates of future land-use history will require construction of land-use scenarios that account for the impacts of human activity and climate shift.

3.5.2.2 Forest Management

Long-rotation forest management and the deployment/non-deployment and intensity of thinning are known to impact short- and long-term forest carbon sequestration (Canadell and Raupach 2008; Campbell et al. 2009; Aun et al. 2021). In Japan, the shortage of forest managers due to population ageing and decline is problematic and can potentially lead to abandonment of planted forests and increased area of un-thinned forests (Forestry Agency 2020). Problems specific to a given country or administrative district can be reflected in estimates of future forest carbon sequestration by incorporating specific data on the intensity of forest management into forest management scenarios that are then analyzed using ecosystem models (e.g., Wang et al. 2013). In fact, the updated version of the Biome-BGC model used in this chapter (Biome-BGCMuSo) includes an assignable thinning intensity parameter (Hidy et al. 2016). Estimates of future carbon sequestration that incorporate forest management information in this manner should prove useful in the formulation of forest management policy at the administrative district level.

3.5.3 Climatological and Meteorological Perspective

As shown by the simulations in this chapter, the impacts of warming on NEP vary substantially by elevation, vegetation type, and season. Accordingly, when estimating the effect of warming on future NEP even in a small area such as Gifu Prefecture, detailed climatological forecasting of the magnitude and spatial distribution of changes in environmental factors such as temperature, precipitation, solar radiation, and humidity for a given season is extremely important. These and other related challenges can broadly be classified into those having to do with the uncertainty of warming estimates from different models, the reproducibility of meteorological

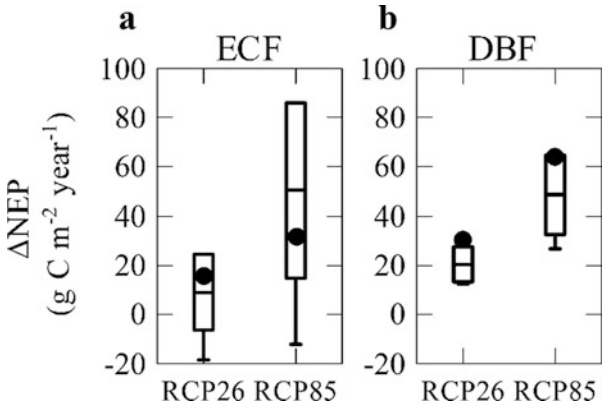

Fig. 3.8 The annual ΔNEP in the future projection relative to the current climate in Gifu prefecture, Japan. Each box and vertical bar indicate average and standard deviation, and maximum and minimum of ΔNEP simulated by each climate model (HadGEM2-ES, MRI-CGCM3, CSIRO-Mk3-6-0, MIROC5, and GFDL-CM3). Black circle indicates ΔNEP simulated by average meteorological values in five climate models

values in complex terrain, and warming-related changes in the frequency of extreme weather events.

First, there is substantial uncertainty regarding the magnitude of temperature rise, change in precipitation, and change in solar radiation associated with climate model warming estimates (IPCC 2013). In this chapter, to reduce uncertainty, we used average meteorological values (e.g., temperature, precipitation, solar radiation) from five climate models as input data for the ecosystem model (Fig. 3.3). Using meteorological values from each of the five climate models separately as ecosystem model inputs in scenarios RCP2.6 and RCP8.5 yields estimates of cumulative annual ΔNEP in Gifu Prefecture ranging from −18 to 19 g C m^{-2} $year^{-1}$ and −12 to 71 g C m^{-2} $year^{-1}$ for evergreen coniferous forests and from 12 to 28 g C m^{-2} $year^{-1}$ and 26 to 65 g C m^{-2} $year^{-1}$ for deciduous broad-leaf forests in scenarios RCP2.6 and RCP8.5, respectively (Fig. 3.8); the substantial breadth of estimates is especially evident for evergreen coniferous forest simulations. The above results highlight the importance of using output data from multiple climate models and discussing uncertainty when estimating future forest carbon sequestration.

Second, in the field of climatology, the reproducibility of meteorological values in complex landscapes including mountains is a challenge (Lundquist et al. 2019). The output values of the climate models used in this chapter are indirectly based on statistically downscaled 1-km climatic data and are able to reproduce elevation-dependent environmental changes with a certain degree of accuracy (Nishimori et al. 2019). That said, the models' ability to reproduce cloud- and water-related mechanical processes remains limited (Nishimori et al. 2019). Accordingly, reproduction of climatic values in regions with large environmental gradients such as mountainous areas requires the use of local climate models driven by the output of climate models

around the target area as boundary conditions to recalculate the climate for the target area (i.e., nesting) (Gutowski et al. 2020).

The third class of challenges has to do with forecasting changes in the frequency of extreme weather events associated with warming. As extreme weather events do not necessarily occur every year, warming-related changes in frequency need to be expressed as probability density functions (Nosaka et al. 2020). This requires large-scale ensemble calculations with over 1000 runs. The Database for Policy Decision making for Future Climate Change (D4PDF) contains output from high-resolution 60- and 20-km-mesh climate simulations for the Earth and Japan (and surrounding areas). The data include 6000-years- ensembles (3000-years- ensembles for Japan and surrounding areas) of future climate simulation data based on present-day climate conditions as well as 5400-years- ensembles of future climate simulation data assuming a mean global temperature rise of 4 °C over pre-industrial levels, which is sufficient to enable changes in extreme weather event frequencies to be expressed as probability density functions (Mizuta et al. 2017). For example, Sasai et al. (2019) and Kawase et al. (2016) have used D4PDF to forecast increase in frequency of heavy snowfall events in certain areas of Japan. Such forecasts, as noted in Sect. 3.5.1.1, are useful for estimating changes in the frequency of extreme weather events and accompanying changes in the spatial distribution of forest disturbance intensity. Simulations based on temperature rise scenarios of 1.5 °C and 2.0 °C over pre-industrial levels have already been conducted (Nosaka et al. 2020); the results of these simulations should prove useful to future research aimed at estimating carbon sequestration in forest ecosystems.

3.6 Conclusions

In this chapter, we introduced our research involving the estimation of changes in carbon sequestration potential in mountainous regions of Japan under ongoing climate change at a spatial resolution of 1 km. In addition to demonstrating the importance of monitoring actual carbon fluxes in the field and characterizing the variability of carbon sequestration responses to climate change in mountainous regions with large environmental gradients, we discussed future directions for research involving regional-scale carbon flux simulations from three perspectives (ecological, forestry, and climatological/meteorological). Overcoming the challenges identified here will require not only further advances in individual disciplines but, also, interdisciplinary research by members of the ecology-atmospheric science community as well as transdisciplinary research linking ecology, forestry, and sociology.

Acknowledgments Biome-BGC v4.2 and MT-CLIM v4.3 were developed by the Numerical Terradynamic Simulation Group, University of Montana. The climate scenario at 1-km resolution (NAROv2.7r) was provided by the Institute for Agro-Environmental Sciences, National Agriculture

and Food Research Organization. This work was supported by JSPS KAKENHI Grant Numbers 20K06144, 20H03041, 21H02245.

References

Ainsworth EA, Long SP (2005) What have we learned from 15 years of free-air CO_2 enrichment (FACE)? A meta-analytic review of the responses of photosynthesis, canopy properties and plant production to rising CO_2. New Phytol 165:351–371. https://doi.org/10.1111/j.1469-8137.2004.01224.x

Allen CD, Macalady AK, Chenchouni H et al (2010) A global overview of drought and heat-induced tree mortality reveals emerging climate change risks for forests. For Ecol Manag 259:660–684. https://doi.org/10.1016/j.foreco.2009.09.001

Amiro B, Barr A, Black T et al (2006) Carbon, energy and water fluxes at mature and disturbed forest sites, Saskatchewan, Canada. Agric For Meteorol 136:237–251. https://doi.org/10.1016/j.agrformet.2004.11.012

Aubinet M, Vesala T, Papale D (eds) (2012) Eddy covariance: a practical guide to measurement and data analysis. Springer, Berlin

Aun K, Kukumägi M, Varik M et al (2021) Short-term effect of thinning on the carbon budget of young and middle-aged silver birch (Betula pendula Roth) stands. For Ecol Manag 480. https://doi.org/10.1016/j.foreco.2020.118660

Bonan G (2008) Ecological climatology: concepts and applications, 2nd edn. Cambridge University Press, Cambridge

Campbell J, Alberti G, Martin J et al (2009) Carbon dynamics of a ponderosa pine plantation following a thinning treatment in the northern Sierra Nevada. For Ecol Manag 257:453–463. https://doi.org/10.1016/j.foreco.2008.09.021

Canadell JG, Raupach MR (2008) Managing forests for climate change mitigation. Science 320:1456–1457

Cao M, Woodward FI (1998a) Net primary and ecosystem production and carbon stocks of terrestrial ecosystems and their responses to climate change. Glob Chang Biol 4:185–198

Cao M, Woodward FI (1998b) Dynamic responses of terrestrial ecosystem carbon cycling to global climate change. Nature 393:249–252

Chang SC, Saitoh TM, Shibata H et al (2021) Recent advances in the understanding of ecosystem processes at eddy covariance CO_2 flux sites in east Asian forest ecosystems: a review. J Agric Meteorol 77:52–65. https://doi.org/10.2480/agrmet.D-20-00018

Chapin FS, Woodwell GM, Randerson JT et al (2006) Reconciling carbon-cycle concepts, terminology, and methods. Ecosystems 9:1041–1050. https://doi.org/10.1007/s10021-005-0105-7

Chisholm RA (2010) Trade-offs between ecosystem services: water and carbon in a biodiversity hotspot. Ecol Econ 69:1973–1987. https://doi.org/10.1016/j.ecolecon.2010.05.013

Chung H, Muraoka H, Nakamura M et al (2013) Experimental warming studies on tree species and forest ecosystems: a literature review. J Plant Res 126:447–460. https://doi.org/10.1007/s10265-013-0565-3

Collatz GJ, Ball JT, Grivet C, Berry JA (1991) Physiological and environmental regulation of stomatal conductance, photosynthesis and transpiration: a model that includes a laminar boundary layer. Agric For Meteorol 54:107–136

Compton JE, Boone RD, Motzkin G et al (1998) Soil carbon and nitrogen in a pine-oak sand plain in Central Massachusetts: role of vegetation and land-use history. Oecologia 116:536–542

Di Sacco A, Hardwick KA, Blakesley D et al (2021) Ten golden rules for reforestation to optimize carbon sequestration, biodiversity recovery and livelihood benefits. Glob Chang Biol 27:1328–1348. https://doi.org/10.1111/gcb.15498

Dusenge ME, Duarte AG, Way DA (2019) Plant carbon metabolism and climate change: elevated CO2 and temperature impacts on photosynthesis, photorespiration and respiration. New Phytol 221:32–49. https://doi.org/10.1111/nph.15283

Dusenge ME, Madhavji S, Way DA (2020) Contrasting acclimation responses to elevated CO2 and warming between an evergreen and a deciduous boreal conifer. Glob Chang Biol 26:3639–3657. https://doi.org/10.1111/gcb.15084

Egusa T, Kumagai T, Shiraishi N (2020) Carbon stock in Japanese forests has been greatly underestimated. Sci Rep 10:7895. https://doi.org/10.1038/s41598-020-64851-2

Erb K-H, Kastner T, Luyssaert S et al (2013) Bias in the attribution of forest carbon sinks. Nat Clim Chang 3:854–856. https://doi.org/10.1038/nclimate2004

Farquhar GD, von Caemmerer SV, Berry JA (1980) A biochemical model of photosynthetic CO2 assimilation in leaves of C3 species. Planta 149:78–90

Fawzy S, Osman AI, Doran J et al (2020) Strategies for mitigation of climate change: a review. Environ Chem Lett 18:2069–2094. https://doi.org/10.1007/s10311-020-01059-w

Forestry Agency (2020) Annual report on forest and forestry in Japan. Ministry of Agriculture, Forestry and Fisheries. Available from https://www.rinya.maff.go.jp/j/kikaku/hakusyo/R2hakusyo/index.html (in Japanese with English abstract)

Goodale CL, Aber JD (2001) The long-term effects of land-use history on nitrogen cycling in northern hardwood forests. Ecol Appl 11:253–267

Gutowski WJ, Ullrich PA, Hall A et al (2020) The ongoing need for high-resolution regional climate models: process understanding and stakeholder information. Bull Am Meteorol Soc 101:E664–E683. https://doi.org/10.1175/bams-d-19-0113.1

Heimann M, Reichstein M (2008) Terrestrial ecosystem carbon dynamics and climate feedbacks. Nature 451:289–292. https://doi.org/10.1038/nature06591

Hidy D, Barcza Z, Marjanović H et al (2016) Terrestrial ecosystem process model biome-BGCMuSo v4.0: summary of improvements and new modeling possibilities. Geosci Model Dev 9:4405–4437. https://doi.org/10.5194/gmd-9-4405-2016

Hui D, Deng Q, Tian H et al (2015) Climate change and carbon sequestration in forest ecosystems. In: Handbook of climate change mitigation and adaptation, pp 1–40. https://doi.org/10.1007/978-1-4614-6431-0_13-2

IPCC (2013) Climate change 2013 - the physical science basis. Cambridge University Press, Cambridge

IPCC (2018) Global warming of 1.5 °C: an IPCC special report on the impacts of global warming of 1.5 °C above pre-industrial levels and related global greenhouse gas emission pathways, in the context of strengthening the global response to the threat of climate change, Sustainable development, and efforts to eradicate poverty. Cambridge University Press, Cambridge

Ito A, Saitoh TM, Sasai T (2015) Synergies between observational and modeling studies at the Takayama site: toward a better understanding of processes in terrestrial ecosystems. Ecol Res 30:201–210. https://doi.org/10.1007/s11284-014-1205-7

Kawase H, Murata A, Mizuta R et al (2016) Enhancement of heavy daily snowfall in Central Japan due to global warming as projected by large ensemble of regional climate simulations. Clim Chang 139:265–278. https://doi.org/10.1007/s10584-016-1781-3

Keenan TF, Williams CA (2018) The terrestrial carbon sink. Annu Rev Environ Resour 43:219–243. https://doi.org/10.1146/annurev-environ-102017-030204

Keenan TF, Luo X, De Kauwe MG et al (2021) A constraint on historic growth in global photosynthesis due to increasing CO_2. Nature 600:253–258. https://doi.org/10.1038/s41586-021-04096-9

Kimball JS, Running SW, Nemani R (1997) An improved method for estimating surface humidity from daily minimum temperature. Agric Forest Meteorol 85:87–98

Kondo M, Ichii K, Ueyama M (2015) Impact of anomalous climates on carbon allocation to biomass production of leaves, woody components, and fine roots in a cool-temperate deciduous forest. Agric For Meteorol 201:38–50. https://doi.org/10.1016/j.agrformet.2014.11.005

Kondo M, Saitoh TM, Sato H et al (2017) Comprehensive synthesis of spatial variability in carbon flux across monsoon Asian forests. Agric For Meteorol 232:623–634. https://doi.org/10.1016/j.agrformet.2016.10.020

Lamb RL, Hurtt GC, Boudreau TJ et al (2021) Context and future directions for integrating forest carbon into sub-national climate mitigation planning in the RGGI region of the U.S. Environ Res Lett 16. https://doi.org/10.1088/1748-9326/abe6c2

Lee X, Massman W, Law B (eds) (2004) Handbook of micrometeorology: a guide for surface flux measurement analysis. Kluwer Academic, Dordrecht

Lee M-S, Lee J-S, Koizumi H (2008) Temporal variation in CO2 efflux from soil and snow surfaces in a Japanese cedar (*Cryptomeria japonica*) plantation, central Japan. Ecol Res 23:777–785. https://doi.org/10.1007/s11284-007-0439-z

Lundquist J, Hughes M, Gutmann E et al (2019) Our skill in modeling mountain rain and snow is bypassing the skill of our observational networks. Bull Am Meteorol Soc 100:2473–2490. https://doi.org/10.1175/bams-d-19-0001.1

Luyssaert S, Inglima I, Jung M et al (2007) CO_2 balance of boreal, temperate, and tropical forests derived from a global database. Glob Chang Biol 13:2509–2537. https://doi.org/10.1111/j.1365-2486.2007.01439.x

Mizoguchi Y, Ohtani T, Takanashi S et al (2012) Seasonal and interannual variation in net ecosystem production of an evergreen needleleaf forest in Japan. J For Res 17:283–295. https://doi.org/10.1007/s10310-011-0307-0

Mizuta R, Murata A, Ishii M et al (2017) Over 5,000 years of ensemble future climate simulations by 60-km global and 20-km regional atmospheric models. Bull Am Meteorol Soc 98:1383–1398. https://doi.org/10.1175/bams-d-16-0099.1

Morimoto J, Aiba M, Furukawa F et al (2021) Risk assessment of forest disturbance by typhoons with heavy precipitation in northern Japan. For Ecol Manag 479. https://doi.org/10.1016/j.foreco.2020.118521

Nagai S, Saitoh TM, Kobayashi H et al (2012) *In situ* examination of the relationship between various vegetation indices and canopy phenology in an evergreen coniferous forest, Japan. Int J Remote Sens 33:6202–6214. https://doi.org/10.1080/01431161.2012.682660

Nagai S, Saitoh TM, Kajiwara K et al (2018) Investigation of the potential of drone observations for detection of forest disturbance caused by heavy snow damage in a Japanese cedar (*Cryptomeria japonica*) forest. J Agric Meteorol 74:123–127. https://doi.org/10.2480/agrmet.D-17-00038

Nakai Y, Kitamura K, Suzuki S et al (2003) Year-long carbon dioxide exchange above a broadleaf deciduous forest in Sapporo, northern Japan. Tellus 55B:305–312

Nishijima K, Maruyama T, Graf M (2012) A preliminary impact assessment of typhoon wind risk of residential buildings in Japan under future climate change. Hydrol Res Lett 6:23–28. https://doi.org/10.3178/hrl.6.23

Nishimori M, Ishigooka Y, Kuwagata T (2019) SI-CAT 1km-grid square regional climate projection scenario dataset for agricultural use (NARO2017). J Jpn Soc Sim Tech 38:150–154. (in Japanese)

Nosaka M, Ishii M, Shiogama H et al (2020) Scalability of future climate changes across Japan examined with large-ensemble simulations at + 1.5 K, +2 K, and + 4 K global warming levels. Prog Earth Planet Sci 7. https://doi.org/10.1186/s40645-020-00341-3

Ohtani Y, Yasuda Y, Mizoguchi Y et al (2005) Seasonal and interannual variability in net ecosystem CO2 exchange in six forest flux sites in Japan. In: Proceedings of the 7th International Carbon Dioxide Conference 79–80

Ohtsuka T, Akiyama T, Hashimoto Y et al (2005) Biometric based estimates of net primary production (NPP) in a cool-temperate deciduous forest stand beneath a flux tower. Agric For Meteorol 134:27–38. https://doi.org/10.1016/j.agrformet.2005.11.005

Ohtsuka T, Mo W, Satomura T et al (2007) Biometric based carbon flux measurements and net ecosystem production (NEP) in a temperate deciduous broad-leaved Forest beneath a flux tower. Ecosystems 10:324–334. https://doi.org/10.1007/s10021-007-9017-z

Ohtsuka T, Negishi M, Sugita K et al (2013) Carbon cycling and sequestration in a Japanese red pine (*Pinus densiflora*) forest on lava flow of Mt. Fuji. Ecol Res 28:855–867. https://doi.org/10.1007/s11284-013-1067-4

Piao S, Ciais P, Friedlingstein P et al (2008) Net carbon dioxide losses of northern ecosystems in response to autumn warming. Nature 451:49–52. https://doi.org/10.1038/nature06444

Pugh TAM, Lindeskog M, Smith B et al (2019) Role of forest regrowth in global carbon sink dynamics. Proc Natl Acad Sci U S A 116:4382–4387. https://doi.org/10.1073/pnas.1810512116

Reichstein M, Bahn M, Ciais P et al (2013) Climate extremes and the carbon cycle. Nature 500:287–295. https://doi.org/10.1038/nature12350

Romero-Olivares AL, Allison SD, Treseder KK (2017) Soil microbes and their response to experimental warming over time: a meta-analysis of field studies. Soil Biol Biochem 107:32–40. https://doi.org/10.1016/j.soilbio.2016.12.026

Saigusa N, Yamamoto S, Murayama S et al (2005) Inter-annual variability of carbon budget components in an AsiaFlux forest site estimated by long-term flux measurements. Agric For Meteorol 134:4–16. https://doi.org/10.1016/j.agrformet.2005.08.016

Saitoh TM, Tamagawa I, Muraoka H et al (2010) Carbon dioxide exchange in a cool-temperate evergreen coniferous forest over complex topography in Japan during two years with contrasting climates. J Plant Res 123:473–483. https://doi.org/10.1007/s10265-009-0308-7

Saitoh TM, Nagai S, Yoshino J et al (2015) Effects of canopy phenology on deciduous overstory and evergreen understory carbon budgets in a cool-temperate forest ecosystem under ongoing climate change. Ecol Res 30:267–277. https://doi.org/10.1007/s11284-014-1229-z

Sasai T, Saigusa N, Nasahara KN et al (2011) Satellite-driven estimation of terrestrial carbon flux over Far East Asia with 1-km grid resolution. Remote Sens Environ 115:1758–1771. https://doi.org/10.1016/j.rse.2011.03.007

Sasai T, Obikawa H, Murakami K et al (2016) Estimation of net ecosystem production in Asia using the diagnostic-type ecosystem model with a 10 km grid-scale resolution. J Geophys Res Biogeosci 121:1484–1502. https://doi.org/10.1002/2015jg003157

Sasai T, Kawase H, Kanno Y et al (2019) Future projection of extreme heavy snowfall events with a 5-km large ensemble regional climate simulation. J Geophys Res Atmos 124:13975–13990. https://doi.org/10.1029/2019jd030781

Seidl R, Schelhaas MJ, Rammer W et al (2014) Increasing forest disturbances in Europe and their impact on carbon storage. Nat Clim Chang 4:806–810. https://doi.org/10.1038/nclimate2318

Setoyama Y, Sasai T (2013) Analyzing decadal net ecosystem production control factors and the effects of recent climate events in Japan. J Geophys Res Biogeosci 118:337–351. https://doi.org/10.1002/jgrg.20038

Shibata H, Hiura T, Tanaka Y et al (2005) Carbon cycling and budget in a forested basin of southwestern Hokkaido, northern Japan. Ecol Res 20:325–331. https://doi.org/10.1007/s11284-005-0048-7

Smith NG, Dukes JS (2013) Plant respiration and photosynthesis in global-scale models: incorporating acclimation to temperature and CO_2. Glob Chang Biol 19:45–63. https://doi.org/10.1111/j.1365-2486.2012.02797.x

Song J, Wan S, Piao S et al (2019) A meta-analysis of 1,119 manipulative experiments on terrestrial carbon-cycling responses to global change. Nat Ecol Evol 3:1309–1320. https://doi.org/10.1038/s41559-019-0958-3

Takanashi S, Kosugi Y, Tanaka Y et al (2005) CO_2 exchange in a temperate Japanese cypress forest compared with that in a cool-temperate deciduous broad-leaved forest. Ecol Res 20:313–324. https://doi.org/10.1007/s11284-005-0047-8

Thom D, Seidl (2016) Natural disturbance impacts on ecosystem services and biodiversity in temperate and boreal forests. Biol Rev 91:760–781. https://doi.org/10.1111/brv.12193

Thornton PE (2010) Biome BGC version 4.2: theoretical framework of biome-BGC. Technical Documentation

Thornton PE, Running SW (1999) An improved algorithm for estimating incident daily solar radiation from measurements of temperature, humidity, and precipitation. Agric Forest Met 93:211–228

Toriyama J, Hashimoto S, Osone Y et al (2021) Estimating spatial variation in the effects of climate change on the net primary production of Japanese cedar plantations based on modeled carbon dynamics. PLoS One 16:e0247165. https://doi.org/10.1371/journal.pone.0247165

Walker AP, De Kauwe MG, Bastos A et al (2021) Integrating the evidence for a terrestrial carbon sink caused by increasing atmospheric CO_2. New Phytol 229:2413–2445. https://doi.org/10.1111/nph.16866

Wang W, Wei X, Liao W et al (2013) Evaluation of the effects of forest management strategies on carbon sequestration in evergreen broad-leaved (Phoebe bournei) plantation forests using FORECAST ecosystem model. For Ecol Manag 300:21–32. https://doi.org/10.1016/j.foreco.2012.06.044

Wang S, Zhang Y, Ju W et al (2020) Recent global decline of CO2 fertilization effects on vegetation photosynthesis. Science 370:1295–1300. https://doi.org/10.1126/science.abb7772

Yashiro Y, Lee NY, Ohtsuka T et al (2010) Biometric-based estimation of net ecosystem production in a mature Japanese cedar (*Cryptomeria japonica*) plantation beneath a flux tower. J Plant Res 123:463–472. https://doi.org/10.1007/s10265-010-0323-8

Yasuda Y, Watanabe T, Ohtani Y et al (1998) Seasonal variation of CO_2 flux over a broadleaf deciduous forest. J Jpn Soc Hydrol Water Resour 11:575–585. (in Japanese with an English abstract)

Yasuda Y, Saito T, Hoshino D et al (2012) Carbon balance in a cool–temperate deciduous forest in northern Japan: seasonal and interannual variations, and environmental controls of its annual balance. J For Res 17:253–267. https://doi.org/10.1007/s10310-011-0298-x

Chapter 4
Woody Biomass Change Monitoring in Temperate Montane Forests by Airborne LiDAR Analysis

Yoshio Awaya

Abstract Airborne laser scanners by light detection and ranging (LiDAR) measure the elevation of ground objects, and canopy height (DCHM) can be estimated as the difference between the canopy surface and ground elevation. A forest area was selected in the east of Takayama city (Gifu Prefecture, Japan) in the cool temperate forest zone. Airborne LiDAR observation was executed in 2005 and 2011. Total dry woody biomass (TDB) was mapped using the two LiDAR data using statistical biomass estimation models, one for evergreen coniferous forests and the other for deciduous broadleaved forests using DCHMs. Changes in TDB were mapped, and man-made evergreen coniferous forests surrounding a village in the west showed greatest TDB and growth in the study area due to human forestry activity. On the other hand, forests in the east were young with less TDB and growth. Hence, forests in the east were younger, and TDB and growth were less, than those in the west. Deciduous broadleaved forests, which were used as fuel woods until the 1960s, generally had smaller TDB and growth. Human forestry activity resulted in TDB and growth differences, and TDB maps showed impacts of the forestry activity in this area.

Keywords Total dry biomass (TDB) · Biomass growth · Airborne LiDAR · Cool temperate forest · Forestry activity

4.1 Introduction

A forest ecosystem provides various ecosystem services, including carbon stock and fixation, timber and fuel supply, water purification, and wildlife habitat. It is essential to identify the forest distribution including forest type, height, and biomass to understand the contribution of a forest to the human community through its ecosystem services. For example, different (e.g. by species, height, density, and age) forest

Y. Awaya (✉)
River Basin Research Center, Gifu University, Gifu, Japan
e-mail: awaya@green.gifu-u.ac.jp

F. Li et al. (eds.), *River Basin Environment: Evaluation, Management and Conservation*, https://doi.org/10.1007/978-981-19-4070-5_4

types support different animals, and geographical forest information is probably necessary and important for animal conservation.

Forest resource information is mandatory for forestry. Stock volume information (both amount and distribution) is important for timber production, and dry biomass information is necessary when calculating the woody fuel supply. Since timber is a renewable resource, it is important to use biomass wisely in order to reduce carbon emissions. Recently, biomass and carbon fixation information from each forest is required for global warming mitigation as well.

The concentration of atmospheric carbon dioxide (CO_2), one of the greenhouse gasses causing climate change, is increasing steadily. Moreover, global mean air temperature seems to have increased greatly since the 1910s in conjunction with the increasing greenhouse gas concentration (Houghton et al. 2001). Internationally there is much interest in the estimation of carbon storage and evaluation of carbon balance in terrestrial ecosystems in order to understand the potential value of ecosystems for carbon reduction.

Net primary productivity (NPP), which is the amount of carbon absorbed by vegetation, may increase under increasing global air temperature in ecosystems where plants can extend the growing period. On the other hand, decreased precipitation may cause NPP reduction in ecosystems due to water stress (Houghton et al. 2001). Estimation of NPP is essential for evaluating the carbon balance, and for understanding the effects of climate change on vegetation.

Biomass is an important variable for forestry as a resource as well as a CO_2 source for carbon balance studies. The biomass and carbon stocks in forests are important indicators of their productive capacity, energy potential, and capacity to sequester carbon (FAO 2016). Biomass is a pool of atmospheric carbon fixed by plants and ranges widely based on tree size in large areas. The difference between biomass and litter falls during a period (usually a year) is the NPP. On the other hand, it is well known that forest disturbances in the tropics release carbon to the atmosphere as CO_2. In addition, tree plantations and silvicultural treatments in some countries such as China result in significant tree growth and support carbon fixation from the atmosphere to trees (FAO 2016). Therefore understanding forest change as the potential carbon sink in a large area is essential for understanding carbon balance on a regional, national, continental, or global scale. However, precise assessment of forest biomass distribution by field survey is a difficult task when the area is large.

Remote sensing provides information concerning landcover by detecting signals such as reflected solar energy from the land surface and analyzing characteristics of signals. For example, optical sensors provide multispectral surface information as digital images (pictures) of a certain mesh size between sub-meter and some kilometers. Optical sensors separate reflected solar energy into some different wavelengths, which is spectra. Obtained images cover areas from about 100 km^2 to 300,000 km^2 as wall-to-wall pixel data and are used for forestry applications.

Thus optical images can be used to estimate spatial coverage of forest information, such as forest types and biomass (Franklin 2001). Providing information in large areas is the greatest advantage of remote sensing, and this technology surpasses the field survey method. On the other hand, the greatest problem of optical sensors is

that they observe not only biophysical parameter directly but also the spectra (color) of trees. Therefore forest information such as biomass is evaluated indirectly (indirect estimation) by identifying any relationship between intensity of spectral reflectance and biophysical parameters such as biomass. Relationships between reflectance and biophysical parameters are not strong and change according to the images. Since observed reflectance values change according to different specifications of the sensors, observation conditions such as atmosphere, solar direction, and topographic shadow. Although removing influence or 'noise' using these factors is mandatory, removing noise is a very hard task. As a result, it is difficult to derive consistent and accurate estimation of biophysical parameters because of the indirect estimation affected by numerous noise sources.

Although optical remote sensing has been used to estimate forest biomass distribution (Peng et al. 2019; Spanner et al. 1990; Peterson et al. 1987), it is very difficult to derive accurate and consistent estimation from optical images due to not only atmospheric and topographic effects but also seasonal changes of tree spectra. Reflectance is saturated in stands with high biomass and the estimation accuracy is low in dense forests with high biomass (Foody et al. 2003). Optical images have been also used for estimation of NPP distribution and for their inter-annual monitoring with environment information such as climate (e.g. air temperature and precipitation) (Awaya et al. 2004; Potter et al. 1993).

The normalized difference vegetation index (NDVI) is linear to the fraction of absorbed photosynthetically active radiation, and NDVI can be used to estimation the amount of solar energy which is used photosynthesis by plants. It is essential to achieve very accurate atmospheric correction, topographic correction, and reduction of effects of bidirectional reflectance distribution function (BRDF) of vegetation species-by-species for precise optical image processing to derive biophysical parameters including biomass and NPP. However accurate high resolution atmospheric information maps for atmospheric correction are not available and BRDF of ground surface at each pixel for accurate BRDF and topographic correction is unknown. Above all, reflectance of visible and infrared wavelengths saturate in dense vegetation. These problems affect accurate biomass and NPP estimation using optical images.

On the other hand, light detection and ranging (LiDAR) technology provides accurate canopy height information (Maltamo et al. 2014), which is one of the biophysical parameters. Although laser scanning emit laser pulses discretely, current laser scanner can emit more than 10 laser pulses per square meter to the ground from the air. Dense laser pulses provide pseudo wall-to-wall height information and can supply accurate canopy height of trees in a large area.

Laser scanning based on LiDAR from the air was introduced for forest measurements in the early 1980s, and a laser profiler revealed that tree canopy height was measurable from the air in a large area (Arp et al. 1982; Aldred and Bonner 1985). Airborne laser scanners emit laser pulses from the air to the ground and receive reflected pulses from objects on the ground. The geographical location of the ground object is determined from the time lag between the emission and receiving of the laser pulse (distance) and the direction from the scanner on airplane geographical

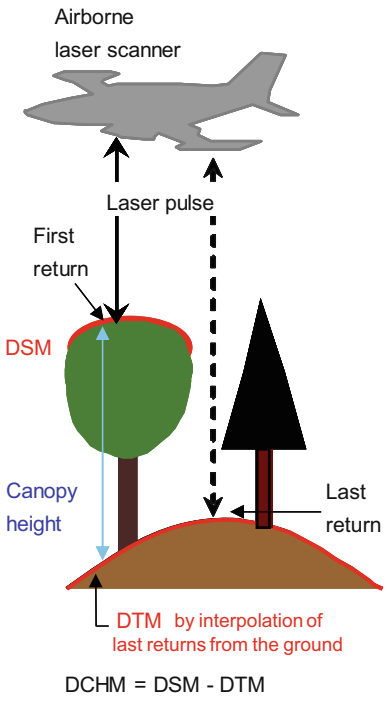

Fig. 4.1 Schematic view of laser scanning

location (Beraldin et al. 2010). Most pulses reflect at the canopy surface (first return) and few pulses reach to the ground (last return). Surface returns show surface elevation of objects and ground returns show the ground elevation. First returns are used to produce a digital surface model (DSM), and ground surface is estimated as a digital terrain model (DTM) using ground returns and numerical interpolation, such as triangulated irregular network (TIN, Maas 2010). The difference between DSM and DTM is the digital canopy height model (DCHM, Fig. 4.1). DCHM is accurate canopy information of not only height but also horizontal and vertical structure. Laser pulses also provide information on foliage.

Various research in this field has been carried out (Leeuwen and Nieuwenhuis 2010; Wulder et al. 2012). For example, stem volume or biomass estimation is the most popular and important research topic for forestry, forest ecology, and carbon circulation studies (Awaya and Takahashi 2017; Breidenbach et al. 2016; Takahashi et al. 2005a, 2010; Maltamo et al. 2004; Holmgren et al. 2003; Næsset 1997; Peng et al. 2019; Cao et al. 2014; Kankare et al. 2013; Mora et al. 2013; He et al. 2012; Rosette et al. 2012; Yao et al. 2011; Zhao et al. 2009; Foody et al. 2003; Lefsky et al. 1999a, b; Nelson et al. 1988).

Forest type or tree species classification using airborne LiDAR data is advantageous in precise canopy detection and species identification using the reflected laser pulse intensity or canopy attributes that are derived from the pulses (Hovi et al.

2016). Airborne LiDAR data provide canopy structure information such as vertical canopy cover (Korhonen et al. 2011) and vertical structure (Morsdorf et al. 2009). Forest gaps, which are open canopy areas in closed forest, can be detected (Zhang 2008) and monitored using time serial LiDAR data (Vepakomma et al. 2008, 2012; Araki and Awaya 2021). Gaps are important for undergrowth plants as they can get more sunlight; therefore, monitoring gaps and undergrowth plants give us prediction of tree regeneration. Scientists commonly use leaf area index (LAI) estimation. Optical images have been commonly used for LAI mapping (Melnikova et al. 2018; Biudes et al. 2014; Sprintsin et al. 2007; Knyazikhin et al. 1998; Spanner et al. 1990; Peterson et al. 1987) despite some difficulties with signal saturation, atmospheric effects, and topographic effects. Although atmospheric and topographic effects were able to be greatly reduced and seasonal and inter-annual LAI monitoring is possible, saturation was still a serious problem (Melnikova et al. 2018).

As for LAI prediction using LiDAR, its data provide better estimates compared to those by optical sensor data and even three-dimensional leaf distribution has been mapped (Sumnall et al. 2021; Almeida et al. 2019; Kamoskea et al. 2019; Hopkinson et al. 2013; Morsdorf et al. 2006). Thus, LiDAR data are useful not only for mapping of forest status but also for monitoring its changes, and the results are useful for forest management.

Among these applications, biomass estimation is the most important among carbon studies for understanding the capacity of a forest as a sink and pool of carbon. If airborne LiDAR data are captured twice within some years over the same forest, then tree growth such as height or biomass can be analyzed accurately over a wide area. The estimation provides growth potential information of trees in the coverage of LiDAR data.

Large-area forest inventory is a time-consuming task; however, biomass estimation using LiDAR point data has become popular for creating wall-to-wall inventories. LiDAR-based inventories are essential now in providing more accurate estimates of biophysical properties than conventional methods. Although airborne laser observation and data processing is costly, it provides forest resource information over large areas with wall-to-wall coverage. Indeed, the use of laser data for forest inventories supply promising results and improved accuracy (Næsset 2014). Various studies revealed the performance of airborne laser sensors for predicting forest variables, such as stem volume and above-ground biomass (AGB) of pine (Nelson et al. 1988), AGB of deciduous broadleaved and evergreen coniferous (Lefsky et al. 1999a, b) forests, and stem volume of evergreen coniferous forests, such as pine forests (Næsset 1997). The advanced LiDAR technology in pulse density and accurate positioning (Næsset 2014) brings accurate small-footprint laser data, which results in precise biomass mapping (Means et al. 2000; Holmgren et al. 2003).

Stem volume is proportional to the space between the canopy surface and the ground (hereafter, canopy space) (Tsuzuki et al. 2006). The average canopy height is determined by the canopy space divided by the stand area. Thus, the canopy space and average canopy height are identical and the average canopy height is useful for stem volume estimation. However, individual tree analysis has become popular for

variables, such as tree height (Kwak et al. 2007), AGB, and stem volume. Double-logarithmic relationships have been applied for single tree analysis between AGB or stem volume and variables from LiDAR data, including the average canopy height (Næsset and Økland 2002; Takahashi et al. 2005a, b; Kankare et al. 2013). Areal-based analysis produced much better results than individual tree-based analysis for stem volume and AGB (Kankare et al. 2013). Since most of numerous studies were stand-level studies, it is important to evaluate the causes of the estimate variation in the stand-level analysis prior to operational use (Breidenbach et al. 2016).

As described above, LiDAR data provide accurate biomass distribution maps, and if two biomass maps in a period are compared, the distribution of biomass changes become clear (Næsset and Gobakken 2005). As for LAI (leaf biomass), accurate estimation seems to be still difficult due to saturation of LAI against a number of return pulses. However, accurate woody biomass estimation is possible (Awaya and Takahashi 2017; Takahashi et al. 2010; Maltamo et al. 2004).

Therefore, woody biomass change can be mapped accurately in a large area using airborne LiDAR data (Næsset and Gobakken 2005). I herein introduce the usefulness of airborne LiDAR data for TDB and growth (TDB change) mapping in mountain forests in the middle of the main (Honshu) island of Japan.

4.2 The Study Site, Data and Method

The Japanese archipelago spreads between 20°N and 45°N between the subtropical and boreal zones. Therefore, various forest types (sub-tropical evergreen deciduous forest, temperate evergreen broadleaved forest, cool temperate deciduous broadleaved forest, and boreal evergreen coniferous forest) exist in the Japanese archipelago. About two-thirds of land in Japan is covered by forest; about 60% of the forest is naturally regenerated forest and the remainder is plantation forest containing coniferous trees such as Japanese cedar or sugi (*Cryptomeria japonica* D. Don), hinoki cypress (*Chamaecyparis obtusa* Sieb. et Zucc.), Japanese larch (*Lalix leptolepis* Gordon), Todo fir (*Abies sachalinensis* Masters), and Ezo spruce (*Picea jezoensis* Carr.).

Part of a small river basin was selected as the study area (36.146°N, 137.386°E). The study site was part of the Namai river basin, which is located near Takayama city in Gifu Prefecture. The elevation ranges between 800 and 1600 m above sea level (ASL) in the west and east, respectively, with a steep topography and an average slope angle of 30 degrees. The area is located in the cool temperate zone with natural deciduous broad-leaved forests and artificial coniferous forests, which are the most common forests in Honshu Island. According to local information, most of the river basin was completely logged about 60–70 years ago (after World War 2) and therefore the forests in the study site are relatively young. Plantation forests of evergreen conifers, including Japanese cedar and hinoki cypress, are dominant in the area below approximately 1000 m ASL. Planting of Japanese cedar seedlings was common in the 1950s and 1960s because Japanese cedar is a fast-growing species

Table 4.1 Summary of plot surveys between 2009 and 2013 (Awaya and Takahashi 2017)

Forest type	Stage	No of plots	Average DBH (cm)			Average tree Height (m)			TDB (Mg ha^{-1})		
Japanese cedar[a]	Young	4	1.1	–	9.4	1.8	–	5.8	2.6	–	86.1
	mature	8	22.6	–	41.2	18.8	–	29.1	325.7	–	467.1
Hinoki cypress[a]	Young-mature	21	14.6	–	34.3	9.6	–	21.4	110.4	–	444.9
Deciduous broadleaved		55	1.1	–	25.7	1.7	–	21.3	7.2	–	317.6

[a] Cedar, cypress and then cedar were planted in conifer plantations after World War II. Area of young cedar plantation is small

used for timber production including the rebuilding of destroyed houses after World War 2.

Hinoki cypress was introduced to Japan between the 1970s and 1990s because of its valuable commercial quality (Forestry Agency of Japan 2014). Japanese cedar has also been planted recently. Therefore the ages of Japanese cedar and hinoki cypress stands are clearly different in the study area. Natural deciduous broadleaved forests dominate in areas above 1000 m ASL, and planted Japanese larch forests exist in areas above 1200 m ASL. The most dominant deciduous broadleaved species in this region are deciduous oak (*Quercus mongoloca* var. grosseseratta Rehder et Wilson), Japanese white birch (*Betula platyphylla* var. japonica Hara), and Erman's birch (*Betula ermanii* Cham.).

Cherry spp. such as Japanese bird cherry (*Prunus grayana* Maxim.), maple spp. such as Redvein maple (*Acer rufinerve* Siebold & Zucc.), and Japanese umbrella tree (*Magnolia obovate* Thunb.) are common and vary with elevation and successional stages of stands. Japanese larch was planted around the 1950s for a short period, and the tree size is similar among larch stands.

Table 4.1 shows the summary of forest field data for biomass mapping. As shown in Fig. 4.2a, coniferous plantations (dark green) cover the lower part of slopes. Cedar has a rounder canopy than cypress (Fig. 4.2b) and it appears darker green than cypress in the areal photo, however, it was difficult to identify these species in the aerial photo (Fig. 4.2d). Deciduous broadleaved trees change in autumn to different leaf colors by species (Fig. 4.2c) and appear in dark brown in Fig. 4.2d.

There are two forest flux measurement sites within this study site (Fig. 4.2d): one at a deciduous broadleaved forest (TKY Takayama deciduous broadleaf forest site http://asiaflux.net/index.php?page_id=112) and the other at an evergreen coniferous forest (TKC Takayama evergreen coniferous forest site http://asiaflux.net/index.php?page_id=111). They have been operated since 1993 and 2005, respectively.

The main objective of the flux measurement sites is to measure atmospheric CO_2 flux, estimate its exchange between ecosystem and atmosphere, then understand the biological mechanisms. Numerous carbon flux (e.g. Saitoh et al. 2012), biological (e.g. Muraoka et al. 2012), and ecological (e.g. Ohtsuka 2012) studies have been executed in the flux measurement sites. Linking biological and ecological findings to

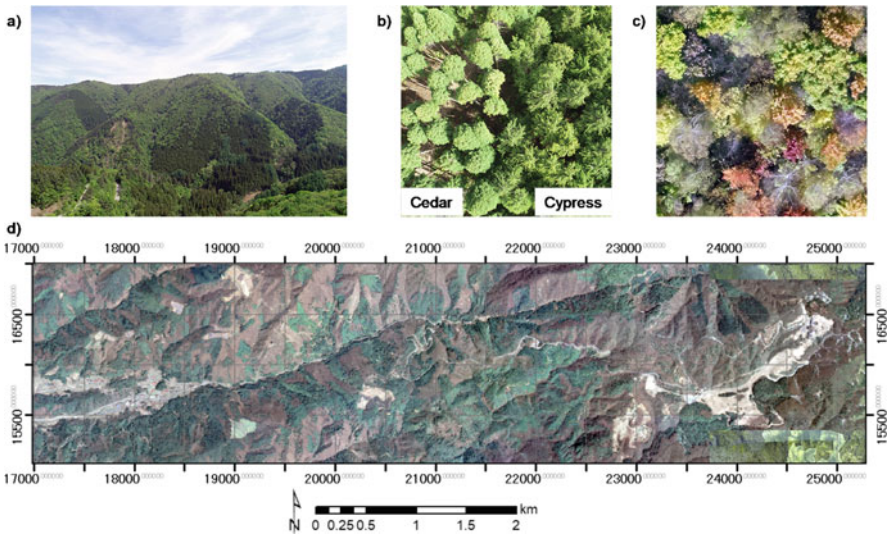

Fig. 4.2 Forest views in the study site and an aerial ortho-photo map. (**a**) A view of forest in this area. Topography is mountainous and steep. Dark green and brighter green parts are evergreen coniferous and deciduous broadleaved forest, respectively. UAV photos over (**b**) evergreen coniferous stands and (**c**) a deciduous broadleaved stand under autumnal coloring. (**d**) The orthophoto which were acquired in autumn, 2012 covers the entire study site. Deciduous trees had dropped leaves at the time of photo acquisition and appear in brown. The coordinate system of the orthophoto is Japan Plane Rectangular Coordinate System VII

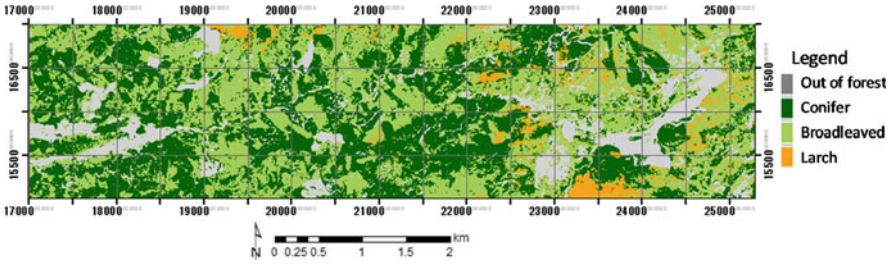

Fig. 4.3 Forest type map of the mapping area (Awaya and Takahashi 2017)

satellite remote sensing is one of primary objectives of the flux measurement sites (Muraoka et al. 2012).

4.2.1 Remote Sensing Data and Forest Type Map

Three airborne LiDAR datasets of the study area were obtained in October 2003, July 2005, and August 2011. The footprint sizes of the three LiDAR datasets were

between 0.2 and ca. 0.4 m, and the point densities were 0.7, 1.8, and 1.0 pulses m^{-2} for the 2003, 2005, and 2011 LiDAR data, respectively (Table 4.2).

LiADR data in 2003 was used to identify forest and non-forest area in the forest type classification with two QuickBird images in April 12, 2007 and May 23, 2007 (Fukuda et al. 2012) using a decision-tree classification procedure. A digital canopy height model (DCHM), comprising the difference between the digital surface model (DSM) and the digital terrain model (DTM), was produced using the LiDAR data of 2003 and used to separate forest and other land covers. Two QuickBird images were used for forest type classification to identify deciduous forest by phenological changes using the maximum likelihood classifier, and separated from evergreen coniferous forest. The forest-type map (Fig. 4.3) was used as a reference to check forest type distribution, and for selection of biomass prediction models by the forest type at each pixel.

Forests were classified into three types in the map: evergreen coniferous forests (Japanese cedar and hinoki cypress), deciduous broadleaved forests, and larch forests. Coniferous plantations seemed prevalent in areas where there was easy access for people (Fig. 4.3). A prefectural road extending from west to east is the main road in the study area. The road appeared in black on DCHM (Fig. 4.4b). Some forest roads extend from this prefecture road to forest plantations. Elevation was higher in the eastern part where deciduous broadleaved forest was common. The acreages of evergreen coniferous forest and deciduous broadleaved forest are almost the same in this area.

The Namai river flows from a mountain peak in the north-east (top of Fig. 4.4a) and then flows alongside flat land. Other parts are mountainous and steep. Tall trees exist mostly in the west along the Namai river, and trees are small in the east, as described previously (Fig. 4.4b).

4.2.2 Biomass Estimation Model

It was pointed out that there was a linear relationship between average canopy height and stem volume or biomass (Tsuzuki et al. 2006). Average canopy height and various canopy parameters are computed from LiADR point cloud data. The LiDAR parameter with highest correlation against TDB was different according to forest type (Awaya and Takahashi 2017); however, there were some parameters that had significant correlation with TDB.

TDB prediction models for evergreen coniferous and deciduous broadleaved forests were produced by a linear regression analysis using parameters with the highest correlation coefficients with TDB among LiDAR parameters. Average canopy height and a half height of canopies were selected as the independent variables for evergreen coniferous and broadleaved deciduous forest, respectively, as shown in Fig. 4.5 (Awaya and Takahashi 2017). The model for deciduous broadleaved forests was used for larch forests.

Evergreen coniferous forest:

Table 4.2 Summary of LiDAR observations

Observation date	Laser scanner	Beam divergence (mrad)	Wavelength (nm)	Flight altitude above ground (m)	Footprint size (m)	FOV (°)	Beam density (pulse m^{-2})	Usage
Oct., 2003	RAMS (EnerQuest, USA)	0.33	1064	2000 (Entire Gifu Prefecture)	–	±22	0.7	Classification
July 25, 2005	ALTM 2050DC (Teledyne Optech, Canada)	0.19	1064	1200	0.24	±22	1.8	Biomass estimation
Aug. 28, 2011	VQ-580 (RIEGL, Horn, Austria)	0.50	1550	600	0.30	±30	1.0	Biomass estimation

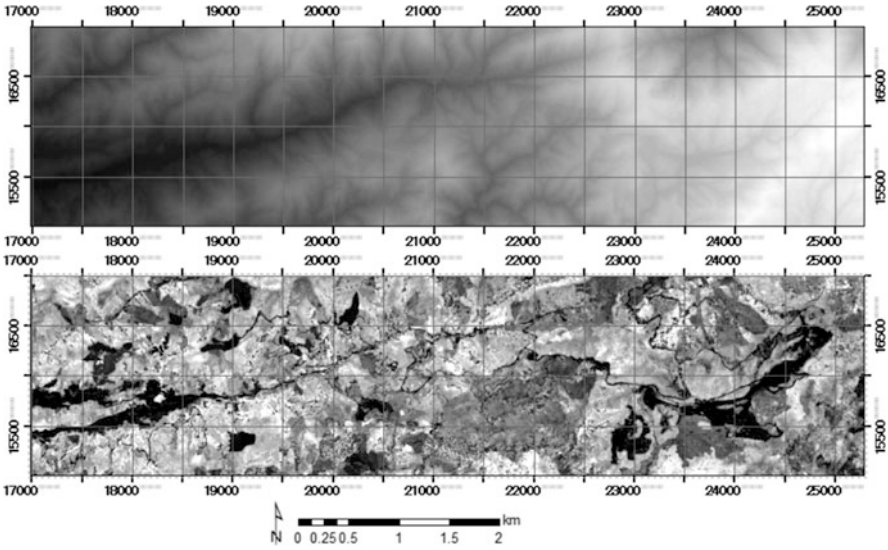

Fig. 4.4 Airborne LiDAR data over the study site. (**a**) A digital surface model (DSM): objects with higher elevation appear brighter. Elevation is lower in the western part which is connecting to the Takayama city area. (**b**) A digital canopy height model (DCHM), which was obtained in August, 2011: black areas are open areas such as roads, crop fields, open recreation areas, and ski slopes

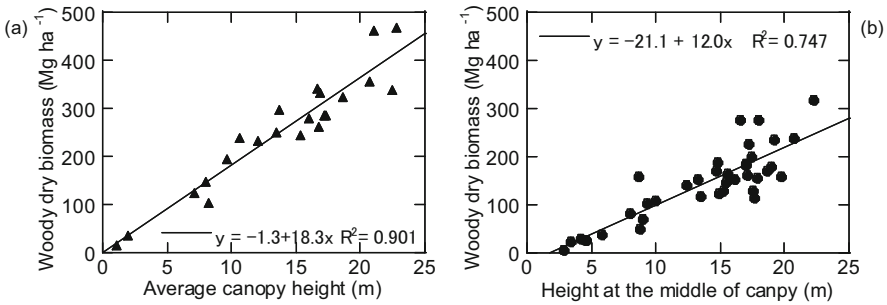

Fig. 4.5 Relationship canopy parameters, which were computed using DCHM in 2011 and field-measured the total (above and below) woody dry biomass. (**a**) Evergreen coniferous forest, and (**b**) deciduous broadleaved forest

$$\mathrm{TDB} = 18.3 \times \mathrm{AHavr} - 1.3 \tag{4.1}$$

Deciduous broadleaved forest:

$$\mathrm{TDB} = 12.0 \times \mathrm{Hd5} - 21.1 \tag{4.2}$$

There is a strong correlation between the independent variables and TDB for the two forest types. The validation results showed the usefulness and weakness of DCHM

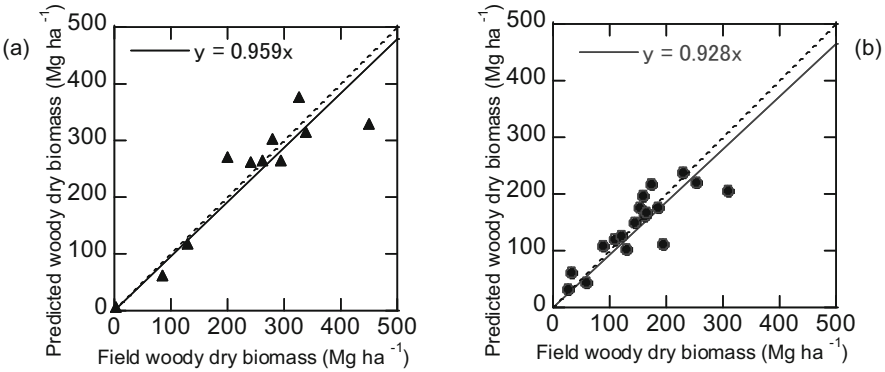

Fig. 4.6 Validation results of TDB prediction based on the comparison of predicted and field TDB. Models (**a**) for evergreen coniferous forests, and (**b**) for deciduous broadleaved forests (Awaya and Takahashi 2017)

derived variables. Predicted TDB tended to be slightly underestimated as the regression lines, with slopes of 0.959 and 0.928 between field measurements (X-axis) and the predictions (Y-axis) in Fig. 4.5. The size variation would be a function of age and, thus, canopy height. Therefore, LiDAR height variables probably correlated with variation in biomass among stands. Reducing standard error is the greatest task in improving the accuracy of TDB estimates, and adding the second height variable may be effective.

The models for coniferous forests might underestimate the Japanese cedar field TDB and overestimate the hinoki cypress field TDB. Japanese cedar trees had a multilayer structure because of intraspecies competition under unthinned conditions. The overstory canopies covered understory trees that were invisible from the air. Therefore the estimated TDB was relatively low, because the understory was not evaluated in the overall estimation using the DCHMs and prediction model.

On the other hand, hinoki cypress stands had an uniform one-layer canopy and relatively low TDB in this area, resulting in an overestimate using the DCHMs and prediction model. Thus, canopy structure influences the biomass estimates (Rosette et al. 2012). The standard errors (SEs) for TDB validation (Fig. 4.6) were 32.3 and 35.8 Mg ha^{-1} for evergreen coniferous forest and deciduous broadleaved forest, respectively. Estimates were sensitive to the tree density or canopy structure. Dense stands tended to result in underestimations with high SEs.

4.3 Biomass Distribution

TDB maps were produced using raster LiDAR parameter files, the forest type map (Fig. 4.3), and selected models (Fig. 4.5). A frequency histogram of the 2011 TDB map (not shown) had a symmetrical frequency distribution peaking at around

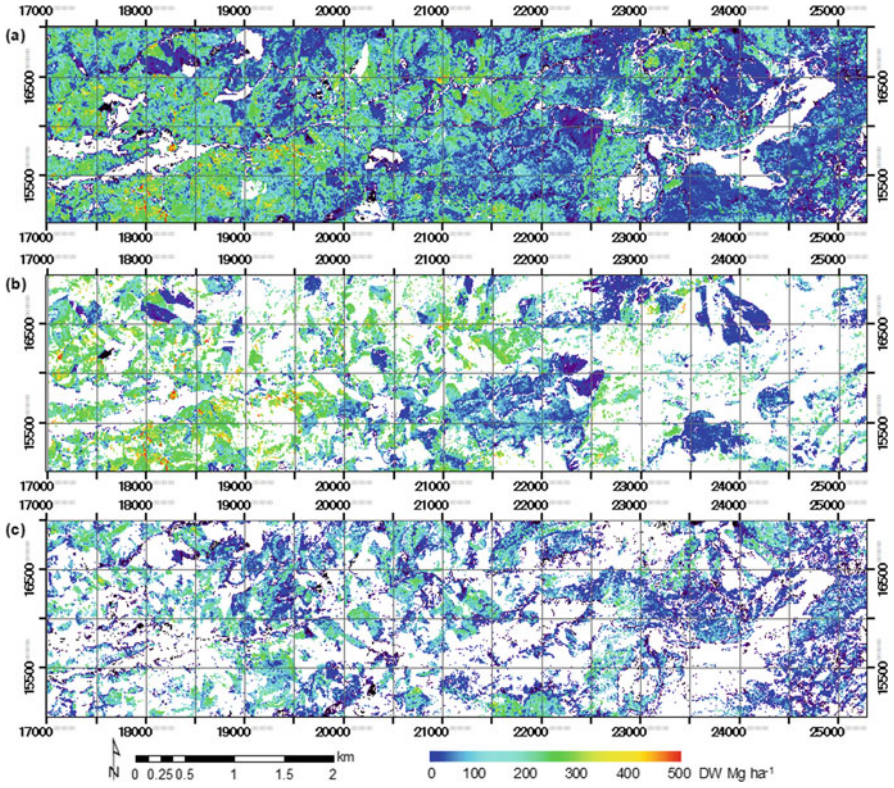

Fig. 4.7 Distribution of TDB 2005 predicted using Eqs. (4.1) and (4.2). (**a**) All forest, (**b**) evergreen coniferous forest, and (**c**) deciduous broadleaved forest

230 Mg ha^{-1} (Awaya and Takahashi 2017), while the average was 239.4 Mg ha^{-1}. There was no clear deviation of biomass frequency when all forests were considered.

TDB maps show forest status regarding woody biomass distribution well. TDB was greater in the western half than that in the eastern half of the study area, both in 2005 (Fig. 4.7a) and 2011 (Fig. 4.8a). TDB was especially great around the open area in the west where local farmers' houses existed. As described previously, Japanese cedar was planted after the World War 2 before the planting of hinoki cypress, therefore it had the highest TDB in the western part in Figs. 4.7a and 4.8a.

A small village was located at the west and forest farmers planted evergreen coniferous trees in their surroundings. Deciduous broadleaved trees were used as fuel wood until about 1960 before the energy revolution, and most broadleaved forest seemed to have been left undisturbed and thus regenerated naturally. Hence, areas with high TDB in the west mainly included mature Japanese cedar forests. On the other hand, there was no residential area in the eastern two-thirds, and planting trees started later than the western area near the village. As a result, broadleaved and

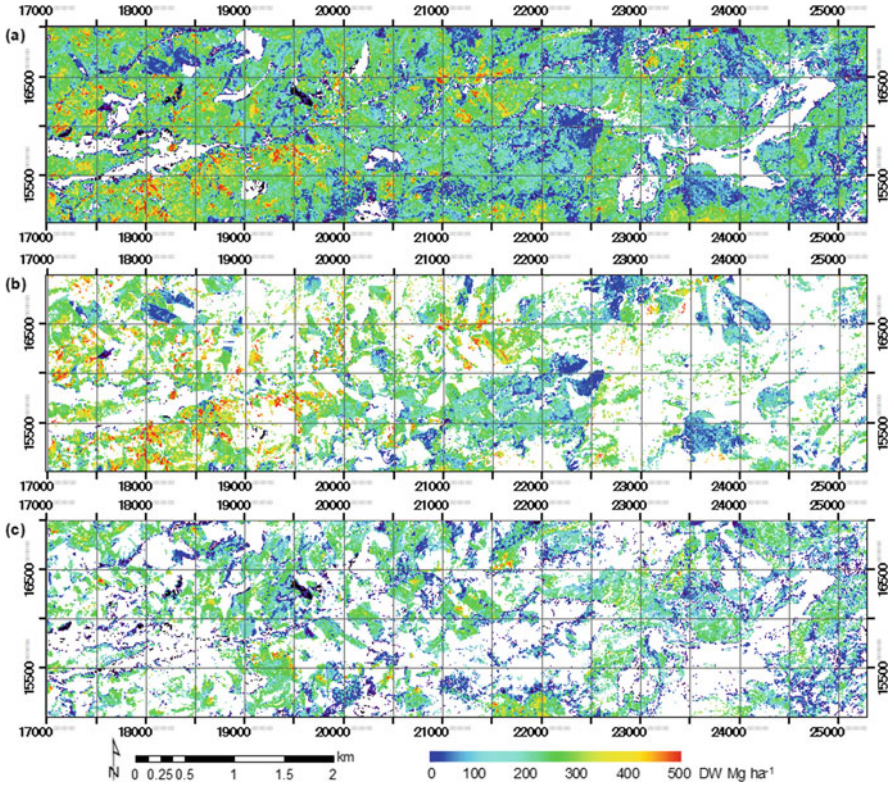

Fig. 4.8 Distribution of TDB 2011 predicted using Eqs. (4.2) and (4.8). (**a**) All forest, (**b**) evergreen coniferous forest, and (**c**) deciduous broadleaved forest (Awaya and Takahashi 2017)

young coniferous forests with small TDB dominated in the eastern two-thirds of the mapping area.

TDB of evergreen coniferous forest exceeded 300 Mg ha^{-1} in 2005 (Fig. 4.7b) and became greater in 2011 (Fig. 4.8b) in the west. On the other hand, TDB of evergreen coniferous forest was mostly less than 200 Mg ha^{-1} with the same level of deciduous broadleaved forest in the eastern one-third in 2005 (Fig. 4.7c), and the trend was the same in 2011 (Fig. 4.8c), although TDB increased up to about 300 Mg ha^{-1}. Thus harvesting and planting history influenced on the biomass distribution in the study site and the TDB maps shows the forestry history activity indirectly. Thus, historical human activity reflected the distribution of forest types and biomass in this area.

4.4 Interannual Biomass Change

Logging was rare between 2005 and 2011 because stands were in the pre-mature stage and mostly less than 50 years old, which is the standard time to harvest cedar and cypress trees in this area. Therefore biomass increased everywhere (Fig. 4.9). On the other hand, biomass decreased in only 2.6% of the forest area. The area in which biomass decreased more than 100 Mg ha^{-1} was only 0.8% of the forest where trees would be logged. The TDB change map shows that TDB increased greater in evergreen coniferous forest than in deciduous broadleaved forest. Japanese cedar grows fast among tree species in Japan so this would be the greatest reason of this difference.

The annual TDB growth of the Japanese cedar almost reaches greatest in about 50 years old, and the stand age of most cedar forests was about 40 to 50 years in the study site. These are probably the reasons of greater TDB increase in the coniferous forests than broadleaved forests, and TDB increase was more than 5 Mg ha^{-1} year^{-1} in large parts of the coniferous forests. On the other hand, TDB increased mostly

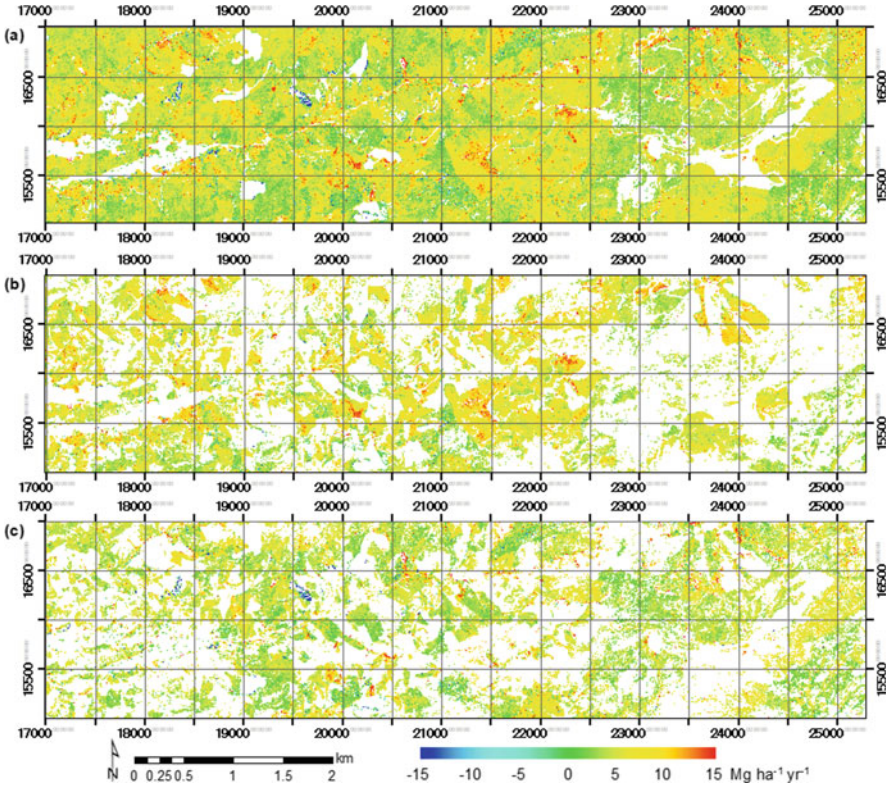

Fig. 4.9 Secular TDB change between 2005 and 2011. (**a**) All forest, (**b**) evergreen coniferous forest, and (**c**) deciduous broadleaved forest

around 5 Mg ha^{-1} year^{-1}, and the area with increase less than 5 Mg ha^{-1} year^{-1} covered about a half of the map (Fig. 4.9).

Table 4.3 shows TDB in 2005 and 2011 along with its change. The average TDB of evergreen coniferous forest was about 1.4 times greater than that of deciduous broadleaved forest, both in 2005 and 2011. Annual TDB changes were 6.6 and 3.6 Mg ha^{-1} year^{-1} for these forest types, respectively, and 5.0 Mg ha^{-1} year^{-1} for all forest.

Thus evergreen coniferous forest had greater TBD and growth rate than deciduous broadleaved forest. Since the forest age is probably similar due to a common harvesting and planting history of trees for the two forest types in this area, the difference would be caused by difference rates of growth between the tree species rather than different stand ages between the two forest types. Since the coverage area of these forest types was similar in this area, TDB of evergreen coniferous forests was about 1.3 times that of broadleaved forests in 2005 and 2011; the ratio was almost same as the ratio of average TDB. Total TDB change or woody biomass growth was 7213 MgDW ha^{-1} year^{-1} or 3607 MgC ha^{-1} year^{-1}, including larch.

Our results showed TDB distribution including above ground and underground woody parts of trees. Average annual change of TDB (growth) of deciduous broadleaved forest was about 3.6 MgDW ha^{-1} over the broadleaved forest and 2.38 MgDW ha^{-1} in TKY. An average annual woody biomass growth of 2.56 MgDW ha^{-1} was recorded between 1999 and 2009 in TKY (Ohtsuka 2012), which was quite close to the prediction by TDB difference. Ohtsuka (2012) also reported that the average annual leaf biomass was 3.66 MgDW ha^{-1}. Therefore the sum of woody biomass growth and leaf biomass, which is NPP, would be nearly twice of our TDB growth estimation in deciduous broadleaved forests.

4.5 Conclusions

As airborne laser scanners provide the most accurate canopy height information in a large area, researchers are keen to validate its accuracy for various forest applications using predicted biomass (stem, woody part, leaf) canopy structure. This article introduced an application of TDB and growth mapping regarding usages of airborne LiDAR data in forestry and carbon circulation.

High coefficients of determination appeared in the TDB prediction models of coniferous forest as well as in the broadleaved forest using canopy height parameters which were computed using airborne LiDAR data in 2011. The TDB prediction models were suitable for TDB mapping in a forested area comprising part of the Namai river basin.

Although field plot surveys provide biomass or carbon amount information, spatial distribution mapping is difficult due to hardiness of numerous plot surveys. The Forestry Agency of Japan has executed national forest inventory for more than 20 years; however, plots are located at 4 km lattice points. Thus spatial distribution of biomass cannot be mapped by plot surveys. Above all, repeating large scale

Table 4.3 Summary of TDB and its change by each forest type

Forest type	Area (ha)	Rate per whole area (%)	Rate per forest (%)	Average TDB (Mg ha^{-1})			Total TDB (Mg)			Rate of TDB (%)		
				2005	2011	Change per year	2005	2011	Change per year	2005	2011	Change
Evergreen Conif.	664.4	40.0	46.1	253.0	292.5	6.6	168,063	194,353	4384	53.9	54.7	60.5
Deciduous DRD	708.6	42.7	49.2	184.4	205.9	3.6	130,695	145,888	2559	41.9	41.1	35.3
Larch	68.4	4.1	4.7	193.9	220.1	4.4	13,261	15,059	299	4.3	4.2	4.1
Sub total or mean	1441.4	86.8	100.0	216.5	246.5	5.0	312,019	355,300	7242	100.0	100.0	100.0
None forest	218.6	13.2										
Total	1660.0	100.0										

precise survey is costly. Airborne laser observations are also costly; however, point clouds height data provide accurate biomass maps and are stored for further analysis.

As shown in this article, biomass (TDB) maps using repetitive observation data resulted in a biomass change (TDB growth or NPP) map which showed carbon fixation by forest plants. Unlike carbon flux measurements, it is impossible to map carbon fixation by forested lands (Net Ecosystem Production, NEP) using airborne LiDAR alone. If soil respiration is estimated using remote sensing data (including climate), carbon fixation can be mapped and would be advantageous. However, a comparison of NPP between LiDAR estimates and field survey in TKY showed a close agreement. Although NEP mapping using LiDAR data is difficult, NPP mapping is quite accurate and LiDAR remote sensing can provide spatial distribution of biomass growth or carbon fixation by trees.

Our results are transferrable to forests of the same species with a similar structure. Unfortunately, our results will not be universal among various forests, however, as pointed out by other studies (Næsset 2014; Rosette et al. 2012). Forest structure varies greatly and is impacted, for example, by planting rates or thinning practices. Estimation errors would be great after thinning which changes stand structure. This can result in changes in the relationship between biomass and LiDAR variables (Rosette et al. 2012). The difference in stand structure, including canopy height and variation, is especially influenced by thinning and must, therefore, have great influence on TDB prediction which was derived using canopy height parameters.

It was necessary to reduce effects by stand density and slope angle, which reduced the accuracy of DCHM using probably very dense point cloud data. LiDAR technology has advanced greatly and precise forest biomass mapping is promising using future airborne LiDAR data.

Acknowledgments This article was the result of a research project "Development of an accuracy assessment method for scaling results of carbon balance using a process based model" supported by JSPS KAKENHI (grant number 22248017, Grant-in-Aid for Scientific Research A). The 2003 LiDAR data and three aerial orthophotos were provided by the Gifu Prefectural Government. The author appreciates the work of Emeritus Professor Tsuyoshi Akiyama who contributed to the research by establishing research facilities in Takayama, such as image processing software, the QuickBird images, and the 2005 LiDAR data. The author greatly appreciates the valuable advice from Dr. Tomoaki Takahashi (Forestry and Forest Products Research Institute). The author also appreciates the field survey support from Mr. Kenji Kurumado (Takayama Research Center of Gifu University), Naoko Fukuda, and Hiroto Kawai (former Awaya Laboratory staff), and Siqinbilige Wang, Nabuti Alatan, and Weilisi (former Awaya Laboratory students).

References

Aldred AH, Bonner GM (1985) Application of airborne lasers to forest surveys (Inst. Information report PI-X-51); Petawawa National Forestry, Petawawa, pp 1–62

Almeida DRA, Stark SC, Shao G, Schietti J, Nelson BW, Bruce W, Silva CA, Gorgens EB, Valbuena R, Papa DA, Brancalion PHS (2019) Optimizing the remote detection of tropical

rainforest structure with airborne lidar: leaf area profile sensitivity to pulse density and spatial sampling. Remote Sens 11(1):92. https://doi.org/10.3390/rs11010092

Araki K, Awaya Y (2021) Analysis and prediction of gap dynamics in a secondary deciduous broadleaf Forest of Central Japan using airborne multi-LiDAR observations. Remote Sens 13(100). https://doi.org/10.3390/rs13010100

Arp H, Griesbach JC, Burns JP (1982) Mapping in tropical forests; A new approach using the laser APR. PE&RS 48:91–100

Awaya Y, Takahashi T (2017) Evaluating the differences in modeling biophysical attributes between deciduous broadleaved and evergreen conifer forests using low-density small-footprint LiDAR data. Remote Sens 9(572). https://doi.org/10.3390/rs9060572

Awaya Y, Kodani E, Tanaka K, Liu J, Zhuang D, Meng Y (2004) Estimation of the global net primary productivity using NOAA images and meteorological data: changes between 1988 and 1993. Int J Remote Sensing 25(9):1597–1613

Beraldin J, Blais F, Lohr U (2010) Laser scanning technology. In: Vosselman G, Mass H (eds) Airborne and terrestrial laser scanning. Whittles Publishing, Scotland, pp 19–30

Biudes MS, Machado NG, Danelichen VH, Souza MC, Vourlitis GL, Nogueira JDS (2014) Ground and remote sensing-based measurements of leaf area index in a transitional forest and seasonal flooded forest in Brazil. Int J Biometeorol 58:1181–1193

Breidenbach J, McRoberts RE, Astrupa R (2016) Empirical coverage of model-based variance estimators for remote sensing assisted estimation of stand-level timber volume. Remote Sens Environ 173:274–281

Cao L, Coops NC, Hermosilla T, Innes J, Dai J, She G (2014) Using small-footprint discrete and full-waveform airborne lidar metrics to estimate total biomass and biomass components in subtropical forests. Remote Sens 6:7110–7135

Food and Agriculture Organization of the United Nations (FAO) (2016) Global forest resources assessment 2015 how are the world's forests changing? 2nd edn. FAO, Rome, pp 1–44

Foody GM, Boydb DS, Cutlerc MEJ (2003) Predictive relations of tropical forest biomass from Landsat TM data and their transferability between regions. Remote Sens Environ 85:463–474

Forestry Agency of Japan (2014) Annual report on Forest and forestry in Japan fiscal year 2013. Forestry Agency of Japan, Tokyo, p 223. (In Japanese with English Summary)

Franklin SE (2001) Remote sensing for sustainable forest management. Lewis Publishers, CRC Press, Florida, 407 pp

Fukuda N, Awaya Y, Kojima T (2012) Classification of forest vegetation types using LiDAR data and Quickbird images – case study of the Daihachiga river basin in Takayama city. J JASS 28: 115–122. (In Japanese with English Summary)

He QS, Cao CX, Chen EX, Sun GQ, Ling FL, Pang Y, Zhang H, Ni WJ, Xu M, Li ZY (2012) Forest stand biomass estimation using ALOS PALSAR data based on LiDAR-derived prior knowledge in the Qilian Mountain, western China. Int J Remote Sens 33:710–729

Holmgren J, Nilsson M, Olsson H (2003) Estimation of tree height and stem volume on plots using airborne laser scanning. For Sci 49:419–428

Hopkinson C, Lovell J, Chasmer L, Jupp D, Kljun N, van Gorsel E (2013) Integrating terrestrial and airborne lidar to calibrate a 3D canopy model of effective leaf area index. Remote Sens Environ 136:301–314

Houghton JH, Ding Y, Grigss DJ, Noguer M, van der Linden PJ, Xiaosu D (eds) (2001) Climate change 2001: the scientific basis. Cambridge University Press, Cambridge, pp 99–237

Hovi A, Korhonen L, Vauhkonen J, Korpela I (2016) LiDAR waveform features for tree species classification and their sensitivity to tree- and acquisition related parameters. Remote Sens Environ 173:224–237

Kamoskea AG, Dahlina KM, Starkc SC, Shawn P, Serbind SP (2019) Leaf area density from airborne LiDAR: comparing sensors and resolutions in a temperate broadleaf forest ecosystem. For Ecol Manag 433:364–375

Kankare V, Vastaranta M, Holopainen M, Räty M, Yu X, Hyyppä J, Hyyppä H, Alho P, Viitala R (2013) Retrieval of forest aboveground biomass and stem volume with airborne scanning LiDAR. Remote Sens 5:2257–2274

Knyazikhin Y, Martonchik J, Diner D, Myneni R, Verstraete M, Pinty B, Gobron N (1998) Estimation of vegetation canopy leaf area index and fraction of absorbed photosynthetically active radiation from atmosphere-corrected MISR data. J Geophys Res Atmos 103:32239–32256

Korhonen L, Korpela I, Heiskanen J, Maltamo M (2011) Airborne discrete-return LIDAR data in the estimation of vertical canopy cover, angular canopy closure and leaf area index. Remote Sens Environ 115:1065–1080

Kwak D, Lee W, Lee J, Biging GS, Gong P (2007) Detection of individual trees and estimation of tree height using LiDAR data. J For Res 12:425–434

Leeuwen M, Nieuwenhuis M (2010) Retrieval of forest structural parameters using LiDAR remote sensing. Eur J Forest Res 129:749–770

Lefsky MA, Harding D, Cohen WB, Parker G, Shugart HH (1999a) Surface lidar remote sensing of basal area and biomass in deciduous forests of eastern Maryland, USA. Remote Sens Environ 67:83–98

Lefsky MA, Cohen WB, Acker SA, Parker GC, Spies TA, Harding D (1999b) Lidar remote sensing of the canopy structure and biophysical properties of Douglas-fir western hemlock forests. Remote Sens Environ 70:339–361

Maas H (2010) Forestry applications. In: Vosselman G, Mass H (eds) Airborne and terrestrial laser scanning. Whittles, Scotland, pp 213–235

Maltamo K, Eerikäinenn J, Pitkänen J, Hyyppä M (2004) Vehmas estimation of timber volume and stem density based on scanning laser altimetry and expected tree size distribution functions. Remote Sens Environ 90:319–330

Maltamo M, Næsset E, Vauhkonen J (eds) (2014) Forestry applications of airborne laser scanning. Springer, Dordrecht, 464 pp

Means JE, Acker SA, Fitt BJ, Renslow M, Emerson L, Hendrix CJ (2000) Predicting forest stand characteristics with airborne scanning lidar. PE&RS 66:1367–1371

Melnikova I, Awaya Y, Saitoh TM, Muraoka H, Sasai T (2018) Estimation of leaf area index in a mountain Forest of Central Japan with a 30-m spatial resolution based on Landsat operational land imager imagery: an application of a simple model for seasonal monitoring. Remote Sens 10:179. https://doi.org/10.3390/rs10020179

Mora B, Wulder MA, White JC, Hobart G (2013) Modeling stand height, volume, and biomass from very high spatial resolution satellite imagery and samples of airborne LiDAR. Remote Sens 5:2308–2326

Morsdorf F, Kötz B, Meier E, Itten KI, Allgöwer B (2006) Estimation of LAI and fractional cover from small footprint airborne laser scanning data based on gap fraction. Remote Sens Environ 104(1):50–61

Morsdorf F, Nichol C, Malthus T, Woodhouse IH (2009) Assessing forest structural and physiological information content of multi-spectral LiDAR waveforms by radiative transfer modelling. Remote Sens Environ 113:2152–2163

Muraoka H, Noda HM, Saitoh TM, Nagai S, Nasahara KN (2012) Long-term and regional scale observation of forest canopy photosynthesis by linking plant ecophysiology and satellite remote sensing. BSJ-Review 3, 16 pp

Næsset E (1997) Estimating timber volume of forest stands using airborne laser scanner data. Remote Sens Environ 61:246–253

Næsset E (2014) Area-based inventory in Norway-from innovation to an operational reality. In: Maltamo M, Næsset E, Vauhkonen J (eds) Forestry applications of airborne laser scanning, vol 27. Springer, Dordrecht, pp 215–240

Næsset E, Gobakken T (2005) Estimating forest growth using canopy metrics derived from airborne laser scanner data. Remote Sens Environ 96:453–465

Næsset E, Økland T (2002) Estimating tree height and tree crown properties using airborne scanning laser in a boreal nature reserve. Remote Sens Environ 79:105–115

Nelson R, Krabill W, Tonelli J (1988) Estimating forest biomass and volume using airborne laser data. Remote Sens Environ 24:247–267

Ohtsuka T (2012) Carbon cycling at Takayama Forest: results from intensive studies in the last decade, and further studies for a next decade. Jpn J Ecol 62:31–44

Peng D, Zhang H, Liu L, Huang W, Huete AR, Zhang X, Wang F, Yu L, Xie Q, Wang C, Luo S, Li C, Zhang B (2019) Estimating the aboveground biomass for planted forests based on stand age and environmental variables. Remote Sens 11(2270). https://doi.org/10.3390/rs11192270

Peterson DL, Spanner MA, Running SW, Teuber KB (1987) Relationship of thematic mapper simulator data to leaf area index of temperate coniferous forests. Remote Sens Environ 22:323–341

Potter CS, Randerson JT, Field CB, Matson PA, Vitousek PM, Mooney HA, Klooster SA (1993) Terrestrial ecosystem production: a process model based on global satellite and surface data. Glob Biogeochem Cycles 7:811–841

Rosette J, Suárez J, Nelson R, Los S, Cook B, North P (2012) Lidar remote sensing for biomass assessment, in remote sensing of biomass—principles and applications. In: Fatoyinbo T (ed) InTech, Rijeka, pp 3–26

Saitoh TM, Nagai S, Yoshino J, Muraoka H, Saigusa N, Tamagawa I (2012) Functional consequences of differences in canopy phenology for the carbon budgets of two cool-temperate Forest types: simulations using the NCAR/LSM model and validation using tower flux and biometric data. Eurasian J Forest Res 15(1):19–30

Spanner MA, Pierce LL, Peterson DL, Running SW (1990) Remote sensing of temperate coniferous forest leaf area index. The influence of canopy closure, understory vegetation and background reflectance. Int J Remote Sens 11:95–111

Sprintsin M, Karnieli A, Berliner P, Rotenberg E, Yakir D, Cohen S (2007) The effect of spatial resolution on the accuracy of leaf area index estimation for a forest planted in the desert transition zone. Remote Sens Environ 109:416–428

Sumnall MJ, Trlica A, Carter DR, Cook RL, Schulte ML, Campoe OC, Rubilar RA, Wynne RH, Thomas VA (2021) Estimating the overstory and understory vertical extents and their leaf area index in intensively managed loblolly pine (Pinus taeda L.) plantations using airborne laser scanning. Remote Sens Environ 112250. https://doi.org/10.1016/j.rse.2020.112250

Takahashi T, Yamamoto K, Senda Y, Tsuzuku M (2005a) Predicting individual stem volumes of sugi (Cryptomeria japonica D. Don) plantations in mountainous areas using small-footprint airborne LiDAR. J For Res 10:305–312

Takahashi T, Yamamoto K, Senda Y, Tsuzuku M (2005b) Estimating individual tree heights of sugi (Cryptomeria japonica D. Don) plantations in mountainous areas using small-footprint airborne LiDAR. J For Res 10:135–142

Takahashi T, Awaya Y, Hirata Y, Furuya N, Sakai T, Sakai A (2010) Stand volume estimation by combining low laser-sampling density LiDAR data with QuickBird panchromatic imagery in closed-canopy Japanese cedar (Cryptomeria japonica) plantations. Int J Remote Sensing 31(5): 1281–1301

Tsuzuki H, Kusakabe T, Sueda T (2006) Long-range estimation of standing timber stock in western boreal forest of Canada using airborne laser altimetry. J Jpn For Soc 88:103–113. (In Japanese with English Summary)

Vepakomma U, St-Onge B, Kneeshaw D (2008) Spatially explicit characterization of boreal forest gap dynamics using multi-temporal lidar data. Remote Sens Environ 112:2326–2340

Vepakomma U, Kneeshaw D, Fortin MJ (2012) Spatial contiguity and continuity of canopy gaps in mixed wood boreal forests: persistence, expansion, shrinkage and displacement. J Ecol 100: 1257–1268

Wulder MA, White JC, Nelson RF, Næsset E, Ørka OH, Coops NC, Hilker T, Bater CW, Gobakken T (2012) Lidar sampling for large-area forest characterization: a review. Remote Sens Environ 121:196–209

Yao T, Yang X, Zhao F, Wang Z, Zhang Q, Jupp D, Lovell J, Culvenor D, Newnham G, Ni-Meister W (2011) Measuring forest structure and biomass in New England forest stands using echidna ground-based lidar. Remote Sens Environ 115:2965–2974

Zhang K (2008) Identification of gaps in mangrove forests with airborne LIDAR. Remote Sens Environ 112:2309–2325

Zhao K, Popescu S, Nelson R (2009) Lidar remote sensing of forest biomass: a scale-invariant estimation approach using airborne lasers. Remote Sens Environ 113:182–196

Chapter 5
Semi-Natural Grasslands Maintained by Controlled Burning in Japan: Air and Soil Temperature and Plant Diversity

Satoshi Tsuda

Abstract There are semi-natural grasslands that are maintained by mowing and livestock grazing in Japan, and some of them are maintained by burning. Mowing and grazing are carried out mainly in the summer when the plants are active, but burning is carried out from winter to spring, which is the dormant period of the plants. The temperature at the time of burning in spring is high above ground, but hardly rises underground, so the damage on plants is considered to be limited. The soil temperature after burning is high enough for seeds areto germinate even in spring when the air tem able perature is low. Many seedlings occur in the burned area because the soil temperature after burning rises. As a result, the biodiversity of semi-natural grasslands increases.

Keywords Grassland burning · Prescribed fire · Semi-natural grassland · Soil temperature · Vegetation structure

5.1 Introduction

The Japanese archipelago is located at latitudes 45° 31′ to 24°3′ N and longitude 122° 56′ to 145 °49′ E. The southern part of the Ryukyu Islands is included in the subtropical zone, and the northern part of Hokkaido is included in the subarctic zone. Most of the rest of the Japanese archipelago belongs to the temperate zone, but the southwestern side is generally classified as a warm temperate zone and the north-eastern side is generally classified as a cool temperate zone. The warm temperate zone is mainly occupied by evergreen broad-leaved trees, and the cool temperate zone is occupied by deciduous broad-leaved trees, both of which develop forest communities.

In most parts of Japan, the annual rainfall is in the range of 1000 mm to 3000 mm, which is sufficient for the formation of forest communities. Therefore, natural

S. Tsuda (✉)
River Basin Research Center, Gifu University, Gifu, Japan
e-mail: tsuda@green.gifu-u.ac.jp

F. Li et al. (eds.), *River Basin Environment: Evaluation, Management and Conservation*, https://doi.org/10.1007/978-981-19-4070-5_5

grasslands are not distributed unless there are some special environments such as alpine zones with low temperature, dryness, and short growing period, coastal grassland with sandy and high salinity, and marshes with excessive water conditions. In Japan, grasslands that are widely and commonly found in areas from flatlands to mountains are semi-natural grasslands, which are premised on human management in order to establish them. Unlike artificial grasslands, semi-natural grasslands are herbaceous communities that are naturally established after human disturbance. The main management methods include mowing, burning, grazing, and combinations of these. If these are not done, the grasslands will grow to bushes in a few years and will transition to a forest community within a few decades. Among these semi-natural grasslands in Japan, the characteristics of burning and subsequent changes in vegetation will be described for grasslands that are managed by burning.

Regarding the effects on plants, reaping and grazing are likely to have similar effects in cutting the plants during the growing season of the plants. On the other hand, grassland burning is likely to be different from the former two in that it has the effect of burning during the dormant period of the plant. I will be explained the characteristics of grassland burning from that point of view.

5.2 Semi-Natural Grassland Maintained by Burning in Japan

Fertilizers made from grass resources such as barnyard manure, compost, and green manure used in agriculture in the past have now been replaced by industrially synthesized chemical fertilizers. In addition, cows and horses that need feed raised by most farmers for cargo handling and agricultural work have been replaced by tractors and other agricultural machinery powered by fuel. Many thatched roof houses (Photo 5.1) which is hard to maintain has changed to a farmhouse with a tin roof and a tiled roof, which is easy maintain. As a result, grasslands for obtaining grass resources are no longer needed around rural areas, and more than 90% of the area of semi-natural grasslands has disappeared compared to 100 years ago (Ogura 2012). Figure 5.1 shows that the grasslands are currently being burned to maintain the grasslands in Japan, and the locations of the grasslands covered in this paper are described place name.

The semi-natural grasslands maintained by grassland burning in Japan extend nationwide from Hokkaido to Kyushu, but are relatively few in Hokkaido and the Chubu region. In Mt. Aso, Akiyoshidai, Mt. Kanpu, Koshimizu Gensei-Kaen, etc., the excellent grassland view was evaluated and it was designated as a National park or a Quasi-national park. These grassland views should be maintained, but the grassland area has decreased as the lifestyles surrounding agriculture have changed. In Mt. Kanpu (Akita Prefecture), the grassland area within the range of the Quasi-national park decreased from 319 ha to 138 ha in the 40 years from 1975 to 2014 (Masui et al. 2017). With the decrease in grassland area, there are concerns about the

Photo 5.1 Thatched-roof houses that were once often seen in rural areas. The Gokayama village including these houses in this photo is designated as a World Heritage Site

extinction of grassland-based plants. For example, *Platycodon grandiflorum*, *Eupatorium japonicum* and *Patrinia scabrioides*, which have been known as the Seven Herbs of Autumn (Aki no Nanakusa), are currently designated as endangered species in the national and prefectural governments due to their lack of habitat.

In the grassland ecosystem maintained by burning, local peoples are diversified in their awareness of grassland burning. Some peoples think that burning for the purpose of improving the grass quality of the rangeland for grazing, while others are not particularly conscious of the purpose and have continued to burn for a long time. In addition, at Watarase Yusuichi (retarding basin), burning is set to grow high-quality Phragmites australis as a raw material for reed screen (Yoshizu), and there are also places where burning is set to maintain the grassland landscape and conserve endangered species.

5.3 Temperature During Grassland Burning

It is expected that if the grasslands are burned, high temperatures will be generated, which will have a considerable impact on the ecosystem. The effects of grassland burning on the ecosystem have been known for a long time, with direct effects such as high temperatures and burned to plant litter, and indirect effects such as the fall of charcoal and ash and changes in the soil conditions (Daubenmire 1968). Even if the

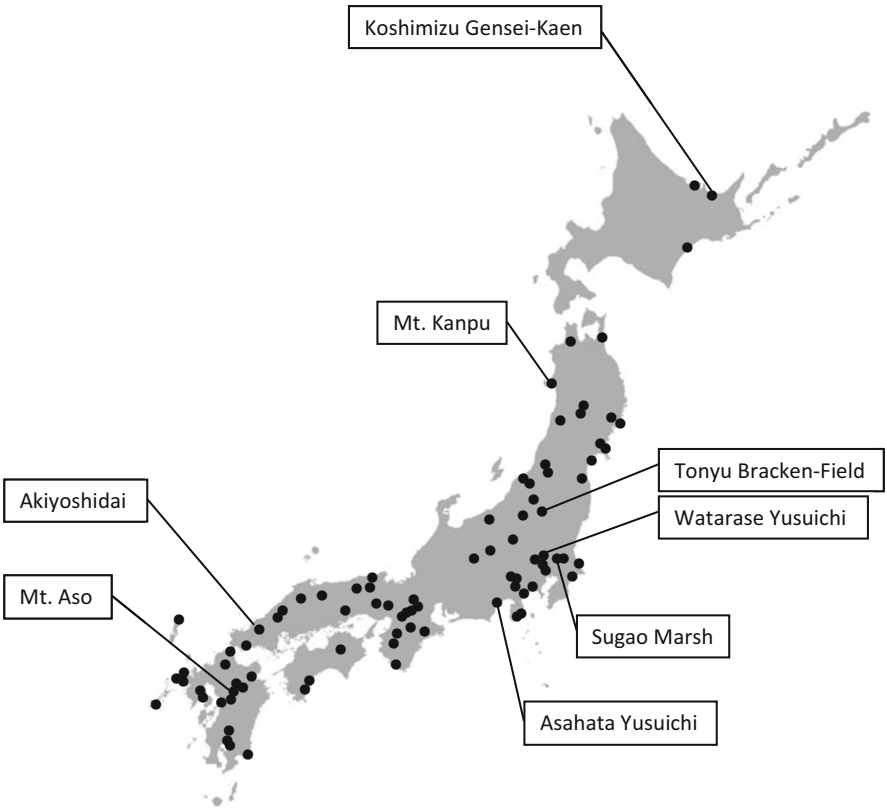

Fig. 5.1 Distribution of semi-natural grasslands managed by burning in Japan. The burned grasslands are indicated by dots, and the grasslands with the names are mentioned in the text

semi-natural grasslands in Japan are burned, the same effects as those of natural grasslands such as prairies should be brought to the ecosystem, so the temperature environment was measured by burning of semi-natural grassland in various places in Japan.

For temperature measurement during grassland burning, six sheath-type K thermocouples were connected to a data logger (Thermic, medel 2300A or 2400A manufactured by Eto Electric Co., Ltd.), as one set. The temperatures in the air at heights of +100 cm and +30 cm, on the ground surface (±0 cm), and in the soil at depths of −2 cm, −5 cm, and −10 cm were recorded at 1-s intervals. The recording device (Thermic) was sealed in a vinyl bag and buried underground, and the electrical wire of the thermocouple was heat-resistant with glass wool, ceramic fiber, heat-resistant aluminum tape, etc. to prevent disconnection due to heating (Photo 5.2).

Figure 5.2 shows the temperature changes during burning in several different types of grasslands. When a community of tall plants such as *Phragmites australis* and *Miscanthus sacchariflorus* with a plant height of 3–4 m is burned, the

Photo 5.2 A system for measuring the burning temperature of grasslands

temperature rises to 700–800 ° C above the ground. On the other hand, when a community with a plant height of about 1–2 m, such as Miscanthus sinensis, Leymus mollis, and Miscanthus intermedius, is burned, the temperature rises only to about 300–500 °C, and in the case of plant height of about 10 cm such as Zoysia japonica, the temperature of the above-ground part rises only up to about 100 ° C. It takes a very short time for temperature sufficient to kill the plant and high temperature lasts for only a few minutes during burning. This is not affected by the type of semi-natural grassland. Furthermore, it can be seen that the lethal temperature is reached only in the above-ground part of all types of grasslands except for the Zoysia japonica community, and there is almost no temperature rise at all three measurement points in the underground part. From this, it is presumed that even if the fire is turned on during the dormant period of the plants in early spring, only the dead leaves and dead stem on the ground are burned, and many living shoots under the ground are not affected. In other words, plants that originally lived in semi-natural grasslands, especially those capable of vegetative propagation, can be regenerated

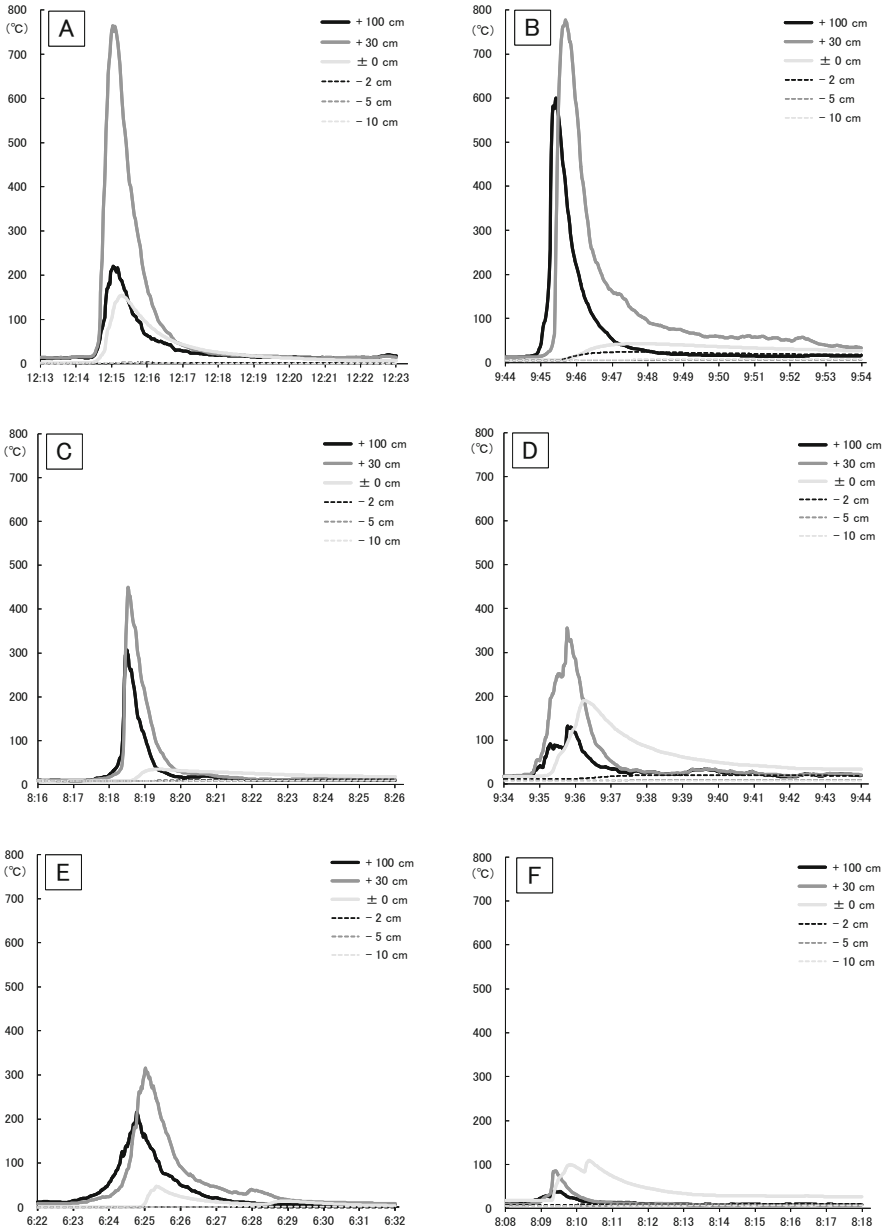

Fig. 5.2 Measurement results of temperature changes by height (+100, +30, ± 0, −2, −5, −10 cm) for 10 min when burning in different grassland types. A: Burning on Janurary 23, 2011 in the Phragmites australis community of the Sugao Marsh, B: Burning on February 8, 2020 in the Miscanthus sacchariflorus community of the Asahata Yusuichi (Drainage basin), C: Burning on April 20, 2019 in the Miscanthus sinensis community in the Mt. Kanpu, D: Burning on May 3, 2019 in the Miscanthus intermedius community in the Tonyu Bracken-Field, E: Burning on April 20, 2010 in the Leymus mollis community in the Koshimizu Gensei-Kaen, F: Burning on April 13 in the Zoysia japonica community in the Mt. Kanpu

from sprouts that survived by the summer of the year, even if they were burned in early spring. Since many species of the components of the semi-natural grassland are vegetatively regenerating species, they do not die even after burning, so the vegetation after burning has almost no structural change compared to the vegetation of the previous year.

Regarding seed germinating species, it is generally known that some Fabaceae species have seeds whose germination rate increases when exposed to high temperatures (Iwata 1966; Martin et al. 1975; Takahashi and Kikuchi 1986; Auld and O'Connell 1991, etc.). There are many *Lespedeza* species such as *Lespedeza bicolor* and *Lespedeza cyrtobotrya* in the *Miscanthus* type semi-natural grassland, and they may germinate due to heat.

5.4 Soil Temperature After Burning

Even if exposed to high temperatures during burning, the effect on vegetative regeneration plants with buds below the ground surface is relatively small. If the seeds are above ground, they may burn to death, but if they are buried underground, they are less likely to die from heat. Conversely, high temperatures during burning can promote seed germination. It is thought that not only heating during burning but also increase in soil temperature due to direct sunlight after burning affects seed germination. Masui et al. (2020) measured the soil temperature after burning in some semi-natural grasslands in eastern Japan and showed that the temperature during the daytime was higher than in unburned grasslands. They predicted that direct sunlight would warm the surface of the soil as a result of lack of litters in the burned grasslands, and the presence of litters in the unburned grasslands would prevent light heating. Figure 5.3 shows changes in soil temperature. Maximum soil temperatures at a depth of 0.5 cm were recorded at 31.9 °C and 28.2 °C on the afternoon of July 27 in burned and unburned grasslands, respectively, and 28.0 °C and 26.5 °C were recorded even at 2 cm underground.

The largest difference in soil temperature between burned and unburned grassland was reached at 12.1 °C (0.5 cm depth) and 7.9 °C (2 cm depth), in the afternoon of May 27. At this time, the soil temperature of the burned grassland was 22.3 °C at a depth of 0.5 cm and 17.2 °C at a depth of 2 cm, which was considerably higher than that of the unburned. Since the germination season of many plants in Japan is spring, it is expected that more plants will be able to germinate in the burned grassland where the soil temperature rises after burning. As Masui et al. (2020) predicted, if the presence of litter blocks sunlight and the soil temperature in the unburned area is lower than that in the burned area, there should be a difference in the amount of litter after burning. In fact, there is a few litter immediately after burning in burned area compared with unburned area of the Koshimizu Gensei-Kaen (Table 5.1).

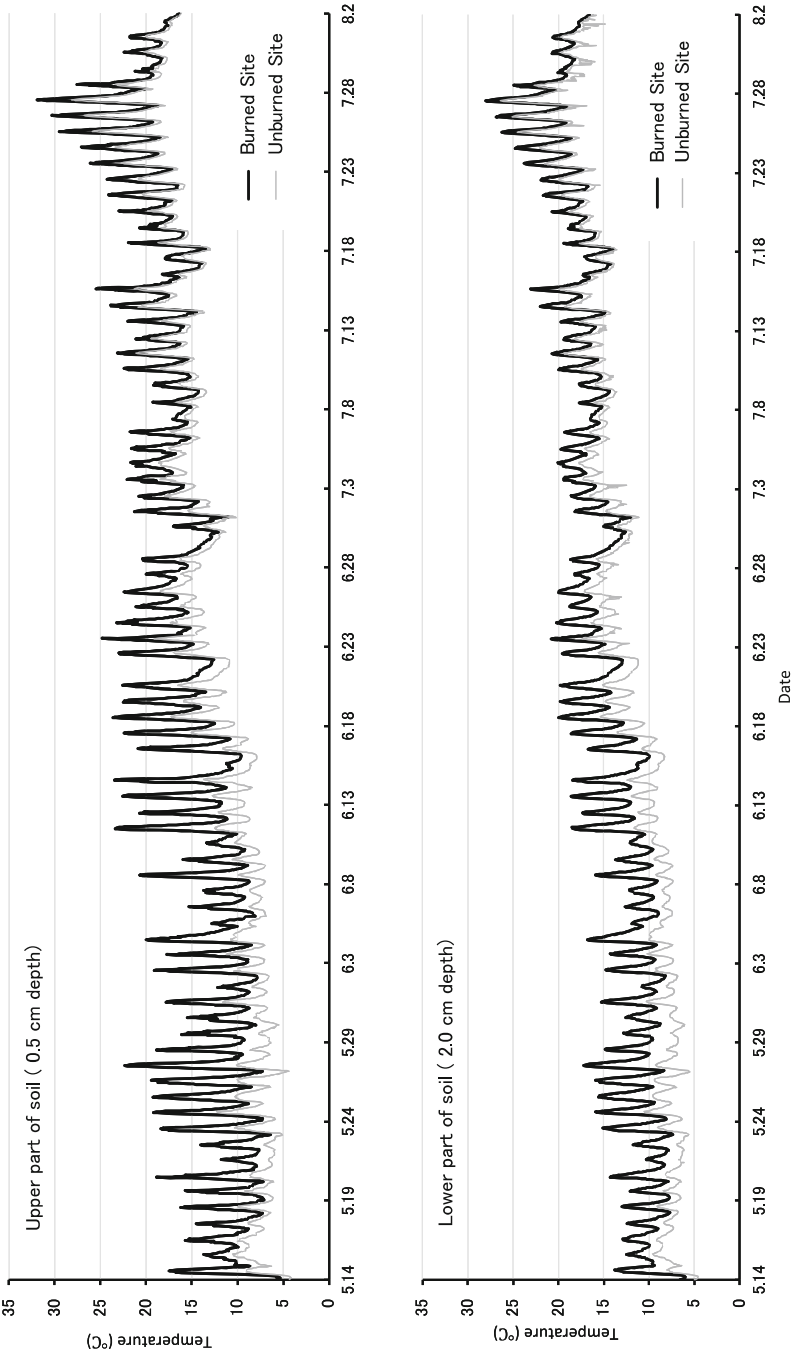

Fig. 5.3 Fluctuations of upper (−0.5 cm) and lower (−2.0 cm) soil temperature in the burned and unburned sites, in coastal grassland of Koshimizu Gensei-Kaen burned on May 13, 1997

Table 5.1 Annual change in the amount of litter in Koshimizu Gensei-Kaen

Sampling time	Fuel weight (g/m^2)	n
Just before burning	979.6 ± 282.9	25
Just after burning	202.1 ± 178.9	22
One year after burning	569.8 ± 184.5	22
Two years after burning	788.3 ± 166.1	22
Three years after burning	893.3 ± 334.4	22

Grassland burning is carried out in spring at intervals of about 5 years in Koshimizu Gensei-Kaen. One square meter of litter was collected from grasslands that had been burned for different year

Table 5.2 Vegetation structure and diversity index in burned and unburned areas of Miscanthus type seminatural grasslands in Mt. Kanpu

	Total number of species	Number of research quadrats (1 × 1 m)	Average number of species in one quadrats	Individual density (m^{-2})		Diversity index (H′)
				Vegetative shoots	Seed germination	
Burned site	61	13	22.08	436.77	67.77	2.82
Unburned site	57	9	17.33	286.75	4.33	2.59

5.5 Characteristics of the Plant Community After Burning

Seedlings are expected to increase due to the high temperature during burning or the rise in soil temperature after burning. Diversity can increase as seedlings are added to grassland vegetation. Table 5.2 shows the results of examining vegetation in the burned and unburned areas of Miscanthus sinensis Type grassland in Mt. Kanpu. Grassland burnings were carried out five times between 2008 and 2021, and some 1 × 1 m quadrat were set up in the summer for vegetation research in the semi-natural grassland. The number of individuals for each species in the quadrat were counted after separating seedlings and vegetative suprouts.

Although the number of research quadrats is slightly different, the total number of species appearing in the burned and unburned areas was 61 and 57, respectively. There was little difference in these numbers, but only 46 of them appeared in both burned and unburned areas. Fifteen species such as *Themeda barbata*, *Patrinia villosa*, and *Erigeron thunbergii* subsp. *thunbergii* appeared only in the burned area, and 11 species such as *Aster iinumae* and *Viburnum dilatatum* appeared only in the unburned area. The number of species and the density of individuals appearing in quadrat were higher in the burned area than in the unburned area. In the burned area, the density of vegetative sprouts increased to 1.5 times that of the unburned area, and the density of seedlings reached more than 15 times that of the unburned area. It is clear that the seed germination was promoted by burning. However the reason why the number of vegetatively regenerated individuals increased in the burned area is currently unknown.

In the study of the semi-natural grasslands of Mt. Kanpu, the total number of species that appeared was not so different between the burned and unburned areas, but the population density increased in the burned areas. In particular, a remarkable increase was observed in seed germinated individuals. If grassland burning is not carried out, vegetatively regenerating individuals will play a major role in maintaining the semi-natural grassland in Japan. Many seedlings appear when grassland burning is carried out, and it is expected that the semi-natural grassland will be composed of many plants. When the diversity index was calculated, it was $H' = 2.59$ in the unburned area, while it was as high as $H' = 2.82$ in the burned area.

5.6 Conclusion

Semi-natural grasslands in Japan are generally burned during the plant dormant period from winter to spring. High temperatures occur during burning, but the lethal temperature of plants is reached only in the above-ground parts, and the underground temperature does not rise. For dormant plants, the shoots and buried seeds below the ground surface are alive, but the above-ground parts are dead. Therefor even if they are burned, the effect of burning for plants is small. On the other hand, the soil temperature after burning becomes higher than the underground temperature during burning due to blackening with charcoal and irradiation with direct sunlight. Seedlings do not appear much in unburned area, but in burned area, seed germination is promoted and many seedlings appear in spring. As a result, highly diverse plant communities are maintained by burning in semi-natural grasslands in Japan.

References

Auld TD, O'Connell MA (1991) Predicting patterns of post-fire germination in 35 eastern Australian Fabaceae. Aust J Ecol 16:53–70

Daubenmire R (1968) Ecology of fire in grasslands. Adv Ecol Res 5:209–266

Iwata E (1966) Germination behavior of shrubby Lespedeza (Lespedeza cyrtobotrya Miq.) seeds with special reference to burning. Ecol Rev 16:217–227

Martin RE, Miller RL, Cushwa CT (1975) Germination response of legume seeds subjected to moist and dry heat. Ecology 56:1441–1445

Masui T, Adachi M, Fujita H, Obata K, Tsuda S (2020) Fluctuation of soil temperature after prescribed burning in some semi-natural grassland in eastern Japan (in Japanese). Vegetat Sci 37:13–25

Masui T, Sawada Y, Tsuda S (2017) Changes in grassland vegetation in Mt. Kanpu, Oga Peninsula of the Akita prefecture (in Japanese). Landscape Plann Horticult 21:1–11

Ogura J (2012) History of radically changed vegetation of Japan (in Japanese). Kokon-Shoin, Tokyo

Takahashi M, Kikuchi T (1986) The heat effect on seed germination of some species in the initial stage of a post-fire vegetation. Ecol Rev 21:11–14

Chapter 6
Detection and Identification of *Phytophthora* Pathogens that Are Threatening Forest Ecosystems Worldwide

Ayaka Hieno, Mingzhu Li, Wenzhuo Feng, Auliana Afandi, Kayoko Otsubo, Haruhisa Suga, and Koji Kageyama

Abstract Introduced *Phytophthora* species are a serious threat to forest trees and nursery plants. These pathogens have spread rapidly and widely due to human activities such as international plant trading, and have caused negative impacts on forest ecosystems. Imported plants should be carefully inspected for the presence of pathogens using molecular detection methods. Since large numbers of specimens are tested in quarantine, the detection method must be simple, rapid and accurate. A loop-mediated isothermal amplification (LAMP) method has the advantage of high tolerance to amplification inhibitors, and thus, simple DNA extraction methods can be used. In this chapter, we will discuss processes for LAMP detection including LAMP primer design; methods for DNA extraction from environmental samples such as plants, soil and water; the applicability various instruments for LAMP assays; and experimental settings for accurate detection with regard to sampling and potential contamination sources. This information will be very useful for researchers in creating detection procedures involving LAMP. LAMP-based

A. Hieno (✉) · K. Otsubo · K. Kageyama
River Basin Research Center, Gifu University, Gifu, Japan
e-mail: hieno@green.gifu-u.ac.jp; otsubo@green.gifu-u.ac.jp; kageyama@green.gifu-u.ac.jp

M. Li
College of Life Sciences, Shaanxi Normal University, Xi'an, Shaanxi, China
e-mail: limz@snnu.edu.cn

W. Feng
College of Agriculture, Guizhou University, Guiyang, Guizhou, China
e-mail: wzfeng@gzu.edu.cn

A. Afandi
Department of Plant Protection, Faculty of Agriculture, Universitas Lampung, Bandar Lampung, Lampung, Indonesia
e-mail: auliana.afandi@fp.unila.ac.id

H. Suga
Institute for Glyco-core Research, Gifu University, Gifu, Japan
e-mail: suga@gifu-u.ac.jp

F. Li et al. (eds.), *River Basin Environment: Evaluation, Management and Conservation*, https://doi.org/10.1007/978-981-19-4070-5_6

detection is expected to have various applications in the future, and is one of the most promising options for pathogen detection, which is needed for disease control.

Keywords *Phytophthora* · LAMP · DNA extraction · QProbe · Multiplex · Internal control

6.1 Introduction

Phytophthora is an oomycete genus with worldwide distribution, and many of its species cause destructive diseases. Several *Phytophthora* species are serious threats to forest trees and nursery plants (Jung et al. 2018). Introduced species including *Phytophthora ramorum*, *Phytophthora lateralis* and *Phytophthora kernoviae* cause tree mortality, mainly in the United States and the United Kingdom (Brasier et al. 2005; Rizzo et al. 2005; Robin et al. 2011; Webber 2009). In Australia, forest dieback is caused by another introduced species, *Phytophthora cinnamomi* (Dell et al. 2005; Garkaklis et al. 2004). These pathogens have spread rapidly and widely due to human activities including the international plant trade, and have resulted in negative impacts on forest ecosystems around the world (Brasier 2008; Jung et al. 2016; Parke and Grünwald 2012). Unfortunately, plant sanitary regulations tend to come into effect only after a problem is identified (Roy et al. 2014). Roy et al. (2014) suggested that regulations should include more proactive approaches for countering pest invasions, including the detection of organisms that have not yet been identified or whose risks are not generally recognized. To achieve early risk management, it is important to conduct large-scale surveys of potential pathogens in the environment and to assess their virulence. In recent years, the diversity of *Phytophthora* species in natural forests has been actively investigated, leading to the discovery of new species and a better understanding of the ecology and pathogenicity of *Phytophthora* species living in natural forest ecosystems (Burgess et al. 2018; Jung et al. 2017a, b; Yang et al. 2017).

Typically, imported plants are subjected to random visual inspection, and if every plant is free of symptoms, the shipment is passed. However, Fichtner et al. (2012) identified symptomless *P. kernoviae* infections in North American native plants. Therefore, imported plants should be carefully screened for the presence of pathogens using molecular detection methods, even if they are accompanied by a phytosanitary certificate. In quarantine, large numbers of specimens need to be tested, so the detection method must be simple, fast and accurate. Various detection methods have been developed for the genus *Phytophthora*, including conventional PCR methods (Martin et al. 2004; Schena et al. 2008; Scibetta et al. 2012), TaqMan-based real-time PCR methods (Bilodeau et al. 2014; Schena et al. 2006), and recombinase polymerase amplification-based methods (Miles et al. 2015). However, high throughput sampling using these methods is technically difficult because the DNA extraction procedures are generally time-consuming. Loop-mediated isothermal amplification (LAMP) methods (Mori et al. 2001; Mori and Notomi 2009; Nagamine et al. 2002; Notomi et al. 2000) have the advantage of high tolerance to

amplification inhibitors (Kaneko et al. 2007) and thus, simple and easy DNA extraction methods are applicable in LAMP-based detection. LAMP can be used to rapidly amplify nucleic acids with high specificity and sensitivity under isothermal conditions by using a DNA polymerase with strand displacement activity. The reactions can be monitored using real-time fluorescence measurements or turbidity measuring systems. Recently, chip technology-based microfluidic, paper-based and digital LAMP detection methods have been developed (Rolando et al. 2019; Zhang et al. 2019). Digital LAMP can also be done using track-etched polycarbonate membranes without the need for special equipment or complicated chip fabrication procedures (Lin et al. 2019). Moreover, LAMP has broader applicability from the laboratory to the field, as demonstrated by numerous studies. LAMP products can be visualized with the naked eye by adding fluorescent DNA-intercalating dyes such as ethidium bromide (Pham et al. 2005), SYBR® Green I (Notomi et al. 2000), propidium iodide (Hill et al. 2008), Quant-iT™ PicoGreen® (Tomlinson et al. 2007), or GeneFinder™ (Almasi et al. 2013); metal-ion indicators such as hydroxynaphthol blue (Goto et al. 2009), $CuSO_4$ (Zhang et al. 2009), or calcein (Tomita et al. 2008); pH indicators such as cresol red (Tanner et al. 2015); or by using 5′-biotinylated loop primers and streptavidin-functionalized gold-nanoparticles (Suwannin et al. 2021). Therefore, the LAMP method is suitable for high throughput detection in the laboratory or for disease diagnosis in the field.

In Japan, all but one species in the genus *Phytophthora* are listed as plant quarantine organisms. The exception is *Phytophthora nicotianae*, which is considered a domestic species because it was reported as far back as 1915 and has infected over 70 species including crops and horticultural species throughout Japan (Genebank Project, NARO, last accessed November 2021). For Japanese quarantine control, we designed genus-specific LAMP primer sets for real-time fluorescence detection of all species in the genus *Phytophthora* (Hieno et al. 2020), and four species-specific primer sets for the detection of *P. ramorum*, *P. lateralis*, *P. kernoviae* (Hieno et al. 2021) and *P. nicotianae* (Hieno et al. 2019). The former three species had not yet been found in Japan but are known pathogens of forest tree species in other countries. Moreover, a *P. nicotianae* species-specific quenching probe (QProbe) was designed for use with the *Phytophthora* genus-specific LAMP primer set, to establish a simultaneous detection method for the genus *Phytophthora* and *P. nicotianae* (Hieno et al. 2020). All the detection methods using these primer sets and the probe were able to be multiplexed with an internal control primer set for detecting plant DNA, which is useful for the accurate detection of pathogens in infected plant tissues (Hieno et al. 2021). The internal control shows whether the amplification was successful, thereby avoiding false negative results caused by enzyme inactivation or amplification inhibitors from plant tissues.

The following sections include practical information with details that may not be included in research papers. We provide detailed tips on designing LAMP primers for the target pathogen, selecting a DNA extraction method for environmental samples, applying LAMP to various instruments, and finally, setting up the procedure for faster, easier and more accurate LAMP detection. This information will be

useful to researchers who are developing new LAMP-based detection methods or adapting existing methods for new applications.

6.2 LAMP Primer Design

Our LAMP primer sets for *Phytophthora* pathogens (F3, B3, FIP and BIP) were designed using the PrimerExplorerV5 software (https://primerexplorer.jp) (Table 6.1). This software can also design loop primers (F-loop and B-loop), however, for this application the loop primers were not designed, because the presence of loop primers could increase the occurrence of primer dimers in multiplex detection. Even without loop primers, the detection time on the portable real-time fluorometer Genie®II (Optigene, UK) was sufficiently short: less than 30 min with 100 pg of mycelial DNA, and the detection limit was 100 fg or less against mycelial DNA (Fig. 6.1). This is equivalent to the sensitivity of PCR.

6.2.1 Appropriate Genomic Regions for Designing Species-Specific Primers

The genus *Phytophthora* has been classified into phylogenetic clades 1 to 10 (Abad et al. 2019) based on the ITS region of the nuclear ribosomal DNA (rDNA-ITS). This DNA region was amplified using the ITS4 and ITS5 primer pair (White et al. 1990). The number of species in each clade is quite variable. For example, as of November 2021 clade 1, which includes *P. nicotianae*, consisted of 18 species (2 are hybrid species); clade 10, which includes *P. kernoviae*, consisted of 13 species; and clade 8, which includes *P. ramorum* and *P. lateralis*, consisted of 23 species. To design species-specific primers, the rDNA-ITS region is the primary choice because it has been used to distinguish between the most recently identified species, and it can be amplified with high sensitivity due to its high copy number. We designed species-specific LAMP primer sets based on the rDNA-ITS region for *P. nicotianae* (Hieno et al. 2019) and *P. kernoviae* (Hieno et al. 2021). On the other hand, *P. ramorum* and *P. lateralis* could not be distinguished from closely related species using the rDNA-ITS region. These species belong to clade 8, which is one of the most species-rich groups in the genus, containing many very closely related species. Our secondary choice of a genomic region for primer design was the cytochrome *c* oxidase subunit I (*cox*1, or COI) gene, which is carried on the mitochondrial DNA and has previously been recommended for species identification (Robideau et al. 2011). Sequence information for the *cox*1 gene, obtained using the OomCoxI Levup and Fm85mod primer pair (Robideau et al. 2011), is available in the public database and was therefore used to design species-specific LAMP primer sets for the *Phytophthora* species. Despite the fact that the *cox*1 gene is AT-rich with limited

Table 6.1 Sequences of LAMP primer sets for *Phytophthora* pathogens and plants (reproduced and modified with permission from Microbes and Environments, adapted from Hieno et al. 2021)

LAMP primer set	Name		Sequence (5′-3′)	Length (bp)	Locus	References
Phytophthora ramorum-specific	Pram	F3	TTACTGCACATGCTTTTATC	20	Cytochrome *c* oxidase subunit I gene	Hieno et al. (2021)
		B3	GAATGTGCTTGTACACTTGA	20		
		FIP	AGGAAATGCCATATCTGGAGTGCCTGCTTTAATTGGTGGG	40		
		BIP	GGCTTTATTATTATTAGTTTTAAACTGTCCAACCAGTACC	40		
Phytophthora lateralis-specific	Plat	F3	TAATGATAGGTGCACCTGAT	20	Cytochrome *c* oxidase subunit I gene	Hieno et al. (2021)
		B3	AATCTACTGAAGGTCCTGAA	20		
		FIP	CGATGAAACTAATAATAATATGGCTTTTCCACGTATGAA	39		
		BIP	GGCTATTGTAGAATCTGGTGGGGCTTGTACACTAGATAAC	40		
Phytophthora kernoviae-specific	Pker	F3	GGTAGTGTTGGTTTCGGC	18	rDNA-ITS region	Hieno et al. (2021)
		B3	CGTGCACACAAAAAATTGTTCC	22		
		FIP	TACACACTACTACGGTACACCTGCTTATTGTGTCTTTTTCCTTGC	45		
		BIP	ACTTTGTGTGCGAAGTAGAGAAAAGGTTTCGTCCCCTCGGC	41		
Phytophthora nicotianae-specific	Pnic	F3	CGGTGGAGGAGATGTCAGAT	20	rDNA-ITS region	Hieno et al. (2019)
		B3	GTTCAGCCGAAGCCAACC	18		
		FIP	TCAGTTTAGTACATTTAAAATGAAGTGTCTTGCGATTGGT	40		
		BIP	AAGGCTGCTATTGTGGCAAAACACTCTTCCATTAACGCCG	40		
Phytophthora genus-specific	Physp	F3	TCTGCTTTTAACTAGATAGC	20	rDNA-ITS region	Hieno et al. (2020)
		B3	CACCACTTTTCGAGCAAAGA	20		
		FIP	GCATACTTCCAGGACTAACCGTAATGCGAATTGCAGGA	38		
		BIP	CCTGTATCAGTGTCCGTACATCTCCTCCACCGACTACACG	40		

(continued)

Table 6.1 (continued)

LAMP primer set	Name		Sequence (5′-3′)	Length (bp)	Locus	References
Plant	COX	F3	TATGGGAGCCGTTTTTGC	18	Cytochrome *c* oxidase subunit I gene	Hieno et al. (2021) Tomlinson et al. (2010 modified)
		B3G	AACTGCTAAGGGCATTCC	18		
		FIPA	ATGGATTTGACCTAAAGTTTCAGGGCAGGATTTCACTATTGGGT	44		
		FIP2	ATGGATTTGACCTAAAGTTTCGGTCGCAGGATTTTACTTTCGGG	44		
		BIPA	TGCATTTCTTAGGGCTTTCGGATCCAGCGTAAGCATCTG	39		
		F-loop	ATGTCCGACCAAAGATTTTACC	22		
		F-Loop2	ATGTTCGACCAGAGATTTTACC	22		
		B-loop	GTATGCCACGTCGCATTCC	19		

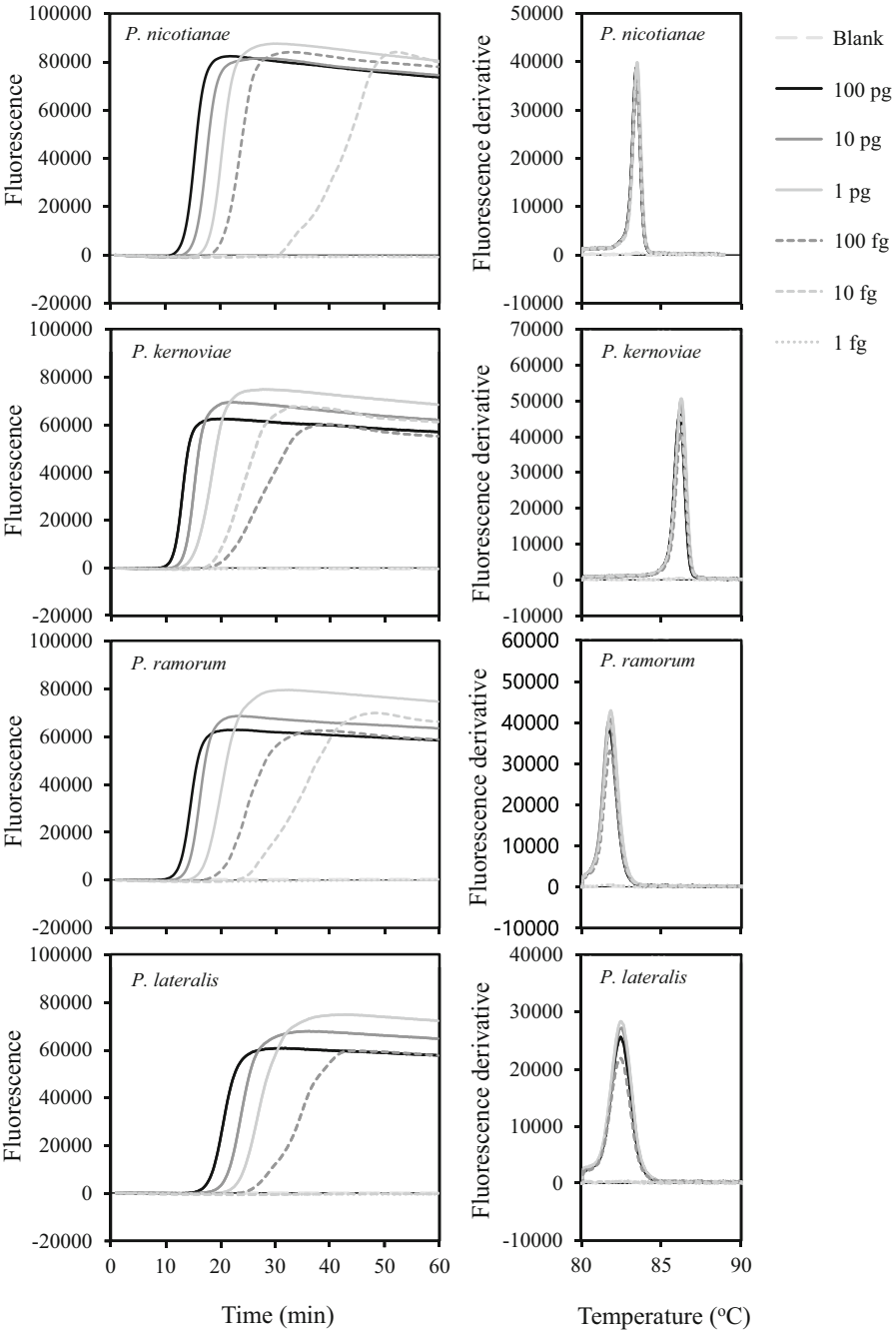

Fig. 6.1 Sensitivity of the four species-specific LAMP primer sets designed for the rDNA-ITS region (*P. nicotianae* and *P. kernoviae*) and the *cox*1 gene (*P. ramorum* and *P. lateralis*) (reproduced and modified with permission from John Wiley and Sons and Microbes and Environments, adapted from Hieno et al. 2019 and Hieno et al. 2021, respectively). The species-specific LAMP assay was performed using the Genie®II system. After amplification at 65 °C for 60 min,

regions suitable for the primer design, we were able to design LAMP primer sets that could distinguish *P. ramorum* and *P. lateralis* from each other and from closely related species (Hieno et al. 2021).

Another choice for species-specific primer design is the triosephosphate isomerase/glyceraldehyde-3-phosphate dehydrogenase (*tigA*) gene, a nuclear gene that has been sequenced for most *Phytophthora* species. As for other marker genes, haplotypes or intra-species sequence variation must be investigated, but we have found that *tigA* is useful for designing species-specific LAMP primer sets (Li et al. 2022). Yang and Hong (2018) identified effective genetic markers for species belonging to each *Phytophthora* clade, and these will be useful in selecting additional genomic regions for species-specific LAMP primer design.

6.2.2 Processes in Species-Specific Primer Design

The four basic LAMP primers (F3, B3, FIP and BIP) lead to the production of dumbbell-shaped DNA molecules with stem-loop structures at each end (Fig. 6.2). The stem-loop structures serve as the starting material for LAMP cycling (Notomi et al. 2000). Within 3 bp at each end of the stem-loop DNA is the most effective site for specific detection. To design a species-specific LAMP primer set, we first identify unique sequences in the target species using multiple alignments with closely related species, and also ensure that the unique sequences are conserved among multiple isolates of the target species from various locations. The most effective sequence variation for primer design is a deletion or insertion that is well conserved within the target species. Next, two sites in the target's unique sequences are selected for F1c and B1c (Fig. 6.3). A long distance between F2 and B2 reduces amplification efficiency, so 120–180 bp is recommended, and then the distance between F1c and B1c should be 40 bp or less. Even if there is only one unique site (1 bp) of the target available for primer design, the ends of the stem-loop DNA can overlap by 1 bp of DNA (Fig. 6.4) (The distance setting for "Distances F1c–B1c" includes −1 bp in the "Detailed Settings" in PrimerExplorerV5). Such overlapping designs can lead to reduced amplification efficiency, and in our case, the sensitivity of detection was 10-fold lower when compared to a LAMP primer set designed with two sites for the stem-loop in nearly the same region. However, if the target organism has a limited number of unique sequences, it can be effective to try overlapping stem loops. After selecting the F1 and B1 sites for stem loops with the "Fixed Primer" button in PrimerExplorerV5, use the "Generate" button to automatically generate other primer sites and modify them to include unique sequences near the resulting primer regions. If there are no "Primer Candidates," you need to modify

Fig. 6.1 (continued) fluorescence derivative data during the annealing phase (98–80 °C) were obtained. A reaction mixture without DNA (Blank) was used as a negative control, and mycelial DNA of each species was used

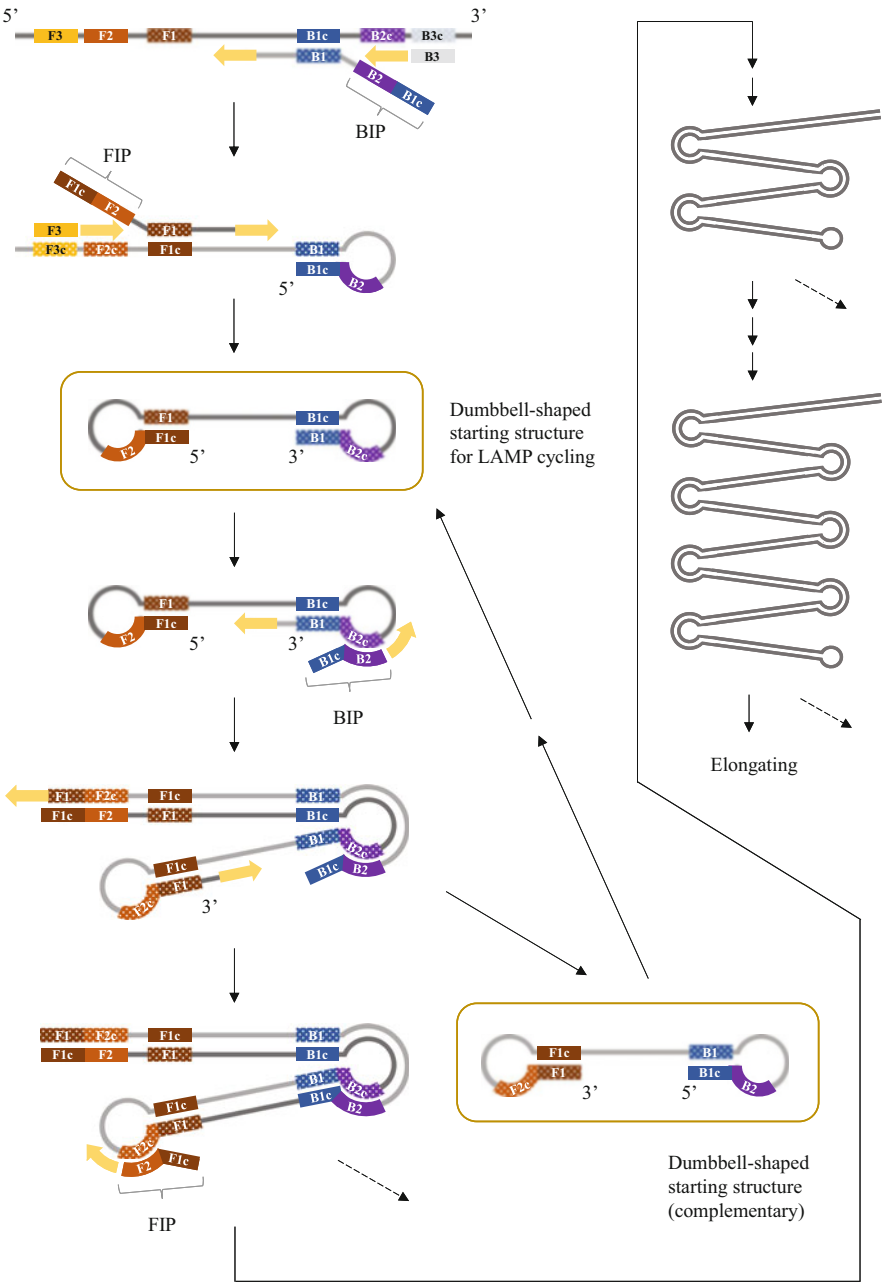

Fig. 6.2 Steps in the LAMP reaction (reproduced and modified with permission from Oxford University Press from Notomi et al. 2000). This figure shows the process that starts from BIP primer

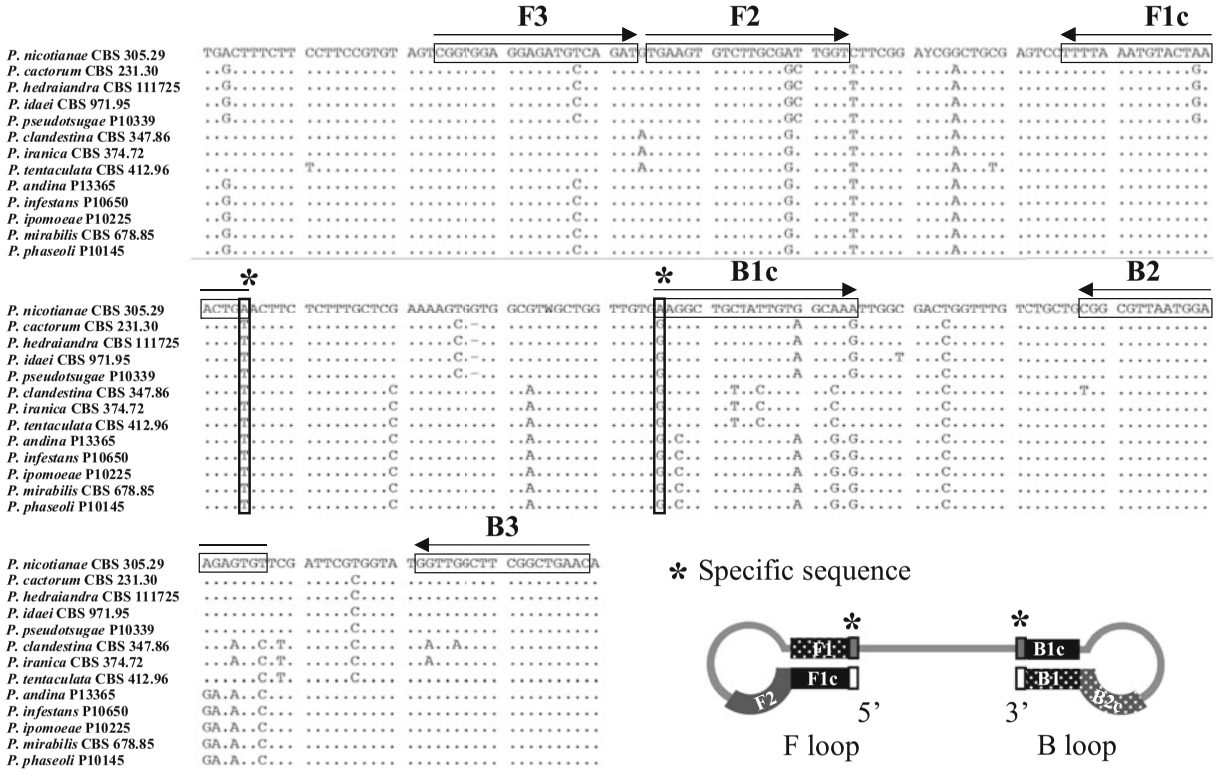

Fig. 6.3 Two unique sites in the target's sequence are selected for F1c and B1c in the LAMP primer region (reproduced and modified with permission from John Wiley and Sons, adapted from Hieno et al. 2019). Asterisks indicated these two sites within the larger species-specific sequence

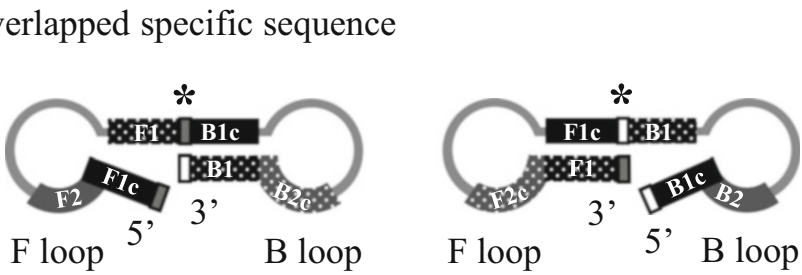

Fig. 6.4 Dumbbell-shaped starting structure with overlapped stem-loop

F1 and B1 and try again. As with PCR primers, the inclusion of a unique target sequence within 3 bp of the amplification start point allows for specific detection. After selecting the six primer sites (F3, F2, F1, B1, B2 and B3), it is important to check for dimerization using PrimerExplorerV5, and make additional modifications if necessary.

6.2.3 Primer Specificity Test with Mycelial DNA

Candidate LAMP primer sets are subjected to specificity tests using mycelial DNA from *Phytophthora* species. Total DNA is extracted from ex-type, authentic, or representative isolates using PrepMan™ Ultra Sample Preparation Reagent (Thermo Fisher Scientific), following the manufacturer's protocol. A typical amount of DNA to use in the specificity tests is 100 pg for 25 μL reaction mixture. Candidate LAMP primer sets are first tested with the most closely related species within the same (sub) clade as the target species, and if the specificity holds, the candidate primer set is tested on all available species in the same clade and representative species from all clades 1 to 10. The specificity of the candidate primer set should be confirmed using soil-borne pathogens that inhabit the same environment as the *Phytophthora* species. These primer tests with mycelial DNA from many isolates of different origins are needed, even though the conservation of the target's unique sequences was already determined by multiple sequence alignments. This is because sequences in the databases are not always correct. If the target species is reported to be a hybrid, or if the presence of a haplotype is reported, additional testing is required depending on the situation. The potential number of *Phytophthora* species is estimated to be between 200 and 600 (Brasier 2009), and the number of described *Phytophthora* taxa is continuously increasing, reaching about 200 as of November 2021. Therefore, the phylogenetic state of the target species must be updated just before the primer set is designed.

The genus-specific LAMP primer sets must also be updated frequently as new taxa are discovered and described. In previous studies, *Phytophthora* genus-specific

PCR primers have been designed using the following sequences: the rDNA-ITS region (Scibetta et al. 2012); the *Ypt*1 gene that encodes the ras-like GTP-binding protein (Schena et al. 2006, 2008); the *cox* subunit 1 and subunit 2 genes (Martin et al. 2004). *Phytophthora* genus-specific TaqMan real-time PCR assays have been designed on two mitochondrial regions, *trnM-trnP-trnM* and *atp9-nad9* (Bilodeau et al. 2014), and for *trnM-trnP-trnM*, recombinase polymerase amplification (RPA) method has also been developed (Miles et al. 2015).

6.3 DNA Extraction Methods from Environmental Samples

Phytopthothora species can be isolated from infested plant samples or environmental samples such as forest soils or river water. In this section, we introduce DNA extraction methods for plant, soils and water that are suitable for LAMP-based detection.

6.3.1 Plant DNA Extraction

As described before, LAMP can be used to detect target sequences in crude DNA samples. We selected a simple plant DNA extraction method by comparing three procedures: a simple water extraction method, the Kaneka Easy DNA Extraction Kit version 2 (hereafter the Kaneka kit) and the Kageyama+Mag method (Li et al. 2015), which is an established method for soil DNA extraction. As a result, we chose the Kaneka kit because the LAMP results were more accurate when this kit was used than when the water extraction method was used. When the water extraction method was used, we sometimes obtained irregular or nonspecific amplification. Furthermore, at 30 min the Kaneka kit was quicker and easier than the Kageyama + Mag method, which takes about 90 min (Hieno et al. 2019). After making this selection, the manufacturer's protocol was improved by adding a beads-beating step (Hieno et al. 2021). In brief, 5 mm squares of thin plant tissues such as leaves, buds and flower buds are collected in 2 mL screw-cap tubes, each containing a stainless steel bead (0.25 inches). For stem and rhizome samples, the tissue is shaved off with a knife and two pieces (lengths of 5 mm) are collected as described above. Solution A of the Kaneka kit (200 μL) is added and the tube is vortexed for 5 min. The tube is then heated at 98 °C for 8 min in a heat block. After cooling to room temperature, 28 μL of Solution B is added, mixed well, and then centrifuged. The supernatant is centrifuged again and the supernatant diluted 20 times, then used as template (Fig. 6.5). This procedure was tested with 176 plant species representing 155 genera and 110 families, and when the plant LAMP primer set was used, it was able to detect 140 species of 124 genera in 87 families (Hieno et al. 2021). Among the weakly detected and non-detected species, an additional DNA purification step using the OneStep™ PCR Inhibitor Removal Kit (Zymo Research) improved detectability

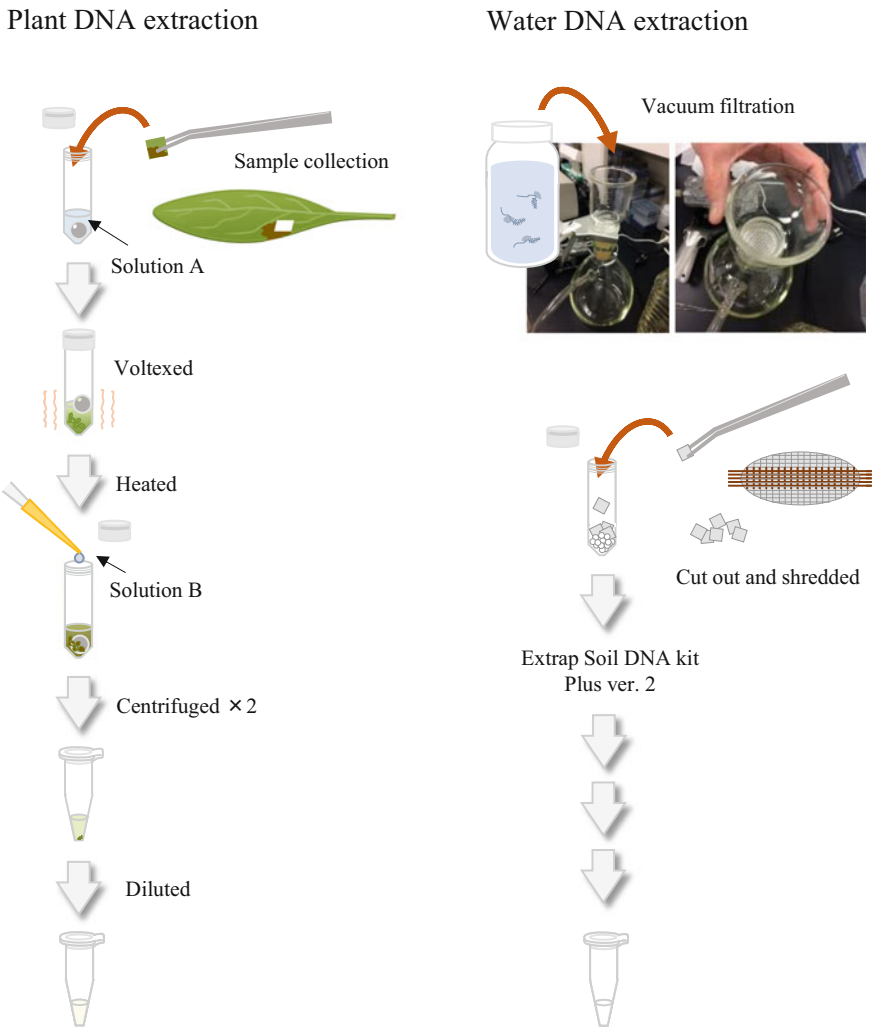

Fig. 6.5 DNA extraction from plant and water samples

for 12 species in 12 genera and 12 families (Hieno et al. 2021), including plants in Pinales (Cupressaceae and Pinaceae), Malpighiales (Salicaceae), Ericales (Ericaceae), Poales (Poaceae and Typhaceae), Zingiberales (Zingiberaceae) and Caryophyllales (Nyctaginaceae and Portulacaceae). These species have hard leaves that may contain more inhibitors. Some other plants with soft leaves in the Oxalidales (Oxalidaceae) and Rosales (Cannabaceae and Ulmaceae) was also improved by the purification, for unknown reasons. Plants containing saponin, such as *Pittosporum tobira* (Pittosporaceae), also showed relatively weak detectability that improved with additional DNA purification.

6.3.2 Soil DNA Extraction

Phytophthora species are generally known as soil-born pathogens. Recent studies revealed a high diversity of unknown *Phytophthora* species in natural ecosystems of Southeast Asia, and these could threaten forests, natural ecosystems or crops on other continents and islands (Jung et al. 2017b). DNA extraction from soil is more difficult than from plants, and requires the removal of inhibitors along with the extraction of enough DNA for LAMP assays. In Japan, ando soils have developed from volcanic ash and contain abundant levels of phosphoric acid and organic compounds. The particles of these soils can strongly bind micro-organisms and DNAs, making DNA extraction very difficult (Li et al. 2015). Other substances, such as allophane, humic acids, polyphenolics, and tannins could inhibit DNA amplification, and such inhibitors must be removed in the purification step (Li et al. 2015). We have tested the original Kageyama+Mag method (Li et al. 2015) and commercial kits including the FastDNA™ SPIN Kit for Soil (MP Biomedicals), the Soil DNA Isolation Kit (NORGEN), ISOIL for Beads Beating (Nippon Gene), and the Extrap Soil DNA kit Plus ver. 2 (Nittetsu Kankyo). Column-based DNA extraction kits tend to have lower DNA yields than kits that use magnetic beads. In our hands, when testing a variety of soils including Japanese soils, the Extrap Soil DNA kit Plus ver. 2 was the most efficient DNA extraction method, and the DNA samples were more stable LAMP amplification than those from other methods and kits.

6.3.3 Water DNA Extraction

Phytophthora is an oomycete, and oomycetes are also known as water molds that live in fresh or brackish water or wet soil. In California, Port-Orford cedars growing adjacent to a stream were killed within a few years after the introduction of *P. lateralis* to the stream (Hansen et al. 2000). Hong and Moorman (2005) suggested that *Phytophthora* species contaminating irrigation water will be a primary source of inoculum for diseases in numerous nurseries and fruit and vegetable crops. Vacuum filtration using an appropriate membrane filter is required for DNA extraction from water samples. In a previous study, Watanabe (2014, written in Japanese) selected Durapore® membranes (5.0 μm pore size, 47 mm diameter, hydrophilic PVDF, SVWG04700, Millipore) to capture zoospores, mycelia, and other tissues in water samples collected from hydroponics. When turbid water samples were filtered, Watanabe et al. (2013, written in Japanese) used 0.1 g per membrane of Hyflo Super-Cel® (Fuji Film Wako) as an effective filter aid. The membrane-filtered water sample, with or without the filter aid, can then be subjected to DNA extraction using the Extrap Soil DNA kit Plus ver. 2. Four rows from the center of the membrane are cut out and shredded into squares along the mass markings, then the pieces are

combined in a 2 mL tube containing beads from the kit, and DNA extraction is carried out according to the manufacture's protocol (Fig. 6.5).

6.4 Instrument Selection

It is important to select an amplification/detection instrument that is suitable for your particular application. All our LAMP primer sets were designed and tested using the Genie®II (OptiGene) system, but we have tested our detection methods and primer sets with other fluorometers and turbidimeters. Users may be able to apply LAMP protocols to instruments that already available in their laboratories.

6.4.1 The Genelyzer™ FII/Genelyzer™ FIII System

The Genie®II instrument is portable and battery powered, making it suitable for field work. However, this instrument is not available for sale in Japan. The Genelyzer™ FII and Genelyzer™ FIII systems (Canon Medical Systems) are good alternatives to Genie®II. When compared with Genie®II, there were no differences in the specificity of the amplification and in the peak temperature in the annealing curve analysis (Hieno et al. unpublished). The Genie®II and Genelyzer™ FII can each process 16 samples at once, whereas the Genelyzer™ FIII has a Peltier cooling mechanism and is smaller (for reactions of 8 samples). These systems are portable, but hence have the disadvantage that the numbers of samples that can be processed at a time are much lower than the numbers processed by larger lab-based systems. For example, the new Genelyzer F-MS (Canon Medical Systems) supports up to 96 samples (8 samples×12 units), and is expected to be used for high-throughput detection.

6.4.2 StepOnePlus™ system/QuantStudio® 3 System

The LAMP assay established by Genie®II can also be applied to the StepOnePlus™ and QuantStudio® 3 real-time PCR systems (Applied Biosystems). These systems can handle up to 96 samples, but we recommend that you use a smaller number of samples, as too many samples will require more time for handling and may cause undesirable amplification due to difficulty of temperature control. For these systems, a melting curve analysis can be used instead of the annealing curve analysis (Hieno et al. 2020). When using the QProbe, free QProbe was detected as non-negligible noise in blank samples, but it did not interfere with the LAMP assay (Hieno et al. 2020) (Fig. 6.6). Between these instruments and Genie®II, there were almost no differences in the specificity and peak temperatures in the annealing curve analysis (Hieno et al. 2020; Hieno et al. unpublished), however, the negative peak

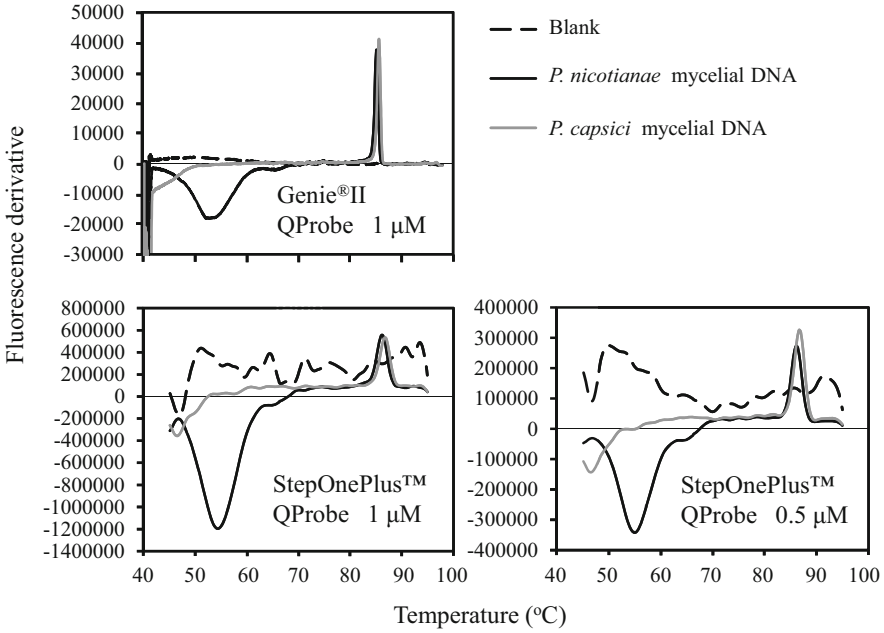

Fig. 6.6 Detection using an alternative real time fluorometer (Reproduced and modified with permission from American Phytopathological Society, adapted from Hieno, A., et al. 2020. Detection of the genus *Phytophthora* and the species *Phytophthora nicotianae* by LAMP with a QProbe. Plant Dis. 104(9): 2469–2480. https://doi.org/10.1094/PDIS-12-19-2523-RE.). The *Phytophthora* genus specific LAMP assay with the *P. nicotianae* specific QProbe was performed using the Genie®II system and the StepOnePlus™ real-time PCR system. After amplification at 68 °C for 60 min, fluorescence derivative data during the annealing phase (98–40 °C) were obtained. A reaction mixture without DNA (Blank) was used as a negative control, and *P. nicotianae* mycelial DNA was used as a positive control. Mycelial DNA from *P. capsici* was used as an additional negative control. *Phytophthora* genus-specific primers was detected as a positive fluorescent peak at around 85 °C, and the correct target of the *P. nicotianae*-specific QProbe was detected as a negative fluorescent peak at about 53 °C in the Genie®II and about 55 °C in the StepOnePlus™ real-time PCR system

temperature for the QProbe was shifted slightly from 53 °C to 55 °C, for unknown reasons (Hieno et al. 2020) (Fig. 6.6). Peak detection at low temperatures is not expected for general LAMP assays, therefore they might cause unexpected compatibility discrepancies between LAMP instruments and other fluorometers.

The biggest difference between these instruments and Genie®II is the setup time. StepOnePlus™ and QuantStudio® 3 take several minutes to warm up the lid after loading the sample, which can cause undesirable amplification. A short pre-run (70 °C, 1 min) with an empty plate (Hieno et al. 2020) was effective in reducing the heating time for the main run.

6.4.3 *The LoopampEXIA® System*

The LAMP primer sets tested in Genie®II were also applicable to the LoopampEXIA® system (Eiken Chemical) when using different reagents for the turbidimeter. LoopampEXIA® is scalable up to six 16-sample amplification units (96 reactions). Our LAMP primer sets do not include loop primers, so the detection time takes an additional 10 min and the detection limit is 10 times higher than fluorescence detection (Hieno et al. unpublished). We found no difference in specificity (Hieno et al. unpublished).

6.5 Experimental Procedures for More Accurate Detection

LAMP-based detection requires special consideration for contamination and handling time. In isothermal amplification, a large amount of DNA is produced, and this can be a source of contamination for following reactions. Moreover, in isothermal amplification, the reaction is initiated at room temperature, resulting in nonspecific amplification. However, these problems can be easily solved by following careful procedures.

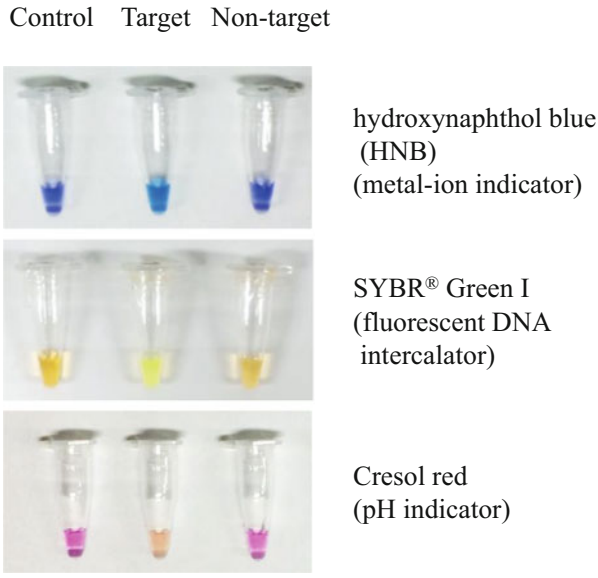

Fig. 6.7 LAMP products visualized with different color indicators. Control, negative control without DNA template; Target, species-specific LAMP assay with 100 pg of target mycelial DNA; Non-target, species-specific LAMP assay with 100 pg of non-target mycelial DNA

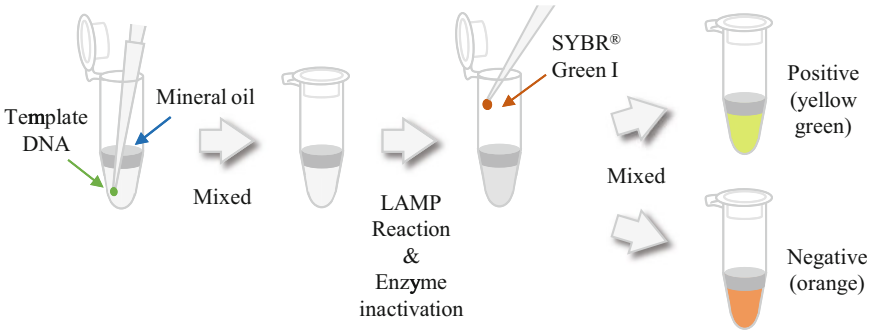

Fig. 6.8 Colorimetric detection using SYBR® Green I with mineral oil

6.5.1 Contamination

The biggest concern in LAMP-based detection is false-positive detection caused by DNA contamination. Due to the high amplification efficiency of the LAMP method, amplified DNA can become an aerosol when the lid of the tube is opened, contaminating the experimental environment. Colorimetric detection (Fig. 6.7) is simple and applicable for on-site detection without special equipment. If a color indicator dye is added after amplification, the lid of the tube can be kept closed until after it has cooled down to room temperature. Mineral oil can also be used to prevent contamination, for example, 20 μL of mineral oil can be added to reaction mixture without the DNA template, then the template is added under the mineral oil using a micropipette (total 25 μL of reaction mixture +20 μL of mineral oil). After amplification followed by enzyme inactivation (80 °C for 5 min) and cooling down, the color indicator is dropped onto the tube wall by micropipette, then mixed into the reaction mixture (Fig. 6.8).

In order to prevent the effects of contamination, it is a good idea to use a separate clean bench for preparation of the reaction solutions and addition of the DNA templates. A filter tip is effective for preventing DNA contamination from the micropipette. Additionally, reagents should be dispensed in small quantities, and water should be replaced frequently.

6.5.2 Sample Amounts

Preparation of the reaction mixture must be quick, because temperature control is important for preventing nonspecific amplification. For accurate detection, the amplification reaction should start within 5 min after adding the DNA template, so that the maximum sample size is around 16 samples. Therefore, for high throughput detection, a simultaneous detection method in a single tube is important. In addition to multiplex LAMP (Hieno et al. 2021) and LAMP with the QProbe (Hieno et al.

2020), many types of single tube detection methods exist, and most are fluorescence-based. These include: fluorescence of the loop primer upon self-dequenching, the use of a fluorophore-modified primer with ethidium bromide, HyBeacon probes, detection of amplification by release of quenching, quenching of unincorporated amplification signal reporters, one-step strand displacement, multiple endonuclease restriction in real-time, the use of a LightCycler or assimilating probe, and mediator displacement (Becherer et al. 2020).

6.5.3 Other Concerns

Unlike in laboratory experimental conditions, the amounts of DNA and amplification inhibitors in samples collected in the field can be very diverse. The amplicons show different peak temperatures in the annealing analysis if the amplification has not reached saturation (Fig. 6.9). Therefore, it is necessary to check whether the increase in fluorescence signal is saturated or not.

6.6 Conclusion

Forests in many parts of the world are being lost or substantially altered as a result of damage by introduced pests (Roy et al. 2014). Currently, *P. ramorum* has been reported to infect at least 109 plant species in 51 genera and 25 families (as of 2019; USDA), and it has been found in 32 countries (Invasive Species Compendium, last

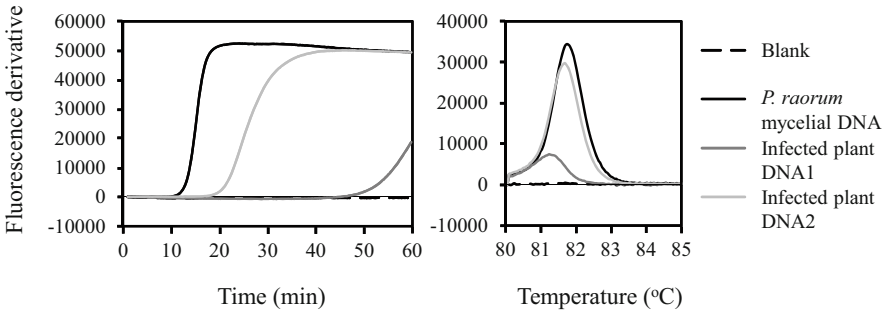

Fig. 6.9 Different peak temperatures in the annealing analysis between saturated and non-saturated amplicons. The *P. ramorum* specific LAMP assay was performed using Genie®II. After amplification at 65 °C for 60 min, fluorescence derivative data during the annealing phase (98–80 °C) were obtained. A reaction mixture without DNA (Blank) was used as a negative control, and *P. ramorum* mycelial DNA was used as a positive control, detected as a peak at around 82 °C. Infected plant DNA1 and 2 were extracted from a *P. ramorum* inoculated rhododendron leaf. The reaction from Infected plant DNA1 was not saturated at the end of the amplification time, resulting in a lower peak temperature

updated on 28 Jul 2021). Tree species of the genera *Camellia*, *Pieris*, *Rhododendron*, *Syringa* and *Viburnum* are the key hosts involved in moving this pathogen to new geographical areas (Grünwald et al. 2008). Recently, *P. ramorum* was found in laurosilva forests in Japan (Jung et al. 2021). Therefore, our LAMP-based detection method is important not only for quarantine detection in imported materials but also for phytosanitary checks of plants intended for export, including Japanese Bonsai trees. Recent developments in LAMP-based detection systems have demonstrated the high potential for many future applications with different user requirements (Becherer et al. 2020). For plant pathogen detection, especially in quarantine control, high-throughput and rapid (within 1 day) detection is important. Detection methods need to be simple and easy, applicable for personnel without special skills, and should require minimal specialized equipment. Moreover, the running cost for one sample should be less than about $8 (1,000 Japanese yen) to account for limited budgets. Most plant pathogens lower do not need to be tightly controlled by detection systems such as those needed for clinical viruses. It is important to take the user's requirements into account when designing detection systems, and to provide a range of options so that the user can select the most appropriate for their situation. LAMP provides many options for detection, and is a favorable choice for the detection of *Phytophthora* pathogens.

Acknowledgments Research for this review was supported by a Grant-in Aid for "Development of detection and identification techniques of pests" in "Research and development of adaptation measures for global warming and abnormal weather" from the Ministry of Agriculture, Forestry, and Fisheries of Japan. We thank Emeritus Prof. E. M. Hansen, Prof. M. D. Coffey, Dr. P. W. Tooley, Prof. C. Hong, Dr. B. S. Weir, Dr. T. I. Burgess, Dr. T. Jung, Mr. S. Uematsu and Dr. H. Watanabe for providing isolates of many important *Phytophthora* spp., and Dr. S. Subandiyah and Dr. A. Wibowo for providing plant DNA samples. We also thank Mr. T. Sakoda, Mr. K. Ueda for technical assistance.

References

Abad, ZG, Burgess T, Bienapfl JC, Redford AJ, Coffey M, Knight L (2019) IDphy: molecular and morphological identification of *Phytophthora* based on the types. USDA APHIS PPQ S&T Beltsville Lab, USDA APHIS PPQ S&T ITP, Centre for Phytophthora Science and Management, and World Phytophthora Collection

Almasi MA, Ojaghkandi MA, Hemmatabadi A, Hamidi F, Aghaei S (2013) Development of colorimetric loop-mediated isothermal amplification assay for rapid detection of the tomato yellow leaf curl virus. J Plant Pathol Microbiol 04:153

Becherer L, Borst N, Bakheit M, Frischmann S, Zengerle R, von Stetten F (2020) Loop-mediated isothermal amplification (LAMP) – review and classification of methods for sequence-specific detection. Anal Methods 12(6):717–746

Bilodeau GJ, Martin FN, Coffey MD, Blomquist CL (2014) Development of a multiplex assay for genus- and species-specific detection of *Phytophthora* based on differences in mitochondrial gene order. Phytopathology 104(7):733–748

Brasier CM (2008) The biosecurity threat to the UK and global environment from international trade in plants. Plant Pathol 57:792–808

Brasier C (2009) *Phytophthora* biodiversity: how many *Phytophthora* species are there? In: Goheen EM, Frankel SJ (tech. coords.) Proceedings of the fourth meeting of the International Union of Forest Research Organizations (IUFRO) working party S07.02.09: *Phytophthoras* in forests and natural ecosystems. Gen. Tech. Rep. PSW-GTR-221. U.S. Department of Agriculture, Forest Service, Pacific Southwest Research Station, Albany, pp 101–115

Brasier CM, Beales PA, Kirk SA, Denman S, Rose J (2005) *Phytophthora kernoviae* sp. nov., an invasive pathogen causing bleeding stem lesions on forest trees and foliar necrosis of ornamentals in the UK. Mycol Res 109(8):853–859

Burgess TI, Simamora AV, White D, Wiliams B, Schwager M, Stukely MJC, Hardy G (2018) New species from *Phytophthora* clade 6a: evidence for recent radiation. Persoonia 41:1–17

Dell B, Hardy G, Vear K (2005) History of *Phytophthora cinnamomi* management in Western Australia. In: Calver M et al (ed) Proceedings 6th National Conference of the Australian Forest History Society, pp 391–406

Fichtner EJ, Rizzo DM, Kirk SA, Webber JF (2012) Infectivity and sporulation potential of *Phytophthora kernoviae* to select North American native plants. Plant Pathol 61(2):224–233

Garkaklis MJ, Calver MC, Wilson BA, Hardy GESJ (2004) Habitat alteration caused by an introduced plant disease, *Phytophthora cinnamomi*: a potential threat to the conservation of Australian forest fauna. In: Lunney D (ed) The conservation of Australia's forest fauna, 2nd edn. Royal Zoological Society of New South Wales, Mosman, pp 899–913

Genebank Project, National Agriculture and Food Research Organization (NARO): database of plant diseases in Japan, based on "common names of plant diseases in Japan" compiled by Phytopathological Society of Japan. URL https://www.gene.affrc.go.jp/databases-micro_pl_diseases_en.php

Goto M, Honda E, Ogura A, Nomoto A, Hanaki K (2009) Colorimetric detection of loop-mediated isothermal amplification reaction by using hydroxy naphthol blue. BioTechniques 46(3): 167–172

Grünwald NJ, Goss EM, Press CM (2008) *Phytophthora ramorum*: a pathogen with a remarkably wide host range causing sudden oak death on oaks and ramorum blight on woody ornamentals. Mol Plant Pathol 9(6):729–740

Hansen EM, Goheen DJ, Jules ES, Ullian B (2000) Managing Port-Orford-Cedar and the Introduced Pathogen *Phytophthora lateralis*. Plant Dis 84(1):4–14

Hieno A, Li M, Afandi A, Otsubo K, Suga H, Kageyama K (2019) Rapid detection of *Phytophthora nicotianae* by simple DNA extraction and real-time loop-mediated isothermal amplification assay. J Phytopathol 167(3):174–184

Hieno A, Li M, Afandi A, Otsubo K, Suga H, Kageyama K (2020) Detection of the genus *Phytophthora* and the species *Phytophthora nicotianae* by LAMP with a QProbe. Plant Dis 104(9):2469–2480

Hieno A, Li M, Otsubo K, Suga H, Kageyama K (2021) Multiplex LAMP detection of the genus *Phytophthora* and four *Phytophthora* species *P. ramorum*, *P. lateralis*, *P. kernoviae*, and *P. nicotianae*, with a plant internal control. Microbes Environ 36(2):ME21019

Hill J, Beriwal S, Chandra I, Paul VK, Kapil A, Singh T, Wadowsky RM, Singh V, Goyal A, Jahnukainen T, Johnson JR, Tarr PI, Vats A (2008) Loop-mediated isothermal amplification assay for rapid detection of common strains of *Escherichia coli*. J Clin Microbiol 46(8): 2800–2804

Hong CX, Moorman GW (2005) Plant pathogens in irrigation water: challenges and opportunities. Crit Rev Plant Sci 24:189–208

Invasive Species Compendium, CABI URL https://www.cabi.org/isc/

Jung T, Orlikowski L, Henricot B, Abad-Campos P, Aday AG, Aguín Casal O, Bakonyi J, Cacciola SO, Cech T, Chavarriaga D, Corcobado T, Cravador A, Decourcelle T, Denton G, Diamandis S, Doğmuş-Lehtijärvi HT, Franceschini A, Ginetti B, Green S, Glavendekić M, Hantula J, Hartmann G, Herrero M, Ivic D, Jung MH, Lilja A, Keca N, Kramarets V, Lyubenova A, Machado H, di San M, Lio G, Mansilla Vázquez PJ, Marçais B, Matsiakh I, Milenkovic I, Moricca S, Nagy ZÁ, Nechwatal J, Olsson C, Oszako T, Pane A, Paplomatas EJ, Pintos

Varela C, Prospero S, Rial Martínez C, Rigling D, Robin C, Rytkönen A, Sánchez ME, Sanz Ros AV, Scanu B, Schlenzig A, Schumacher J, Slavov S, Solla A, Sousa E, Stenlid J, Talgø V, Tomic Z, Tsopelas P, Vannini A, Vettraino AM, Wenneker M, Woodward S, Peréz-Sierra A, Deprez-Loustau ML (2016) Widespread *Phytophthora* infestations in European nurseries put forest, semi-natural and horticultural ecosystems at high risk of Phytophthora diseases. For Pathol 46(2):134–163

Jung T, Jung MH, Cacciola SO, Cech T, Bakonyi J, Seress D, Mosca S, Schena L, Seddaiu S, Pane A, di San M, Lio G, Maia C, Cravador A, Franceschini A, Scanu B (2017a) Multiple new cryptic pathogenic *Phytophthora* species from *Fagaceae* forests in Austria, Italy and Portugal. IMA Fungus 8(2):219–244

Jung T, Jung MH, Scanu B, Seress D, Kovacs GM, Maia C, Perez-Sierra A, Chang TT, Chandelier A, Heungens K, van Poucke K, Abad-Campos P, Leon M, Cacciola SO, Bakonyi J (2017b) Six new *Phytophthora* species from ITS Clade 7a including two sexually functional heterothallic hybrid species detected in natural ecosystems in Taiwan. Persoonia 38:100–135

Jung T, Perez-Sierra A, Duran A, Jung MH, Balci Y, Scanu B (2018) Canker and decline diseases caused by soil- and airborne *Phytophthora* species in forests and woodlands. Persoonia 40:182–220

Jung T, Jung MH, Webber JF, Kageyama K, Hieno A, Masuya H, Uematsu S, Pérez-Sierra A, Harris AR, Forster J, Rees H, Scanu B, Patra S, Kudláček T, Janoušek J, Corcobado T, Milenković I, Nagy Z, Csorba I, Bakonyi J, Brasier CM (2021) The destructive tree pathogen *Phytophthora ramorum* originates from the laurosilva forests of East Asia. J Fungi 7(3):226

Kaneko H, Kawana T, Fukushima E, Suzutani T (2007) Tolerance of loop-mediated isothermal amplification to a culture medium and biological substances. J Biochem Biophys Methods 70(3):499–501

Li M, Ishiguro Y, Kageyama K, Zhu Z (2015) A simple method for normalization of DNA extraction to improve the quantitative detection of soil-borne plant pathogenic oomycetes by real-time PCR. Lett Appl Microbiol 61(2):179–185

Li M, Guo Q, Liang M, Zhao Q, Lin T, Gao H, Hieno A, Kageyama K, Zhang X, Cui L, Yan Y, Qiang Y (2022) Population dynamics, effective soil factors, and LAMP detection systems for *Phytophthora* species associated with kiwifruit diseases in China. Plant Dis 106(3):846–853

Lin X, Huang X, Urmann K, Xie X, Hoffmann MR (2019) Digital loop-mediated isothermal amplification on a commercial membrane. ACS Sens 4(1):242–249

Martin FN, Tooley PW, Blomquist CL (2004) Molecular detection of *Phytophthora ramorum*, the causal agent of sudden oak death in California, and two additional species commonly recovered from diseased plant material. Phytopathology 94(6):621–631

Miles TD, Martin FN, Coffey MD (2015) Development of rapid isothermal amplification assays for detection of *Phytophthora* spp. in plant tissue. Phytopathology 105(2):265–278

Mori Y, Notomi T (2009) Loop-mediated isothermal amplification (LAMP): a rapid, accurate, and cost-effective diagnostic method for infectious diseases. J Infect Chemother 15(2):62–69

Mori Y, Nagamine K, Tomita N, Notomi T (2001) Detection of loop-mediated isothermal amplification reaction by turbidity derived from magnesium pyrophosphate formation. Biochem Biophys Res Commun 289(1):150–154

Nagamine K, Hase T, Notomi T (2002) Accelerated reaction by loop-mediated isothermal amplification using loop primers. Mol Cell Probes 16(3):223–229

Notomi T, Okayama H, Masubuchi H, Yonekawa T, Watanabe K, Amino N, Hase T (2000) Loop-mediated isothermal amplification of DNA. Nucleic Acids Res 28(12):E63

Parke JL, Grünwald NJ (2012) A systems approach for management of pests and pathogens of nursery crops. Plant Dis 96(9):1236–1244

Pham HM, Nakajima C, Ohashi K, Onuma M (2005) Loop-mediated isothermal amplification for rapid detection of Newcastle disease virus. J Clin Microbiol 43(4):1646–1650

Rizzo DM, Garbelotto M, Hansen EM (2005) *Phytophthora ramorum*: integrative research and management of an emerging pathogen in California and Oregon forests. Annu Rev Phytopathol 43:309–335

Robideau GP, De Cock AW, Coffey MD, Voglmayr H, Brouwer H, Bala K, Chitty DW, Desaulniers N, Eggertson QA, Gachon CM, Hu CH, Kupper FC, Rintoul TL, Sarhan E, Verstappen EC, Zhang Y, Bonants PJ, Ristaino JB, Levesque CA (2011) DNA barcoding of oomycetes with cytochrome *c* oxidase subunit I and internal transcribed spacer. Mol Ecol Resour 11(6):1002–1011

Robin C, Piou D, Feau N, Douzon G, Schenck N, Hansen EM (2011) Root and aerial infections of *Chamaecyparis lawsoniana* by *Phytophthora lateralis*: a new threat for European countries. For Pathol 41(5):417–424

Rolando JC, Jue E, Schoepp NG, Ismagilov RF (2019) Real-time, digital LAMP with commercial microfluidic chips reveals the interplay of efficiency, speed, and background amplification as a function of reaction temperature and time. Anal Chem 91(1):1034–1042

Roy BA, Alexander HM, Davidson J, Campbell FT, Burdon JJ, Sniezko R, Brasier C (2014) Increasing forest loss worldwide from invasive pests requires new trade regulations. Front Ecol Environ 12(8):457–465

Schena L, Hughes KJ, Cooke DE (2006) Detection and quantification of *Phytophthora ramorum*, *P. kernoviae*, *P. citricola* and *P. quercina* in symptomatic leaves by multiplex real-time PCR. Mol. Plant Pathol 7(5):365–379

Schena L, Duncan JM, Cooke DEL (2008) Development and application of a PCR-based molecular tool box for the identification of *Phytophthora* species damaging forests and natural ecosystems. Plant Pathol 57(1):64–75

Scibetta S, Schena L, Chimento A, Cacciola SO, Cooke DE (2012) A molecular method to assess *Phytophthora* diversity in environmental samples. J Microbiol Methods 88(3):356–368

Suwannin P, Polpanich D, Leelayoova S, Mungthin M, Tangboriboonrat P, Elaissari A, Jangpatarapongsa K, Ruang-Areerate T, Tangchaikeeree T (2021) Heat-enhancing aggregation of gold nanoparticles combined with loop-mediated isothermal amplification (HAG-LAMP) for *Plasmodium falciparum* detection. J Pharm Biomed Anal 203:114178

Tanner NA, Zhang Y, Evans TC Jr (2015) Visual detection of isothermal nucleic acid amplification using pH-sensitive dyes. BioTechniques 58(2):59–68

Tomita N, Mori Y, Kanda H, Notomi T (2008) Loop-mediated isothermal amplification (LAMP) of gene sequences and simple visual detection of products. Nat Protoc 3(5):877–882

Tomlinson JA, Barker I, Boonham N (2007) Faster, simpler, more-specific methods for improved molecular detection of *Phytophthora ramorum* in the field. Appl Environ Microbiol 73(12): 4040–4047

Tomlinson JA, Dickinson MJ, Boonham N (2010) Rapid detection of *Phytophthora ramorum* and *P. kernoviae* by two-minute DNA extraction followed by isothermal amplification and amplicon detection by generic lateral flow device. Phytopathology 100:143–149

USDA Agricultural Research Service URL https://nt.ars-grin.gov/fungaldatabases/fungushost/fungushost.cfm

Watanabe H (2014) The detection methods for high-temperature-*Pythium* species in hydroponic culture by bait and membrane filter. Plant Protect (written in Japanese) 68(6):309–313

Watanabe H, Muramoto Y, Adachi M, Fukuta S, Takahashi R, Kageyama K (2013) Reducing clogging by using a filter aid for the detection of plant pathogen using a membrane filter method. Ann Rept Kansai Pl Prot (written in Japanese) 55:65–66

Webber JF (2009) Management of *Phytophthora kernoviae* and *P. ramorum* in Southwest England. In: Goheen EM, Frankel SJ (eds) Phytophthoras in forests and natural ecosystems. General Technical Report PSW-GTR-221. USDA Forest Service, Albany, pp 177–183

White TJ, Bruns T, Lee S, Taylor J (1990) Amplification and direct sequencing of fungal ribosomal RNA genes for phylogenetics. In: Innis MA, Gelfand DH, Sninskey JJ, White TJ (eds) PCR protocols: a guide to methods and applications. Academic, San Diego, pp 315–322

Yang X, Hong C (2018) Differential usefulness of nine commonly used genetic markers for identifying *Phytophthora* species. Front Microbiol 9:2334

Yang X, Tyler BM, Hong C (2017) An expanded phylogeny for the genus *Phytophthora*. IMA Fungus 8(2):355–384

Zhang ZP, Zhang Y, Liu JP, Zhang JT, An ZX, Quan FS, Zhang L, Cai X, Pu SW (2009) Codeposition of dNTPs detection for rapid LAMP-based sexing of bovine embryos. Reprod Domest Anim 44(1):116–121

Zhang H, Xu Y, Fohlerova Z, Chang H, Iliescu C, Neuzil P (2019) LAMP-on-a-chip: revising microfluidic platforms for loop-mediated DNA amplification. Trends Anal Chem 113:44–53

Part II
Water, Soil and Hydrometeorological Dynamics

Chapter 7
Water Quality Safety and Security: From Evaluation to Control

Fusheng Li

Abstract Water is a central part of river basin that sustains the life of humans and all essential social and natural functions and activities. The safety and security of water for both its quantity and quality is the issue that directly links with the SDG for Clean Water and Sanitation and is the key leading to a safe and sustainable river basin environment, the foundation for achieving other SDGs, such as Life below Water, Life on Land, No Poverty and Zero Hunger. This chapter focuses on water quality evaluation and control based on review of information available in literature and some research data of the author relating to river water quality and its changes during rainstorm, the internal load of phosphorous in freshwater reservoir sediment and its release potential differences under condition with and without aeration, river bed bacterial community for integrated water quality evaluation related to heavy metal pollution and bacteria accumulation of cesium in water The contents and some findings described through this chapter are consistent with the SDGs of the United Nations that require concrete actions, and can serve as reference for better evaluation and management of water environment.

Keywords Water quality · Water safety and security · SDGs · Phosphorus · Heavy metal · Bacteria

7.1 Introduction

Water is necessary for the survival of all living species on earth and plays irreplaceable roles in human life, from our health to all social and economic activities. The quality of water, normally described as Water Quality, is used to reflect the suitability of water for various types of usages and all involved living, industrial and agricultural processes. Requirement for water quality differs greatly in accordance with the usages with respect to the physical, chemical, and biological aspects of

F. Li (✉)
River Basin Research Center, Gifu University, Gifu, Japan
e-mail: lifs@gifu-u.ac.jp

F. Li et al. (eds.), *River Basin Environment: Evaluation, Management and Conservation*, https://doi.org/10.1007/978-981-19-4070-5_7

water properties or characteristics. For safe drinking water supply, the maximum allowable levels for toxic substances and pathogenic microbial agents are the items with the strictest requirement for waterworks to satisfy, in addition to the requirements on items such as pH, turbidity, color, odor and smells that affect consumers' feeling and accessing will towards tap water, and on the management and maintenance of the water supply system as a whole from source water intake to water treatment process and finally to treated water distribution. Consequently, water quality is reflected, regulated, and managed by a wide range of parameters and approaches and, depending on the sources and usages of water, some can be very specific and some very common.

The quality formation of water in natural water environment is a result of many natural and human influences. Natural influences generally refer to those in relations to geological, hydrological and climatic aspects of watersheds or associated entire environment. The transfer, diffusion and transformation of naturally occurring substances and elements as well as microbial agents are also important factors that should be included in the sphere of multiple factors greatly affecting the quality and, in many cases, the quantity of water available for use as well. The influences of human activities on water quality are widespread and also very tremendous with respect to the extent to which they can disrupt and bring about adversary or detrimental impacts to ecosystems and inhibit or restrict water use.

The quality of water from most natural water sources is getting more and more complicated due to further intensified industrial, agricultural and living activities, as well as increasingly diversified living styles and rising living standard. In addition to conventional contaminants that have been followed in the past, newly emerging chemical compounds and microbial and viral agents of health and taste concerns are found existent in rivers and lakes of many countries. On the other hand, as a fact, consumers' requirement for the quality of tap water has been consistently increasing, not only for the drinking purpose but also for other usages (e.g., bath, washing and kitchen). Failure in responding to the requirement is a reason that continuously promotes and accelerates people's escaping from public water supplies seen in many countries, which, if not solved properly, will affect the sustainable development of the public water supply infrastructure, and make the operation of water works more difficult.

Water security is "the capacity of a population to safeguard sustainable access to adequate quantities of acceptable quality water for sustaining livelihoods, human well-being, and socio-economic development, for ensuring protection against waterborne pollution and water-related disasters, and for preserving ecosystems in a climate of peace and political stability.," as defined by the United Nations. To cope with the complicating source water quality and rising consumer requirement, integrated water management from source to the tap is important, together with the necessity for building or assembling new water treatment systems on the basis of the existing and new technologies (including biological filtration, activated carbon adsorption, membrane filtration, and even such technologies as ion exchange and nanofiltration adopted for pure water production).

This chapter is aimed to emphasize the importance and significance of evaluation and control of water quality for safe, secure, and sustainable water environment management and water supply; and provide information of reference value for further water quality study and practical water quality control. It includes the following four parts described based on literature review and relevant research data of the author: Dissolved and particulate organic carbon, nitrogen, and phosphorus; Phosphorous release to water from sediment; Sediment bacteria as a potential index for comprehensive water quality evaluation; and Cesium accumulation by bacteria in freshwater sediment.

7.2 Dissolved and Particulate Organic Carbon, Nitrogen and Phosphorus

Organic carbon (C), nitrogen (N) and phosphorus (P) are important elements monitored for natural water systems and various wastewater sources. Their content, together with the content of some hazardous substances and pathogenic microorganisms, are crucial criteria for evaluation of the suitability of a given surface water source as the source of water supply for relevant social, industrial and/or agricultural purposes. For drinking water production, it is well known that, although similar physicochemical treatment processes are applied, the quality of finished water differs markedly depending on the sources of water due mainly to their physical, chemical and biological features. C, N and P are essential elements of almost all lives, their content also affect the community of aquatic microorganisms with respect to their species and numbers. In many cases, inorganic P acts as the limiting factor of primary production (Elser et al. 1990) in natural water environment. PO_4-P at about 0.01 mg/L can cause nutrient limitation, affecting the growth and cell tissue of most microorganisms (Elwood et al. 1981). From the viewpoint of water quality and water environment conservation, however, an excessive presence of nutrients is not favored. Higher concentrations of nutrients are often blamed for eutrophication of many surface water bodies, which not only disturbs the balance of aquatic microbial community but can also lead to furthered water quality deteriorations.

Organic matter (OM) in surface water generally exhibits the features of naturally occurring organic substances and is a heterogeneous mixture of organic compounds having variable physicochemical properties. Arising mainly from the decay of plant and animal residuals and other metabolic activities of microorganisms, humic substances constitute for a major proportion of dissolved organic matter (DOM) of most natural water sources and can form trace hazardous disinfection byproducts during water treatment. They may also affect the fate and behavior of coexisting contaminants through their involvement in redox-processes (Bierg et al. 1995), and their capability in binding hydrophobic trace organic species (Chiou et al. 1986) and in forming complexes with metals (Christensen et al. 1996). The heterogeneity of DOM is reflected in many aspects (including molecular weight or size, structure,

functional group, charge density, aromaticity, etc.) (Chandrakanth and Amy 1998; Myllykangas et al. 2002; Li et al. 2002; 2003a, b). Molecular weight (MW) or size is an important aspect since it greatly affects the removal of the constituents of DOM from water (Myllykangas et al. 2002; Li et al. 2002).

In addition to dissolved ones, organic and inorganic components in their particulate forms also play significant roles. Derived from such sources as plant litter, microbial biomass and its by-products, and weathering and dissolution of minerals, the fate of particulate components varies with the environmental, biochemical, and hydrologic characteristics of water bodies (Morris et al. 1995; Dawson and Billett 1998; Mortimer et al. 1998). Characterizing the composition of suspended particles based on C, N, P, and heavy metals, endocrine disrupting compounds, antibiotic resistance genes and pathogenic bacterial and viral agents of health concerns is receiving increasing attentions because it provides the information for better understanding their features and also some important insights towards the fate of dissolved trace organic and inorganic species. Dissolved impurities or pollutants of natural or anthropogenic origins may transport along with suspended particles because of physical sorption and/or chemical interactions. The information also benefits the characterization of sources, sinks and movement of aquatic elements through catchments to receiving water bodies.

Heavy rainstorm is an important natural phenomenon and a typical non-point source contributor. It brings into surface water large quantities of suspended substances, greatly affecting the water chemistry of river and lake systems, depending on the associated stream conditions, catchment types and land uses. In regard of this, information on the changes of particulate C, N and P during typical typhoon-induced heavy storm events is scarce.

7.2.1 Dissolved Organic Matter, Nitrogen and Phosphorus

In most cases, a storm of rain causes distinct changes for river water quality evaluated by such indices as pH, electrical conductivity (EC), suspended solids (SS), ultraviolet absorbance at 260 nm or 254 nm (UV260 or UV254), dissolved organic carbon (DOC), particulate organic matter (POM), particulate organic carbon (POC), total phosphorus (TP), dissolved phosphorus (DP), total nitrogen (TN) and dissolved nitrogen (DN). Compared to the changes in SS, the changes in the content of DOM can be smaller depending on their content of occurrence and accumulation in associated catchments and the easiness of transportation through the rainwater' pathway to receiving rivers or lakes. Like the trend of SS, remarkable changes in the concentrations of TP and TN can occur, and the changing extent can differ along the flow direction from upstream to downstream. For TP, in many cases, the contribution from its suspended form (SP) is generally larger than that from its dissolved form (DP); for nitrogen, however, although the suspended form (SN) can increase by several folds, its contribution to TN is less significant.

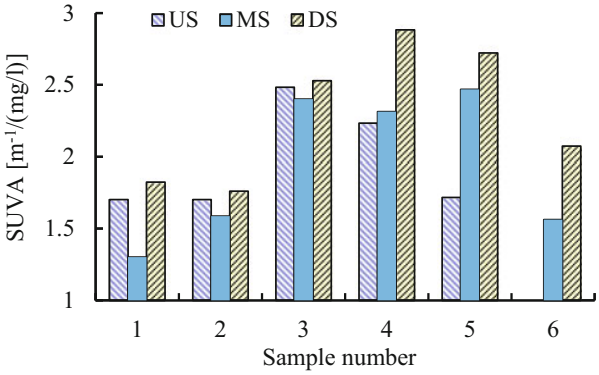

Fig. 7.1 Changes in the composition of dissolved organic matter reflected by SUVA in water of Nagara River (a major river in central Japan area) along the river line (166 km in length) during a heavy storm of rain. US is the upstream site, MS the midstream site and DS the downstream site. Sample number 1 was collected hours before the storm, 2, 3, 4 and 5 during the storm following the course of river water level ascending (with sample 5 corresponding to the time point where river water level the DS site reached its highest level), and 6 after the storm when water level had returned back to that before the storm. SUVA is specific ultraviolet absorbance defined as the ratio of UV260 to DOC

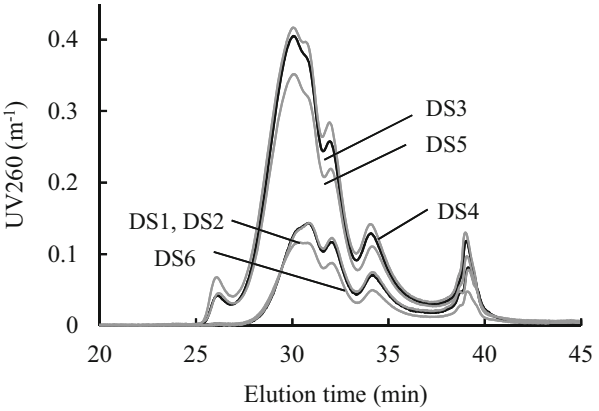

Fig. 7.2 Changes in the composition of dissolved organic matter reflected by molecular weight distribution in water of Nagara River. DS1-DS6 represent the six downstream samples described earlier in Fig. 7.1

A good accordance of the changing trends of SS and DOM with varying river water level may suggest the origin of relevant substances, i.e., the increased SS and DOM are brought newly into river sources via the storm event. The increased proportion of DOM may contain a higher content of UV-absorbing organic constituents (Fig. 7.1) and have a molecular size range like that of DOM present in its headwater (Fig. 7.2). Beyond the small fractions of larger-molecular sizes, the newly emerged DOM constituents may have a molecular size range like that of organic constituents existed in water before the rainstorm (Fig. 7.2).

7.2.2 *Organic Matter, Nitrogen and Phosphorus in Particulate Form*

POM in rivers can vary at each monitory site from upstream to downstream and during rainfall, thus indicating substantial changes in suspended particles' organic content along the river line and during heavy storm of rain. A general decreasing trend of POM from upstream to downstream (Fig. 7.3) may suggest suspended particles merged into the river water along the river line contained lower content of organic matter. Similarly, the smaller values of POM noticed for samples at higher river water levels (US3, MS4 and DS4, for instance), as compared to the reference samples (US1, MS1 and DS1), may suggest the lower organic content for particles newly brought into the river via the stormwater although the presence of SS increased markedly.

Following the changes in the POM, the mass percentages of organic carbon fixed in suspended particles may also change (Fig. 7.3). In case, the observed trends for POM and POC are similar along flow direction or during rainfall or snow-thawing seasons, it is reasonable to infer that the carbon content in particulate organic matter, defined as POC divided by POM, differs less significantly. Taking also into consideration the indication that POM is mainly derived from such sources as plant litter, microbial biomass and its by-products, and precipitated DOMs, the higher POM

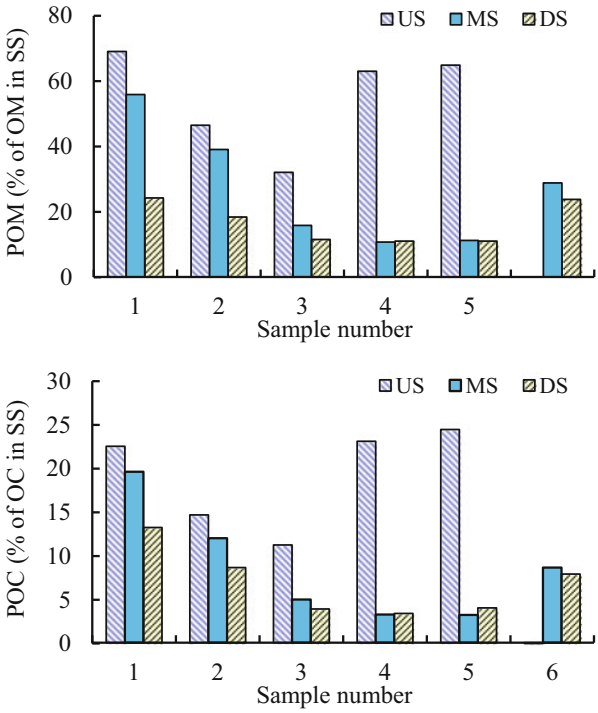

Fig. 7.3 Changing trends of particulate organic matter and particulate organic carbon (by mass) in water of Nagara River along the river line during a heavy storm of rain (the results for samples described earlier in Fig. 7.1)

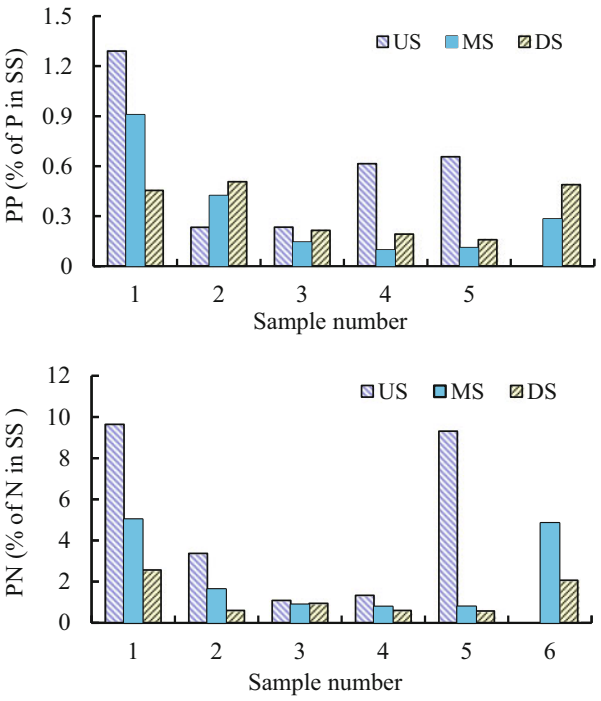

Fig. 7.4 Changing trends of particulate nitrogen and particulate phosphorus (by mass) in water of Nagara River along the river line during a heavy storm of rain (the results for samples described earlier in Fig. 7.1)

values for upstream water samples can be considered because of contribution from the higher forest coverage in the upstream catchment of most natural rivers.

Like organic C, the mass percentages of nitrogen and phosphorus in suspended particles (PN and PP) also vary within different ranges. Indicating a general decreasing trend as the river water flowed downstream and a similar trend as the river water level increased due to the storm of rain, the content of PN can change in different ranges along the flow direction in rivers. Our results on PN of water samples collected during a complete storm rain event of Nagara River in central Japan were 1.1–9.6%, 0.8–5.0% and 0.6–2.6% for samples from upstream, midstream, and downstream sites, respectively (Fig. 7.4). Comparison of our results with documented ones (Neal et al. 1997) for three Tweed basin river sites (1.04–3.15%) and three LOIS Humber River sites (0.43–1.06%) indicated that suspended particles in water of the Nagara River, especially those in its upstream, generally contained higher content of nitrogen. For PP, a general decreasing trend due to storm rain was also observed although its values were much smaller than PN and fluctuated only in the ranges of 0.23–1.3%, 0.1–0.9% and 0.16–0.45% along the river line (Fig. 7.4). The PP values resembled those determined for samples of the above-referenced Tweed basin river sites (0.58–1.31%) and LOIS Humber River sites (0.19–0.65%).

7.2.3 Inter Relationships of Dissolved and Particulate C, N and P

C:N and N:P are well-used indexes reflecting the nutrient structure of natural water systems. In most cases even if rainfall could bring about enhanced presence of C and N in water, the changes of C:N in dissolved form are comparatively smaller than those in the particulate form. For samples collected from the up-, mid- and downstream of Nagara River, for instance, dissolved C:N varied in 4.0–6.7, 0.74–1.79 and 0.66–1.18; while the particulate ones in 2.34–17.32, 3.91–7.36 and 5.16–14.41, respectively. A trend of decreases in dissolved C:N along the river flow direction was revealed, indicating that water merged into the river along its flow direction contained larger content of dissolved N (in relation to the dissolved C) than the headwater at the upstream site. For samples collected during the storm of heavy rain, larger ratio values of particulate C:N were revealed. It was thus conceived that, compared to suspended particles in the river water before the storm, those newly brought into the river through stormwater contained higher content of C (in relation to N).

The ratio values of N:P also vary with the sources of water, irrespective of the existing form of both nitrogen and phosphorus, dissolved or particulate. If an apparent trend of either increasing or decreasing for N:P as water flows downstream exists or not depends greatly on the land coverage and use in the catchment and the discharge loadings of the both elements-relevant substances and compounds. So is the case when the impacts of rainfall are considered. Larger ratio values of N:P for the dissolved form than the particulate form may exist as a feature different from C:N, suggesting that in relation to the content of N, the content of P contained in suspended particles is higher.

Dissolved organic carbon, nitrogen and phosphorus in natural water sources are generally transported from such sources as soil, vegetation, sewage discharge, agriculture and industries. Since such sources are not uniformly distributed in the catchment of most river basins and also because the interplay of associated physicochemical and biological processes during mass transportation from catchment to river and along the river line is very complex, the concentrations of these elements can vary in a manner less relevant. This was confirmed by poor inter concentration correlations obtained among these three indices (DN vs. DOC, DP vs. DOC and DP vs. DN) for three sites designed along the mainstream of Nagara River. For particulate C, N and P in natural water systems, the major source of these three elements is generally considered as soil-transported organic matter from decayed vegetation and animal residues. Although not linear, the author's observation result for Nagara River showed increases of PN and PP with the increases of POC; and increases of PP with the increases of PN (Fig. 7.5). The parametric increasing trends may imply that suspended particles from the vegetation rich Nagara River basin were similar with respect to the content of nutrients.

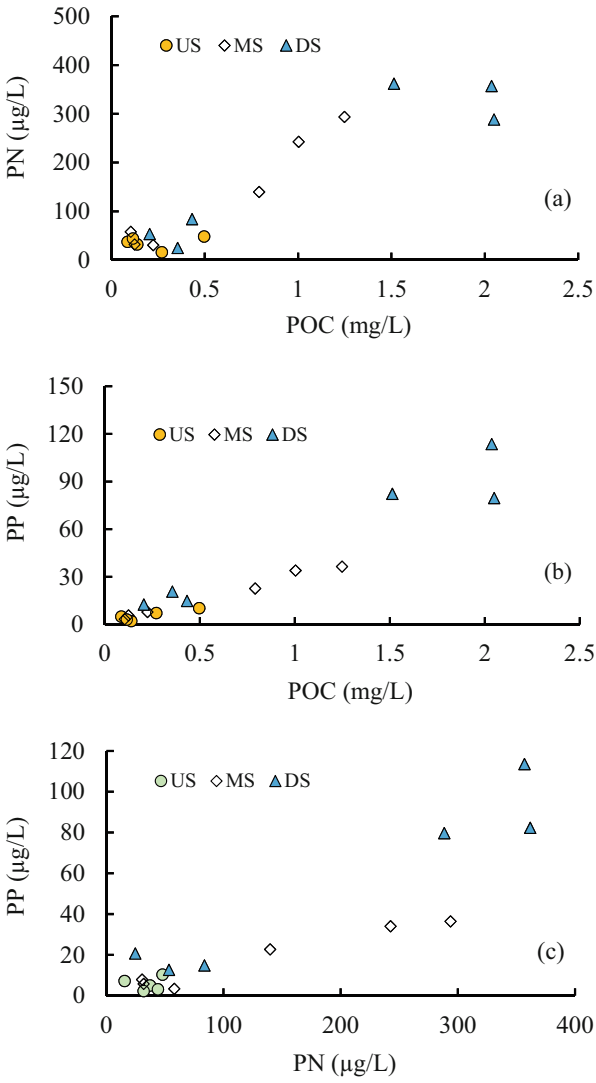

Fig. 7.5 Concentration inter relationships suspended particulate organic carbon, nitrogen and phosphorus: (**a**) PN vs. POC, (**b**) PP vs. POC and (**c**) PP vs. PN, in water samples collected at all three sampling sites

7.3 Phosphorous Release to Water from Sediment

Many elements can accumulate in sediment of river, lake, and reservoir water sources. Due to physical, chemical, and biological reactions occurring in the sediment phase and the interface formed between the overlaying water phase and sediment phase, they can release to water, hence affecting and regulating the concentrations and composition of the elements in water. In most cases, phosphorus released from sediment sustains the eutrophication process of most closed water bodies and the cycles between overlying water and sediment through algal growth,

Photo 7.1 Sediment sampling from freshwater reservoir using core sampler for analysis and evaluation of the properties of sediment and the release potential of nutrients (photo taken by the author)

organic deposition, decomposition, and release (Elser et al. 1990; Wang et al. 2003). Information on how and to what extent phosphorus is released from sediment is thus crucial for better water resource management, which requires quantitative evaluation of phosphorus bound within sediment, especially the categories or fractions of phosphorus that could change their status from particulate forms to dissolved ones with the involvement of complex biological and physicochemical reactions (Li et al. 2005; Wang et al. 2003). Estimation of the releasing potentials of phosphorus from sediment under different oxygen condition is also desired to establish the likely relations between releasing potentials and the internal load of all categories of particulate phosphorus (Photos 7.1 and 7.2).

7.3.1 Phosphorus in Sediment

Phosphorus in sediment exists in particulate form and is generally classified into five categories, namely organic phosphorus (organic P), calcium-, aluminum- and ferric-combined inorganic phosphorus (Ca-P, Al-P and Fe-P), and insoluble phosphorous (insoluble-P). The classification can be done using frozen dried sediment samples following analytical approaches, such as the one documented (Measurement Method Assessment Committee for Soil Nutrients 1997). This approach involves direct measurements of total phosphorus (total P), organic P, and consecutively extracted Ca-P, Al-P and Fe-P using corresponding decomposed, washed, and extracted solutions. The fraction of total inorganic P is defined as the difference between total P and organic P, and the category of insoluble-P is determined by deducting the

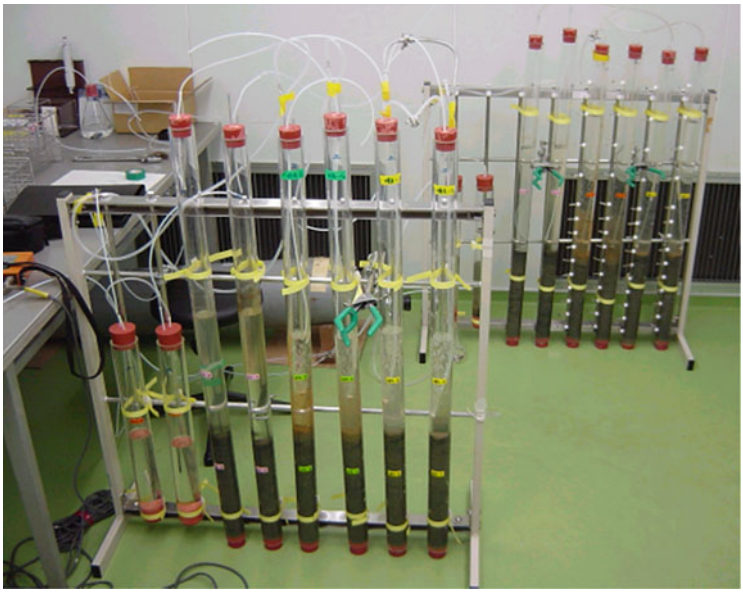

Photo 7.2 Column setup for evaluation of nutrient release from sediment core of a freshwater reservoir under conditions with and without the existence of dissolved oxygen (photo taken by the author)

combined forms of Ca-P, Al-P and Fe-P from the computed total inorganic P category.

The content of each P category can change along the vertical direction of the sediment and may also change depending on the seasons.

Insoluble-P was a major category bound within sediment, with its occupation decreasing vertically in accordance with the decreases in the total bound phosphorus content. For combined categories with Ca, Al and Fe, the percentages of Fe-P and Al-P were larger and increased from the surface layer to the bottom layer. The combined inorganic categories are reactive phosphorus that can dissociate according to changes in the redox potential of sediment and then release into water phase for algae to ingest and are thus greatly concerned (Wang et al. 2003).

Although there are some exceptions, a general trend of decreases in the total content of phosphorus existed as the sediment lowered its position from the sliced surface layer to bottom layer. As shown (Fig. 7.6), the averaged content of total-P bound within SL, ML and BL layers throughout the studied time span of about a year was 1.86, 1.58 and 1.13 mg-P/g-dry, respectively, and was apparently smaller than 0.1–1.3% measured for suspended particles present in the water samples of a major river (Nagara River) in a central Japan rich with vegetation coverage collected along the river line during a critical typhoon-induced heavy rain storm event (Li et al. 2005), and 0.58–1.31% and 0.19–0.65% for samples of the Tweed basin river sites and three LOIS Humber river sites, respectively (Neal et al. 1997).

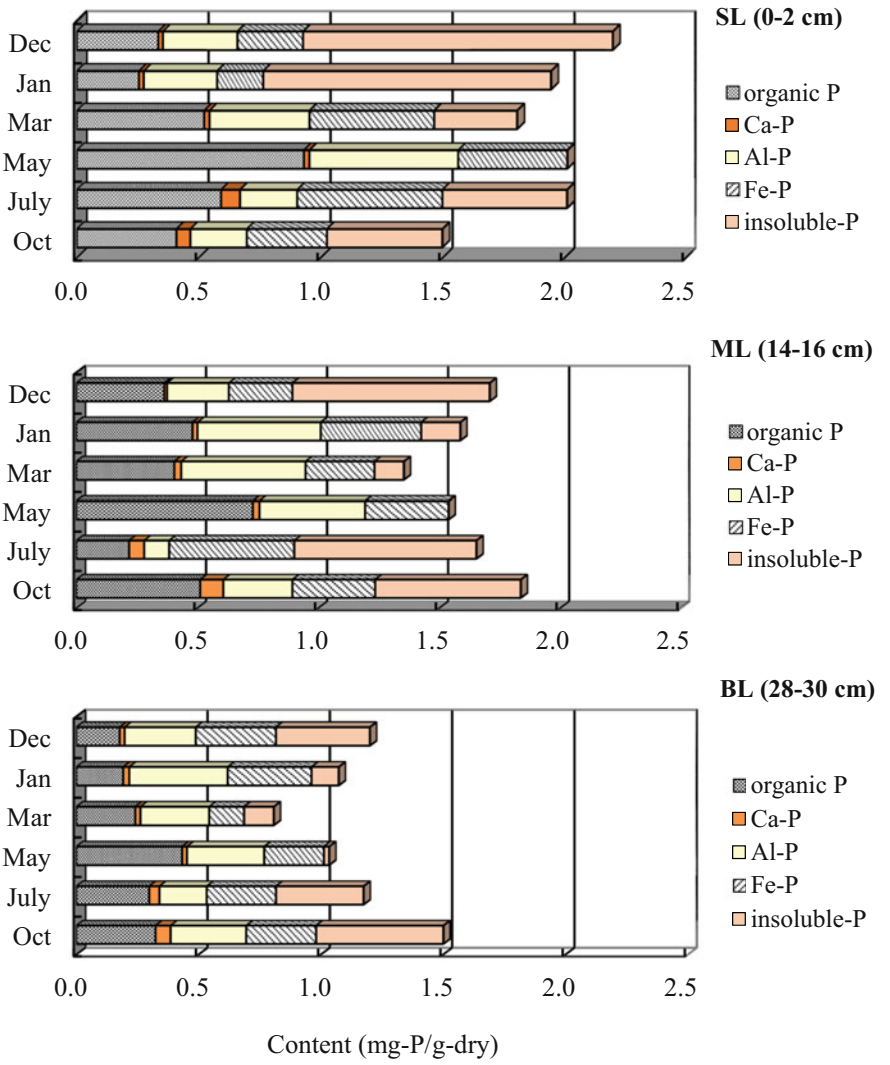

Fig. 7.6 Particulate phosphorus composition in three different sediment layers of a freshwater reservoir in eastern Japan and their seasonal changes (SL: surface layer, ML: middle layer, BL: bottom layer, sliced from a core sample about 35 cm in thickness from the surface of the sediment

Moreover, differences with seasons also exist in the total content of phosphorus in sediment, although the extent of differences is not always significant enough for singling out the likely reasons behind. Enhanced release of phosphorus as a result of enhanced microbial activities is conceivable as temperatures in the sediment-water interface and within the sediment (a combined system of sediment particles and pore water) become higher from early spring to late autumn, which may lead to reductions

in the bound content of the exchangeable phosphorus (organic-P) and the combined inorganic phosphorus categories (Ca-P, Al-P and Fe-P).

Organic phosphorus is a category of greater concern since it can convert into reactive phosphorus through microbial activities of inhabited microbes in sediments. For this category, a broader variance in its content along the vertical direction also exists in most cases. As could be seen from the results (Fig. 7.6), the content varied in 13–55% for the three sediment layers collected over a year, with the averaged content value getting decreased vertically from 0.51 (SL) to 0.45 (ML) and 0.28 mg-P/g-dry (BL). The broader variance is conceivable, taking into consideration that in lake and reservoir sediment environment organic phosphorus deposited from the overlying water may transport horizontally and vertically through bioturbation mixing and burial. And, during transportation, biological decomposition may take place.

For the combined categories of inorganic phosphorus, the content of Ca-P, Al-P and Fe-P also changes depending on the sediment layer position and the seasons. As could be seen from the results (Fig. 7.6), the total content of combined inorganic phosphorus bound in sediment of SL, ML and BL varied in 0.51–1.08, 0.53–0.95 and 0.45–0.77 mg-P/g-dry, respectively, with the averaged values revealing a decreasing trend from 0.78 (SL) to 0.75 (ML) and to 0.60 mg-P/g-dry (BL).

7.3.2 Release Behavior of Phosphorus from Sediment

Batch experiment is an effective way to evaluate the fundamental release behavior of phosphorus from sediment under different dissolved oxygen concentration condition. This can be achieved using sliced sediment layers from core sediment samples supplied with and without the introduction of air to water in batch experiment reactors. For experiments without the introduction of air, to ensure no oxygen can penetrate the reactors, continuous supply of wetted nitrogen directly into the reactors is a very effective approach. From the observed time profiles, the releasing rate and potential of phosphorus can be estimated.

The water phase PO_4-P concentration increased with time for all three sediment layers, indicating consistent release of phosphorus from sediment (Fig. 7.7). The increasing extent was markedly larger for water-sediment interaction occurring under the condition without dissolved oxygen (anaerobic). In the reactors supplied with wetted-air (aerobic), although being several-folds lower than the concentration values observed in the anaerobic rectors, dissolved PO_4-P increased its presence from the initial 0.05 to the final 0.6, 0.71 and 0.41 mg/L after running for 380 hours with SL, ML and BL, respectively. These values are much larger than the documented ones found to regulate the growth and activities of microorganisms in water environments. Inorganic phosphorus often acts as an important limiting factor for primary production (Elser et al. 1990). Dissolved PO_4-P at around 0.01 mg/L is reported to cause nutrient limitation, leading to lowered growth rate and elevated N: P ratio in the cell tissues of P-limited microorganisms (Elwood et al. 1981).

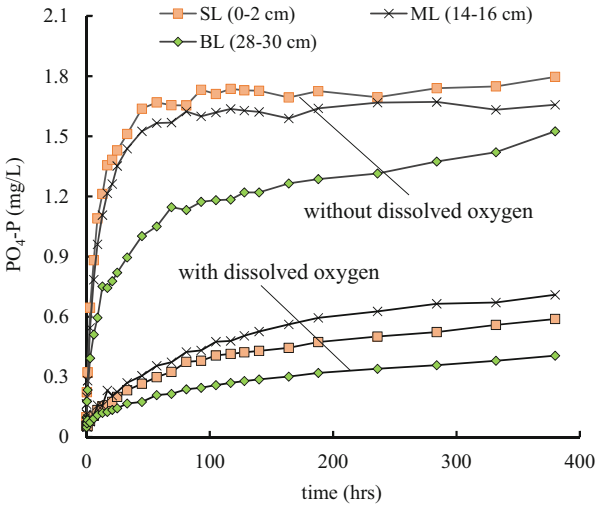

Fig. 7.7 Time profiles of PO_4-P released from sediment of a freshwater reservoir (the same reservoir described earlier in Fig. 7.6) in reactors with and without dissolved oxygen at 20 °C. The dose of sediment was 6.7 g/L in wet after centrifugal separation, and 2.47, 2.56 and 3.23 g/L in dry for surface layer (SL), middle layer (ML) and bottom layer (BL), respectively. The content of VSS of these three layers was 14.0, 11.1 and 10.4%, respectively. The three layers were sliced from a core sample about 35 cm in thickness from the surface of the sediment

The unexpected relatively higher content of PO_4-P in the aerated reactors, within which saturated oxygen at about 8.5 mg/L was always confirmed, can be considered to be mainly originated from the degradation of organic matter bound within sediment. The content of organic matter reflected by volatile suspended solids generally varies based on the locations and surrounding environment of the water bodies as well as such factors as hydraulic retention time and water and sediment depths. The content of organic matter was 14.0, 11.1 and 10.3%, and the content of organic carbon was 2.7, 2.3 and 1.7%, respectively for sediment layers of SL, ML and BL of the reservoir. For PO_4-P released in environment with only limited concentration of dissolved oxygen or without dissolved oxygen, a contribution from the degradation of organic matter by anaerobic microbes is also conceivable. However, since organic degradation by anaerobic microbes occurs in a rate which is generally much slower than degradation by aerobic microbes, its contribution to the total release is probably less significant. The significant proportions of the released phosphorus (Fig. 7.7) were thus considered to be mainly originated from the bound categories of combined inorganic phosphorus (Ca-P, Fe-P and Al-P) which dissociated due to changes in the redox potential induced by anaerobic microbial reactions occurring within relative reactors.

7.3.3 *Releasing Potential of Phosphorus from Sediment*

The releasing potential of phosphorus represented by its initial releasing rate and the maximum released amount can be estimated based on the observed time profile of dissolved phosphorus under a certain experiment condition. The initial releasing rate can be defined as the change in the released phosphorus concentration divided by the time interval involved and can thus be determined based on the slope of the linear line best fitting the observed initial time profile data. For the index of maximum released amount, its value can be generated by dividing the maximum released phosphorus concentration with the dose of sediment; while the maximum released concentration is the value after the concentration of dissolved phosphorus in water becomes relatively stable, i.e., the release is reaching its steady state.

The initial releasing rate of phosphorus form sediment varies with seasons when sediment is sampled and subjected to evaluation and with the position of sediment in its vertical direction, so does with the maximum released amount of phosphorus. As could be seen from the author's results (Fig. 7.8) that, under aerobic conditions, the releasing rate from sediment of SL, ML and BL varied with time in 0.6–7.3, 0.7–7.6 and 0.47–3.15 μg h^{-1}/g-dry, respectively; while, under anaerobic conditions, the releasing rate was markedly higher, varying in 9.9–75.5, 13.4–45.1 and 2.2–23.6 μg h^{-1}/g-dry.

Using the sediment samples collected in December and January, Li et al. (2004) studied the behavior of a natural estrogen (17β estradiol) spiked into batch reactors

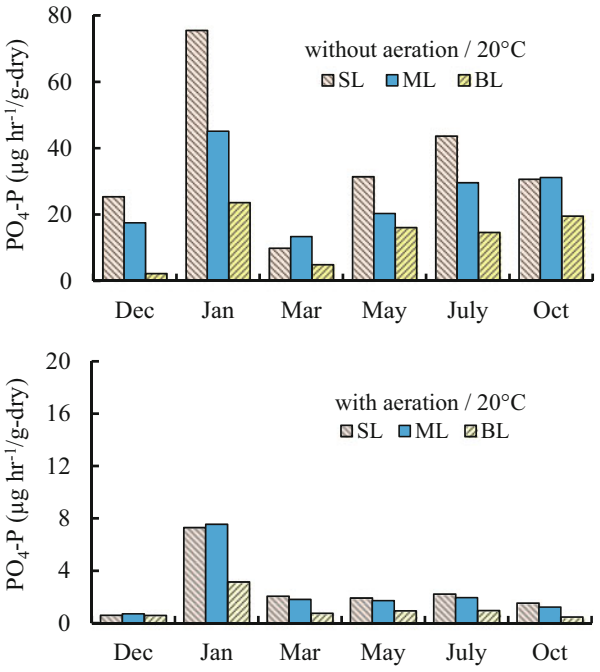

Fig. 7.8 Differences in the initial releasing rate of PO_4-P from sediment of different seasons of a freshwater reservoir (the same reservoir described earlier in Fig. 7.6) in reactors with and without dissolved oxygen at 20 °C. The dose of sediment was 6.7 g/L in wet after centrifugal separation, and 2.47, 2.56 and 3.23 g/L in dry for surface layer (SL), middle layer (ML) and bottom layer (BL), respectively. The content of VSS of these three layers was 14.0, 11.1 and 10.4%, respectively. The three layers were sliced from a core sample about 35 cm in thickness from the surface of the sediment

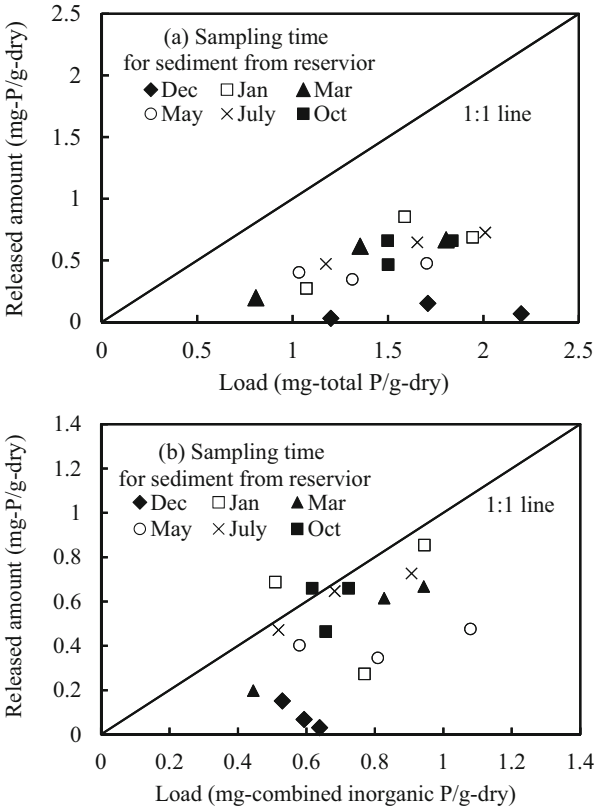

Fig. 7.9 Relationships of the maximum released amount of phosphorus in reactors without dissolved oxygen at 20 °C with (**a**) the load of total P and (**b**) the load of the total combined inorganic P of SL, ML and BL layers of sediment of a freshwater reservoir (the same reservoir described earlier in Fig. 7.6). The dose of sediment was 6.7 g/L in wet after centrifugal separation, and 2.47, 2.56 and 3.23 g/L in dry for surface layer (SL), middle layer (ML) and bottom layer (BL), respectively. The content of VSS of these three layers was 14.0, 11.1 and 10.4%, respectively. The three layers were sliced from a core sample about 35 cm in thickness from the surface of the sediment

of sediment-water suspensions. The dissipation rate of this estrogen, given by the first order reaction rate parameter, for anaerobic runs at 20 °C varied in 0.005–0.062 h^{-1}/g-dry, a difference of about ten-folds between the layers of SL and BL. This difference resembled that noticed for the releasing potentials discussed above, thus suggesting that microbial activities occurring within anaerobic sediment environment be a major factor responsible for phosphorus release from sediment. In other words, by assessing microbe activities through degradation studies with a tracer organic molecule, glucose for instance, the releasing potentials of phosphorus possessed by sediment might be predicted, given the load of bound phosphorus in sediment be known.

Knowing the relationship of the maximum released PO_4-P amount under anaerobic condition with the load of total phosphorus and the load of total combined inorganic phosphorus are also important. As the plots of the author's results (Fig. 7.9) show, compared to the use of total P which also includes the content of insoluble P, the use of the total combined inorganic P which includes Fe-P, Al-P and Ca-P can lead to a result allowing the plots to distribute in positions apparently closer to the 1:1 line drawn in the figure. The standard redox potential values of Fe, Al and Ca, with their oxidative form/reductive form as Fe(III)/Fe(II), Al(III)/Al and Ca(II)/

Ca, are 0.771, −2.07 and −2.84 volts, respectively. Since an element having a larger redox potential value could be reverted into its reductive from easier, it was thus conceived that the phosphorus category combined with iron (Fe-P) was preferentially released from the sediment particles.

A furthered correlation analysis of the maximum released amount phosphorus with the load of Fe-P, the load of Al-P and finally the load of Ca-P was also performed. Compared to the latter two combined phosphorus categories, the former Fe-P led to a correlation coefficient comparatively higher ($r = 0.51$). Considering the surface sediment layer alone, the maximum released amount from the layer corresponded to about 50–100% of the total combined inorganic phosphorus load (0.51–1.08 mg-P/d-dry) within the stirred anaerobic sediment-water suspensions. This provided a hint for development of some new approaches for reducing sediment-bound internal nutrient load within closed water environments, in addition to such conventional ones as chemical dosing and dredging, whose adversary impacts on sediment ecosystems could never be neglected.

7.4 Sediment Bacteria as a Potential Index for Comprehensive Water Quality Evaluation

The pollution of water and soil environments by heavy metals is consistently a major issue in many parts of the world due to their adversary effects on associated ecosystems and detrimental effects on the health of humans and animals. For natural water environment, many water quality indexes related to the species and concentrations of heavy metals are included in respectively national standards and regulations and are used for evaluation of water quality and the extent of water pollution by heavy metals originated from natural sources and human activities (social, agricultural, and industrial activities).

In the freshwater environment mainly including rivers, lakes and dam reservoirs, a sediment phase always exists even if its thickness and composition may change with many factors, such as the coverages and uses of the associated catchment, hydraulic conditions and meteorological conditions (Li et al. 2003a, b, 2005, 2008a, b; Haller et al. 2011). Compared to the flowing water phase, the sediment phase is relatively stable and contains bacterial communities whose composition and structure may reflect the quality of the flowing water. This feature enables the bacterial community populated in the sediment to serve as a likely new biomonitoring index to assist in existing chemical analysis for realizing more comprehensive water quality evaluation.

When water sediment bacteria are considered for use as a potential index, comprehensive understanding of the responses of sediment bacteria to heavy metals is necessary. For this, there is the need to conduct integrated evaluations based on the three aspects: bacterial density, activity, and community structure. The reason is because sediment bacterial species may differ in their capability of tolerance against

heavy metals (Zhang et al. 2016), their growth rate under the condition with and/or without the presence of heavy metals (Gillan et al. 2005), and their uptake rate for substrate available in the water environment (Murata et al. 2005). The conclusion may differ according to the aspect from which evaluation is conducted. For instance, in regard of the responses of soil and marine sediment bacterial community to heavy metals in density, previous studies have reported that heavy metal contamination may lead to a reduction of total microbial biomass (Brookes and McGrath 1984; Fliessbach et al. 1994), and a decrease in the numbers of specific bacterial populations such as infecting rhizobia (Chaudri et al. 1993) or mycorrhizae (Koomen et al. 1990). However, there are also other studies that have shown that metal stress does not always reduce productivity (Shi et al. 2002; Wenderoth and Reber 1999) or biomass (Shi et al. 2002; Chodak et al. 2013; Zhang et al. 2016).

Similarly, regarding the impacts of heavy metals on the diversity of soil and water sediment bacterial community, findings reported in previous studies are also different. Through analysis of bacterial communities in heavy metal-contaminated soils at different levels of resolution, Sandaa et al. (1999) reported that heavy metal contamination may lead to a reduction of bacterial diversity. However, other researchers observed either an increase in microbial diversity (Sorci et al. 1999) or no significant variation (Gillan et al. 2005). The contrary findings are considered to be explainable by factors other than metals (such as environmental variables, the time of exposure, etc.) (Haller et al. 2011). For field studies, toxic organic compounds, if coexisted with heavy metals, are also a factor that makes the evaluation of the impacts of heavy metals more complicated (Shi et al. 2002).

The responses of bacterial communities in natural environments to heavy metals are considered to be mainly in association with the toxicity of heavy metals. For bacterial species too sensitive to heavy metals, their growth may be inhibited (Koomen et al. 1990; Chaudri et al. 1993; Lahra et al. 2003; Barkay 1987; Rasmussen and Sørensen 2001; Smit et al. 1997). For bacterial species with strong resistance against heavy metals and those with weak resistance but can recover after adapting to the toxicity, they may maintain their growth as dominating ones or become new dominating ones (Rasmussen and Sørensen 2001; Gillan et al. 2005). For observed increases or no variation in microbial diversity of marine sediments along with heavy metal contamination (Sorci et al. 1999; Gillan et al. 2005), the reason was speculated due mainly to the appearance of new dominant species, rather than a reversion to the original community (Gillan et al. 2005). In addition to the differences of bacterial species in their tolerance capability against heavy metals, the differences in their uptake rate for substrate are also a probable factor contributing in part, if not all, to the observed differences as hinted in previous studies (Hattori 1992; Murata et al. 2005). Such a hypothesis probably applies since, within bacterial community, there might be some bacterial species that have strong tolerance against heavy metals and could grow readily only when the substrate available for their use is ensured. If such bacterial species exist, depending on their density and the substrate availability for them as against other coexisted bacterial species, increases or no apparent variations in the overall density of the bacterial community are likely. To find new evidence to prove this, relatively long-term incubation experiments under well-controlled

conditions are necessary since field studies are difficult to differentiate the impacts of heavy metals from those of many environmental variables and hazardous organic compounds if coexisted.

7.4.1 *Sediment Bacterial Responses to Heavy Metals in Density*

The extent of sediment bacteria's response to Cu was more obvious than that to Pb, Cr and Cd. In the beginning a few days, incubation spiked with middle and high concentrations of Cu showed bacterial density lower than control (Ctrl) (Fig. 7.10). After the short beginning period, however, the density turned to rapid increases and reached levels about 3 orders higher than Ctrl. For incubation with the low concentration, the density was about 2 orders higher than Ctrl. In Ctrl, the density increased by about 2 orders after incubation started for one day and then maintained slight fluctuations till the end of incubation. The increases in Ctrl were probably due to abundant substrate in the reactor (provided daily by the addition of glucose) than in the field of the river. For Cd, obvious bacterial growth occurred for incubation with high Cd concentration where the density values increased by 1–2 orders as compared to Ctrl. For incubation spiked with Pb and Cr, a distinct trend of either increases or decreases against Ctrl did not appear, suggesting the response of sediment bacteria to these two metals is not strong. A short-term inhibition effect followed by a distinct long-term promotion effect by Cu was also revealed for sediment bacteria from other two tributary rivers in the Nagara River system.

For general bacteria detected through culturing with higher substrate concentration under higher temperature than heterotrophic bacteria, the changing trends of bacterial density during incubation spiked respectively with Cu, Pb, Cr and Cd were very similar to those of heterotrophic bacteria. The extent of responses of the sediment bacteria differed with the targeted three tributary rivers of the Nagara River system, and the difference was probably caused by the differences in the extent of their exposure to the metals in the field of the rivers.

The initial reductions of relative bacterial density in incubation with Cu might be explained by the inhibition effect on the growth of certain bacterial species, if not all, due to the toxicity of the metal element, as reported by Baath (1989) and Giller et al. (1998). The stronger inhabitation effect of Cu was also reported by Murata et al. (2005) who compared soil bacterial responses to Cu, Sb, In and Zn through incubation experiment using 96-well microtiter plates. The long-term promotion effect of Cu and Cd was partly supportive of the previous findings (Sorci et al. 1999), and could serve as a direct evidence showing the possibility of increases in the density of bacteria in water environment contaminated with heavy metals, even if the standard plate count method has its limitations in detecting all heterotrophic bacterial species populated in river sediment.

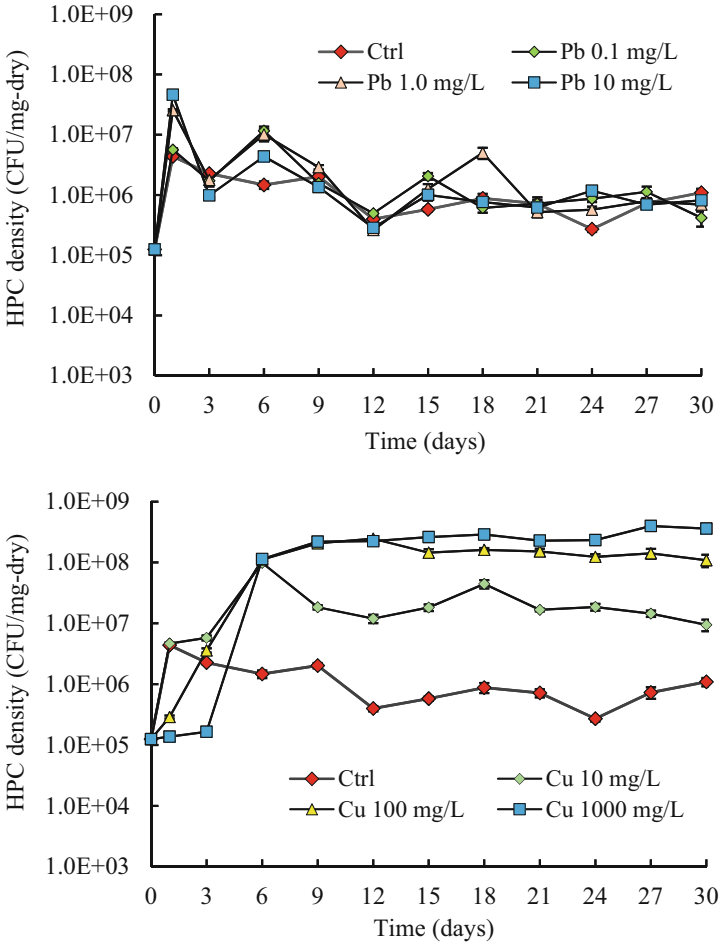

Fig. 7.10 Changes in the density of heterotrophic bacteria (HPC) during sequencing batch incubation spiked with different concentrations of Pb and Cu for riverbed sediment from a tributary river (Kurisugawa) of the Nagara River system in central Japan. The density of HPC is described as the number of colonies divided by the dry mass of sediment added to each incubation reactor. The initial sediment solid concentration was 780 mg/L (dry weight), the carbon source (10 mg-C/L as glucose) and nitrogen source (1 mg-N/L as ammonium nitrogen) were added to each reactor on a daily basis, and temperature was controlled at 20 °C). The plot and error bar show the mean value and standard deviation of six measurements for HPC (duplicate incubation runs and three measurements for each run). Ctrl represents the data of the control experiment conducted without spiking metals

It is inferable from the incubation experiment results that the observed responses of the riverbed sediment bacteria to Cu and Cd in density were probably a result of the following involvements: (1) the activity of all bacterial species was inhibited in the initial time period and then recovered after adapted to the incubation condition;

(2) some bacterial species having faster uptake rate for substrate and can grow even under relatively low field substrate concentration were highly sensitive to the metals and their growth was inhibited (the likely reason for the observed initial bacterial density reductions); and (3) some bacterial species, who had strong tolerance capability against metals and could grow readily under rich substrate condition, existed and turned into rapid growth when the growth of the bacterial species having faster uptake rate for substrate was inhibited (the likely reason for the observed long-term bacterial density increases). A fourth explanation (4) was also conceivable: the sediment contained some major species, which were present in high proportion but were sensitive to metals, and some species present at very low density in the sediment but could emerge after a lag time because they were more resistant to metals than the major species. The apparently higher density values for incubation spiked with the metal than control noticed in the period of long-term promotion effect could further lead to the inference that the contribution of (3) was relatively significant for the incubation conditions of this study. To support this inference requires results on bacterial community structures.

7.4.2 Sediment Bacterial Responses to Heavy Metals in Activity

The activity of bacteria can be described by the first order rate constant k of glucose estimated by fitting data obtained through sequencing batch incubation using sediment. k values for incubation in rectors spiked with heavy metals are generally lower, with the extent of impact from Cu being more prominent (Fig. 7.11).

The changes in the bacterial activity defined as the rate constant k divided by the HPC concentration showed that, of the four metal elements, the activity of bacteria became particularly weaker for incubation spiked with Cu and Cd, if compared to Cr and Pb (Fig. 7.12).

The response of sediment bacteria to heavy metals also differs with the rivers. In regard of the impact of Cu, for instance, heterotrophic bacteria in the sediment of the upstream of Kurisu River responded obviously, followed by the downstream Gyaku River and then the mid-stream Ijira River, three tributary rivers of the Nagara River system. To Cd under the concentration of 10 mg/L, a distinctly stronger response was associated with the bacteria in the sediment of the upstream Kurisu River. For bacteria in the sediment of the mid-stream Ijira River and the downstream Gyaku River, the responses were weaker and similar. The adversary impact of heavy metals on the activity of river sediment bacteria is also supported by incubation with bacteria of other sources, such as soil environment evaluated based on dehydrogenase activity, CO_2 respiration or the decomposition rates of organic matter added to soils (Wlike 1991; Hattori 1992; Murata et al. 2005). In dose-response incubation of bacteria extracted from soils through measurement of protein synthesis, Pb was found more toxic than Cr in affecting microbial activities (Shi et al. 2002). The

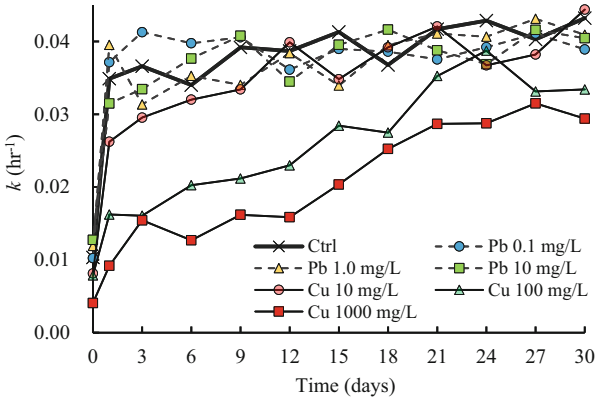

Fig. 7.11 Changes in the first-order degradation rate constant of glucose by riverbed sediment heterotrophic bacteria (HPC) from a tributary river (Kurisugawa) of the Nagara River system in central Japan during sequencing batch incubation spiked with different concentrations of Pb and Cu. The initial sediment solid concentration was 780 mg/L (dry weight), the carbon source (10 mg-C/L as glucose) and nitrogen source (1 mg-N/L as ammonium nitrogen) were added to each reactor on a daily basis, and temperature was controlled at 20 °C). The plot and error bar show the mean value and standard deviation of six measurements for HPC (duplicate incubation runs and three measurements for each run). Ctrl represents the data of the control experiment conducted without spiking metals

bacterial response to heavy metals also differs greatly with the pH levels in the environment. When pH is at around 7.0, dissolved concentrations of Pb, Cu and Cd available for sediment bacteria can be lower, compared to pH at the acid side. For Cr with high solubility in water, microbial activity could lead to reduction of Cr (VI) into Cr (III). Therefore, it is worthy of special mention that the observed effects of the heavy metals on bacterial density and activity through incubation experiments are a result of the likely involvement of both dissolved and not dissolved metal species (for Pb, Cu and Cd) and of the different existence forms (for Cr); and were probably lower than those in water environment with lower pH levels.

Taking also into consideration the revealed responses in density, i.e., the long-term density increases of heterotrophic bacteria in the reactors spiked with Cu of different concentrations (for instance, 10, 100 and 1000 mg/L) and Cd (10 mg/L), the decreases in the relative bacterial activity evaluated on the basis of the mineralization rate for dissolved organic carbon can probably be explained by the following: the bacterial species that have strong tolerance against the metals and grew to greater abundance probably possess a slower consumption rate for substrate. The reported inhibition effect due to the toxicity of the metals through, for instance, direct inhibition of the metabolic systems is also possible and cannot be excluded (Wlike 1991; Hattori 1992; Shi et al. 2002; Murata et al. 2005).

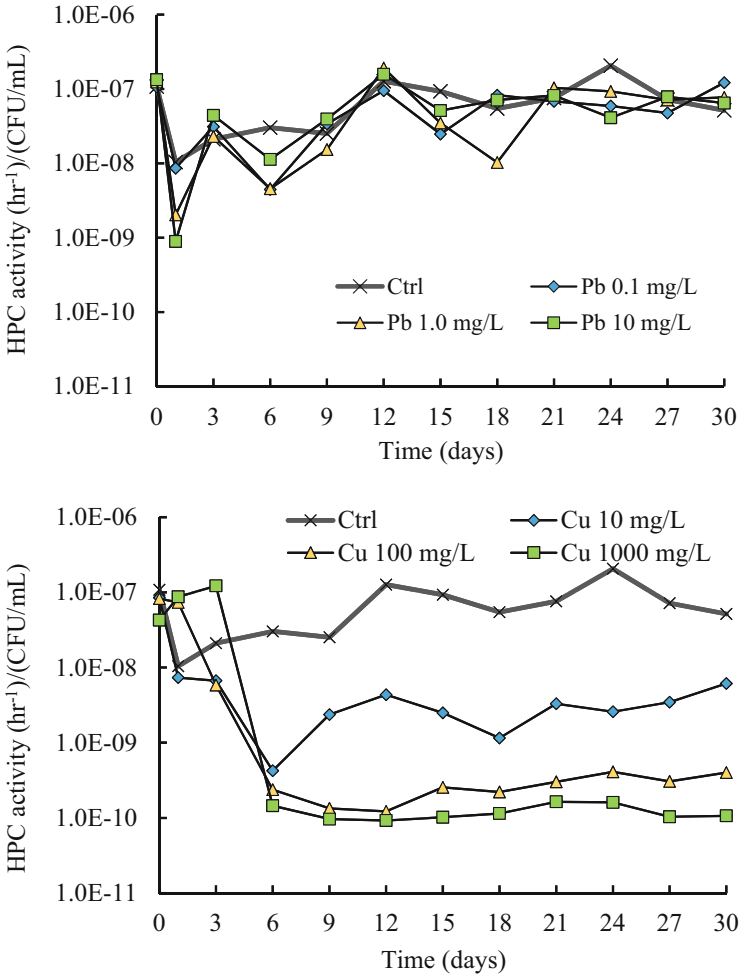

Fig. 7.12 Changes in the activity of heterotrophic bacteria (HPC) during sequencing batch incubation spiked with different concentrations of Pb and Cu with riverbed sediment from a tributary river (Kurisugawa) of the Nagara River system in central Japan. The initial sediment solid concentration was 780 mg/L (dry weight), the carbon source (10 mg-C/L as glucose) and nitrogen source (1 mg-N/L as ammonium nitrogen) were added to each reactor on a daily basis, and temperature was controlled at 20 °C). Ctrl represents the data of the control experiment conducted without spiking metals

7.5 Cesium Accumulation by Bacteria in Freshwater Sediment

The water environment pollution by radioactive cesium is consistently a great concern. Cesium can accumulate in living organisms and gets condensed through food chains, thus threatening the safety and health of humans, animals, and ecosystems. While the direct effect of the Fukushima power plant accident occurred 10 years ago is still lasting, the way to deal with the large amount of wastewater from the plant has appeared as a hot debate of recent days.

Sediment in most closed freshwater bodies is a sink for many pollutants. A recent study by Ivanov et al. (2021) showed that 137Cs in the sediment of Schekino reservoir after the Chernobyl Nuclear Power Plant accident had reached 496 kBq/m^2. The fate and behavior of Cs in sediment greatly affects the safety of the whole water environment and is a result of complicated interactions with the major constituting components in sediment (including pore water, sediment particles, vegetation debris and various microorganisms) through sorption, desorption, diffusion, bioaccumulation, and biotransformation. For all these interactions, the involvement of microbial community in sediment can be enormous.

The microbial community in sediment generally includes bacteria, algae, protozoa, and metazoan. Bacteria can account for 90–99% of the total biomass that existed therein. The larger specific surface area provided by bacteria (100–1000 times higher than typical eukaryotic cells) (Nealson 1997) also suggests the possibility of bacteria as the predominant microbial group in water environment that regulates the fate and behavior of cesium even if evidence through systematical experimental and field studies is necessary. Microbial accumulation of cesium has been documented in literature based on research targeting on larger aquatic organisms than bacteria, such as benthic creatures (Shigenobu et al. 2015), demersal fish (Wada et al. 2013), aquatic plants (Sasaki et al. 2016). However, information on the accumulation of cesium by the tiny species of bacteria in sediment is lacking where bacteria also function as the food source for ingestion by organisms larger than them beyond their role as decomposers. Ingestion by larger organisms may also affect the fate and transport of cesium in the entire water environment.

Bacteria in freshwater sediment are a mixture of multiple species having different sizes and a variety of extracellular and intracellular constituting substances. Different functional groups may contribute differently to the sorption capacity for ionic elements. For instance, the carboxyl groups of the extracellular polymeric substances were reported advantageous in adsorbing cadmium; while amine, carboxyl, hydroxyl and phosphate groups and the extracellular proteins were advantageous in binding cesium ions (Yu et al. 2020). The transport systems for ions may also differ with bacteria, which probably lead to differences in the transfer of cesium into the cytoplasm. Previous studies in literature showed that potassium transport systems were essential for cesium accumulation in microalgae, cyanobacteria, and bacteria (Lee et al. 2019; Avery et al. 1991; Tomioka et al. 1992; Bakker 1993). The number of enzymes (such as potassium-transporting P-type ATPase) may also

affect the induced active intracellular accumulation for cesium (Lee et al. 2019). Some specific substances in the bacteria possessing the capability to trap cesium in the cytoplasm, such as polyphosphate (Kuwahara et al. 2011), may also affect its accumulation. Different bacterial species in sediment may have different accumulation capabilities for cesium. The accumulation capability may also change as the temperature in water environment changes. All these require detailed validation through experiments under well-controlled conditions. The effect of temperature was reported for many trace contaminants in water environment (Freeman et al. 2017; Deng et al. 2014; Sanz-Lázaro et al. 2015).

7.5.1 *Bacterial Species from the Sediment*

Bacteria in water and soil environment are very diverse. The sequencing analysis result for isolated bacteria after plate culture for a freshwater sediment sample identified the bacteria as 5 species in the phylum of Proteobacteria, 9 species of Firmicutes, and another two species of uncertain (Table 7.1). From a coastal sediment sample studied in parallel, 12 species were found in the phylum of Proteobacteria, and 6 of Firmicutes and another one of Bacteroidetes. It is thus clear that most isolated bacteria belonged to the phyla of Proteobacteria and Firmicutes. However, judging from the species levels, they were quite different, implying that bacterial community in the sediment of freshwater environment can be

Table 7.1 Species identified by sequence analysis of heterotrophic bacteria isolated from freshwater reservoir sediment cultured following conventional plate culture method (Standard Methods 2017)

Name	Accession No.	Identities (%)	Phylum
Ensifer sp.	KF437393	100	Proteobacteria
Bacillus sp.	KF501477	100	Firmicutes
Bacillus aryabhattai	JX524506	100	Firmicutes
Bacillus megaterium	KF460569	99	Firmicutes
Bacillus anthracis	KF436681	99	Firmicutes
Bacillus sp.	AB847892	99	Firmicutes
Bacillus sp.	KF562337	99	Firmicutes
Bacterium	JN118420	99	–
Ensifer sp.	JX028785	91	Proteobacteria
Ensifer sp.	AB552886	95	Proteobacteria
Ensifer adhaerens	JX042455	88	Proteobacteria
Bacillus megaterium	KF460567	98	Firmicutes
Bacterium	DQ117542	97	–
Bacillus sp.	HM117832	75	Firmicutes
Bacillus aryabhattai	KF436619	99	Firmicutes
Ensifer adhaerens	KF030956	88	Proteobacteria

distinctly different from that of the coastal water environment, even if the number of bacterial species is limited only to those that can be cultured through the conventional cultural method and isolated.

7.5.2 *Accumulation Capability of Bacteria for Cs*

All isolated bacteria from a sample of freshwater reservoir sediment showed their capability in accumulating cesium. For bacteria from a freshwater sediment, the lowest accumulation concentration was 3.95×10^{-6} ng-Cs/cell and the highest was 5.68×10^{-4} ng-Cs/cell, with the difference being more than 2 orders (Fig. 7.13). It is reasonable to infer that the density and fate of bacterial species in the sediment may greatly affect the distribution and behavior of the metal element in the whole environment of the relevant freshwater bodies.

The significant difference was probably due to the difference of bacteria in the following aspects involved in accumulation of cesium, as could be inferred by also referencing to the very limited literature reports on accumulation of cesium by microorganisms: an actinomycete Streptomyces sp. K202 (Kuwahara et al. 2011), fungal Rhodosporidium fluviale (Lan et al. 2014), and a cyanobacterium

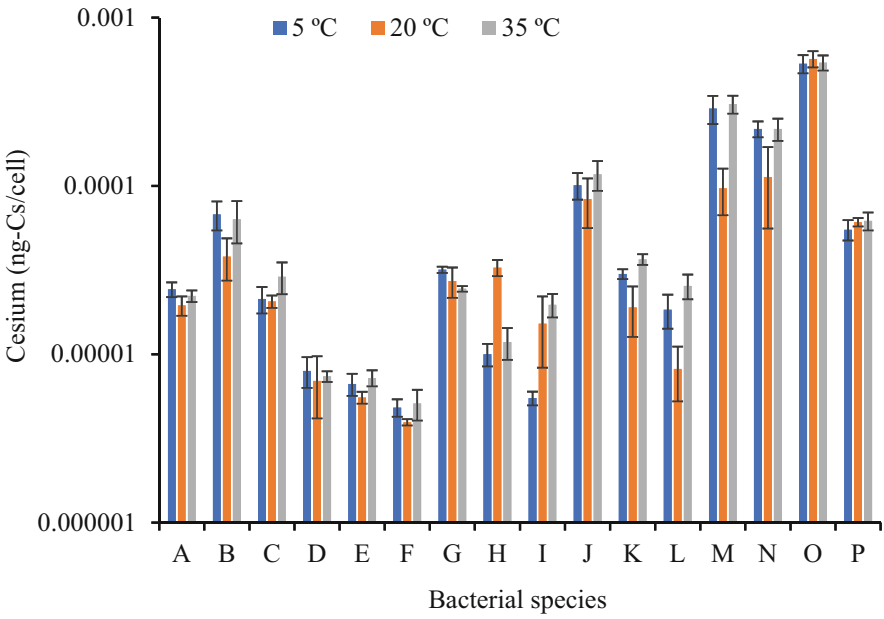

Fig. 7.13 Accumulation of cesium by heterotrophic bacteria isolated through plate culture method from freshwater reservoir sediment. Accumulation was determined after incubation for 72 h at three different temperatures (5, 20 and 35 °C). The initial Cs concentration in each test tube was 200 μg/L. The labels A-P of the x-axis represent the isolated bacterial species

Synechococcus PCC7002 (Yu et al. 2020). The first aspect is in association with the sites where cesium can probably be accumulated through the process of sorption to the cell surface and then fixation into the cytoplasm. For this aspect, the shapes and size of the cells, as well as the content and composition of both extracellular and intracellular polymeric substances exhibiting different physicochemical features (for instance, the features related to functional groups such as carboxylic, phosphate, phosphodiester, amino, and hydroxyl) can be considered as important factors. They may differ greatly among bacterial species. The second aspect is probably related to the scale of the channels where transportation for cesium ion could take place, as suggested by Lee et al. (2019), and to the activity of enzymes that could induce active intracellular accumulation for cesium, like potassium-transporting P-type ATPase (Lee et al. 2019). The difference in the quantity of some specific substances among bacteria that could trap cesium in cytoplasm, like polyphosphate reported by Kuwahara et al. (2011), is also conceivable. Studies on the involvement of these factors in regulating the accumulation of cesium are necessary for obtaining direct evidence to support the inferences.

In the phylum level, the isolated bacteria in the freshwater sediment belonged to Proteobacteria, Firmicutes and two unknown phyla. Averaging the values of the Cs accumulation capacity of the bacterial species in each phylum showed that the accumulation capacity in the phylum level was 1.21×10^{-4}, 6.12×10^{-4}, 3.80×10^{-5} and 8.18×10^{-6} ng-Cs/cell, respectively, with the accumulation capacity of the Firmicutes being about five times as large as that of Proteobacteria. Similarly, for bacteria in the coastal sediment studied in parallel, the accumulation capacity followed the order of Firmicutes > Proteobacteria > Bacteroidetes, with the capacity value of 9.31×10^{-4}, 4.93×10^{-4} and 1.28×10^{-4} ng-Cs/cell, respectively.

Although the bacteria in this study were randomly isolated from the cultural colonies, the obtained results can benefit to better understanding and control of the fate and behavior of radioactive cesium in water environment and ecosystem associated with bacteria. They can also serve as an important reference for further studies related to the effect of cell size, shape, and extracellular and intracellular polymeric substances of bacteria on cesium accumulation, diffusion, and transportation in the water environment, and to the involvement and contributions of other factors that function together with bacteria. In addition, since bacteria in aquatic environment are very diverse, studies using more bacterial species such as bacteria for nitrification, denitrification, desulfurization and methane generation are expected, together with analysis and discussion of cesium accumulation at higher taxonomic levels (Photo 7.3).

Photo 7.3 Particulate organic matter sampling for evaluation of water quality responses to dam construction and operation (photo taken by the author)

7.6 Water Quality Control and Needs for Research and Technology Development

Water quality is a complex issue affected by factors of local, regional, and global features and origins. To realize the SDG for Clean Water and Sanitation and other relevant SDGs, and to ensure better water and living environment under the challenges of dynamic global urban development and climate change, integrated water quality evaluation and water environment management is and will continue to be a topic of concern. Water quality control and water treatment based on conventional and new unit processes (including coagulation, sedimentation, sand filtration, biological filtration, chlorination, ozonation, activated carbon adsorption, membrane filtration, and even such technologies as ion exchange and nanofiltration adopted for pure water production) are indispensable, together with development of new systems based on both new and conventional technologies.

Acknowledgement The author thanks Mr. Jun Tsumori for his great cooperation in the study leading to part of the data used in the section on phosphorous release from sediment. The author also thanks his students who have joined either filed or laboratory studies or both that led to the data used in other sections of this chapter.

References

Avery SV, Codd GA, Gadd GM (1991) Caesium accumulation and interactions with other monovalent cations in the cyanobacterium synechocystis PCC 6803. J Gen Microbiol 137(2): 405–413

Bakker EP (1993) In: Bakker EP (ed) Alkali cation transport systems in prokaryotes. CRC Press, Boca Raton, pp 253–276

Barkay T (1987) Adaptation of aquatic microbial communities to Hg2+ stress. Appl Environ Microbiol 53:2725–2732

Bierg PL, Rugge K, Pedersen JK, Christensen TH (1995) Distribution of redox sensitive groundwater quality parameters downgradient of a landfill (Grindsted, Denmark). Environ Sci Technol 29:1387–1394

Baath E (1989) Effects of heavy metals in soil on microbial processes and populations (a review). Water Air Soil Pollut 47(3–4):335–379. https://doi.org/10.1007/BF00279331

Brookes PC, McGrath SP (1984) Effects of metal toxicity on the size of the soil microbial biomass. J Soil Sci 35:341–346

Chandrakanth M, Amy G (1998) Effects of NOM source variations and calcium complexation capacity on ozone-induced particle destabilization. Water Res 32:115–124

Chaudri AM, McGrath SP, Giller KE, Rietz E, Sauerbeck DR (1993) Enumeration of indigenous *Rhizobium leguminosarum* biovar trifolii in soils previously treated with metal-contaminated sewage sludge. Soil Biol Biochem 25:301–309

Chiou CT, Malcolm RL, Brinton TI, Kile DE (1986) Water solubility enhancement of some organic pollutants and pesticides by dissolved humic and fulvic acids. Environ Sci Technol 20:502–508

Chodak M, Gołębiewski M, Morawska-Płoskonka J, Kuduk K, Niklińska M (2013) Diversity of microorganisms from forest soils differently polluted with heavy metals. Appl Soil Ecol 64:7–14

Christensen JB, Jensen DL, Christensen TH (1996) Effect of dissolved organic carbon on the mobility of cadmium, nickel and zinc in leachate polluted groundwater. Water Res 30:3037–3049

Dawson JJC, Billett MF (1998) The separation of suspended particulate material into organic, mineral and organo-mineral fractions. Water Res 32:1725–1731

Deng J, Qin B, Paerl HW, Zhang Y, Wu P, Ma J, Chen Y (2014) Effects of nutrients, temperature and their interactions on spring phytoplankton community succession in Lake Taihu. China PLoS One 9(12):1–19

Elser JJ, Marzolf ER, Goldman CR (1990) Phosphorus and nitrogen limitation of phytoplankton growth in the freshwaters of North America: a review and critique of experimental enrichments. Can J Fish Aquat Sci 47:1468–1477

Elwood JW, Newbold JD, Trimble F, Stark RW (1981) The limiting role of phosphorus in a woodland stream ecosystem: effects of P enrichment on leaf decomposition and primary producers. Ecology 62:146–158

Fliessbach A, Martens R, Reber HH (1994) Soil microbial biomass and microbial activity in soils treated with heavy metal contaminated sewage sludge. Soil Biol Biochem 26:1201–1205

Freeman O, Ovie O, Omoregie I (2017) Effect of climate change through temperature increase on heavy metals concentrations in water and sediment of Ekpan Creek, Delta state. Nigeria Adv Res 10(5):1–16

Giller KE, Witter E, Mcgrath SP (1998) Toxicity of heavy metals to microorganisms and microbial processes in agricultural soils: a review. Soil Biol Biochem 30(10–11):1389–1414. https://doi.org/10.1016/S0038-0717(97)00270-8

Gillan DC, Danis B, Pernet P, Joly G, Dubois P (2005) Structure of sediment-associated microbial communities along a heavy-metal contamination gradient in the marine environment. Appl Environ Microbiol 71:679–690

Haller L, Tonolla M, Zopfi J, Peduzzi R, Wildi W, Pote J (2011) Composition of bacterial and archaeal communities in freshwater sediments with different contamination levels (Lake Geneva, Switzerland). Water Res 45:1213–1228

Hattori H (1992) Influence of heavy metals on soil microbial activities. Soil Sci Plant Nutr 38:93–100

Ivanov MM, Konoplev AV, Walling DE, Konstantinov EA, Gurinov AL, Ivanova NN, Kuzmenkova NV, Tsyplenkov AS, Ivanov MA, Golosov VN (2021) Using reservoir sediment deposits to determine the longer-term fate of Chernobyl-derived 137Cs fallout in the fluvial system. Environ Pollut 274:116588

Koomen I, McGrath SP, Giller KE (1990) Mycorrhizal infection of clover is delayed in soils contaminated with heavy metals from past sewage sludge applications. Soil Biol Biochem 22: 871–873

Kuwahara C, Fukumoto A, Nishina M, Sugiyama H, Anzai Y, Kato F (2011) Characteristics of cesium accumulation in the filamentous soil bacterium Streptomyces sp. K202. J Environ Radioact 102(2):138–144

Lahra J, Maas-Diepeveenb J, Stuijfzandc SC, Leonardsd PEG, Drukea JM, Luckera S, Espeldoornb E, Kerkumb LCM, van Steed LLP, Hendriks AJ (2003) Responses in sediment bioassays used in the Netherlands: can observed toxicity be explained by routinely monitored priority pollutants? Water Res 37:1691–1710

Lan T, Feng Y, Liao J, Li X, Ding C, Zhang D, Yang J, Zeng J, Yang Y, Tang J, Liu N (2014) Biosorption behavior and mechanism of cesium-137 on *Rhodosporidium fluviale* strain UA2 isolated from cesium solution. J Environ Radioact 134:6–13

Lee KY, Lee SH, Lee JE, Lee SY (2019) Biosorption of radioactive cesium from contaminated water by microalgae *Haematococcus pluvialis* and *Chlorella vulgaris*. J Environ Manag 233: 83–88

Li F, Yuasa A, Ebie K, Azuma Y, Hagishita T, Matsui Y (2002) Factors affecting the adsorption capacity of dissolved organic matter onto activated carbon: modified isotherm analysis. Water Res 36:4592–4604

Li F, Yuasa A, Chiharada H, Matsui Y (2003a) Polydisperse adsorbability distribution of several natural and synthetic organic matrices. J Colloid Interface Sci 265:265–275

Li F, Yuasa A, Chiharada H, Matsui Y (2003b) Storm impacts upon the composition of organic matrices in Nagara River-a study based on molecular weight and activated carbon adsorbability. Water Res 37:4027–4037

Li F, Tsumori J, Yamashita N, Tanaka H, Suzuki Y (2004) Biodegradation and biotransformation pathways 17β-estradiol by reservoir sediment under aerobic and anaerobic conditions. Environ Eng Res JSCE 41:447–458. (in Japanese with English abstract)

Li F, Yuasa A, Muraki Y, Matsui Y (2005) Impacts of a heavy storm of rain upon dissolved and particulate organic C, N and P in the main river of a vegetation-rich basin area in Japan. Sci Total Environ 345:99–113

Li F, Tsumori J, Suzuki Y, Tanaka H (2008a) Vertical distribution of nonylphenol ethoxylates and their derivatives in sediments of a freshwater reservoir. Water Air Soil Pollut 189:265–277

Li F, Desmiarti R, Yuasa A, Horio A (2008b) Behavior of natural estrogens in semicontinuous activated sludge biodegradation reactors. Bioresour Technol 99:2964–2971

Measurement Method Assessment Committee for Soil Nutrients (ed) (1997) Analytical methods for soil nutrients. YONEDO

Morris AW, Allen JI, Howland RJM, Wood RG (1995) The estuary plume zone: source of sink for land-derived nutrient discharges? Estuarine Coastal Shelf Sci 40:387–420

Mortimer RJG, Krom MD, Watson PG, Frickers PE, Davey JT, Clifton RJ (1998) Sediment-water exchange of nutrients in the intertidal zone of the Humber estuary. UK Mar Pollut Bull 37(3–7): 261–279

Murata T, Koshikawa M, Takamatsu T (2005) Effects of Pb, cu, Sb, in and ag contamination on the proliferation of soil bacterial colonies, soil dehydrogenase activity, and phospholipid fatty acid profiles of soil microbial communities. Water Air Soil Pollut 164:103–118

Myllykangas T, Nissinen TK, Rantakokko P, Martikainen PJ, Vartiainen T (2002) Molecular size fractions of treated aquatic humus. Water Res 36:3045–3053

Neal C, Robson AJ, Harrow M, Hill L, Wickham H, Bhardwaj CL, Tindall CI, Ryland GP, Leach DV, Johnson RC, Bronsdon RK, Cranston M (1997) Major, minor, trace element and suspended

sediment variations in the river tweed: results from the LOIS core monitoring programme. Sci Total Environ 194(195):193–205
Nealson KH (1997) Sediment bacteria: who's there, what are they doing, and what's new? Annu Rev Earth Planet Sci 25:403–434
Rasmussen LD, Sørensen SJ (2001) Effects of mercury contamination on the culturable heterotrophic, functional and genetic diversity of the bacterial community in soil. FEMS Microbiol Ecol 36:1–9
Sandaa RA, Torsvik V, Enger O, Daae FL, Castberg T, Hahn D (1999) Analysis of bacterial communities in heavy metal-contaminated soils at different levels of resolution. FEMS Microbiol Ecol 30:237–251
Sanz-Lázaro C, Valdemarsen T, Holmer M (2015) Effects of temperature and organic pollution on nutrient cycling in marine sediments. Biogeosciences 12(15):4565–4575
Sasaki Y, Funaki H, Iri S, Dohi T, Hagiwara H (2016) Fate of radiocesium in freshwater aquatic plants and algae in the vicinity of the Fukushima Daiichi nuclear power plant. Limnology 17(2): 111–116
Shi W, Becker J, Bischoff M, Turco RF, Konopka AE (2002) Association of microbial community composition and activity with lead, chromium, and hydrocarbon contamination. Appl Environ Microbiol 68:3859–3866
Shigenobu Y, Ambe D, Kaeriyama H, Sohtome T, Mizuno T, Koshiishi Y, Yamasaki S, Ono T (2015) Investigation of Radiocesium translation from contaminated sediment to benthic organisms. Impacts of the Fukushima Nuclear Accident on Fish and Fishing Grounds, pp 91–98
Smit E, Leeflang P, Wernars K (1997) Detection of shifts in microbial community structure and diversity in soil caused by copper contamination using amplified ribosomal DNA restriction analysis. FEMS Microbiol Ecol 23:249–261
Sorci JJ, Paulauskis JD, Ford TE (1999) 16 rRNA restriction fragment length polymorphism analysis of bacterial diversity as a biomarker of ecological health in polluted sediments from New Bedford Harbor, Massachusetts, USA. Mar Pollut Bull 38:663–675
Standard Methods (2017) Standard Methods for the Examination of Water and Wastewater, 23rd ed., American Public Health Association (APHA), American Water Works Association (AWWA), and Water Environment Federation (WEF), Washington, DC
Tomioka N, Uchiyama H, Yagi O (1992) Isolation and characterization of cesium-accumulating bacteria. Appl Environ Microbiol 58(3):1019–1023
Wada T, Nemoto Y, Shimamura S, Fujita T, Mizuno T, Sohtome T, Kamiyama K, Morita T, Igarashi S (2013) Effects of the nuclear disaster on marine products in Fukushima. J Environ Radioact 124:246–254
Wang H, Appan A, Gulliver JS (2003) Modelling of phosphorous dynamics in aquatic sediments: I-model development. Water Res 37:3928
Wenderoth D, Reber H (1999) Correlation between structural diversity and catabolic versatility of metal affected prototrophic bacteria in soil. Soil Biol Biochem 31:345–352
Wlike BM (1991) Effects of single and successive additions of cadmium, nickel and zinc on carbon dioxide evolution and dehydrogenase activity in a sandy luvisol. Biol Fertil Soils 11:34–37
Yu R, Chai H, Yu Z, Wu X, Liu Y, Shen L, Zeng W (2020) Behavior and mechanism of cesium biosorption from aqueous solution by living Synechococcus PCC7002. Microorganisms 8(4): 491
Zhang C, Nie S, Liang J, Zeng G, Wu H, Hua S, Liu J, Yuan Y, Xiao H, Deng L, Xiang H (2016) Effects of heavy metals and soil physicochemical properties on wetland soil microbial biomass and bacterial community structure. Sci Total Environ 557–558:785–790

Chapter 8
Energy Recovery from Wastewater

Kayako Hirooka

Abstract Wastewater treatment is essential for maintaining a healthy water environment, but conventional wastewater treatment technology has a serious problem in that a large amount of energy is required due to oxygen supply for aeration to supply oxygen to the microorganisms and treat and dispose of the excess sludge. On the other hand, organic matter in wastewater is a potentially large source of energy, and it is important to recover and utilize it. In this chapter, methane fermentation, microbial fuel cells, and microbial electrolysis cells are introduced as technologies that can recover energy from wastewater as well as purify it.

Keywords Methane fermentation · Microbial fuel cell · Microbial electrolysis cell

8.1 Introduction

Human beings consume a large amount of water every day for their daily life and industrial activities. After its usage, used water is contaminated and becomes wastewater, which contains a plethora of pollutants such as biodegradable and non-biodegradable organic matter, suspended inorganic matter, nutrients, heavy metals, and pathogenic microorganisms. If this wastewater is not properly treated before discharge into an aquatic environment, such as a river, lake, or sea, and the amount of discharged pollutant exceeds the environmental carrying capacity (the limit at which nature can accept pollutants without adversely affecting the environment through its inherent self-purification), this unclean water becomes a problem. Water pollution causes human health hazards, adverse effects on natural ecosystems, and decreased water use for human activities. Therefore, it is necessary to remove pollutants from wastewater by wastewater treatment.

There are various kinds of wastewater treatment methods, such as physicochemical treatment, biological treatment, electrochemical treatment, or a combination of

K. Hirooka (✉)
River Basin Research Center, Gifu University, Gifu, Japan
e-mail: khirooka@gifu-u.ac.jp

F. Li et al. (eds.), *River Basin Environment: Evaluation, Management and Conservation*, https://doi.org/10.1007/978-981-19-4070-5_8

these methods, where the most appropriate technique is selected and applied depending on the type and concentration of pollutants in the wastewater to be treated. Most wastewater generated in modern society is organic wastewater containing organic matter as the main pollutant, such as municipal wastewater, food industry wastewater, and livestock wastewater, which are commonly treated by biological treatments using aerobic microorganisms such as activated sludge. However, the activated sludge process requires large amounts of energy for aeration to supply oxygen to the microorganisms and treat and dispose of the excess sludge (excess microorganisms that are withdrawn to maintain a constant microbial concentration in the biological reactor). For example, in the case of Japan, the volume of sewage is about 14.5 billion m^3/year, which uses 7.2 billion kWh/year of electricity, and is equivalent to 0.67% of Japan's total electricity consumption (Japan Sewage Works Agency 2010).

On the other hand, the organic matter contained in wastewater has potential energy and can be used as biomass energy. In recent years, as global warming has become a serious problem worldwide, biomass, along with wind and solar power, is expected to become a carbon-neutral renewable energy to replace fossil fuels and nuclear power. It is said that the potential energy contained in wastewater is about 9.3 times as much as the electrical energy required for its treatment (Shizas 2004), so there are high expectations for biomass as an energy source. Among the various types of biomass, bioethanol is one of the most popular types of biomass. But it is derived from crops competing with the use of foodstuffs, which leads to higher prices, and also requires energy to grow crop-based raw materials. Wastewater, on the other hand, does not compete with food because it is waste, and it does not require energy for production. Therefore, it is highly desirable to recover and utilize energy from wastewater to build a low-carbon society. In light of this, there is a growing need for wastewater treatment technology that removes pollutants and recovers energy at the same time. This chapter introduces methane fermentation as a popular and already widely used such technology, and Microbial Fuel Cell and Microbial Electrolysis Cell as newly focused on and actively studied.

8.2 Methane Fermentation

Methane fermentation, also known as anaerobic digestion, uses anaerobic microorganisms called methanogens to decompose and remove organic matter from wastewater while simultaneously recovering methane gas that can be used as an energy source. It is said that the phenomenon of methane fermentation was first reported in the eighteenth century, when Alessandro Volta described in a letter that gas bubbles collected from a swamp were combustible (McCarty 1981). Its application in the treatment of highly concentrated organic wastes, such as livestock waste, food waste, and excess sludge from biological wastewater treatment, has already been around for more than a century. It has also been applied to wastewater treatment since the 1980s with the development of high-speed methane fermentation

technology represented by the UASB method. Methane fermentation is the most mature of the energy recovery wastewater treatment technologies and is currently in widespread use around the world.

Wastewater treatment by methane fermentation is an anaerobic process, which means there is no need for aeration of the biological reactor. In addition, since the bacterial yield of anaerobic microorganisms is lower than that of aerobic microorganisms, the amount of excess sludge generated is significantly reduced. Therefore, the energy required for aeration and treatment/disposal of excess sludge is reduced, which is a major advantage over the activated sludge process as a wastewater treatment technology. Furthermore, energy recovery from wastewater is possible. However, the quality of the treated water is lower than that of the activated sludge process and it cannot be discharged as it is, so it needs to be treated again using other aerobic treatment such as the activated sludge process. In addition, the activated sludge process can remove nutrients by modifying the process, but methane fermentation cannot remove nutrients.

8.2.1 Microorganisms Contributing to Methane Fermentation

The microorganisms that are directly contributing to methane production in methane fermentation are methanogens, the obligate anaerobic archaea. Methanogens are found in a variety of anaerobic environments in nature, such as lakes, rice paddies, swamps, river sediment, cattle rumen, and the hindgut of white ants. Since the methanogens used in practical methane fermentation are both mesothermophilic and thermophilic archaea, methane fermentation tanks are usually heated to 37 °C–55 °C. In addition, most methanogens can take only specific substrates, using only hydrogen or acetic acid. The respective reactions of the decompositions are as follows,

$$4H_2 + HCO_3^- + H^+ \rightarrow CH_4 + 3H_2O$$

$$CH_3COO^- + H_2O \rightarrow CH_4 + HCO_3^-$$

The methane generated above can be burned to generate electricity. It can also be used simply as a heat source.

By the way, since most of the organic matters in wastewater and sludge are other than acetic acid and hydrogen, methanogens alone cannot treat it efficiently. Therefore, microorganisms that decompose the organic matter into hydrogen or acetic acid that can be used by methanogens are working in the methane fermentation reactor. These microorganisms carry out the following processes: (1) solubilization and hydrolysis of high-molecular organic matter including solids, (2) acid generation to decompose the hydrolyzed products into volatile fatty acids (acetic acid, propionic

acid, butyric acid, formic acid, etc.) and alcohols, and (3) acetic acid or hydrogen generation process from fatty acids above C3.

Furthermore, in actual methane fermentation reactors, different reactions by various anaerobic microorganisms occur in addition to the major reactions described above. A typical one is the biological sulfate reduction reaction, which results in the biogas from the methane fermentation reactor usually containing hydrogen sulfide gas. The composition of the biogas from a typical methane fermentation is about 60% methane, 40% CO_2, and 1000–2000 ppm H_2S.

8.2.2 Methane Fermentation Process

According to the total solid concentration (TS concentration) of the solids in the reactor, the methane fermentation process is classified into wet treatment (TS concentration $< 10\%$) and dry treatment (TS concentration $> 10\%$). In the case that wastewater and excess sludge generated from wastewater treatment are to be treated, wet treatment is used.

The wet treatment process is based on the complete mixing reactor, and various modifications have been developed. The main direction of development has been to increase the concentration of microorganisms in the reactor and shorten the treatment time. To achieve this, the following methods have been proposed: the return of concentrated sludge to the reactor (anaerobic contact process, anaerobic baffled reactor), formation of biofilm using a carrier (anaerobic filter reactor, anaerobic fluidized bed reactor), and prompting self-granulation of microorganism (upflow anaerobic sludge blanket [UASB] reactor, expanded granular sludge bed [EGSB] reactor). In the following, the complete mixing reactor as the basic form, and the UASB reactor as a process which is often applied to wastewater treatment, are introduced.

8.2.2.1 Complete Mixing Reactor

The methane fermentation tank of the complete mixing reactor has a mixing device installed in the tank, and generated biogas including methane gas is collected from the top of the tank, while digested sludge (excess sludge) is discharged from the bottom (Fig. 8.1). Therefore, the amount of influent wastewater and sludge discharge are equal. In order to maintain a stable concentration of active microorganisms and the performance of organic matter decomposition, the treatment time (hydraulic retention time: HRT) is generally set at 15–30 days when treating sewage sludge or livestock wastewater. Mixing methods include suction of the generated biogas with a blower and blowing it into the tank, mechanical mixing of the reactor with a pump and rotating machinery, and a combined method of several methods.

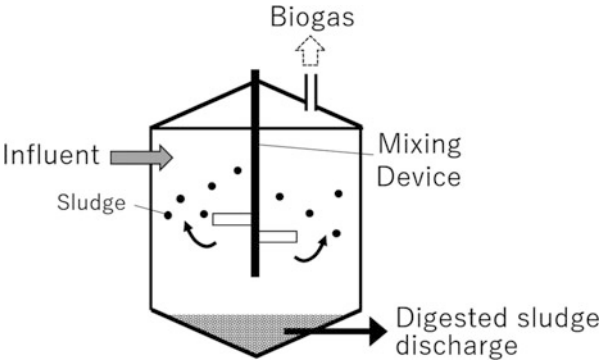

Fig. 8.1 Methane fermentation tank of the complete mixing reactor

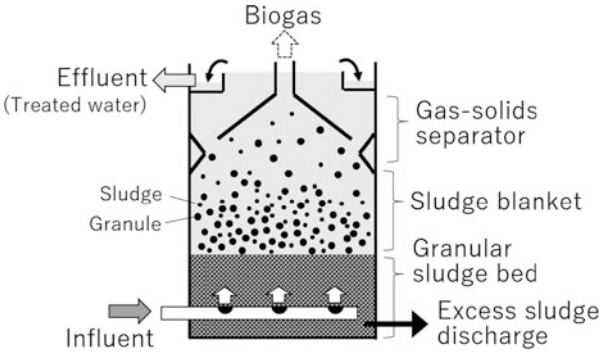

Fig. 8.2 Upflow Anaerobic Sludge Blanket (UASB) Reactor

8.2.2.2 Upflow Anaerobic Sludge Blanket (UASB) Reactor

This method is a type of high-speed methane fermentation technology developed by Lettinga et al. in the Netherlands in the 1970s. It was originally developed for wastewater containing high concentrations of easily biodegradable organic matter, but is now being applied to wastewater with low concentrations of organic matter such as sewage. It is widely used mainly in developing countries with warm climates.

The main feature of this method is that it uses the aggregation and granulation abilities of anaerobic microorganisms to form and retain granular sludge with excellent sedimentation properties in the reactor, thereby retaining a high concentration of microorganisms in the reactor, which enables high-speed (several hours) treatment of organic matter in the wastewater. The UASB reactor consists of a single tank, a device at the bottom of the tank to disperse and evenly inflow the wastewater flow, a gas-solids separator (GSS) at the top of the tank to separate the gas, granules, and treated water, a treated water overflow section, and an excess sludge discharge section. The system consists of a gas-solids separator (GSS) at the top of the tank to separate gas, granules, and treated water, a treated water overflow section, and an excess sludge discharge section (Fig. 8.2). The wastewater that flows in from the bottom of the reactor passes through the granular sludge bed (an area with dense

granules) and sludge blanket (an area where a small number of granules and sludge are flowing) in an upward flow. Due to the gentle agitation caused by the rising biogas, the granules in the sludge bed are efficiently in contact with the organic matter in the wastewater. Organic matter decomposition, methane gas production, and biomass growth take place mainly in the sludge bed region. Biogas is separated and collected in the upper air collecting chamber of the GSS, while solid-liquid separation of treated water and granules is performed in the settling area. The separated treated water is discharged from the overflow section.

8.3 Microbial Fuel Cell: MFC

Methane fermentation is a technology that has already been put to practical use, but there are still some issues to be overcome. In this context, microbial fuel cells (MFCs) are expected to be a new wastewater treatment technology. The MFC is a type of fuel cell technology, which recovers the chemical energy of organic matter as electrical energy using special microorganisms that can transport electrons generated during the decomposition of organic matter directly to the electrodes. The major difference between conventional wastewater treatment (including methane fermentation) and MFCs is that the oxidation-reduction reaction associated with the removal of organic matter is divided into an organic matter oxidation reaction at the anode and an oxygen reduction reaction at the cathode so that electrical energy can be extracted.

As with methane fermentation, the advantages of MFCs include the fact that the amount of excess sludge generated is less than in the activated sludge process, so the energy required for excess sludge treatment is less, and the aeration energy is also unnecessary in the single-chamber MFC described previously. Furthermore, it has several advantages over methane fermentation, such as a higher treatment rate compared to anaerobic treatment like methane fermentation, which is sometimes similar to aerobic treatment 3), and higher theoretical energy efficiency (see below).

8.3.1 MFC Structure and Principle of Power Generation

There are various types of MFC structures, which can be broadly categorized into single-chamber MFCs, dual-chamber MFCs, and sediment MFCs. Typically, single-chamber and dual-chamber MFCs are used for wastewater treatment.

First, let's start with the dual-chamber MFC (Fig. 8.3), whose structure is easy to understand. In the dual-chamber MFC, the water chamber is divided by a membrane (such as a proton exchange membrane) into an anaerobic anode chamber and an aerobic cathode chamber. The anode is installed in the anode chamber, and the cathode is installed in the cathode chamber, which are then connected by an external circuit. Wastewater containing organic pollutants flows into the anode chamber and

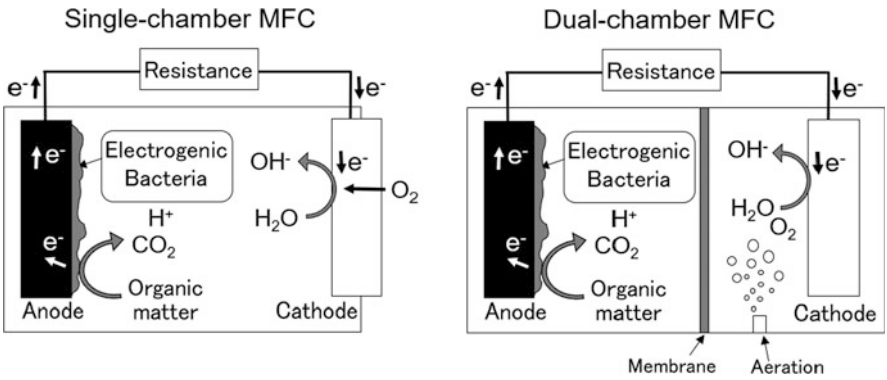

Fig. 8.3 Single-chamber MFC and dual-chamber MEC

is treated. Here organic matter is decomposed into CO_2, H^+, and electrons by microorganisms. This half-reaction equation can be simplified as follows

$$C_xH_yO_z + (2x - z)H_2O \Leftrightarrow xCO_2 + (4x + y - 2z)H^+ + (4x + y - 2z)e^-$$

For this reaction to proceed, the microorganism must release the electrons produced by the decomposition of organic matter to the outside of the body, so it passes the electrons to the electrode (anode). These electrons flow through the external circuit and reach the other electrode (cathode). At this point, the load on the circuit causes the electrons to work, which refers to energy extraction.

The electrons reaching the cathode are used in the reduction reaction of the oxidant. To accelerate this reaction, a catalyst such as platinum is often used at the cathode. Oxygen, nitric acid, potassium ferricyanide, etc. can be used as the oxidant supplied to the cathode chamber. For example, when oxygen is used as the oxidant, the half-reaction equation is as follows: oxygen, water, and electrons react to produce hydroxide (OH^-) ions.

$$O_2 + 2H_2O + 4e^- \rightarrow 4OH^-$$

When considering practical applications, the use of oxygen, which is abundant in the environment and does not require energy for production, is considered to be promising. When oxygen is supplied, aeration is performed in the cathode chamber. However, since the solubility of oxygen in water is low, the efficiency of oxygen supply to the cathode is poor, and additional energy for aeration is required.

The single-chamber (Fig. 8.3) MFC was developed to overcome the disadvantages of the dual-chamber MFCs, in which there is no partition in the chamber and only an anode chamber. The anode is installed inside the chamber the same as in the dual-chamber MFC, but the cathode is an air cathode, a waterproof and gas-permeable electrode, and is installed as part of the outer wall of the chamber. In the single-chamber MFC, only oxygen is used as the oxidant in the cathode and is

supplied from the outside atmosphere through the air cathode. This eliminates the need for aeration. In addition, the oxygen supply is more efficient than in the dual-chamber MFC, resulting in a higher level of power generation than in the dual-chamber MFC. The wastewater flows into the anode chamber and is treated, and the principle of power generation is the same as in the dual-chamber MFC. The membrane can be installed on the surface of the water side of the air cathode but is unnecessary.

8.3.2 Microorganisms in MFCs

Microorganisms that pass electrons obtained from the decomposition of organic matter in wastewater to the anode are generally called electrogenic microorganisms. Dissimilated metal-reducing bacteria of the genus *Shewanella* and *Geobacter* are popular, but many other microbial species have been reported. These microorganisms are ubiquitous on earth and can be sampled from mainly anaerobic environments such as sediments of seabed, rivers and lakes, various wastewaters, paddy field soils, and wetlands. When a MFC is operated using these as an inoculum, the MFC will generate electricity in a few days to a few weeks due to the selective pressure in the chamber that favors the electrogenic microorganisms. When operated with actual wastewater, the microbial community is usually a mixed culture. At this time, there are some microorganisms in the culture that compete with the electrogenic microorganism in organic matter uptake. However, not all microorganisms that do not directly contribute to power generation are nuisances, and some may play an important role. That is, they decompose complex organic matter that is difficult for electrogenic microorganisms to utilize and make it available to them. Therefore, in actual wastewater containing various kinds of organic materials, a mixed culture with other microorganisms is considered to be more efficient than a pure culture of only electrogenic microorganisms.

8.3.3 Comparison Between Methane Fermentation and MFCs

The characteristics of MFCs compared with methane fermentation are as follows:

1. Methane fermentation requires heating to 35 °C–55 °C to improve treatment performance, but MFCs can be operated at room temperature since electrogenic microorganisms are not as negatively impacted by low temperature than methanogenic archaea, so heating is unnecessary.
2. Methane fermentation requires a certain degree of scale to ensure economic efficiency due to the needs for heating and sealing, but MFCs have less impact on economic efficiency due to such scaling down.

3. In methane fermentation, a generator is required to generate electricity using the recovered methane. MFCs, on the other hand, can generate electricity directly from wastewater and do not require a generator.
4. Since MFCs are not heat engines, they are not limited by the Carnot cycle and have high theoretical energy efficiency. On the other hand, methane fermentation is subject to this limitation when generating electricity from methane gas.
5. Methane is a flammable gas, and therefore there is a risk of gas explosion. On the other hand, in an ideally operated MFC, no flammable gas is generated, so there is no danger of gas explosion.
6. In methane fermentation, biogas contains toxic gases such as hydrogen sulfide, but hydrogen sulfide is not generated in an ideally operated MFC.
7. Methane fermentation is an anaerobic process, and the wastewater treatment rate is several to several dozen times slower than that of aerobic treatment. On the other hand, the energy available to electrogenic microorganisms in MFCs is determined between anaerobic and aerobic reactions. Therefore, the removal rate of organic matter and the growth rate of electrogenic microorganisms are theoretically located between anaerobic and aerobic treatment. Sometimes, depending on the type of wastewater, the rate is close to that of aerobic treatment.

8.3.4 Performance of MFCs

The power generation of MFCs is usually expressed in terms of electrical power per electrode area (W/m^2) or per reactor volume (W/m^3). Removal of organic matter as a wastewater treatment technology is often expressed in terms of COD removal ratio. Although it varies depending on the structure of the equipment and the type of wastewater, the highest power generation and organic matter removal of MFCs reaches about 2870 W/m^3 (Fan et al. 2012) and 98% (Lu et al. 2009). The coulombic efficiency, the ratio of the removed organic matter used for power generation, is over 90% in an ideal case. A MFC with a power generation of 2870 W/m^3 has an impractical structure in which the thickness of the anode chamber is extremely thin (about 3 mm) to increase the power per volume, but many MFCs with less extreme structures have been reported to be capable of generating power of about 100 W/m^3 (Chen et al. 2012; Wen et al. 2011; Velasquez-Orta et al. 2009). However, most of these studies have been conducted on a laboratory scale using small devices of tens of mL to a few liters at most.

8.3.5 Challenges for Practical Application of MFCs

As mentioned above, most research on MFCs has been conducted at the laboratory scale. In actual wastewater treatment, the treatment volume is several m^3/day, even in small-scale plants, and more than 100,000 m^3/day in large-scale plants. Therefore,

it is necessary to scale up MFCs, but various physical limitations, such as the water pressure on the air cathode, which is not a problem with small MFC reactors, become apparent at larger sizes. Therefore, it is not possible to simply increase the size of the structure of a lab-scale MFC. In addition, the cost and effort of operating a larger MFC are much greater than those of a smaller MFC, so it is not possible to conduct experiments casually, but in recent years, there have been increasing reports on the operation of pilot-scale MFCs of 100 L or more (Feng et al. 2014; Ge and He 2016; Vilajeliu-Pons et al. 2017; Liang et al. 2018; Rozendal et al. 2008). However, these large MFCs tend to have significantly lower power generation than small MFCs. This is probably because the performance of small MFCs is pursued without regard to profitability, while the performance of large MFCs is sacrificed to reduce costs, and this tendency is more obvious for larger MFCs.

In addition, it is essential to reduce the cost of the equipment for practical use. At present, the equipment cost of MFCs is estimated to be significantly higher than that of conventional aerobic or anaerobic treatment (Sleutels et al. 2012). AlSayed et al. estimate that the cost of equipment for large MFCs is 30–90 times the cost of the activated sludge method (2020). Therefore, significant cost reduction of electrode materials, catalysts, and membranes is necessary in the future. Positively, the number of MFC researchers has been increasing in recent years (Kumar et al. 2018) and their research is becoming more active, so we can expect further technological development in the future.

8.4 Microbial Electrolysis Cell: MEC

By modifying the MFC system, it is possible to recover flammable gas (hydrogen or methane gas) from wastewater instead of electricity. This technology is called a microbial electrolysis cell (MEC). It differs from MFCs in that it cuts off the supply of oxygen to the cathode and also applies a voltage between the anode and cathode (Fig. 8.4). This allows the MEC to generate hydrogen or methane gas at the cathode.

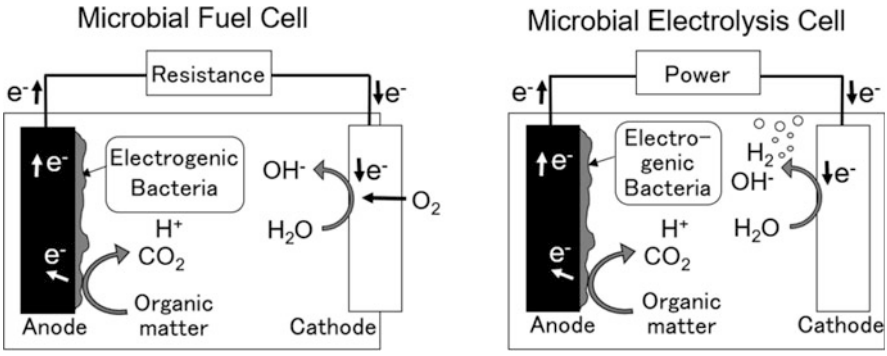

Fig. 8.4 Comparison of MFC and MEC

Although energy must be supplied to apply the voltage, the energy contained in the resulting gas is greater than the amount of energy required to apply the voltage, which means that energy can be recovered overall.

8.4.1 Principle of MECs

The anode reaction of a MEC is the same as that of a MFC, where electrogenic microorganisms oxidize organic matter and transfer electrons to the electrodes. On the other hand, at the cathode, the oxygen supply is cut off, so the oxygen reduction reaction does not take place as in the MFC. In the case of hydrogen generation, for example, a water reduction reaction ($2H_2O + 2e^- \Leftrightarrow H_2 + 2OH^-$) occurs when the electrode potential is lowered by applying a voltage. Theoretically, the amount of voltage that must be applied can be considered as follows. For example, when acetic acid is used as a substrate, the anodic reaction and potential are as follows

$$CH_3COO^- + 4H_2O \Leftrightarrow 2HCO_3^- + 9H^+ + 8e^-$$

($E = -0.296$ V vs. SHE, but 298 K, pH = 7, $CH_3COO^- = 5$ mM, $HCO_3^- = 5$ mM) (Logan 2008)

The water reduction reaction and potential at the cathode are as follows

$$2H_2O + 2e^- \Leftrightarrow H_2 + 2OH^-$$

($E = -0.414$ V vs. SHE, but 298 K, pH = 7)

Therefore, to operate the MEC, it is necessary to apply a voltage higher than 0.118 V, since $(-0.414\ V) - (-0.296\ V) = -0.118$ V. However, in practice, a voltage of about 0.3–1.1 V is often applied due to various energy losses (Liu et al. 2010; Wrana et al. 2010). In the case of obtaining hydrogen by electrolysis of water, the theoretical voltage is more than 1.23 V, while the actual electrolysis voltage is about 1.8–2.0 V (Logan 2008). Therefore, the MEC can be used to produce hydrogen at a much lower voltage than water electrolysis.

8.4.2 Structure of MECs

The MEC consists of a water chamber, an anode, a cathode, an external power supply, and an external circuit connecting them (Fig. 8.4). The basic principle of the MEC is the same as that of the MFC: the electrogenic microorganisms pass electrons to the anode, and the electrons flow through the circuit and are used in the reduction reaction at the cathode. Therefore, the requirements for the structure of the MEC and the materials for the device are almost the same as those for the MFC. Moreover, the

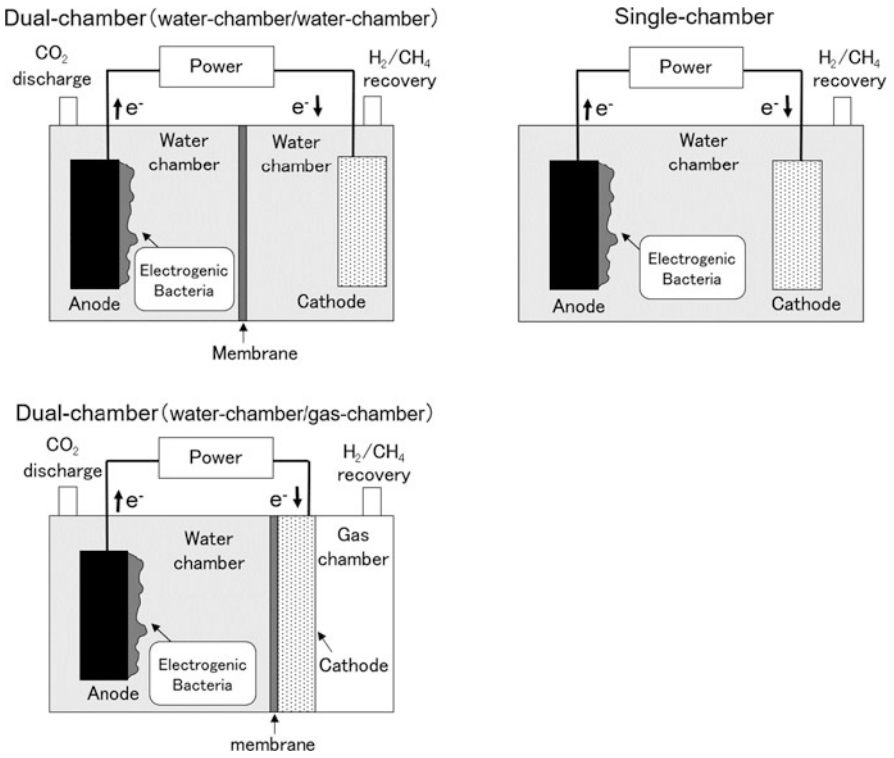

Fig. 8.5 Structure of MECs

community structure of electrogenic microorganisms in the anode is unlikely to be different between MFCs and MECs (Liu et al. 2010).

In considering the unique structure of the MEC, it is important to focus on the improved efficiency of the target gas generation at the cathode and the recovery of the generated gas. The presence or absence of a membrane and the location of the gas collection port play a major role in this, and the structure of the MEC can be classified into three types: single-chamber type, dual-chamber type (water chamber/water chamber), and dual-chamber type (water chamber/gas chamber) (Fig. 8.5).

8.4.2.1 Dual-Chamber MEC (Water Chamber/Water Chamber)

The dual-chamber MEC (water chamber/water chamber) is the earliest and easiest to understand MEC. It consists of dual-chambers separated by a membrane: an anode chamber where wastewater containing organic matter flows in and electrogenic microorganisms work, and a cathode chamber where gases are produced. The gas is collected from the headspace above the cathode chamber. The membrane prevents

microorganisms and organic matter from flowing into the cathode chamber from the anode chamber and increases the purity of the produced gas.

8.4.2.2 Single-Chamber MEC

The single-chamber MEC contains both an anode and cathode in a single-chamber with the membrane removed. When the distance between the anode and cathode is short, a separator, such as an insulating membrane, may be placed between the cathode and anode to avoid short-circuiting the electrodes. The major advantage of the single-chamber system is that there is no internal resistance due to the membrane, which increases the cell current and gas production rate compared to the dual-chamber system (water chamber/water chamber). Liu et al. (2010) reported that the gas production rate of a single-chamber type hydrogen-producing MEC was in the range of about 0.5–3.1 m^3/day/m^3 (hydrogen gas production rate per treated volume of wastewater), while that of a dual-chamber MEC (water chamber/water chamber) was about 0.015–1.1 m^3/day/m^3. Another advantage is the absence of various problems associated with membranes, such as membrane fouling, membrane degradation, and membrane cost. On the other hand, the gas produced at the cathode is consumed by other bacteria flowing in from the anode side, and the purity of the recovered gas is reduced due to contamination with CO_2 gas produced in the anodic reaction.

8.4.2.3 Dual-Chamber Type (Water Chamber/Gas Chamber)

The dual-chamber type (water chamber/gas chamber) has a structure similar to that of the single-chamber MEC, with an air cathode, which is an air-permeable electrode, embedded in part of the chamber wall of the anode chamber (water chamber). In the case of MFCs, one side of the air cathode is exposed to the atmosphere, but in the case of MECs, a sealed gas chamber is installed to maintain the anaerobic environment at the cathode. The gas produced by the cathode is then collected in the gas chamber. Since the gas is released directly into the gas phase, there is no mass transfer resistance when the gas moves from the liquid phase to the headspace, and the gas can be recovered efficiently. However, since an air cathode is used, the water pressure on the cathode becomes a problem. The membrane can be installed in contact with the inside surface of the chamber of the air cathode. However, it should be noted that the installation of the membrane has both advantages and disadvantages.

8.4.3 Comparison of MFCs and MECs

While MFCs and MECs have many similarities, they also have some differences, which result in different advantages and considerations in design and maintenance.

First, energy from wastewater is recovered in the form of H2 gas or methane gas in MECs but is electrical energy in MFCs. In the case of MFCs, it is necessary to store the energy in a battery for transportation and storage, but there is a loss due to natural discharge over time. On the other hand, in MECs, the gas is stored in a sealed container, so there is no loss due to spontaneous discharge, which is advantageous for long-term storage. However, the storage of flammable gas is challenging, requiring high-pressure chambers or inducing risk related to gas leakage or explosion. In addition, the MEC requires a more hermetically-sealed system than the MFC, because it is very important to collect the generated gas efficiently.

Next, MFCs require oxygen to be supplied to the cathode, while MECs do not. Therefore, in MFCs, the oxygen supplied to the cathode is used by aerobic microorganisms to take organic matter, which may compete with the anodic electrogenic microorganisms, but in MECs, this is not the case, so the coulombic efficiency tends to be higher than in MFCs. In addition, the MEC can maintain a strictly anaerobic state more easily than the MFC, which is advantageous for the acclimation of ubiquitous anaerobic bacteria (for example, bacteria of the genus *Geobacter*, which are well known as electrogenic microorganisms, are ubiquitous anaerobes).

In addition, the problem of water pressure on the air cathode is a major issue in a single-chamber MFC. Although this is not a problem for small MFC systems used in the laboratory, the deeper the water, the greater the water pressure on the cathode, which is a major issue related to scale up. On the other hand, microbial electrolysis cells do not have such a problem because the cathode is immersed in water, except for the dual-chamber type (water chamber/gas chamber).

References

AlSayed A, Soliman M, Eldyasti A (2020) Microbial fuel cells for municipal wastewater treatment: from technology fundamentals to full-scale development. Renew Sust Energ Rev 134:110367

Chen Y, Lv Z, Xu J, Peng D, Liu Y, Chen J, Sun X, Feng C, Wei C (2012) Stainless steel mesh coated with MnO_2/carbon nanotube and polymethylphenyl siloxane as low-cost and high-performance microbial fuel cell cathode materials. J Power Sources 201:136–141

Fan Y, Han SK, Liu H (2012) Improved performance of CEA microbial fuel cells with increased reactor size. Energy Environ Sci 5(8):8273–8280

Feng Y, He W, Liu J, Wang X, Qu Y, Ren N (2014) A horizontal plug flow and stackable pilot microbial fuel cell for municipal wastewater treatment. Bioresour Technol 156:132–138

Ge Z, He Z (2016) Long-term performance of a 200 liter modularized microbial fuel cell system treating municipal wastewater: treatment, energy, and cost. Environmental Science: Water Research & Technology 2(2):274–281

JSWA (Japan Sewage Works Association) (2010) Heisei-20-nendo-ban Gesuidou Toukei (in Japanese). JSWA

Kumar R, Singh L, Zularisam AW, Hai FI (2018) Microbial fuel cell is emerging as a versatile technology: a review on its possible applications, challenges and strategies to improve the performances. Int J Energy Res 42(2):369–394

Liang P, Duan R, Jiang Y, Zhang X, Qiu Y, Huang X (2018) One-year operation of 1000-L modularized microbial fuel cell for municipal wastewater treatment. Water Res 141:1–8

Liu H, Hu H, Chignell J, Fan Y (2010) Microbial electrolysis: novel technology for hydrogen production from biomass. Biofuels 1(1):129–142

Lu N, Zhou SG, Zhuang L, Zhang JT, Ni JR (2009) Electricity generation from starch processing wastewater using microbial fuel cell technology. Biochem Eng J 43(3):246–251

Logan BE (2008) Microbial Fuel Cells. John Wiley & Sons

McCarty PL (1981) One hundred years of anaerobic digestion, anaerobic digestion. Elsevier Biomedical Press 7

Rozendal RA, Hamelers HV, Rabaey K, Keller J, Buisman CJ (2008) Towards practical implementation of bioelectrochemical wastewater treatment. Trends Biotechnol 26(8):450–459

Shizas I (2004) Experimental determination of energy content of unknown organics in municipal wastewater streams. J Energy Eng 130(2):45–53

Sleutels TH, Ter Heijne A, Buisman CJ, Hamelers HV (2012) Bioelectrochemical systems: an outlook for practical applications. ChemSusChem 5(6):1012–1019

Velasquez-Orta SB, Curtis TP, Logan BE (2009) Energy from algae using microbial fuel cells. Biotechnol Bioeng 103(6):1068–1076

Vilajeliu-Pons A, Puig S, Salcedo-Dávila I, Balaguer MD, Colprim J (2017) Long-term assessment of six-stacked scaled-up MFCs treating swine manure with different electrode materials. Environmental Science: Water Research & Technology 3(5):947–959

Wen Q, Kong F, Zheng H, Cao D, Ren Y, Yin J (2011) Electricity generation from synthetic penicillin wastewater in an air-cathode single chamber microbial fuel cell. Chem Eng J 168(2): 572–576

Wrana N, Sparling R, Cicek N, Levin DB (2010) Hydrogen gas production in a microbial electrolysis cell by electrohydrogenesis. J Clean Prod 18:S105–S111

Chapter 9
Management of On-Site Household Wastewater Treatment Systems (*Johkasou*) in Japan

Yasushi Ishiguro and Fusheng Li

Abstract *Johkasou* is an on-site wastewater treatment system that was developed and is widely used in Japan. In this chapter, the actual usage of *Johkasou* in Japan, as well as their design, maintenance, and management are introduced. In addition, the knowledge gained from our research on their management and the operating conditions required to improve the quality of treated water is discussed.

Keywords *Johkasou* · On-site wastewater treatment · Household wastewater · Management

9.1 Introduction

When wastewater is discharged into the aquatic environment, it is mixed with water, and the pollutants are purified over time by the self-cleaning processes. However, if the amount of pollutants exceeds the self-cleaning ability of the rivers and other water bodies, the pollutants will flow into the water, and water pollution will progress. The main domestic wastewater treatment systems in Japan are sewage systems, rural sewage systems, community plants, and *Johkasou*. Among these, the centralized wastewater treatment system collects water from many remote buildings through pipes and treats all the water at a remote site. These include different types of sewage systems and rural sewage systems. On the other hand, when the wastewater is treated on the same premises as the building, it is called "onsite treatment system", and *Johkasou* is a typical example. These include small-scale *Johkasou* installed in individual homes and medium- and large-scale *Johkasou* that treat wastewater from housing complexes and public facilities such as schools, city halls, stores, and hospitals.

Johkasou is an on-site wastewater treatment system developed in Japan. *Johkasou* was mainly built to process wastewater generated in households that are

Y. Ishiguro (✉) · F. Li
River Basin Research Centre, Gifu University, Gifu, Japan
e-mail: ishiguro@green.gifu-u.ac.jp; lifs@gifu-u.ac.jp

F. Li et al. (eds.), *River Basin Environment: Evaluation, Management and Conservation*, https://doi.org/10.1007/978-981-19-4070-5_9

not yet connected to public sewage systems. *Johkasou,* together with the sewage system, which collects and treats wastewater from larger areas, plays an important role in maintaining a clean and comfortable living environment and preserving the natural environment. In addition, treated water from *Johkasou* is discharged into natural water bodies such as rivers and lakes in a dispersed manner through ditches and waterways, thus greatly affecting the surrounding river basin and contributing to the pollution in rivers and lakes.

Since *Johkasou* are installed in individual houses, the amount of wastewater inflow and the concentration of the pollutants varies greatly throughout the day. However, the performance of *Johkasou* in treating the wastewater is generally good. *Joukasou* performance varies depending on their type, the conditions of their usage, and their state of maintenance and inspection, which affects the treated water quality.

In this chapter, the design, maintenance, and management of *Johkasou*, their actual conditions of use in Japan are introduced. In addition, the knowledge gained from our research on the management and operating conditions of *Johkasou* to improve the quality of treated water is discussed.

9.2 Actual Usage of *Johkasou* in Japan

9.2.1 Current Status of Wastewater Treatment and Usage of Johkasou *in Japan*

There are two main types of wastewater treatment facilities in Japan: "centralized treatment systems" and "on-site treatment systems." These two systems are used appropriately in different situations, sharing roles and responsibilities, and taking advantage of the local conditions and their respective features.

"Centralized treatment systems" transport wastewater from households and businesses in large areas through a pipeline to a wastewater treatment plant. "Centralized treatment systems" include "sewage systems" (under the jurisdiction of the Ministry of Land, Infrastructure, Transport and Tourism, Japan), which primarily eliminate and treat wastewater in urban areas, "rural sewage systems" (under the jurisdiction of the Ministry of Agriculture, Forestry and Fisheries, Japan), which treat wastewater in agricultural promotion areas, and "community plants" (under the jurisdiction of the Ministry of the Environment, Japan), which independently treat wastewater in residential complexes unconnected to public sewage systems.

On the other hand, the main type of "on-site treatment system" is the "*Johkasou*" (under the jurisdiction of the Ministry of the Environment). In areas where centralized treatment is inefficient or has yet to arrive, *Johkasou* can be installed by individuals. There are two types of *Johkasou*: *tandoku-syori Johkasou*, which treats only wastewater from toilets, and *gappei-syori Joukasou*, which treats wastewater from toilets and miscellaneous wastewater, called "gray water" such as that from kitchens, laundry rooms, and bathrooms. In *tandoku-syori Johkasou*, only

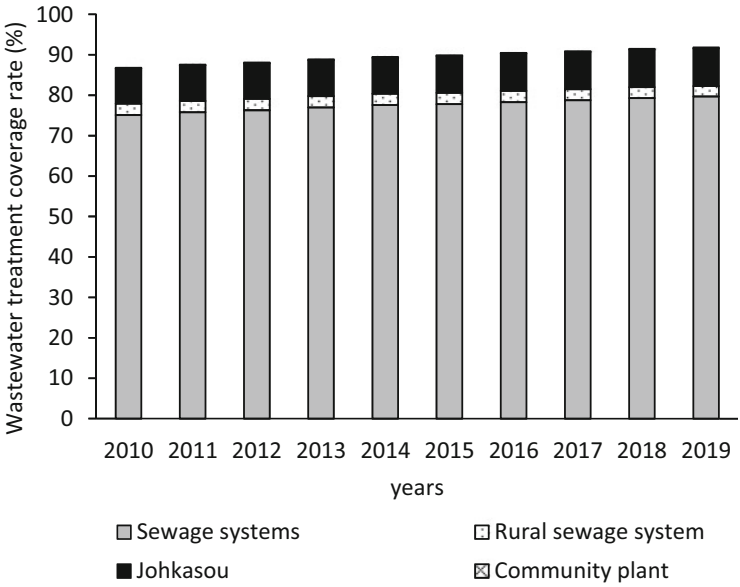

Fig. 9.1 Wastewater treatment coverage rate in Japan (data from the Ministry of the Environment, Japan)

wastewater from the toilet is treated, and the other miscellaneous wastewater is discharged directly into the environment. Thus, installing new *tandoku-syori Johkasou* has been prohibited since 2001, and now only *gappei-syori Johkasou* are permitted to be installed.

Figure 9.1 shows the wastewater treatment coverage rate in Japan for the 10-year period from 2009 to 2019. In Japan, the wastewater treatment coverage rate is high; it reached 86.9% in 2010 and gradually increased to 91.7% in 2019. Out of these wastewater treatment systems, sewage systems are the most widespread, and their coverage rate increased from 75.1% in 2010 to 80.1% in 2019. In the case of rural sewage systems, the rate remains between 2.6 and 2.8%. For community plants, the rate has always been 0.2%, and there has been no significant change over the past 10 years. The rate of *Johkasou* usage was at 8.7% in 2010, and has gradually increased since then, reaching 9.3% in 2019. This indicates that *Johkasou* play an important role in household wastewater treatment in Japan.

The trend in the number of septic tanks installed in Japan from 2009 to 2019 is shown in Fig. 9.2. In 2010, the number of *tandoku-syori Johkasou* was larger than that of *gappei-syori Johkasou*, but in 2019, the number of *gappei-syopri Johkasou* installed exceeded that of *tandoku-syori Johkasou*. Installing new *tandoku-syori Johkasou* has been prohibited since 2001, indicating that the shift to *gappei-syori Johkasou* is progressing. However, there are still many *tandoku-syori Johkasou* in operation, and it is hoped that they will be transitioned to *gappei-syori Johkasou* as soon as possible.

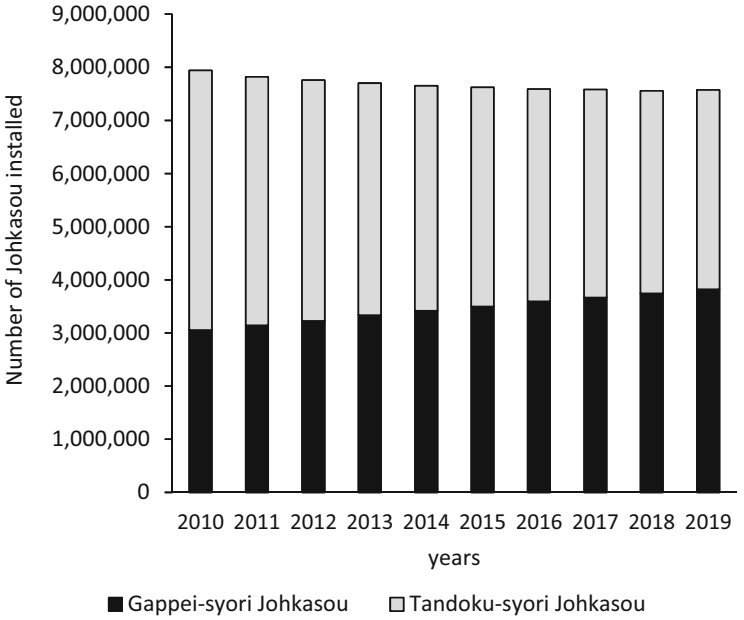

Fig. 9.2 The number of *Johkasou* installed in Japan (data from the Ministry of the Environment, Japan)

9.3 Design and Management of *Johkasou*

9.3.1 Johkasou *Designs*

Johkasou are facilities that treat wastewater discharged mainly from toilets and gray water. They purify the wastewater to a certain level before the water is discharged. In this section, we explain small-scale *gappei-syori Johkasou*, which are mainly installed in houses.

The structure of *gappei-syori Johkasou* consist of features such as (1) an "anaerobic tank" where suspended solids in the wastewater settle and then anaerobic microorganisms decompose part of the organic matter, (2) an "aerobic tank" where air is blown in by a blower and aerobic microorganisms attached to the contact media decompose most of the organic matter, and (3) a "segmentation tank" where the sludge and supernatant contained in the treated water are separated.

The main body of the *gappei-syori Johkasou* structure is composed of fiberglass reinforced with plastic (FRP) and other materials and is manufactured in one piece at a factory. These types of *Johkasou* can be installed in the basement of each individual house parking lot and other spaces, and the treated water is then discharged into a channel or river. Their performance is equivalent to that of a sewage system, with an biochemical oxygen demand (BOD) removal rate of 90% or higher, and has a treated water quality of BOD 20 mg/L or lower (an advanced

treatment type that can remove nitrogen and phosphorus is also available). As these types of facilities are important for conserving the aquatic environment, subsidies are available from the government, prefectures, and municipalities for their installation.

9.3.1.1 Wastewater Treatment by *Johkasou*

The amount of domestic wastewater discharged from households is approximately 200 L per person per day, and it has a BOD load of approximately 40 g as pollutants. Of this, approximately 13 g of pollutants is discharged from toilets, and about 27 g of pollutants in gray water.

During the period of high economic growth in 1980, *tandoku-syori Johkasou* were widely used to treat wastewater from toilets. However, in this case, gray water discharged untreated, and the performance of the septic tanks themselves was not as good as that of today, so many pollutants were discharged into the environment. *Tandoku-syori Johkasou* were replaced by the development and widespread use of *gappei-syori Johkasou*, a technology unique to Japan that simultaneously treats wastewater from toilets as well as gray water. The "biological membrane method, "which has a high capacity to cope with temporal changes in wastewater load (quantity and quality), was applied to septic tanks, and the technology was established in the 1950s. Since then, improvements have been made, and technical progress has been made at a level comparable to other treatment facilities, such as sewage systems.

9.3.1.2 Characteristics of *Gappei-Syori Johkasou*

Gappei-syori Johkasou, which are facilities that treat household wastewater, have the following features and are compared to a sewage system.

1. *Gappei-syori Johkasou* are installed where domestic wastewater is generated, and they treat and discharge wastewater on-site, so they do not require a network of pipelines to collect wastewater such as sewage systems.
2. In sewage systems, the discharge of treated water is concentrated at the discharge outlet of the wastewater treatment plant, resulting in large local changes in the river water volume. On the other hand, *gappei-syori Johkasou* do not cause large changes in water volume in local rivers and channels because only small volumes of domestic wastewater are treated on-site and then discharged.
3. Properly treated water can be used as emergency water during disasters. In addition, because industrial wastewater is not mixed in, the sludge contains less heavy metals and is easy to reuse.
4. When sewage systems are installed in cities with small populations, the cost per capita increases. On the other hand, *gappei-syori Johkasou* are mostly unaffected by this problem and can be efficiently maintained even in municipalities with small populations.

5. They are installed underground, are about the size of a car, and are not easily affected by the installation's location, topography, or geology.
6. *Gappeisyori Johkasou* are individually distributed facilities, and it is possible to make appropriate responses to changes such as a decrease in population.

9.3.1.3 Types of *Gappei-Syori Johkasou*

There are various types of *gappei-syori Johkasou* that differ in their performance and treatment methods. For example, in addition to the standard BOD of 20 mg/L or less, there are those that can reduce BOD to 10 mg/L or less, or 5 mg/L or less, and there are also those that can remove nitrogen and phosphorus.

In addition, the "anaerobic filter bed and aerobic contact process" is the most widespread treatment method. However, there are also other methods, such as the "carrier fluidization and biological filtration system, "in which a "carrier fluidization section" and a "biological filtration section" are installed in place of the contact material in the "aerobic tank" to increase the treatment efficiency and reduce the overall capacity.

Small scale *gappei-syori Johkasou* are divided into units called "ninsou" in Japanese, which are based on the number of people in the home to be treated, and their size is determined according to the size of the house, such as "5 ninsou," "7 ninsou" or "10 ninsou." In areas that are not connected to a sewage system, large-scale *Johkasou* are sometimes used to treat wastewater from commercial and public facilities, some of which are large enough to serve more than 10,000 people. In this case, it is the same type of facility as a sewage system, but it is legally considered a *Johkasou*.

9.3.1.4 Structure of the *Gappei-Syori Johkasou*

The *gappei-syori Johkasou* treatment mainly involves biological treatment using microorganisms, which is similar in principle to the treatment of wastewater in other wastewater treatment systems. A typical example of the treatment process in a septic tank is shown in Fig. 9.3.

1. Anaerobic tank

   In an anaerobic tank, suspended solids in the wastewater are usually precipitated and separated. Some of the pollutants in the wastewater are decomposed by anaerobic microorganisms (microorganisms that do not like oxygen). Depending on the model of the septic tank, the microorganisms are attached to filter media of various shapes to enhance the treatment.

2. Aerobic tank

   An aerobic tank is where aerobic organisms primarily carry out wastewater treatment. A blower sends fine bubbles of air to the bottom of the tank, and the

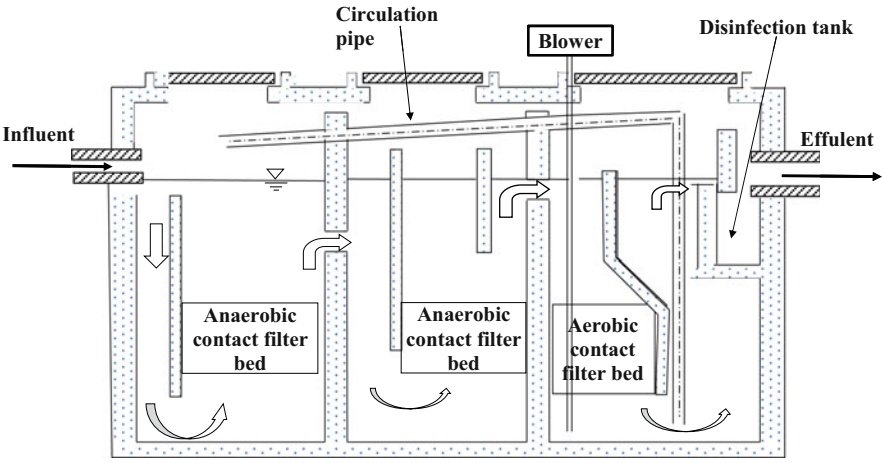

Fig. 9.3 Schematic diagram of a *gappei-syori Johkasou* and treatment flow

biofilm of aerobic microorganisms attached to the surface of the contact filter medium decomposes the pollutants in the wastewater.

The activated sludge process, in which microorganisms are suspended, is the mainstream method in sewage systems, while the biological membrane process is the mainstream method used in *Johkasou*. Unlike the activated sludge process, the biological membrane process retains the sludge microorganisms in the reaction tank, resulting in less sludge return and the generation of less excess sludge by promoting self-oxidation.

3. Sedimentation tank

   In the sedimentation tank, sludge consisting of waste material such as proliferated microorganisms is sedimented and separated.

4. Disinfection tank

   The treated water is discharged after chlorination in the disinfection tank. In the disinfection tank, a plastic cylinder is filled with a tablet-type chlorine agent in the flow path, and the treated water meets the chlorine agent at the bottom of the cylinder and is disinfected.

In recent years, the structures used in *gappei-syori Johkasou* have been diversifying, and in addition to the conventional specifications set by the government (notified type), there are also compact types with smaller capacities (approximately 70%) and advanced treatment types with advanced nitrogen, phosphorus, and BOD removal in consideration of eutrophication in areas with strict water quality regulations (closed water bodies). Most newly installed *gappei-syori Johkasou* are equipped with a function to promote denitrification by transferring the treated water from the sedimentation tank to the anaerobic tank using an airlift pump.

9.3.2 *Management of* Johkasou

Johkasou are facilities that use microorganisms to treat wastewater. Therefore, it is important to maintain an environment in which the microorganisms can actively work. If they are not managed properly, the function of the *Johkasou* will gradually deteriorate, degrading the aquatic environment and the surrounding habitat For this reason, administrators of *Johkasou* (users and installers) are required by *Johkasou* law to conduct periodic maintenance, desludging, and legal inspections.

9.3.2.1 Legal Inspections

Legal inspections are conducted to check whether the *Johkasou* have been installed correctly and are functioning properly. There are two types of inspections: water quality inspections after installation (legal inspection by Article 7) and periodic inspections (legal inspection by Article 11). According to the provisions in *Johkasou* law, only inspection bodies designated by the prefectural government (designated inspection bodies) are allowed to conduct legal inspections.

- Legal inspection by Article 7(Inspection after installation)
  This is an inspection stipulated by the provisions of Article 7 in *Johkasou* law. This type of inspection is conducted to ensure that the septic tank was properly installed and is functioning properly. It should be conducted during the first 3 to 8 months of use and aims to correct any problematic issues as soon as possible.
- Legal inspection by Article 11 (Periodic inspection)
  This is an inspection stipulated by the provisions of Article 11 in *Johkasou* law. Once a year, it must be confirmed that regular maintenance and cleaning is being carried out properly and that the septic tank is functioning normally.

9.3.2.2 Operation/Maintenance

Operation/maintenance maintains the normal functioning of the septic tank by checking whether each device and piece of machinery in the *Johkasou* is working normally, the operation process of the *Johkasou* as a whole, the treated water, the accumulation of sludge, and whether the pipes and filter media are clogged. *Johkasou* are facilities that treat wastewater using microorganisms; therefore, it is necessary to maintain an environment in which the microorganisms can thrive. In particular, the blower, which supplies oxygen to the microorganisms, needs to be checked because it operates continuously. In addition, consumables, such as disinfectants, need to be replenished and replaced periodically. Another important role of the operation/maintenance checks is to determine when to desludge and contact a *Johkasou* desludging vendor, if necessary. The frequency of operation/maintenance varies depending on the processing method and usage conditions, but it should be performed at least three times per year. Operation/maintenance must be carried out in

accordance with the technical standards based on the Septic Tank Law. Maintenance and inspections must be entrusted to a contractor registered with the prefectural government.

9.3.2.3 Desludging

Desludging is the process of removing the sludge and scum that accumulates in *Johkasou*, and cleaning and washing the attached equipment and machinery. In most cases, desludging is performed annually. Neglecting desludging can cause deterioration of the *Johkasou*, sludge leakage, and a bad odor.

9.4 Actual Usage of *Johkasou* and Original Efforts in Gifu Prefecture

Gifu Prefecture is located almost in the center of Japan, and the Hida region in the northern part of Gifu Prefecture has several mountains over 3000 m above sea level. In contrast, in the southern part of the prefecture, the Mino region, three major rivers—the Kiso River, the Nagara River, and the Ibi River flow through the Nono Plain. This section introduces a case study of wastewater treatment, the usage of *Johkasou* in Gifu Prefecture, and the original efforts made through cooperation among *Johkasou's* three different maintenance and management industry groups.

9.4.1 Current Status of Wastewater Treatment and Usage of Johkasou *in Gifu Prefecture*

Figure 9.4 shows the wastewater treatment coverage rate in Gifu Prefecture over a 10-year period from 2009 to 2019. In Gifu Prefecture, the wastewater treatment coverage rate was 87.7% in 2010, and it gradually increased to 92.9% in 2019. This rate is slightly higher than that of Japan as a whole. For example, using 2019 as an example, the sewage systems coverage rate of Japan was 79.7%, while that of Gifu Prefecture was lower at 76.8%. As a result, rural sewage systems and *Johkasou* accounted for 5.6% and 10.7% of the total, respectively, which is slightly higher than that of Japan as a whole. This is probably due to topographical factors and the population distribution in Gifu Prefecture. This suggests that the role of *Johkasou* is comparatively more important in Gifu Prefecture.

The trend in the number of septic tanks installed in Gifu Prefecture for the 10-year period from 2009 to 2019 is shown in Fig. 9.5. From 2010 to 2019, the number *of gappei-syori Johkasou* increased and the number of *tandoku-syori Johkasou* decreased, indicating that the shift away from *tandoku-syori Johkasou* to

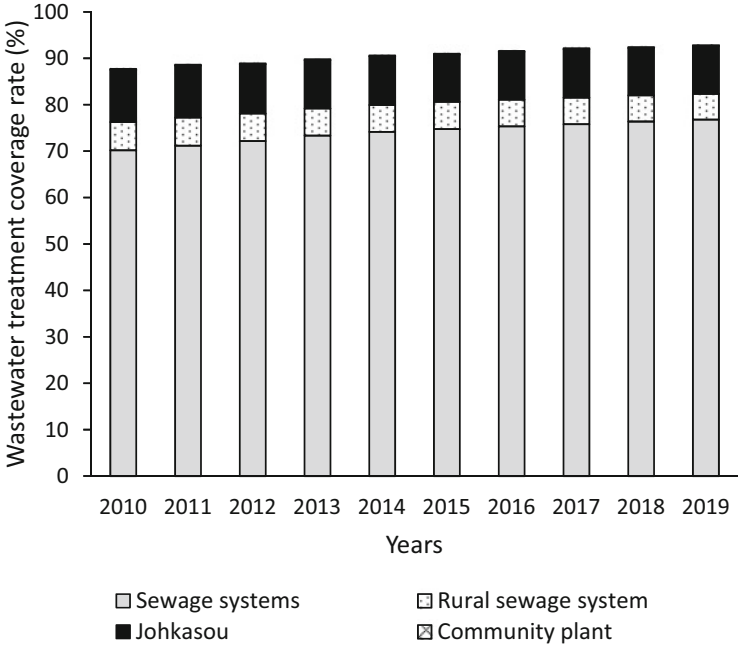

Fig. 9.4 The wastewater treatment coverage rate in Gifu Prefecture (data from the Ministry of the Environment, Japan)

gappei-syori Johkasou has progressed. However, in Gifu Prefecture, the number of *tandoku-syori Johkasou* installed in 2019 still exceeded the number of *gappei-syori Johkasou* installed by 16,000, indicating that the shift to *gappei-syori Johkasou* was delayed compared to the rest of Japan. In Gifu Prefecture, it is anticipated that there will be a faster shift to *gappei-syori Johkasou* in the future.

9.4.2 Original Efforts in Gifu Prefecture

9.4.2.1 "Water Reclamation Facilities" Recognition System for *Johkasou*

The "Water Reclamation Facilities Recognition System for *Johkasou*" was launched in April 2007 to certify excellent *gappei-syori Johkasou* are undergoing advanced maintenance and management (Akabane et al. 2014, Watanabe 2014). Under this system, a legal inspection agency designated by Gifu Prefecture certifies that *gappei-syori Johkasou* conforms to a stricter standard (treated wastewater transparency of 30°) than the Ministry of the Environment's guideline (treated wastewater transparency of 20°) and is a facility equivalent to a sewage system. *Gappei-syori Johkasou*,

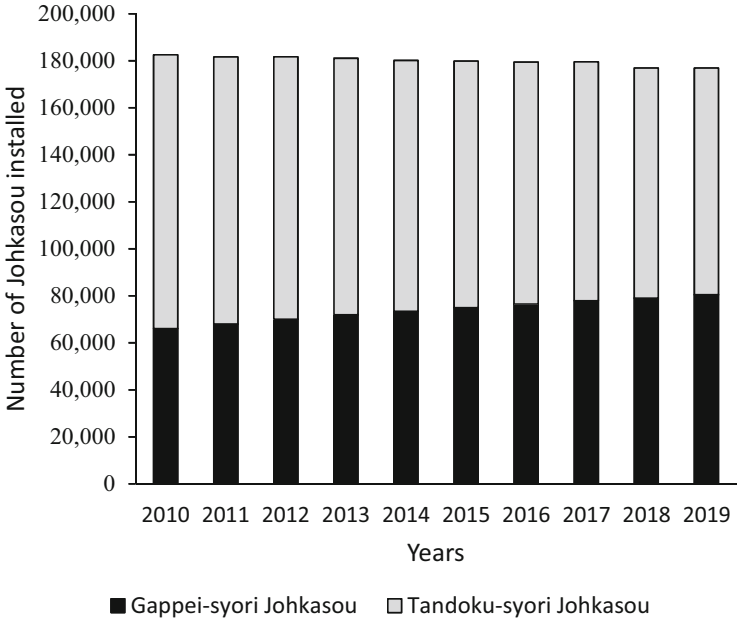

Fig. 9.5 The number of *Johkasou* installed in Gifu prefecture (data from the Ministry of the Environment, Japan)

which complied with the recognition standards for the past three consecutive years, are recognized as "Water Reclamation Facilities."

The following four criteria must be met to be recognized.

1. Compliance with the judgment criteria for the past three consecutive years in legal inspections, including inspections by Articles 7 and 11, conducted by the Gifu Environmental Management Technology Center.
2. Operation/maintenance and desludging were carried out in accordance with the frequency and technical standards specified in *Johkasou* law.
3. The treated water must have a transparency of 30°or higher.
4. An alarm is installed to notify someone when the blower has stopped.

As of November 2021, 61,323 *gappei-syori Johkaso*u have been recognized. When a septic tank is certified under this system, a seal of recognition is affixed to the home by the *gappei-syori Johkasou* installer, and there is no fee to apply for this designation.

9.4.2.2 Cooperation among *Johkasou*'s Three Different Maintenance and Management Industry Groups

The maintenance and management industry groups of *Johkasou* in Gifu Prefecture have set the standard for treated water quality at a transparency of 30° or higher. A transparency of 30° is approximately equal to 13 mg/L or less in BOD, which is equivalent to or higher than the BOD discharge standard of sewage systems. In addition, the guidelines for the maintenance and management of *gappei-syori Johkasou* state that the desirable range of water transparency is 30 cm or more because the probability of the BOD being over 20 mg/L is extremely high if the transparency of the effluent is 30 cm or more. A certain degree of transparency in the treated water has been ensured in the maintenance of *Johkasou* without coordination among the three operation/maintenance, desludging, and legal inspection organizations. However, in order to achieve a higher transparency of the treated water, *Johkasou's* three different maintenance and management industry groups in Gifu Prefecture have established an effective and efficient *Johkasou* maintenance and management system by using tablet computers to "send-off" and share information (Murai et al. 2014, Watanabe 2014). As a result of this effort, the ratio of *Johkasou's* with a treated water transparency 30° or higher increased from 76.0% in 2007 to 92.2% in 2017.

9.5 Effect of *Johkasou's* Operational Conditions on the Quality of the Treated Water

As mentioned in the previous section, the goal for the treated water as designated by the association involved in the on-site maintenance of *gappei-shori Johkasou* is above 30° of transparency in Gifu Prefecture. However, approximately 8% of the *gappei-shori Johkasou* did not meet this maintenance goal.

This section introduces a part of the research on the operating conditions that the contractor can set during the maintenance and cleaning of *gappei-syori Johkasou* to improve the quality of the treated water (Ishiguro et al. 2016, 2017, 2017b, 2018). In this section, unless otherwise noted, "*Johkasou*" is used to refer to "*gappei-syori Jophkasou*."

9.5.1 Effect of Water Circulation on the Quality of the Treated Water

Three small-scale *gappei-syori Johkasou* models with nitrogen removal functions that were operating in ordinary households in Gifu Prefecture were selected for this study. *Johkasou* use a contact filter bed system and have the following treatment

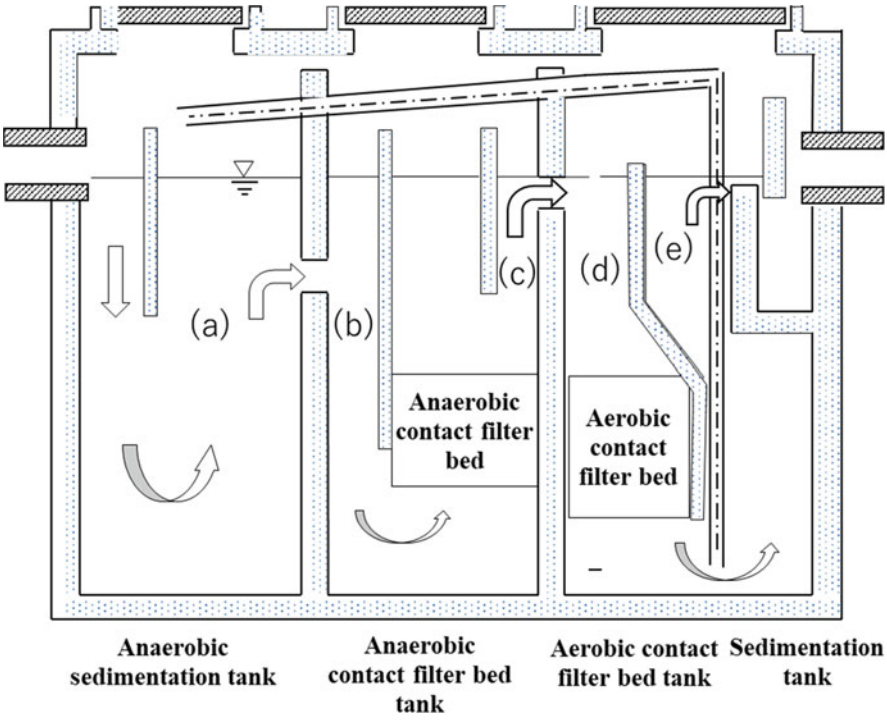

Fig. 9.6 Flowchart of the studied *Johkasou* and sampling points for water collection. (**a**) water in the anaerobic sedimentation tank, (**b**) inlet water of the anaerobic contact filter bed tank, (**c**) outlet water of the anaerobic contact filter bed tank, (**d**) water in the aerobic contact filter bed tank, and (**e**) water in the sedimentation tank

performance: BOD = 20 mg/L or less, total nitrogen = 20 mg/L or less, and suspended solids (SS) = 20 mg/L or less. Wastewater is treated in four tanks: an anaerobic sedimentation tank, an anaerobic contact filter bed tank, an aerobic contact filter bed tank, and a sedimentation tank; the treated water is then chlorinated in a disinfection tank before being discharged. (Fig. 9.6). The anaerobic contact filter bed tank is equipped with a filter filled with skeletal-like spherical anaerobic filter media. The aerobic contact filter bed tank remains aerobic, and constant aeration is performed using a blower. In the aerobic contact filter bed tank, plate-like filter materials are installed at the top, and net-like cylindrical filter materials are installed at the bottom. The circulating water was returned from the bottom of the sedimentation tank to the anaerobic sedimentation tank using a circulating airlift pump.

This case study was conducted from April 23 to August 27, 2015. During the study period, the circulating water volume of the treated water circulation was varied to investigate the effect of water circulation on the treated water quality, and the relationship between the two was analyzed using multivariate analysis. Surveys were

conducted once a week, and water samples were collected from five locations (a)–(e), as shown in Fig. 9.6.

Dissolved Oxygen (DO), pH, and redox potential (ORP) were measured at the sampling sites, and the circulating water volume, the scum thickness in each tank, and the sludge thickness in each tank were also measured. The circulating water volume was measured at the outlet of the circulation pipe in the anaerobic sedimentation tank.

Turbidity, suspended solids (SS), volatile suspended solids (VSS), biochemical oxygen demand (BOD), carbonaceous biochemical oxygen demand (C-BOD), dissolved organic carbon (DOC), total nitrogen, ammonia nitrogen, nitrite-nitrogen, nitrate-nitrogen, and total phosphorus were measured in the laboratory.

Figure 9.7 shows the changes in BOD, total nitrogen, and total phosphorus in one of the three *Johkasou* surveyed as an example. BOD without circulation (WCR: 0; WCR means the water circulation ratio) was high in the water of the anaerobic sedimentation tank and the inlet water of the anaerobic contact filter bed tank, and low in the outlet water of the anaerobic contact filter bed tank, the water in the aerobic contact filter bed tank, and in the water in the sedimentation tank (Fig. 9.7a). The BOD in the water in the anaerobic sedimentation tank and in the inlet water of the anaerobic contact filter bed tank decreased with a water circulation ratio of 3 (WCR: 3), in which the water in the sedimentation tank was returned to the anaerobic sedimentation tank at three times the daily average inflow water volume rate, and at a circulation ratio of 2 (WCR: 2), in which the water in the sedimentation tank was returned at two times the daily average inflow water volume rate. However, there was no significant difference in the BOD of the water in the sedimentation tank.

Total nitrogen was high in the water in the anaerobic sedimentation tank without circulation (WCR 0), but it decreased in WCR 3 and WCR 2. In addition, the total nitrogen in the water in the sedimentation tank showed a tendency to decrease in WCR3 and WCR2 compared to the WCR 0. The pattern of total phosphorus was similar in all tanks with and without water circulation, and no increase or decrease was observed with water circulation (Fig. 9.7c).

A decrease in total nitrogen due to the change in water circulation in the three tanks suggests that nitrate-nitrogen produced by nitrification in the contact filter bed tank is returned to the impurity removal tank by circulating water (Fujimura and Nakajima 1998), resulting in denitrification and consequently a decrease in total nitrogen in the water in the treatment tank.

Due to the circug water, a clear change in BOD was observed in the primary treatment (the anaerobic sedimentation tank and anaerobic contact filter bed tank). In contrast, the BOD of water in the aerobic contact filter bed tank and the water in the sedimentation tank did not increase, even though water with a high pollution load was pushed out to the secondary treatment (the aerobic contact filter bed tank and the sedimentation tank) by circulating water. This suggests that the organic matter removal performance was maintained in the secondary treatment, which could remove the organic matter that flowed in from the primary treatment.

Figure 9.8 shows the results of the cluster analysis and Fig. 9.9 shows the results of the principal component analysis of water in the sedimentation tank of a

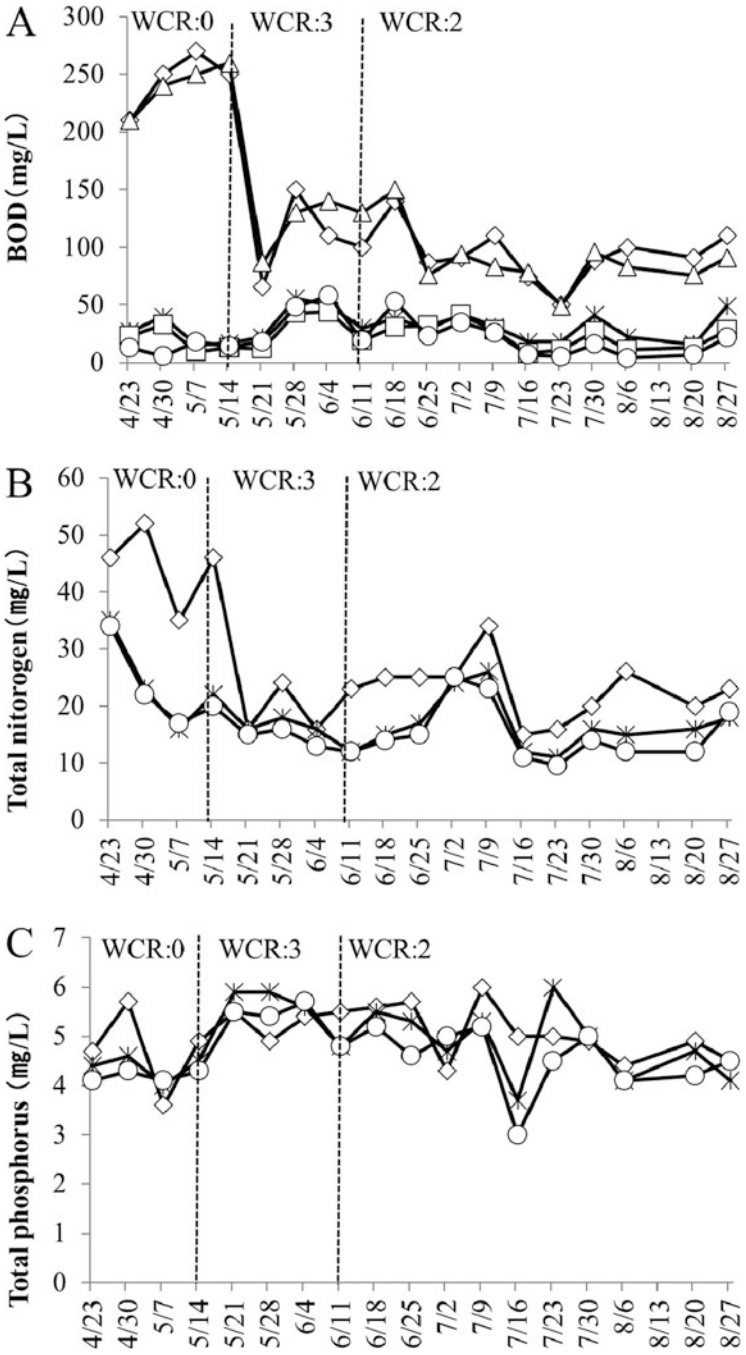

Fig. 9.7 Changes in biological oxygen demand (BOD), total nitrogen, and total phosphorus due to circulation changes in the treated water. (◇) Water in the anaerobic sedimentation tank, (△) inlet water of the anaerobic contact filter bed tank, (*) outlet water of the anaerobic contact filter bed tank, (□) water in the aerobic contact filter bed tank, and (○) water in the sedimentation tank. WCR

Johkasou, as examples of the multivariate analyses. In the cluster analysis (Fig. 9.8), the data were classified into three clusters by a coupling distance of 2.0 or less.

When the results of principal component analysis and cluster analysis were combined, SS, VSS, and organic nitrogen were included in the index that constituted cluster I and had the highest degree of correlation with the first principal component axis, along with BOD, C-BOD, and turbidity.

These results indicate that suspended organic matter is strongly related to BOD, C-BOD, and turbidity. Total nitrogen, ammonia nitrogen, pH, and nitrate nitrogen, which constitute clusters II and III and have a high degree of correlation with the second principal component axis, are a group of indices related to denitrification and nitrification.

The loadings expressed by BOD, C-BOD, SS, VSS, and organic nitrogen were similarly distributed in the three *Johkasou* and could be grouped together. In addition, total phosphorus was included in the same group. In contrast, DOC was grouped into a different group from BOD and C-BOD in all *Johkasou*. These results indicate that suspended organic matter is strongly related to the organic load (BOD and C-BOD).

However, ammonia nitrogen, nitrate-nitrogen, total nitrogen, pH, and ORP were considered to be related to nitrification and denitrification.

The indexes that made up these two groups were grouped together on the first and second principal component plane without mixing, indicating that the relationship between these groups was low.

These results suggest that, when considering improvements made to the treated water from *Johkasou*, there is little relationship between the nitrogen load and the organic load represented by BOD and C-BOD. Therefore, water circulation is effective for nitrogen removal; however, other measures should be considered for reducing the organic load.

9.5.2 Effect of Aeration Rates on the Treated Water

Eleven *Johkasou*, the same type as those surveyed in Section 4.1, were among those surveyed in houses in Gifu Prefecture, and did not meet the required water transparency of 30°. The effect of the aeration volume on the treated water was investigated by changing the aeration volume setting based on the DO of the water in the aerobic contact filter bed tank and the sedimentation tank in each *Johkasou*. The relationship between aeration volume and treated water quality was analyzed using multivariate analysis.

Fig. 9.7 (continued) means the water circulation ratio, that is, the circulation water volume/influent water (reproduced from Ishiguro et al. 2016)

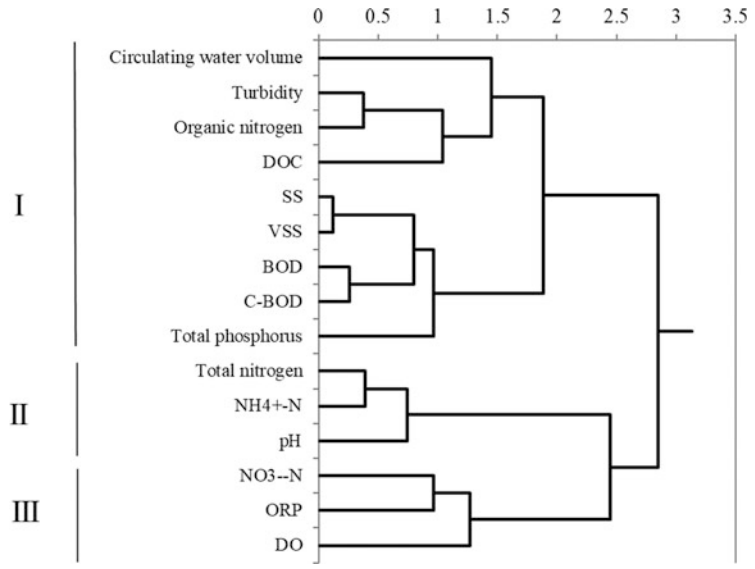

Fig. 9.8 Cluster analysis results for water samples in a sedimentation tank under the influence of circulating water (reproduced from Ishiguro et al. 2016)

A field survey and sample collection were conducted on the first day of the survey, and the aeration volume of the aerobic contact filter bed tank was changed.

Four weeks after the setting change, a field survey and sample collection were conducted. If the transparency of the treated water was improved to 30° or higher, the survey was deemed complete. If the transparency of the treated water did not meet 30°, the aeration volume was changed. In addition to the indices described in Section 4.1, the number of particles, the sludge volume index (SVI) of the sludge in the sedimentation tank, and the amount of biofilm attached to the contact material in the aerobic contact filter bed tank were measured.

As a result of changing the aeration volume of the aerobic contact filter bed tanks, the transparency of the treated water in three *Johkasou* increased to more than 30°, and the BOD decreased with the increasing aeration volume. In six *Johkasou*, decreasing the aeration volume of the aerobic contact filter bed tanks increased the transparency of the treated water to more than 30° and decreased the BOD. The total nitrogen and total phosphorus did not show a constant trend with changing aeration volume. These results suggest the possibility of reducing the organic load by increasing the aeration volume.

The results of the cluster analysis and principal component analysis of the sedimentation tank are shown in Figs. 9.10 and 9.11, respectively.

In the cluster analysis, four clusters were formed when the bond distance was less than 2.0.

The results of the cluster analysis (Fig. 9.10) and principal component analysis (Fig. 9.11) showed that total BOD and C-BOD were linked to turbidity, organic

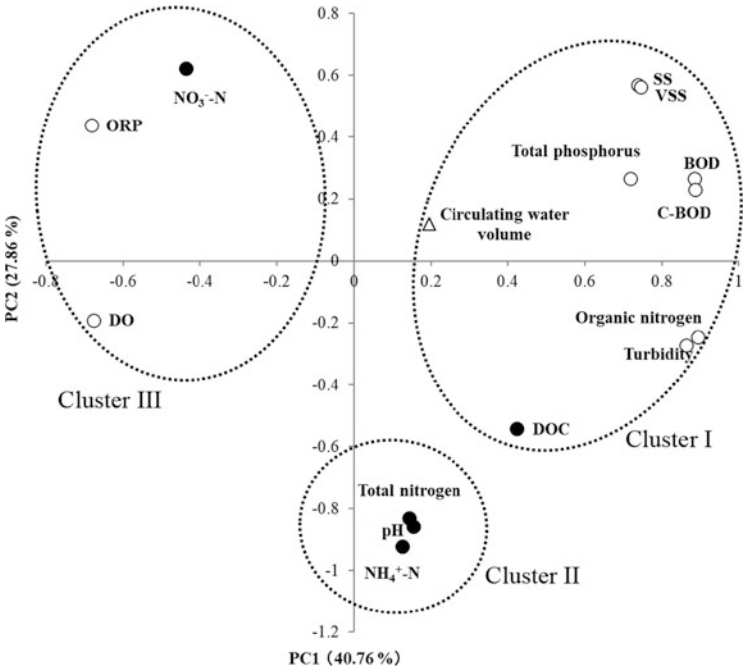

Fig. 9.9 Principal component analysis results for water samples in a sedimentation tank under the influence of circulating water. (○)The first principal component, (●)the second principal component, and (△) the third principal component, with the highest loading values (reproduced from Ishiguro et al. 2016)

nitrogen, SS, VSS, and particles with sizes from 0.5–1 μm. The results of the principal component analysis also showed a close link between aeration volume and these water quality indices.

The results suggest that increasing the aeration volume is one way to improve the quality of the treated water in *Johkasou*. In addition, we suggest that particles with sizes from 0.5–1 μm are related to the quality of the treated water, especially to the organic loading.

9.5.3 Small Particles Are Related to Treated Water Quality

To investigate how small particles are related to the treated water quality in detail, water in the sedimentation tanks of *Johkasou*, whose transparency increased from 10° to 83° by increasing the aeration volume of the aerobic contact filter bed tank from 30 L/min to 63 L/min, was placed onto a filter, freeze-dried, platinum-deposited, and then observed with a scanning electron microscope (Fig. 9.12). A large number of bacteria-like substances were observed in the water that had a

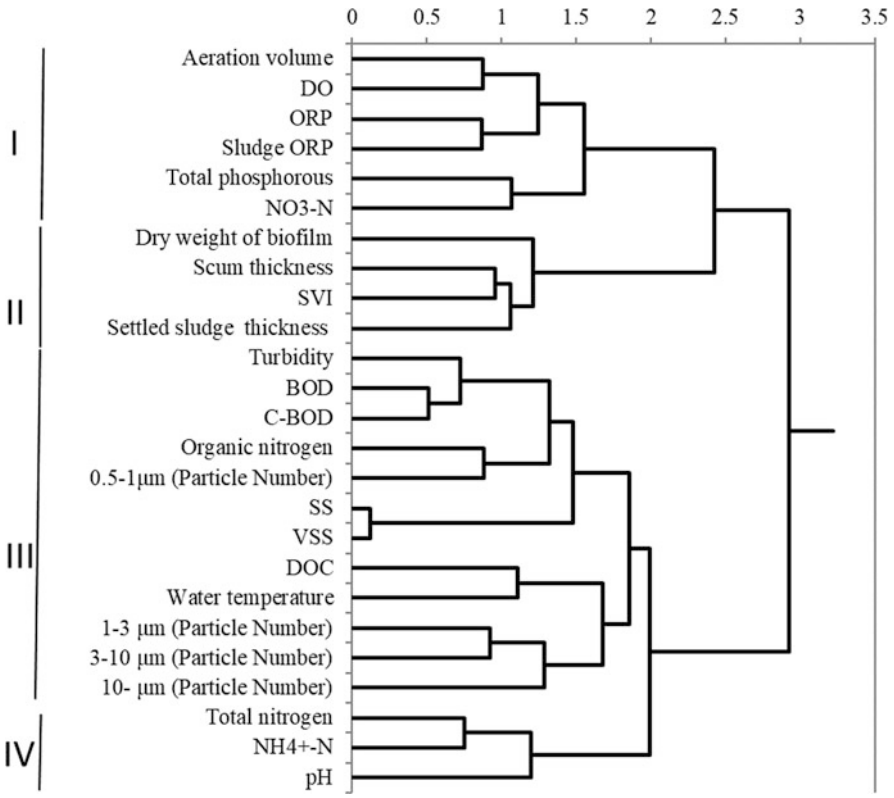

Fig. 9.10 Cluster analysis results for water and sludge samples in the sedimentation tank. (reproduced from Ishiguro et al. 2017b)

transparency of 10° (left side of Fig. 9.12). On the other hand, although bacteria-like substances were also present in the water in the treatment tank that had 83° of transparency, the amount of bacteria-like substances was clearly lower (right side of Fig. 9.12).

The number of bacteria was measured using a flow cytometer (Fig. 9.13). There was a large difference in the number of bacteria in the outlet water of the anaerobic contact filter bed tank, the water in the aerobic contact filter bed tank, and the water in the sedimentation tank. The number of bacteria in the sedimentation tank was lower at an aeration volume of 63 L/min and a transparency of 83° compared to an aeration volume of 30 L/min and a transparency of 10°. Furthermore, there was a significant correlation between the number of bacteria and the reciprocal of the water transparency of the water collected from the sedimentation tank (Fig. 9.14). This suggests that the bacteria in the treated water are related to the quality of the treated water, especially the organic load.

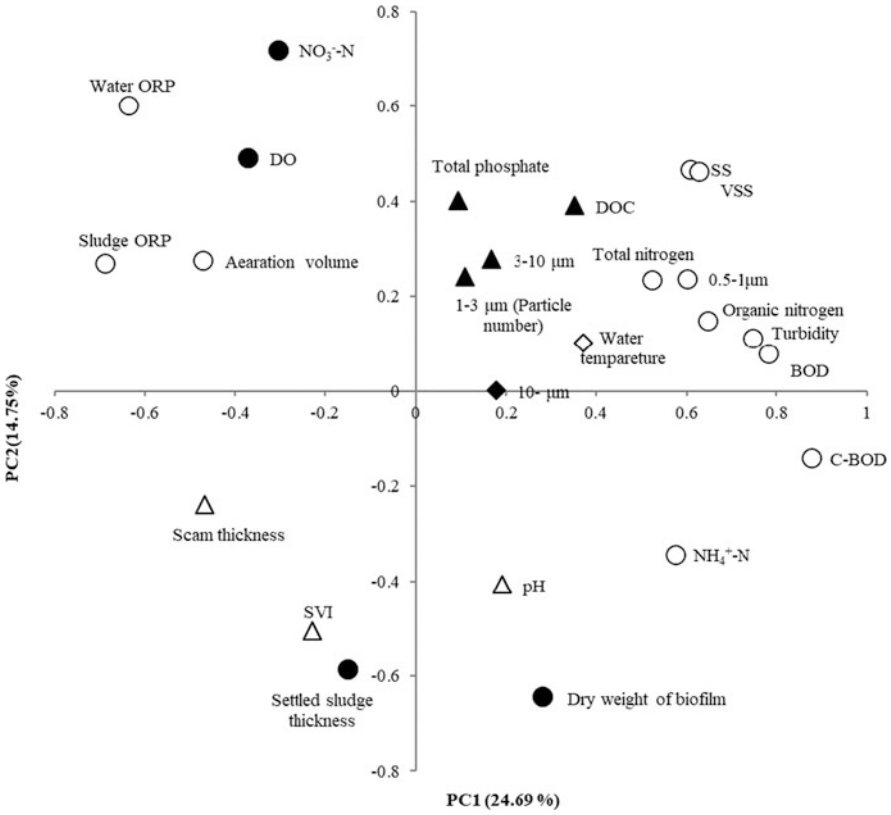

Fig. 9.11 Principal component analysis of the water and sludge samples collected from the sedimentation tank. (○) The first principal component, (●) the second principal component, (△) the third principal component, (▲) the fourth principal component, (◇) the fifth principal component, and (◆) the sixth principal component with the highest loading values (reproduced from Ishiguro et al. 2017b)

9.6 Conclusion

Johkasou are excellent on-site wastewater treatment systems that were developed and are widely used in Japan. They are small wastewater treatment facilities that mainly treat wastewater in households. They are responsible for about 10% of the wastewater treatment in Japan and support a clean and comfortable living environment and preserve the natural environment. However, the treatment performance of *Joukasou* vary depending on their type, conditions of usage, and state of maintenance and inspection, and this affects the quality of the treated water. Treated water from *Johkasou* is discharged into natural water bodies such as rivers and lakes in a dispersed manner through ditches and waterways, thus greatly affecting the environment of the river basin. Therefore, *Johkasou* must be properly maintained and

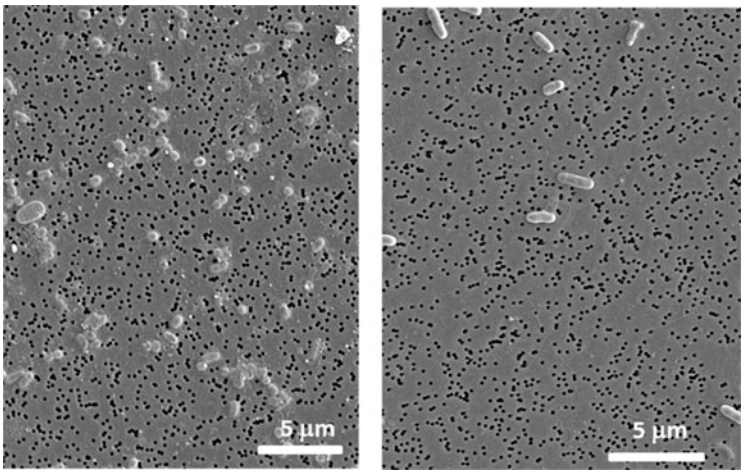

Fig. 9.12 Small particles in the water collected from the sedimentation tank and observed with a scanning electron microscope. Left: aeration volume of 30 L/min and a transparency of 10°. Right: aeration volume of 63 L/min and a transparency of 83° (reproduced from Ishiguro et al. 2017b)

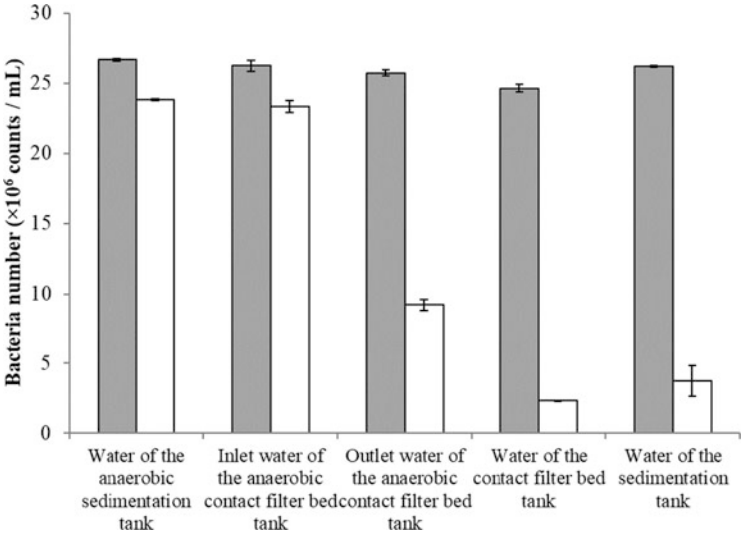

Fig. 9.13 Change in the number of bacteria within change the aeration volume. ▒: Aeration volume of 30 L/min and a transparency of 10°. □: Aeration volume of 63 L/min and a transparency of 83°. The bars indicate the standard deviation (reproduced from Ishiguro et al. 2017b)

managed. In our study, we presented some suggestions that can be used in the maintenance and management of *Johkasou*.

In the future, we anticipate that the installation of *gappei-syori Johkasou* will become more widespread in areas that have not yet been connected to public sewage

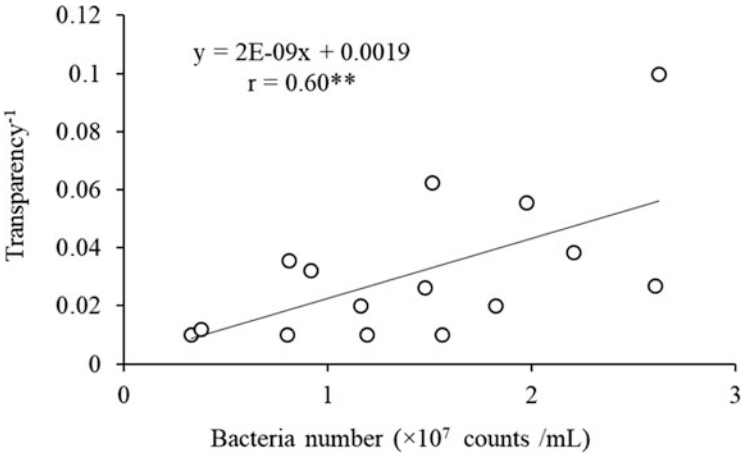

Fig. 9.14 Relationship between the number of bacteria and the reciprocal of the water transparency in the water collected from the sedimentation tank. **P < 0.05 (reproduced from Ishiguro et al. 2017b)

systems and that this will help preserve the environment of the surrounding river basin. In addition, we will continue to study the maintenance and management of *Johkasou*.

Acknowledgments We would like to express our gratitude to the Gifu Environmental Management Technology Center for their extensive cooperation in sampling and conducting the research. We would like to thank Editage (www.editage.com) for English language editing.

References

Akabane C, Yamamoto Y, Yokoi M (2014) Original recognition system of Gifu prefecture: water restoration facility recognition system for Johkasou. J Environ Con Eng 43(9):6–9

Fujimura Y, Nakajima J (1998) Ffluent water quality of small-scale on-site treatment facilities for household waste-water and nitrogen removal performance with recycle operation. J Jpn Soc Water Environ 21(3):157–162

Ishiguro Y, Cui G, Fujisawa T, Yasufuku K, Okumura S, Tamagawa T, Joni AF, Li F (2018) Changes of microparticles and bacteria in *gappei-syori Johkasou* and Rwsidual organic matter in water if the treated water tank. J JSCE, ser G 74:III_415–III_422

Ishiguro Y, Fujisawa T, Trianda Y, Yasufuku K, Okumura S, Tamagawa T, Joni AF, Li F (2017b) Effect of operational conditions of *Johkasou* on the treated water quality. J Environ Con Eng 46(8):13–17

Ishiguro Y, Fujisawa T, Trianda Y, Yasufuku K, Okumura S, Tamagawa T, Li F (2017) Effect of aeration rates on the treated treated water quality of *gappe-syori Johkasou*. J JSCE Ser G 73(7): III_53–III_62

Ishiguro Y, Trianda Y, Fujisawa T, Yasufuku K, Okumura S, Tamagawa T, Joni AF, Li F (2016) Effect of water circulation on the treated water quality of *Johkasou*. J JSCE ser. G72:III_255-III_265

Murai K, Nakino Y, Yonezawa M (2014) Cooperation between *Johkasou's* three different maintenance and management industry groups and on-line systematization. J Environ l Con Eng 43(9):15–20

Watanabe N (2014) Problem and solution measures for domestic wastewater treatment in Gifu prefecture. J Env l Con Eng 43(9):2–5

Chapter 10
Predicting Fine Sediment Deposition Rate in Lowland River Channel: Comparison of Two Adjacent Rivers

Morihiro Harada and Shigeya Nagayama

Abstract In this chapter, the response of lowland rivers after excavation works to secure flood capacity, especially after excavation of the flood channel along the main channel, is described in detail from several perspectives. The excavation works and subsequent monitoring of the Ibi River ($A = 1196$ km^2) and Nagara River ($A = 1914$ km^2), which are located near the central part of Japan and flow adjacent to each other, are described. First, an overview of river rehabilitation in the plains of Japan is presented. Then, the necessity and significance of excavation work and vegetation clearing to secure flood capacity are explained. The response that occurs after excavation is the redeposition of sediment and establishment of plants. These factors can rapidly reduce flood capacity, but can also have natural restoration implications for organisms that prefer floodplain habitats. However, the habitats formed by flood-channel excavations have a finite lifespan. Finally, a practical model for calculating the sediment deposition rate is presented, using the relationship between sediment concentration and flow rate during floods as an input condition. The results of this chapter may help implement adaptive river channel management in lowland rivers.

Keywords Lowland rivers · River management · Flood-channel excavation · Sedimentation rate · Inter-levee flood plain

M. Harada (✉)
River Basin Research Center, Gifu University, Gifu, Japan
e-mail: m_harada@gifu-u.ac.jp

S. Nagayama
Regional Adaptation Research Center, Gifu University, Gifu, Japan
e-mail: nagayama@gifu-u.ac.jp

F. Li et al. (eds.), *River Basin Environment: Evaluation, Management and Conservation*, https://doi.org/10.1007/978-981-19-4070-5_10

10.1 Introduction

10.1.1 Improvement of Lowland Rivers of Japan

In the alluvial plains of Japan, the frequency of river flooding was greatly reduced after the rehabilitation of frequently flooded natural rivers, excavation of new river channels, and construction of continuous levees on both sides of the river channels. Such river improvements were partially undertaken in each region in the early modern period. However, most of the drastic river channel improvement works were intensively carried out by the Meiji government in the late 19th and early 20th centuries.

The rivers covered in this chapter are the Ibi River and the Nagara River, which are in central Japan and flow through the Nobi Plain. Earlier, these rivers were connected by multiple channels and flowed across the lowland floodplain with complex topographic surfaces, but major renovation work from 1887 to 1912 succeeded in separating the interconnected major rivers (Fig. 10.1). Simultaneously, continuous levees were constructed on both sides of the new river channels. Since then, river administrators have continuously worked on river channels to improve the safety of continuous levees. Specifically, they have: (1) created a flood channel between the continuous levee and the main channel by embankment, (2) dug down the main channel, (3) raised the levee and widened its cross section, and (4) installed revetments on the levee to protect it from erosion by flowing water. As a result, many of the large rivers in the alluvial plains of Japan have been transformed into

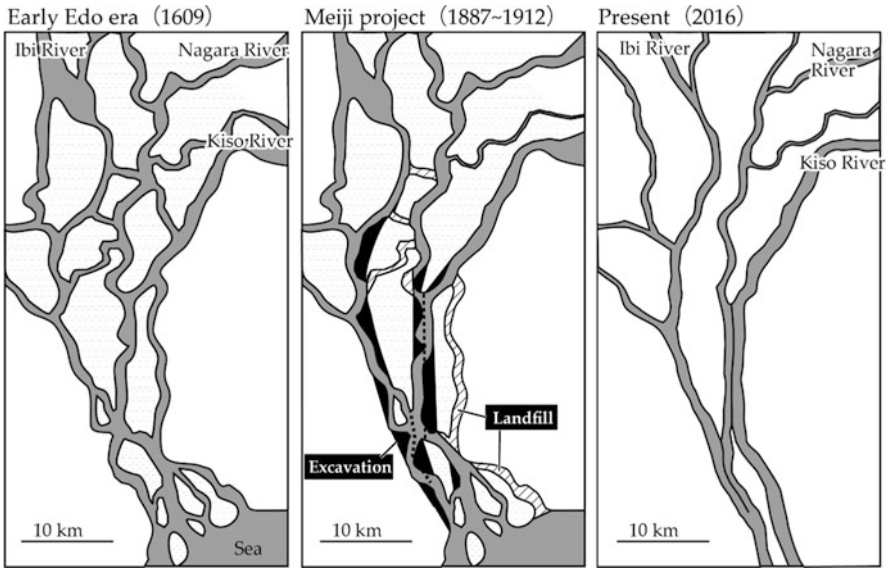

Fig. 10.1 Plan view of the river renovation that separated the interconnected rivers flowing through the Nobi Plain, located in central Japan. (Reproduced from Nagayama et al. 2017b)

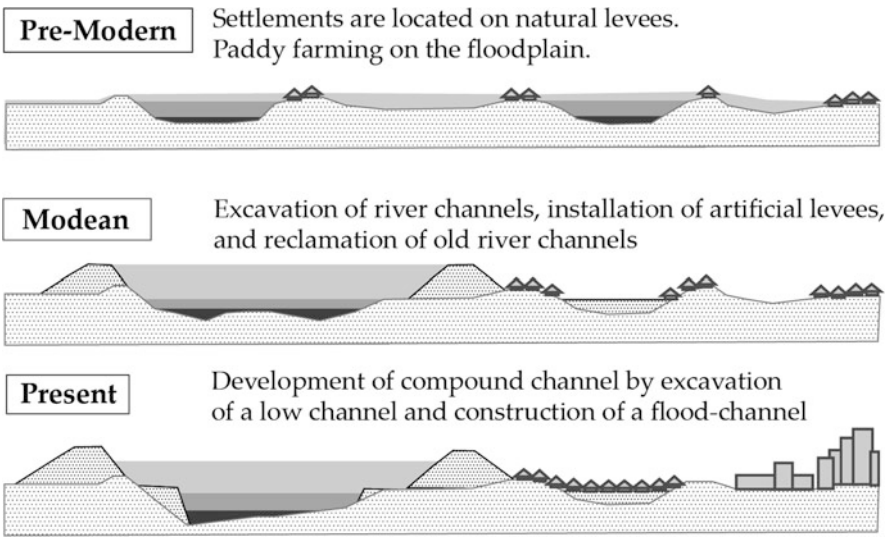

Fig. 10.2 Schematic cross-sectional view of a natural river in an alluvial plain being modified into an artificial compound channel

compound channels consisting of levees, flood channels, and main channels (Fig. 10.2). These improvements have further increased the flood capacity of river channels and the safety of levees.

In recent decades, major rivers in Japan have been experiencing riverbed degradation due to the combined effects of human activities, such as gravel extraction for construction materials and the reduction of sediment supply to river channels caused by the construction of large dams. As a result of riverbed degradation, the specific height between the main channel and the inter-levee floodplain has increased. Furthermore, the inter-levee floodplain environment has changed due to decrease in the frequency and intensity of flood disturbance on the relatively elevated terrain surface, and subsequent tree establishment has progressed (Nakamura et al. 2006). This had led to a direct and indirect effect on the biological communities dependent on the floodplain (Negishi et al. 2012, 2014). Thus, the landscape of large rivers in the Japanese plains has changed significantly.

10.1.2 Clearing Riparian Vegetation and Conducting Excavation to Secure the Flood Capacity

Riparian vegetation has a variety of important ecological functions in river ecosystems (Tabacchi et al. 1998). However, riparian vegetation growing in the river channel acts as an obstacle to water flow during floods and reduces flood capacity. In addition, in-channel vegetation can cause sediment deposition (Cotton et al.

2006). The flow through submerged vegetation is calm (Wu et al. 2005), and fine sediments can be deposited. Periodic vegetation clearance and excavation of accumulated sediment are necessary to maintain the flood capacity of the river channel. Furthermore, record-breaking heavy rainfall disasters have been increasing in many parts of the world due to the effects of global warming. According to the assessment of flood intensity and frequency using the large ensemble climate model product d4PDF to evaluate the impact of climate change, the magnitude and frequency of floods in Japanese rivers are predicted to increase (Harada et al. 2020a, b; Tanaka et al. 2021). Therefore, in many large rivers that flow through the alluvial plains of Japan, forest clearance in the river channel and flood channel excavation are carried out as part of the river channel management work to lower the water level during floods.

10.1.3 Flood-Channel Excavation Works in Ibi River and Nagara River

This chapter focuses on the Ibi River and the Nagara River as a typical example of flood-channel excavation. The following topics are covered: (1) topographical changes after flood channel excavation in the Ibi River, (2) restoration of floodplain environments in the Ibi River, and (3) prediction of sediment deposition rates in the Ibi and Nagara Rivers.

The catchment area of the Ibi River basin is 1196 km^2 at the Mangoku water gauging station near the study section. The catchment area of the Nagara River basin is 1914 km^2 at the Sunomata water gauging station near the study section. The average annual precipitation in the Ibi River and Nagara River basins is about 2500 mm, which is about 1.5 times the national average of about 1700 mm. While there are several large dams for power generation and flood control in the Ibi River basin, there are no large dams on the mainstem of Nagara River.

In the Ibi River, flood channel excavation was carried out from 2001 to 2007 in a section that ranged between approximately 32 KP (Kilometer Post from the river mouth) and 39 KP. In the Nagara River, flood channel excavation was carried out from 2009 to present in a section from approximately 39KP to 44 KP. As shown in Fig. 10.3, both sections are located slightly downstream of the alluvial fan section, which is the transition zone from the alluvial fan to the lowland floodplain. The slope of the riverbed in the study section was approximately 1/3300, but at the upstream end of the section, which was approximately 40 KP, the slope changed to approximately 1/1700, and thus the riverbed material in the main channel changed significantly within the section. Coarse sand and fine gravel were dominant at the upstream reach of the section, whereas fine and medium sand were dominant at the downstream reach.

The flood-channel excavation sites in the Ibi and Nagara rivers are shown in Fig. 10.4. The Ibi River has the 14 excavation sites with a variety of heights (relative

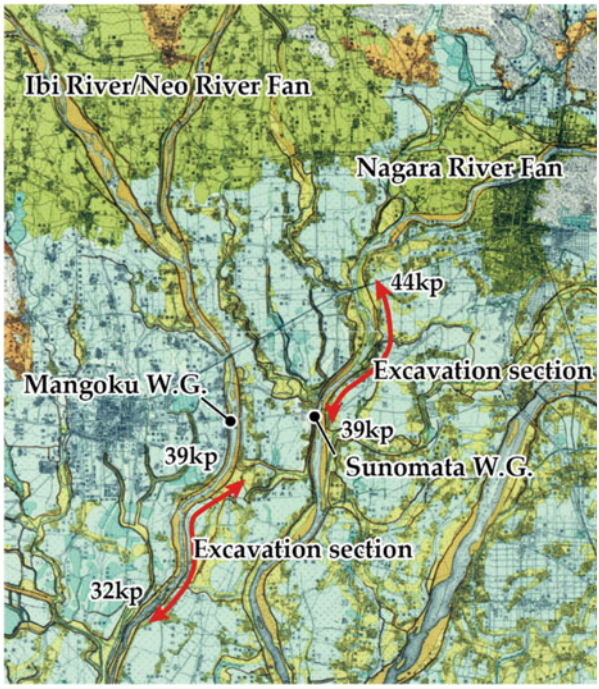

Fig. 10.3 The location of the flood-channel excavation sections in the Ibi and Nagara Rivers. Both excavation sections are located downstream of the alluvial fan section

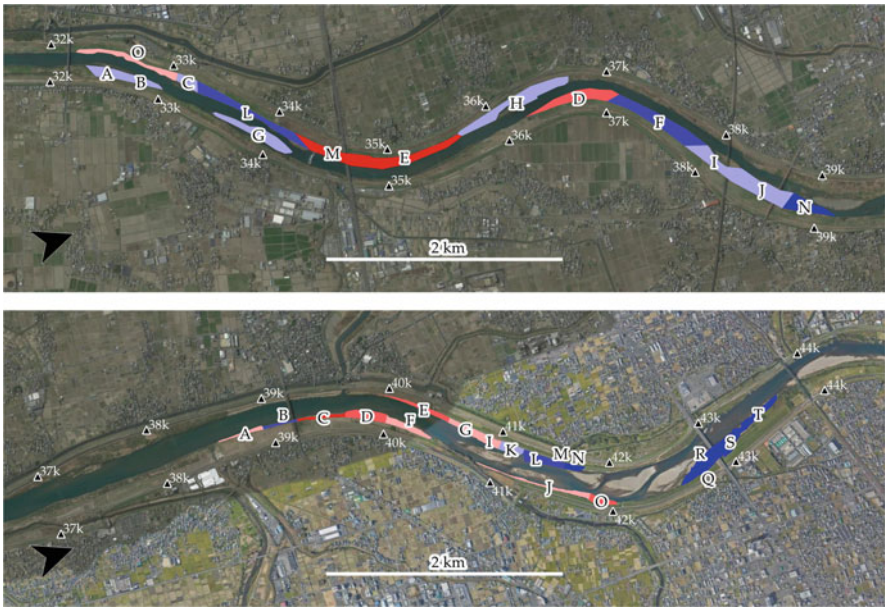

Fig. 10.4 Flood-channel excavation sites in the Ibi River (Upper) and the Nagara River (Lower). The relative height of the excavated area is lowest for dark red and highest for dark blue

to normal water level) along the main channel to study the effect of different excavation heights on the response. A field survey was conducted focusing on the topographical and ecological responses in the floodplain after the excavation work. The Ibi River was targeted because the excavation work here was experimental.

10.2 Formation Process of Microtopography after Flood Channel Excavation

10.2.1 Formation of Topography of Lowland Floodplain

To understand the mechanism of topography formation in artificially channelized rivers, it is important to understand the outline of those processes in natural river channels. In the natural levee zone, which is located downstream of the alluvial fan and has a gentle topographic gradient, a large floodplain consisting of natural levees, flood plains and backswamps is formed. It is well known that pristine rivers inundate once every few years. During inundation, medium sand contained in the floodwater is deposited on both sides of the river channel, forming a natural levee (Hudson 2005; Klasz et al. 2014). Although natural levees are primarily associated with lowland meandering river floodplains, they are formed on any type of river floodplain (Hudson 2005). The fine sand and silt contained in the floodwater are slowly deposited on the inundated floodplain. Even in the artificial compound channel, the sediments are transported by running water, and the topography of the river channel is changed by erosion and sedimentation.

10.2.2 Sediment Deposition after Flood Channel Excavation in Compound Channel

Harada et al. (2015) investigated the stratigraphy of sediments deposited in the excavated sites of the Ibi River. They focused on two sites (sites D and O in Fig. 10.4) that were excavated at a height between the drought and normal water levels, and selected 10 sampling sites considering the plane shape of the main channel and the distance from the main channel. The field survey was conducted in February 2014. At the time of the survey, 12 years had passed since the excavation work in the site D and 8 years in the site O, respectively. To understand the grain size distribution and stratigraphy of the sediment deposited after the excavation work, the sediment was sampled from the different layers with a variety of grain size and sediment color by digging down the deposited sediment at the sampling sites. The sediment samples were examined for grain size distributions by sieving tests and sedimentation particle size analysis. The sampling sites and the landscape changes of

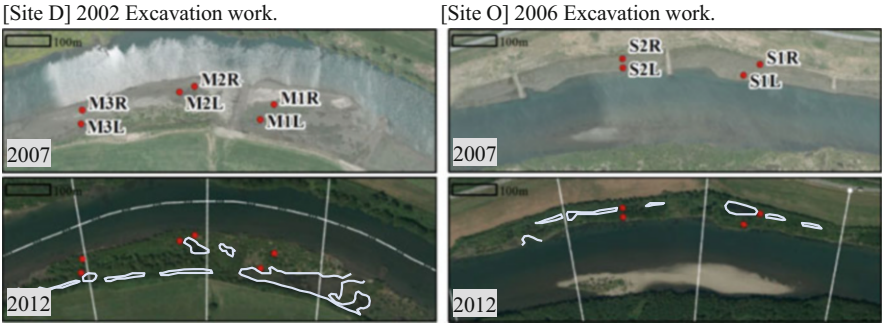

Fig. 10.5 Landscape changes and sampling sites of the two study sites on the Ibi River. The red circle indicates the sampling sites for sediment. The white line indicates the floodplain water bodies formed after excavation

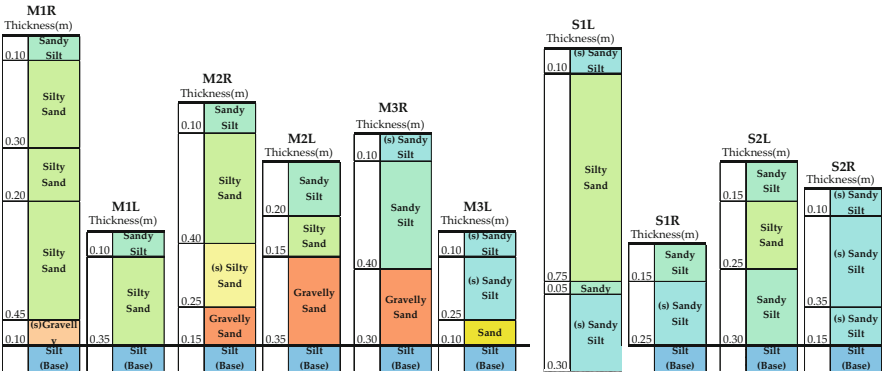

Fig. 10.6 Columnar view of sediment deposition after excavation of the flood channel. The columnar view and thickness of the sediment (m) are shown with respect to the base of the excavation site. The (s) in the sediment grain size classification means "slightlly"

the two study sites are shown in Fig. 10.5. The results of the analysis of the sediment deposits are shown in Fig. 10.6.

Figure 10.6 shows five pairs of columnar plots of sediment deposited after excavation work; one of each pairs shows the site near the low channel and the other shows the site farther away from low channel. According to the river administrator, the elevation of the compacted silt layer was exposed as the base surface after the excavation. In this survey, the elevation of the compacted silt layer was measured by GPS surveying as the base layer of excavation works. The elevation of the base layer was almost unchanged from that recorded in the construction plan. At survey points M1R, M2R, M2L, and M3R in Area D, gravel mixed with sand was deposited just above the surface of base layer. These coarse sediments were considered to be bedloads transported by the floods just after the excavation works. According to the hydrological observations by the river administrator, extreme flood near the design flood of the river channel occurred immediately after the

excavation of area D in the spring of 2002. After the extreme flooding in the spring–summer of 2002, the excavation site was inundated by floods of various magnitudes. Baring a few exceptions, the majority of deposited sediments were middle to fine sand or silt. Comparing each of the five pairs, we find that the sediment deposited near the low channel (M1R, M2R, M3R, S1L, S2L) tends to have coarser grain size and greater sediment thickness than sediment deposited farther from the low channel (M1L, M2L, M3L, S1R, S2R). The sites facing the low channel had higher ground and contained more sand. Such microtopography is very similar to natural levees formed by natural rivers. Behind the natural levee-like microtopography, there was a wetland with finer sediments and water bodies. Thus, the topography resembled that of a natural levee in a natural river channel.

The following events were considered to have occurred at the excavation sites: (1) the ground at the excavation site became low and flat owing to the excavation work; (2) repeated flooding deposited sediment in the excavation site, forming a natural levee-like topography along the main channel, (3) finer sediment was deposited behind the natural levee-like topography; and (4) the wetland and flood-plain water bodies were separated by being surrounded by land formed by the accumulation of sediment. As a result, the flat excavated area was transformed into four types of microtopography: natural levees, lowlands behind natural levees, isolated water bodies, and connected water bodies. Sediment deposition after flood channel excavation reduced flood capacity, but also created an environment similar to the flood plain formed by a natural river channel.

10.2.3 Relationship Between Sediment Deposition and Vegetation Transition

The major trees that thrive in Japanese river channels are willows, bamboos, and *Robinia pseudoacacia* (invasive alien species in Japan). In this study rivers, willow trees are representative pioneer plants after the excavation works. Results of a survey conducted prior to excavation work on the Ibi River, the Late goldenrod (*Solidago altissima*) community, the Ogi (*Miscanthus sacchariflorus*) community, and the willows (*Salix chaenomeloides*, *Salix eriocarpa*, *Salix subfragilis*, and *Salix gilgiana*) are common species before the excavation works. However, as shown in Fig. 10.5, the excavation sites of the Ibi River were heavily forested after excavation.

As mentioned in Sect. 10.1, trees in the river channel provide resistance to flood flow and promote sediment deposition. Therefore, forestation is not desirable in the excavated area. To determine when and how willow species invaded the site after excavation work, a survey was conducted in 2014 to determine the size and age of the willows (Harada et al. 2015). The height, diameter at breast height, and number of annual rings at breast height of willow trees were recorded in the vicinity of the ten sites where sediment surveys were conducted. The number of samples was $N = 5$ or 6 at each site, and a total of 55 samples were obtained. There was no statistically

significant difference ($p > 0.05$) between the number of annual rings in areas D and O, which were excavated in 2002 and 2006, respectively. The most common number of annual rings was six (25 of 55), followed by five (14 of 55). This result suggests that the establishment of willows in both areas occurred at approximately the same time. However, in both areas, the average number of annual rings was higher in the natural levee-like topography than in the backswamp-like wetland. Based on the above, it can be inferred that the natural levee-like topography was elevated above the water surface at an early stage, allowing willow seeds to become established. This is because willow seed dispersal occurs in the spring, when the seeds float on the water and drift to the water's edge. The age of willow trees growing in excavated areas could be an indicator of the time when bare ground above the water surface was formed by sediment deposition. However, the actual age of the willow trees was estimated to be older than the number of annual rings because the willow trees were disturbed by sediment deposition and flooding, and they fell down and sprouted again. The willow trees have strong vitality that allow them to sprout and regenerate from their stumps even after being cut down. Since it is not desirable for the bare land to be covered by willows after excavation, techniques are being developed to induce the surface to be covered by herbaceous species after excavation.

10.3 Restoration of Inter-Levee Floodplain Environment by Flood Channel Excavation

10.3.1 Natural Floodplain and Inter-Levee Floodplain

Flood plains are formed by the accumulation of sediment in the flowing water from rivers during floods and play an important role in biodiversity. For example, the varied microtopography of flood plains creates different physical and hydrological environments in relation to flood disturbances, such as frequency and intensity of flooding, and allows a variety of terrestrial and aquatic organisms to inhabit the floodplains (Junk et al. 1989; Robinson et al. 2002; Tockner and Stanford 2002). Flood plains also store nutrients and organic matter and reduce rapid runoff downstream, thereby increasing primary production on the flood plain and affecting ecosystem functions, including decomposition (Bayley 1995; Tockner et al. 1999).

Flood channel excavation creates lowlands that are vulnerable to flood disturbances. In gently sloping lowland rivers that flow through natural embankment zones, excavation can increase the frequency of flooding in the lowlands created by the excavation, thus providing a means to regenerate and maintain a wetland-like environment. Flood channel excavation has a high affinity for the rehabilitation of the floodplain environment. In recent years, it has been seen as a project that balances flood control and environmental restoration (Nakamura et al. 2006; Osugi et al. 2007; Akamatsu et al. 2008). The project is also likely to be effective in

addressing issues, such as the alteration of ecosystems and conservation of rare organisms in the floodplain outside the levee (Takenaka et al. 1996; Washitani 2007; Negishi et al. 2012).

Landscape distributions in alluvial riverscapes before and after levee construction. Pristine floodplain with meandering channel in the upper illustration and inter-levee floodplain with straightened channel in the lower illustration.

10.3.2 Lifespan of Freshwater Mussel Habitat Created by Flood Channel Excavation

Nagayama et al. (2017a) examined the relationship between the excavation height and elapsed years, and the mussel habitat created by excavation in the Ibi River to understand efficient management of the floodplain environment using flood-channel excavation. A field survey of mussel abundance was conducted in December, 2011. The results revealed the following: In the sites with lower excavation heights (but higher than drought water level), mussel abundance and the proportion of the pond occupied by the mussels were higher, and sediment depths and deposition rates were lower. Mussel abundance and the amount of ponds increased and then decreased with peaks of 5 and 6–9 years after the excavations, respectively, in the context of continuing sedimentation. These results suggest that flood-channel excavations should be strategically implemented so that low excavation sites with 5–9 years elapsed since excavation are always present somewhere in a target river segment Nagayama et al. (2017a).

Thus, sediment deposition after excavation creates an environment that resembles a pristine floodplain, which produces a habitat for organisms that use the floodplain; however, the life span of the habitat is short. It is considered that the rate of change in topography shortens the life span of the habitat formed on the inter-levee floodplain of the Ibi River. Hori et al. (2011) investigated sediment deposition rates on natural levees and hinterland wetlands in an area along the old channel of the Ibi River near the study site. They estimated that the sedimentation rate of hinterland wetland sediments was 0.1–0.2 cm/year and that of natural levee sediments was approximately 1.5 cm/year. The sedimentation rate in the excavated area in the present river channel was approximately one order of magnitude higher than that in the old river channel. As shown in Fig. 10.7, the most significant difference between natural and artificial river channels is the presence or absence of a continuous artificial levee. Natural river channels are inundated by bankfull water levels once every few years. On the other hand, artificial river channels in Japan are designed to avoid overflowing even during floods that occur once every few decades or once every hundred years. Therefore, external forces acting on the inter-levee floodplain are high, both in terms of water flow and sediment content. This is the cause for high rate of topographic change in the inter-levee floodplain. In addition, in rivers where the flow channel is not restricted by bank revetments, various riverine landscapes are

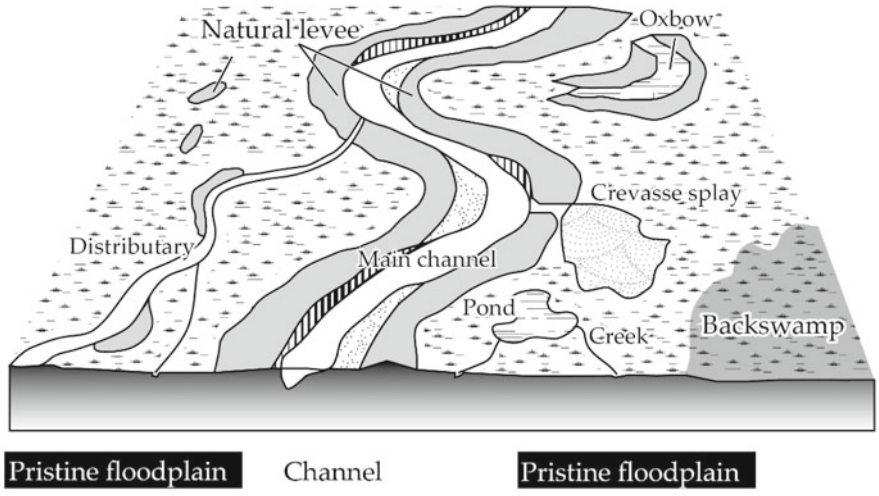

(a) Pristine lowland floodplain

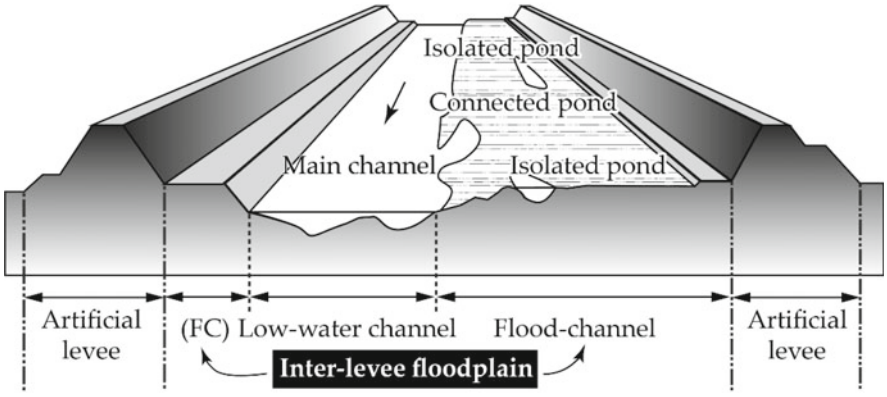

(b) Inter-levee floodplain

Fig. 10.7 Schematic image of (**a**) Pristine lowland floodplain and (**b**) Inter-levee floodplain (Reproduced from Kitamura et al. 2017)

renovated by the lateral movement of the flow channel due to the erosion of sediment on the riverbank. This phenomenon, which is common in highly natural rivers, is called "shifting habitat mosaic" (Stanford et al. 2005; Nakamura et al. 2007). In artificial channels where channel migration is not allowed, it is difficult to naturally form mosaics. Thus, excavation and vegetation clearing are expected to be the means of inducing a shifting mosaic by artificial disturbance.

10.4 Predicting Fine Sediment Deposition Rate in Lowland River Channel

10.4.1 Relationship Between Suspended Load Concentration and Flow Rate

The response after the flood channel excavation naturally depends on the characteristics of the river. Sediment accumulation may be caused by a combination of flow regime and sediment regime of the river, and not just on the method of excavation work. The sediment deposition trends observed at the excavation sites after excavation work in the two adjacent rivers (Fig. 10.4) were very different.

Figure 10.8 shows the grain size distribution (GSD) in the three excavation sites each in the Ibi River and Nagara River. The GSD of the natural levee-like

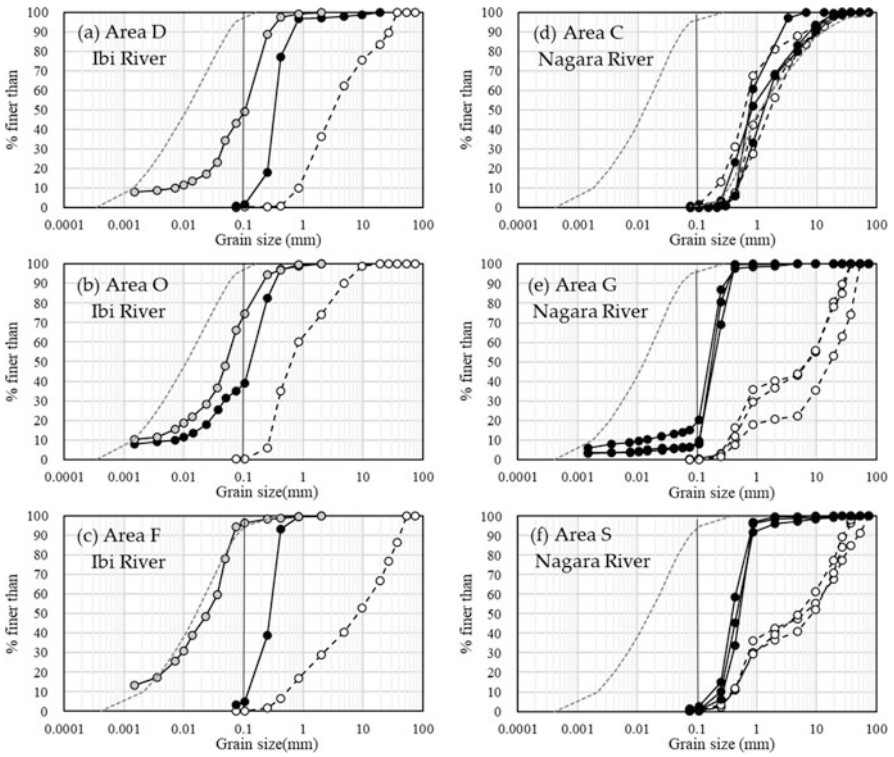

Fig. 10.8 Grain size distribution (GSD) of the sediments around excavation sites in the Ibi and Nagara River. In the Ibi River, GSD plots with white filled circle, black filled circle, gray filled circle show the GSD of the low channel bed, natural levee-like topography, and hinter land-like topography, respectively. The gray dotted line indicates the GSD of the washload in the flood water. In the Nagara River, black filled circle shows the GSD of the deposited sediment found in excavated area

topography of the Ibi River, is mostly sand, presumably deposited by suspended load that was rolled up from the riverbed of the low channel. On the other hand, the GSD of the hinterland-like topography is similar to the GSD of the washload in the sampled water during flood runoff. Since most of the area of the Ibi River excavation area has a landscape similar to that of a hinterland wetland, it can be said that the majority of the sediment deposited is fine-grained sediment equivalent to "washload". Washload is considered to be a fine-grained component that is rarely present in riverbed materials. With respect to physical properties, washload is generally defined as sediment less than 0.1–0.2 mm in diameter size that transitions to a suspended state directly when the movement limit is exceeded. Contrary, in the Nagara River excavation area, there appears to be some deposition of sand rolled up from the low channel bed, but very little deposition of washload. What factors contributed to the differences observed between the two rivers?

Harada et al. (2020a, b) analyzed water samples under a wide range of flow conditions, assuming that the difference in sediment deposition between the Ibi River and the Nagara River was due to the difference in sediment concentration during the flood. Surface water samples were collected at a particular point on the Ibi and the Nagara River (bridges that serve as high-flow observation points) between high-flow observations, which were conducted multiple times during a flood. The aim was to simultaneously observe flow and sediment concentration relations. Two liters of water samples were collected at each point in the middle of the main channel. Although it is desirable to have a larger volume sampled, it is dangerous to work during floods and at night. Therefore, the minimum volume required for analysis was collected.

Water sampling and sediment concentration analysis during floods were performed with the help of river managers from 2018 to 2019. Sediment concentrations in surface water samples from the two rivers are shown in Fig. 10.9. The basin areas of the Ibi and Nagara River are 1196 km^2 and 1914 km^2, respectively. The flood discharge observed in the Nagara River, which has a larger basin area, is generally higher. The circle plots in Fig. 10.9 show the results of a survey conducted by the river administrator at the same location on the Nagara River in the 1960s. The results revealed considerable variation in sediment concentration, even in the same river.

The relationship between suspended sediment concentration C and water discharge Q is not simple. Even within a single flood hydrograph, the sediment concentration can be different for the same flow rate. Williams (1989) presented a pioneering study that divided the C-Q relationship into five common patterns. However, to make the handling of sediment concentration as practical as possible, the definition of the sediment transport rate Q_s was a function of water discharge, Q. A relation that gives Q_s as a function of Q is called a sediment rating curve as a power function (Wilcock et al. 2009).

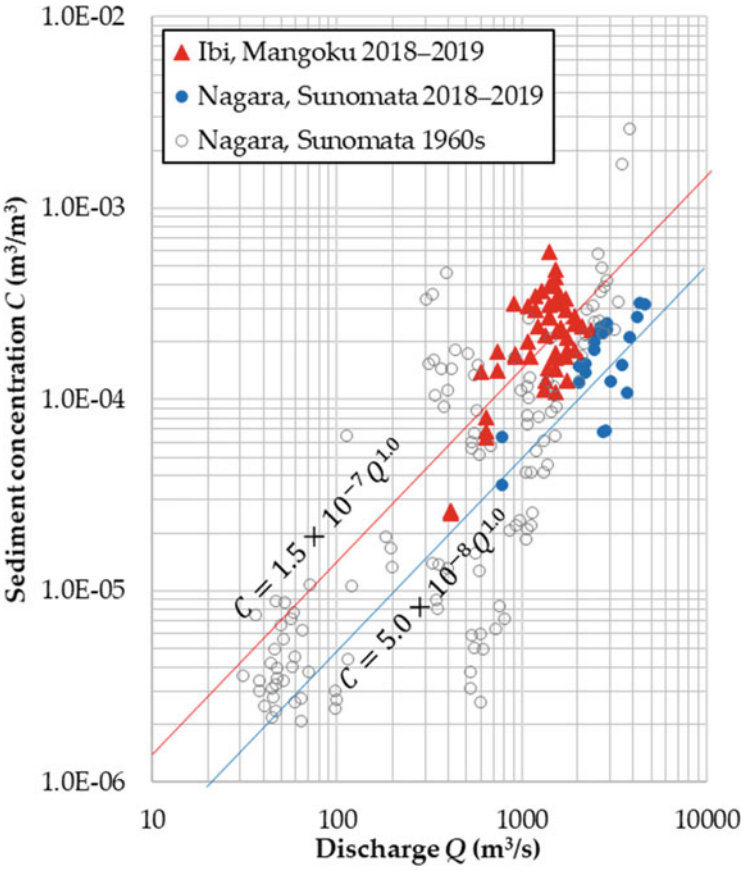

Fig. 10.9 Sediment concentration in surface water samples (Ibi River and Nagara River)

$$Q_s = aQ^b \tag{10.1}$$

Where, sediment transport rate Q_s is the product of the sediment volume concentration C and the water discharge Q. Equation 10.2, which presents the sediment concentration C in terms of the water discharge Q can be expressed as follows:

$$C = aQ^{b-1} \tag{10.2}$$

C-Q relationship was established for the measured sediment concentrations in the Ibi and Nagara Rivers (Fig. 10.9). Focusing on the same flow discharge, the sediment concentration was higher in the Ibi River, that is about three times more that in the Nagara River (Fig. 10.9). According to a survey of sediment concentrations conducted by river administrators in the 1960s, the average sediment concentration in Japanese rivers was approximately $C = 1.0 \times 10^{-7} Q$.

10.4.2 Method for Predicting Fine-Grained Sediment Deposition Rate

Harada et al. (2020a, b) established a method to predict the sedimentation rate of fine-grained sediment using the relationship between water discharge Q and sediment concentration C as an input condition. The performance of this method was verified by reproducing the annual sediment deposition at three excavation sites each in the Ibi and Nagara Rivers.

The basic calculation procedure of the simplified suspended sediment model is as follows: (1) set the time–frequency distribution of the water level at the cross section to be calculated. In this study, the frequency distribution is created using the last 10 years of hourly water levels at the nearest water level gauging station (n = 87,648 if there are no missing measurements) in increments of 1 cm; (2) set up the H-Q equation for the calculated cross section to relate the calculated water level H to the flow rate Q; (3) set the particle size to be calculated; (4) calculate the sedimentation rate dz_b/dt (m/s) using Eq. (10.3) by changing the water level in increments of 1 cm; (5) calculate the annual sedimentation rate (m/year) by integrating the calculated sedimentation velocity at each water level multiplied by the time corresponding to the frequency of occurrence of the calculated water level.

With respect to the suspended sediment transport in model calculation, a boundary surface is assumed at a reference point height z_a near the riverbed, and the exchange of sediment between the transport equation of suspended sediment in the flowing water and Eq. (10.3) is expressed by the balance of uplifting and settling through the boundary surface.

$$\frac{dz_b}{dt} = \frac{1}{1-\lambda}(w_0 C_b - q_{su}) \tag{10.3}$$

Where, z_b is the bed height (m), λ is the porosity, w_0 is the terminal settling velocity (m/s), C_b is the sediment concentration at the reference surface (m^3/m^3), q_{su} is the sediment volume uplifted from the river bed in unit time and unit area ($=w_0 \cdot C_a$, m/s), and C_a is the concentration at the reference surface in equilibrium. The left-hand side is the rate of change in the riverbed height, that is, the sedimentation rate (m/s). In this study, the sedimentation rate was calculated at the excavation site using Eq. (10.3).

In our research, the use of only washload in Eq. (10.3) is based on the study by Fujita et al. (1996), who discussed channel narrowing due to washload sedimentation. The porosity is assumed to be 0.40 for simplicity. The amount of uplift q from the river bed at the excavation site is given by the Lane-Kalinske equation as the reference surface concentration C_a at the reference surface height $z_a = 0.05\ h$. The particle terminal settling velocity w_0 is given by the Rubey equation.

The concentration C of the washload flowing over the excavated area is given directly by the equation (Q-C equation) related to the flow rate Q, which is set in advance for each river. In this study, the Q-C equation based on the results of the

water sampling survey was used for calculation. The authors confirmed that the concentration of fine sediment in the center of the main channel and near the boundary of the flood channel was similar. In addition, strong horizontal mixing, which is a large-scale flow structure, occurred in the compound channels. The concentration distribution of the washload in the cross-sectional direction was assumed to be uniform.

The concentration C_b at the reference height z_a of the excavation site should be set, considering the vertical distribution of the sediment concentration according to the grain size. Although the shape of the vertical distribution differs slightly based on various distribution formulas, the vertical distribution is almost uniform if the grain size is small. For example, when the Lane-Kalinske equation is calculated for 0.1 mm, the relative sediment concentration C/C_a near the water surface is 0.46, while it is 0.82 for 0.05 mm and 0.99 for 0.01 mm, indicating that the concentration is almost uniform from near the bottom to near the water surface. The particle size distribution of sediment obtained from the surface water sampling is almost the same in the Ibi and Nagara rivers, ranging up to 0.2 mm; furthermore, 80 to 90% of them are less than 0.05 mm. Therefore, the vertical distribution of the sediment concentration is considered to be almost uniform and $C_b = C$.

The ratio of the settling velocity w_0 to the friction velocity u^* (Rouse number) is the dominant variable not only in the L–K equation, but also in the equation for calculating the reference surface concentration C_a. The friction velocity u^* is calculated as $u^* = (ghI_e)^{1/2}$ using the water depth h and energy gradient I_e at the excavation site. Because the method of setting I_e has a great influence on the results of the model, three methods are considered in this study: the first method assumes that the I_e at the excavation site is the same as the I_e at the main channel; the second method assumes that the I_e at the excavation site is constant, which is the same as the bed gradient; the third method assumes that the I_e energy gradient at the excavation site is remarkably small (≈ 0) and does not consider the amount of uplifting q_{su}.

Figure 10.10 shows the results of the model calculation of the annual sedimentation rate with the energy gradient I_e set in three different ways. The particle size to be calculated was 0.013 mm, which corresponded to the particle size distribution of the surface water sample. The terminal settling velocity w_0 was set at 0.15 mm/s according to the Rubey equation. Methods 1 and 2 resulted in almost no washload sedimentation. Method 1 resulted in no deposition at any of the calculated water levels. In Method 2, because the energy gradient of the excavation site was smaller than that of Method 1, the sedimentation rate was positive in the range of high water levels, but the temporal frequency of high water levels was significantly small, so the amount of sedimentation was calculated to be almost zero. Method 3, in which the uplifting q_{su} from the excavation site was set to zero, yielded sedimentation rates closest to the field values. In particular, in the Ibi River, the order and magnitude of sedimentation rates at the three study sites were close to the local conditions. Although it was predicted that washload deposition would occur in the Nagara River, almost no washload sedimentation was observed in the field.

By experimenting with Methods 1 to 3 to determine the sedimentation of washloads, it was confirmed that in order to have washload sedimentation with

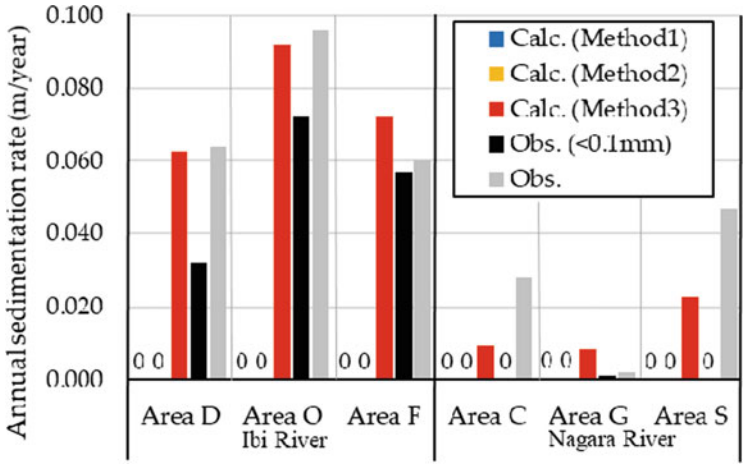

Fig. 10.10 Calculation results of annual sedimentation rate for six excavation sites (Ibi River and Nagara River). The observed sediment deposition rates are shown for all grain sizes (Obs.) and for the fraction of grain sizes smaller than 0.1 mm

small sedimentation rates, the amount of uplifting q_{su} in Eq. (10.3) and C_a must be almost zero. Method 3 assumes zero uplifting, and is a simple calculation to represent the sedimentation situation in the field. It was estimated that the sedimentation rate of the washload was small, and the vertical concentration distribution was almost uniform. Therefore, in order for sedimentation to occur, a calm environment is required in which particles suspended near the riverbed can settle and deposit despite low settling velocity. In other words, a microenvironment in which the flow is stagnant only in the vicinity of the riverbed is sufficient. A flow field with dense vegetation is one of the places that satisfies this condition. In the vertical structure of the flow with vegetation, the turbulence near the bottom was suppressed, and no upwelling took place. Therefore, Method 3 can be interpreted as calculating the washload deposition rate under the condition that the ground surface is covered with vegetation. In fact, in the study area of the Ibi River, after the flat excavation site was differentiated into a terrestrial area and a floodplain waterbody, sediment deposition continued on the vegetated terrestrial area, while sediment deposition did not occur in the waterbodies. In most of the excavated areas of the Nagara River, no fine-grained sediment was deposited. However, only in excavation area G, where the Japanese barberry *Miscanthus sacchariflorus* grows densely, fine-grained sediment was deposited. These observations support the above discussion and suggest that dense vegetation on the ground surface in the Nagara River may result in sedimentation to the extent predicted by the model. It is not only the flow regime and sediment regime of each river that affects sediment deposition after flood-channel excavation, but also the presence of vegetation has a dominant effect on the sediment deposition rate.

10.5 Conclusion

In this chapter, the response of the river environment after excavation work is explained using various aspects of the flood channel excavation, which is conducted to secure the flood capacity of the river channel. These responses are shaped by the interaction between flowing water, sediment, and vegetation. The topographic changes that occur in the inter-levee floodplain are similar to those that occur in the natural channel and its floodplain, but the rate of change is much faster. Excavation works can also contribute to the rehabilitation of the inter-levee floodplain environment. To effectively manage river channels in terms of both flood management and river environment restoration, it would be effective to understand the characteristics of rivers in terms of both flow and sediment regimes, and to develop an adaptive management cycle using model calculations and field monitoring.

Acknowledgments This work was partly supported by JSPS KAKENHI (Grant Numbers: JP17H03311 and JP19K04625), and MLIT River Sabo Technology Research and Development Grant (FY2017-2019). The authors would like to thank the Kisogawa-jouryu River Office of the MLIT for providing the observation data. The authors are also grateful to laboratory members Mika Tsunoda, Shohei Iwata, Hiroki Tomita, and Daisuke Tozaki for their contributions to this study.

References

Akamatsu F, Shimano K, Denda M, Ide K, Ishihara M, Toda H (2008) Effects of sediment removal on nitrogen uptake by riparian plants in the higher floodplain of the Chikuma River, Japan. Landsc Ecol Eng 4:91–96

Bayley PB (1995) Understanding large river-floodplain ecosystems. Bioscience 45:153–158

Cotton JA, Wharton G, Bass JAB, Heppell CM, Wotton RS (2006) The effects of seasonal changes to in-stream vegetation cover on patterns of flow and accumulation of sediment. Geomorphology 77(3–4):320–334

Fujita KI, Moody JA, Uda T, Fujii M (1996) Accretion of flood-plains by wash load deposit and resulting channel narrowing. Doboku Gakkai Ronbunshu 1996(551):47–62

Harada M, Akahori R, Takeda S (2020a) Estimating sedimentation rates based on simple mesurement of fine sediment concentration. Advances in River Engineering. J Jpn Soc Civil Eng 26:585–590

Harada M, Maruya Y, Kojima T, Matsuoka D, Nakagawa Y, Kawahara S, Araki F (2020b) Flood frequency analysis and impact assessment for climate change in the nagara river basin. J Jpn Soc Civil Eng 8(1):79–86

Harada M, Nagayama S, Oishi T, Kayaba Y (2015) Microtopography formation after Flood-Channel excavation in Ibi-River. J Jpn Soc Civil Eng, Ser B1 (Hydraulic Engineering) 71(4): I_1171–I_1176

Hori K, Usami S, Ueda H (2011) Sediment facies and Holocene deposition rate of near-coastal fluvial systems: an example from the Nobi plain. Jpn J Asian Earth Sci 41(2):195–203

Hudson PF (2005) Natural levees. Encyclopedia of water. Science 10

Junk JW, Bayley PB, Sparks RE (1989) The flood pulse concept in river-floodplain systems. Canadian J Fish Aquatic Sci Special Publications 106:110–127

Kitamura J, Tashiro T, Nagayama S (2017) Inland water system planning: Management for Ecosystem Rehabilitation. In: Shimizu H, Takatori C, Kawaguchi N (eds) Labor forces and landscape management. Springer, Singapore

Klasz G, Reckendorfer W, Gabriel H, Baumgartner C, Schmalfuss R, Gutknecht D (2014) Natural levee formation along a large and regulated river: the Danube in the National Park Donau-Auen, Austria. Geomorphology 215:20–33

Nakamura F, Shin N, Inahara S (2007) Shifting mosaic in maintaining diversity of floodplain tree species in the northern temperate zone of Japan. For Ecol Manag 241(1–3):28–38

Nakamura K, Tockner K, Amano K (2006) River and wetland restoration: lessons from Japan. Bioscience 56(5):419–429

Nagayama S, Harada M, Sagawa S, Kayaba Y (2017a) Mussel habitat in excavated flood-channels in the Ibi River with reference to initial ground heights and elapsed years. Ecol Civ Eng 19(2):131–142

Nagayama S, Tashiro T, Kitamura J (2017b) Inland water landscape: structural and functional changes in the ecosystem. In: Shimizu H, Takatori C, Kawaguchi N (eds) Labor forces and landscape management. Springer, Singapore

Negishi JN, Sagawa S, Kayaba Y, Sanada S, Kume M, Miyashita T (2012) Mussel responses to flood pulse frequency: the importance of local habitat. Freshw Biol 57(7):1500–1511

Negishi JN, Katsuki K, Kume M, Nagayama S, Kayaba Y (2014) Terrestrialization alters organic matter dynamics and habitat quality for freshwater mussels (U nionoida) in floodplain backwaters. Freshw Biol 59(5):1026–1038

Osugi T, Tate S, Takemura K, Watanabe W, Ogura N, Kikkawa J (2007) Ecological research for the restoration and management of rivers and reservoirs in Japan. Landsc Ecol Eng 3:159–170

Robinson CT, Tockner K, Ward JV (2002) The fauna of dynamic riverine landscapes. Freshw Biol 47:661–677

Stanford JA, Lorang MS, Hauer FR (2005) The shifting habitat mosaic of river ecosystems. Internationale Vereinigung für theoretische und angewandte Limnologie: Verhandlungen 29(1):123–136

Tabacchi E, Correll DL, Hauer R, Pinay G, Planty-Tabacchi AM, Wissmar RC (1998) Development, maintenance and role of riparian vegetation in the river landscape. Freshw Biol 40(3): 497–516

Takenaka A, Washitani I, Kuramoto N, Inoue K (1996) Life history and demographic features of Aster kantoensis, an endangered local endemic of floodplains. Biol Conserv 78:345–352

Tanaka T, Kobayashi K, Tachikawa Y (2021) Simultaneous flood risk analysis and its future change among all the 109 class-a river basins in Japan using a large ensemble climate simulation database d4PDF. Environ Res Lett 16(7):074059

Tockner K, Stanford JA (2002) Riverine flood plains: present state and future trends. Environ Conserv 29:308–330

Tockner K, Pennetzdorfer D, Reiner N, Schiemer F, Ward JV (1999) Hydrological connectivity, and the exchange of organic matter and nutrients in a dynamic river-floodplain system (Danube, Austria). Freshw Biol 41:521–535

Washitani I (2007) Restoration of biologically-diverse floodplain wetlands including paddy fields. Glob Environ Res 11:135–140

Wilcock P, Pitlick J, Cui Y (2009) Sediment transport primer: estimating bed-material transport in gravel-bed rivers. Gen. Tech. Rep. RMRS-GTR-226. Fort Collins, CO: US Department of Agriculture, Forest Service, Rocky Mountain Research Station. 78 p., 226

Williams GP (1989) Sediment concentration versus water discharge during single hydrologic events in rivers. J Hydrol 111(1–4):89–106

Wu W, Shields FD Jr, Bennett SJ, Wang SS (2005) A depth-averaged two-dimensional model for flow, sediment transport, and bed topography in curved channels with riparian vegetation. Water Resour Res 41(3)

Chapter 11
Relationship between Forest Stand Condition and Water Balance in a Forested Basin

Toshiharu Kojima

Abstract Water dynamics in forest basins is highly complex. Although some investigations on long-term change in forest water balance following forest fires exist, limited information is available in long-term observation of forest watersheds composed of a single tree species and forest age. Therefore, a detailed water balance model, based on forest structure parameters using observation data from the literature, was developed to evaluate how forest structures, such as forest age, density, and tree height, affect the water balance of a forested watershed. It is suggested that the available water resources in Japanese cedar forests decline from young forest to age 100 years and then remain almost constant. Similar trends about the water balance in the forested watershed have been observed in existing studies, and the impact of aboveground areas, which have a significant effect on forest age, on the water balance appears to correspond to the results of this study, which were validated by the detailed model.

Keywords LAI · Evapotranspiration · Interception · Forest growth · Forest thinning

11.1 Introduction

Water dynamics in forest basins is a highly complex process that involves interception evaporation (where rainwater that hits the trees' body evaporates during rainfall), stem flow (where rainwater flows down the tree stem to the forest floor), infiltration of rainwater that reaches the forest floor into the soil layer, storage in porosity in the soil layer, and pipe flow (in which rainwater flows down through large porosity in the soil layer). These water movement processes, also known as hydrological processes, are influenced by forest and soil conditions, topography, and microclimate. However, the long-term water balance is relatively explainable. R denotes the total rainfall to the basin; Q, the total discharge from the basin; E,

T. Kojima (✉)
River Basin Research Center, Gifu University, Gifu, Japan
e-mail: kojima@green.gifu-u.ac.jp

F. Li et al. (eds.), *River Basin Environment: Evaluation, Management and Conservation*, https://doi.org/10.1007/978-981-19-4070-5_11

the total evapotranspiration from the basin; and S, the water storage in the basin. The basin water balance can be expressed as follows:

$$\frac{dS}{dt} = R - Q - E \tag{11.1}$$

where dS/dt denotes the time variation of S. Time t is assumed as a sufficiently long period, then $dS/dt = 0$, and the total discharge from the basin can be expressed as follows:

$$Q = R - E \tag{11.2}$$

Therefore, the total amount of available river flow mainly depends on the evapotranspiration from the basin, assuming the same amount of rainfall. Evapotranspiration from forest basins occurs in two forms: evaporation from tree bodies wetted by rain and transpiration *via* plant stomata. Various researchers have modeled forest evapotranspiration and interception according to forest conditions. However, the set parameters in different models vary depending on the tree species, forest type, forest condition, etc. Therefore, these parameters must be adjusted based on observation results when applied to a real forest. Although some investigations on long-term forest water balance change following forest fires exist, information on forest watersheds composed of a single tree species and forest age is insufficient. This study describes the relationship between forest condition and forest water balance using a detailed model based on several literature values.

11.2 Evapotranspiration

Evapotranspiration from forests significantly impacts the water balance in a forested basin. This section outlines the methods for estimating evapotranspiration from the forest.

11.2.1 Method with Potential Evapotranspiration

Potential evapotranspiration is a widely adopted and relatively simple method for estimating evapotranspiration. According to Thornthwaite, potential evapotranspiration is the maximal rate of evaporation from a large area completely and uniformly covered by actively growing vegetation with adequate moisture at all times (Thornthwaite 1948; Brutsaert 2005). In addition to the Thornthwaite method, other possible evapotranspiration methods, such as the (Hamon 1961) and Makkink methods (Makkink 1957), have been proposed. These are empirical methods based on temperature, sunshine duration, and solar radiation. In addition, the actual

evapotranspiration is involved in such biological effects as stomatal impedance to the diffusion of water vapor and the stage in the growth cycle of the vegetation; thus, a correction factor is necessary, which is presented as follows:

$$E = fE_p \tag{11.3}$$

where E denotes the actual evapotranspiration; E_p, the potential evapotranspiration; and f, a correction factor. Therefore, this paragraph outlines the procedures for estimating evapotranspiration with potential evapotranspiration and correction factor.

11.2.1.1 Thornthwaite Equation

Thornthwaite (1948) defined the relationship between mean monthly temperature and potential evapotranspiration adjusted to a standard month of 30 d, with each having 12 h of possible sunshine in the following form:

$$E_{p,th} = 1.6\left(\frac{D_0}{12}\right)\left(\frac{10T_i}{I}\right)^a \tag{11.4}$$

where $E_{p,\ th}$ denotes the monthly potential evapotranspiration (cm/30 days); T_i, the mean monthly temperature in i-th month ($^\circ C$); and I, an appropriate heat index in the following form:

$$I = \sum_i^{12}\left(\frac{T_i}{5}\right)^{1.514} \tag{11.5}$$

The exponent a is closely approximated by the following expression:

$$a = 0.0000006751I^3 - 0.0000771I^2 + 0.01792I + 0.49239 \tag{11.6}$$

D_0 is the mean monthly possible sunshine time (h) defined as follows:

$$D_0 = 24\left(\frac{\omega_0}{\pi}\right) \tag{11.7}$$

$$\omega_0 = \cos^{-1}(-\tan\varphi\tan\delta) \tag{11.8}$$

$$\delta = 0.4093\cos\{0.01689(D - 173)\} \tag{11.9}$$

where φ is the latitude at the target area (rad), and D is the day of the year.

11.2.1.2 Hammon Equation

Hamon (1961) also proposed average daily potential evapotranspiration, represented as proportional to the product of day-time hour squared and concentration of saturated water vapor at a mean temperature in the following form:

$$E_{p,h} = 0.14\left(\frac{D_0}{12}\right)^2 \rho_{w,sat} \tag{11.10}$$

where $E_{p,\ h}$ denotes the average daily potential evapotranspiration (mm/d); D_0, the mean monthly possible sunshine time (h); and $\rho_{w,\ sat}$, the saturated water vapor concentration at mean temperature defined as follows:

$$\rho_{w,sat} = \frac{217 e_t}{T + 237.15} \tag{11.11}$$

$$e_t = 6.11 \times 10^{7.5T/(T+237.15)} \tag{11.12}$$

where e_t denotes the saturated water vapor pressure (hPa) at mean monthly temperature T ($^\circ C$).

11.2.1.3 Makkink Equation

The Makkink equation is defined as follows:

$$E_p = a\frac{\Delta}{\Delta + \gamma}\frac{R_s}{\iota} + b \tag{11.13}$$

where ι denotes the latent heat of vaporization; R_s, the total amount of solar radiation; and γ and Δ, psychrometric coefficient and rate of change of saturated specific humidity at air temperature (hPa/ $^\circ C$), respectively, and can be approximated as $\Delta/(\Delta + \gamma) = 1/[1.05 + 1.4 \exp(-0.0604T)]$. Moreover, a and b are parameters that depend on the location. Nagai (1993) proposed the following modified Makkink equation that considers surface albedo α.

$$E_p = (a + 0.05 - \alpha)\frac{\Delta}{\Delta + \gamma}\frac{R_s}{\iota} + b \tag{11.14}$$

11.2.1.4 Correction Factor

The oldest correction factor f, which reflects the moisture availability, is defined by the following equations:

$$f = \begin{cases} 1 & (w > w_0) \\ \\ (w - w_c)/(w_0 - w_c) & (w \leq w_0) \end{cases} \tag{11.15}$$

where w denotes the soil water contents; w_0, a critical soil water content above which E equals E_p; and w_c, a lower cut-off value below which E is zero (Brutsaert 2005).

$$f = \begin{cases} 1 & (\theta_{0-2} \geq 30\%) \\ \\ 0.76\left[\frac{1}{2}\left\{1 - \cos\left(\frac{\theta_{0-2}}{30}\pi\right)\right\}\right]^{3.5} + 0.24 & (\theta_{0-2} < 30\%) \end{cases} \tag{11.16}$$

However, some correction factors with LAI for vegetation area are also proposed. In this paper, the following equation proposed by Kondo (1998) is used to estimate actual evapotranspiration based on potential evapotranspiration.

$$f = \frac{0.78}{1 + \exp\{-0.78(LAI - 2.2)\}} \tag{11.17}$$

11.2.2 Penman–Monteith Method

The Penman–Monteith method, a so-called big leaf model, which considers a forest as a big leaf, is one of the relatively simple and frequently used methods to estimate evapotranspiration in vegetation area; it is defined as the following equation:

$$\iota E = \frac{\Delta(R_n - G) + c_p\rho\{q_{sat}(T) - q\}g_A}{\Delta + \gamma\left(1 + \frac{g_A}{g_C}\right)} \tag{11.18}$$

where ιE denotes the latent heat flux (W/m^2); ι, the latent heat of vaporization (2.5 MJ/kg); E, the evapotranspiration (kg/s/m^2); R_n, the net radiation (W/m^2); G, the ground heat flux (W/m^2); c_p, the constant pressure specific heat of air (1006 J/kg/K at 1.0 a.t.m); ρ, the wet gas density (kg/m^3); q, the specific humidity (kg/kg); $q_{sat}(T)$, the saturated specific humidity at air temperature T; Δ (dq_{sat}/dT), the rate of change of saturated specific humidity at air temperature; γ, the psychrometeric constant (c_p/ι); and g_A and g_C, the aerodynamic conductance and canopy conductance, respectively. The Penman–Monteith method is unique since it uses g_A and g_C as the conductivity to evapotranspiration at the canopy scale instead of the bulk exchange coefficient. g_A and g_C are parameters influenced by forest structure, such as canopy height and stand density.

Moreover, the Penman–Monteith method also considers heat balance. R_n is defined as follows:

$$R_n = (1 - ref)S^{\downarrow} + L^{\downarrow} - \sigma {T_s}^4 \tag{11.19}$$

where $S^{\downarrow}$ is the solar radiation (W/m^2); $L^{\downarrow}$, the longwave radiation from the atmosphere (W/m^2); *ref*, the surface albedo (0.1 to 0.3 for the forested area); σ, the Stefan–Boltzmann constant; and T_s, the ground surface temperature (K).

11.2.2.1 Aerodynamic Conductance

Aerodynamic conductance can be estimated using the following equation, which considers the ground surface roughness:

$$g_A = \frac{\kappa^2 u(z)}{\left(\ln \frac{z-d}{z_0}\right)^2} = C_H u(z) \tag{11.20}$$

where $u(z)$ denotes the wind speed (m/s) at altitude z from the ground surface; κ, the Kalman constant; z_0, the ground surface roughness length (m); d, the zero-plane displacement (m); and C_H, the bulk exchange coefficient for sensible heat. In the forest area, d and z_0 are affected by forest structure as the following equations:

$$\frac{d}{h} = 1.1 \ln \left[1.0 + (c_d LAI)^{\frac{1}{4}}\right] \tag{11.21}$$

$$\frac{z_0}{h} = \begin{cases} \frac{z_0'}{h} + 0.3\sqrt{c_d LAI} & (c_d LAI \leq 0.2) \\ 0.3\left(1.0 - \frac{d}{h}\right) & (c_d LAI > 0.2) \end{cases} \tag{11.22}$$

where h is the canopy height (m); c_d, the mean drag coefficient (0.2); and z_0', the roughness length of the soil surface (m). $z_0'/h = 0.000860$ was used for bare soil (Shaw and Pereira (1982)). Nakai et al. (2008) proposed the following equations with stand density N (trees/ha) and LAI:

$$\frac{d}{h} = 1.0 - \frac{1.0 - \exp(-\alpha N)}{\alpha N} \frac{1.0 - \exp(-\beta LAI)}{\beta LAI} \tag{11.23}$$

$$\frac{z_0}{h} = 0.264\left(1.0 - \frac{d}{h}\right) \tag{11.24}$$

where $\alpha = 0.000724$, $\beta = 0.274$.

11.2.2.2 Canopy Conductance

Canopy conductance g_C is a parameter that corresponds to stomatal conductance g_s when a canopy is considered a single leaf. Jarvis (1976) proposed the following equation for stomatal conductance g_s, which is a function of leaf temperature, leaf water potential, vapor pressure deficit, etc.

$$g_s = g_s(\delta q) g_s(T) g_s(Q_P) g_s(\Psi_1) g_s(C_a) \tag{11.25}$$

where $g_s(\delta q)$, $g_s(T)$, $g_s(Q_P)$, $g_s(\Psi_1)$, and $g_s(C_a)$ are the response of g_s to vapor pressure deficit δq, leaf temperature T, photon flux density Q_P, leaf water potential Ψ_1, and ambient CO_2 concentration C_a. Based on the Jarvis model, the environmental dependence of g_s is assumed to be separable and dependent on each environmental variable. X_i is described by an individual response function f_i, which lies between 0 and 1. A commonly used g_s model is derived as the product of the maximum stomatal conductance $g_{s,\,max}$ and each response function:

$$g_s = g_{s,max} \prod_i f_i(X_i) \tag{11.26}$$

where g_s is applicable for detailed phenomena at the individual leaf level; however, it needs to be expanded to the canopy scale to evaluate the water balance at the basin scale. Based on the relationship between the net canopy photosynthesis and the net photosynthesis of the top leaf layer, Cox et al. (1998) proposed the following equation for g_C and g_s:

$$g_C = g_s \frac{1 - \exp(-k \cdot LAI)}{k} \tag{11.27}$$

where g_s is the stomatal conductance of the top leaf layer; g_C, the canopy conductance; and k, the extinction coefficient for PAR. However, the following simple equation has also been proposed (e.g., Whitely et al. 2009):

$$g_C = g_s \cdot LAI \tag{11.28}$$

According to the Jarvis model, several g_C equations have been proposed with the observed evapotranspiration:

$$g_C = g_{Cref} \cdot f_1(\delta q) \cdot f_2(S) \cdot f_3(T) \tag{11.29}$$

where $f_1(\delta q)$, $f_2(S)$, and $f_3(T)$ are the response functions of vapor pressure deficit δq (kPa), solar radiation S (W/m^2), and air temperature T ($^\circ C$), respectively, as follows.

$$f_1(\delta q) = 1.00 - \beta \cdot \ln(\delta q) \tag{11.30}$$

$$f_2(S) = \min\left\{\left(\frac{S}{600}\right)^{\delta}, 1.00\right\} \tag{11.31}$$

$$f_3(T) = \begin{cases} 1.00 & (T \geq \epsilon) \\ \dfrac{T-\zeta}{\epsilon-\zeta} & (\zeta < T < \epsilon) \\ 0.00 & (T \leq \zeta) \end{cases} \tag{11.32}$$

where β, δ, ϵ, and ζ are parameters. g_{Cref} is a parameter related to a stand structure. Komatsu et al. (2014) proposed the following equation, which is related to stand density N and diameter at breast height d_m.

$$g_{Cref} = a \cdot N \cdot {d_m}^k \tag{11.33}$$

where a and k are parameters. However, photosynthesis and respiration in the trees are related to the total number of stomata in living leaves, as presented by Shinozaki's pipe model (Shinozaki et al. 1964); thus, g_{Cref} should be more closely related to the diameter under the live branch or LAI, and so on. Therefore, in this study, the following equation with LAI is used to estimate g_C:

$$g_C = \alpha \cdot LAI \cdot g_1(\delta q) \cdot g_1(S) \cdot g_1(T) \tag{11.34}$$

where α is a constant value (0.0018). $g_1(\delta q)$, $g_1(S)$, and $g_1(T)$ are response functions of vapor pressure deficit δq (hPa), solar radiation S (W/m^2), and air temperature T ($^\circ C$), respectively, and are defined by the following equations:

$$g_1(\delta q) = \frac{\exp(-0.569\delta q)}{\exp(-0.569)} \tag{11.35}$$

$$g_1(S) = \frac{1180S}{1000 + 180S} \tag{11.36}$$

$$g_1(T) = \frac{39(T-5)}{25(T+9)} \tag{11.37}$$

11.3 Canopy Interception

Rainwater that falls on the forest canopy reaches the forest floor as throughfall R_t and stemflow R_s. If the gross rainfall to the forest canopy is R_g, there is the following relationship between R_g, R_t, and R_s:

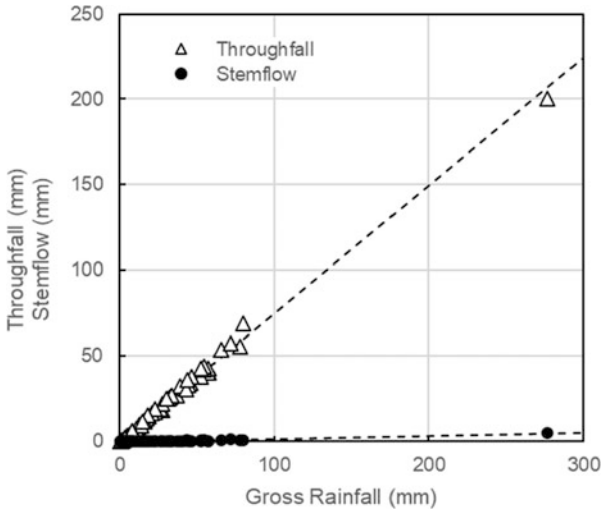

Fig. 11.1 Relationship between gross rainfall and throughfall/stemflow observed at Takayama Site of Gifu University

$$I = R_g - R_t - R_s \tag{11.38}$$

where I is the canopy interception, i.e., the loss of rainfall on the forest canopy. The relationships between R_g and R_t / R_s are often linear, as presented in Fig. 11.1, and can be defined by the following equations:

$$R_t = a_1 R_g + b_1 \tag{11.39}$$

$$R_s = a_2 R_g + b_2 \tag{11.40}$$

where a_1, a_2, b_1, and b_2 are coefficients that depend on forest factors such as forest species and forest age, with many estimation results reported for various forests. In deciduous broadleaf forests, where LAI changes with the seasons (e.g., Watanabe et al. 2012), these coefficients also change seasonally, indicating that canopy interception is influenced by forest structures like LAI. Several interception evaporation models that account for the forest structure have been proposed. This study uses the following interception model for each rainfall event (Kondo and Ishii 1992; Kondo et al. 1992; Kondo and Watanabe 1991):

$$I = I_{POT} \times (\tau/24) + S \tag{11.41}$$

where I is interception evaporation (mm); I_{POT}, the potential interception evaporation (mm); τ, the duration of a rainfall event (h); and S, the water storage capacity of tree surface (mm). Potential interception evaporation I_{POT} is defined by the following equation:

$$\frac{\iota I_{POT}}{R_n - G - \sigma T^4} = \frac{\Delta}{\gamma}\{T^+ + q^+(1 - rh)\}J \tag{11.42}$$

where rh is relative humidity, and σ is the Stefan–Boltzmann constant. T^+, q^+, and J are defined by the following equations.

$$T^+ = \frac{1 - J(\Delta/\gamma)(1 - rh)q^+}{1 + J(1 + \Delta/\gamma)} \tag{11.43}$$

$$q^+ = \frac{1}{R_n - G - \sigma T^4}\frac{4\sigma T^3 q_{sat}(T)}{\Delta} \tag{11.44}$$

$$J = \left(c_P\rho/4\sigma T^3\right)C_H u \tag{11.45}$$

where u is wind speed; the water storage capacity S is defined by the following equation:

$$S = s_{Leaf}LAI + s_{branch}BAI + s_{stem}SAI \tag{11.46}$$

where s_{Leaf}, s_{branch}, and s_{stem} are the water storage capacity of leaf, branch, and stem, respectively (mm/LAI). BAI and SAI are branch and stem area indices, respectively. Here the probability of precipitation impacting a tree body Ω^* is defined by the following equation:

$$\Omega^* = \Omega\left\{1 - \exp\left(-\frac{f \cdot LAI}{\Omega}\right)\right\} \tag{11.47}$$

where Ω is the canopy closure rate, and f is the factor of leaf tilt, usually 0.5. When $\Omega^* \times P_g > I_{POT} \times (\tau/24) + S$, canopy interception can be estimated as $I = I_{POT} \times (\tau/24) + S$; otherwise, $I = \Omega^* \times R_g$. It is known that the light intensity $I(z)$ at the altitude z in a forest confirms the Beer–Lambert law as follows:

$$I(z) = I_0 \exp\{-kF(z)\} \tag{11.48}$$

where I_0 is the light intensity on the canopy; $F(z)$, the total LAI from the top of the canopy to altitude z; and k, the light extinction coefficient. Assuming that $I_0 = 1$, the canopy openness at the forest floor, that is, the complement of canopy closure Ω, is expressed by the following equation:

$$1 - \Omega = \exp\{-k \cdot LAI\} \tag{11.49}$$

The extinction coefficient is affected by the angle of the leaves. Many studies have been conducted on the vertical distribution of the light environment in the forest to evaluate the photosynthetic rate and on the indirect measurement method of LAI using these relationships (e.g., van Gardingen et al. 1999; Tsuruta et al. 2014;

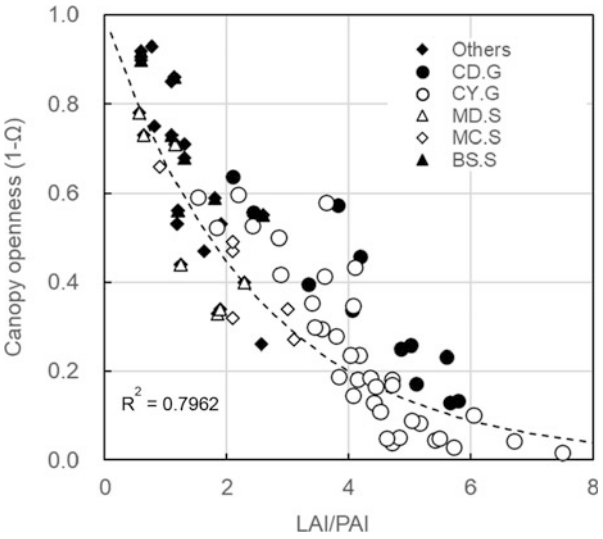

Fig. 11.2 Relationship between canopy openness and LAI/PAI. Each data point is as follows: CD. G and CY.G are Japanese cedar and cypress, respectively, by Ena Regional Agriculture and Forestry Office and JFCE (2008). MD.S, MC.S, BS.S, and Others are mixed deciduous, mixed coniferous, black spruce, and other species, respectively, by Leblanc et al. (2005)

Leblanc et al. 2005). In this study, the relationship $1 - \Omega$ and *LAI* is plotted in Fig. 11.2 from the list of PAI and canopy openness as described by Leblanc et al. (2005), whereas the list of stand conditions such as DBH, tree height, and canopy closure described in Ena Regional Agriculture and Forestry Office of Gifu Prefecture and Japan Forest Engineering Consultants (2008), and the value of $k = 04030$ ($R^2 = 0.7962$) was obtained.

11.4 LAI Estimation

As explained in the previous section, the water balance in the forest area is closely related to the leaf area index (LAI). It is challenging to directly observe LAI; therefore, several estimating equations have been proposed using allometry formulas, often used as equations for the relative growth relationships of organisms. Some equations suggested, such as the equation associated with DBH (e.g., Watanabe and Moteki 2007), are the easiest to survey in the forest, whereas the equation related to the stem area at the crown base height is discussed later. Forest survey is very labor-intensive, and most researchers often do not publish the surveyed data; however, only the results from the analysis are published in most cases. Forest survey results are not included in papers submitted to journals but rather in university forests and research institutes bulletins; therefore, it is important to prudently examine such small reports. Moreover, it is also vital to use publicly available datasets, such as BAAD (Falster et al. 2015) and World Forest Biomass and Primary Production Data (Cannell 1982). In this study, considering that LAI varies with stand structure, the following procedure was applied and constructed based on the survey results obtained from the various literature for Japanese cedar forest.

11.4.1 Forest Growth Model

Japanese forestry industries use yield density diagrams in predicting tree growth and timber harvest. In this study, the forest growth model was developed based on the forest harvest table of Gifu Prefecture (e.g., Forestry Resources Management Division of Gifu Prefecture (1992)). The tree height of a top layer H_t is defined by the following growth curve equations:

$$H_t = M\{1 - L\exp(-Kt)\} \tag{11.50}$$

where t is the forest age (y), and M, L, and K are the parameters. The above equation is the so-called Mitscherlich's curve. In addition to Mitscherlich's curve, the logistic and Gompertz curves are often used as forest growth models. The Japanese cedar forest in Gifu Prefecture grows according to Mitscherlich's curve, as presented in Fig. 11.3. In Fig. 11.3, the plots reveal the results of observations in Gifu Prefecture. The center curve (Condition III) follows the above growth equation. The other curves show the difference in growth rate depending on the forest growth condition, such as slope direction and soil water condition.

As the forest grows, some trees naturally die from competition. The following equation can express the maximum tree density during the forest growth process:

$$\log_{10} N_{Rf} = \log_{10} K_4 + K_3 \log_{10} H_t \tag{11.51}$$

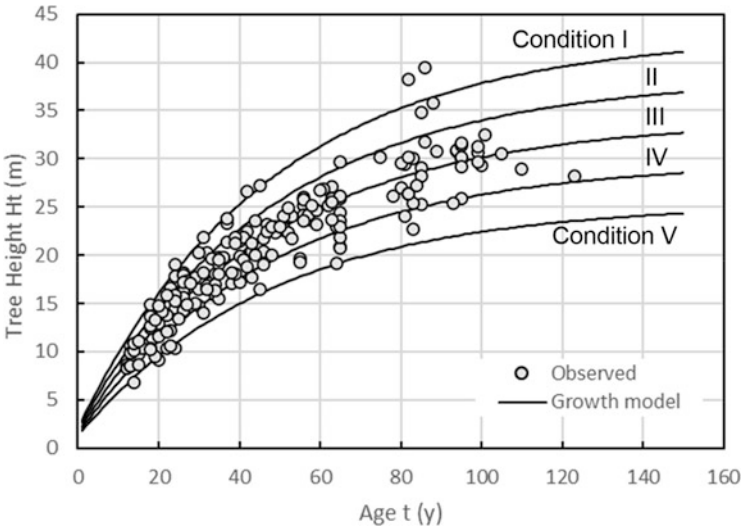

Fig. 11.3 Forest growth model for Japanese cedar in Gifu Prefecture. Conditions I to V are the difference in growth rate depending on the forest growth condition

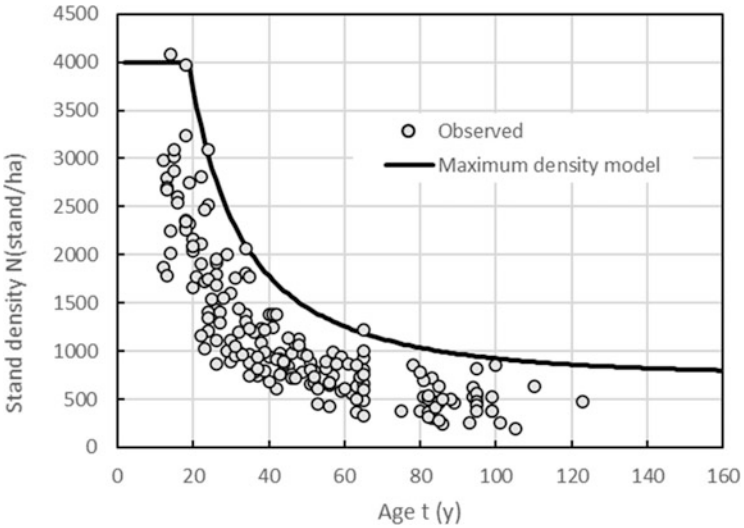

Fig. 11.4 Maximum stand density model for Japanese cedar in Gifu Prefecture

where N_{Rf} is the maximum stand density (trees/ha), and K_3 and K_4 are the parameters based on the forest density control chart. Figure 11.4 presents the maximum stand density curve for Japanese cedar forest in Gifu Prefecture, with the initial number of trees planted being 4000 trees/ha. Each data point is the observation result of forest age and stand density. The maximum stand density curve parameters are defined as a tangent to the plots' upper limit. Since the maximum stand density is determined by tree height, it gradually decreases with forest age, as presented in Fig. 11.4. Except for disturbances resulting from thinning and fallen trees due to wind and snow damage, the forest stand density changes with time according to the maximum tree density equation.

Diameter at breast height (DBH) D (cm) is estimated according to the following equations:

$$D = \beta_1 + \beta_2 D_g + \beta_3 \sqrt{N} H_t / 100 \tag{11.52}$$

$$D_g = 200\sqrt{G/(\pi N)} \tag{11.53}$$

$$G = V/H_F \tag{11.54}$$

$$H_F = \alpha_1 + \alpha_2 H_t + \alpha_3 \sqrt{N} H_t / 100 \tag{11.55}$$

$$V = \left(b_1 {H_t}^{b_2} + \frac{b_3 {H_t}^{b_4}}{N} \right)^{-1} \tag{11.56}$$

where N is the stand density (trees/ha); D_g, the average diameter (cm); G, the stem area (m^2/ha); H_F, the shape ratio (m); V, the stand volume (m^3/ha); and α_1, α_2, α_3, β_1,

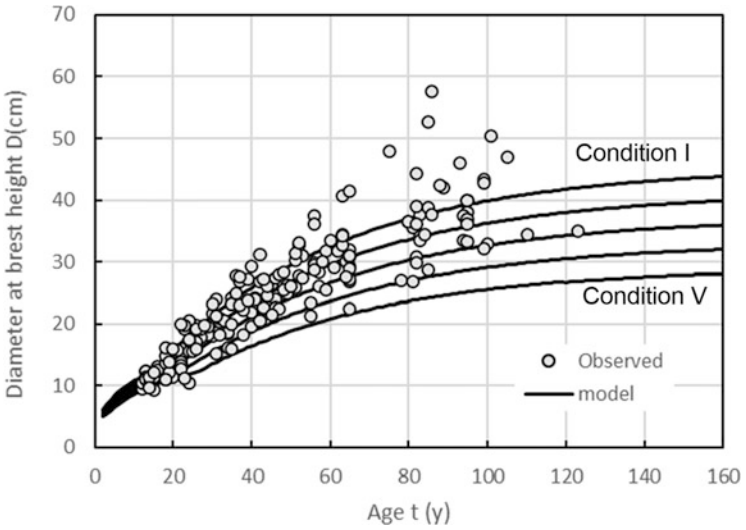

Fig. 11.5 Changes in diameter at breast height for Japanese cedar in Gifu Prefecture with stand age. Each curve represents the difference in growth conditions

β_2, β_3, b_1, b_2, b_3, b_4, the parameters determined for each species and region. Figure 11.5 presents the diameter changes at breast height with stand age of Japanese cedar forest in Gifu Prefecture, estimated using the above equation.

11.4.2 Crown Base Height

LAI is related to the total mass in living leaves, as presented by Shinozaki's pipe model (Shinozaki et al. 1964). As shown in Fig. 11.6, assuming that the tree stem shape is trapezoidal, the stem area at crown base height A_B (m^2) is estimated as follows:

$$A_B = A_0(H - H_B)/(H - H_0) \tag{11.57}$$

where A_0 denotes the stem area at breast height (m^2); H, the tree height (m); H_B, the crown base height (m); and H_0, the breast height, usually 1.3 (e.g., Inagaki et al.,2020). Figure 11.7 presents the relationship between observed stem area at crown base height and estimated using the above equation for Japanese cedar. Each data point is based on data extracted from works of literature, such as those of Kawanabe and Ando (1988), Ishii et al. (1998), Saito and Shidei (1973), and Saito et al. (1967). From Fig. 11.7, the following equation between the observed stem area at crown base height $A_{B,\,obs}$ and estimated $A_{B,\,est}$ was obtained.

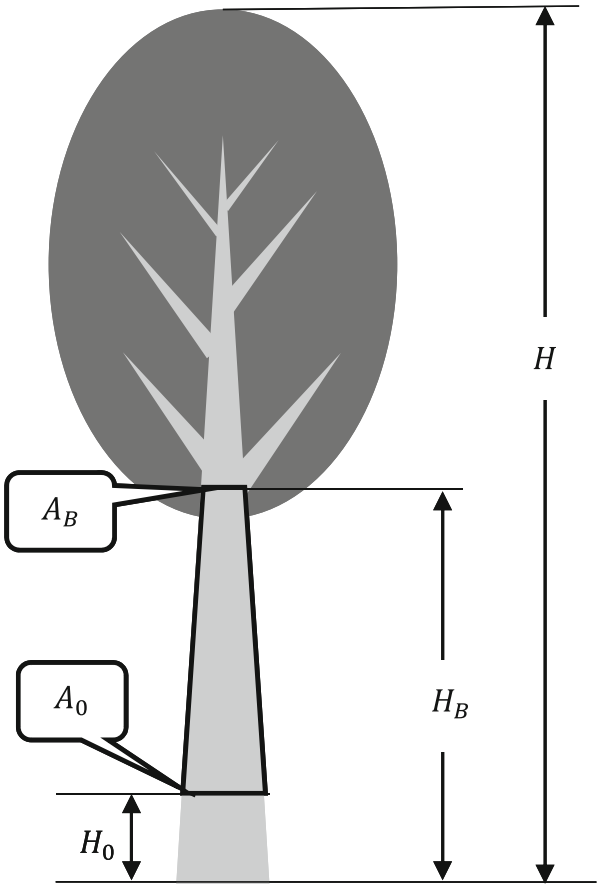

Fig. 11.6 Illustration of the relationship between the stem area at the crown base height and the stem area at the breast height

$$\log A_{B,obs} = 0.992 \log A_{B,est} - 0.0908 \tag{11.58}$$

Crown base height H_B is affected by forest management such as pruning and influenced by the stand structure. As can be seen from Fig. 11.8, the equation relating crown base height and stand density often expresses the following cumulative function form (e.g., Chiba 2009):

$$H_B = aN^{-b} \tag{11.59}$$

where N is the stand density, and a and b are the coefficients. Figure 11.9 presents the relationship between the estimated crown base height using the coefficients obtained from Fig. 11.8 and the actual ones. However, Fig. 11.9 demonstrates that the coefficient of determination (R^2) is 0.4325, indicating that the accuracy is not excellent. However, the following equation, considered with relative spacing index, is also proposed by the following equation (e.g., Kanazawa et al. 1985):

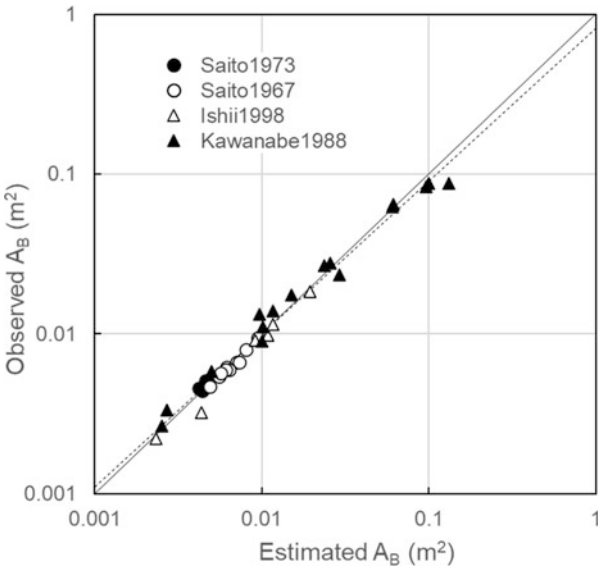

Fig. 11.7 Relationship between the observed and estimated stem area at the crown base height. Each data point is based on the following literature: Kawanabe1988: Kawanabe and Ando (1988), Ishii1998: Ishii et al. (1998), Saito1973: Saito and Shidei (1973), and Saito1967: Saito et al. (1967)

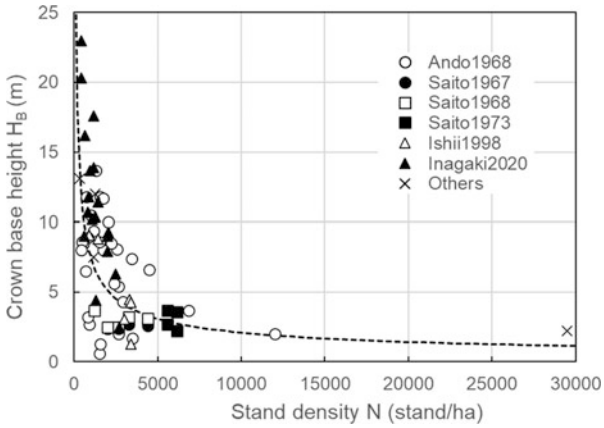

Fig. 11.8 Relationship between the stand density and the crown base height for Japanese cedar. Each data point is based on the following references: Ando1968: Ando et al. (1968), Saito1967: Saito et al. (1967), Saito1968: Saito et al. (1968), Saito1973: Saito and Shidei (1973), Ishii1998: Ishii et al. (1998), Inagaki2020: Inagaki et al. (2020), and Others: Tadaki and Kawasaki (1966), Tadaki et al. (1967) and Watanabe and Moteki (2007)

$$H_B = \frac{H}{aS_r^{\,b} + 1} \tag{11.60}$$

where S_r is the relative spacing index obtained using the following equation:

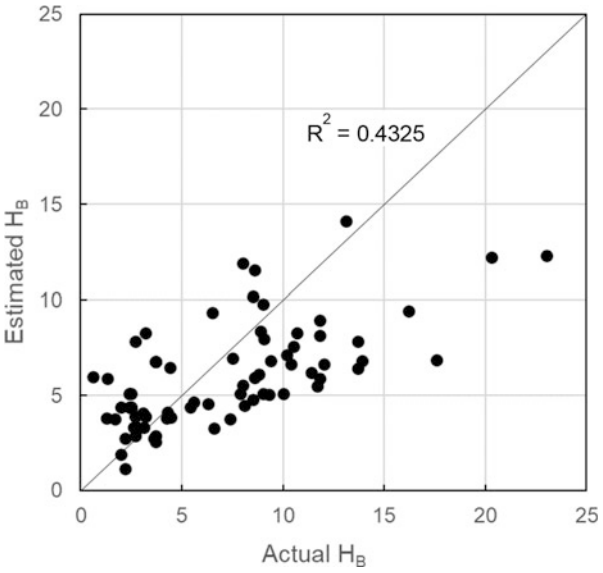

Fig. 11.9 Relationship between the estimated crown base height with the cumulative function form and the actual one. Each data point is the same as that in Fig. 11.8

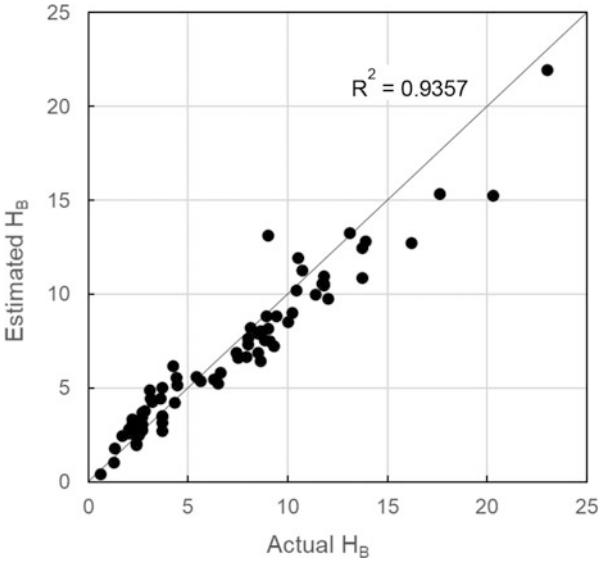

Fig. 11.10 Relationship between the estimated crown base height with the equation considered with relative spacing index and the actual one. Each data point is the same as that in Fig. 11.8

$$S_r = \frac{10000}{H\sqrt{N}} \tag{11.61}$$

where H is the tree height, and a and b are the coefficients. Figure 11.10 presents the relationship between the estimated crown base height using the equation, considered with relative spacing index, and the actual one. The coefficient of determination is

0.9357, indicating a very high accuracy. From Fig. 11.10, the values $\log_{10} a = -1.6906$, $b = 1.3839$ are obtained.

11.4.3 Dry Leaf Weight

Due to the difficulty in measuring each leaf area, the leaf weight is measured instead to develop allometric equations. Allometric equations for trees are designed with DBH or stem area at breast height, which are usually easy to survey. From numerous literature values, the relationship between stem area at breast height A_0 (m^2) and dry leaf weight w_L (kg) of a stand tree was obtained as presented in Fig. 11.11. From Fig. 11.11, the relationship was derived by the following equation:

$$\log w_L = 0.8227 \log A_0 + 2.2789 \tag{11.62}$$

However, as aforementioned, the total leaf mass is related to the stem area at the crown base height shown by Shinozaki's pipe model. Therefore, the relationship between the stem area at the crown base height A_B (m^2) and w_L (kg) of a stand tree

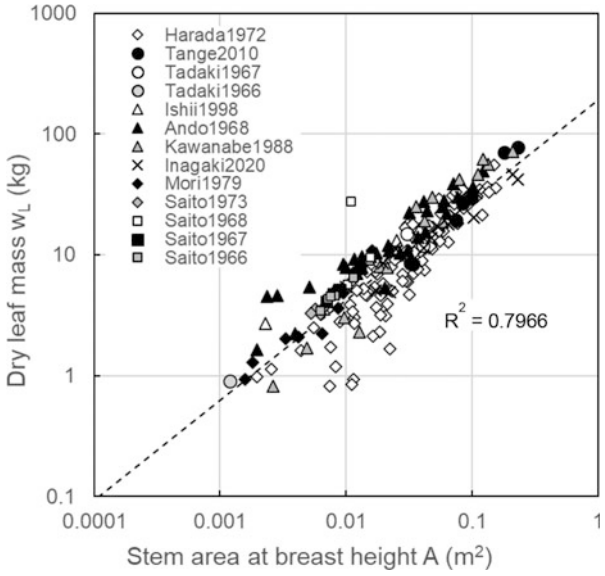

Fig. 11.11 Relationship between dry leaf mass and stem area at breast height for Japanese cedar. Each data point is obtained from the following literature: Harada1972: Harada et al. (1972), Tange2010: Tange and Kojima (2010), Tadaki1967: Tadaki et al. (1967), Tadaki1966: Tadaki and Kawasaki (1966), Ishii1998: Ishii et al. (1998), Ando1968: Ando et al. (1968), Kawanabe1988: Kawanabe and Ando (1988), Inagaki2020: Inagaki et al. (2020), Mori1979: Mori et al. (1979), Saito1973: Saito and Shidei (1973), Saito1968: Saito et al. (1968), Saito1967: Saito et al. (1967), and Saito1966: Saito et al. (1966)

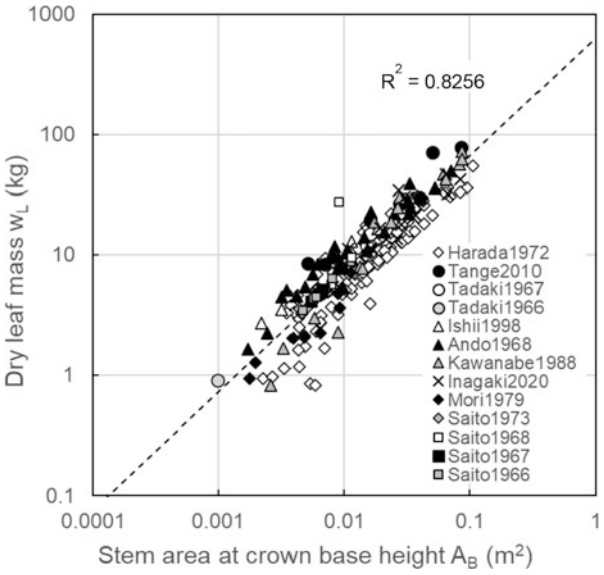

Fig. 11.12 Relationship between dry leaf mass and stem area at crown base height for Japanese cedar

was derived with similar literature values as in Eq. (11.59), as presented in Fig. 11.12. From Fig. 11.12, the relationship was obtained by the following equation:

$$\log w_L = 0.9823 \log A_B + 2.8045 \tag{11.63}$$

Equation (11.63) was more accurate than Eq. (11.62), with $R^2 = 0.8256$. It was confirmed that the dry leaf weight could be estimated more accurately using the stem area at the crown base height.

11.4.4 Relationship Between Dry Leaf Weight and Leaf Area

The leaf area measurement is labor-intensive compared with the leaf weight measurement, with a few published data on their relationship. Tadaki et al. described the data on leaf area, fresh leaf weight, and dry leaf weight of Japanese cedar in several references (Tadaki et al., 1965, 1967; Tadaki and Kawasaki 1966). However, the leaf area was estimated using the fresh leaf weight and leaf area equation by Yuruki (1964). Therefore, when the estimation results for several forests are plotted, they appear as a straight line, as presented in Fig. 11.13. However, since the dry leaf weight is not similar to the fresh leaf weight, the relationship between dry leaf weight and LAI is described in Fig. 11.14. However, Ishii et al. (1998) published data on leaf area and dry leaf weight in comparing the LAI estimated from LAI-2000 and satellite images with the actual value of LAI obtained by stratified cutting. The

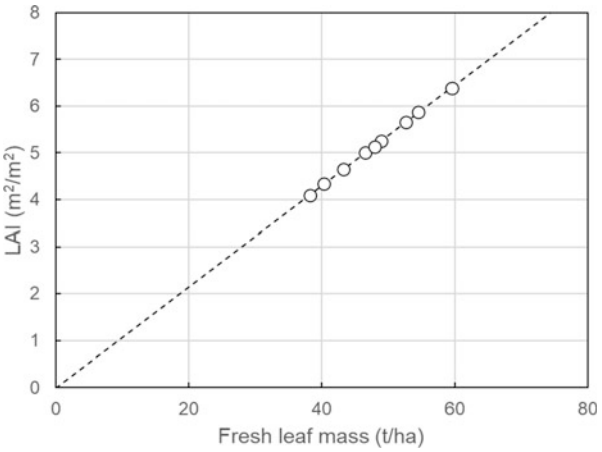

Fig. 11.13 Relationship between fresh leaf mass and LAI. Each data point from Tadaki et al. (1965)

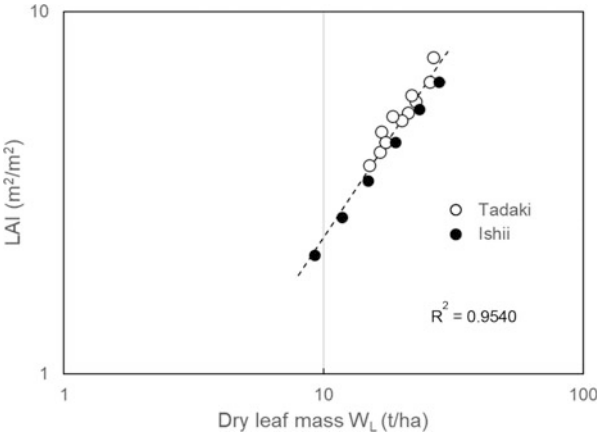

Fig. 11.14 Relationship between dry leaf mass and LAI. Each data point from Ishii: Ishii et al. (1998), Tadaki: Tadaki et al. (1965), Tadaki and Kawasaki (1966) and Tadaki et al. (1967)

following conversion equation was obtained by displaying the data of Ishii et al. (1998) in conjunction with Fig. 11.14.

$$\log LAI = 1.074 \log W_L - 0.6981 \tag{11.64}$$

where W_L denotes the dry leaf weight per ha (t/ha), which is calculated from stand density N (trees/ha) and dry leaf weight of a tree w_L (kg/tree), and is expressed as follows:

$$W_L = w_L \times N / 10000000 \tag{11.65}$$

11.5 Results and Discussions

11.5.1 Relationship Between the Stand Structure and LAI

There are few investigations on LAI and numerous investigations on dry leaf weight. Using Eq. (11.64), many LAI data can be calculated using the many observed dry leaf weights. The relationship between forest age and LAI with many observations of Japanese cedar forest is demonstrated in Fig. 11.15. LAI ranged from 2 to 12. For the forest aged above 80 years, the relationship between forest age and LAI was not well understood due to the few observations obtained. However, some of the scatter plots presented in Fig. 11.15 include observations of very dense forests with a density of more than 10,000 trees/ha. Figure 11.16 presents the dense forests with less than 15 the observations of high-density forest are excluded and the maximum values of the remaining sunspot data are draw, the envelope line with the maximum value at LAI = 8 can be draw, as shown by the dotted line, in Fig.11.16. Vertessy et al. (2001) reported that the total LAI, which include LAI of mountain ash and LAI of understory, of mountain ash forests in Australia rapidly rise to by age 7 years, and then decline steadily to 3.6. Therefore, the envelope line in Fig.11.16 might be drawn to decline to 6.0 after age 60 years, but this is uncertain due to the lack of observations. On the other hands, based on the growth model of Japanese cedar forest in Gifu Prefecture described so fa, the change of LAI for a general forest in Gifu Prefecture can be calculated as shown in Fig. 11.17. Forest in average condition is shown as the solid line, good condition as the dashed line, and poor condition as the single-dotted line. It rises rapidly by about 15 years, gradually rises by about

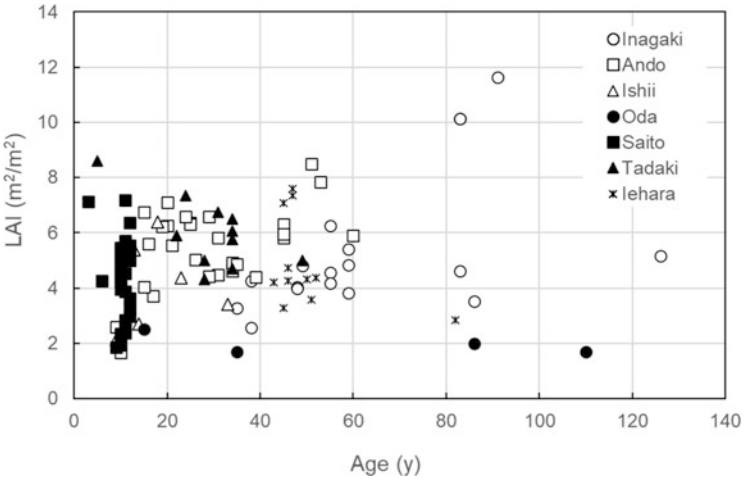

Fig. 11.15 Relationship between observed LAI and forest age. Each data point from Inagaki: Inagaki et al. (2020), Ando: Ando et al. (1968), Ishii: Ishii et al. (1998), Oda: Oda (2015), Saito: Saito et al. (1966), Saito et al. (1967), Saito et al. (1968), Saito and Shidei (1973), Tadaki: Tadaki et al. (1965), Tadaki and Kawasaki (1966), Tadaki et al. (1967), Others: Iehara et al. (2003)

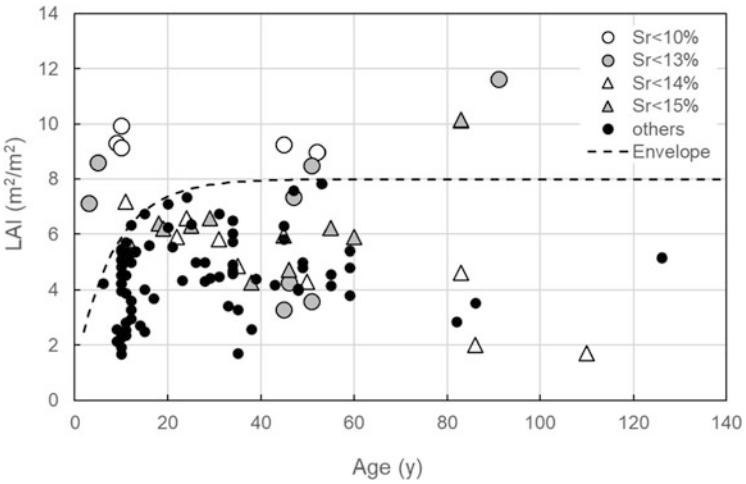

Fig. 11.16 Relationship between observed LAI and forest age

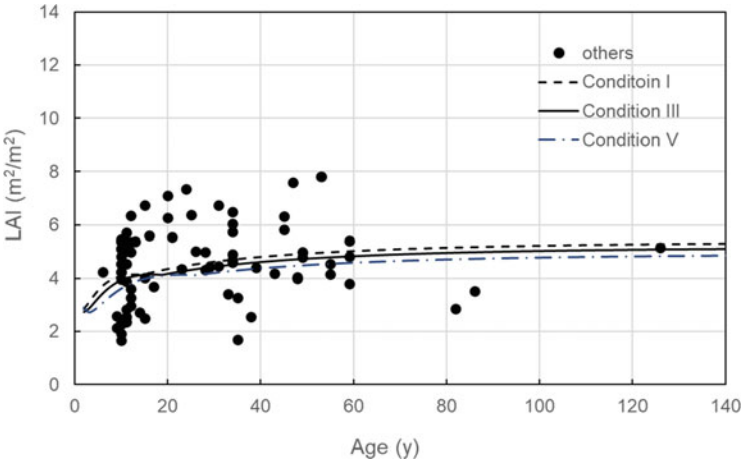

Fig. 11.17 Relationship between observed LAI and forest age

60 years, and then became almost constant. As described above, the detailed model described so far can estimate average changes in LAI as observed. The results in Fig. 11.17 are based on the Gifu Prefecture model, and it is expected that the maximum LAI will be as large as the observed value in warmer regions with good growing conditions. Here, let me consider the reason why LAI does not increase with forest age. LAI (m^2/m^2) is the product of the leaf area of a single tree A_L (m^2/tree) and stand density N (trees/ha).

$$LAI = A_L \times N/10000\#(11.66) \tag{11.66}$$

Therefore, even if a tree growth and the leaf area of a single tree increases, LAI, which is the product of A_L and N, is not expected to increase much because N decreases due to natural mortality.

11.5.2 Relationship of Stand Structure and Water Balance

Evapotranspiration was calculated using the evapotranspiration model, the interception model, and the forest growth model described in Sections 11.2 to 11.4. The meteorological data such as air pressure, temperature and wind speed, obtained from the TKC site in Takakayama City, Gifu Prefecture, Japan (e.g. Saito et al. 2012). Stand structure, such as tree height, LAI, and stand density, was set using the forest growth model assuming age 50 year of Japanese cedar forest and normal condition (Condition III). The results of calculation using daily data from January 1 to December 31, 2010 are shown in Fig. 11.18. *Et* is the sum of evapotranspiration by Penman-Montieth method and interception evaporation. In the case of rainy days,

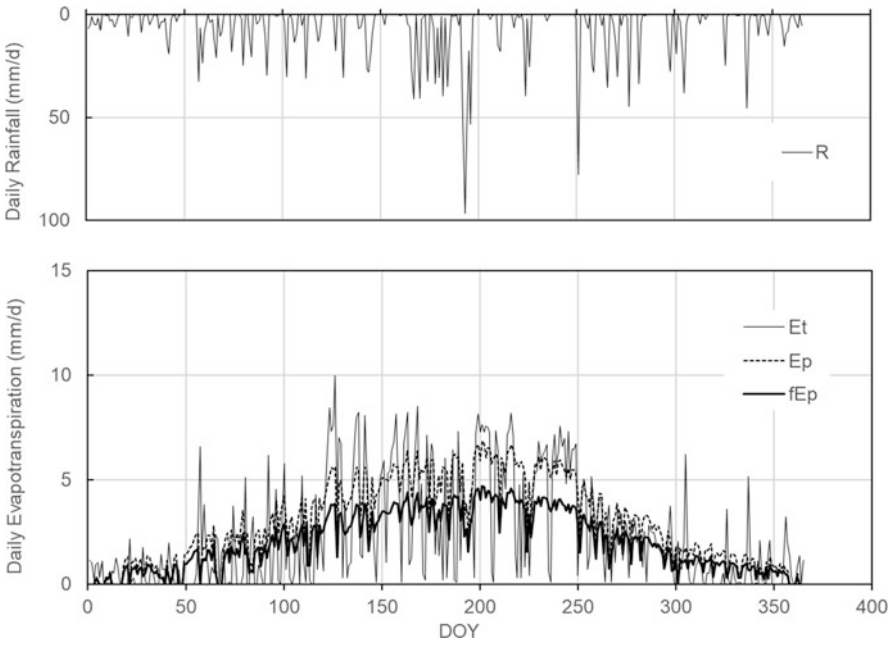

Fig. 11.18 Seasonal variation of simulated daily evapotranspiration and daily rainfall. R: rainfall, Ep: potential evapotranspiration using the Makkink method, fEp: actual evapotranspiration using Eq. (11.14), Et: evapotranspiration using the Penman–Monteith method and interception evaporation

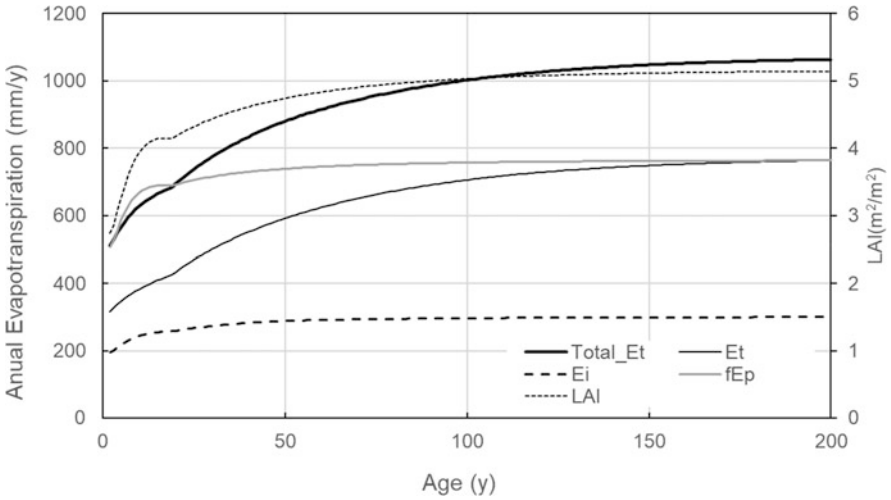

Fig. 11.19 Relationship between simulated annual evapotranspiration and forest age. Et: actual evapotranspiration using the Penman–Monteith method, Ei: interception evaporation, Total_Et: Et + Ei, fEp: actual evapotranspiration using the Makkink method and correction factor

interception evaporation was employed, and evapotranspiration using the Penman–Monteith method was adopted on a non-rainy day. *Ep* is the potential evapotranspiration using the Makkink method, whereas *fEp* is the actual evapotranspiration calculated from the product of *Ep* and the correction factor by Eq. (11.14). Also, the average forest evapotranspiration in Japan has been calculated, indicating that the annual rainfall is 2064.5 mm/yr., estimated annual evapotranspiration by *fEp* is 741.1 mm/y, and estimated annual evapotranspiration by Et is 892.0 mm/y.

Figure 11.19 presents the changes in simulated annual evapotranspiration and LAI when the forest age varied from 2 to 200 years, using similar meteorological data for TKC in 2010. The shift in *fEp*, which rapidly increased during the young forest, but did not change much after the mature forest, collaborates with the change in LAI. Since the correction factor of Eq. (11.14) depends only on LAI, the change in *fEp* follows the change in LAI. *Ei* has a similar change to *fEp*. Although *Ei* as a model depends only on LAI, the probability of rainfall impacting a tree body Ω^* and water storage capacity S is highly dependent on LAI; thus, the change in *Ei* almost follows the change in LAI. Alternatively, evapotranspiration using the Penman–Monteith method rapidly increases by age 100 and then gradually increases. The evapotranspiration using the Penman–Monteith method depends on g_A and g_C. While g_C is highly dependent on LAI, g_A is associated with forest structure parameters other than LAI, such as tree height and density, and therefore has a distinct tendency to change in response to forest growth. Figure 11.20 presents water resource provision changes, excluding evapotranspiration (Total_Et = Et + Ei) from annual rainfall. In this study, during the forest condition setup, the provision of water resources rapidly declined by age 100 and gradually decreased. Vertessy et al. (2001) and Yamaura et al. (2021) reported that the change in water resources

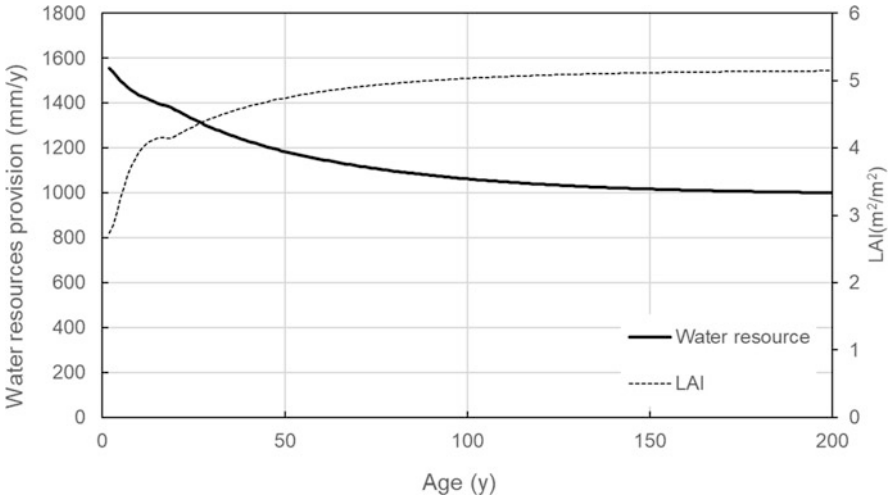

Fig. 11.20 Relationship between water resources provision and forest age

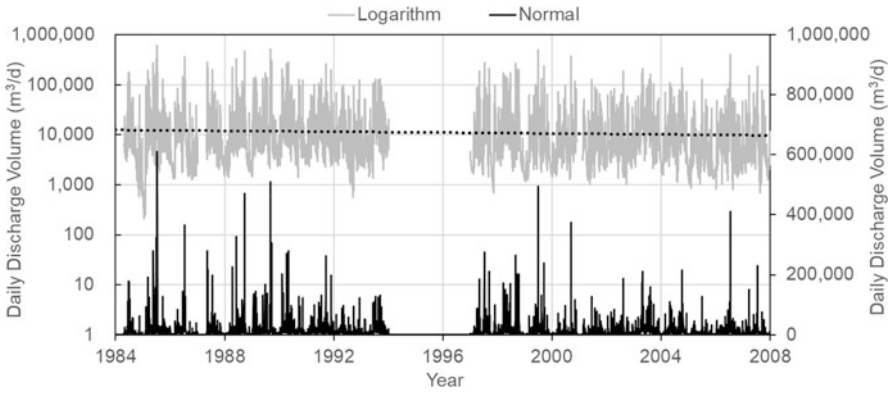

Fig. 11.21 Changes in daily discharge volume in a small forested watershed "Gaman-Sawa" in Nakatsugawa City, Gifu Prefecture, Japan (300 ha)

provision declined with forest growth by a certain forest age and then tended to be almost constant. Figure 11.21 presents the daily discharge volume from 1985 to 2007 in a small forested watershed "Gaman-Sawa" in Nakatsugawa City, Gifu Prefecture, Japan. Gaman-Sawa is a small watershed comprising Japanese cedar, Japanese cypress, and broadleaf trees whose ages are mainly about 50 years, from 10 to 100 years. The black line indicates the normal daily discharge volume, and the gray line shows logarithmic discharge volume enabling an easy understanding of the changes over the year. As mentioned in a similar figure in the work of Tani (2016), the black line is significantly affected by rainfall variability, making the changes not easily visible over a year at first glance. Alternatively, the gray line, displayed

logarithmically, shows a light decline trend (−144 m^3/y, about 1% per year). The forest age in the Gaman-Sawa watershed is about 50 years, similar to the period in Fig. 11.20 when the decreasing trend of water resources provision gradually decelerated. Therefore, the model developed in this research can evaluate the change in water balance in the forested watershed in response to the change in forest condition.

11.6 Conclusion

The detailed water balance model is developed to evaluate how different forest structures, such as forest age, density, and tree height, affect the water balance of a forested watershed based on forest structure parameters using observed data obtained from numerous literature. Since a real forested watershed includes various forest ages and types, making direct comparisons between observation and modeled values is challenging; however, the developed model can reproduce the general characteristics of the secular changes in water resources. Assuming that the model produces the water balance of the forested watershed, it is suggested that the available water resources in Japanese cedar forests decline from young forest to age 100 years, later remaining almost constant. Similar trends of the water balance in the forested watershed have been documented in existing studies. Furthermore, the impact of aboveground areas, which have a significant effect on forest age, on the water balance seems to correspond to the results of this study, which were validated by the detailed model.

However, the model proposed in this study and its calculation results is mainly limited to the aboveground parts. In addition, the water balance in the forested watershed is also immensely influenced by the water dynamics in the soil layer. Several studies on the forest soil layer and water dynamics include porosity, pipe flow, intermediate flow, and soil infiltration. However, even at a similar forest age, the relationship between forest age and water dynamics could be different when reforestation with sufficient forest soil remaining is done to the forest and also when it is reforested after the soil layer has disappeared. This trend is caused by the fact that the difference between the forest structure and the runoff characteristics by the soil layer is extremely complex than the relatively simple aboveground layer. In addition, the development of discharge models based on the forest structure is not yet adequately advanced. However, various researchers have gathered knowledge on the condition of soil layers and runoff characteristics. Therefore, it is desirable to conduct further modeling that integrates such knowledge.

Acknowledgments This work was supported by JSPS KAKENHI Grant Number JP20K04747, JP20K12284. I would like to thank K. Kanematsu of Chubu Forest Engineering Consultants and Ena Regional Agriculture and Forestry Office of Gifu Prefecture for providing Gaman-Sawa data.

References

Ando T, Hatiya K, Doi K, Kataoka H, Kato Y, Sakaguchi K (1968) Studies on the system of density control of sugi (*cryptomeria japonica*) stand. Bulletin of the Government Forestry Experiment Station 209:1–76

Brutsaert W (2005) Hydrology. Cambridge University Press, Cambridge, U.K.

Cannell MGR (1982) World forest biomass and primary production data. Academic, London, pp 146–149

Chiba Y (2009) Expected duration for canopy re-closure after thinning in plantation forests. Kanto Journal of Forest Research 60:149–150. (in Japanese)

Cox PM, Huntingford C, Harding RJ (1998) A canopy conductance and photosynthesis model for use in a GCM land surface scheme. J Hydrol 212-213:79–94

Ena Regional Agriculture and Forestry Office of Gifu Prefecture and Japan Forest Engineering Consultants (2008) Report of the Kiso River basin forest hydrologic function study. Futatsumori, Fukuoka, Nakatsugawa city. Gifu Prefecture-(in Japanese)

Falster DS et al (2015) BAAD: a biomass and allometry database for woody plants. Ecology 96(5): 1445–1445

Forestry Resources Management Division of Gifu Prefecture (1992) Forest harvest table/forest density control chart for Japanese cedar (in Japanese)

Hamon WR (1961) Estimating potential evapotranspiration. J Hydraul Div 87(3):107–120

Harada H, Satoo H, Hotta I, Hatiya K, Tadaki Y (1972) Study on the nutrient contents of mature Cryptomeria forest. Bulletin of the Government Forest Experiment Station 249:17–74

Iehara T, Fukuda M, Hosoda K, Ishibashi S, Nishizono T, Tanaka K, Kotani E, Kondo H, Matsuura Y (2003) Study on transparent and verifiable method of evaluating carbon sinks, Report of Global Environment Research Coordinate System, Ministry of the Environment, Japan. http://www.env.go.jp/earth/kenkyuhi/report/pdf/03_5_2_1.pdf (last Accessed at 7, Feb., 2022) (in Japanese)

Inagaki Y, Nakanishi A, Tange T (2020) A simple method for leaf and branch biomass estimation in Japanese cedar plantations. Trees 34:349–356

Ishii T, Nashimoto M, Shimogaki H (1998) Development of forest observation method using remote sensing data–Estimation of leaf area index, Annual Research Report. Central Research Institute of Electric Power Industry

Jarvis PG (1976) The interpretation of the variations in leaf water potential and stomatal conductance found in canopies in the field, philosophical transactions of the Royal Society of London, series. B. Biological Sciences 273:593–610

Kanazawa Y, Kiyono Y, Fujimori T (1985) Crown development and stem growth in relation to stand density in even-aged pure stands (II) clear-length model of Cryptomeria japonica stands as a function of stand density and tree height. Journal of the Japanese Forest Society 67(7): 391–397

Kawanabe S, Ando M (1988) Studies on regeneration of natural forest on lower limit of cool temperate deciduous broad-leaved forest V -biomass and growth in natural forest of Cryptomeria japonica. Bulletin of the Kyoto University Forests 60:67–76

Komatsu H, Sinohara Y, Kumagai T, Kume T, Tsuruta K, Xiang Y, Ichihashi R, Tateishi M, Shimizu T, Miyazawa Y, Nogata M, Laplace S, Han T, Chiu C, Ogura A, Saito T, Otsuki K (2014) A model relating transpiration for Japanese cedar and cypress plantations with stand structure. For Ecol Manag 334:301–312

Kondo J (1998) Dependence of evapotranspiration on the precipitation amount and leaf area index for various vegetated surfaces. Journal of Japan Society of Hydrology and Water Resources 11(7):679–693

Kondo J, Ishii M (1992) Estimation of rainfall interception loss from forest canopies and comparison with measurements. Journal of Japan Society of Hydrology and Water Resources 5(1): 27–34

Kondo J, Watanabe T (1991) A guide to study on evaporation from the complex land surface. Tenki 38(11):699–710. (in Japanese)
Kondo J, Watanabe T, Nakazono M, Ishii M (1992) Estimation of forest rainfall interception. Tenki 39(3):159–167. (in Japanese)
Leblanc SG, Chen JM, Fernandes R, Deering DW, Conley A (2005) Methodology comparison for canopy structure parameters extraction from digital hemispherical photography in boreal forests. Agric For Meteorol 129:187–207
Makkink GF (1957) Ekzameno de la formulo de Penman, Netherland. J Agric Sci 5:290–305
Mori M, Inuma M, Sato A, Saito K (1979) Managements and land use in Fagus crenata natural forest region in Tohoku district, Technical Report 5, Agriculture, Forestry and Fisheries Research Council
Nagai A (1993) Estimation of pan evaporation by Makkink equation, journal of Japan Society of Hydrology and Water. Resources 6(3):238–243
Nakai T, Sumida A, Daikoku K, Matsumoto K, van der Molen MK, Kodama Y, Kononov AV, Maximov TC, Dolman AJ, Yabuki H, Hara T, Ohta T (2008) Parameterization of aerodynamic roughness over boreal, cool-and warm-temperate forests. Agric For Meteorol 148(12): 1916–1925
Oda T (2015) Report of the river fund of the river foundation, Japan, Grand Number 27–1263-0006, http://public-report.kasen.or.jp/271263006.pdf. Accessed at 7, Feb., 2022 (in Japanese)
Saito H, Kan M, Shidei T (1966) Studies on the effects of thinning from small diameter trees (I). Changes in stand condition before and after thinning. Bulletin of the Kyoto University Forests 38:50–67
Saito TM, Nagai S, Yoshino J, Muraoka H, Saigusa N, Tamagawa I (2012) Functional consequences of differences in canopy phenology for the carbon budgets of two cool-temperate forest types: simulations using the NCAR/LSM model and validation using tower flux and biometric data. Eurasian Journal of Forestry Research 15(1):19–30
Saito H, Shidei T (1973) Studies on the productivity and its estimation methodology in a young stand of Cryptomeria japonica D. Don. Journal of the Japanese Forest Society 55(2):52–62
Saito H, Tamai S, Ogino K, Shidei T (1968) Studies on the effects of thinning from small diametered trees (III). Changes in stand condition after the second growing season. Bulletin of the Kyoto University Forests 40:81–92
Saito H, Yamada I, Shidei T (1967) Studies on the effects of thinning from small diameter trees (II). Changes in stand condition after single growing season. Bulletin of the Kyoto University Forests 39:64–78
Shaw RH, Pereira AR (1982) Aerodynamic roughness of a plant canopy: a numerical experiment. Agric Meteorol 26:51–65
Shinozaki K, Yoda Y, Hozumi K, Kira T (1964) A quantitative analysis of plant form-the pipe model theory I. Basic analysis, Japanese Journal of Ecology 14(3):97–105
Tadaki Y, Kawasaki Y (1966) Studies on the production structure of forest. IX. Primary productivity of a young Cryptomeria plantation with excessively high stand density. Journal of Japanese Forest Society 48(2):55–61
Tadaki Y, Ogata N, Nagatomo Y (1965) The dry matter productivity in several stands of cryptomeria japonica in Kyushu. Bulletin of the Government Forestry Experiment Station 173:45–66
Tadaki Y, Ogata N, Nagatomo Y (1967) Studies on production structure of forest. XI. Primary productivities of 28-years-old plantations of Cryptomeria of cuttings and of seedlings origin. Bulletin of the Government Forestry Experiment Station 199:47–65
Tange T, Kojima K (2010) Aboveground biomass data of anno growth monitoring stands of Cryptomeria japonica in the university Forest in Chiba. The University of Tokyo, miscellaneous Information, the Tokyo University Forests 49:1–6. (in Japanese)
Tani M (2016) Mizu to tuti to mori no kagaku. Kyoto University Press, Japan. (in Japanese)
Thornthwaite CW (1948) An approach toward a rational classification of climate. Geogr Rev 38(1): 55–94

Tsuruta K, Nogata M, Shinohara Y, Komatsu H, Otsuki K (2014) The correction coefficient for leaf area index measurement based on the optical method in a Japanese cedar forest. Bulletin of Kyusyu University Forest 95:88–92

van Gardingen PR, Jackson GE, Hernandez-Daumas S, Russell G, Sharp L (1999) Leaf area index estimates obtained for clumped canopies using hemispherical photography. Agric For Meteorol 94:243–257

Vertessy RA, Watson FGR, O'Sullivan SK (2001) Factors determining relations between stand age and catchment water balance in mountain ash forests. For Ecol Manag 143:13–26

Watanabe N, Kojima T, Shinoda S, Ohashi K, Tamagawa I, Saitoh T (2012) Observation and modeling of rainfall interception in evergreen forest and deciduous forest. Journal of Japan Society of Civil Engineers, Ser B1 68(4):I_1759–I_1764

Watanabe H, Moteki Y (2007) Growth progress and biomass in 92-years-old plantation of Japanese cedar. Bulletin of the Gifu Prefectural Research Institute of Forest 36:7–13. (in Japanese)

Whitely R, Medlyn B, Zeppel M, Macinnis-Ng C, Eamus D (2009) Comparing the penman-Monteith equation and a modified Jarvis-Stewart model with artificial neural network to estimate stand-scale transpiration and canopy conductance. J Hydrol 373:256–266

Yamaura Y, Yamada Y, Matsuura T, Tamai K, Taki H, Sato T, Hashimoto S, Murakami W, Toda K, Saito H, Nanko K, Ito E, Takayama N, Tsuzuki N, Takahashi M, Yamaki K, Sano M (2021) Modeling impacts of broad-scale plantation forestry on ecosystem services in the past 60 years and for the future. Ecosyst Serv 49:101271

Yuruki T (1964) Analytical studies on factors controling tree growth. Bulletin of the Kyushu University Forest 37:85–179

Chapter 12
Plant Pathogenic Oomycetes Inhabiting River Water Are a Potential Source of Infestation in Agricultural Areas

Koji Kageyama, Akihiro Hayano, Hina Kikuchi, Kayoko Otsubo, Haruhisa Suga, and Ayaka Hieno

Abstract In recent years, plant pathogenic oomycetes have become a cause of destruction of nature due to their contribution to new forest diseases and damages to agricultural production, and have attracted attention as important pathogens. It is essential to understand the ecology of pathogenic fungi to elucidate the causes of disease outbreaks. However, there has been little focus on how pathogenic fungi behave in the environment. In this study, we investigated several parameters of two representative genera of plant pathogenic oomycetes, *Pythium* and *Phytopythium* species, in terms of (a) their distribution in Japan, (b) seasonal variation from upstream to downstream of rivers with different anthropogenic impacts, (c) morphological and molecular phylogenetic characteristics of river water isolates and (d) pathogenicity. The results suggest that phytopathogenic oomycetes are naturally found in rivers and can act as pathogens when they invade agricultural production sites, indicating the need to pay attention to river water and irrigation water as one of the pathogen transmission routes.

Keywords *Pythium* · *Phytopythium* · Irrigation · Water supply · Crop production · Horticulture

12.1 Introduction

Oomycetes grow on filamentous mycelia like true fungi, but they belong to the kingdom Stramenopile (Chromista) and are genetically distantly related to true fungi (Cavalier-Smith and Chao 2006; Schroeder et al. 2013). In recent years, plant pathogenic oomycetes have attracted attention as important pathogens by

K. Kageyama (✉) · A. Hayano · H. Kikuchi · K. Otsubo · A. Hieno
River Basin Research Center, Gifu University, Gifu, Japan
e-mail: kageyama@green.gifu-u.ac.jp

H. Suga
Institute for Glyco-core Research, Gifu, Japan

F. Li et al. (eds.), *River Basin Environment: Evaluation, Management and Conservation*, https://doi.org/10.1007/978-981-19-4070-5_12

contributing to the destruction of nature through spreading new forest diseases and causing damage to agricultural production through new diseases (Kageyama 2015). The first step in disease control is to identify and classify the species of pathogens that cause the disease. In recent years, the introduction of molecular biological methods has opened major avenues for species classification (Kageyama 2014). In addition, it is essential to understand the ecology of pathogenic fungi to elucidate the causes of disease outbreaks. However, there has been little research on how pathogenic fungi behave in the environment.

12.1.1 Classification of Phytopathogenic Oomycetes

A molecular phylogenetic analysis of the taxonomic system within the oomycetes was conducted based on the nucleotide sequences of the small subunit (SSU), large subunit (LSU), internal transcribed spacer region of nuclear ribosomal DNA, and the mitochondrially encoded cytochrome oxidase gene 1 and 2 (Beakes and Sekimoto 2009; Martin 2000; Matsumoto et al. 1999; Robideau et al. 2011). Based on this analysis, oomycetes are divided into "basal oomycetes" and "crown oomycetes". The "basal oomycetes" include five orders, Haptoglossales, Eurychasmales, Haliphthorales, Olpidiopsidales, and Atkinsiellales, that do not form sexual organs, but form sporangium and zoospore, the asexual organs, instead. The "crown oomycetes" include six orders, Rhipidiales, Leptomitales, Pythiales, Albuginales, Saprolegniales, and Peronosporales, all of which have oogonium, antheridium and oospore as sexual organs, in addition to the asexual organ. This system was developed not only from the molecular phylogenetic analysis, but also considering their morphological, histological and ecological characteristics. The orders reported as plant pathogens are the Leptomitales, Pythiales, Albuginales, Saprolegniales, and Peronosporales, which consist of a highly evolved group of oomycetes. The phytopathogenic fungi used in this study are species that belong to the genera *Pythium* and *Phytopythium* of the order Pythiales.

It is estimated that more than 200 species of *Pythium* and *Phytopythium* have been described, of which over 50 new species have been described since 2000, and more than 300 species have not been described due to insufficient comparison with other species or lack of type strains (Schroeder et al. 2013).

12.1.2 Morphological Characteristics of Pythium *and* Phytopythium *Species*

Both these species grow into a mycelium when active. The nuclear phase of the mycelium is diploid, whereas fungi are usually haploid. The cell wall is made of cellulose and does not contain chitin, unlike fungi. The mycelium is usually

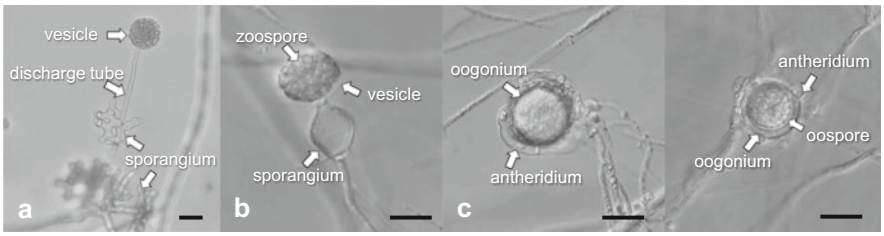

Fig. 12.1 Morphological characteristics of *Pythium* and *Phytopythium* species. (**a**, **b**) asexual propagative structures, filamentous sporangium (**a**), spherical sporangium (**b**). (**c**, **d**) sexual propagative structures, oogonia, antheridia, oospore. Bars = 20 μm

coenocytic without septa, and septa are found at the borders of various reproductive organs (van der Plaats-Niterink 1981; Waterhouse 1968).

During asexual reproduction, a spherical or filamentous sporangium is formed (Fig. 12.1a, b), and zoospores are produced in the spherical vesicle formed by the transfer of protoplasm from the sporangium through the discharge tube. The zoospores have two flagella of different lengths, a feather-shaped one, extending forward from the side of the cell, and a sheath shaped one extending backward. The zoospores play a role in expanding the habitat by swimming in water. The sexual reproductive organs are the oogonia in the female, the antheridia in the male, and the oospores are fertilized by these organs (Fig. 12.1c, d). In sexual reproduction, the diversity of the species is maintained by crossbreeding, and the thick-walled oospore formed by fertilization is a survival organ that can withstand the environment when nutrients are depleted until a new source of nutrients is found.

12.1.3 Habitat and Life Cycle of Pythium *and* Phytopythium *Species*

The habitats of *Pythium* and *Phytopythium* spp. vary from aquatic to terrestrial. For example, *Py. porphyrae* is a marine organism and is an important pathogen causing red rot in seaweed cultivation (Kawamura et al. 2005). *Phytopythium helicoides* is both aquatic and terrestrial and causes root rot in many plants such as rose, kalanchoe and poinsettia (Kageyama et al. 2002; Takahashi et al. 2014; Watanabe et al. 2007) and is soil-transmitted by its oospore. *Pythium intermedium* is a less virulent pathogen of crops and does not form zoospores. Instead, it forms hyphal swellings as asexual organs and adapts to the soil (Li et al. 2010, 2021).

In terms of their life cycle, they adapt to their living environment by strategically forming asexual and sexual reproductive organs. When infecting organic matter or roots, the mycelium actively absorbs nutrients while simultaneously the sporangium is formed and the zoospores with flagella released from the sporangium are used to swim and spread through the water. They are attracted to new organic matter and to attractants leached from the roots of the host plant. After attaching to organic matter

or roots, the flagella are discarded and the zoospore becomes an encysted spore. The encysted spores germinate on the surface to which they are attached and infect organic matter and roots by invading through their mycelium. After absorbing all the nutrients, they form sexual structures. The oospores germinate in response to new organic matter or host-approaching attractants and become infectious (Kageyama 2014).

12.1.4 Pythium *and* Phytopythium *Species as Plant Pathogens*

Many species of *Pythium* and *Phytopythium* live as saprophytic fungi that decompose organic matter such as fallen leaves (Hendrix and Campbell 1973; Jacobs 1982). However, some species are parasitic on living plants such as crops and destroy them. Phytopathogenic species cause a wide range of plant diseases, including seed rot, seedling blight, and root rot of mature plants. In addition, a single species can be pathogenic to multiple plants. For example, *Py. aphanidermatum* has been reported on 43 species of crops in Japan, including soybean blight, cucumber root rot, watermelon rot, geranium stem rot, chrysanthemum blight, and Alstroemeria rhizome rot. *Phytopythium helicoides* has been reported on 14 species of crops in Japan, including strawberry root rot, chrysanthemum vertical blight, verruca root rot, gerbera root rot, and lotus rot. Occasionally, multiple *Pythium* and *Phytopythium* pathogens cause different diseases even on the same plant. Seedling blight of *Pp. vexans,* root rot of *Py. myriotylum*, and cotton rot of *Py. aphanidermatum* have been reported in tomato plants (Gene Bank of Agricultural Production Resources, https://www.gene.affrc.go.jp/databases-micro_pl_diseases.php).

In recent years, protected horticulture and hydroponic cultivation that are less affected by external environmental conditions have been developed to ensure stable agricultural production. In both cases, the plants are cultivated in a closed space and at a constant temperature, which is preferable for the plants, but since the temperature is kept at an optimum level with little temperature variation and the conditions are humid, they are conducive for the growth of *Pythium* and *Phytopythium* spp. In addition, in facility cultivation, anniversary cultivation is carried out for effective use of facilities. These conditions facilitate the growth of *Pythium* and *Phytopythium* spp. that are tolerant to high temperatures (optimum growth temperature around 35 °C) in the summer and induce damage.

12.1.5 *Distribution of Plant Pathogenic* Pythium *and* Phytopythium *Species*

The distribution of *Pythium* and *Phytopythium* spp. has been investigated in agricultural soils, irrigation water and reservoirs (Abdelzaher et al. 1994a, b, 1995;

Jacobs 1982; Hong and Moorman 2005; Nechwatal et al. 2008; Sánchez and Gallego 2000; Watanabe 1981, 1984), but few studies have been conducted in non-agricultural areas such as forests and rivers (Abdelzaher and Kageyama 2020). *Pythium, Phytophthora*, and *Phytopythium* spp. have been reported to be isolated from forest soil and river water in non-crop areas, and *Pp. helicoides* and *Py. myriotylum*, which are also plant pathogens, from forest soil and river water in the subtropical and cool temperate regions of Japan (Kageyama 2010). Although irrigation water has been investigated in other countries (Zappia and Hüberli 2014), there have only been few studies in non-agricultural areas, conducted in Korea (Nam and Choi 2019) and USA (Shrestha et al. 2013).

If plant pathogens are found in rivers, the use of river water through agricultural canals to irrigate crops and as culture media for nutrient cultivation would mean the artificial introduction of a primary source of infection. In addition, in recent years, guerrilla rains caused by abnormal weather conditions have resulted in river flooding, increasing the likelihood of river water intruding into farmland. Since river flooding is widespread, it may lead to the expansion of pathogen infestations regionally. Therefore, investigating *Pythium* and *Phytopythium* spp. that pose a threat to agricultural production in the natural environment can contribute to providing some guidelines for disease control measures.

12.1.6 Objectives of this Study

In this study, we investigated the hypothesis that pathogenic species such as *Pythium* and *Phytopythium* spp. present in river water invade agricultural production sites and cause damage to agricultural crops in Japan. Toward this end, we tested several parameters, including (a) the distribution of *Pythium* and *Phytopythium* spp. (b) seasonal variation of their distribution from upstream to downstream of rivers with different anthropogenic impacts, (c) morphological and molecular phylogenetic characteristics of river water isolates and (d) their pathogenicity.

12.2 Materials and Methods

12.2.1 Isolation of Pythium *and* Phytopythium *Species from Water*

Thirty to fifty grass blades cut into 5 mm pieces were placed in a 250 ml plastic bottle, which was sterilized by autoclaving and used as a sampling bottle. The water from the river was collected from a location where the river flow was slow and where organic matter such as fallen leaves had accumulated. Two samples were taken by filling the bottle with about 80% volume of river water (Fig. 12.2). After one week of

Fig. 12.2 Sampling and baiting methods for isolation of *Pythium* and *Phytopythium* species from water

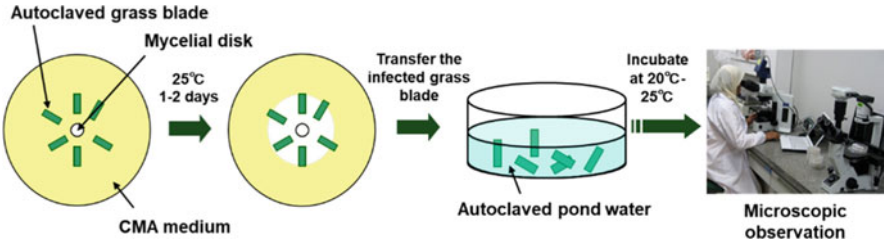

Fig. 12.3 Method for morphological observation

incubation at 25 °C, the grass pieces were collected on paper towels, lightly drained, and placed on NARM medium (Morita and Tojo 2007), a selective medium for *Pythium* spp.

The NARM medium was sterilized by adding 17 g/L of corn meal agar (Becton, Dickinson and Company) and 10 g/L of bacto agar (Becton, Dickinson and Company), and then cooled to about 50 °C. The mixture was prepared by adding 10 mg/L of nystatin, 250 mg/L of ampicillin sodium, 250 mg/L of rifampicin, and 1 mg/L of miconazole nitrate (all from Wako Pure Chemical Industries, Ltd.). The mycelial tips were transferred to CMA slope medium and used as isolates.

12.2.2 Species Identification of the Isolates

Morphological characteristics and DNA sequences were used to identify the species of isolates.

Morphological observations were made using the grass-blade method (Waterhouse 1967, 1968), which involves infecting grass blades with the isolate and floating it on water (Fig. 12.3). Sections (1.0–1.5 cm) of turfgrass were sterilized by high pressure steam and incubated in the dark at 25 °C for 1–3 days. Sections of grass blades infected with the fungus were floated in a 1: 2 mixture of filtered pond water and distilled water sterilized by high-pressure steam and incubated in the dark at 20 °C for 1–7 days. The morphology of asexual organs such as sporangium, spermatogonia, and oocysts was observed under a microscope.

In oomycetes, the internal transcribed spacer region of rDNA (the rDNA-ITS region) and mitochondrial cytochrome c oxidase subunit 1 gene coding region (*cox*1) are recognized as useful DNA barcode regions capable of accurate species identification (Robideau et al. 2011). Therefore, we carried out the BLAST search based on the sequences of ITS and *cox*1. DNA was extracted from mycelia using PrepMan Ultra Reagent (Thermo Fisher Scientific, Tokyo, Japan) according to the manufacturer's instructions. PCR was conducted using the ITS4 (5-′-TCCTCCGCTTATTGATATGC-3′) and ITS5 (5-′-GGAAGTAAAAGTCGTAACAAGG-3′) primers for the rDNA-ITS region, and OomCoxI-Levup (5′-TCAWCWMGATGGCTTTTTTCAAC-3′) and Fm85mod

(5′-RRHWACKTGACTDATRATACCAAA-3′) primers for *cox*1, according to the method described by White et al. (1990) and Robideau et al. (2011), respectively. The 25 µl reaction mixtures contained 1 µl DNA, 2 µM of each primer, 0.4 mg/ml BSA, 0.4 mM dNTPs, 0.125 U of TaKaRa Taq DNA polymerase (Takara Bio, Kusatsu, Japan), and PCR buffer (10 mM Tris–HCl, pH 8.3, 50 mM KCl, and 1.5 mM $MgCl_2$). The PCR reactions were carried out in a T100 DNA Thermal Cycler (Bio-Rad Laboratories, Hercules, CA, USA). The rDNA-ITS region and *cox*1 were amplified under the following conditions: 94 °C for 2 min, followed by 35 cycles at 94 °C for 1 min, 55 °C for 30 s (annealing step), 72 °C for 1 min, with a final extension at 72 °C for 10 min. PCR products were checked for successful amplification by electrophoresis in 2% (w/v) agarose gels (Agarose S, FUJIFILM WAKO, Tokyo, Japan). The PCR product was purified using ExoSAP-IT Express (Thermo Fisher Scientific). Sequencing of the purified PCR product was performed using BigDye Terminator v3.1 (Thermo Fisher Scientific).

For the strains that showed two bands in electrophoresis, the DNA was collected by cutting the band of the target size from the electrophoresed gel. For DNA extraction from the gel, Thermostable β-Agarase (NIPPON GENE CO., LTD., Tokyo, Japan) was used according to the manufacturer's instructions, and BigDye Terminator v3.1 was used for sequencing as before.

The rDNA-ITS region could not be sequenced in some cases due to intra-strain polymorphism; in which case, PCR products were cloned using the TOPO TA Cloning Kit for Sequencing (Thermo Fisher Scientific) according to the instructions. Direct PCR was performed from the colonies formed on the culture medium by cloning. The primers used were M13M4 (5'-GTTTTCCCAGTCACGAC-3′) and M13rv (5'-CAGGAAACAGCTATGAC-3′). The PCR was performed using the same reaction solution composition and reaction conditions as for the ITS region. For sequencing, BigDye Terminator v3.1 was used as before.

The nucleotide sequences were subjected to BLAST searches using DNA Data Bank of Japan (DDBJ; http: //www.ddbj.nig.ac.jp/index-j.html), and species with high homology were selected as candidate species.

Phylogenetic analysis of representative isolates in all species recovered from river water was conducted based on the sequences of the rDNA ITS region (Table 12.1). The phylogenetic tree was constructed from the sequences aligned using Clustal X and MEGA X software (Kumar et al. 2018) with the maximum-likelihood method and Tamura-Nei model (Tamura and Nei 1993). Bootstrap values were calculated with 1000 replicates.

12.2.3 Pathogenicity Test

To determine whether the widely distributed riverine strains of *Pp. helicoides, Py. myriotylum* and *Py. dissotocum* are actually pathogenic to plants, we conducted pathogenicity tests on crops that have been reported as hosts. Inoculation tests were

Table 12.1 List of *Pythium* and *Phytopythium* isolates used in phylogenetic analysis

Isolate	Isolation year	Location	Species
FIW5–11	2010	Fukui	*Py. aphanidermatum*
FIW5–13	2010	Fukui	*Py. arpisium*
GF19JW1–1-6	2019	Gifu	*Py. arrhenomanes*
GF19JW4–2-3	2019	Gifu	*Py. apleroticum*
GF20AW2–1-1	2020	Gifu	*Py. oopapillum*
GU20SRW1–2-1	2020	Gifu	*Pp. vexans*
HOW1–6	2010	Hokkaido	*Pp. litorale*
HSW1–11	2013	Hiroshima	*Py. myriotylum*
HSW2–1	2013	Hiroshima	*Py. catenulatum*
HSW3–11	2013	Hiroshima	*Py. oopapillum*
IKW1–6	2014	Ishikawa	*Py. inflatum*
ITW1–3	2014	Iwate	*Py. apleroticum*
ITW2–4	2014	Iwate	*Pp. helicoides*
MGW1–9	2014	Miyagi	*Py. dissotocum*
NRW2–3	2010	Nara	*Py. irregulare*
On11W3–2	2011	Okinawa	*Py. myriotylum*
On11W3–3	2011	Okinawa	*Pp. helicoides*
On11W6–2	2011	Okinawa	*Py. inflatum*
On11W9–8	2011	Okinawa	*Pp. vexans*
SGW1–1	2010	Saga	*Py. aphanidermatum*
SZW4–2	2012	Sizuoka	*Pp. litorale*
SZW10–14	2012	Shizuoka	*Py. catenulatum*
SZW12–2	2012	Shizuoka	*Py. marsipium*
TTW2–7	2012	Tottori	*Py. dissotocum*
TTW3–1	2012	Tottori	*Py. arrhenomanes*

conducted on sedum and gerbera plants grown in soil, and on lettuce and tomato plants grown hydroponically.

12.2.3.1 Pathogenicity Test by Soil Cultivation

Three isolates of *Pp. helicoides*, GF19AgW 2–2-3, GF19AgW 3–2-2, and GF19OW 4–2-3, were isolated from the Ijira river in Gifu Prefecture, Japan.

Pathogenicity tests by soil inoculation were conducted on sedum and gerbera plants, which have been reported as hosts of *Pp. helicoides* (Hayashi et al. 2018; Suzuki et al. 2009). In the case of sedum, cell trays (40 mm × 40 mm × 40 mm/cell) were filled with horticultural culture soil (Hanogokoro Co., LTD., Nagoya, Japan) that had been sterilized by high-pressure steam (120 °C, 60 min). The plants were cultivated for three weeks (25 °C, 12 h light: 12 h dark). For gerbera, the seeds (variety: Festival Scarlet Eye) were treated with 10% hydrogen peroxide water for 20 minutes and washed three times with sterile water to sterilize the surface. Two

seeds per square were sown in cell trays prepared in the same way as for sedum, and the trays were thinned as necessary so that one seedling remained and cultivated for four weeks.

The inoculum source was prepared as follows: 2 g of bentgrass seeds and 10 ml of distilled water were placed in a 200 ml flask and sterilized by high-pressure steam. Five sheets of fungus-containing agar were placed in the flask, and the tips of the mycelium of the test strain, which had been cultured on CMA medium for 2 days (25 °C, dark), were punched out with a 4-mm diameter cork borer. After 3 weeks, 50 ml of sterile water and the culture were mixed in a homogenizer and this fungal suspension was used as the inoculum source. The control was cultured in the same way with plain agar instead of fungus-containing agar.

For inoculation, five sedum seedlings were transplanted into a polycarbonate box (13.2 cm × 8.9 cm × 5.8 cm) filled with sterilized culture soil, and 5 ml of the fungal suspension was inoculated per plant. After inoculation, the plants were cultivated in an artificial climate for 4 weeks (25 °C, 12 h light: 12 h dark). For gerbera, the roots of the grown seedlings were washed under running water and then immersed in the fungal suspension for 1 minute. After that, gerberas were planted in cell trays (50 mm × 50 mm × 50 mm/cell) with high-pressure steam sterilized culture soil and cultivated for two weeks in an artificial climate machine under the same conditions.

For investigating disease development, the soil on the roots was washed with running water and the condition of the roots was evaluated. Disease development was evaluated by the disease index (0 = no disease to 3 = significant delay in growth and severe root browning) based on the condition of the above-ground parts and roots. The disease severity was calculated from the disease index by the following formula:

$$\text{Disease severity} = \{\Sigma(\text{disease index} \times \text{number of plants})/(\text{number of seeds} \times 3)\} \times 100$$

For re-isolation, diseased parts of five individual plants were placed on a 9 cm Petri dish of NARM medium (see above) after the disease survey. This was incubated in an incubator (25 °C, in the dark) for 1–2 days to check for mycelial growth.

12.2.3.2 Pathogenicity Test by Hydroponics

For hydroponic cultures, the following isolates were used: for *Pp. helicoides*, GF19AgW2–2-3, GF19AgW3–2-2, and GF19OW4–2-3; for *P. dissotocum*, GF19AW4–1-3, GF19AgW1–2-1, and GF19OW1–2-2, and for *P. myriotylum*, GF20JW2–2-3, GF20AgW2–2-2, and GF19OW4–2-3.

Lettuce, which has been reported as a host for *Pp. helicoides* and *Py. dissotocum* (Stanghellini and Kronland 1986) and tomato, which has been reported as a host for *Py. myriotylum* (Feng et al. 2018), were used as test plants. Surface sterilization was

performed for both by treating them with 10% hydrogen peroxide water for 20 min followed by rinsing with sterile water three times.

Before inoculation, lettuce seeds (variety: Green Wave) were placed in a glass Petri dish (pore size: 8.5 cm) lined with a Kim-towel moistened with sterile water and grown in an artificial climate machine for 2 days. Tomatoes were grown in a hydroponic kit (20 cm × 6 cm × 5 cm, Living Farm Co., Ltd. Japan) by placing surface sterilized tomato seeds (cultivar: House Momotaro) in the slits on a sponge with slits. Liquid fertilizer was applied during the first week of culture.

For inoculation of lettuce, 4 mm diameter mycelium tips of the test strain cultivated on CMA medium for 2 days (25 °C, in the dark) were placed along with the seeds in the slits of the sponge of the hydroponics kit described above, and cultivated for 3 weeks at 20 °C with 12 h of light and 12 h of darkness. For tomatoes, fungus-containing agar made in the same way as for lettuce was placed in the sponge slit from the side of the tomato seedlings and incubated for three weeks at 25 °C with 12 h light and 12 h of darkness.

The disease survey and re-isolation were done in the same way as in the soil cultivation.

12.3 Results and Discussion

12.3.1 Distribution of Phytopathogenic Oomycetes in Water Systems in Japan

In order to investigate the flora of *Pythium* and *Phytopythium* species in water systems in Japan, we collected isolates from rivers and irrigation water in 10 regions and 20 prefectures throughout Japan from 2007 to 2020. Either or both species of both genera were detected in all survey sites. Many of the isolates did not form sexual organs even though the identified species originally sexually reproduced, and the asexual organs formed filamentous or swollen filamentous, earlobe-shaped, or club-shaped sporangia, which released a large number of zoospores in water. A BLAST search of these strains based on the nucleotide sequence of the rDNA ITS region or the *cox*1 gene, which is the DNA barcoding region of oomycetes (Robideau et al. 2011), revealed many strains that appeared to be new species.

Some of the isolates were reported as phytopathogenic species and their distribution pattern revealed that they are widely distributed in rivers, even though the survey sites, except for irrigation water, were mainly in forested areas upstream of rivers. We detected a large number of species, including 10 *Pythium* spp. and 3 *Phytopythium* spp. *Py. dissotocum*, *Py. catenulatum*, and *Pp. helicoides* detected in more than 10 prefectures. The next most frequent species were *Py. arrhenomanes*, *Py. marsupium*, *Py. myriotylum*, *Py. oopapillum*, and *Pp. litorale*, which were detected in 6 to 9 prefectures. The others were *Py. apleroticum*, *Py. aphanidermatum*, *Py. inflatum*, *Py. irregulare*, and *Pp. vexans* isolated in one to

three prefectures (Table 12.2, Fig. 12.4). *Pythium inflatum*, *Py. oopapillum*, *Pp. litorale* and *Pp. vexans* were also isolated from forest water in Korea (Nam and Choi 2019). *Pythium apleroticum*, *Pp. helicoides*, *Pp. litorale* and *Pp. vexans* were isolated in Tennessee, USA (Shrestha et al. 2013).

Comparing the species detected in irrigation water with those in river water, we found no unique species, with the same species detected in irrigation water also seen in river water. However, *Py. irregulare* was detected only at one site in irrigation water, and *Py. aphanidermatum* was detected at two sites, one of which was irrigation water.

We did not observe any regional bias in the species detected. For example, *Py. myriotylum* and *Pp. helicoides*, which are known to be tolerant to high temperatures, were not found more frequently in southern regions, but were found even in northern regions such as Yamagata and Iwate prefectures. In addition, there was no region where a particularly large number of species was detected.

12.3.2 *Positional and Seasonal Variations of Phytopathogenic* Pythium *and* Phytopythium *Fauna in Ijira River, Gifu, Japan*

Rivers are influenced by human activities such as agriculture and drainage as they move downstream. It is interesting to investigate whether the impact of human activities on rivers can be assessed by studying the changes in the diversity of *Pythium* and *Phytopythium* fauna depending on the location of the river. In addition, examining the seasonal variation of both the genera and the species at the same site will provide important information for setting the timing of the mycological survey and for discussing the results of the survey. We chose the Ijira river, which is a tributary of the Nagara river and flows from Yamagata City to Gifu City in Gifu Prefecture, as the study river, and four sites (A-D; A: upstream, B: upper midstream; C: lower midstream; D: downstream) (Table 12.3) were set up from upstream to downstream of this river. River water was collected every two months from February 2019 to December 2020, and the detected species were examined.

We detected 8 *Pythium* species and 2 *Phytopythium* species in the Ijira river, and the number of species detected was almost the same as the number of species detected in the Japan survey (10 and 3, respectively). The species that were not detected in the Ijira river were *Py. aphanidermatum, Py. irregulare* and *Pp. vexans*, all of which have rarely been detected in Japan (Table 12.3). On the other hand, *Py. dissotocum, Py. catenulatum, Py. marsipium, Py. oopapillum* and *Pp. helicoides* were detected in many sites as in other areas of Japan (Fig. 12.4). In comparison with the 18 other rivers and irrigation water sources in Gifu Prefecture, the number of species detected in the Ijira River was 10, whereas the number of species detected in Gifu Prefecture was 8, including *Phytopythium* species (Tables 12.2 and 12.3).

Table 12.2 Phytopathogenic *Phytopythium* and *Pythium* species isolated from rivers, lakes, and irrigation water from 2007 to 2018

Sampling site and year			Sites[a] and numbers		*Pythium*[b]										*Phytopythium*[c]		
					Aph	*Apl*	*Arr*	*Cat*	*Dis*	*Inf*	*Irr*	*Mar*	*Myr*	*Oop*	*Hel*	*Lit*	*Vex*
Hokkaido		2010, 2011	Ri	3					○							○	
Tohoku region																	
	Akita	2014	Ri	1					○								
	Iwate	2014	Ri	2		○			○					○	○		
	Yamagata	2014	Ri	3					○			○	○		○		
			Ic	3					○				○		○		
	Miyagi	2014	Ri	2					○					○	○		
Koshinetsu region																	
	Yamanashi	2012	Ri	5			○	○	○								
			Ic	1				○	○								
Hokuriku region																	
	Ishikawa	2014	Ri	4			○		○	○				○		○	○
	Fukui	2010	Ri	5	○			○					○		○		
Tokai region																	
	Shizuoka	2012, 2013	Ri	5			○	○	○			○			○		
			Ic	2				○	○			○			○	○	
	Gifu	2010, 2012	Ri	15				○	○			○	○	○	○		
		2014, 2019	Ic	3											○		
	Aichi	2008, 2009	Ic	7			○		○						○	○	
Kinki region																	
	Nara	2010	Ic	3							○				○		
Chugoku region																	
	Hiroshima	2013	Ri	3			○	○	○				○	○	○		
	Tottori	2012	Ri	4			○	○	○						○		

(continued)

Table 12.2 (continued)

Sampling site and year			Sites[a] and numbers		*Pythium*[b]										*Phytopythium*[c]		
					Aph	*Apl*	*Arr*	*Cat*	*Dis*	*Inf*	*Irr*	*Mar*	*Myr*	*Oop*	*Hel*	*Lit*	*Vex*
	Okayama	2013	Ri	2			○					○		○	○		
	Yamaguchi	2018	Ri	2									○		○		
Shikoku region																	
	Ehime	2012	Ri	6									○		○		
Kyushu region																	
	Saga	2010	Ic	4	○			○				○			○		
	Kagoshima (Amami Island)	2018	Ri	7					○						○	○	
Okinawa region																	
	Main Island	2011	Ri	4								○				○	○
			Ic	6						○			○		○		

[a] Ri: River, Ic:irrigation canel

[b]Aph: *P. aphanidermatum*, *Apl: P. apleroticum, Arr: P. arrhenomanes, Cat: P. catenularum, Dis: P. dissotocum, Inf: P. inflatum,* Irr*: P. irregulare*, Mar: *P. marpsium*, Myr: *P. myriotylum*, Oop; *P. oopapillum*

[c]Hel: *Pp. helicoides*, Lit: *Pp. litorale*, Vex: *Pp. vexans*

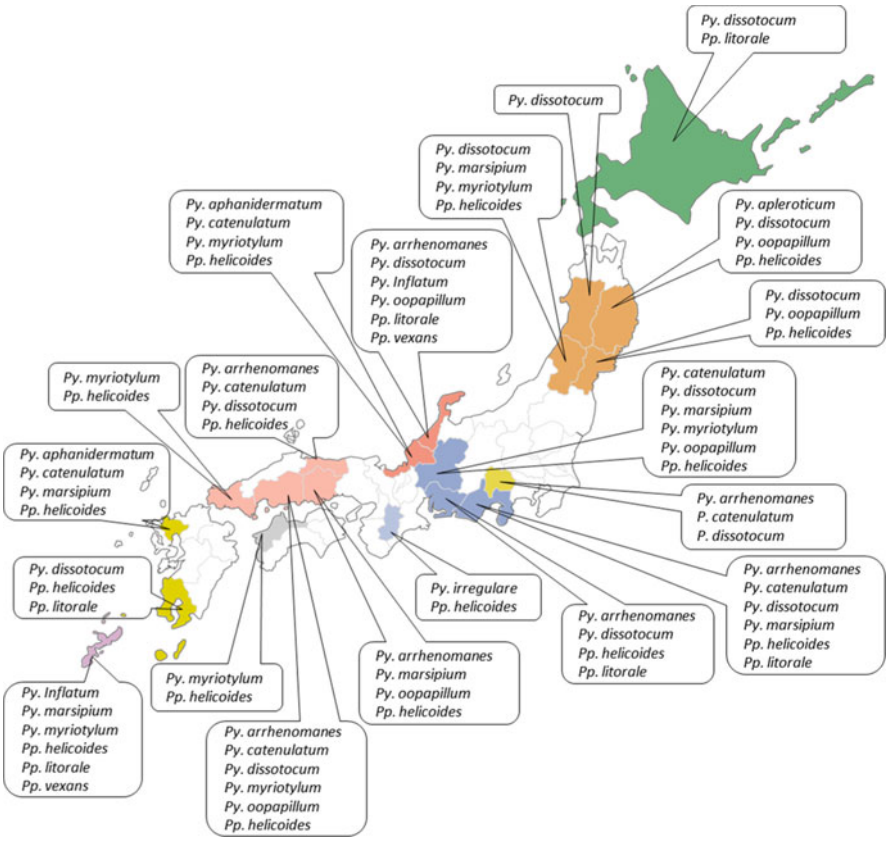

Fig. 12.4 Distribution of plant pathogenic *Pythium* and *Phytopythium* species in river waters in Japan

Pythium arrhenomanes, Py. apleroticum and *Pp. litorale* were detected in the upper to middle streams of the river, while *Py. catenulatum*, *Py. marsipium* and *Pp. helicoides* were not detected in the upper stream (Site A; Table 12.3). On the other hand, *Py. dissotocum* and *Py. oopapillum* were detected from upstream to downstream regardless of location (Table 12.3). The diversity tended to be low in the upstream of the river, with the highest diversity at site B in the upper-middle streams, where all eight species of *Pythium* spp. that were detected in other survey sites in the Ijira River were detected, and two of the three *Phytopythium* species was detected.

With regards to yearly variation (Table 12.3), *Pythium apleroticum* and *Pp. litorale* were detected only in 2019 in the upstream to midstream areas (sites A, B, and C, respectively). On the other hand, *P. inflatum* and *P. myriotylum* were detected only in 2020 in the upstream to midstream areas (sites B and C, respectively).

In terms of seasonal variation, high-temperature tolerant *Pp. helicoides* was not detected during the winter months of December to February (water temperature

Table 12.3 Positional and seasonal variation of plant pathogenic Phytopythium and Pythium fauna in water from upstream to downstream of Ijira river in Gifu, Japan

Sampling date		Isolated phytopathogenic species			
		Site A	Site B	Site C	Site D
2019	Feb.		*P. dissotocum*	*Phpy. litorale*	
		-		*P. catenulatum*	
				P. dissotocum	
	Apl.	*Phpy. litorale*	*P. oopapillum*	*P. dissotocum*	*P. dissotocum*
		P. dissotocum			
	Jun.	*P. oopapillum*	*Phpy. litorale*	*Phpy. litorale*	*Phpy. helicoides*
				P. catenulatum	
	Aug.	*P. arrhenomanes*	*Phpy. helicoides*	*Phpy. helicoides*	*Phpy. helicoides*
		P. dissotocum			
	Oct.	*P. dissotocum*	*P. apleroticum*	*Phpy. helicoides*	*P. marsipium*
		P. apleroticum	*P. marsipium*	*P. arrhenomanes*	*P. oopapillum*
	Dec.	*P. dissotocum*	*P. dissotocum*	*P. dissotocum*	
			P. oopapillum		
2020	Feb.		*P. dissotocum*	*P. dissotocum*	*P. dissotocum*
	Apl.	*P. dissotocum*	*P. dissotocum*	*P. catenulatum*	*Phpy. helicoides*
			P. oopapillum	*P. dissotocum*	*P. catenulatum*
					P. dissotocum
					P. oopapillum
	Jun.	*P. dissotocum*	*P. arrhenomanes*	*Phpy. helicoides*	*P. dissotocum*
			P. dissotocum	*P. dissotocum*	*P. inflatum*
			P. myriotylum	*P. marsipium*	*P. marsipium*
					P. oopapillum
	Aug.	*P. dissotocum*	*Phpy. helicoides*	*Phpy. helicoides*	
			P. marsipium	*P. marsipium*	
			P. myriotylum		
	Oct.		*Phpy. helicoides*	*P. dissotocum*	*Phpy. helicoides*
			P. dissotocum	*P. marsipium*	*P. catenulatum*
			P. marsipium		*P. dissotocum*
			P. oopapillum		*P. marsipium*
	Dec.		*P. catenulatum*	*P. dissotocum*	*P. catenulatum*
			P. dissotocum		*P. oopapillum*
			P. oopapillum		

8–18 °C, Table 12.3, Fig. 12.5). *P. myriotylum*, another species tolerant to similar levels of high temperatures, was detected only twice during the summer months of June and August (water temperature 24 °C and 31 °C, respectively). On the other hand, *Py. dissotocum* was detected throughout the year regardless of season, even though its optimum growth temperature was 25 °C, suggesting that it might have a wide range of temperature adaptation.

The number of species detected tended to be high in the relatively warm months between June and October (water temperature: 16–26 °C), although it was lower in

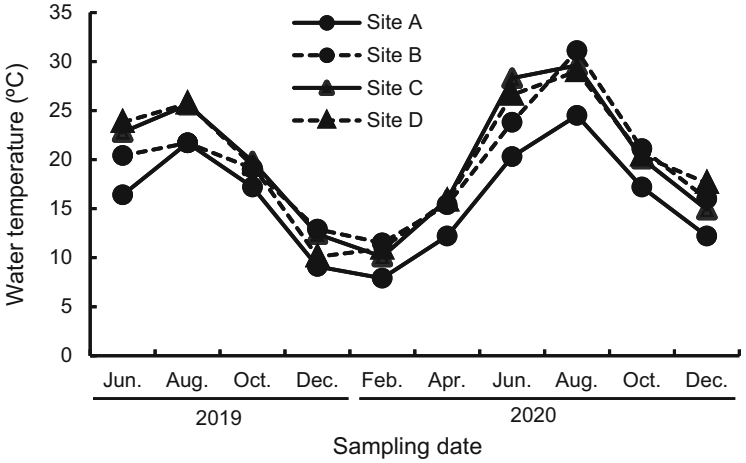

Fig. 12.5 Seasonal changes in water temperature in Ijira river located in Gifu prefecture, Japan

August (water temperature: 22–31 °C), the middle of summer, regardless of whether it was upstream or downstream. However, *Py. dissotocum*, *Py. catenulatum*, and *Py. oopapillum* were also detected in the winter months of December through February (water temperature 8–18 °C). It is not clear whether the survival form of *Py. dissotocum*, *Py. catenulatum*, and *Py. oopapillum* at this time was that of active zoospores or not.

These results suggest that *Py. dissotocum*, a pathogen of rice that is isolated more frequently upstream, may be a threat in rice paddies. *Pythium myriotylum* and *Pp. helicoides,* which have a wider host range, are found in the middle and down streams of the river, indicating that the use of river water for hydroponics is dangerous. It is also possible that these pathogens may enter the river with the effluent from the cultivation facilities.

From our results, it is apparent that the best time to conduct the survey of *Pythium* and *Phytopythium* fauna, is in June and October, when the water temperature is warm (15–25 °C). In addition, we consider that the middle streams of rivers are the best sites for the survey of plant pathogens.

12.3.3 Morphological Characteristics of Strains Isolated from Rivers

Next, we set out to understand the morphology of the sporangium, the organ that forms zoospores, and the characteristics of the sexual organs, which are durable survival organs in aquatic species compared to those species that live mainly in soil.

Pythium species we detected in water in this study were overwhelmingly the species that formed filamentous sporangia and had a high ability to form zoospores from the sporangia, even though they were not plant pathogens. Eight of the ten phytopathogenic *Pythium* species we detected (*Py. apleroticum*, *Py. aphanidermatum* (Fig. 12.6a-c), *Py. arrhenomanes* (Fig. 12.6d-f), *Py. catenulatum* (Fig. 12.6g-h), *Py. dissotocum* (Fig. 12.6i-k), *Py. inflatum*, *Py. myriotylum* (Fig. 12.7a-c) and *Py. oopapillum*) formed filamentous sporangia. For the genus *Phytopythium*, we detected three species in this study, *Pp. helicoides* (Fig. 12.7d-f), *Pp. littorale* (Fig. 12.7g-i), and *Pp. vexans* (Fig. 12.7j-l), with the first two forming sporangia with papillae and the latter forming sporangia without papillae.

Phytopythium litorale is not capable of forming sexual organs (Nechwatal and Mendgen 2006). The strains identified as *Py. inflatum, Py. marsipium*, and *Py. oopapillum* were reported to form sexual organs (van der Plaats-Niterink 1981), but in our observations, they only formed asexual organs. Among *Py. arrhenomanes*, *Py. dissotocum* and *Pp. helicoides*, although some strains formed sexual organs, most formed only asexual organs. Some strains of *Pp. helicoides* have been reported to have lost the ability to form sexual organs despite their pathogenicity (Kageyama et al. 2003) These asexual reproductive organ-dependent life cycles suggest that aquatic fungi have strong saprophytic capacity and lose the ability to form sexual organs as they are able to survive due to the constant supply of nutritive organic matter in water unlike in field soil, and don't need to resort to forming survival structures.

The characteristics of the sexual organs differ among species: the oogonia of *Py. arrhenomanes*, *Py. myriotylum*, and *Pp. helicoides* have a smooth surface and are large (around 30 μm), whereas those of *Py. dissotocum* and *Pp. vexans* are around 20 μm in size. *Pythium irregulare* has spines on the oogonia and is smaller than 20 μm in size. *Pythium catenulatum* does not form sexual organs in a single culture but forms them in mating culture with compatible strains. The sexual organs of the species isolated from water did not have any special features unlike that of asexual organs.

12.3.4 Molecular Phylogenetic Analysis of Strains Isolated from Rivers

In order to determine the molecular phylogenetic position of the isolates recovered from river and irrigation water, we constructed a molecular phylogenetic tree based on the nucleotide sequence of the rDNA-ITS region for both *Pythium* and *Phytopythium* (Table 12.1; Figs. 12.8 and 12.9).

In the genus *Pythium*, the morphological characteristic of the sporangium, (both filamentous and spherical sporangia), is to form a large cluster, which is the first divergence point in the molecular phylogeny (Lévesque and de Cock 2004; Matsumoto et al. 1999; Martin 2000; Villa et al. 2006). We identified that the

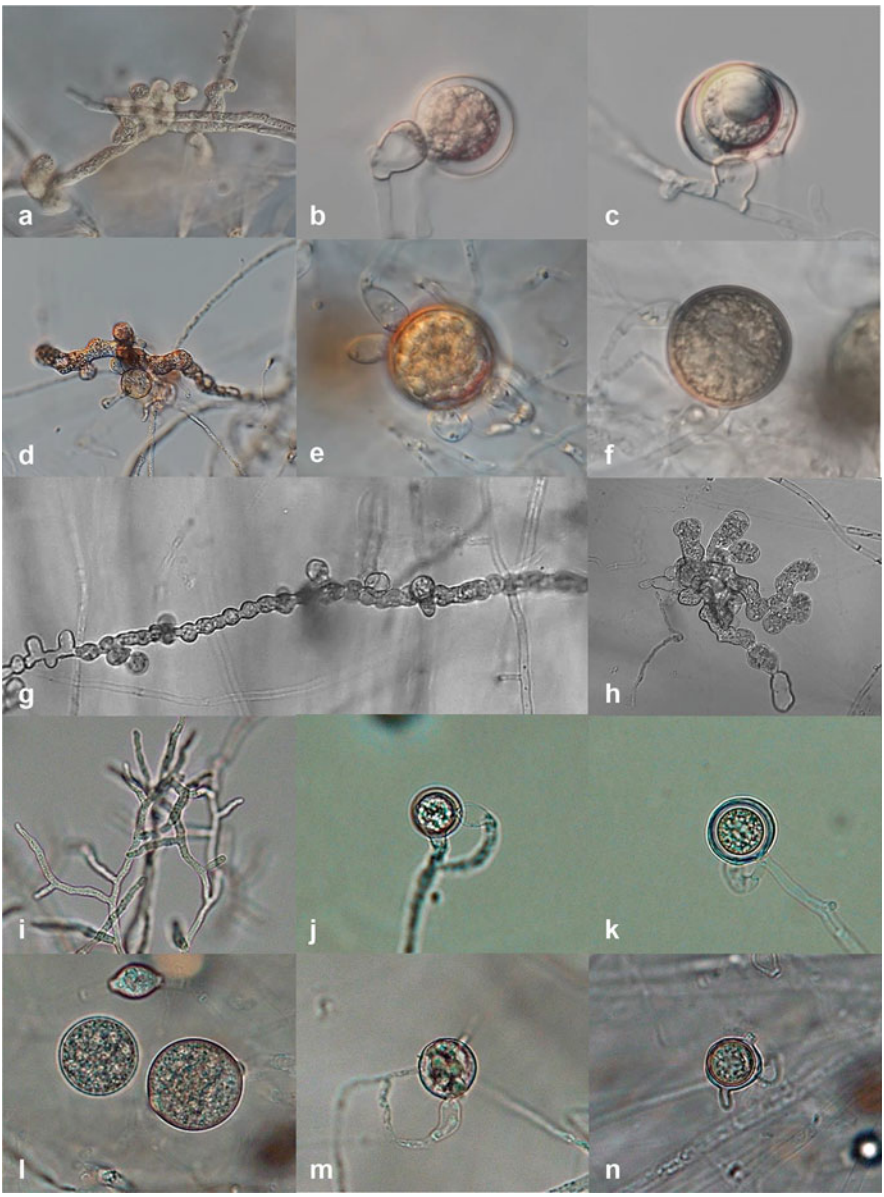

Fig. 12.6 Morphological characteristics of *Pythium aphanidermatum*, *Py. arrhenomanes*, *Py. catenulatum*, *Py. dissotocum* and *Py. irregulare*. (**a**-**c**) *Py. aphanidermatum*, (**a**) filamentous inflated sporangium, (**b**, **c**) smooth oogonium with an intercalary antheridium and aplerotic oospore, (**d**-**f**) *Py. arrhenomanes*, (**d**) lobulate sporangium, (**e**, **f**) smooth oogonia with multiple antheridia and nearly plerotic oospore, (**g**, **h**) *Py. catenulatum*, (**g**) catenulate hyphal swelling, (**h**) lobulate sporangia, (**i**-**k**) *Py. dissotocum*, (**i**) filamentous sporangia, (**j**, **k**) smooth oogonium with a monoclinous antheridium, aplerotic oospore, (**l**-**n**) *Py. irregulare*, (**l**) spherical sporangia, (**m**, **n**) irregularly spined oogonium with a monoclinous antheridium

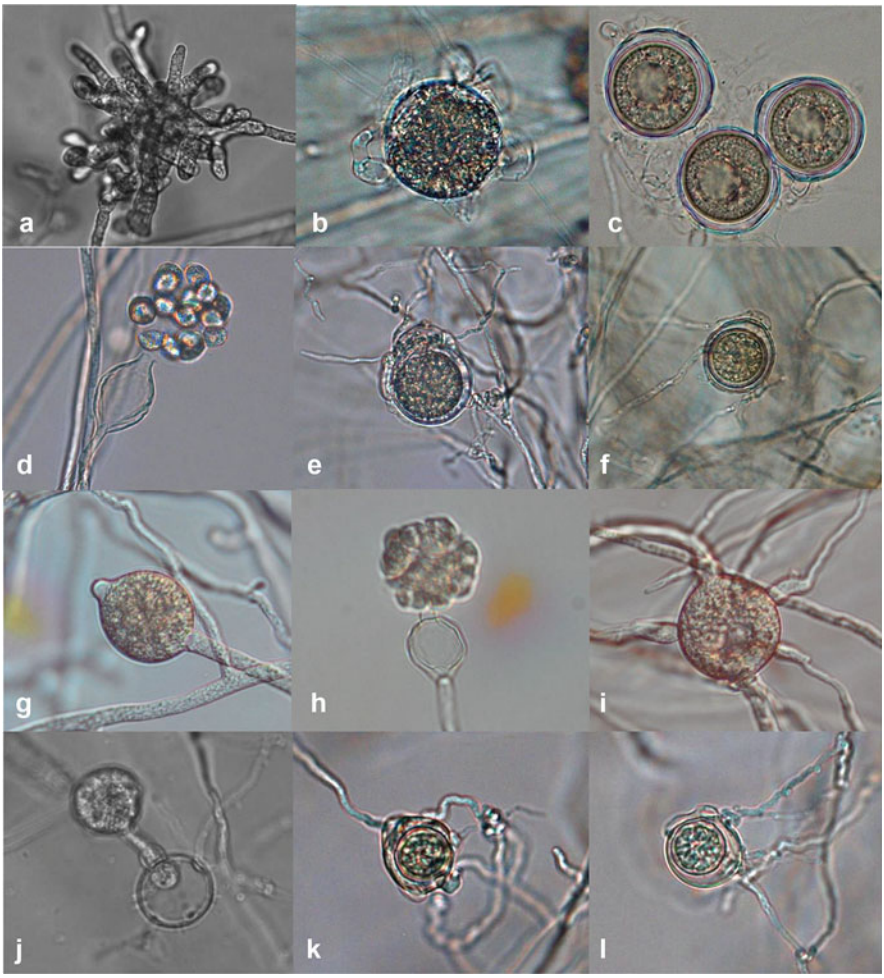

Fig. 12.7 Morphological characteristics of *Pythium myriotylum*, *Phytopythium helicoides*, *Pp. litorale* and *Pp. vexans*. (**a**-**c**) *Py. myriotylum*, (**a**) lobate sporangium, (**b**, **c**) smooth oogonium with multiple antheridia and aplerotic oospore, (**d**-**f**) *Pp. helicoides*, (**d**) zoospore formation in vesicle from sporangium, (**e**, **f**) smooth oogonium with broadly contacted antheridia and aplerotic oospore, (**g**-**i**) *Pp. litorale,* G; papillate sporangium, (**e**) zoospore formation in vesicle from sporangium, (**f**) direct germination of sporangium, (**j**-**l**) *Pp. vexans*, (**j**) spherical sporangia and vesicle formation from sporangia, (**k**, **l**) smooth oogonium with monoclinous antheridia and aplerotic oospore

phytopathogenic species isolated from rivers belonged to molecular phylogenies Clades A and B (to which filamentous sporangium-forming species belonged) as 8 out of 10 species were filamentous spore-forming species, and the species belonging to Clade B were dominant. *Py. aphanidermatum* belonged to Clade A. Other two phytopathogenic species, *Py. irregulare* and *Py. marsipium*, which form spherical

Fig. 12.8 Maximum likelihood tree of the river isolates with the ex-types of the genus *Pythium* inferred from the sequences of the rDNA ITS region. The isolate numbers used for the phylogenetic analysis are showed after the taxon name. The circled isolates were representative of the phytopathogenic species in the river isolates. *Phytopythium helicoides* was used as out group. The clade names referred to Lévesque and de Cock (2004). The numbers on the branches represent bootstrap values obtained from 1000 replications (only values greater than 60% are shown)

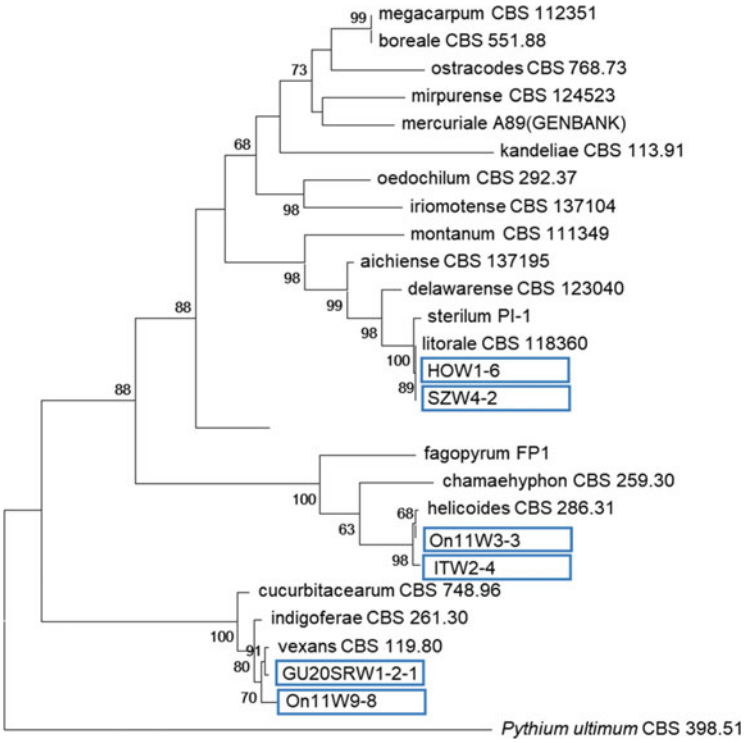

Fig. 12.9 Maximum likelihood tree of the river isolates with the ex-types of the genus *Phytopythium* inferred from the sequences of the rDNA ITS region. The isolate numbers used for the phylogenetic analysis are showed after the taxon name. The circled isolates were representative of the phytopathogenic species in the river isolates. *Pythium ultimum* was used as out group. The numbers on the branches represent bootstrap values obtained from 1000 replications (only values greater than 60% are shown)

sporangia, belong to Clade E and Clade F, respectively. These indicate that the species of *Pythium* present in the river are genetically related, although there are some exceptions.

The genus *Phytopythium* was initially a molecular lineage Clade K of the genus *Pythium*. However, a molecular phylogenetic analysis by Villa et al. (2006), which included the genus *Phytophthora*, showed that it is a Clade genetically closer to *Phytophthora* than to *Pythium*, and a new genus was subsequently proposed by Bala et al. (2010). Three species detected in rivers did not belong to any special Clade (Baten et al. 2014; de Cock et al. 2015). With only about 20 species belonging to this genus, it was difficult to observe any special trends. However, many of the species in this genus were isolated from water in other countries (Shrestha et al. 2013; Nam and Choi 2019; Zappia and Hüberli 2014) and were considered to be a group of aquatic species.

Table 12.4 Pathogenicity of *Phytopythium helicoides* to sedum and gerbera plants in soil culture

	Disease incidence %	Disease severity	Re-isolation %
Sedum			
Control	0	0	0
GF19AgW2–2-3	100	75	100
GF19AgW3–2-2	100	73	100
GF19OW4–2-3	100	83	100
Gerbera			
Control	0	0	0
GF19AgW2–2-3	100	88	100
GF19AgW3–2-2	100	81	100
GF19OW4–2-3	100	79	100

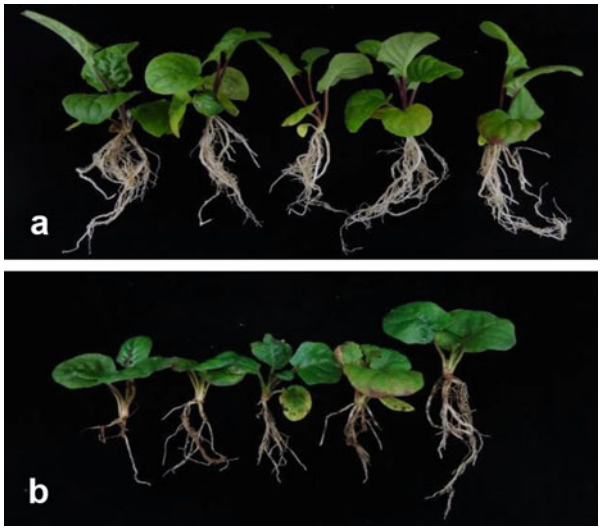

Fig. 12.10 Pathogenicity of *Phytopythium helicoides* from river water to gerbera plants grown in soil culture. (**a**) non-inoculated, (**b**) inoculated

12.3.5 Pathogenicity of Strains Isolated from River Water to Plants

In order to determine whether strains isolated from river water are actually pathogenic even if they are reported as plant pathogens, we examined the pathogenicity of the frequently encountered species, *Py. dissotocum*, *Py. myriotylum*, and *Pp. helicoides*, in soil and in hydroponic cultivation.

In soil cultivation, *Pp. helicoides* was tested for pathogenicity against sedum and gerbera plants, which have been reported as its natural targets. All three tested strains of *Pp. helicoides* caused significant root inhibition in sedum, and even when roots were produced, they were brown and decayed (Table 12.4). The growth of aboveground parts was also significantly inhibited. In gerbera, all three tested strains caused significant root brown rot and suppressed growth (Table 12.4, Fig. 12.10).

Table 12.5 Pathogenicity of *Phytopythium* and *Pythium* species in hydroponic culture

	Disease incidence %	Disease severity	Re-isolation %
Phytopythium helicoides to lettuce			
Control	0	0	0
GF19AgW2–2-3	100	85	80
GF19AgW3–2-2	100	80	90
GF19OW4–2-3	100	63	80
Pythium dissotocum to lettuce			
Control	0	0	0
GF19AW4–1-3	100	88	100
GF19AgW1–2-1	100	93	100
GF19OW1–2-2	100	88	100
Pythium myriotylum to tomato			
Control	0	0	0
GF20JW2–2-3	100	90	100
GF20AgW2–2-2	100	93	100

Fig. 12.11 Pathogenicity of *Pythium dissotocum* from river water to lettuce plants grown in hydroponic culture. (**a**) non-inoculated, (**b**) inoculated

Both *Pp. helicoides* and *Py. dissotocum* were tested for their pathogenicity against lettuce, which has been reported as their natural targets (McGehee et al. 2018). The pathogenicity of *Py. myriotylum* against tomato was also investigated, (Li et al. 2014; Feng et al. 2018) and both strains caused brown rot of the roots and consequent growth inhibition (Table 12.5, Fig. 12.11).

These results indicate that the strains isolated from river water are also pathogenic to plants as the strains isolated from diseased plants. In other words, we have clarified one of the important factors in testing the hypothesis that pathogenic species in river water invade agricultural production sites and cause damage to crops.

12.3.6 Conclusion

The presence of plant pathogens in river water has posed a problem for several plant species. In terms of the host range of plant pathogens detected in river and irrigation water, *Py. aphanidermatum* and *Py. myriotylum* have been reported on more than 40 plant species while *Py. irregulare* and *Pp. helicoides* on more than 20 plant species. These four species have been attracting attention not only in field crops but also in vegetables and flowering plants due to the widespread use of hydroponics and other greenhouse cultivation methods in recent years (Feng et al. 2015, 2018; Fukuta et al. 2013, 2014; Li et al. 2014; Suzuki et al. 2013; Takahashi et al. 2014). In particular, the three species other than *Py. irregulare* are important pathogens for tomatoes and flowering plants that are grown in greenhouses year-round even at high temperatures during the summer because of their heat tolerance and their ability to grow even at 40 °C, with an optimum growth at 30 °C or higher (Ishiguro et al. 2013). *Pythium dissotocum* is also a problematic pathogen in hydroponics, although its host range is not as wide as the four species mentioned above. Our results suggest that phytopathogenic oomycetes are naturally found in rivers and can act as pathogens when they invade agricultural production sites, emphasizing the need to pay attention to river water and irrigation water as one of the pathogen-transmission routes.

Although *Py. myriotylum* and *Pp. helicoids*, which were detected frequently, are high temperature tolerant species, their distribution shows that they are not necessarily found only in warm regions but are also present in the cold Hokkaido and Yamagata prefectures suggesting that they have a high ability to survive in winter. Considering the wide host range of these species, it is necessary to keep in mind that they can be harmful to plants even in cold areas.

Our morphological analyses showed that *Pythium irregulare* form spherical sporangia in water, but do not release zoospores. *Py. irregulare* has a wide host range and is commonly found in agricultural areas (Li et al. 2021). These findings suggest that the species was detected incidentally in river water due to the inflow of river water into agricultural fields caused by rising water levels, and their low detection frequency suggests that these species will be not active inhabitants of river water. If further studies prove this, this species could be used as a biological indicator of sediment inflow into rivers.

Although a broad host range is thought to be associated with a wide distribution, our results suggest that there need not be a strong correlation between the two factors. For example, *Py. myriotylum* and *Pp. helicoides* have a broad host range and are widely distributed, but *Py. aphanidermatum* and *Py. irregulare* do not have a

wide distribution in rivers but have a wide host range. Similarly, *Py. catenulatum*, *Py. marsupium*, and *Py. oopapillum*, which have a narrow host range (they have only been reported as pathogens of rice), have a wide distribution. Moreover, the life cycle of pathogens differs from species to species. While some aquatic species have acquired pathogenicity in crops, there may be others whose life cycle is mainly in soil but could still cause pathogenicity. It is necessary to consider the distribution of pathogens in soil as well as water for investigating the transmission modes of a plant pathogen.

References

Abdelzaher HMA, Ichitani T, Elnaghy MA (1994a) *Pythium marsipium* from pond water in Osaka. Mycol Res 98:920–922

Abdelzaher HMA, Ichitani T, Elnaghy MA (1994b) *Pythium flurninurn* var. *fluminurn* from pond water in Osaka. Mycol Res 98:982–984

Abdelzaher HMA, Ichitani T, Elnaghy MA, Samy KMH, Ezzat MF-A (1995) Materials for *Pythium* flora of Japan. X. Occurrence, identification and seasonality of *Pythium* spp. in three pond waters and mud soils in Osaka. Mycoscience 36:71–85

Abdelzaher HMA, Kageyama K (2020) Diversity of aquatic *Pythium* and *Phytopythium* spp. from rivers and a pond of Gifu city. Japan Novel Res Microbiol J 4(6):1029–1044

Bala K, Robideau GP, Lévesque CA, de Cock AWAM, Abad ZG, Lodhi AM, Shahsad S, Ghaffar A, Coffey MD (2010). *Phytopythium* Abad et al. Gen. Nov. and *Phytopythium sindhum* Lodhi et al. sp. nov. fungal planet 49. Persoonia 24:136–137

Baten MA, Asano T, Motohashi K, Ishiguro Y, Rahman MZ, Inaba S, Suga H, Kageyama K (2014) Phylogenetic relationships among *Phytopythium* species, and re-definition of *Phytopythium fagopyrinum* comb. nov., recovered from damped-off buckwheat seedlings in Japan. Mycol Prog 13:1145–1156

Beakes GW, Sekimoto S (2009) The evolutionary phylogeny of oomycetes–insights gained from studies of holocarpic parasites of algae and invertebrates. In: Lamour K, Kamoun S (eds) Oomycete genetics and genomics. Wiley-Blackwell, pp 1–24

Cavalier-Smith T, Chao EEY (2006) Phylogeny and megasystematics of phagotrohic heterokonts (kingdom Chromista). J Mol Evol 62:388–420

de Cock AWAM, Lodhi AM, Rintoul TL, Bala K, Robideau GP, Abad ZG, Coffey MD, Shahzad S, Lévesque CA (2015) *Phytopythium*: molecular phylogeny and systematics. Persoonia 34:25–39

Feng M, Ishiguro Y, Hotta K, Watanabe H, Kageyama K (2015) Simple detection of *Pythium irregulare* using loop-mediated isothermal amplification assay. FEMS Microbiol Lett 362. https://doi.org/10.1093/femsle/fnv174fnv174

Feng M, Nukaya A, Satou M, Fukuta N, Ishiguro Y, Suga H, Kageyama K (2018) Use of LAMP detection to identify potential contamination sources of plant pathogenic *Pythium* species in hydroponic culture systems of tomato and eustoma. Plant Dis 102:1357–1364

Fukuta S, Takayashi R, Kuroyanagi S, Miyake N, Nagai H, Suzuki H, Hashizume F, Tsuji T, Taguchi H, Watanabe H, Kageyama K (2013) Detection of *Pythium aphanidermatum* in tomato using loop-mediated isothermal amplification (LAMP) with species-specific primers. Eur J Plant Pathol 136:689–701

Fukuta S, Takahashi R, Kuroyanagi S, Ishiguro Y, Miyake N, Nagai H, Suzuki H, Tsuji T, Hashizume F, Watanabe H, Kageyama K (2014) Development of loop-mediated isothermal amplification assay for the detection of *Pythium myriotylum*. Lett Appl Microbiol 59:49–57

Hayashi M, Suga H, Kageyama K (2018) Root rot of Sedam caused by *Pythium* and *Phytopythium* species. Jpn J Phytopathol 84:32

Hendrix FF, Campbell WA (1973) Pythium as plant pathogens. Annu Rev Phytopathol 11:77–98
Hong CX, Moorman GW (2005) Plant pathogens in irrigation water: challenges and opportunities. Crit Rev Plan Sci 24:189–2005
Ishiguro Y, Asano T, Otsubo K, Suga H, Kageyama K (2013) Simultaneous detection by multiplex PCR of the high-temperature-growing *Pythium* species: *P. aphanidermatum*, *P. helicoides* and *P. myriotylum*. J Gen Plant Pathol 79:350–358
Jacobs RPWM (1982) Pythiaceous fungi associated with the decomposition of *Nymphoides peltata*. Antonie Van Leeuwenhoek 48:433–445
Kageyama K (2010) Mycobiota in the subtropical and cool temperate areas in Japan. IFO Res Commun 24:117–156
Kageyama K (2014) Molecular taxonomy and its application to ecological studies of *Pythium* species. J Gen Plant Path 80:314–326
Kageyama K (2015) Studies on the taxonomy and ecology of oomycete pathogens. J Gen Plant Path 81:461–465
Kageyama K, Aoyagi T, Sunouchi R, Fukui H (2002) Root rot of miniature roses caused by *Pythium helicoides*. J Gen Plant Pathol 68:15–20
Kageyama K, Suzuki M, Priyatmojo A, Oto Y, Ishiguro K, Suga H, Aoyagi T, Fukui H (2003) Characterization and identification of asexual strains of *Pythium* associated with root rot of rose in Japan. J Phytopathol 151:485–491
Kawamura Y, Yokoo K, Tojo M, Hishiike M (2005) Distribution of *Pythium porphyrae*, the causal agent of red rot disease of *Porphyrae* spp., in the Ariake Sea. Japan Plant Dis 89:1041–1047
Kumar S, Stecher G, Li M, Knyaz C, Tamura K (2018) MEGA X: molecular evolutionary genetics analysis across computing plat forms. Mol Biol Evo 35:1547–1549
Lévesque CA, de Cock AWAM (2004) Molecular phylogeny and taxonomy of the genus *Pythium*. Mycol Res 108:1363–1383
Li M, Hieno A, Motohashi K, Suga H, Kageyama K (2021) *Pythium intermedium*, a species complex consisting of three phylogenetic species found in cool-temperate forest ecosystems. Fungal Biol 125:1017–1025
Li M, Senda M, Komatsu T, Suga H, Kageyama K (2010) Development of real-time PCR technique for estimation of population density of *Pythium intermedium* in forest soils. Microbiol Res 165: 695–705
Li M, Ishiguro Y, Otsubo K, Suzuki H, Tsuji T, Miyake N, Nagai H, Suga H, Kageyama K (2014) Monitoring by real-time PCR of three water-borne zoosporic *Pythium* species in potted flower and tomato greenhouses under hydroponic culture systems. Eur J Plant Pathol 140:229–242
Martin FN (2000) Phylogenetic relationships among some *Pythium* species inferred from sequence analysis of the mitochondrially encoded cytochrome oxidase II gene. Mycologia 92:711–727
Matsumoto C, Kageyama K, Suga H, Hyakumachi M (1999) Phylogenetic relationships of *Pythium* species based on ITS and 5.8S sequences of the ribosomal DNA. Mycoscience 40:321–331
McGehee C, Raudales RE, Elmer WH (2018) First report of *Pythium dissotocum* causing Pythium root rot on hydroponically grown lettuce in Connecticut. Plant Dis 102:2043
Morita Y, Tojo M (2007) Modifications of PARP medium using fluazinam, miconazole, and nystatin for detection of *Pythium* spp. in soil. Plant Dis 91:1591–1599
Nam B, Choi Y-J (2019) *Phytopythium* and *Pythium* species (Oomycota) isolated from freshwater environments of Korea. Mycolobiol 47:261–272
Nechwatal J, Mendgen K (2006) *Pythium litorale* sp. nov., a new species from the littoral of lake Constance. Germany FEMS Microbiol Lett 255:96–101
Nechwatal J, Wielgoss A, Mendgen K (2008) Diversity, host, and habitat specificity of oomycete communities in declining reed stands (*Phragmites australis*) of a large freshwater lake. Mycol Res 112:689–696
Robideau GP, de Cock AWAM, Coffey MD, Voglmayr H, Bo-nants PJM, Ristaino JB, Chitty D, Rintoul T, Désaulniers N, Eggertson Q, Bala K, Gachon CMM, Smith ML, Lévesque A (2011) DNA barcoding of oomycetes with cytochrome c oxidase subunit I (COI). Mol Ecol Resour 11: 1002–1011

Sánchez J, Gallego E (2000) *Pythium* spp. present in irrigation water in the Poniente region of Almeria (South-Eastern Spain). Mycopathologia 159:29–38

Shrestha SK, Zhou Y, Lamour K (2013) Oomycetes baited from streams in Tennessee 2010-2012. Mycologia 105:1516–1523

Schroeder KL, Martin FN, de Cock AWAM, Lèvesque CA, Spines CFJ, Okubara PA, Paulitz TC (2013) Molecular detection and quantification of *Pythium* species: evolving taxonomy, new tools, and challenges. Plant Dis 97:4–20

Stanghellini ME, Kronland WC (1986) Yield loss in hydroponically grown lettuce attributed to subclinical infection of feeder rootlets by *Pythium dissotocum*. Plant Dis 70:1053–1056

Suzuki M, Kageyama K, Ichikawa T, Uchiyama T (2009) Occurrence of Pythium root rot of garbera caused by *Pythium helicoides*. Jpn J Phytopathol 75:237

Suzuki H, Tsuji T, Hashizume F, Fujita A, Kuroda K (2013) Population dynamics of high-temperature-growing *Pythium* species on tomato in hydroponic and effects of water temperature on incidence. Jpn J Phytopathol 79:58

Takahashi R, Fukuta S, Kuroyanagi S, Miyake N, Nagai H, Kageyama K, Ishiguro Y (2014) Development and application of a loop-mediated isothermal amplification assay for rapid detection of *Pythium helicoides*. FEMS Microbiol Lett 355:28–35

Tamura K, Nei M (1993) Estimation of the number of nucleotide substitutions in the control region of mitochondrial DNA in humans and chimpanzees. Mol Biol Evo 10:512–526

Van der Plaats-Niterink AJ (1981) Monograph of the genus *Pythium*. Stud Mycol 21:1–242

Villa ON, Kageyama K, Asano T, Suga H (2006) Phylogenetic relationships of *Pythium* and *Phytophthora* species based on ITS rDNA, cytochrome oxidase II and β-tublin gene sequences. Mycologia 98:410–422

Watanabe H, Taguchi Y, Hyakumachi M, Kageyama K (2007) *Pythium* and *Phytophthora* species associated with root and stem rots of kalanchoe. J Gen Plant Pathol 73:81–88

Watanabe T (1981) Distribution and populations of *Pythium* species in the northern and southern part of Japan. Ann Phytopath Soc Japan 47:449–456

Watanabe T (1984) Detection and quantitative estimations of *Pythium aphanidermatum* in soil with cucumber seeds as a baiting substrate. Plant Dis 68:697–698

Waterhouse GM (1967) Key to *Pythium* Pringsheium. Mycol Paper 109:1–15

Waterhouse GM (1968) The genus *Pythium* Pringsheim. Mycol Paper 110:1–71

White TJ, Bruns TD, Lee SB, Taylor JW (1990) Amplification and direct sequencing of fungal ribosomal RNA genes for phylogenetics. In: Innis MA, Gelfand DH, Sninskey JJ, White TJ (eds) PCR protocols: a guide to methods and applications. Academic, San Diego, California, pp 315–322

Zappia RE, Hüberli D, Hardy GESJ, Bayliss KL (2014) Fungi and oomycetes in open irrigation systems: knowledge gaps and biosecurity implications. Plant Path 63:961–972

Chapter 13
Soil Contamination and Conservation

Yongfen Wei and Huijuan Shao

Abstract Healthy soils are essential to food security and provide significant contributions to the Sustainable Development Goals (SDGs) by conserving biodiversity, improving water quality, and enhancing resilience against extreme weather. However, the introduction of contaminants from various sources into the soil environment has degraded the soil ecosystem and endangered human health. Soil contamination often cannot be visually detected; therefore, soil must be properly utilized, appropriately managed, comprehensively studied, and efficiently conserved. This chapter firstly introduces the types and sources of soil contamination, global soil contamination status, and soil remediation technologies. It then briefly describes the soil contamination in Japan by radioactive cesium (Cs) and the related decontamination practices implemented to address this problem. Furthermore, the results of our previous research on treating Cs contaminated soil using industrial waste materials are introduced. Finally, the efforts and challenges in managing and controlling soil contamination are presented to provide reference for soil remediation.

Keywords Soil contaminants · Soil remediation · Cesium · Recycling material · Immobilization · SDGs

13.1 Introduction

Humans have considerably changed the soil environment to acquire benefits. These changes have caused unintended negative consequences to soil property and most organisms, thereby challenging their survival. Soil contamination is a classic example of such a scenario because in many cases it is not directly observed, and its effects could become apparent after several decades since its commencement.

Y. Wei (✉)
River Basin Research Center, Gifu University, Gifu, Japan
e-mail: weiyf@gifu-u.ac.jp

H. Shao
College of Resources and Environment, Shandong Agricultural University, Tai'an, China

F. Li et al. (eds.), *River Basin Environment: Evaluation, Management and Conservation*, https://doi.org/10.1007/978-981-19-4070-5_13

Unfortunately, 25% of global soils have been reported to be contaminated. Moreover, in many parts of the world, several decades of industrial activities, farming activities, and improper urban waste disposal have saturated and exceeded the capacity of soil to retain contaminants.

To emphasize the importance of soil as an important component of the natural system, as a vital contributor to human commonwealth due to its contribution to food, water and energy security, and as a mitigator of biodiversity loss and climate change, along with the significance of soil conservation, the 68th UN General Assembly adopted a resolution (A/RES/68/232) in December 2013 to officially declare December fifth as the World Soil Day (WSD). After the recognition of the WSD, the International Year of Soils, 2015 (IYS 2015) was also declared by the 68th session of the United Nations General Assembly. Further, in 2018, "Be the Solution to Soil Pollution" global campaign was adopted to create awareness regarding the importance of maintaining healthy soil ecosystems and encouraging societies to combat soil pollution and improve soil health. In the same year as the IYS 2015, the Sustainable Development Goals (SDGs), also known as the Global Goals, were approved by the United Nations as a universal call to action to end poverty, protect the planet, and ensure that by 2030 all people enjoy peace and prosperity. Soil is the at the core of sustainable development; improving soil quality is an integral step towards achieving the SDGs, specifically the Goals on zero hunger (SDG 2), climate action (SDG 13), and life on land (SDG 15).

This chapter describes the types and sources of soil contaminants, global status of soil contamination and soil remediation technologies; moreover, the soil contamination situation in Japan after the Fukushima Daiichi nuclear power plant (FDNPP) accident, and the decontamination practices implemented by the country to deal with the soils contaminated with radioactive ^{137}Cs are described. The results of our previous research on the methods to in-situ remediate ^{137}Cs contaminated forest soil using industrial waste materials are also introduced. Finally, efforts and challenges faced in managing and controlling soil contamination are briefly presented.

13.2 Soil Contaminants and Global Status of Soil Contamination

13.2.1 Soil Contaminants

Soil contaminants can be broadly divided into chemical (inorganic and organic), physical, biological and radioactive types. Chemical contamination is the most common. Inorganic chemical contaminants mainly include acids, alkalis, heavy metals (HMs) and salts, whereas organic chemical contaminants mainly include pesticides, petroleum, synthetic detergents, PAHs and PCBs. Recently, the effects of new soil contaminants such as microplastics, antibiotic resistance genes and e-wastes are also becoming an increasing concern. The sources of soil contamination mainly

Table 13.1 Main sources of soil contamination in different regions (FAO and UNEP 2021)

Region	Main sources of soil contamination
Asia	East Asia: Industrial activities, mining, coal-burning, and solid waste disposal
	Southeast Asia: Increasing number of chemical industries and weak environmental regulations, along with agriculture and forestation-deforestation
	Central Asia: Mining, oil industries, metal sectors, and agricultural activities
Europe	Released radionuclides from Chernobyl accident, military activities, industrial and commercial activities, mining, waste disposal, agricultural activities
Latin America and the Caribbean	Agricultural practices, urban waste management, mining, quarrying and smelting activities, transport exhaust emissions, energy production, industrial and livestock activities
North America	Mining, industrial and agricultural activities, energy production, solid waste, military activities and nuclear weapons
Near east and North Africa	Dispersal of wind-blown contaminated dust, agricultural and industrial activities, intensive oil production, mining, inappropriate waste disposal
Sub-Saharan Africa	Mining and quarrying, fossil fuel extraction, agricultural and industrial activities, transport, energy sector, waste disposal and processing

include mining, smelting, industrial activity, sewage irrigation, solid waste stacking, chemical fertilizers and pesticides. Table 13.1 lists some examples of the main sources of soil contamination in different regions of the world. As shown, most contaminants originate from human activities such as industrial processes and mining, poor waste management, unsustainable farming practices, accidents ranging from small chemical spills to nuclear power plant damage, as well as the armed conflicts (FAO and UNEP 2021).

13.2.2 Global Status of Soil Contamination

According to Kumar et al. (2019), more than ten million sites worldwide have been contaminated. For example, in the United States, more than 100,000 contaminated sites have been reported (Tu et al. 2020). In 2020, 2.5 million sites across Europe were potentially contaminated, according to the European Environment Agency. Further, out of the total number of radioactive contaminated areas (34 million hectares) after the Chernobyl accident in 1986, 20 million hectares of highly contaminated soils were in Europe, 70% of which were in Eastern European countries, including Belarus, Ukraine, and the Russian Federation (Boubriak et al. 2016). In Australia, approximately 80,000 sites were estimated to be contaminated.

In Asia, due to the diversity in the economic development, lifestyles, environmental policies, and recognition of sustainable development in different countries

(IMF 2018), the issues of soil contamination are becoming complex and diverse. For example, in Japan, approximately 1.16 million acres of agricultural soil have been contaminated by HMs (Xu et al. 2016). And the soil contamination by radioactive substances, mainly due to the FDNPP accident occurred in 2011 also remains a significant problem. In 2015, the South Korean Ministry of Environment monitored soils at 1000 sites for eight trace elements and 13 other compounds, found that Hg and Zn were the most common contaminants (KOR-MOE 2017). In Thailand, the proportion of contaminated sites is increasing because of not only their domestic wastes but also the imported wastes (Diss 2019). There are approximately 52 major contaminated sites in Thailand, and the main sources of contamination are mining, petrochemical industries, illegal dumping, waste processing facilities, and imported e-wastes (FAO and UNEP 2021). Although the Bengal Delta is one of the most heavily arsenic (As) contaminated areas worldwide, soil conservation has not been prioritized in Bangladesh. In India, soils have been significantly contaminated with trace elements because of rapid economic growth through industrial, agricultural, and mining activities. In Sri Lanka, the use of agrochemicals, such as inorganic fertilizers and pesticides, is one of the main causes of soil contamination. Additionally, the lack of municipal solid waste collection facilities and poor waste management practices continue to cause severely soil contamination in Sri Lanka (Bandara et al. 2008). In China, the Ministry of Environmental Protection estimated that almost 16.1% of the total arable land and 19.4% of the cultivated land exceeded the permissible limit for HMs. Moreover, out of all the contaminated soils, 82.8% were contaminated with trace elements, such as As, Cd, Cu, Pb, and Hg; additionally, 13.7%, 2.8%, 1.8%, and 1.1% of the total cultivated land have been reported to be slightly, mildly, moderately, and heavily contaminated, respectively (Zhao et al. 2015). Notably, trace element contamination is generally more serious in southeast China than that in northwest China.

In summary, soil contamination has become one of the most challenging environmental problems worldwide due to its great harm to the ecological environment and public health. To conserve and maximize the use of limited and difficult-to-regenerate soil resources, remediation of contaminated soil is very important and urgent.

13.3 Soil Remediation Technologies and Approaches toward Reducing the Risk of Cs Contaminated Soil in Japan

13.3.1 Soil Remediation Technologies

Soil remediation technologies tend to remove hazardous substances or reduce their amount accumulated in the soil, and to limit their spread so that the contaminated areas cease to pose a threat to the state of the environment and human health.

Generally, soil remediation can be broadly divided into physical, chemical and biological methods (Liu et al. 2018).

13.3.1.1 Physical Remediation Method

Physical remediation is using certain technologies to separate the contaminants from the soil and restore the available value of the soil. Physical remediation methods mainly include landfilling, soil surface capping or encapsulation, vitrification, thermochemical treatment, and electrokinetic remediation. Landfilling is one of the simplest soil remediation techniques through which the contaminated soil is removed from its original site and transported to a secure landfill for disposal. Soil surface capping or encapsulation method refers to covering the contaminated soil with a layer of waterproof material to form a properly designed physical barrier system. This technique is not truly a soil "remediation" method, as no efforts are made to remove or reduce contaminants in the soil. Nevertheless, the method can efficiently eliminate the risk of exposure to the contaminated soil. Vitrification is a thermal remediation technique that uses heat to transform contaminated soil into glass-like solids. Although this method requires high temperature and high pressure which means large energy consumption, it has high remediation efficiency. Thermochemical treatment is using high or low temperatures to heat the contaminated soil to volatilize the contaminants. Notably, thermal treatment technology can only remove volatile soil contaminants. Electrokinetic remediation is to reduce the scope of soil remediation and reduce the amount of engineering. Based on the principles of electrochemistry and electrophoresis, contaminants are moved to the electrode for centralized treatment or separation. It is only suitable for soil with high humidity. It has a certain danger, and the cost is high due to the electric energy consumption.

13.3.1.2 Chemical Remediation Method

Chemical remediation is the process of changing the contaminant structure or reducing the mobility and toxicity of contaminants by means of chemical decomposition or fixation. It mainly includes soil washing, chemical oxidation/reduction, and solvent extraction.

Soil washing has been commonly used to remove organic contaminants from the soil by flushing surfactant solutions or passing extraction fluids through the contaminated soil. Extraction fluids in the form of chemical solutions are typically injected or infiltrated into the soil. This technique is applicable to homogenous coarse-textured soils with high permeability. Although this method is economic and user-friendly, installing solution collection wells or subsurface drains is challenging and expensive. Chemical oxidation-reduction technology purifies the soil by allowing the reaction between the chemical oxidants added to the soil and the contaminants, and chemically converting hazardous contaminants to nonhazardous or less toxic compounds. The most used oxidants are K_2MnO_4, H_2O_2 and ozone gases. Solvent

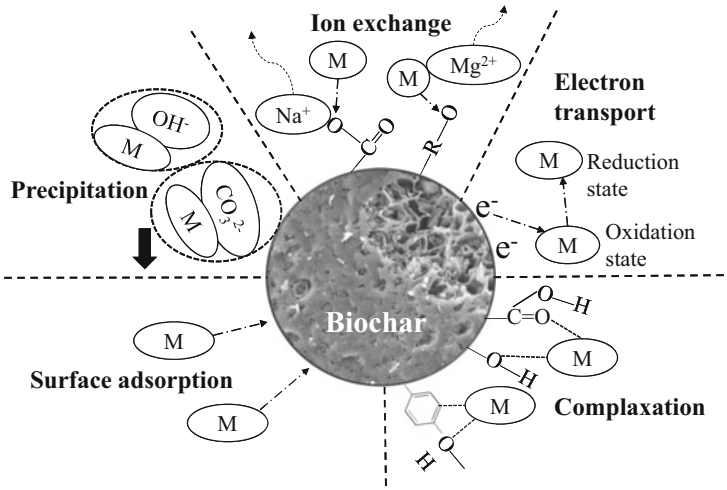

Fig. 13.1 Possible immobilization mechanisms of heavy metals (M) by biochar

extraction remediation is a technology that uses solvents to extract or remove harmful chemicals from contaminated soil. This technology is suitable for organic contaminated soil, and the effectiveness of extracting contaminants from soil depends on the intimate contact between the soil and the solvent mixture.

The above-mentioned conventional physicochemical remediation techniques are highly efficient and can be applied to severely contaminated soils but only at small scales (Dada et al. 2015). Moreover, they exhibit other disadvantages, such as high energy requirements and costs, destruction of soil structure and quality, and secondary contamination due to the released chemical substances during the remediation processes (Cristaldi et al. 2017). Therefore, some safe and effective remediation methods have been developed. For example, soil photocatalytic degradation, a novel deep-soil oxidation remediation technology, can be applied to remediate pesticide contaminated soils. Stabilization/ solidification is a well-developed and effective method for immobilizing potentially toxic elements in contaminated soils via adsorption, hydration, precipitation, or alkaline activation (Li et al. 2021; Shen et al. 2019). Besides, several studies have been conducted to reuse various low-cost or recycling materials, such as biochar, fly ash, blast-furnace slag, incinerated sewage sludge ash, zeolite, red mud and phosphogypsum, to immobilize soil contaminants (Shao et al. 2021; Tian and Sasaki 2019; Wang et al. 2021).

Biochar has been reported to adsorb or passivate soil contaminants and has been used primarily for in-situ remediation because of its large specific surface area, abundant active functional groups, good complexation, and adsorption property (Fig. 13.1). Additionally, biochar immobilizes HMs in soil through physicochemical adsorption with an aim of changing the specific chemical forms of HMs and inhibiting the bioavailability of HMs (Lu et al. 2014). Zheng et al. (2013) reported that adding biochar acquired from rice residues significantly decreased Cd, Zn and

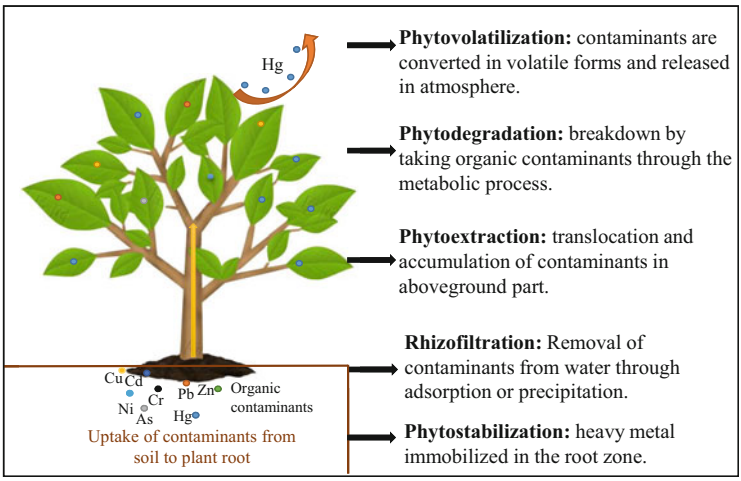

Fig. 13.2 Phytoremediation strategies

Pb concentrations by 71%, 37% and 61% in the plant shoot, respectively. Liu et al. (2020) also revealed that the application of lychee biochar enhanced sunflower growth and immobilized HMs in the contaminated soil.

13.3.1.3 Biological Remediation Method

Bioremediation uses plants, microorganisms, or microbial/plant enzymes to detoxify, remove, or degrade contaminants to benign forms or low concentrations (Kumar et al. 2011). Compared to physicochemical methods, bioremediation is an environmentally friendly, safe and inexpensive technology for soil reclamation (Xiao et al. 2019). Among the available bioremediation technologies, phytoremediation is commonly used because it is easily operated, requires fewer human resources, and improves the aesthetic value of the environment. It uses vegetation to remove contaminants from the soil or decrease the availability of contaminants, thereby restoring the soil to a healthy level (Lajayer et al. 2019).

Hyperaccumulators tolerate high concentrations of contaminants and possess distinct capabilities to efficiently absorb contaminants from soil, translocate them from roots to shoots, detoxify and sequester contaminants in plant tissues. Phytoremediation of organic-contaminated soils is mainly manifested through the direct absorption of organic pollutants by plants, biodegradation promotion of organic pollutants by various secretions or enzymes released by plants, and enhancement of organic pollutants mineralization by plant rhizosphere. Phytoremediation is usually grouped into several sub classes including phytovolatilization, phytodegradation, phytoextraction, rhizofiltration and phytostabilization (Fig. 13.2). Phytovolatilization is using plants to take up contaminants from soil, convert these toxic elements into less toxic volatile form, and subsequently release

them into the atmosphere by plant transpiration process via the leaves or foliage system (Yan et al. 2020). Phytodegradation is the breakdown of organic compounds by metabolic processes of plants or enzymes. Phytoextraction, also known as phytoaccumulation, is the uptake of contaminants from soil by hyperaccumulator roots and their translocation and accumulation in the aboveground biomass, followed by seasonal harvesting until the concentrations of soil contaminants decrease to an acceptable level. Rhizofiltration is the reclamation of soil pore water, wastewater, surface and groundwater with low levels of contaminants by plant roots. Phytostabilization refers to the decreases in the mobility and bioavailability of contaminants in the soil, as well as the limitation of their leaching into groundwater and entering to the food chain, due to their stabilization from off-site transport with the help of certain vegetations.

Phytoremediation has been recently receiving increasing attention because of its low-cost, feasibility, and eco-friendly natures. However, phytoremediation also shows some challenges, for example, it is time-consuming, proper disposal of contaminated plants is an important concern. Moreover, the remediation efficiency depends on many factors including soil contamination level, soil characteristics, plant growth rate and biomass, root depth, as well as favorable meteorological conditions (Mahar et al. 2016; Cameselle and Gouveia 2019). Besides, phytoremediation is only applicable for medium to low degree of soil contamination, because plant growth can be restricted under a high degree of contamination. Contaminants that are tightly embedded in the soil are difficult to be eliminated through phytoremediation due to their low bioavailability. To increase the bioavailability of contaminants and improve the remediation efficiency, phytoremediation should be supplemented with other physical, chemical and biological methods; therefore, future research should focus on combined soil remediation technology.

13.3.2 Practical Approach to Reduce the Risk of Cs Contaminated Soil in Japan

13.3.2.1 Fukushima Daiichi Nuclear Power Plant Accident

In March 2011, the FDNPP accident triggered by a large earthquake and tsunami occurred and released 6000–12,000 PBq of ^{33}Xe, 100–500 PBq of ^{131}I, 15–20 PBq of ^{137}Cs, and 15–20 PBq of ^{134}Cs (Komatsu et al. 2021). This resulted in extensive radioactive contamination and caused detrimental effects to life and property in northeastern Japan, particularly in Fukushima Prefecture.

Among the radionuclides released during the FDNPP accident, radioactive Cs (^{134}Cs and ^{137}Cs) was the most harmful element that affected the current and could affect the future health of the local population. ^{137}Cs contamination in the environment was more significant than that of ^{134}Cs, and posed as a long-term hazard. This is because its long half-life (approximately 30 years) could potentially contaminate the environment for long periods and threaten present and future generations of

living organisms. Additionally, its structural analog of an alkali element, such as K, could facilitate its immediate absorption by the plants from the soil, mainly through the K uptake system in the roots during K deficiency, and accumulate in plants following similar pathways, consequently, inhibiting plant growth, further damaging living organisms, and increasing the risks to cancer via the food chain.

To reduce the risk of exposure to radioactive materials, the Japanese government ordered immediate evacuation of the residents living around the FDNPP after the accident on March 12, 2011. Initially, only the areas within a 3-km radius of the FDNPP were evacuated, but as the effects of the accident became severe, areas within a radius of 20–30 km from the FDNPP were ordered to evacuate. Subsequently, on April 22, 2011, the government designated the 20-km radius around the FDNPP as a restricted area and prohibited entry for public, excluding those engaged in emergency response. Moreover, to minimize the effects of radioactive exposure, the contaminated area was divided into different areas based on the degree of contamination such as deliberate evacuation areas, specific areas recommended for evacuation, and evacuation prepared areas in case of emergency. Simultaneously, the government also set the criteria for radioactive Cs (sum of ^{134}Cs and ^{137}Cs) concentrations in food as 100 Bq kg^{-1} to ensure that annual internal exposure to Cs by food ingestion is less than 1 mSv per year (Ministry of Health, Labor and Welfare 2018). In municipalities where food products exceeded the standard criteria, shipping restrictions were introduced.

13.3.2.2 Soil Decontamination

To radically reduce the impact of radioactive Cs on human health and environment and to facilitate quick rehabilitation of the evacuated local population, the government decided to implement soil decontamination projects on an extensive scale. Accordingly, the Japanese Ministry of the Environment adopted the Act on Special Measures concerning the Handling of Environment Pollution by Radioactive Materials in August 2011. The law was established to ensure that the government will be responsible for promoting decontamination and will continually provide the technical information necessary for decontamination, including effective decontamination methods, funds, and considerations, through model projects in each region, especially in areas with particularly high doses of radioactive Cs.

Additionally, the Act on Special Measures for Decontamination was also enacted in November 2011. To supplement these acts, decontamination guidelines were released by the Japanese Ministry of Environment in December 2011 and updated in 2013 by incorporating knowledge and new technologies. The guidelines consisted mainly of three parts: Guidelines for Methods for Investigating and Measuring the Status of Environmental Pollution in Intensive Contamination Survey Areas, Guidelines Pertaining to Decontamination and Other Measures, and Guidelines Pertaining to the Collection and Transfer of the Removed Soil. They outlined the methods necessary for surveying and quantifying the contamination levels, preparing the contaminated areas for remediation, and treating the removed contaminated soil.

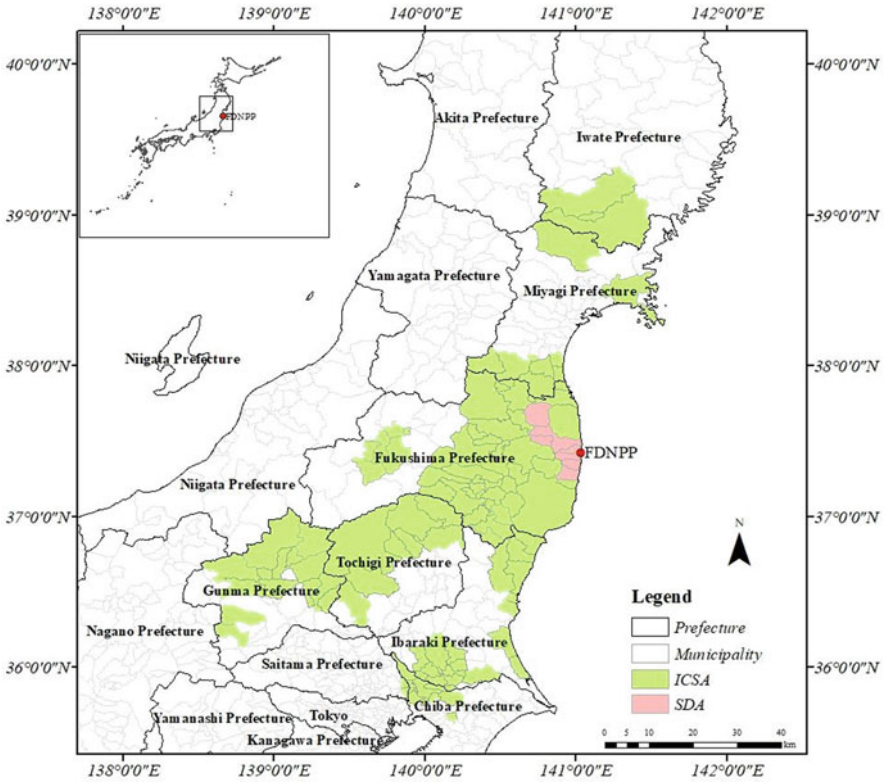

Fig. 13.3 Soil decontamination areas (cited from HP of the Ministry of Environment (Japan), https://www.env.go.jp/jishin/rmp/conf/law-jokyo06/lj06_mat02.pdf)

Accordingly, under the direct supervision of the government, a decontamination road map (the special decontamination zone decontamination policy) was published in January 2012.

Soil decontamination began in January 2012, mainly in agricultural and residential areas. Decontamination activities were focused on the special decontamination area (SDA), including 11 districts, which were evacuated after the accident, and the intensive contamination survey area (ICSA), including 97 districts affected by lower, but significant radioactivity levels (not evacuated in 2011) (Fig. 13.3).

Decontamination was conducted in accordance with the circumstances of respective areas. In the cultivated areas within the SDA, the soil surface layer was removed till a depth of 5 cm and replaced with "new soil" comprising locally available crushed granite. In areas farther from the plant, materials that could fix or substitute radioactive Cs (zeolite, K fertilizers, etc.) were applied to the soil. In residential areas, ditch cleaning, roof cleaning, and gutter cleaning were conducted, and vegetable gardens were treated as cultivated areas. Moreover, forested areas located within a radius of 20 m of the houses were treated by cutting branches and collecting

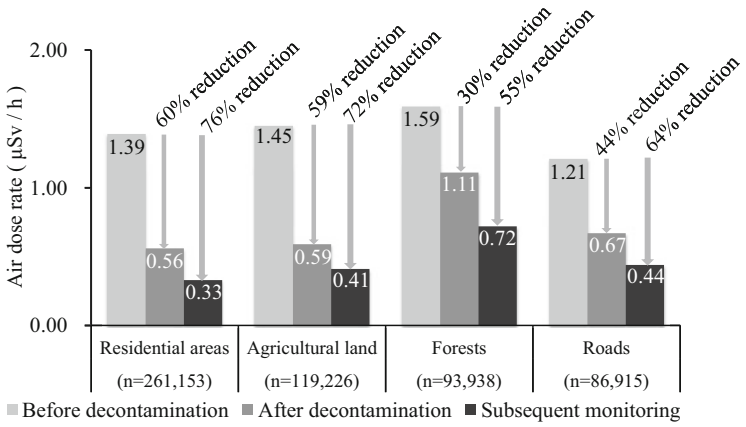

Fig. 13.4 Soil decontamination effects in Fukushima Prefecture (Air dose rate was measured at a height of 1 m from the ground surface. The chart shows the average value of air dose rate in residential areas, agricultural land, forests and roads. Residential areas included schools, parks, graveyards and large-size facilities. Agricultural land included fruit farms. Forests also included slopes, plains and grasslands. Data were acquired from HP of the Ministry of Environment (Japan), http://josen.env.go.jp/area/index.html)

the corresponding litter. However, for difficult-to-return zones (within the SDA area) in the immediate vicinity of the FDNPP, decontamination work was not implemented because these areas were difficult to access.

13.3.2.3 Decontamination Effects and Limitations

According to the Japanese Ministry of the Environment, the entire area covering more than 9000 km^2 was decontaminated. As shown in Fig. 13.4, this decontamination work in the residential areas reduced the radiation dose by 60%, and a subsequent investigation showed that it had further decreased by 76%. In other land types, such as agricultural lands, forests, and roads, evident decontamination effects were also reported.

The decontamination strategy after the FDNPP accident provides valuable insights into the effective removal of Cs from the environment; however, certain limitations exist. For example, the method used to clean the contaminated lands reduced Cs concentrations by 72–76% in treated agricultural and residential areas, but the removal cost of the uppermost part of the soil in cultivated land was approximately 3000 billion Japanese yen. The costs could increase further if the forested areas are decontaminated. In addition, this method generates a significant amount of waste that is difficult to treat, transport, and store before its shipment to final disposal sites. Moreover, according to the reports by Mainichi Japan on May 27, 2021, a survey by the Japanese Board of Audit showed that the radiation doses in almost 12,900 locations subject to decontamination near the FDNPP or around 2%

of the sites (561,232 locations) cleaned after the nuclear disaster, did not fall below the pre-decontamination levels.

13.3.3 Experimental Approach to Reduce the Risk of Cs Contaminated Forest Soil

Although the decontamination in agricultural and residential lands has resulted in relatively satisfactory results, decontamination in large contaminated forests is difficult, due to increased costs and labor, destructive impacts on forest ecosystems, and additional expenses required to dispose large amounts of waste soil.

To alleviate the adverse effects of ^{137}Cs contamination, the Japanese Ministry of Agriculture, Forestry, and Fisheries utilized different methods, such as removing topsoil and fallen leaves, cutting trees, and covering the forest floor with wood chips in the experimental sites in Kawauchi village, Hirono town, and the Iitate village of Fukushima Prefecture, after the FDNPP accident from April 2012 to June 2013. However, despite a reduction in the dose by 12–14%, the release and diffusion of ^{137}Cs from the forest ecosystems, especially for those located in sloped areas were confirmed.

To reduce the pollution risk to the surrounding water and vegetation, the use of immobilization additives is considered as a promising alternative treatment to inhibit the ^{137}Cs from being washed off and transferred from contaminated soil to vegetation. Several adsorbent materials, including wood charcoal, bamboo charcoal, and zeolite, have been used to fix ^{137}Cs in soil and thus, inhibit its transfer from the soil to the surrounding environments (Aung et al. 2015; Burger and Lichtscheidl 2018). However, few studies have focused on the inhibitory effect of ^{137}Cs transfer from soil using biochar and other industrial waste-based recycling material adsorbents; correspondingly, the associated knowledge is also insufficient.

To select effective additives for ^{137}Cs immobilization, provide valuable references for the sorption and transfer behavior of ^{137}Cs in water, vegetation, and soil environments, and address ^{137}Cs contamination problem in forested soil, we collected soil samples from the topsoil of evergreen coniferous forest (0–15 cm depth), which is most widely distributed soil in Japan, from the vicinity of Ijira Lake in Gifu Prefecture. ^{133}Cs stable isotope was used as the surrogate for ^{137}Cs because both show similar physicochemical properties. After evaluating the fixation capability of Cs on different recycling materials based on sorption experiments, candidate recycling materials as Cs-fixing additives were selected. Subsequently, through pot cultivation experiments, the inhibitory effects of the selected recycling materials on Cs transfer from contaminated forest soil to vegetation and water penetrated from the potting soil were investigated and are described comprehensively in the subsequent sections.

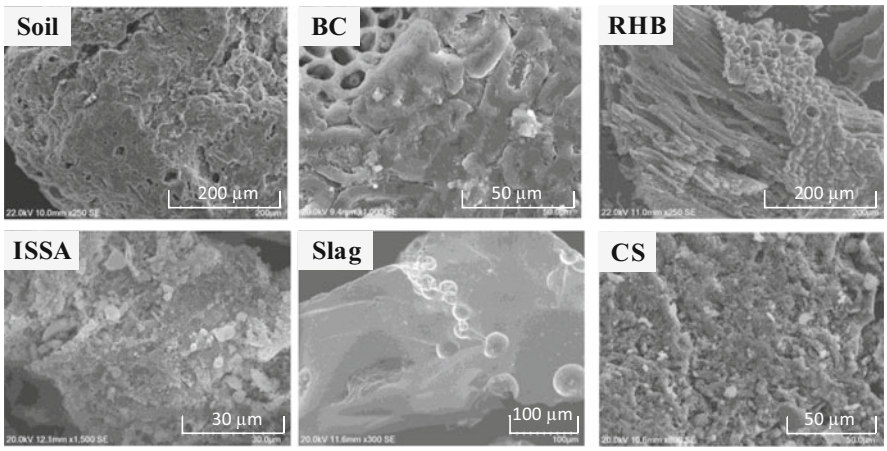

Fig. 13.5 SEM micrographs of soil and the five recycling materials. *BC* coconut shell biochar, *RHB* rice husk biochar, *ISSA* incinerated sewage sludge ash, *CS* carbonized sludge

13.3.3.1 Fixation Capability Comparison of Recycling Materials for Cs Immobilization in Contaminated Forest Soil

Five recycling materials were used for comparison: coconut shell biochar (BC), rice husk biochar (RHB), blast furnace slag (hereafter referred to as slag), incinerated sewage sludge ash (ISSA), and carbonized sludge (CS). BC and RHB were obtained from the TAKII Seed Corporation and KANSAI Corporation, Japan, respectively, and the slag was obtained from the NISSHIN KOGYO Corporation, Japan. ISSA was acquired after P was recovered from the North Wastewater Treatment Plant of Gifu City in central Japan Gifu Prefecture. CS was a product of carbonization using mixed sludge from several small biological wastewater treatment facilities and was obtained from the Japan Environmental Management Center Co. Ltd., Kaizu City, Gifu Prefecture, Japan. The scanning electron microscopy (SEM) images of the recycling materials and the soil used are shown in Fig. 13.5.

Bottle-point batch sorption experiments were conducted to generate isotherm data for Cs after conducting sorption on each recycling material, soil, and recycling material-soil mixtures having different mixing ratios (7:3, 5:5, and 3:7 by weight). The initial Cs concentration varied at 0, 10, 50, 100, 500, and 1000 µg L^{-1}. The sorbent added to all bottles was fixed to an identical amount of 0.1 g in the dry state. After adding 30 mL of the Cs solution diluted to the designated concentration in each bottle, all bottles were shaken at 20 °C for 48 h to ensure sorption equilibration. Subsequently, the mixed solution in each bottle was centrifuged at 3500 rpm for 5 min, and the supernatant was filtered through a 0.2-µm membrane filter. The filtrate was then subjected to Cs quantification using inductively coupled plasma mass spectrometry (ICP-MS) (Agilent 7500 Series, Agilent, USA). The distribution of Cs adsorbed on the sorbent was analyzed using SEM/ energy dispersive X-ray

analysis (EDX) (Hitachi SU-3500). In addition, the basic physicochemical properties of the recycling materials, soil, and their mixtures under different mixing ratios were also pre-analyzed.

The acquired isotherm data were described by the Freundlich isotherm model. The Freundlich K and Cs distribution after sorption on the recycling materials analyzed by SEM/EDX indicated that CS followed by BC and ISSA had larger fixation capability for Cs than the sample soil, suggesting that these materials can serve as potential additives for Cs immobilization in contaminated forest soils (Shao et al. 2018). In addition, parametric positive correlations were observed between the fixation capability of Cs and the property-related indexes of the recycling materials (cation exchange capacity, CEC; organic matter content; and K mass concentration).

13.3.3.2 Examination of Inhibition Effects of the Selected Recycling Materials on the Cs Transfer to Vegetation and Water

To examine the inhibitory effects of the BC, ISSA, and CS, on Cs transfer from contaminated forest soils to vegetation and penetrated water, a pot experiment was conducted in a greenhouse at the Gifu University.

The potting soil in each pot was obtained by separately adding BC, ISSA, and CS at three different concentrations (0, 5%, and 10%, w/w) to the forested soil, which was pre-adjusted to three different ^{133}Cs contamination levels (0, 25, and 50 mg kg^{-1}). Moreover, Napier grass (*Pennisetum purpureum*) was cultivated because it can accumulate high Cs concentrations (Kang et al. 2012).

After 30 d, all grasses were harvested and washed with tap water to remove all soil particles from the surface. This was followed by washing with deionized water. Subsequently, the grasses were separated into different parts (leaf blade, leaf sheath, and root), and freeze-dried under vacuum freeze-drying conditions for 24 h to obtain a constant dry weight. The dried grass samples were crushed using a crusher and digested with nitric acid in an autoclave (Navarrete-López et al. 2012). The Cs and K concentrations of the digested samples were measured using ICP-MS (Agilent

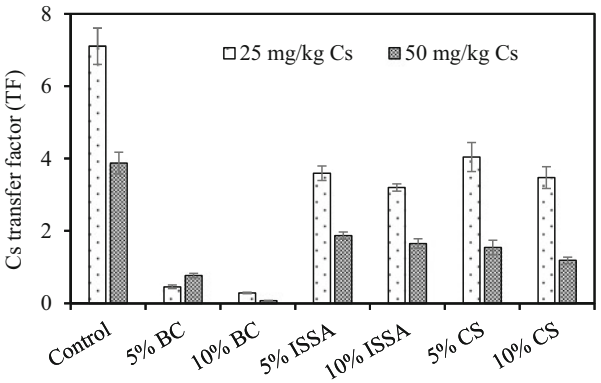

Fig. 13.6 Soil-to-plant transfer factor of Cs under different Cs contamination levels and additive additions. *BC* coconut shell biochar, *ISSA* incinerated sewage sludge ash, *CS* carbonized sludge

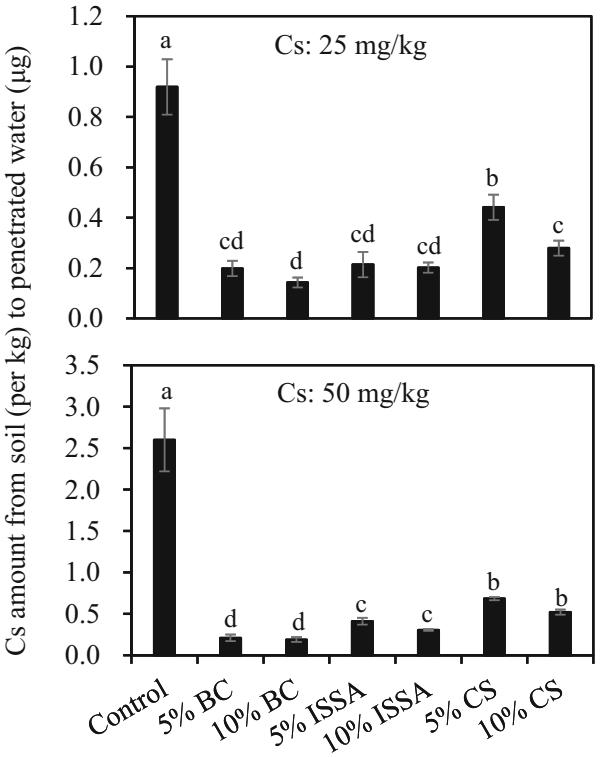

Fig. 13.7 Amount of Cs released from soil (per kg) to the penetrated water. Different letters (**a**–**d**) indicate significant differences ($p < 0.01$) between different additive additions (reproduced from Shao et al. 2019). *BC* coconut shell biochar, *ISSA* incinerated sewage sludge ash, *CS* carbonized sludge

7700x). The distributions of Cs and other elements in the grasses and potting soils were analyzed using SEM/EDX. The penetrated water was collected during the final watering stage, and the Cs concentration in the water was also measured using ICP-MS.

As shown in Fig. 13.6, the value of the soil-to-plant transfer factor, which is an important parameter used in transfer models for predicting the contaminant concentration in plants and for estimating the impacts of internal dose on humans (Ban-Nai et al. 1999), significantly decreased after BC, ISSA, or CS applications, indicating that the Cs transfer from soil to grass was restrained. Thus, it can be concluded that all sorbent materials used in the study could inhibit Cs transfer to the food chain through plants, but the best performance was achieved by BC compared to ISSA and CS.

The Cs amount released from per unit of soil to the penetrated water is shown in Fig. 13.7. Compared to the control group (without additives), all three additives significantly reduced the Cs amount released from the soil to the penetrated water at different Cs contamination levels. At the 25 mg kg^{-1} Cs contamination level, adding BC, ISSA, and CS reduced the amount of released Cs by 78.4–84.4%, 76.7–78.0%, and 51.9–69.6%, respectively. Moreover, at the 50 mg kg^{-1} Cs contamination level, the released Cs was reduced by 91.9–92.7%, 84.4–88.2%, and 73.7–79.9% for BC,

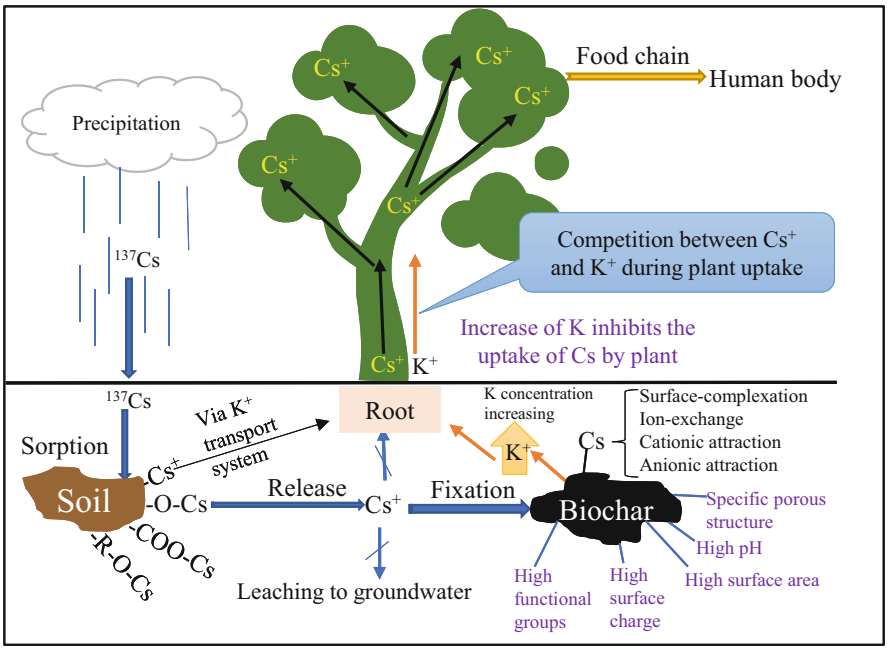

Fig. 13.8 Proposed interactions among Cs, soil, biochar, and plants (reproduced from Shao et al. 2020)

ISSA, and CS additions, respectively, and the amount of released Cs showed significant differences among the three additives and followed the order: BC < ISSA < CS.

The possible mechanisms of Cs immobilization by biochar are shown in Fig. 13.8. The bioavailability of Cs in plants is influenced by several processes, including the transfer of Cs from soil particles to water, uptake of Cs by plant roots, and translocation of Cs within plants (Yoshida et al. 2004). Biochar can enhance Cs immobilization in soil by increasing the specific adsorption of Cs and inhibiting plant uptake due to competition with K. Cs was adsorbed onto biochar mainly through cation exchange, surface interaction, and complexation with functional groups (such as –COOH and –OH) on the biochar surface (Uchimiya et al. 2011). In addition, soil properties could influence both the Cs availability in the soil and the phase of Cs absorbed by plant roots (Fujimura et al. 2015). For instance, biochar addition could increase the negative charges of soil particles, thereby increasing the adsorption affinity for cations (Jiang et al. 2012). Biochar properties, such as large surface area, high porosity, pH, and CEC, promote the fixation of mobile Cs onto biochar and facilitate the conversion of Cs into more stable forms (Beesley et al. 2011; Xie et al. 2015). Conversely, the increased K concentration in biochar-amended soil suppresses Cs uptake by plant roots and Cs transfer from roots to

aboveground parts due to the competitive relationship between Cs and K (Shao et al. 2020).

13.4 Efforts and Challenges in Managing and Controlling Soil Contamination Worldwide

Most countries have formulated management and control strategies for soil contamination. For example, in the United States, the Comprehensive Environmental Response, Compensation, and Liability Act (commonly known as the Superfund Law) was enacted as the first law on soil pollution in 1980, and it has achieved significant results to address soil contamination. According to this law, approximately 800 substances have been designated as harmful substances. Along with this law, the United States implemented other laws, such as the Resource Conservation and Recovery Act, Safe Drinking Water Act, and Water Quality Purification Act, with an aim to prevent soil and water contamination.

Germany has a long history of industrial development. Apart from soil contamination caused by industrial activities, military-based soil contamination due to defense projects associated with the two World Wars has also become a social problem. As a measure against soil contamination, Germany enforced the Federal Soil Protection Law in March 1999 and the Soil Conservation Contamination Site Ordinance in July of the same year. These laws have established permissible limits for different contaminants according to land use; additionally, according to these laws, purification targets can be determined based on the agreement between regulators and landowners for specific applications in each category. Moreover, the enforcement of these laws unifies disparate soil contamination countermeasures in different regions, thereby leading to increased rational and effective soil conservation efforts.

After Europe and the United States, soil contamination in China has become increasingly serious in recent years. To conserve soil resources and safeguard human health, in 2016, the Chinese central government allocated funds for soil contamination prevention and control and issued 28.5 billion RMB to support source control, risk control, restoration, and supervision of soil contamination; and promote the establishment of funds and multi-channel support for soil contamination prevention and control at the provincial level. According to the global Environmental Research Network, the market capacity of soil remediation industry in China during the 13th Five-Year Plan was 72.45 billion RMB, of which 15 billion RMB, 48.8 billion RMB, and 8.65 billion RMB were allocated for cultivated land restoration, site restoration, and coal mine restoration, respectively. Along with this financial capital, soil remediation began attracting social capital.

However, most countries worldwide still face various challenges regarding soil conservation. For example, data on non-point source emissions at the national level are scarce, especially in the developing countries. In some countries, the primary

cause of soil contamination is lack of awareness among the general population. For example, a survey revealed that more than 68% respondents in Bangladesh were unaware of the hazards of e-waste, while 12% believed that e-waste did not have negative effects (Islam et al. 2016). In addition, lack of information on the extent of contamination in the food chain reduces the understanding of the risks to health and food security. In addition, the soil management capacity varies widely among different countries. The foundation for soil environmental supervision and management is weak, and the technical support is insufficient in many developing countries, all of which have made the prevention and control of soil contamination difficult.

Soil remediation is characterized by a long cycle, high cost and slow effects. Thus, the lack of national-level infrastructure, standard or advanced technology, and systematic treatment make it difficult to ensure effective soil restoration. Moreover, financial resources for soil remediation and environmentally sound waste management are insufficient. For example, although China adopted its first soil contamination law as its latest effort to address environmental problems, strategies to finance the remediation of the existing damages remain unclear. During the 12th Five-Year Plan (2011–2015), only $4.546 billion was allocated for soil remediation, and mainly in urban areas. Further, the estimated cost of remedial work was approximately $1.3 trillion for 2016–2020. The Chinese government estimated that this amount possibly includes only a fraction of the total cost.

Restoring contaminated soil is a long-term and arduous task for all countries in the world. Soil remediation strategies are subjected to the concentrations and amounts of the contaminants, geographical conditions as well as financial resources. In addition, for successful soil remediation the integrated implementation of different physical, chemical and biological technologies will be the key.

13.5 Conclusion

Soil is an important component of the ecosystem, as most of the food we consume originates from it. Therefore, maintaining soil purity, fertility and its toxin-free characteristic is important. However, with the increase in the impacts of human activities on the environment, soil has become increasingly contaminated. Contaminants such as heavy metals and radioactive ^{137}Cs which cannot be easily degraded and will persist in the environment for a long duration. Consequently, this may cause serious problems for the next generations.

This chapter introduces the types and sources of soil contaminants, global status of soil contamination, soil remediation technologies, soil contamination situation in Japan after the FDNPP accident, and effective soil decontamination practices to reduce the impact of radioactive ^{137}Cs on human health and the environment. Moreover, a case study to address ^{137}Cs contaminated forest soil using different industrial waste materials based on sorption and pot experiments was introduced. We found that the application of biochar significantly decreased the accumulated Cs concentration in vegetation and inhibited Cs transfer from soil to vegetation and

water, thus, showing high performance in reducing the bioavailability of Cs in soil. This finding serves as a valuable reference for addressing the Cs contamination problem in forest areas because biochar as a soil amendment is inexpensive and can improve soil fertility, soil water holding capacity, and aeration status. However, the safety and biological toxicity of biochar needs to be further studied through long-term field experiments before large-scale application in different soil types.

Efforts to address soil contamination have been undertaken for several years. Improving the soil environment is a long-term and arduous task for all countries worldwide. With the improvements in public awareness regarding environmental protection and governmental support, more economical and efficient soil remediation technologies have been recently developed and applied. Furthermore, with the increasing awareness on green and sustainable remediation in many countries, soil contamination will be completely controlled and the sustainable development of soil resources will be achieved by using the most optimum remediation technology.

References

Aung HP, Aye YS, Mensah AD, Omari RA, Djedidi S, Oikawa Y, Ohkama-Ohtsu N, Yokoyama T, Bellingrath-Kimura SD (2015) Relations of fine-root morphology on ^{137}Cs uptake by fourteen brassica species. J Environ Radioact 150:203–212

Bandara JMRS, Senevirathna DMAN, Dasanayake DMRSB, Herath V, Bandara JMRP, Abeysekara T, Rajapaksha KH (2008) Chronic renal failure among farm families in cascade irrigation systems in Sri Lanka associated with elevated dietary cadmium levels in rice and freshwater fish (tilapia). Environ Geochem Hlth 30(5):465–478

Ban-Nai T, Murmatsu Y, Yanagisawa K (1999) Transfer of some selected radionuclides (Cs, Sr, Mn, Co, Zn and Ce) from soil to root vegetables. J Radioanal Nucl Chem 241:529–531

Beesley L, Moreno-Jiménez E, Gomez-Eyles JL, Harris E, Robinson B, Sizmur T (2011) A review of biochars' potential role in the remediation, revegetation and restoration of contaminated soils. Environ Pollut 159:3269–3282

Boubriak I, Akimkina T, Polischuk V, Dmitriev A, McCready S, Grodzinsky D (2016) Long term effects of Chernobyl contamination on DNA repair function and plant resistance to different biotic and abiotic stress factors. Cytol Genet 50(6):381–399

Burger A, Lichtscheidl I (2018) Stable and radioactive cesium: a review about distribution in the environment, uptake and translocation in plants, plant reactions and plants' potential for bioremediation. Sci Total Environ 618:1459–1485

Cameselle C, Gouveia S (2019) Phytoremediation of mixed contaminated soil enhanced with electric current. J Hazard Mater 361:95–102

Cristaldi A, Conti G, Jho E, Zuccarello P, Ferrante M (2017) Phytoremediation of contaminated soils by heavy metals and PAHs. A brief review Environ Technol Inno 8:309–326

Dada E, Njoku K, Osuntoki A, Akinola M (2015) A review of current techniques of physico-chemical and biological remediation of heavy metals polluted soil. Ethiop J Environ Stud Manag 8(5):606–615

Diss K (2019) Recycled electronics are turning Thailand into a 'dumping ground for hazardous waste'. ABC, 16 July 2019. Available at https://www.abc.net.au/news/2019-07-16/recycled-tech-from-western-nations-destroying-thai-villages/11274578

FAO and UNEP (2021) Global assessment of soil pollution: report, Rome. https://doi.org/10.4060/cb4894en

Fujimura S, Muramatsu Y, Ohno T, Saitou M, Suzuki Y, Kobayashi T, Yoshioka K, Ueda Y (2015) Accumulation of ^{137}Cs by rice grown in four types of soil contaminated by the Fukushima Dai-ichi nuclear power plant accident in 2011 and 2012. J Environ Radioact 140:59–64

IMF (2018) Regional economic outlook. Asia Pacific: good times, uncertain times, a time to prepare., p. 76. Regional Economic Outlook No. 0258–7440. Washington, DC, International Monetary Fund. https://www.imf.org/en/Publications/REO/APAC/Issues/2018/04/16/areo0509

Islam MT, Abdullah AB, Shahir SA, Kalam MA, Masjuki HH, Shumon R, Rashid MH (2016) A public survey on knowledge, awareness, attitude and willingness to pay for WEEE management: case study in Bangladesh. J Clean Prod 137:728–740

Jiang TY, Jiang J, Xu RK, Li Z (2012) Adsorption of Pb (II) on variable charge soils amended with rice-straw derived biochar. Chemosphere 89:249–256

Kang DJ, Seo YJ, Saito T, Suzuki H, Ishii Y (2012) Uptake and translocation of cesium-133 in napiergrass (*Pennisetum purpureum Schum.*) under hydroponic conditions. Ecotoxicol Environ Saf 82:122–126

Komatsu M, Hashimoto S, Matsuura T (2021) Effects of species and geo-information on the ^{137}Cs concentrations in edible wild mushrooms and plants collected by residents after the Fukushima nuclear accident. Sci Rep 11:22470

KOR-MOE (2017) Soil & groundwater related organizations discussion. http://me.go.kr/home/web/index.do?menuId=10264

Kumar A, Bisht B, Joshi V, Dhewa T (2011) Review on bioremediation of polluted environment: a management tool. Int J Environ Sci 1(6):1079–1093

Kumar S, Prasad S, Yadav K, Shrivastava M, Gupta N, Nagar S, Bach Q, Kamyab H, Khan S, Yadav S, Malav L (2019) Hazardous heavy metals contamination of vegetables and food chain: role of sustainable remediation approaches- a review. Environ Res 179 (Part A) 108792

Lajayer B, Moghadam N, Maghsoodi M, Ghorbanpour M, Kariman K (2019) Phytoextraction of heavy metals from contaminated soil, water and atmosphere using ornamental plants: mechanisms and efficiency improvement strategies. Environ Sci Pollut Res 26:8468–8484

Li J, Chen L, Zhan B, Wang L, Poon C, Tsang D (2021) Sustainable stabilization/solidification of arsenic-containing soil by blast slag and cement blends. Chemosphere 271:129868

Liu J, Huang W, Mo A, Ni J, Xie H, Hu J, Zhu Y, Peng C (2020) Effect of lychee biochar on the remediation of heavy metal-contaminated soil using sunflower: a field experiment. Environ Res 188:109886

Liu L, Li W, Song W, Guo M (2018) Remediation techniques for heavy metal-contaminated soils: principles and applicability. Sci Total Enviro 633:206–219

Lu K, Yang X, Shen J, Robinson B, Huang H, Liu D, Bolan N, Pei J, Wang H (2014) Effect of bamboo and rice straw biochars on the bioavailability of cd, cu, Pb and Zn to sedum plum bizincicola. Agric Ecosyst Environ 191:124–132

Mahar A, Wang P, Ali A, Awasthi M, Lahori A, Wang Q, Li R, Zhang Z (2016) Challenges and opportunities in the phytoremediation of heavy metals contaminated soils: a review. Ecotoxicol Environ Saf 126:111–121

Ministry of Health, Labour and Welfare (2018). Information on the great East Japan earthquake: food http://www.mhlw.go.jp/english/topics/2011eq/index_food.html

Navarrete-López M, Jonathan MP, Rodríguez-Espinosa PF, Salgado-Galeana JA (2012) Autoclave decomposition method for metals in soils and sediments. Environ Monit Assess 184(4): 2285–2293

Shao H, Wei Y, Li F (2018) Fixation capability of recycling materials as potential additives for cesium immobilization in contaminated forest soil. J Radioanal Nucl Chem 319(1):315–326

Shao H, Wei Y, Li F (2019) Inhibition effects of industrial waste-based sorption materials on cesium transfer from contaminated soil to vegetation and penetrated water. Environmental Science 32(1):1–10

Shao H, Wei Y, Zhang F, Li F (2020) Effects of biochars produced from coconut shell and sewage sludge on reducing the uptake of cesium by plant from contaminated soil. Water Air Soil Pollut 231(550):1–12

Shao H, Wei Y, Wei C, Zhang F, Li F (2021) Insight into cesium immobilization in contaminated soil amended with biochar, incinerated sewage sludge ash and zeolite. Environ Technol Inno 23: 101587

Shen Z, Jin F, O'Connor D, Hou D (2019) Solidification/stabilization for soil remediation: an old technology with new vitality. Environ Sci Technol 53:11615–11617

Tian Q, Sasaki K (2019) Application of fly ash-based materials for stabilization/ solidification of cesium and strontium. Environ Sci Pollut Res 26:23542–23554

Tu C, Wei J, Guan F, Liu Y, Sun Y, Luo Y (2020) Biochar and bacteria inoculated biochar enhanced cd and cu immobilization and enzymatic activity in a polluted soil. Environ Int 137: 105576

Uchimiya M, Klasson KT, Wartelle LH, Lima IM (2011) Influence of soil properties on heavy metal sequestration by biochar amendment. 1. Copper sorption isotherms and the release of cations. Chemosphere 82:1431–1437

Wang F, Xu J, Yin H, Zhang Y, Pan H, Wang L (2021) Sustainable stabilization/ solidification of the Pb, Zn, and cd contaminated soil by red mud-derived binders. Environ Res 284:117178

Xiao R, Ali A, Wang P, Li R, Tian X, Zhang Z (2019) Comparison of the feasibility of different washing solutions for combined soil washing and phytoremediation for the detoxification of cadmium (cd) and zinc (Zn) in contaminated soil. Chemosphere 230:510–518

Xie T, Reddy KR, Wang C, Yargicoglu E, Spokas K (2015) Characteristics and applications of biochar for environmental remediation: a review. Crit Rev Envi Sci Tec 45(9):939–969

Xu L, Cui H, Zheng X, Zhu Z, Liang J, Zhou J (2016) Immobilization of copper and cadmium by hydroxyapatite combined with phytoextraction and changes in microbial community structure in a smelter-impacted soil. RSC Adv 6(106):103955–103964

Yan A, Wang Y, Tan SN, Mohd Yusof ML, Ghosh S, Chen Z (2020) Phytoremediation: a promising approach for revegetation of heavy metal-polluted land. Front Plant Sci 11:359

Yoshida S, Muramatsu Y, Dvornik A, Znuchenko T, Linkov I (2004) Equilibrium of radiocesium with stable cesium within biological cycle of contaminated forest systems. J Environ Radioact 75:301–313

Zhao F, Ma Y, Zhu Y, Tang Z, Mc Grath S (2015) Soil contamination in China: current status and mitigation strategies. Environ Sci Technol 49:750–759

Zheng R, Chen Z, Cai C, Wang X, Huang Y, Xiao B, Sun G (2013) Effect of biochar from rice husk, bran, and straw on heavy metal uptake by pot-grown wheat seedling in a historically contaminated soil. Biol Res 8:5965–5988

Chapter 14
Evaporation in Arid Regions

Ichiro Tamagawa

Abstract Arid areas are among the typical ground types. In this chapter, evaporation in arid areas is introduced. Evaporated water vapor is carried by turbulence in the surface boundary layer, as is well described by the Monin–Obukhov similarity theory. A practical method of evaluating the evaporation amount from deserts is introduced here. Additionally, the dry surface layer in sandy soil is mentioned. Evaporation occurs under the soil surface, and the behavior of the evaporated water vapor in the dry surface layer connects the ground and the atmosphere.

Keywords DSL · HEIFE · Monin–Obukhov similarity · Sand desert · SBL · Turbulence

14.1 Introduction

This chapter introduces the basic idea for treating water and water vapor movement over or under the ground surface in arid areas, especially from the viewpoint of direct in situ observations.

The United Nations Environment Program (2006) said that the aridity index, which is the ratio of the precipitation amount to the potential evaporation amount, is one of the estimators commonly used to measure aridity. Aridity indices less than 0.20 mean that precipitation supplies under 20% of the water required for optimum plant growth. Areas with aridity indices less than 0.05 are classified as "hyperarid" and occupy 7.5% of the world. In contrast, areas with aridity indices from 0.05 to 0.20, occupying 12.1% of the world, are classified as "arid." The land covers in these areas are mostly sparse with no vegetation.

In this chapter, sand deserts are imaged as the simplest samples to describe the water movement through the ground surface, although there are other types of surfaces, such as oases, lakes, rivers, and other types of deserts. The water movement

I. Tamagawa (✉)
River Basin Research Center, Gifu University, Gifu, Japan
e-mail: tama@green.gifu-u.ac.jp

F. Li et al. (eds.), *River Basin Environment: Evaluation, Management and Conservation*, https://doi.org/10.1007/978-981-19-4070-5_14

from rivers or lakes to deserts and its consumption by evaporation are of great interest and importance to the understanding of the water budget of an area. However, this chapter focuses on one-point scale processes as basic components of water movement. As frequently done, we considered them one-dimensionally, which implies a horizontally homogeneous surface and that water and water vapor move only vertically. These processes seem simple because only evaporation occurs on the sand surface (i.e., without vegetation activity). Thus, simple physical processes are expected to describe these phenomena.

14.2 Water and Water Vapor Movement over the Ground Surface and the Boundary Layer

Generally speaking, water vapor evaporating from the surface is carried by atmospheric motion, forms clouds, and falls as precipitation. In this chapter, we focused on the processes near the surface.

The air at the bottom of the atmosphere touches the ground surface and is heated by solar radiation during daytime and cooled by radiative cooling. Usually, air parcels (i.e., small volumes of air) can move in limited layers and cannot move into the upper atmosphere because the potential temperature of the upper atmosphere is higher than that of the lower atmosphere. Potential temperature is defined as the temperature of the air compressed adiabatically to the reference pressure 1000 hPa, where the state with no heat exchange is called the adiabatic state. It is useful in considering the vertical movement of air because the air temperature varies by expansion or compression because of pressure. The difference in the potential temperature between an air parcel and the surrounding atmosphere determines the buoyancy force acting on the parcel. Only nonadiabatic processes, such as condensation heating, heat exchange on the ground surface, and radiative heating/cooling, can change the potential temperature. Thus, meteorologists prefer using the potential temperature in comparing the air at different altitudes.

The air parcel heated on the ground surface has a higher potential temperature and thus obtains an upward buoyancy force. However, the upward movement of the air parcel eventually stops, and it stays inside a shallow layer because the upper atmosphere has a higher potential temperature. The heated air is then mixed into the layer. Even at nighttime, the lower part of the mixed layer is cooled on the cooled surface, but the air over the cooled layer remains mixed because the cooled air layer does not grow well because of the negative buoyancy force.

The shallow layer where the air affected by surface conditions mostly stays is called the atmospheric boundary layer (ABL). Its depth is typically about 1 km, which varies because of climate and weather conditions. The water vapor coming into the atmosphere from the ground surface is well mixed in the ABL at daytime but does not spread well and stays in cool shallower layers at nighttime. We call the daytime ABL the mixing layer, where the water vapor concentrations become

uniform, except that for the surface layer. The surface layer is the lowest part of the ABL, where the short distance from the ground surface limits turbulent mixing. This lowest layer is called the surface boundary layer (SBL), typically the lowest 10% of the ABL. At nighttime, the atmosphere is cooled mainly by the radiatively cooled ground surface. The potential temperature decreases from the bottom. This stabilizes the layers near the ground surface (i.e., the vertical motion of air is reduced). If evaporation occurs, the evaporated water vapor stays in the lowest part of the ABL on the surface (almost the SBL), and its concentration increases at lower heights. These processes are explained in many textbooks of meteorology (e.g., Chap. 4 of Fleagle and Businger 1980; Chap. 1 of Stull 1988).

In summary, water vapor is produced by evaporation at the bottom of the atmosphere (i.e., the ground surface) and expands in the ABL. The SBL has a big role in bringing water vapor from the surface to the atmosphere. Additionally, we may ask about how water vapor can move into the atmosphere over the ABL. On the upper boundary of the ABL, turbulent mixing brings water vapor into the upper atmosphere through entrainment, but the amount of mixing is relatively much smaller than that in the SBL. Convective clouds, such as cumulonimbus, bring much water vapor through the convective air motion, which is driven by the heat released through condensation. In such a case, the ABL becomes a substructure under the cloud. In this chapter, we discuss an atmosphere without strong cloud activity to neglect such process. This is consistent with our topic on arid areas.

14.2.1 Surface Heat Budget and Turbulent Transport of Water Vapor

Evaporation consumes energy. Energy is another limiting condition of evaporation besides water existence itself. From the energy conservation law, the surface energy budget (14.1) shows the limiting condition for evaporation. The equation is written for the energy emitted from or absorbed by a unit area of the surface for a unit of time, and it shows the energy conservation law. Each term is called the vertical component of heat flux, frequently abbreviated as "heat flux." Its unit is W m^{-2} in the S.I. unit system. Because we considered only vertical components, the equation can avoid complicated vector mathematics. The equation can be written as

$$(1-\alpha)Q_s + Q_{ld} - Q_{lu} = H + \lambda E + G, \quad (14.1)$$

where Q_s is the shortwave (solar radiation) flux on the surface, α is the surface albedo, which is the reflectivity of the shortwave radiation, Q_{ld} is the downward longwave radiation flux from the atmosphere to the surface, Q_{lu} is the longwave radiation emitted from the ground surface to the atmosphere, H is the heat transported from the surface to the atmosphere, called the sensible heat flux, λE is the latent heat consumed by evaporation E at the ground surface, called the latent

heat flux, and G is the heat flux going into the ground. The sign of each term follows its explanation, and the terms can be negative to indicate the opposite direction. The left side of the equation shows radiative fluxes into the surface, and the right side shows fluxes from the surface. The equation is correct when water evaporates from the surface, when other chemical reactions or physical processes relating to energy do not occur, and the surface is just plain without depth. However, for surfaces with vegetation, the energy heating or cooling vegetation must be considered. In such cases, the canopy layer with some height is considered instead of an ideal surface without depth. However, such treatment was skipped here for simplicity. Still, including the heat budget of the ground with heat capacity variation due to the soil water content is important. The heat brought by precipitation must also be considered to close the heat budget correctly. As for arid surfaces, evaporation and heat consumption may occur under the surface. This point will be mentioned in a later section. Here we treat evaporation as occurring at the surface.

The sensible heat flux H and latent heat flux λE are carried by atmospheric processes. Heat and water vapor transported by molecular diffusion processes may dominate just on the surface; molecular diffusion loses its dominance only in the millimeter scale, where turbulent transfer processes dominate in other layers.

Air motion is turbulent in almost all the atmosphere. A textbook on fluid dynamics said that the Reynolds number $R_e = Uz/\nu$ indicates whether a flow is laminate or turbulent, where U is the speed of the air motion, z is the height used as the typical length scale of the air motion, and ν is the dynamic viscosity coefficient of the air. For example, a 1- m s^{-1} wind speed at a 1- m height above the ground surface and at 300 K ($\nu = 15.8 \times 10^{-6}$ $m^2 s^{-1}$) has a Reynolds value of more than 6×10^4, which is high enough to indicate turbulent motion.

Under turbulent conditions, wind and other atmospheric variables show much fluctuation in time and space. Horizontal homogeneity should be redefined to show the horizontal homogeneity of the turbulence statistics. Under turbulent conditions, heat, water vapor, and momentum are transferred by turbulence. The effects of molecular diffusion can be neglected from the viewpoint of transferring processes but not for the dissipation processes of turbulent motion. This is because turbulent motion progresses from large to small scales and dissipates its fluctuation in very small scales because of molecular diffusion and viscosity.

The turbulent fluxes H and λE can be measured using the vertical wind speed, temperature, and humidity. Only the vertical components of wind are important because we assumed horizontally homogeneous conditions and that the horizontal movement of heat and water vapor has no effect on the surface-to-atmosphere transport. Turbulent transfer processes can be measured using sensors in the field. The measurement must cover the turbulent fluctuation of water vapor, wind, and so on. Usually, sonic anemometer thermometers (SATs) and infrared gas analyzers are used. These instruments can measure at a sampling rate of greater than 10 Hz. The gas analyzer can measure the water vapor density and, often, the CO_2 density. Thus, it is frequently used to observe CO_2 absorption rates such as that over forests. The results of such carbon-related studies may be shown in some other chapters.

Back to the description of H and λE, the turbulent transport of H and λE can be evaluated using (14.2) and (14.3) in a technique called the eddy covariance method:

$$H = \rho\, C_{\mathrm{p}}\, \overline{w'T'}, \tag{14.2}$$

$$\lambda E = \lambda\, \rho\, \overline{w'q'}, \tag{14.3}$$

where ρ is the density of air, C_{p} is the specific heat of a unit mass of air at constant pressure, w is the vertical component of wind velocity, T is the absolute temperature, and q is the specific humidity, which is the water vapor mass per unit mass of air. The symbols $\bar{}$ and $'$ show the average and turbulent fluctuation components of each variable. For the temperature turbulent fluctuation, $T' = T - \bar{T}$, $q' = q - \bar{q}$, and $w' = w - \bar{w}$. The averaging period and sampling rate should be considered the statistics of turbulence such as those written in terms of the cospectral density function in Kaimal and Finnigan (1994). Roughly saying, 30-min recording with 10-Hz sampling is a typical configuration for observations on the point from a height of several tens of meters.

The meaning of the covariance $\overline{w'q'}$ can be explained as follows: the amount of water vapor transported vertically by wind for a unit horizontal area for a unit time can be expressed as $\rho_{\mathrm{v}} w$, where ρ_{v} is the density of water vapor, considering that w multiplied by a short time is the volume passing the unit area for this short time and that the density multiplied by the volume gives the mass. So, on average, $E = \overline{\rho_{\mathrm{v}} w} = \overline{\rho q w}$. The air density can be usually treated as a constant. Here, we used ρ to represent the constant air density, including water vapor itself. In this case $\rho_{\mathrm{v}} = \rho q$. When w, q are divided into mean components $\bar{w}, \bar{q}$ and turbulent components $w'q'$, given $\overline{w'} = 0$ and $\overline{q'} = 0$, the average water vapor flux (i.e., evaporation) can be shown as

$$E = \rho\, (\bar{w}\, \bar{q} + \overline{w'q'}). \tag{14.4}$$

The mass conservation law gives

$$\frac{\partial \rho}{\partial t} = -\left(\frac{\partial (\rho u)}{\partial x} + \frac{\partial (\rho v)}{\partial y} + \frac{\partial (\rho w)}{\partial z} \right), \tag{14.5}$$

where x, y represent the horizontal coordinates and u, v are the horizontal components of wind. (14.5) can be read as the convergence of mass flux resulting in increased mass. Then, we assumed horizontally homogenous conditions with constant ρ. (14.5) thus becomes $\frac{\partial \bar{w}}{\partial z} = 0$ because $\frac{\partial \rho}{\partial t} = \frac{\partial (\rho u)}{\partial x} = \frac{\partial (\rho v)}{\partial y} = 0$. On the surface, $\bar{w} = 0$ leads to $\bar{w} = 0$ everywhere. Therefore,

$$E = \rho\, \overline{w'q'}. \tag{14.6}$$

In the same way, $H = \rho\, C_\mathrm{p}\, \overline{w'T'}$, considering that the heat consumed for the temperature change in open conditions can be expressed using C_p. The heat passed to or removed from the air on the surface gives the temperature fluctuation $C_\mathrm{p}T'$ because the heating process occurs at constant pressure conditions. H can be so as in (14.2).

The temperature T is not conserved in vertical motions, as mentioned earlier. Thus, the potential temperature must be used in considering atmospheric motion. Here, we assumed that the turbulence measurement is done at a fixed position not so far from the surface. The atmospheric pressure at some height is determined by the gravitational force acting on the air column above the height because vertical air motion usually has small acceleration to keep the balance between the pressure gradient force and gravity. This pressure is called hydrostatic pressure. The pressure changes only gradually because it is caused by the vertically integrated gravity force for all air above the point. Therefore, the pressure on the surface can be thought of as constant in a short time (e.g., 30 min). The pressure difference between the surface and the measurement height can be thought of as very small. Thus, the measured T' can be used as the surface value. In very strict discussions, small temperature corrections due to the pressure difference between the measuring height and surface might be needed, but these are usually negligible. Only the heat used at constant pressure conditions, which includes the work done by the density change due to temperature change, is considered to obtain the heat flux in (14.2).

In actual conditions, we must consider a bit more factors than those from the simple ideal conditions used in the above discussions. For instance, the ground surface may not be perfectly horizontally flat and may have some slopes and undulations. The direction of the heat flux must also be reconsidered. We can assume average wind flows along the surface, and we can use the direction perpendicular to the surface instead of the geometrically vertical direction because such coordinate change can keep the assumed horizontally homogenous surface. The assumption used over the horizontally homogenous surface means $\left|\frac{\partial s}{\partial x}\right|, \left|\frac{\partial s}{\partial y}\right| \ll \left|\frac{\partial s}{\partial z}\right|$ for some variable s to disregard its horizontal difference. Especially for wind, the important vertical component of the wind velocity obeys $\frac{\partial \bar{w}}{\partial z} = 0$, and $\bar{w} = 0$ at the surface gives $\bar{w} = 0$ everywhere. No mean vertical wind condition is important because the fluxes caused by the mean wind often show very large heat and water vapor transport. Moreover, if a geometrical $\bar{w}$ exist, the mean transport seems to be canceled over other places because the amount of air mass between the observation height and the surface is expected to be conserved. Vertically, we may expect the turbulent transfer to be more representative than the mean transfer. The turbulence statistical values along to the direction with the largest gradient of some variables are expected to be more representative, and the gradient perpendicular to the surface is the largest over the generally sloped and undulated surface.

For a more detailed calculation, we may have to consider the average of the vertical mass flux by turbulence. Warm air tends to move upward and cold air downward over a heated surface at daytime, resulting in a downward mass transfer by turbulence because lower-density air is exchanged with higher-density air and

vice versa at nighttime. These phenomena result in compensating flow through a very small mean motion of air, which may be smaller than the sensor's resolution and preciseness. Quantifying the water vapor produced by evaporation may be necessary to give the mean vertical transfer of heat aside from vapor transfer. If we have a perfectly flat uniform observation place with a perfectly precise sensor, transport can be detected as a vertical motion. However, the resolution and preciseness of the sensors and the flatness or homogeneity are not enough. Thus, we must consider these points in what is called the Webb, Pearman, and Leuning correction (Webb et al. 1980; Leuning 2007). This correction is sometimes important in evaluating CO_2 flux, but we do not want to dwell on this point here. For details, the readers are referred to Chap. 4 of Foken (2008).

14.2.2 Monin–Obukhov Similarity Describing Turbulence Statistics

The turbulent fluxes and other statistics relating to turbulence can be connected to each other, including the mean field by the Monin–Obukhov similarity (Chap. 5 of Stull 1988). The theory was developed in the 1940s and validated using turbulent observation experiments from the 1960s. Only a brief introduction is included here to discuss arid conditions.

The target is a horizontally homogenous and steady condition in the SBL with a roughly 100-m depth. Each turbulent flux becomes constant because the horizontally homogenous and steady condition gives no vertical divergence or convergence. In this condition where no other variations exist, the most important values in determining the vertical profile of the average values are the turbulent fluxes. In the simplest case when the buoyancy force does not work because of the constant potential temperature, only the Reynolds stress transfers horizontal momentum in the vertical direction through $\overline{u'w'}$. The vertical gradient of the averaged wind is $\partial\bar{u}/\partial z$, where $\bar{u}$ shows the mean wind component along the averaged wind direction, which is horizontal over the horizontally uniform surface, and z, w are the vertical coordinate and component of wind, respectively. The turbulent fluctuation of wind mixes the air parcel originally moving with other air on average. This means that larger $\bar{u}$ values at high altitudes give positive u' to the smaller $\bar{u}$ values at low altitudes because of the downward vertical motion with negative w' and vice versa. The covariance $\overline{u'w'}$ is always statistically negative over horizontally homogeneous and steady conditions. The drag velocity u_* is defined as $u_*^2 = -\overline{u'w'}$ to show the scale of the turbulent fluctuation. Considering the dimensions of each variable, $\frac{z}{u_*}\frac{\partial\bar{u}}{\partial z}$ can be a nondimensional variable. Thus, if there is no other variable, it should be constant.

$$\frac{kz}{u_*}\frac{\partial \bar{u}}{\partial z} = 1, \tag{14.7}$$

where the constant k is called the *von Kármán* constant, whose value is found to be almost 0.4. This kind of discussion is called "dimensional analysis" and gives a useful framework for complicated phenomena, and discussions on turbulence frequently use it. The essential point of dimensional analysis is in the selection of variables based on physical images. This relationship can also be modeled using simple physical models such as $|u'| \sim |w'| \sim l\frac{\partial \bar{u}}{\partial z}$, where l shows the length scale of the turbulent motion by considering the Taylor expansion of $\bar{u}$ as a function of z. The air parcel with different mean wind speeds at different heights gives a wind speed fluctuation $l\frac{\partial \bar{u}}{\partial z}$, and the turbulent wind is well mixed to forget the direction $|u'| \sim |w'|$. One more assumption is that the turbulent length scale is proportional to the height, $l = kz$. Then, $u_*^2 = -u'\bar{w}' = -\left\{kz\left|\frac{\partial \bar{u}}{\partial z}\right|\right\}^2$ can be written as (14.7), with k as the coefficient of the turbulent length scale, which is the eddy size including the information of the correlation coefficient for the momentum flux. The covariance $u'\bar{w}'$ becomes negative because the upward moving ($w' > 0$) air parcel has a lower mean wind speed ($u' < 0$), as mentioned earlier. Integrating (14.7) from $z = z_0$ to z, the average wind speed $\bar{u}$ as the function of height z,

$$\bar{u} = \frac{u_*}{k}\log\left(\frac{z}{z_0}\right), \tag{14.8}$$

is obtained, where z_0 is the imaginary lower limit of the turbulent layer to have $u = 0$. z_0 is called the roughness height, and it shows the surface roughness for drag efficiency. It is worth mentioning that hydraulics uses a little bit different definition. Thus, we must be careful in using roughness values from hydraulics.

The relationship shown in (14.8) is called the logarithmic law, which is frequently observed in the near-wall region of many fluids without buoyancy force. The height z is not necessarily the geometrical height from the surface. Often, $z - d$ is used to show the appropriate turbulent eddy size using the zero plane displacement d, and the definition of z itself may be ambiguous over very rough surfaces. The values of z_0 and d are frequently connected to the representative height of the obstacle over surfaces like a building height or a forest height. Here, we considered a flat surface to ignore such point, but sand dunes usually exist on real sand deserts. We skipped these details and focused on a flat surface.

The thermal stratification of the atmosphere gives another buoyancy force effect. Thus, the turbulent status must be considered with buoyancy force caused by temperature fluctuations. Temperature turbulence must have a strong relation to the sensible heat flux at the surface with the coefficient $\frac{g}{T}$, which connects the temperature fluctuation with the buoyancy acceleration, where g is the gravitational acceleration. The Monin–Obukhov stability

$$\frac{z}{L} = \frac{kzgT_*}{\bar{T}\,u_*^2}, \tag{14.9}$$

is a nondimensional parameter showing the effect of buoyancy on turbulence. T_* is the scale parameter of the temperature fluctuation defined as $u_*\,T_* = -\overline{w'T'}$ using u_*. By the same kind of turbulent transfer expression as u_*, $L = \frac{\bar{T}\,u_*^2}{kgT_*}$ is called the Obukhov length. The physical meaning of the Obukhov stability can be considered using the kinematic energy equation of turbulence motion in a horizontally uniform and steady condition. z/L corresponds to the ratio of the buoyancy decay (negative production) rate and the shear production rate of turbulent kinematic energy in the form of a scaling parameter. For details, please see Stull (1988). The sign of z/L is determined by T_*, in other words, by $-\overline{w'T'}$. A positive z/L shows that the turbulent kinetic energy produced by wind shear is decreased by the negative buoyancy force suppressing the turbulence under "stable" conditions. In contrast, a negative z/L shows that the turbulent energy additionally produced by buoyancy force enhances turbulence under "unstable" conditions. z/L equal to zero means no buoyance force under "neutral" conditions, which are the same as the logarithmic law condition. Strictly speaking, the virtual temperature should be used instead of T and the one used for T_* to include the effects of humidity on air density, but we did not use it here for simplicity and as it has little effect in arid conditions.

(14.7) can be expanded by incorporating it with z/L:

$$\frac{kz}{u_*}\frac{\partial \bar{u}}{\partial z} = \phi_m\left(\frac{z}{L}\right). \tag{14.10}$$

ϕ_m shows some experimental function of z/L, which is expected to be universal to all measurements satisfying the used assumption. The temperatures $T, \bar{T}$, and T_* are used instead of the potential temperature variables. This has been widely accepted in the literature because the potential temperature $\theta = T\left(\frac{P_0}{P}\right)^{\frac{C_p}{R}}$, where P, P_0 are the air pressure at the point and that at reference, respectively, and R is a gas constant for a unit mass of air, which has a factor determined only by pressure and is treated as a constant value. Thus, the $\frac{\theta'}{\theta} = \frac{T'}{T}$ relationship exists in the equations used above. For the vertical gradient, we must consider the difference between θ and T because θ is conserved in adiabatic motion, where turbulence is included, whereas T is not. By using the dry adiabatic lapse rate Γ_d,

$$\frac{\partial \bar{\theta}}{\partial z} = \left(\frac{P_0}{P}\right)^{\frac{C_p}{R}}\left(\frac{\partial T}{\partial z} + \Gamma_d\right), \tag{14.11}$$

where $\Gamma_d = \frac{g}{C_p} \sim 0.01\ \mathrm{K/m}$, which is small enough to neglect. In this case, the temperature profile is written as.

$$\frac{kz}{T_*}\frac{\partial \bar{T}}{\partial z} = \phi_h\left(\frac{z}{L}\right), \tag{14.12}$$

where ϕ_h is the empirical function of z/L for temperature, which is thought to be same for other scalar variables such as the specific humidity of water vapor and CO_2 concentration. For specific humidity,

$$\frac{kz}{q_*}\frac{\partial \bar{q}}{\partial z} = \phi_h\left(\frac{z}{L}\right), \tag{14.13}$$

where q_* is defined as $\overline{w'q'} = -u_*q_*$.

The integration of (14.10), (14.12), and (14.13) between appropriate heights, sensible heat flux, and latent heat flux may be written as

$$H = \rho C_p(-u_*T_*) = \rho C_p C_h U(T_s - T_a), \tag{14.14}$$

$$\lambda E = \rho\lambda(-u_*q_*) = \rho\lambda C_e U(q_1 - q_a), \tag{14.15}$$

where C_h, C_e are the so-called bulk coefficients for heat and water vapor, respectively. These coefficients are not only functions of z/L but also parameters expressing surface conditions such as roughness height and integration range. In this chapter, (14.10) is integrated from the roughness height to the observation height, (14.12) is done from the surface to the observation height, and (14.13) is from some lower height to the observation height. The Monin–Obukhov similarity theory is for turbulence statistics; however, the region very near the surface is out of the applicable region, and some other relationships, including molecular diffusion, may be assumed applicable to determine the relationship between the surface temperature and the air temperature. The integration itself can be done with some accuracy, and (14.14) may be expected.

The bulk equation of heat fluxes is used in numerical models such as weather prediction models because of its lower boundary condition with the surface heat budget equation. Even if we measure the turbulent flux directly, the comparison between the measured turbulence statistical values and the mean values can indicate the representativeness of the measurement by considering the assumptions used in the model to connect them.

Turbulence statistics other than fluxes can also be applied using the Monin–Obukhov similarity. For example, the standard deviation of the turbulent fluctuation of the vertical component of wind σ_w and temperature σ_T can be expressed as functions of z/L after normalization using u_* and T_*:

$$\frac{\sigma_W}{u_*} = \phi_w\left(\frac{z}{L}\right), \tag{14.16}$$

$$\frac{\sigma_T}{T_*} = \phi_T\left(\frac{z}{L}\right), \tag{14.17}$$

where ϕ_w and ϕ_T represent some function.

14.2.3 Surface Heat Budget and Turbulent Transportation of Water Vapor in Arid Areas

In arid areas, the fundamental physics is same, but the assumptions used in the above discussion might not be so. Thus, observed data are needed to elucidate these problems. The results of the Heihe River Basin Field Experiment (HEIFE; 1989–1993) (Mitsuta 2005) are introduced as examples. Intensive observations were made over a sand desert in northwest China in 1991 and 1992 for an early project measuring turbulent fluxes for a long-time evaluation of heat and water budgets. The Kaijo DAT-300 used as the SAT for the project was an already matured one, and the infrared gas analyzer for water vapor Kaijo AH-300 was in the development stage as an open-path gas analyzer of water vapor for field observations. A stable gas analyzer for water vapor and carbon dioxide started to be used for observations about after 2000. The data recording system had abilities inferior to those of current systems, especially as regards storing capacity. For these reasons, we could not continuously observe turbulent fluxes in those days but could observe mean meteorological variables. We had to connect the mean observation results with the turbulent flux measurement results at that time. Now, we can use continuous turbulent observations with solar panels and tough data loggers with Internet connection in our laboratory. However, considering the relationships among many statistics is still largely unexplored.

As for the turbulence statistics, (14.17) and the same relationship for q are examined:

$$\frac{\sigma_q}{|q_*|} = \phi_q\left(\frac{z}{L}\right). \tag{14.18}$$

The denominator in the left figure must be an absolute value because the signs of q_* and T_*, which correspond to the sign of z/L, are independent. Figure 14.1 shows the relationships between T and q for unstable conditions. ϕ_T and ϕ_q are expected to be the same because they are passively transferred by wind. ϕ_T in Fig. 14.1 shows a very large scatter in the range of $-\frac{z}{L} < 0.1$. This is because the temperature fluctuation and sensible heat flux must reach zero in neutral conditions. If the turbulent fluctuation of temperature were driven only by the movement of the air parcel due to turbulent motion as assumed by the Monin–Obukhov similarity, the temperature fluctuation and vertical transport of heat would vanish at all. This means that the value of ϕ_T is undefined in neutral conditions, which means $\frac{z}{L} = 0$. Usually, we have some temperature fluctuations caused by horizontal inhomogeneity or other

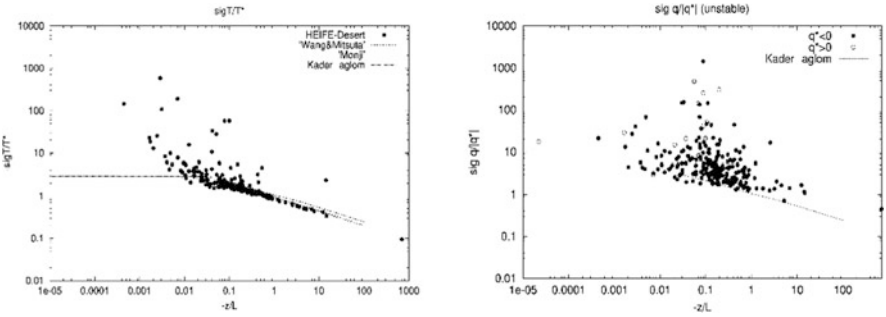

Fig. 14.1 The nondimensional standard deviation of the turbulent fluctuation of temperature and specific humidity. "sigT" and "sig q" are σ_T and σ_q in (14.17) and (14.18), respectively. Wang and Mitsuta (1991), Monji (1973), and Kader and Yaglom (1990) showed such relationship in previously published papers but only for temperature. Even in right figure, because of the unavailability of turbulence data of water vapor from the literature, the same relationship as that of temperature was expected. These figures were reproduced from Tamagawa (1996)

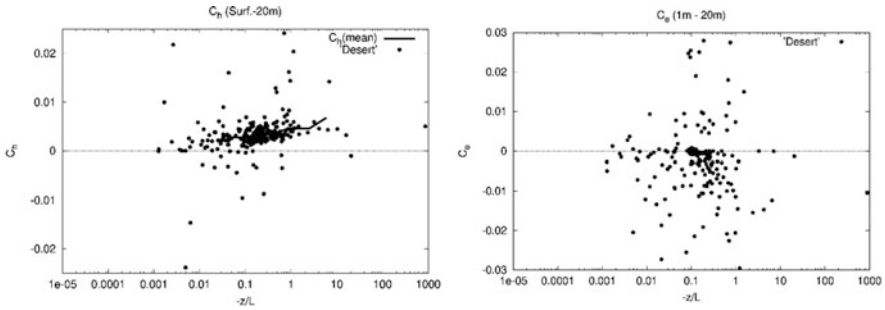

Fig. 14.2 The bulk coefficients calculated using observations (14.14) and (14.15). Data were taken from a desert station of the HEIFE project (1989–1993). The block averaged values are represented by thick lines in the Ch figure (after Tamagawa 1996)

phenomena, even in neutral conditions. Such fluctuations do not contribute to the vertical turbulent flux for T_* but contribute to σ_T, producing large σ_T/T_*. In unstable and stable conditions, temperature fluctuations caused by vertical motions and gradients become dominant, as supposed by the Monin–Obukhov similarity theory. As for ϕ_q in Fig. 14.2, the points show very large scatters. Only the lower edge of the distribution of points shows the same tendency as that seen in the temperature figure. This feature can be understood in the same way as that in the near-neutral condition and ϕ_T. The evaporation $\rho\, \overline{w'q'}$ from the arid surface is small due to the lack of moisture to give turbulent fluctuation and the vertical gradient of specific humidity. These contribute to the vertical transfer of water vapor, giving the q_* value, and some fluctuation caused by inhomogeneity or other factors gives σ_q to produce large ϕ_q. Only when the vertical transport of water vapor prevails can ϕ_q show the same behavior as that of ϕ_T outside of near-neutral conditions. The turbulent fluctuation of

water vapor may be considered the same as that of temperature with strong contamination of other fluctuations not related to the vertical transport of water vapor.

The first step in evaluating the amount of evaporation is connecting turbulent fluxes with the mean observation data. Figure 14.2 shows examples of the evaluation of the bulk coefficients for sensible heat and latent heat fluxes. The fluxes measured by the turbulent observation were compared with the mean temperature, specific humidity, and wind speed using (14.14) and (14.15). The observations of U, T_a, q_a were on the top of the observation tower (20 m), and the height of q_1 is the lowest point of the tower (1 m). The data were not screened so we could use all observed data to evaluate fluxes, although we selected data to very carefully evaluate, for example, the amount of carbon absorbed by a forest. Figure 14.2 shows only unstable conditions as examples. For the sensible heat and temperature, the bulk coefficient C_h shows some related, densely distributed points, although several data points show large scattering. C_h could be determined experimentally. The effect of the sand dune topography was included in the C_h behavior. In any way, the averaged C_h could be obtained. However, the data points scatter in a wide area for C_e, and even its negative values were frequently seen. This could be understood as follows: the small amount of evaporation from the dry sand surface gave a small q_*, $\partial q/\partial z$, giving unstable C_e, as recognized by looking (14.13). Also, the accuracy and resolution of the mean humidity might be doubtful. The directly measured turbulent water vapor flux E had reasonable results, showing water budget analysis in several weeks of evaporation in Mitsuta et al. (1995). The heat budget analysis that used (14.1) was done using the observed values in Mitsuta et al. (1995). The heat budget is almost close with a 10-day averaging with small residuals under 10 Wm^{-2}. The error of the daily heat budget was suggested to be caused by the heat flux into the ground G. We evaluated the very large variations in the soil temperature in very shallow depths caused by strong heating and cooling on the surface. Additionally, the temperature variation in deeper soil layers must be quantified. The annual cycle of deep soil temperature variations was evaluated using a thermal diffusion equation under the deepest observation temperature. The soil thermal characteristics were measured using sampled sand in a laboratory.

In the heat budget of (14.1), the radiation fluxes were measured using a pyranometer and a pyrgeometer for both directions. H could be evaluated from the mean temperature and the wind speed, and G could be determined using ground thermometers with special consideration for annual-scale long-time temperature variations. The remaining term LE could be evaluated as a residual of (14.1). Then, the evaporation rate E could be evaluated. Figure 14.3 shows the observed precipitation after 10-day averages with precipitation amount. Evaporation was stimulated by precipitation. The annual average of evaporation was about 120 mm/year, and that of precipitation was about 100 mm/year. The precipitated water was evaporated, and just a little more evaporation occurred to consume groundwater. The observed region is not so far from oases, and river water was used for irrigation. As the river “Heihe” flows into the desert to disappear with an endorheic lake of the Juyan Lake, the evaluated results seem reasonable.

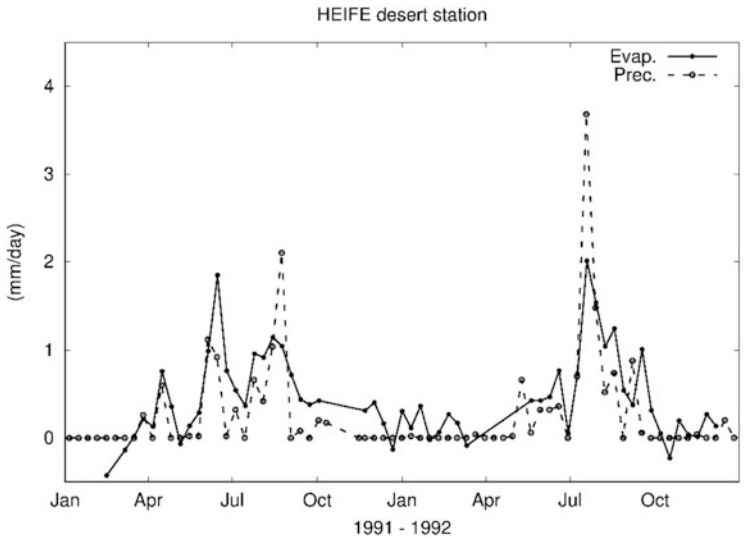

Fig. 14.3 The evaluated evaporation rate and observed precipitation at a desert station of HEIFE in 10-day averages (after Mitsuta et al. 1995)

Heat budget and analysis using turbulence were introduced to show an evaluation sample of evaporation in arid areas. The observation itself was of course tough, and careful analyses based on the knowledge of meteorology were required even in the simple surface condition of sand desert.

14.3 Water and Water Vapor Movement in Soil

One more short section is added to introduce the water movement in sands. Water movement in porous media is generally described by Darcy's law. The gradient of the water potential gives force for water to move against the resistant drag force caused by the flow with hydraulic conductivity. However, if large spaces (i.e., macropores) exist in soil, the water flow becomes turbulent, breaking Darcy's assumptions (Hillel 2004). The ground soil in humid areas has a crumb structure with macropores relating to vegetation activity, and vegetation has transpiration activities. Water movement in humid areas may be more difficult, but the soil in the sand desert is rather simple. The sand and the soil in the desert are well mixed by the wind, making them uniform without macropores or vegetation. Instead, of this simplicity, the soil pores are not filled with water, and the unsaturated layer of the soil must be considered. Even in humid areas, unsaturated zones may exist just on the surface, which we usually do not consider because they are shallow and because other points are more important. In arid areas, the unsaturated layer is developed much. For unsaturated soil, Philip and de Vries (1957) and de Vries (1958) gave a

framework for treating water and water vapor movement with temperature variations in soil using a set of equations. The full equations are skipped here to avoid too many equations and variables. They demonstrated the movement of liquid water due to its potential gradient and the water vapor movement due to the water vapor density gradient in unsaturated layers. The surface heat budget of (14.1) appears for temperature in the water movement analysis. In arid conditions, such as in sand deserts, the so-called dry surface layer (DSL) forms in the uppermost region of the soil. In DSL, liquid water does not move because the water in pores does not continue but is adsorbed on soil particles. Water vapor evaporates at deeper layers and diffuses in pores through the DSL to the sand surface and goes out to the atmosphere. Some brief details are shown below. The water vapor density in pores ρ_v, in the equilibrium state with the water in pores, is expressed as

$$\rho_v = \rho_0 e^{-\frac{\Psi g}{R_v T}}, \tag{14.19}$$

where R_v shows the gas constant for a unit mass of water vapor, and ρ_0 shows the saturated water vapor density at temperature T over the plain water surface. Ψ is expressed in units of height, following common usage in soil physics. Ψg shows the potential, that is, the energy for unit mass, of liquid water differing from the plain surface state due to capillary and adsorption by sand. The value of Ψ decreases rapidly as the soil water content decreases.

(14.19) is called Kelvin's equation. ρ_0 is a function of T, and the exponent of e also includes the temperature T. From both effects, ρ_v is determined by T and Ψ. The factor $e^{-\frac{\Psi g}{R_v T}}$ very rapidly decreased as the soil water content decreased. In the DSL, the profile of ρ_v becomes a quasi-steady state because changes ρ_v is connected to soil water content through Ψ and soil water works as the source or sink of water vapor. The water vapor flux becomes constant in the DSL to keep a steady ρ_v. This short consideration gives a picture of DSL: evaporation occurs at the bottom of DSL, which is called the drying front, and the produced water vapor is transported to the surface. The direct evaporation from the sand surface is negligible. ρ_v at the surface is approximately the same as that of the atmosphere because in arid conditions, the gradient of specific humidity q is small because of the small evaporation in SBL, as shown in (14.13). The evaporation rate E can be expressed as

$$E = K \frac{\rho_v(D) - \rho_{va}}{D}, \tag{14.20}$$

where $\rho_v(D)$ is the water vapor density in the soil at a depth D in the DSL, ρ_{va} is the atmospheric water vapor density near the surface, and K is the coefficient of diffusion in our DSL. K can be expressed by the molecular diffusivity of water vapor and soil air content to show the effective area for vertical diffusion, tortuosity, and so on. Kobayashi and Nagai (1995) reported the evaluation of evaporation of several days at the same desert station above-mentioned using a laboratory evaluated K as a function of water content and temperature. The water also brings soil solute

materials and releases them during evaporation. Thus, evaporation in arid areas is important in considering salinization. Experimental studies in laboratories were done using sample sand in Shimojima and Tamagawa (2001) and those in other studies where the DSL condition is considered.

As shown briefly, even in the simple conditions of sand deserts, evaporation still involves several processes, including water vapor diffusion in unsaturated layers, especially in the DSL. The water vapor gradient in the DSL connected the groundwater condition at the bottom of the DSL to the atmospheric humidity to determine the evaporation rate E. E affects the water amount in sand and thus can change the DSL depth. The processes in the DSL determine the evaporation amount in arid areas. The amount of evaporation is not large, but it determines soil water conditions. For the heat budget, λE in (14.1) disappears, and cooling by evaporation occurs in the evaporation level around the bottom of the DSL. This thin layer cooling may not be correctly measured with the thermometer in the sand. The amount of total cooling due to evaporation is still λE, and (14.1) can be applied to analyzing the observed data.

The most numerical simulation model on land surface processes assumes that the water content of the top layer of soil determines the evaporation rate. This is a little bit of rough treatment for evaporation in arid areas, although the computed water content is roughly adaptable, and the evaporation amount is small in arid areas. Several models were developed to include these processes. For example, Katata et al. (2007) included water and water vapor processes in soil and compared their results with commonly used land surface models in arid conditions. The developed model could perform well in showing the behavior of nightly adsorbed water in the DSL and its effects on surface temperature variations. Scanlon et al. (2003) also applied for the Philip and de Vries type model for the long-term simulation of water and chloride simulation.

As very shortly stated above, processes in soil layers are very important in arid areas. This is an actual limiting evaporation stage in arid areas. Measurements in soil seem to be still difficult in arid areas, for example, because sand-surface-level changes due to the movement of sand by wind and the high density of solute materials affect the electromagnetic characteristics of the water used in the water content measurement.

14.4 Conclusion

Topics relating to evaporation in arid areas were introduced. First, meteorological processes related to evaporation, such as the surface heat budget and turbulent transfer of heat and water vapor with Monin–Obukhov similarity theory, were explained with care for arid conditions. The results obtained from an old HEIFE project were used to explain the processes applied to evaluate evaporation. We explained the eddy covariance observation for a measured evaporation rate directly with turbulence observation as well as the heat budget relationship and the Monin–

Obukhov similarity in considering the observed results to connect the direct observed turbulent flux with the mean atmospheric variables. We suggest that the readers refer to the suggested readings for a more comprehensive understanding of micrometeorology. Soil physics was also briefly introduced, focusing on the DSL. The processes in the DSL microphysically determined the evaporation rate. Atmospheric processes only transferred water vapor and gave boundary conditions to the DSL from a soil process viewpoint. We have to recognize that the soil and the atmosphere are strongly connected to each other and must be considered as one system.

This kind of observational work has been done over many places in the world. The readers may read the results in other climate regions. Even operationally, worldwide meteorological observation networks and numerical weather or climate simulations are now available. However, it should be noted that observation networks and numerical models are neither perfect nor dense enough. Thus, observational studies are necessary for understanding phenomena in detail. These are also useful as ground truth data for simulations and remote sensing to validate and improve results.

References

de Vries DA (1958) Simultaneous transfer of heat and moisture in porous media. Trans Am GeophysUnion 39:909–916

Fleagle RG, Businger JA (1980) An introduction to atmospheric physics, 2nd edn. Academic press Inc., 432

Foken T (2008) Micrometeorology. Springer 306

Hillel D (2004) Introduction to environmental soil physics. Elsevier Science, p 494

Kader BA, Yaglom AM (1990) Mean fields and fluctuation moments in unstably stratified boundary layers. J Fluid Mech 212:637–662

Kaimal JC, Finnigan JJ (1994) Atmospheric boundary layer flows. Oxford University Press, p 289

Katata G, Nagai H, Ueda H, Agam N, Berliner PR (2007) Development of a land surface model including evaporation and adsorption processes in the soil for the land–air exchange in arid regions. J Hydrometeorol 8(6):1307–1324

Kobayashi I, Nagai H (1995) Measuring the evaporation from a sand surface at HEIFE desert station by the dry surface layer (DSL) method. J Meteorol Soc 73:937–945

Leuning R (2007) The correct form of the Webb, Pearman and Leuning equation for eddy fluxes of trace gases in steady and non-steady state, horizontally homogeneous flows. Boundary-Layer Meteorol 123:263–267

Mitsuta Y (2005) Sino-Japanese joint research project HEIFE: general view and results. J Nat Disaster Sci 22(1):45–51

Mitsuta Y, Tamagawa I, Sahashi K, Wang J (1995) Estimation of annual evaporation from the linze desert during HEIFE. J Meteor Soc Japan 73:967–974

Monji N (1973) Budgets of turbulent energy and temperature variance in transition zone from forced to free convection. J Meteor Soc Japan 51:133–145

Philip JR, de Vries DA (1957) Moisture movement in porous materials under temperature gradients. Eos Trans AGU 38:222–232

Scanlon BR, Keese K, Reedy RC, Simunek J, Andraski BJ (2003) Variations in flow and transport in thick desert vadose zones in response to paleoclimatic forcing (0–90 kyr): field measurements, modeling, and uncertainties. Water Resour Res 39:1179

Shimojima E, Tamagawa I (2001) Salinity on water and solute movement in a sand column induced by evaporation. J Japan Soc Hydrol Water Res 14(2):121–130

Stull RB (1988) An introduction to boundary layer meteorology. Springer 688

Tamagawa I (1996) Turbulent characteristics and bulk transfer coefficients over the desert in the HEIFE area. Boundary-Layer Meteorol 77:1–20. https://doi.org/10.1007/BF00121856

United Nations Environment Programme (2006) Global desert outlook, Edited by Exequiel Ezcurra, Division of Early Warning and Assessment (DEWA), United Nations Environment Programme, P.O. Box 30552, Nairobi 00100, Kenya, ISBN: 92–807–2722-2, UNEP Job No. DEW/0839/NA, 148

Webb EK, Pearman GI, Leuning R (1980) Correction of flux measurements for density effects due to heat and water vapour transfer. Quart J Roy Meteorol Soc 106:85–100

Wang J, Mitsuta Y (1991) Turbulence structure and transfer characteristics in the surface layer of the HEIFE Gobi area. J Meteor Soc Japan 51:587–593

Part III
Disaster Mitigation

Chapter 15
Feature Extraction and Analysis of Earthquake Motion

Masumitsu Kuse and Nobuoto Nojima

Abstract The evaluation of earthquake motion is basic problem in the earthquake engineering. Deep understanding of the earthquake motion characteristics of the amplitude, period and duration included in observation records is essential. In this chapter, the feature quantity that can explain the engineering characteristics included in the earthquake motion, makes proposal. First, the 99-dimensional feature vector representing the temporal characteristics of a strong motion on the basis of Husid plot was proposed. The Husid plot is defined as the time history of cumulative power of earthquake motion normalized to the total power. In addition, the Gaussian mixture model was applied to the 99-dimensional feature vector was proposed. The Gaussian mixture model approximates the original data in terms of mixture of multiple Gaussian distributions. Next, the time-frequency analysis of earthquake motion, the period-dependent feature vector based on the evolutionary power spectrum, which is proportional to displacement response envelope, was defined. The period-dependent feature vector was calculated from the time history of cumulative power of evolutionary power spectrum normalized to the total power with reference to Husid plot. Furthermore, the Gaussian mixture model was applied to the period-dependent feature vector.

Keywords Feature vector · Gaussian mixture model · Husid plot

M. Kuse (✉)
River Basin Research Center, Gifu University, Gifu, Japan
e-mail: kuse@gifu-u.ac.jp

N. Nojima
Department of Civil Engineering, Gifu University, Gifu, Japan
e-mail: nojima@gifu-u.ac.jp

F. Li et al. (eds.), *River Basin Environment: Evaluation, Management and Conservation*, https://doi.org/10.1007/978-981-19-4070-5_15

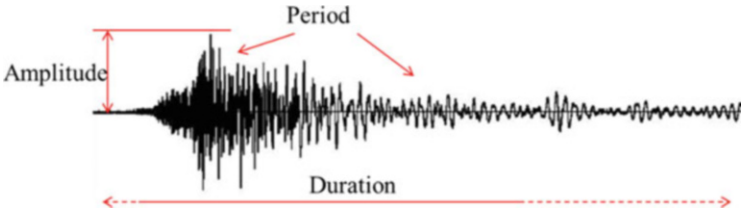

Fig. 15.1 Earthquake motion characteristics

15.1 Introduction

The evaluation of earthquake motion is basic problem in the earthquake engineering. Figure 15.1 shows the outline about the earthquake motion characteristics. As shown Fig. 15.1, deep understanding of the earthquake motion characteristics of the amplitude, period and duration included in observation records is essential. For example, the response spectrum gives useful information about earthquake motion representing period-dependent response amplitude. The group delay time representing the characteristics of duration is the evaluation of the phase characteristics of the earthquake motion. The average of the group delay time represents the position of the center of gravity on time axis, and the variance of the group delay time has the information of the duration characteristics. Using the group delay time, the prediction model of earthquake motion was developed (Sato et al. 1996). Nojima (2014) proposed the prediction equations for the JMA seismic intensity duration considering the shortest distance of the fault, shallow and deep ground data, and the earthquake type. Miyamoto and Honda (2009) proposed of the feature indices of earthquake motion by response value of nonlinear structural model. In the evaluation, the maximum response displacement and the historical absorbed energy were used. Ishii (2012) developed the response duration spectrum as period and duration characteristics of earthquake motion.

The wavelet transform (Iyama and Kawamura 1998) and the nonstationary spectrum (Kamiyama 1979) can describe the characteristics of the amplitude, period, and duration. These parameters show the time variation for each period. The amount of data expressing the earthquake motion is the same as the earthquake time history and the discrete wavelet transform. On the other hand, the amount of data for the continuous wavelet transform and the nonstationary spectrum drastically increases compared to that for the earthquake time history.

In this chapter, for the analysis of earthquake motion, the feature quantity that can explain engineering characteristics included in the earthquake motion, the 99-dimensional feature vector representing the temporal characteristics of strong motion on the basis of the Husid plot was proposed by the authors (Nojima et al. 2017, Kuse et al. 2017). The Husid plot is defined as the time history of cumulative power of earthquake motion normalized to the total power. In addition, the Gaussian mixture model was applied to the 99-dimensional feature vector was proposed. The Gaussian mixture model approximates the original data in terms of mixture of

multiple Gaussian distributions. The Gaussian mixture model approximates the 99-dimensional feature vector with much less amount of data. Next, for the time-frequency analysis of earthquake motion, the period-dependent feature vector based on the evolutionary power spectrum, which is proportional to displacement response envelope, was defined. The period-dependent feature vector was calculated from the time history of cumulative power of evolutionary power spectrum normalized to the total power with reference to Husid plot. Furthermore, the Gaussian mixture model was applied to the period-dependent feature vector.

15.2 Outline of Feature Vector and Gaussian Mixture Model

In this chapter, the 99-dimensional feature vector representing the temporal characteristics of a strong motion is used. The feature vector is calculated from the Husid plot that is defined as the time history of cumulative power of earthquake motion normalized to the total power. Figure 15.2 shows the conceptual diagram of the Husid plot $Pc(t)$ and the feature vector $\mathbf{t}$. $Pc(t)$ is calculated from the Eq. (15.1) using the acceleration time history $A(t)$. The 99-dimensional feature vector t defines from the percentile values t_i $(i = 1, \ldots, 99)$ discretized in every 1% steps of $Pc(t)$.

$$P_C(t) = \frac{100 \int_0^t A^2(\tau)\, d\tau}{\int_0^{t_{\text{end}}} A^2(\tau)\, d\tau} \tag{15.1}$$

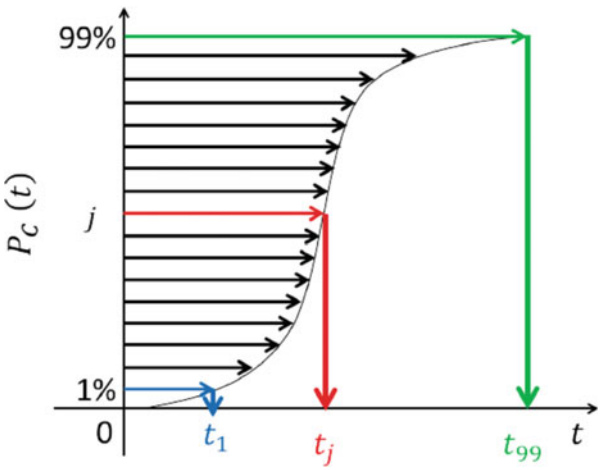

Fig. 15.2 Husid plot and the feature vector **t**

Next, in order to represent of earthquake motion with more less the amount of data, the Gaussian mixture model was applied. The Gaussian mixture model approximates the original data in terms of mixture of multiple Gaussian distributions. The Gaussian distributions $\phi(t)$ with mean μ and standard deviation σ is shown Eq. (15.2).

$$\phi(t) = \frac{1}{\sqrt{2\pi}\,\sigma} \exp\left\{-\frac{(t-\mu)^2}{2\sigma^2}\right\} \tag{15.2}$$

The probability density function represented by the Gaussian mixture model of M elements is shown Eq. (15.3).

$$p(t;\theta) = \sum_{m=1}^{M} \pi_m \phi(t;\mu_m,\sigma_m) \tag{15.3}$$

where $\pi_m(1,\ldots,M)$ is the mixture fraction of element model m, and π_m satisfies Eq. (15.4). As shown Eq. (15.5), the vector θ represents the all parameters.

$$\pi_m \geq 0, \quad \sum_{m=1}^{M} \pi_m = 1 \tag{15.4}$$

$$\theta = \{\pi_m, \mu_m, \sigma_m; m = 1, \ldots, M\} \tag{15.5}$$

The number of element model M is defined from the information criterion. In this paper, BIC(Bayesian Information Criterion) is used.

$$\mathrm{BIC}\left(\widehat{\theta}\right) = -2\sum_{i=1}^{I} \ln p\left(t_i;\widehat{\theta}\right) + k \ln I \tag{15.6}$$

where I is number of data and k is degree of freedom with this model. In this study, $I = 99$ because the 99-dimensional feature vector is used, and k is $k = 3\,M$-1 from Eq. (15.4) and Eq. (15.5).

In addition, for the time-frequency analysis of earthquake motion, the period-dependent feature vector based on the evolutionary power spectrum (Kameda 1975), which is proportional to displacement response envelope, is defined. The evolutionally power spectrum $G(t,\omega)$ is defined as Eq. (15.7).

$$G(t,\omega) = \frac{2h\omega^3}{\pi}\left\{y^2(t) + \frac{\dot{y}^2(t)}{\omega^2}\right\} \tag{15.7}$$

where h is the damping constant (5%), $y(t)$ is the relative displacement of the single degree of freedom system by acceleration time history $A(t)$, ω is the natural circular frequency.

The period-dependent feature vector is defined from the time history of cumulative power of evolutionary power spectrum normalized to the total power with reference to Husid plot. The time history of period-dependent $P_e(t, \omega)$ can be calculated from Eq. (15.7) based on Fig. 15.2 and Eq. (15.1).

$$P_{\mathrm{e}}(t, \omega) = \frac{100 \int_0^t G(\tau, \omega)\, d\tau}{\int_0^{t_{\mathrm{end}}} G(\tau, \omega)\, d\tau} \tag{15.8}$$

The period-dependent feature vector $\mathbf{t_e} = \{t_{\omega j}\}$ is defined from the percentile values $t_{\omega j}\,(j = 1, \ldots, 99)$ discretized in every 1% steps of $P_e(t, \omega)$. The natural period T is calculated $N = 101$ components by Eq. (15.9).

$$T_i = 0.1 \times 10^{\left(\frac{2}{100}\right)(i-1)} \quad (i = 1, \ldots, 101) \tag{15.9}$$

15.3 Application to Earthquake Motion and Consideration

15.3.1 Consideration of Feature Vector and Gaussian Mixture Model

For numerical example, the acceleration records observed from the 2011 Off the Pacific Coast of Tohoku Earthquake were applied the 99-dimensional feature vector. Figure 15.3 shows the acceleration time histories observed at three K-NET stations (National Research Institute for Earth Science and Disaster Resilience 2021a) which are the observation network operated by National Research Institute for Earth Science and Disaster Resilience, and the envelope calculated by Gaussian mixture model. In Fig. 15.3, the envelope calculated by Gaussian mixture model is the approximate result with the optimal number of element models calculated from Eq. (15.6). In these acceleration records, AKT008 is the long duration motion and the standard shape of acceleration envelope. CHB003 has the single peak with sharp amplitude, and MYG004 has two peaks with large amplitude. As compared to the acceleration time history and shape of envelopes calculated by proposed method, the shape of envelope of AKT008 and CHB003 are similar to the earthquake motion. The shape of envelope at MYG004 have significant emphasis on the peak of amplitude, but the shape of envelope is sufficiently approximated.

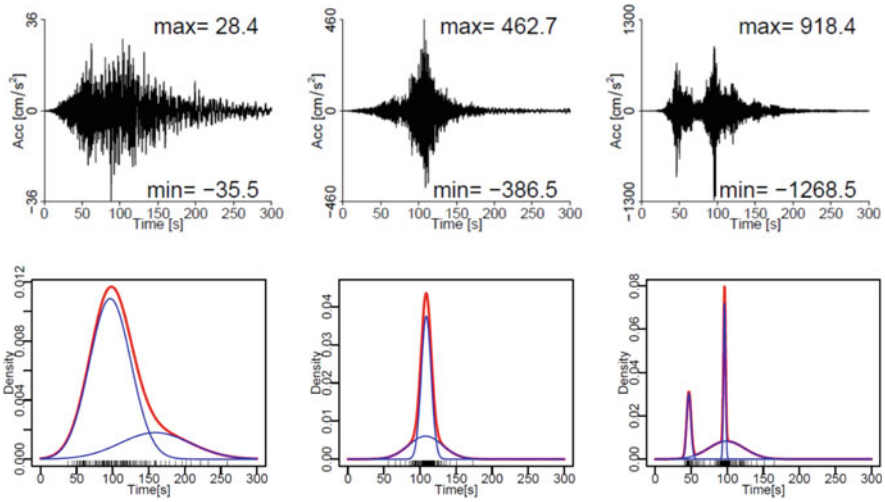

Fig. 15.3 Comparison of acceleration time history and the envelope calculated by Gaussian mixture model (Kuse and Nojima 2021, The red line is the envelope by Gaussian mixture model. The Blue line is the element model. The black line at the bottom is time distribution of the 99-dimensional feature vector.) (**a**) AKT008 (**b**) CHB003 (**c**) MYG004

15.3.2 Consideration of Period-Dependent Feature Vector and Gaussian Mixture Model

The period-dependent feature vector is applied to the earthquake motions observed from the Tokaido-oki earthquake that occurred at 23:57 on September 5, 2004. In this study, the earthquake motion observed in around the Nobi Plain are used. Figure 15.4 shows the location of the observation stations. The earthquake motion records were obtained at K-NET and KiK-net stations (National Research Institute for Earth Science and Disaster Resilience 2021a). Figure 15.5 shows the observed earthquake motion converted into three-dimensional components (radial, transverse and vertical). These earthquake motions have relatively long period characteristics. Figure 15.6 shows the dispersion curve of surface wave calculated using the deep ground model released by Japan Seismic Hazard Information Station(J-SHIS) (National Research Institute for Earth Science and Disaster Resilience 2021b). Figure 15.6 is used in the discussion of surface wave described later in 15.3.3. These three stations shown in Fig. 15.6 are in the Noubi Plain composed of thick sedimentary layers.

Figures 15.7, 15.8, and 15.9 show the evolutionally power spectrum, the period-dependent feature vector, and the envelope applied the Gaussian mixtre model, respectively, for AIC001. The blue and red horizontal lines in Figs. 15.8 and 15.9 are minimum value of group velocity for Love wave and Rayleigh wave. The blue

Fig. 15.4 Location of observation stations around the Noubi Plain

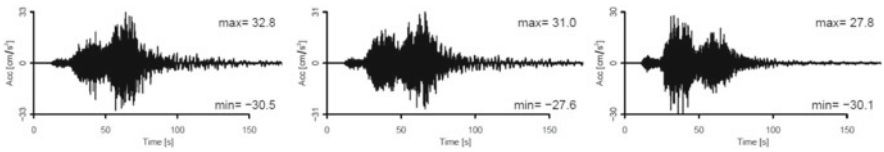

(a) (b) (c)

Fig. 15.5 Comparison of acceleration time history (Kuse and Nojima 2021). (**a**) Radial (**b**) Transverse (**c**) UD

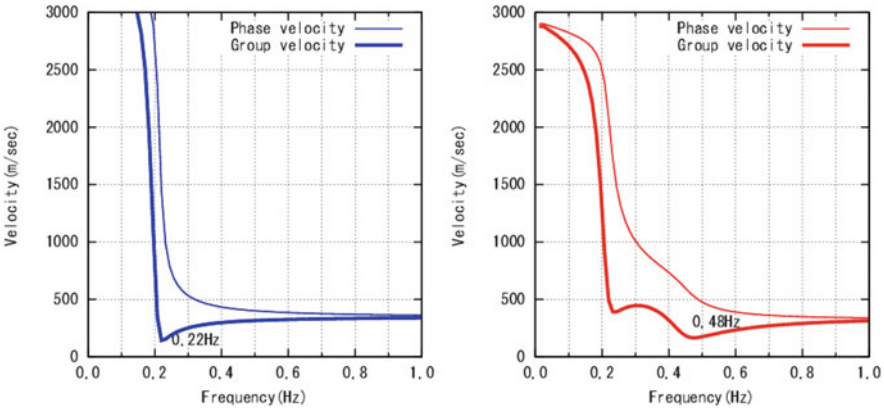

Fig. 15.6 Comparison of dispersion curve of surface wave. (**a**) Love wave (**b**) Rayleigh wave

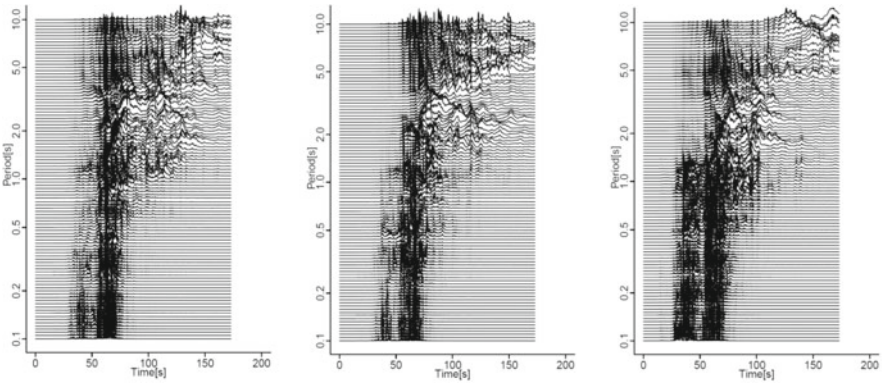

Fig. 15.7 Comparison of evolutionally power spectrum at AIC001 (Kuse and Nojima 2021). (**a**) Radial (**b**) Transverse (**c**) UD

and red curves on Fig. 15.8 are group delay time about Love wave and Rayleigh wave calculated using the group velocity in Fig. 15.6. The group delay time in Fig. 15.8 does not take account of the propagation of earthquake motions from epicenter to observation station. The group delay time calculated using the Fig. 15.6 assumes that the earthquake motion propagated in the Noubi Plain, and the propagation distance in the Noubi Plain is assumed as 10 km, 20 km and 30 km.

In Fig. 15.7, the large amplitude around 30 s to 50 s that seems to be the primary wave is shown in the band of period shorter than about 0.5 s of radial and transverse components, and about 1.2 s in UD component. The large amplitude that appears around 50 s to 80 s at all periods in each component of Fig. 15.7 is principal motion as compared with the acceleration time histories in Fig. 15.5. In addition, the

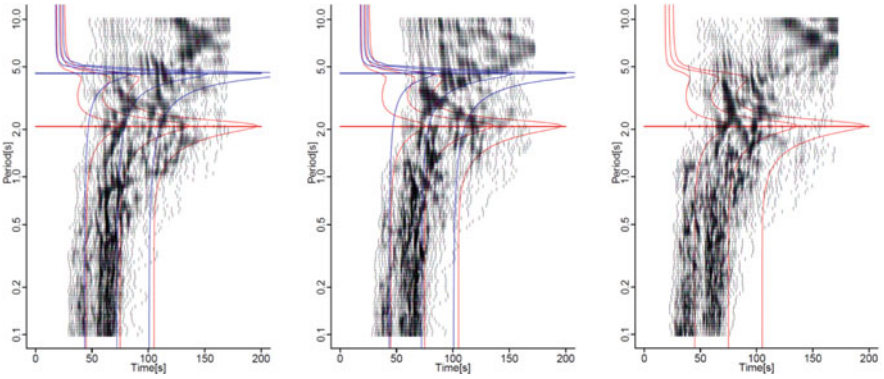

Fig. 15.8 Comparison of the period-dependent feature vector at AIC001 (Kuse and Nojima 2021). (**a**) Radial (**b**) Transverse (**c**) UD

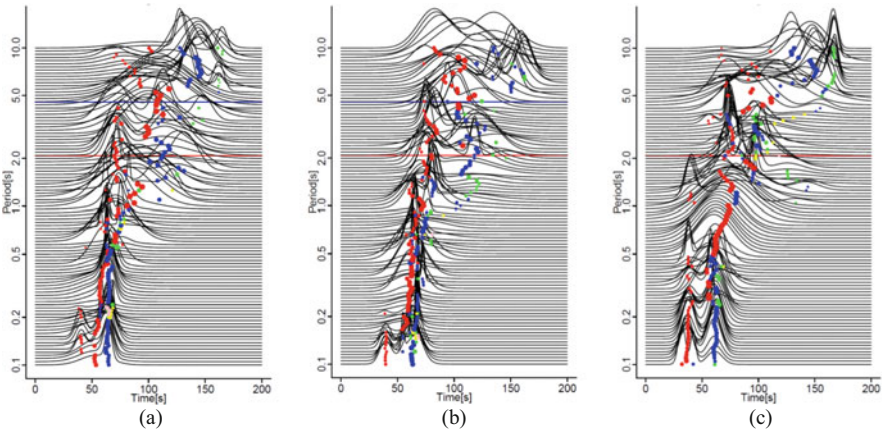

Fig. 15.9 Comparison of the envelope applied the Gaussian mixture model at AIC001 (Kuse and Nojima 2021). (**a**) Radial (**b**) Transverse (**c**) UD

amplitude which is considered to be the surface wave is confirmed in the long period band.

The period-dependent feature vector shown in Fig. 15.8 is calculated from the time history of cumulative power of evolutionary power spectrum normalized to the total power with reference to Husid plot. As previously explained, The period-dependent feature vector is defined by the time of every 1% steps of $P_e(t, \omega)$. Therefore, the time when the feature vector is concentrated corresponds to the time of the large amplitude of the evolutionally power spectrum.

Figure 15.9 shows the approximate envelopes from the Gaussian mixture model calculated with the optimal number of element models. In this figure, the points are the mean of the element model μ_m, and the size of points are the mixture fraction of

the element model π_m. As shown Fig. 15.9, the shape of envelopes calculated by Gaussian mixture model are similar to those by the original evolutionally power spectrum. In Fig. 15.9, the points around 40 s that seen in the short period is considered to be the primary wave. The points around 60 s that seen in the band of period shorter than about 1 s are considered to be principal motion. In the long period range, the μ_m are longer than the 60 s due to the surface wave.

15.3.3 Examination of the Dispersibility of Surface Wave

Next, the proposed period-dependent feature vector was applied to examination of the dispersibility of surface wave. Kamiyama (1979) showed that the dispersibility of surface wave can explain by use of the nonstationary spectrum. Sato et al. (1996) compared the theoretical group delay time of Love wave, and the nonstationary spectrum. Sato et al. showed long-period earthquake motion with dispersibility can be simulated by using the average and standard deviation of group delay time. Sugito et al. (1984) focused on the dispersibility of surface wave, and proposed the method to detect the surface wave using by the evolutionary power spectrum. Figure 15.10 shows the example of evolutionary power spectra. As shown Fig. 15.10a, in the earthquake motion containg surface wave, the peak of amplitude around long period appears later than principal motion. On the contrary, Fig. 15.10b shows the example

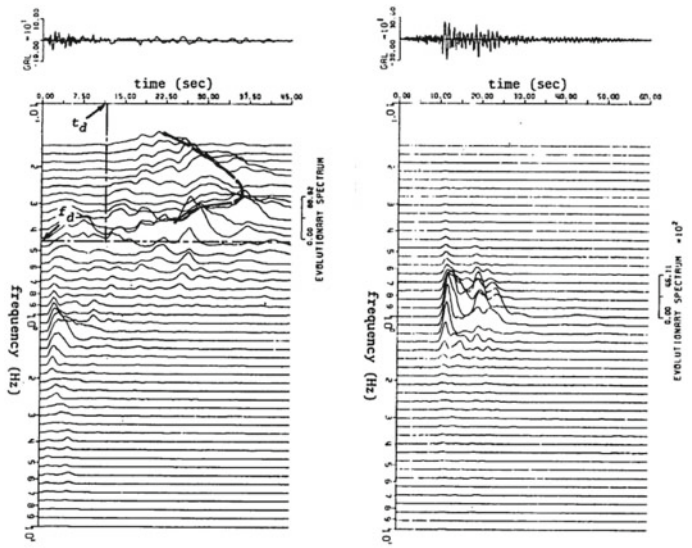

(a) (b)

Fig. 15.10 Example evolutionary power spectra (Sugito et al. 1984) (Radial component). (**a**) Izu-Oshima Kinkai Earthquake (1978) (**b**) Miyagiken-oki Earthquake (1978). Shimizumiho site. Shiogama kojyo site

for the earthquake motion that contains no surface wave component, in which the peak of amplitude around long period does not appear.

Figure 15.7 is considered to contain surface wave from the discussion in Sect. 15.3.2. In Fig. 15.7 showing the radial component, the dispersibility characteristics of surface wave is seen at around 80 s of period 3 s. In the same way, the dispersibility characteristics are seen at around 80 s of period 3.5 s in transverse components, and around 80 s of period 3 s, around 100 s of period 4 s in UD components. In the period-dependent feature vector shown in Fig. 15.8, the dispersibility characteristics of surface wave appears the triangle-shaped distribution that the feature vector is dense. Comparing Figs. 15.7 and 15.8, the triangle-shaped distribution is seen at the time and period when the dispersibility characteristics of surface wave. The Rayleigh wave is contained in the radial and UD components, and the Love wave is contained in the transverse component. Figure 15.6 showed the dispersion curve of surface wave, and Fig. 15.8 showed the group delay time. In Figs. 15.7 and 15.8, the dispersibility of surface wave was found, but the component of surface wave is unclear whether Rayleigh wave or Love wave that compared with Figs. 15.6, 15.7, and 15.8. Figure 15.9 shows the envelope from Gaussian mixture model and the element model μ_m. In Fig. 15.9, the dispersibility characteristics of surface wave are seen in the Transverse component, but The Radial and UD component cannot be seen.

15.4 Conclusion

In this chapter, the feature quantity that can explain the engineering characteristics included in the earthquake motion was proposed. The major results derived in this study can be summarized as follows.

1. The 99-dimensional feature vector representing the temporal characteristics of a strong motion on the basis of Husid plot was proposed. The amount of data for proposed feature quantity is far less than that for earthquake time history.
2. The Gaussian mixture model was applied to the 99-dimensional feature vector. As numerical example, the acceleration records observed in the 2011 Off the Pacific Coast of Tohoku Earthquake were used. The shape of envelopes calculated by proposed method were similar to those by the original earthquake motion.
3. For the time-frequency analysis of earthquake motion, the period-dependent feature vector based on the evolutionary power spectrum, which is proportional to displacement response envelope, was defined. The period-dependent feature vector was calculated from the time history of cumulative power of evolutionary power spectrum normalized to the total power with reference to Husid plot. Furthermore, the Gaussian mixture model was applied to the period-dependent feature vector.

4. As the case study of the earthquake motion analysis, the proposed period-dependent feature vector was applied to examination of the dispersibility of surface wave. The feature vector, the Gaussian mixture model and the dispersion curve calculated from the soil profiles were compared. As a result of comparison of these parameters, the dispersibility of surface wave observed in the evolutionally power spectrum was confirmed.

References

Ishii T (2012) Response duration time spectra of earthquake ground motions. J Struct Constr Eng AIJ 77(676):843–850. (in Japanese)

Iyama J, Kawamura H (1998) Time-frequency analysis of earthquake ground motions by wavelet transform. J Struct Constr Eng AIJ 514:59–64. (in Japanese)

Kameda H (1975) On a method of computing evolutionary power spectra of strong motion seismograms. Proceedings of the Japan Society of Civil Engineers 235:55–62. (in Japanese)

Kamiyama M (1979) Nonstationary characteristics and wave interpretation of strong earthquake ground motions. Proceedings of the Japan Society of Civil Engineers, No 284:35–48. (in Japanese)

Kuse M, Nojima N, Takashima T (2017) Application of the self-organizing maps for duration characteristics of earthquake motion. J Jpn Soc Civil Eng, Ser. A1, 73 (4), I_558-I_567. (in Japanese)

Kuse M, Nojima N (2021) Analysis of earthquake motion and surface motion using the Gaussian Mixture Model, Proc. of the 17th World Conference on Earthquake Engineering, ID: 1d-0099 (On-line)

Miyamoto T, Honda R (2009) Similarity estimation of seismic waves from the viewpoint of the effects on structural systems based on nonlinear structural response as feature indices. JSCE J Earthquake Eng 30:88–96. (in Japanese)

National Research Institute for Earth Science and Disaster Resilience (2021a) Strong-motion Seismograph Networks (K-NET, KiK-net). http://www.kyoshin.bosai.go.jp/. Accessed December 10th, 2021

National Research Institute for Earth Science and Disaster Resilience (2021b) Japan Seismic Hazard Information Station (J-SHIS). http://www.j-shis.bosai.go.jp/map/?lang=en. Accessed December 10th, 2021

Nojima N (2014) Conditional prediction equations for duration of specified intensity levels under given predicted or observed JMA seismic intensity. J Jpn Assoc Earthquake Eng 14(5):50–67. (in Japanese)

Nojima N, Kuse M, Takashima T (2017) Feature extraction and classification of temporal characteristics of earthquake motions. J Jpn Assoc Earthquake Eng 17(2):2_128–2_141. (in Japanese)

Sato T, Sato T, Uetake T, Sugawara Y (1996) A fundamental study for envelope characteristics of long period strong motions by using group delay time. J Struct Constr Eng, AIJ 480:57–65. (in Japanese)

Sugito M, Goto H, Aikawa F (1984) Simplified separation technique of body and surface waves in strong motion accelerograms. Proc of JSCE Structural Eng/Earthquake Eng 1(2):71–76

Chapter 16
Involving the Community to Manage Natural Disasters: A Study of Japanese Disaster Risk Reduction Practices

Maki Koyama

Abstract Effective implementation of disaster risk reduction requires the initiative and participation of local residents. This chapter describes how to build and implement a local disaster prevention system that enables residents to proactively participate in disaster prevention, based on a Japanese case study. Specifically, the section discusses the development of disaster prevention information for local residents, institutions, human resource development, and networking to mitigate damage caused by natural disasters. The need for effective dissemination and communication of information is also examined. Disaster prevention information for local residents includes disaster prevention weather information, evacuation information, and hazard maps using Web-GIS. Efforts taken to develop human resources and networks at community levels are also presented in this chapter. Although this chapter focuses on Japan, the basic ideas or strategies could be applicable to other countries as well.

Keywords Local community · Networking · Human development · Collaboration · Information utilization

16.1 Introduction

Responses to natural disasters often have three levels. The first level comprises all responses from the national and local government, the second is the community aid provided by people living in the area, and the third is self-help by individuals (Cabinet Office, Government of Japan 2021). Among the three levels, the most important and effective response is self-help, where individuals take precautions to protect their lives from immediate disasters. For example, during an earthquake, individuals should attempt to stay in earthquake-resistant buildings, secure furniture to increase interior safety, and stockpile enough food for 3 to 7 days after the

M. Koyama (✉)
River Basin Research Center, Gifu University, Gifu, Japan
e-mail: maki_k@gifu-u.ac.jp

F. Li et al. (eds.), *River Basin Environment: Evaluation, Management and Conservation*, https://doi.org/10.1007/978-981-19-4070-5_16

disaster. Similarly, individuals living in areas that are prone to flooding or landslides must be prepared to evacuate while it is safe to do so during heavy rains.

In a super-aged society like Japan, not everyone can financially afford to live in earthquake-resistant buildings, and those who live alone or have reduced physical and mental functions, may have difficulty securing furniture by themselves. The number of people who are unable to evacuate without the help of others is also increasing, especially in rural areas.

Furthermore, most of the land area of Japan is classified as natural disaster hazard areas, which makes it difficult to uniformly restrict residences in hazard areas. The effective countermeasure for those who already live in a hazardous area is relocation or evacuation. However, it is difficult for public institutions to enforce them under Japanese law, as these measures are related to private property or basic human rights.

Disaster management problems, that are difficult to solve by either self-help or public assistance, can often be resolved through the mutual help of neighborhood residents, concerned parties, and civic groups. This chapter describes the impact of mutual help and collaboration in times of disaster. It also discusses the role of information in establishing community aid services.

16.2 Evacuation from Flood and Landslide

One of the most anticipated mutual help activities is reaching out to neighbors during an evacuation and providing support to those who need assistance during an evacuation (Sakamoto et al. 2021). In order to take appropriate evacuation actions, it is important to check the flood and landslide hazards in the area in advance, and decide whether evacuation actions are necessary and, if so, where they should be taken. In addition, when the risk of flooding or landslides is actually increasing due to heavy rainfall, it is important to start evacuation activities at the appropriate time, referring to disaster prevention weather information. This section describes examples of the use of hazard maps and disaster prevention weather information, as well as examples of local initiatives.

16.2.1 Creating an Evacuation Plan

To ensure safe evacuation, it is important to prepare an evacuation plan during normal times when there are no disasters, confirm its effectiveness through drills, and continuously revise it. Due to climate change, floods and landslides caused by heavy rain have been increasing in recent years. Intense rainfall is characterized by a short grace period between the perception of danger and the occurrence of a disaster, as it rapidly increases the risk of disaster in a short period. This means that it is difficult to evacuate safely if one begins to consider evacuation only after sensing danger.

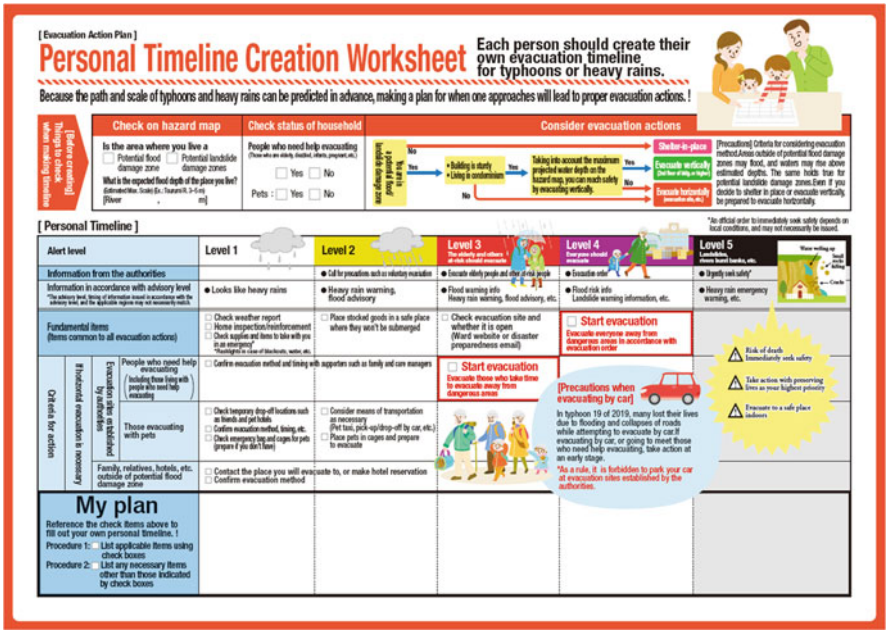

Fig. 16.1 Example of Evacuation Plan Worksheet (Yokohama City, Kanagawa Prefecture, Japan 2021)

A well-designed evacuation plan at the individual and community level should include information on the flood and sediment hazards of the area, the location to be evacuated, the means of transportation, what to take with you when evacuating, and what to do when and if the risk of a disaster increases. Figure 16.1 shows an example worksheet for evacuation planning. In this figure, the stages of disaster risk are shown using national and local government disaster prevention weather information and evacuation information. It is reasonable to use such a sheet for those who have never thought about such a plan, as it is difficult to create one's own evacuation plan without a guide. In Japan, efforts are underway to develop individual evacuation plans at local community-based workshops (Water and Disaster Management Bureau, Ministry of Land, Infrastructure, Transport, and Tourism 2021). Such workshops provide a good opportunity to identify mutual support needs and establish an evacuation plan that is relevant to the community. When considering evacuation plans for a community, it is necessary to consider ways to provide information that residents can use to evaluate the degree of risk during a disaster and act accordingly. The next section describes the available disaster prevention information that can be used by residents.

16.2.2 Use of Hazard Map

Hazard maps, prepared in advance, can help residents check the risk of flood and landslide disasters. In Japan, maps of the expected inundation areas of all large rivers managed by the national government are currently available (Fig. 16.2), and it has been decided that maps of small and medium-sized rivers managed by prefectural governments will also be made available in due course (Ministry of Land, Infrastructure, Transport, and Tourism 2021b). It would be very useful if hazard maps of small- and medium-sized rivers were made public, because the risk of flooding of small and medium-sized rivers increases in steep terrains such as that of Japan during sudden heavy rainfall. Hazard maps at appropriate levels must be developed for each country and region.

Hazard maps can be broadly classified into two types, based on their utilization. One is image-based, such as those published on paper or as pdf files, and the other is web-GIS-based, which allows users to overlay many pieces of information based on location information. Figure 16.2 shows an example of a web-GIS hazard map. This hazard map allows you to check the estimated inundation depth and landslide hazard level by clicking on the location you wish to check. To consider an evacuation plan for each individual, such Web-GIS-based hazard maps are very easy to use.

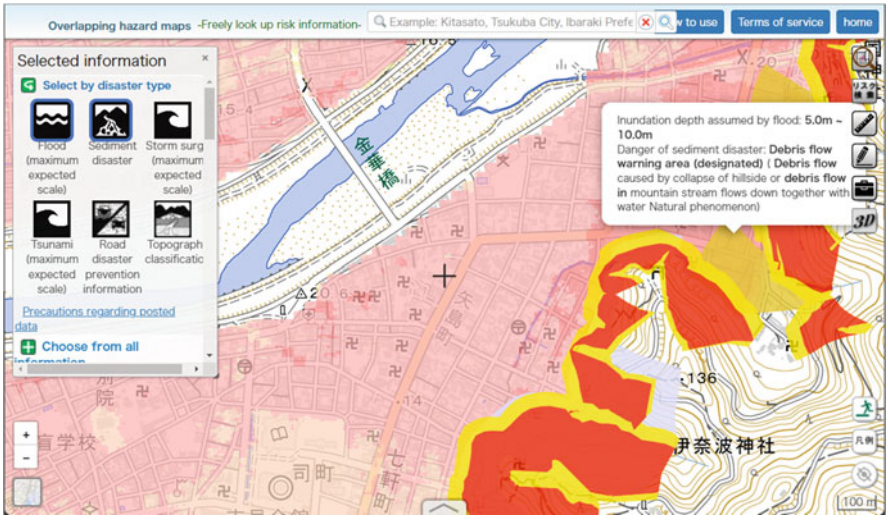

Fig. 16.2 An example of a Web-GIS Hazard Map (Ministry of Land, Infrastructure, Transport, and Tourism 2021a). The original site is only in Japanese, and the screenshots are from Google Translation

16.2.3 Use of Disaster Prevention Weather Information

In order to determine the timing of evacuation for individuals who need to evacuate, it is necessary to comprehensively consider the extent of the current flood or landslide hazard, what means of transportation are available for evacuation, and how much time is needed for evacuation preparation and travel. Among these, the means of transportation available for evacuation and the time required for evacuation should be considered according to the circumstances of each evacuee. However, residents who do not have the expertise to evaluate the risk of flood or landslide disasters may have difficulties with timing their evacuation. Therefore, the national government, local governments, or specialized organizations should provide information on disaster risks.

For example, the Japan Meteorological Agency (JMA) publishes risk maps of precipitation nowcasts, river flooding, inland flooding, and landslide disasters (Fig. 16.3). Precipitation nowcasts provide information on the current and future movement of rain clouds. River flooding, inland water flooding, and landslide disaster risk maps provide information on the risk of occurrence at a given time. These disaster occurrence risks are determined based on the forecast of the occurrence of each disaster. This information can be used to estimate the approximate time before the threat of a disaster reaches a critical level.

The JMA also provides Weather Warnings/Advisories, Tropical Cyclone Information, Hazardous Wind Watch, Heavy Rain Information, Heat Stroke Alert,

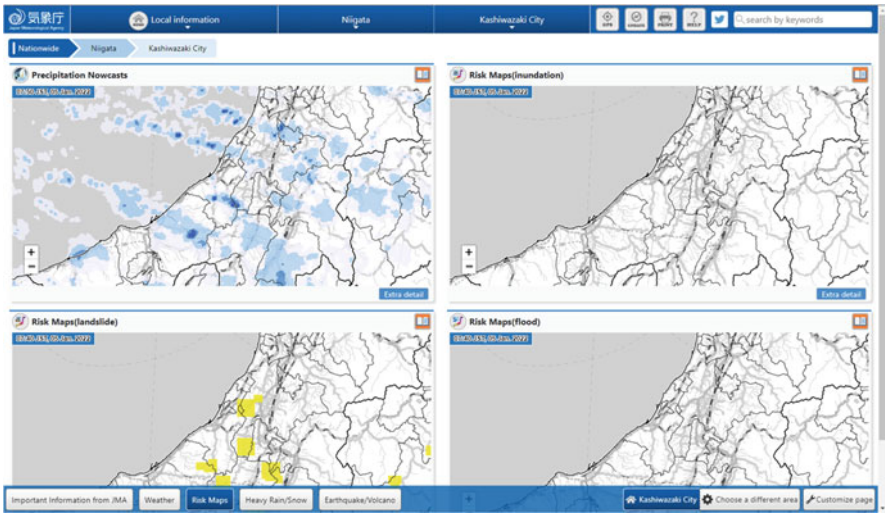

Fig. 16.3 An example of Risk Maps by JMA. From the upper left to the Z direction, precipitation nowcasts, river flooding, inland flooding, and landslide disasters are shown. On the risk map, the degree of danger is expressed in yellow, red, light purple, and dark purple, in that order. Dark purple indicates a level of risk that a disaster has already occurred. However, only some of the colors are shown in the figure due to the lack of screen captures during the heavy rainfall

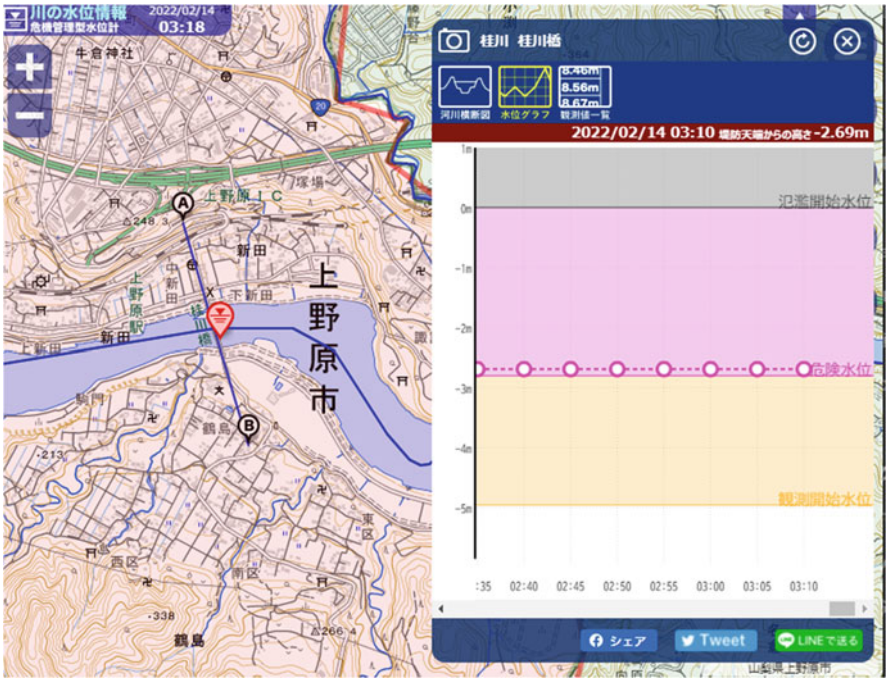

Fig. 16.4 River level information (Ministry of Land, Infrastructure, Transport, and Tourism 2021c). Real-time water levels can be checked at each water level gauge

Precipitation Nowcasts, Precipitation Analysis/Forecasts, Snow Analysis/Forecasts, Tsunami Warnings/Advisories, Earthquake Information, Volcanic Warnings, Volcanic Ash Fall Forecasts, and other disaster prevention information. In addition, the Ministry of Land, Infrastructure, Transport and Tourism has a website (https://k.river.go.jp/) where information on water level gauges installed in rivers can be viewed (Fig. 16.4), and river levels can be checked in real time. These maps can be used to know the current and projected values of flood and sediment hazard risk.

Easy access to all this information can enable residents to customize their evacuation strategies according to their circumstances. For example, a person who has a safe place to evacuate to in the neighborhood and is able to evacuate quickly on their own may perform the evacuation action after the danger is imminent. In contrast, for those who need assistance from others, the time required for evacuation is longer, and thus an earlier evacuation is required. In addition, during periods of infectious disease outbreaks, such as the COVID-19 pandemic, it is necessary to take measures such as dispersing evacuation sites to relieve congestion at evacuation sites and moving the treatment sites for positive cases out of the disaster hazard area.

16.3 Collaboration of Local Residents

As mentioned at the beginning of this chapter, effective measures for damage mitigation include long-term measures (taken by the national and local governments) and short-term measures (taken by individuals or in collaboration with local residents).

16.3.1 Community Disaster Management Plan

In Japan, the community disaster management planning system is a mechanism to encourage community-level collaboration on disaster prevention measures (Cabinet office, Government of Japan 2021). This is a system whereby residents of a local community work together to create a disaster management plan for their community, which is then submitted to a municipal disaster prevention meeting and, if approved, becomes part of the municipal disaster prevention plan. The program went into effect in 2014, and as of April 1, 2020, 4170 districts have worked to develop local disaster management plans and 901 districts have been approved as part of their municipal disaster management plan (Cabinet office, Government of Japan 2021). While there are communities that are prepared to take necessary measures even without a system, the existence of a system facilitates such efforts in some ways. Under this system, a prepared community disaster management plan can be proposed to the municipal disaster prevention council. If the disaster management council approves the plan, the proposed community disaster management plan is recognized as part of the municipal disaster prevention plan. This recognition as part of an official plan is expected to reduce the number of residents who refuse to cooperate.

The community disaster management planning system is a highly flexible system that allows the type of disaster to be handled, the content of countermeasures, and the community unit to be freely set up according to the circumstances of each region. As shown in Fig. 16.5, the published disaster prevention plans differ from region to region in terms of the types of disasters they handle, indicating that plans are prepared according to the characteristics of each region. The following table shows the results of the survey.

It is common to collaborate with local residents in units of communities that are already active in the respective areas. In Japan, community activities are often conducted by neighborhood associations. Therefore, collaboration among local residents regarding disaster management is often conducted by these associations. However, in an increasing number of urban areas, there is a rapid turnover of people, and relationships between neighbors are becoming weaker. Neighborhood associations have been dissolved or are no longer functioning. In these cases, it is necessary to work on a community basis, such as through the management association of a condominium, in accordance with the local community.

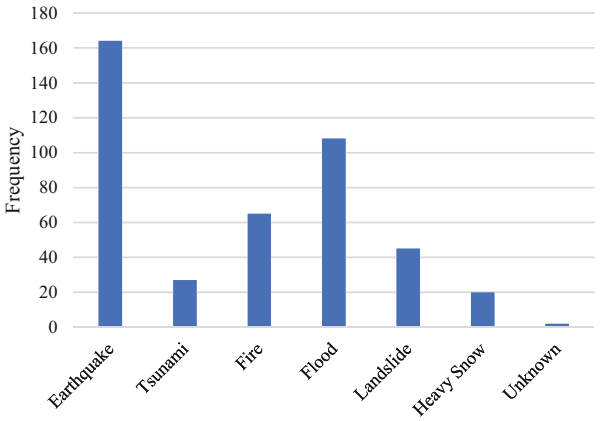

Fig. 16.5 Disaster types listed in published community disaster management plans

16.3.2 Impact of Declining Birthrate and Aging Population

Japan has one of the lowest birth rates and one of the most aged populations worldwide, with an aging rate of 29.1% in 2021. Changes in the demographic composition of communities due to declining birth rates and an aging population significantly impact collaboration among local residents in the field of disaster management. For example, when providing support for evacuation within a community, it is not so difficult to provide support if more people in the community can provide evacuation support than those who cannot evacuate on their own. Conversely, if many people need evacuation assistance and few people can provide assistance, it becomes difficult to provide support within the community.

As mentioned above, local communities in Japan are mainly composed of neighborhood associations. Figure 16.6 shows an estimate of neighborhood associations in Gifu Prefecture, where the need for evacuation support per person was less than four persons during each flood and landslide disaster. As the polygon data for the neighborhood associations is not publicly available, the tabulation was based on the census basic unit blocks. The basic unit blocks (hereafter referred to as BUB) in the Japanese census are generally set in the smallest units of residential blocks, and are the closest to the area of the neighborhood association in the publicly available residential block data. The total BUB in Gifu Prefecture is 7619. In this figure, the census and future population estimates are used to show the number of regions from 2015 to 2065. As the birthrate declines and the population ages, the number of communities with fewer than four supporters per person in need of assistance will increase each year. Thus, the areas where supporters are in short supply will rise from 45% of all BUBs in 2015 to 66% in 2065 in flood hazard areas, and from 13% to 20% in landslide hazard areas.

As discussed so far, collaboration among local residents is effective in mitigating disaster damage, but the declining birthrate and aging population have reduced the number of residents who can work for damage mitigation, making collaboration among residents difficult in some areas. In this case, it is necessary to consider

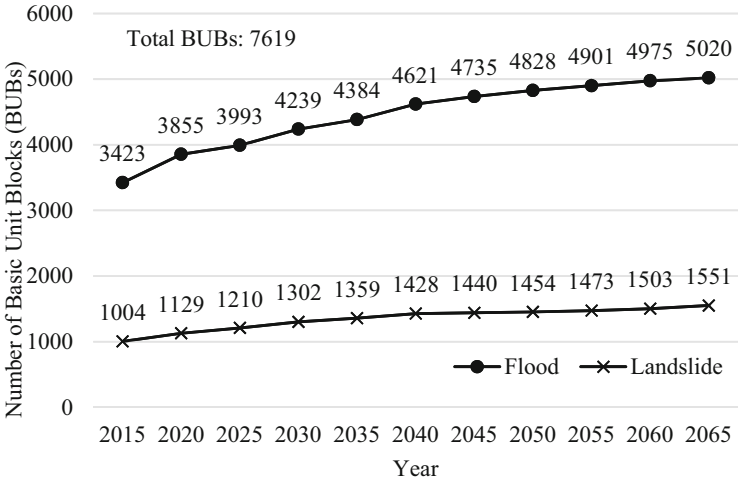

Fig. 16.6 Change in the number of BUBs with four or fewer supporters for each person vulnerable to exposure from 2020 to 2065 in Gifu prefecture (estimation by the author)

measures tailored to the circumstances of each individual and region, such as interregional cooperation and cooperation between welfare offices and neighboring companies.

16.3.3 Human Resource Development for Disaster Risk Reduction for Local Residents

As discussed above, disaster prevention measures taken by residents themselves can effectively reduce the damage caused by disasters. However, many local residents lack the knowledge of disaster information and countermeasures, the skills to develop countermeasures, and the skills to collaborate with various sectors, as described in this chapter. Therefore, it is necessary to develop leaders who can lead disaster prevention activities in their communities. This section describes the human resource development for disaster prevention for the general public in a local community.

16.3.3.1 Skills Required for those Who Take the Initiative in Disaster Reduction Activities in the Community

There is no general definition of the skills required for proactive disaster management in local communities. For example, the members and staff involved in local disaster prevention human resource development at the "Gifu Disaster Mitigation

Table 16.1 Meta-rubric for human resources for regional disaster risk reduction

	Level 1	Level 2	Level 3
	Good followers	People who can do it if shown how	People who can develop their own methods
Knowledge and basic activities	People who have knowledge of disaster prevention and can act independently.	People with basic skills in disaster prevention and mitigation activities.	People with applied skills in disaster prevention and mitigation activities.
Educational skills	People who can pass on the knowledge of disaster reduction.	People who can develop human resources to work on disaster reduction activities.	People who can develop programs for leadership in disaster mitigation.
Networking skills	People who can build face-to-face relationships.	People who can connect related organizations and people and people to people.	People who can work in collaboration with related organizations and people.
Planning and practice	People who can do it if they are shown how.	People who can do without being shown how.	People who can plan, formulate, and implement disaster prevention and mitigation measures from normal times to disaster times.

Center" have organized a list of skills that disaster prevention personnel living in the community need to acquire. The Gifu Disaster Mitigation Center was established by Gifu Prefecture and Gifu University to develop local disaster prevention human resources and promote local disaster prevention measures (https://gfbosai.jp/). Membersand staff include university faculty, Gifu Prefecture officials, and local residents.

Table 16.1 summarizes the skills of the general population living in a community that promotes disaster reduction activities in the form of a rubric used in the field of education. It was developed by the faculty, coordinators, and staff of the Gifu Disaster Mitigation Center, who are responsible for training local human resources. This rubric is not intended to specifically assess the level of skills possessed, but rather to provide a conceptual representation of the skill requirements of local disaster management personnel. Such a conceptual representation of the overall program skills is called a "meta-rubric."

16.3.3.2 Human Resource Development Programs for Disaster Reduction at the Basic Level

Level 1 of the meta-rubric shown in Table 16.1 represents human resources or people who have a basic level of disaster preparedness skills. People at this level lack the skills to act as leaders on their own, but have enough knowledge and skills to support the leader as a "good follower." In Japan, many local governments are implementing human resource development programs at this level (Koseki et al.

Table 16.2 Sample Curriculum for a Basic Level Human Resource Development Program

Period	Lecture Style	Day1	Day2	Day3	Day4
1	Seated lecture	Activities expected of disaster reduction leaders	Impact of disasters caused by earthquake and tsunami	Disaster relief and emergency response by the government	Mental health care during disasters
2		Introduction to meteorological disasters, wind, and flood damage	Ways to secure lifeline and available information about transportation and other facilities	Recovery and reconstruction and support for disaster victims	Disaster volunteer activities
3		Accessing disaster-related information and forecasts and warnings	Business continuity for companies and organizations	Measures for people who need assistance during disasters	Disaster prevention activities during normal times
4	Workshop	Damage estimates, hazard maps and evacuation information	Disaster awareness activities for community use	Local disaster prevention and consideration of diversity	Application of the course information for community disaster prevention
5					
6					

2020). The most of these courses are free of charge. The target audience for the program is the general population. The program to develop human resources for disaster reduction at the basic level provides basic knowledge of disaster mechanisms and disaster prevention measures through classroom lectures and emphasizes the importance of collaboration through group work. Table 16.2 shows an example of the curriculum for a basic-level human resource development program for disaster prevention at the Gifu Disaster Mitigation Center. Individuals can take these basic-level courses and improve their skills by supporting those who are already engaged in disaster reduction activities in their community and by participating in actual disaster reduction activities.

16.3.3.3 Intermediate Level Disaster Management Human Resource Development Program

Level 2 of the meta-rubric (Table 16.1) can be considered the intermediate level of disaster preparedness skills. Although people at this level are unable to plan and develop a program on their own, they are able to act independently based on scenarios and methods given to them. These skills can be acquired through classroom lectures, virtual training, and interactive learning activities.

The Gifu Disaster Mitigation Center runs a program called “Gensai Mirai Juku” to develop human resources at this level. Here, Gensai means disaster mitigation, Mirai means the future, and Juku means a private-tutoring school. The Gensai Mirai Juku is a one-year program in which participants acquire intermediate-level skills through the practice of disaster prevention activities (Koyama et al. 2017). Instruction is provided on an individualized basis by supervisors. Supervisors are university faculty members in the field of community disaster prevention and people who have Level 3 skills listed in the meta-rubric (Table 16.1) and are actively engaged in prevention activities in the community. The individualized instruction method makes it impossible to train a large number of trainees at one time. The current system (8 supervisors) trains 3 to 10 trainees per year. Forty-four students have graduated from the program since its inception in 2016 through 2021.

The Gensai Mirai Juku program consists of the following three sub-programs.

1. Practice of disaster prevention activities
   Students take the initiative to practice disaster prevention activities on their own. The content of the disaster prevention activities is planned by the students themselves, but their supervisors will provide advice when needed. Activities to disseminate disaster prevention knowledge to local residents and the development and implementation of disaster prevention training programs, are examples of disaster prevention activities.
2. On-the-job training (OJT)
   The participants acquire skills through practice by working as support staff for the basic level disaster management human resource development program (Sect. 16.3.3.2), in disaster management training programs where their supervisors serve as instructors, and in community disaster management activities in which their supervisors are involved. Involvement in a large number of actual disaster management activities enables participants to build their own network of resources.
3. Presentation, communication, and facilitation lectures
   Presentation and communication skills are indispensable for disaster reduction activists. However, many local residents, in general, have no experience with presentations or facilitation. Many people have never had the opportunity to learn about communication skills for collaboration. Therefore, training to develop these skills is essential.

The Gensai Mirai Juku has been in place since 2016, and Fig. 16.7 shows the average skill ratings of participants from 2016 to 2021 at the beginning and end of the program. The numbers in the figure refer to the levels on the rubric in Table 16.1, the dotted line represents the time of admission to the school, and the dark line represents the time of graduation.

Thus, it can be seen that a program with 1 year of practical activities improves the skills of all the participants. Participants who were between levels 1 and 2 (basic level) when they entered the program, progressed to levels between 2 and 3 (intermediate level) when they graduated from the program.

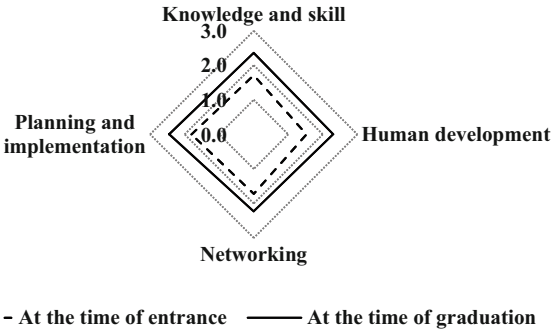

Fig. 16.7 Change in skills between entry and graduation levels

16.3.4 Establishing a Network of People Involved in Disaster Reduction Activities in the Community

Community disaster prevention activities can only be successful when individuals cooperate with the community. However, if we look at community units, there are only a limited number of people who can act as leaders on their own initiative. In such cases, the number of people who can work in complement with the leader may be limited, and this increases the leader's burden. Those who can act as proactive leaders, cooperate, and collaborate with others, and form networks with like-minded people across the region can help solve these problems. Networking with people engaged in disaster reduction activities can reduce the loneliness and burden of leaders and enable them to compensate for each other's shortcomings.

In the Gensai Mirai Juku (Sect. 16.3.3.3), both current and former students participate in OJT, allowing for interactions. Graduates also participate in the interim report meetings of current students and interact with them. In addition, mailing lists and social media, such as Facebook, are also used to promote mutual interaction. Participation in Gensai Mirai Juku provides an opportunity to establish a network between current students and graduates, and encourages mutual cooperation. Examples of mutual cooperation include inviting a person active in another community as a lecturer for a disaster prevention training session for local residents of another community, or organizing study sessions where current and former students learn from each other.

Another network is the network of "Bousaisi," a private qualification offered by the Japan Bousaisi Organization, a non-profit organization involved in disaster prevention. A Bousaisi can be obtained by attending a Level 1 human resources development program (Sect. 16.3.3.2) and passing an examination. This certification was established in 2003, and by the end of February 2022, about 226,120 people had been certified as Bousaisi. The term "Bousai" is Japanese for disaster prevention. The original meaning of the word "si" is one who is capable of handling matters. However, as mentioned above, simply being certified as a Bousaisi does not mean that a person has reached a level where they can handle managing disaster prevention activities by themselves.

However, many Bousaisi have been engaged in community disaster management activities for a long time, and some of them have reached intermediate or advanced levels. The Bousaisi Organization, a national networking organization for Bousaisi, also provides support for community disaster mitigation planning in cooperation with the Japan Society of Community Disaster Management Plan (SCDMP).

16.4 Conclusion

This chapter discussed the need for the development of disaster prevention information systems, human resource development, and networking to mitigate damage caused by natural disasters. For disaster risk reduction, it is important to organically link these efforts and realize an effective cooperative system. As it is difficult for local residents to do this alone, establishing a system of mutual support with a disaster prevention center established at a university or by a non-profit organization, such as the Japan Bousaisi Organization, can be a more effective means to manage disaster prevention activities. Although this is a Japanese case study, the ideas and strategies discussed here could be applicable to other countries as well.

Acknowledgments I would like to thank Editage (www.editage.com) for English language editing.

References

Cabinet office, Government of Japan (2021) Disaster prevention white paper, https://www.bousai.go.jp/kaigirep/hakusho/r03/honbun/1b_1s_01_01.html (in Japanese)

Koseki T, Koyama M, Takagi A, Nojima N, Muraoka H (2020) Design and use of a rubric to assess for basic course of community-based disaster risk reduction. Journal of Social Safety Science 37:269–277. (in Japanese)

Koyama M, Takagi A, Nojima N, Muraoka H (2017) A prototype education program to foster talented people who take actions at their own initiative for regional disaster prevention, 4th Asian conference on urban disaster reduction. Sendai, Japan

Ministry of Land, Infrastructure, Transport and Tourism (2021a) Overlapping hazard map. https://disaportal.gsi.go.jp/maps/

Ministry of Land, Infrastructure, Transport and Tourism (2021b) Press release at 2nd February 2021, https://www.mlit.go.jp/report/press/mizukokudo02_hh_000027.html (in Japanese)

Ministry of Land, Infrastructure, Transport and Tourism (2021c) River level information, https://k.river.go.jp

Sakamoto M, Matta N, Hiroi U, Koyama M (2021) The study on evacuation triggers during heavy rain -based on evacuation behavior survey of 2018 Western Japan heavy rain Disster. Journal of Japan Society for Natural Disaster Science 39(4):439–457. (in Japanese)

Yokohama city (2021) Personal Timeline Creation Worksheet. https://www.city.yokohama.lg.jp/kurashi/bousai-kyukyu-bohan/bousai-saigai/wagaya/timeline.files/0022_20210527.pdf

Water and Disaster Management Bureau, Ministry of Land, Infrastructure, Transport and Tourism (2021) Collection of case studies of My Timeline initiatives in the region. (in Japanese)